

# Advanced Numerical Methods For Polarized Line Formation Theory

A Thesis Submitted to the Mangalore University  
for the Award of the Degree of  
Doctor of Philosophy in Physics



Submitted by

**L. S. Anusha**

Under the Supervision of

**Prof. K. N. Nagendra**

**Indian Institute of Astrophysics**

**Koramangala 2nd Block**

**Bengaluru – 560034**

**India**

**April 2012**



# Declaration

I hereby declare that this thesis, submitted to the Physics Department, Mangalore University, for the award of Ph.D. degree, is a result of the investigations carried out by me at the Indian Institute of Astrophysics, Bengaluru, under the supervision of Professor K. N. Nagendra. The results presented herein have not been subject to scrutiny for the award of a degree, diploma, associateship or fellowship whatsoever, by any other university or institute. Whenever the work described is based on the findings of other investigators, due acknowledgment has been made. Any unintentional omission is regretted.

Prof. K. N. Nagendra  
(Thesis Supervisor)  
Indian Institute of Astrophysics,  
2nd Block, Koramangala,  
Bengaluru 560 034,  
India.

April 2012

L. S. Anusha  
(Ph.D. Candidate)  
Indian Institute of Astrophysics,  
2nd Block, Koramangala,  
Bengaluru 560 034,  
India.

April 2012



– Dedicated to –

my beloved parents Shri. Seetharama Bhasari and Smt. Parvathi Bhasari  
who educated, supported and encouraged to pursue my PhD

– and also to –

my sister Dr. L. S. Deepa, brother Dr. L. S. Sharath Chandra and my  
husband Mr. R. Sandeep



# Acknowledgments

I avail this opportunity to express my deepest gratitude with profound respect towards my beloved and revered preceptor, teacher and guide Prof. K. N. Nagendra, whose masterly suggestions and ablest guidance at every step inspired me and gave me considerable impetus throughout my research career. I would like to impart my indebtedness to him for his fatherly affection and limitless knowledge bestowed on me, which has molded, shaped, and enlightened me to successfully accomplish the work presented here. Worth mentioning is his confidence on me to give unsurpassed freedom to write sophisticated research codes. Through his expertise in specialized research area namely the polarized line formation theory and numerical methods he laid the basis to the advanced research carried out in this thesis. He gave sufficient time for scientific discussions which helped for rapid progress of the work. He also helped me to get associated with many of the eminent researchers like Prof. Hélène Frisch, Prof. Jan Olof Stenflo, Dr. M. Bianda, Dr. F. Paletou, Dr. R. Holzreuter, Dr. R. Ramelli, and Dr. L. Léger who have helped me to gain deeper knowledge in many research areas. I thank him for providing me opportunities to visit the Observatoire de la Côte d'Azur (OCA) at Nice, France, Instituto Ricerche Solari Locarno (IRSOL) at Locarno, Switzerland and Institute of Astronomy, ETH at Zurich, Switzerland, participate in Solar Polarization Workshop (SPW6) held at Hawaii, USA and a summer school on "solar and stellar polarization" held at the Bamboo Sea, China. I cannot express in words the help rendered by him by calling me on telephone or Skype to discuss progress on scientific projects, when I was working in foreign countries for collaboration. From my early student days as an undergraduate student, he motivated me to pursue a career in astrophysics. Although I pursued masters degree in Mathematics I wished to change the field and work in Astrophysics. It was impossible without his support, guidance and encouragement. He was always there to take right decisions at the right time. He stood by me in hard times, encouraged me in sad moments of failure and appreciated in joyous

moments of success. From the time I worked on a summer project with him in 2005, he taught me how to work hard like almost 12 hours a day. He taught me the importance of time, focus and perfection in every single thing we do. Starting from how to write a scientific correspondence, he has taught me how to present a clear talk, how to write a research paper and most importantly, he has taught me how to do independent research. I would like to convey my gratitude to him through the following quotation.

“The dream begins with a teacher who believes in you, who tugs and pushes and leads to next plateau, sometimes poking with a sharp stick called truth – Dan Rather”

I wish to thank Prof. Siraj Hasan, Director, Indian Institute of Astrophysics (IIA) for providing excellent research facilities and constant encouragement during the course of this thesis project. I also thank Prof. H. C. Bhatt, Dean of faculty, IIA, and Prof. S. K. Saha, Chairman, BGS for encouragement and constant support over the years. I would like to thank the BGS secretaries Prof. Annapurni Subramaniam and Prof. R. Ramesh for their help in various official matters during my PhD career. I would like to thank all the lecturers from various Institutes such as IIA, NCRI, IISc., RRI and ISAC who taught me during the course work in the first year of my PhD. Special thanks are due to Prof. C. Sivaram who not only inspired me by his delightful lectures, but also encouraged my research. I am grateful to Prof. Arun Mangalam, Prof. K. E. Rangarajan, Prof. Sunetra Giridhar, Prof. D. C. V. Mallik, Prof. Prasad Subrahmanyam, Prof. Eswar Reddy, Prof. Dipankar Banarjee, Prof. Gopal Krishna, Prof. Chanda Jog, Prof. Ravi Subrahmanyam, Prof. Uday Shankar, and Prof. Seetha from whom I acquired knowledge in several Astrophysical areas. I thank Prof. R. T. Gangadhara for wonderfully guiding me on a course work project on Pulsars and helping me to present the work on this project in the form of a talk. I thank Prof. Usha Devi (Bangalore University), Prof. K. E. Rangarajan (IIA), Prof. Sunetra Giridhar (IIA) and Prof. Annapurni Subramaniam (IIA) who are the members of the Doctoral committee for their kind words and encouragement and for taking care of the progress of my PhD work.

I would to express my sincere thanks to my senior Dr. M. Sampurna, who is presently working as a Chandrasekhar post doctoral fellow at IIA, for her immense help starting from the time of my summer project, during the course work, and all through the PhD career. I am grateful to her for providing moral support and care at hard times and encouragement during the successful moments. She took Physics quiz to me on many Sundays during the course work so that I could learn several aspects of physics. She provided her masters degree notes whenever I needed to learn the concepts in detail. Her guidance to learn the



technique of  $\mathcal{T}_Q^K$ 's (the irreducible tensors for polarimetry) introduced by Egidio Landi Degl'Innocenti is greatly acknowledged as it formed the basis of most of the work presented in this thesis. I thank her for carefully reading the manuscripts of my research papers which form part - II of my thesis and for providing useful comments and suggestions on them. I have learnt many things from her for which my gratitude is inexpressible in words.

I would like to acknowledge my profound gratitude to Prof. Hélène Frisch, for her joint guidance along with Prof. K. N. Nagendra on the work on Hanle turbulence. I thank her also for her collaboration on modeling the spectro-polarimetric data. She organized three short term visits for me at the Observatoire de la Côte d'Azur, Nice, France (during 2008, 2009 and 2010). The discussions during her visit to Bangalore in December 2010 were of great help. Apart from direct discussions, the long scientific correspondences were of immense help. I have learnt from her many techniques such as asymptotic analysis and interpretation of the results, exact theory of solving radiative transfer equations involving integral equation methods. She also introduced me to multi-scale analysis techniques. I would like to place on record the immense help rendered by her through careful reading of the manuscripts of my research papers which form part - II of my thesis and for providing very helpful comments and suggestions on them which greatly helped to improve their presentation. My special thanks to her for her impetus and discussions to prove the symmetry properties of the polarized radiation field in a non-magnetic two-dimensional medium. In fact she provided freedom to complete a publication on part-II of my thesis during my visit to Nice. I thank her for taking me to Paris for four days during my first visit to France in 2008 and providing me an opportunity to visit the beautiful Eiffel tower, La Louvre museum etc. It was wonderful to walk in the streets of Paris for hours and hours. I thank the hospitality by her mother and daughter during my visit to Paris. I would like to thank Prof. Uriel Frisch for interesting discussions on India, Sanskrit and for teaching me several computer commands during my visits to Nice. I thank both Prof. Hélène Frisch and Prof. Uriel Frisch for taking me to sight seeing around of Mediterranean sea coast, a beautiful drive to Monaco to visit a Japanese exhibition and many more. I cherish the moments spent in her home and the interesting discussions. I would like to thank Prof. Thierry Passot, Director, Laboratoire Cassiopee, for extending the research facilities during my visits. I thank the other staff members of OCA - the library staff, and the secretaries for their hospitality and careful handling of the official matters. It needs a special mention and thanks to Dr. Geneviève Amieux who kindly took me on weekends for sight seeing of the beautiful Nice city. I remember the moments spent with her in her classic car (which is nearly 35 years old), for a beautiful drive to Monaco, several views

of the colorful Mediterranean sea, old Nice city, and several other places in and around the Nice city. She introduced me to special vegetarian food of Nice such as special Pizzas, ‘Socca’, pulp of Passion fruit etc. She was kind enough to come and have vegetarian Indian dishes prepared by me at the OCA guest house.

I would like to acknowledge my profound gratitude to Prof. J. O. Stenflo for his joint guidance along with Prof. K. N. Nagendra on the modeling of the spectro-polarimetric data. He, with his wife Joyce, visited Bangalore during December 2009. I was amazed by his deep intuitive knowledge of Physics, astrophysics and of the various fields of research he has mastered. He kindly visited IRSOL, Locarno, Switzerland during my visits there, to discuss the modeling projects which we were then working on. He also kindly provided time to discuss on the relevant project during my very short one-day visit to ETH, Zurich, Switzerland. Apart from these direct discussions, his constant guidance through long scientific correspondences is greatly acknowledged. I have learnt several observational aspects from him. I have greatly benefited by the great lectures by him at the 2nd International summer school at China, on polarized line formation theory. I cherish the wonderful moments with him during the excursions and dancing with him and other co-participants at the barbecue at the Bamboo sea in China. I also thank him for kindly taking me with him for a day of excursion and a wonderful drive to Hana in Hawaii, USA.

Very special thanks are due to Dr. Michele Bianda for organizing two visits to IRSOL at Locarno, Switzerland during 2009 and 2010. He introduced me, who is basically from pure mathematics, to actual observations with instruments such as ZIMPOL (Zurich IMaging POLarimeter). He explained the complex workings of those instruments in a lucid and simple language in way that I could get a feel for them. I have learnt the basics of data analysis in IDL from him. He often stayed till late evenings at IRSOL, which was of great help as I could work without feeling home-sick. He provided enough time for scientific discussions and listened to the updates of my work on each day. I thank him for helping me in all the official matters related to my stay at IRSOL. He kindly organized for me, two one-day visits to ETH, Zurich to discuss with Prof. J. O. Stenflo and Dr. Rene Holzreuter. I thank also Dr. Renzo Ramelli for his help in performing observations and computer related help extended by him. I thank Dr. Bianda and Dr. Ramelli also for their collaboration on the modeling projects. Dr. Bianda also took me to nearby Institute “Specola Solare” at Locarno, and showed me the full solar spectrum, craters on the moon, satellites of Jupiter etc. His hospitality is memorable and I am indebted as he and his wife Mrs. Anna Michele took me for food shopping every week, cooked Indo-Italian dishes several times, took me on excursions to wonderful vallies in the Alps and also around the

beautiful landscapes of Locarno and Ascona. An ever lasting memory is of the drive to Valle Verzasca. We cooked Italian and Indian foods on alternate days and had a memorable time at IRSOL. I remember him also for introducing me to the tasty castania (chestnuts), Pizza of Locarno and many other Italian dishes. I also thank Dr. Ramelli and Mrs. Anna Michele for taking us to a wonderful excursion to Rhone river Glacier, the experience of which is inexpressible in words. I thank Dr. Renzo and his wife Mrs. Katya Renzo for who kindly took me to a castania party. I thank Mrs. Annaliese whom I call Nonna (meaning granny in Italian) who affectionately took care of me very well. I have spent good time with her which included humorous discussions. I thank her for inviting me to mouth watering pizza lunches prepared by her. She did not hesitate to taste my cooking of Indian dishes also. I thank Mrs. Elena for introducing to me the weather forecast Institute (METEO Svizzera), Locarno, for the dinner party at her home and her hospitality. It was very nice to play with little Aline, Michele's daughter, and also to learn few Italian words from her. It was good also to play with Rafaele, son of Dr. Renzo. I wish to thank Michele's mother for her affection and hospitality at her home in Ascona. I am grateful to Dr. Philippe Jetzer for supporting my visits to Locarno. I thank Katya, secretary at IRSOL for helping me in official matters.

I would like to thank Dr. Frédéric Paletou for his collaboration on the work on developing fast numerical methods for radiative transfer. I thank him for all the scientific correspondences, in particular for sending the link to the e-book by Saad (2000) which was of great help to learn basics of the projection methods. I thank Dr. Ludovick Léger for his collaboration.

I am grateful to Dr. Rene Holzreuter, for his collaboration on the modeling projects, the delightful discussions and scientific correspondences. He kindly visited IRSOL for a day in 2009 and provided his time for a day in ETH, Zurich in 2010 in order to help me learn the modeling codes. I thank him for his hospitality and taking care of me when I visited ETH, Zurich.

I wish to thank Dr. Han Uitenbroek and Dr. Marianne Faurobert who briefly visited OCA, Nice, France during my visits there and with whom I could discuss and gain deeper knowledge in several areas of theoretical radiative transfer. I thank Dr. Han Uitenbroek whose unpolarized modeling code has been used for the works carried out in part - III of my thesis. I thank Dr. J. Adam whose finite volume method of solving three-dimensional unpolarized radiative transfer equation has been used in one of the chapters in this thesis. I thank Prof. Véronique Bommier and Dr. A. Asensio Ramos at the Observatory of Paris

for useful discussions.

It was not possible to visit OCA, Nice and IRSOL, Locarno during 2008, 2009 and 2010, without the financial support provided by OCA, Nice, France, Henri Poincaré Junior Fellowship, OCA, Nice, France, Indo-Swiss Joint Fellowship program, which is jointly funded by Department of Science and Technology (DST), New Delhi, India, and École polytechnique fédérale de Lausanne (EPFL), Switzerland, and IRSOL, Locarno Switzerland. I wish to acknowledge my sincere thanks to all these agencies for making possible these visits. I wish to thank University of Hawaii and Dr. Jeff Kuhn for providing full financial support for my visit to Hawaii in 2010. I am grateful to the DST, New Delhi, India and IIA for jointly supporting my visit to China in 2011.

Dr. Baba Varghese of IIA is greatly acknowledged for his kind help and timely solutions to computer related problems on numerous occasions, including handling large memory, graphics, programming and installing several softwares in my laptop and other computers that I used. His help during my stay in foreign countries, to connect to the computers at IIA are also greatly acknowledged. I fall short of words to express my gratitude to him for his timely help whenever needed. I thank computer committee for providing the excellent computing facilities without which the computations of solutions to complicated and numerically expensive scientific problems presented in this thesis could not have been undertaken. I thank all the IIA administrative staff for their support in official matters. Very special thanks to Mr. A. Narasihma Raju who kindly helped me in several official matters such as office room related problems, accommodation problems, reimbursement of the funds, and many more. I also thank Mr. K. T. Rajan, Mrs. Malini Rajan and Mrs. Pramila for their timely help related to the issues of foreign visits. I would also like to thank Mr. Dhananjaya, Mr. K. Shankar and Mr. Rajendran for their help in official as well as transportation facilities.

An important part of my PhD career is the IIA library. Often I worked in quiet environment of the library, which was very much motivating and inspiring. It is my duty to thank all the library staff for their help and co-operation. Particularly, I wish to thank Dr. A. Vagiswari, Dr. Christina Birdie, Mr. B. S. Mohan, Mr. P. N. Prabhakar. Mr. B. S. Mohan especially helped me on number of occasions such as in photo copying, scanning, procuring books and publications from other sources and many more. I wish to thank the library trainees namely Prathibha, Sidhu, Ghouse, Shahin and Kiran for their immense help to find books. Sidhu and Ghouse are also thanked for their help in photo copying several times. Mr. Murali is thanked for his help in arranging the auditorium facility

during my seminars and also for providing copies of photographs. I thank the dispatch section for providing timely facilities for sending official mails to the University, DST etc. The stores department and purchase departments are thanked for providing stationaries and purchasing indented items in time.

I am grateful to the Heads of the Physics Department and the administrative staff of the Mangalore University for their co-operation in all the official matters. I am especially grateful to Mrs. Jayashree Kamat, Mrs. Jayashree and Ms. Anitha of the Mangalore University for kindly providing timely information over the telephone and their assistance in all the administrative matters connected with the PhD program.

I thank all my classmates who helped me during my course work. Especially I thank Roopashree, Bhavya, Smitha, S. and Koshy who extended timely help to understand several concepts in physics. I thank them also for their constant support and encouragement. Special thanks to Bhavya whom I know from the time of my summer project with whom I have shared several memorable moments. I thank Vyas for his brotherly help in several occasions in several ways. I also thank my classmates Kshitij, Sumangala and Mamta with whom I have spent memorable time. I also thank all other classmates during course work. Special thanks are due to Nishant, who was not only my classmate but a great friend all through my PhD career. I thank him also for his support and encouragement on several occasions and for many interesting and enlightening discussions on science, philosophy and music. I have no words to thank my little junior brother Avijeet, whom I know from my 2nd year of PhD. Since then, he has accompanied me for going back from IIA to Bhaskara every night after I complete my day's work at my office. He stood by me in tough times and helped infinite number of times and filled the place of my own brother. I thank my juniors Avijeet and Sumat for providing me their computers when I urgently needed more and faster computing facilities. I thank my junior friends Hema and Anantha for letting me share my happy and sad moments with them and for supporting me. I also thank my other juniors H. N. Smitha, Supriya, Sowmya, Sangeetha, Indu, Ramya, Manpreet, Arya, Shubham and Sumat with whom I have spent several memorable moments. I thank Hema, Anantha, Manpreet, Arya, Avijeet for their wonderful company and help during our visit to New Delhi. I thank my seniors Tapan, Bharat and Vigeesh for their timely help in academic matters. I thank my room mate Ramya for her co-operation during my stay at Bhaskara. I thank my office mates Madhulita, Hema and Sumangala for their co-operation. I thank all other students of IIA for their co-operation. I am grateful to Dr. Yogeshwaran at IISc., for his guidance and useful tips to clear the entrance exams for PhD. I also thank Dr. Pradeep, IISc., and staff members of HRA for their encouragement to take up PhD as

my career.

I deeply acknowledge my gratitude to all the Professors at the post-graduate studies at the Mysore University. The lectures by Prof. D. D. Somashekhar, Prof. H. N. Ramaswamy, Prof. Chandrasekhar Adiga, Prof. Huche Gowda and Prof. Rangarajan have made me passionate about pure mathematics. I thank them for imparting to me, their deep knowledge in mathematics, the foundation of which turned out to be my academic strength during my research career. I specially thank encouragement by Prof. H. N. Ramaswamy for pursuing higher studies. I thank all my friends at the post-graduate studies – Sunitha, Teena, Ashwini, Manjula, Bindu, Aparna, Sahana, Sowbhagya, Shilpa (late), Pavitra, Chetana, Medha, Raji and Jesna for their constant support and encouragement. I also thank Raghuanna and Sudarshan for inspiring discussions on mathematics.

I take this opportunity to thank all the lecturers at the graduate studies at the S. D. M. College, Ujire. I specially acknowledge Prof. Yasho verma, Prof. V. Jayalakshmi, Prof. Nagabhushan, Prof. P. P. Prabhu, Mrs. Saroja, Mr. Abhay (late), Mr. Purushotham Tulupule, Mr. Venkappa, Mr. Sampath Kumar and Mr. Nagesh Puranik for passing on to me their deep knowledge in mathematics, statistics and computer applications through lectures and discussions. I thank Prof. V. Jayalakshmi also for her support and encouragement to pursue higher studies. I thank all my friends at S. D. M. College and Mytreiy hostel – Ganesh, Shakila, Shubha, Ashwini, Malathi, Sharija, Manu, Vinu, Ajay, Amutha, Shruthi, Deepika, Smitha, Sumakka, Bharatiakka, Aswiniakka, Shainy, Indira, Amrutha, Prateeksha, Vidya, Geeta, Trupti and Deepti.

A major role in the success of my career is played by the training that I received at the boarding school ‘Jawahar Navodaya Vidyalaya’ (JNV), at Balehonnur, where I studied from my 6th grade to 12th grade. I am grateful to inspired teaching by my beloved teacher Mr. R. S. Suresh who laid the foundation of basic sciences in me. I thank all the teachers for their encouragement and support – Mr. Epan Luke, Mr. Prabhakar, Mr. Ratnakar, Mr. Uday Nayak, Mrs. Hemalatha, Mr. Nagaraj Tigadi, Mr. Madhusoodan, Mrs. Roopa, Mrs. Vanashree, Mr. Kurian, Mr. V. Suresh, Mr. Rajesh, Mr. Padmanabh, Mr. Killedar, Mrs. Surekha, Mrs. Suchetha, Mrs. Ujwala, Mrs. Revankar, Mr. Ganesh Hegde, Mr. James, Mr. Shaju Joseph, Mrs. Myna, Mrs. Manjula, Ms. Parvati, Mrs. Girija, Mr. Babu, Mr. Prakash, Mr. Arun Nayak, Mr. Hanumesh, Mr. Sareesh, Mrs. Pothuamani, Mr. Devasia, Mr. Guru Prasad Mr. Shyamanna and Mr. Nagaraj. I wish to thank all my friends at JNV especially – Smitha, Namratha, Sowmya mala, Arathi, Nandini, Shakunthala, Sowrabha, Rekha, Sheela, Mala, Navya, Chitra, Deepa, Mamatha, Madhu,

Asha, Sushma, Nithyananda, Lavanya, Chinmaya, Gayana and many more with whom I have spent several memorable moments. I wish to thank Lavanya for her support during my PhD career by visiting me often at IIA. I thank Nithyananda, Smitha also for visiting me at IIA and for their encouragement.

I wish to thank my primary school teachers Mr. Lingappa (late), Mrs. Subhashini and Mr. Shrinivasa moorthy (late) for their encouragement and excellent teaching. I thank all my primary school friends also for sharing good moments with me. I wish to thank Mr. Jayadev (late), Mr. Sheshagiri for their immense encouragement in my younger age.

The patience by my parents Mr. L. C. Seetharama Bhasari and Mrs. K. S. Parvathi Bhasari knows no bounds. Their kindness and support has been a source of inspiration and strength to work hard and reach my goal. My sister Dr. L. S. Deepa and brother-in-law Dr. K. J. Girish, are acknowledged for their affection and support. I am extremely grateful to my brother Dr. L. S. Sharath Chandra who supported, guided and encouraged throughout my life. Without his advice I would not have taken research as my career. It is my brother who has been my idol for the path I chose. Words fall short to express how grateful I am to my beloved brother. I thank my sister-in-law Dr. Soma Banik for her encouragement. It was very nice to play with my little nephews Aprameya, Anirudh, Abijnan, and little niece Anchita.

I thank my special friend and husband R. Sandeep for his limitless encouragement and boundless support. I thank him for his help also at France during my visits there. I am indebted to him for his promise to support my research career throughout my life.

It is my pleasure to thank my uncles Mr. Sridhar and Mr. Radhakrishna for providing a studying environment at their homes and for the hospitality of their family members during my days at Bangalore before joining IIA. I also thank my uncle Mr. Raviprakash and family, aunt Mrs. Rathna and family for their encouragement. I thank all my cousins Anitha, Vasudha, Vasuki, Soujanya, Sameera, Rashmi and Shreesha with whom I have shared nice moments.

I would like to thank Mrs. S. Vimala Nagendra for her motherly affection and support during my visits to Nice in 2008 and to IRSOL during 2009. I thank her for providing home made cooking materials in both the visits which were of great help. During one month of her stay at IRSOL in 2009, her presence made me feel at home. I am grateful to her for her kind advises. It is a pleasure to meet and talk to Mrs. Shamala (mother of Mrs. Vimala), Sumana and Aaditya (daughter and son of Dr. K. N. Nagendra).

It is my great pleasure to acknowledge my music teacher Vidwan Ramachandra Rao with whom I learnt Indian classical music every week. It was a great change from the continuous and monotonous scientific work and helped to reduce the fatigue and enable me to work hard again. I also thank his family members.

Apart from the people whom I am directly connected with, I am greatly inspired by several books. First and foremost is the book “Chandra” – biography of Prof. S. Chandrasekhar written by Kameshwar Wali and the book “Madam Curie” – biography of Madam Curie written by Ève Curie. I have learnt basics and advanced topics in radiative transfer theory and polarized scattering theory through famous books such as “Radiative Transfer” by S. Chandrasekhar, “Stellar Atmospheres” by Dimitri Mihalas, “Solar Magnetic Fields” by Jan Olof Stenflo and “Polarization in Spectral Lines” by Landi Degl’Innocenti & Landolfi. I carry with me for ever the inspiration that I have drawn from these great authors.

Finally I would like to express my deep gratitude to all those who have played a role in shaping me into a successful researcher. My apologies to those, whose names I may have left out inadvertently, who have directly and indirectly helped me during my career.

Bangalore  
April 2012

L. S. Anusha



# List of Publications

This Thesis is based on the following publications

## In International Journals

1. The Hanle effect in a random magnetic field: *Dependence of the polarization on statistical properties of the magnetic field.*: Frisch, H., **Anusha, L. S.**, Sampoorna, M., & Nagendra, K. N., 2009, **A&A**, 501, 335–348
2. Preconditioned Bi-Conjugate Gradient Method for Radiative Transfer in Spherical media.: **Anusha, L. S.**, Nagendra, K. N., Paletou, F., & Lèger, L., 2009, **ApJ**, 704, 661–671
3. Polarized line formation in Multi-dimensional media-I: *Decomposition of Stokes parameters in arbitrary geometries.*: **Anusha, L. S.**, & Nagendra, K. N., 2011a, **ApJ**, 726, 6–19
4. Polarized line formation in Multi-dimensional media-II: *A high speed method to solve problems with partial frequency redistribution.*: **Anusha, L. S.**, Nagendra, K. N. & Paletou, F., 2011a, **ApJ**, 726, 96–109
5. Polarized line formation in Multi-dimensional media-III: *Hanle effect with partial frequency redistribution.*: **Anusha, L. S.**, & Nagendra, K. N., 2011b, **ApJ**, 738, 116–135
6. Polarized line formation in Multi-dimensional media-IV: *A Fourier decomposition technique to formulate the transfer equation with angle dependent partial frequency redistribu-*

tion.: **Anusha, L. S.**, & Nagendra, K. N., 2011c, **ApJ**, 739, 40–48

7. Polarized line formation in Multi-dimensional media-V: *Effects of angle-dependent partial frequency redistribution*.: **Anusha, L. S.**, & Nagendra, K. N., 2012, **ApJ**, 746, 84–99

8. Generalization of the Last Scattering Approximation for the Second Solar Spectrum modeling; *The Ca I 4227 Å line as case study*.: **Anusha, L. S.**, Nagendra, K. N., Stenflo, J. O., Bianda, M., Sampoorna, M., Frisch, H., Holzreuter, R., & Ramelli, R., 2010a, **ApJ**, 718, 988–1000

9. Analysis of the forward scattering Hanle effect in the Ca I 4227 Å line.: **Anusha, L. S.**, Nagendra, K. N., Bianda, M., Stenflo, J. O., Holzreuter, R., Sampoorna, M., Frisch, H., Ramelli, R. & Smitha, H. N., 2011b, **ApJ**, 737, 95–112

10. Observations of the forward scattering Hanle effect in the Ca I 4227 Å line.: Bianda, M., Ramelli, R. **Anusha, L. S.**, Stenflo, J. O., Nagendra, K. N., Holzreuter, R., Sampoorna, M., Frisch, H., & Smitha, H. N., 2011, **A&A**, 530, L13–L16

11. Origin of spatial variations of scattering polarization in the wings of the Ca I 4227 Å line.: Sampoorna, M., Stenflo, J. O., Nagendra, K. N., Bianda, M., Ramelli, R., & **Anusha, L. S.**, 2009, **ApJ**, 699, 1650–1659

12. Projection methods for line radiative transfer in spherical media.: **Anusha, L. S.**, & Nagendra, K. N., 2009, **Mem.S.A.It**, 80, 631–634

13. Polarization: Proving ground for methods in radiative transfer.: Nagendra, K. N., **Anusha, L. S.**, & Sampoorna, M. 2009, **Mem.S.A.It**, 80, 678–689

## In Refereed Conference Proceedings

1. The Hanle Effect as Diagnostic Tool for Turbulent Magnetic Fields.: **Anusha, L. S.**, Sampoorna, M., Frisch, H., & Nagendra, K. N., 2010b, in **Astrophysics and Space Science Proceedings: Magnetic Coupling between the Interior and the Atmosphere of**

- the Sun, eds. S. S. Hasan, & R. J. Rutten (Heidelberg, Berlin: Springer-Verlag), 390–394
2. Recent developments in polarized line formation in magnetic fields.: Nagendra, K. N., Sampoorna, M., & **Anusha, L. S.**, 2010, in **Recent advances in Spectroscopy; Astrophysical, Theoretical and Experimental Perspective**, eds. R. Chaudhary, M. V. Mekkaden, A. V. Raveendran, A. Satyanarayanan (Heidelberg, Berlin: Springer-Verlag), 139–153
  3. Linear Polarization of the Solar Ca I 4227 Å line: Modeling based on radiative transfer and last scattering approximations.: **Anusha, L. S.**, Stenflo, J. O., Frisch, H., Bianda, M., Holzreuter, R., Nagendra, K. N., Sampoorna, M., & Ramelli, R., in ASP Conf. Ser. 437, Solar polarization 6 (SPW6), 2010c, 57
  4. Observations of the solar Ca I 4227 Å line.: Bianda, M., Ramelli, R., Stenflo, J. O., **Anusha, L. S.**, Nagendra, K. N., Sampoorna, M., Holzreuter, R., & Frisch, H. in ASP Conf. Ser. 437, Solar polarization 6 (SPW6), 2010, 67



# Abstract

This thesis aims to develop methods to solve radiative transfer (RT) problems in several astrophysical contexts. A major part of the thesis is devoted to develop an understanding of the effects of multi-dimensional (multi-D) RT on the polarized line formation. We consider partial frequency redistribution (PRD) of line radiation in the presence/absence of external magnetic fields. The thesis consists of three parts. In the first part we develop modern numerical methods to solve the line RT equation in one-dimensional (1D) planar and spherical media. In the second part, we formulate and solve the problem of polarized line RT equation in multi-D media. In the third part we focus our attention on realistic modeling of the spectro-polarimetric observations of the linearly polarized spectrum of the Sun (the well known second solar spectrum).

In Chapter 1 we give a general introduction. Chapters 2 and 3 deal with Part-I of the thesis. Chapters 4–8 are devoted to the Part-II. Chapters 9 and 10 concern Part-III. Chapter 11 presents future outlook on the work presented in this thesis. The mathematical details are given in the form of Appendices. A detailed list of references are given in the bibliography. A glossary of mathematical symbols used in the thesis are given at the end of the thesis, for convenience.

## **Part-I of the Thesis : Advanced numerical methods to solve line radiative transfer equation in 1D media**

In this part we consider two examples. (Ia) concerns the polarized line formation in magneto-turbulent scattering media. (Ib) aims to devise a new and fast numerical method of solving the line RT equation in spherical media.

(Ia) A study of the origin of turbulent weak magnetic fields in the solar atmosphere through

observations of linear polarization suggests that the scale of variation of the magnetic fields is small compared to the mean free path of the photons, and hence ‘micro-turbulence’ is a good approximation. This allows us to replace the magnetic field dependent physical variables by their turbulent averages over the magnetic field vector probability density function (PDF). The line scattering on atomic bound states produces linearly polarized line radiation (called resonance scattering). The magnetic field modification of this phenomenon is called Hanle effect. We develop numerical techniques to solve the line RT equation in the presence of a weak turbulent magnetic field. It can handle a general situation of magneto-turbulence in scattering media (called turbulent Hanle effect), of which the micro- and macro-turbulence are the limiting cases. We undertake a study of the effect of PDFs on the shapes and magnitudes of the linearly polarized emergent Stokes profiles. We show that the linear polarization is very sensitive to the choice of the PDF (the nature of turbulence). Therefore the turbulent Hanle effect can be used as a sensitive diagnostic tool to measure weak small scale fields on the Sun. The necessary theoretical framework for this purpose is presented in Chapter 2.

(Ib) The solution of polarized line RT equation is computationally expensive for realistic mechanisms of scattering, and for multi-D geometries. As a first step towards devising modern techniques which are even more efficient than the existing iterative methods (which are already very fast), we develop a new method called Stabilized preconditioned Bi-Conjugate Gradient (Pre-BiCG -STAB). We consider the example of line transfer in 1D spherical media. It is also an iterative method, based on the construction of a set of bi-orthogonal vectors. We show that this method is quite versatile compared to the traditional iterative methods like Jacobi, Gauss-Seidel and successive over-relaxation. The theory of this numerical method, the computing algorithm, and the bench-mark tests are presented in Chapter 3. This method is also applied to multi-D RT described in later chapters.

## **Part-II of the Thesis : Polarized line formation in multi-dimensional media**

This problem is theoretically complex and computationally very expensive. Due to this the topic has rarely been addressed in the past, although clearly the polarization diagnostics is the most sensitive to explore the finite dimensional structures. With the high spatial resolution polarimetric observations which have now become available from ground based and space platforms, it is imperative that we keep pace with the observations, by developing necessary theoretical knowledge. In six chapters of this thesis, we formulate and solve some of the most complex problems in multi-D geometries (Chapters 4–8). This covers the

formulation of the transfer equation in terms of irreducible spherical tensors (instead of the traditional Stokes parameters); the solution of these equations in two-dimensional (2D) and three-dimensional (3D) geometries using the efficient Pre-BiCG-STAB method, for problems involving PRD and Hanle effect; developing the Fourier decomposition technique to solve the formidable problem of polarized multi-D transfer with angle-dependent PRD. All these topics are covered in Chapters 4– 8.

### **Part-III of the Thesis : Realistic modeling of the spectro-polarimetric observations of the second solar spectrum**

To model the second solar spectrum, one needs to solve the polarized RT equation. For strong resonance lines the PRD effects must be accounted for. To explore the weak solar magnetic fields (both turbulent and oriented), we have to formulate and solve the polarized RT equation that includes Hanle effect. It has been a tradition in spectro-polarimetry of scattering polarization, to conduct observations near the solar limb positions, and model them. After modeling such limb observations (through a case study of Ca I 4227 Å line in non-magnetic quiet Sun observations), we venture to model the observations of ‘forward scattering Hanle effect’- which opens up an entirely new and interesting possibility to study the weak oriented magnetic fields near the solar disk center. In Chapters 9 and 10 we describe in detail the modeling of limb and near disk center observations of the Ca I 4227 Å line scattering polarization. The experience gained in 1D modeling of the actual observations would be useful later when we apply the same modeling techniques in future, to the observations of finite dimensional structures of the solar atmospheres, which clearly require the techniques of multi-D transfer developed in Chapters 4–8. The goals achieved in this thesis and the possibilities for future work are described in Chapter 11.





# Contents

<b>Acknowledgments</b>	<b>i</b>
<b>List of Publications</b>	<b>xi</b>
<b>Abstract</b>	<b>xv</b>
<b>1 General introduction</b>	<b>1</b>
1.1 Polarization of light and its representation . . . . .	2
1.1.1 Polarization ellipse . . . . .	3
1.1.2 Representation of polarized light . . . . .	3
1.2 The polarized light in stellar atmospheres . . . . .	4
1.2.1 Resonance scattering in spectral lines . . . . .	4
1.2.2 The Hanle effect . . . . .	6
1.2.3 The second solar spectrum . . . . .	7
1.2.4 Polarization phase matrices . . . . .	7
1.2.5 Irreducible spherical tensors $\mathcal{T}_Q^K$ . . . . .	7
1.3 Partial frequency redistribution in line scattering . . . . .	8
1.3.1 Angle-averaged redistribution functions . . . . .	10
1.3.2 Complete frequency redistribution function . . . . .	11
1.4 The polarized redistribution matrices . . . . .	11

1.5	Line radiative transfer equation and its solution . . . . .	12
1.5.1	Multi-D radiative transfer . . . . .	12
1.5.2	Methods to solve radiative transfer equation . . . . .	13
1.5.3	Applications of multi-D radiative transfer . . . . .	21
1.6	Modeling of the second solar spectrum . . . . .	22
1.7	Outline of the thesis . . . . .	23
1.7.1	Outline on part–I of the thesis . . . . .	23
1.7.2	Outline on part–II of the thesis . . . . .	24
1.7.3	Outline on part–III of the thesis . . . . .	27
<b>Part-I</b>	<b><u>Advanced numerical methods to solve line radiative transfer</u></b>	
	<b><u>equation in one-dimensional media</u></b>	<b>29</b>
<b>2</b>	<b>The Hanle effect in a random magnetic field</b>	<b>31</b>
2.1	Introduction . . . . .	31
2.2	Assumptions . . . . .	32
2.3	The transfer problem . . . . .	35
2.3.1	Transfer equation for the conditional mean Stokes parameters . . . . .	36
2.3.2	Integral equation for $\mathcal{S}(\tau \mathbf{B})$ . . . . .	37
2.4	A PALI type numerical method of solution . . . . .	38
2.5	A choice of magnetic field vector PDFs . . . . .	41
2.6	Dependence of the polarization on the correlation length . . . . .	44
2.7	A series expansion for the calculation of the polarization . . . . .	45
2.7.1	Construction of the expansion . . . . .	45
2.7.2	Numerical results . . . . .	50
2.7.3	Magnetic field with a finite correlation length . . . . .	54

---

2.8	Dependence of the polarization on the magnetic field vector PDF . . . . .	55
2.9	Concluding remarks . . . . .	58
<b>3</b>	<b>Bi-Conjugate Gradient methods for radiative transfer</b>	<b>61</b>
3.1	Introduction . . . . .	61
3.2	Radiative transfer in a spherical medium . . . . .	63
3.2.1	The transfer equation . . . . .	63
3.2.2	The constant impact parameter approach . . . . .	65
3.2.3	Benchmark models . . . . .	67
3.2.4	Iterative methods of ALI type for a spherical medium . . . . .	68
3.3	Preconditioned BiCG method for a spherical medium . . . . .	71
3.3.1	The Preconditioned BiCG Algorithm . . . . .	72
3.4	Transpose free variant - Pre-BiCG-STAB . . . . .	75
3.4.1	Pre-BiCG-STAB algorithm . . . . .	76
3.5	Comparison of ALI and Pre-BiCG methods . . . . .	77
3.5.1	The behaviour of the maximum relative change (MRC) . . . . .	77
3.5.2	A study of the True Error . . . . .	80
3.5.3	A theoretical upper bound on the number of iterations for convergence in the Pre-BiCG method . . . . .	81
3.6	Results and discussions . . . . .	82
3.7	Concluding remarks . . . . .	84
<b>Part-II</b>	<b><u>Polarized line formation in multi-dimensional media</u></b>	<b>87</b>
<b>4</b>	<b>Decomposition of Stokes parameters in multi-D media</b>	<b>89</b>
4.1	Introduction . . . . .	89
4.2	Polarized radiative transfer in a 3D medium – Stokes vector basis . . . . .	92

4.3	Decomposition of Stokes vectors for multi-D transfer . . . . .	95
4.3.1	A multipolar expansion of the Stokes source vector and the Stokes intensity vector in a 3D medium . . . . .	95
4.3.2	Polarized radiative transfer equation for the real irreducible intensity vector in a 3D medium . . . . .	102
4.4	The Numerical Method of Solution . . . . .	105
4.4.1	The formal solution in 3D geometry . . . . .	105
4.5	Results and Discussions . . . . .	108
4.5.1	A validation test for the 3D polarized radiative transfer solution . . . . .	108
4.5.2	The nature of irreducible intensity components $\mathcal{I}$ in a 3D medium . . . . .	108
4.5.3	Linear polarization in 3D medium of finite optical depths . . . . .	111
4.5.4	The effect of collisional redistribution on the Stokes parameters in a 3D medium . . . . .	113
4.6	Concluding remarks . . . . .	115
<b>5</b>	<b>Solution of partial redistribution problems in multi-D media</b>	<b>119</b>
5.1	Introduction . . . . .	119
5.2	The Polarized transfer equation in a 2D medium . . . . .	121
5.3	A short characteristics method for 2D radiative transfer . . . . .	126
5.4	Computational details . . . . .	129
5.4.1	The angle quadrature in 2D/3D geometries . . . . .	129
5.4.2	The spatial and frequency gridding . . . . .	131
5.5	A Preconditioned BiCG-STAB method . . . . .	131
5.6	Results and Discussions . . . . .	137
5.7	Concluding remarks . . . . .	142
<b>6</b>	<b>Hanle effect with partial redistribution in multi-D media</b>	<b>145</b>

---

6.1	Introduction . . . . .	145
6.2	The polarized radiative transfer in a magnetized multi-D media . . . . .	146
6.3	Decomposition of $\mathbf{S}$ and $\mathbf{I}$ in a magnetized multi-D media . . . . .	149
6.3.1	The irreducible transfer equation in multi-D geometry for the Hanle scattering problem . . . . .	154
6.4	A 3D formal solver based on the short characteristics approach . . . . .	155
6.5	Numerical method of solution . . . . .	156
6.5.1	The Preconditioner matrix . . . . .	158
6.5.2	Computational details . . . . .	158
6.6	Results and discussions . . . . .	159
6.6.1	The Stokes profiles formed due to resonance scattering in 2D and 3D media . . . . .	159
6.6.2	The Stokes profiles in 2D and 3D media in the presence of a magnetic field . . . . .	164
6.6.3	The spatial variation of emergent $(Q/I, U/I)$ in a 3D medium . . . . .	168
6.7	Concluding remarks . . . . .	172
<b>7</b>	<b>Angle-dependent PRD in multi-D media: Formulation</b>	<b>177</b>
7.1	Introduction . . . . .	177
7.2	Transfer equation in terms of Stokes parameters . . . . .	179
7.3	Transfer equation in terms of irreducible spherical tensors . . . . .	183
7.4	Transfer equation in terms of irreducible Fourier coefficients . . . . .	185
7.4.1	Symmetry properties of the irreducible Fourier coefficients . . . . .	189
7.5	Numerical considerations . . . . .	192
7.6	Concluding remarks . . . . .	193
<b>8</b>	<b>Angle-dependent PRD in multi-D media: Radiative transfer</b>	<b>195</b>

8.1	Introduction . . . . .	195
8.2	Polarized transfer equation in a multi-D medium . . . . .	196
8.2.1	The radiative transfer equation in terms of irreducible spherical tensors	197
8.2.2	A Fourier decomposition technique for domain based PRD . . . . .	203
8.3	Numerical method of solution . . . . .	209
8.4	Results and Discussions . . . . .	211
8.4.1	Nature of the components of $\mathcal{I}$ and $\tilde{\mathcal{I}}^{(k)}$ . . . . .	213
8.4.2	Emergent Stokes Profiles . . . . .	217
8.4.3	Radiation anisotropy in 2D media–Stokes source vectors . . . . .	221
8.5	Conclusions . . . . .	222
 <b>Part-III    <u>Realistic modeling of the spectropolarimetric observations</u></b>		
<b>                  <u>of the second solar spectrum</u></b>		<b>225</b>
<b>9</b>	<b>Last scattering approximation: Case study with Ca I 4227 Å</b>	<b>227</b>
9.1	Introduction . . . . .	227
9.2	The Radiative Transfer (RT) approach . . . . .	229
9.3	The details of observations and solar model atmospheres . . . . .	233
9.3.1	The observation of $(I, Q/I)$ in the Ca I 4227 Å line . . . . .	233
9.3.2	The smearing effect . . . . .	235
9.3.3	The model atmosphere and the model atom . . . . .	235
9.4	The anisotropy factor $k_G(\lambda, \mu, \tau_\lambda)$ . . . . .	235
9.5	The Last Scattering Approximations (LSA) . . . . .	237
9.5.1	LSA-3 . . . . .	239
9.5.2	LSA-2: Eddington-Barbier approximation . . . . .	243

9.5.3	LSA-1: semi-empirical approach . . . . .	243
9.6	Results and Discussions . . . . .	245
9.6.1	Theoretical validation of the LSA approaches . . . . .	245
9.6.2	Observational validation of the LSA-3 and the RT approaches . . . . .	246
9.7	Concluding remarks . . . . .	249
<b>10</b>	<b>Forward scattering Hanle effect in Ca I 4227 Å line</b>	<b>255</b>
10.1	Introduction . . . . .	255
10.2	The Radiative Transfer (RT) formulation . . . . .	258
10.2.1	Radiative transfer with the Hanle effect . . . . .	258
10.2.2	Radiative transfer with the Zeeman effect . . . . .	263
10.3	Polarization observations of Ca I 4227 Å line . . . . .	265
10.4	Modeling procedure . . . . .	267
10.4.1	The model atmosphere and the model atom . . . . .	269
10.4.2	Step 1. Polarization profiles for $V/I$ . . . . .	270
10.4.3	Step 2. Polarization diagrams for $Q/I$ and $U/I$ at line center . . . . .	270
10.4.4	Step 3. Polarization profiles for $Q/I$ and $U/I$ . . . . .	270
10.5	Results and Discussions . . . . .	271
10.5.1	$V/I$ profiles from the Zeeman effect . . . . .	271
10.5.2	Polarization diagrams from the Hanle effect . . . . .	272
10.5.3	$Q/I$ and $U/I$ profiles from the Hanle effect . . . . .	273
10.5.4	The effect of model atmospheres . . . . .	275
10.5.5	The role of collisions . . . . .	276
10.5.6	The role of a filling factor . . . . .	277
10.6	Concluding remarks . . . . .	280

<b>11 Conclusions and future outlook</b>	<b>283</b>
11.1 Summary of the thesis . . . . .	283
11.2 Future Outlook . . . . .	288
<b>Appendices</b>	<b>291</b>
<b>A Integral equations for the components of the source vector</b>	<b>291</b>
<b>B Exact expressions of the mean coefficient <math>\langle \mathcal{M}_{00}^2 \rangle</math></b>	<b>294</b>
<b>C Construction of <math>\hat{A}</math> matrix and Preconditioner matrix <math>\hat{M}</math></b>	<b>296</b>
<b>D A core-wing method for the 3D polarized line transfer</b>	<b>300</b>
<b>E Expansion of Stokes parameters into irreducible components in non-magnetic 2D media</b>	<b>303</b>
<b>F Symmetry of polarized radiation field in 2D geometries</b>	<b>304</b>
<b>G Expansion of Stokes parameters into the irreducible components</b>	<b>309</b>
<b>H The magnetic redistribution matrices in the irreducible tensorial form</b>	<b>310</b>
<b>I The magnetic redistribution matrices in the matrix form</b>	<b>313</b>
<b>J The reduced scattering phase matrix in real form</b>	<b>315</b>
<b>K The magnetic redistribution matrices in the matrix form</b>	<b>317</b>
<b>L Symmetry breaking properties of the angle-dependent PRD</b>	<b>320</b>
<b>M The non-magnetic redistribution matrices</b>	<b>323</b>



---

<b>N</b>	<b>The magnetic redistribution matrices</b>	<b>327</b>
<b>O</b>	<b>The Zeeman radiative transfer in the atmospheric reference frame</b>	<b>331</b>
	<b>Bibliography</b>	<b>333</b>



# Chapter 1

## General introduction

Analysis of the spectra of the Sun and stars requires calculation of the radiation emerging from these objects. Such a quantitative information can be obtained through a solution of the radiative transfer (RT) equation, which describes the interaction of radiation with matter through micro-physical processes like the absorption, emission and scattering of radiation on atoms and molecules. These processes cause the energy to be removed from or added to the radiation field. They are characterized by macroscopic coefficients specified by atomic cross-sections and occupation numbers of energy levels of the material that the stellar atmosphere is made up of. In the macro-physical level, the transfer of radiation is governed by quantities such as geometrical shape, the physical extent of the stellar atmosphere, and the presence of external magnetic fields. For example the diffuse radiation field in a planar or spherical medium is quite different from what prevails in a 3D structure. These aspects are studied by representation of the atmosphere by proper idealizations, by taking care to include essential characteristics of the medium.

The polarization of the radiation gives a much deeper insight into the physical processes taking place in the stellar atmosphere. The inclusion of polarization states in the transfer equation brings in an increased level of complexity. For this reason the ‘polarized RT equation’ is formulated and subsequently solved only in the past six decades starting with the seminal papers by S. Chandrasekhar (see Chandrasekhar 1950). This fundamental work established the path to be taken when formulating the polarized RT equation for new astrophysical problems. This thesis concerns the polarization of radiation arising due to scattering of anisotropic radiation on atomic bound states. Scattering polarization in the presence or absence of an external magnetic fields is also considered in detail.

The thesis consists of three parts. In the first part we develop advanced numerical

methods of solving the line RT equation in one-dimensional (1D) media. The second part is devoted to the polarized line formation studies in multi-dimensional (multi-D) geometries. In the third part of the thesis the emphasis is on application of the polarized line formation theory to model the actual polarimetric observations.

## 1.1 Polarization of light and its representation

The vectorial nature of light is called polarization. A ray of light can be represented by an electro-magnetic wave which has three independent oscillations  $E_x(\mathbf{r}, t)$ ,  $E_y(\mathbf{r}, t)$  and  $E_z(\mathbf{r}, t)$ . Correspondingly, three independent wave equations are required to describe the propagation of these oscillations (see Collett 1993) namely

$$\nabla^2 E_i(\mathbf{r}, t) = \frac{1}{c^2} \frac{\partial^2 E_i(\mathbf{r}, t)}{\partial t^2}, \quad i = x, y, z, \quad (1.1)$$

where  $c$  is the velocity of propagation of the oscillation and  $\mathbf{r} = \mathbf{r}(x, y, z)$ . In Cartesian system the components  $E_x(\mathbf{r}, t)$  and  $E_y(\mathbf{r}, t)$  are said to be transverse components and  $E_z(\mathbf{r}, t)$ , the longitudinal component. From solution of Equation (1.1) we obtain radiation field components to be

$$E_x(\mathbf{r}, t) = E_{0x} \cos(\omega t - \mathbf{k} \cdot \mathbf{r} + \delta_x), \quad (1.2)$$

$$E_y(\mathbf{r}, t) = E_{0y} \cos(\omega t - \mathbf{k} \cdot \mathbf{r} + \delta_y), \quad (1.3)$$

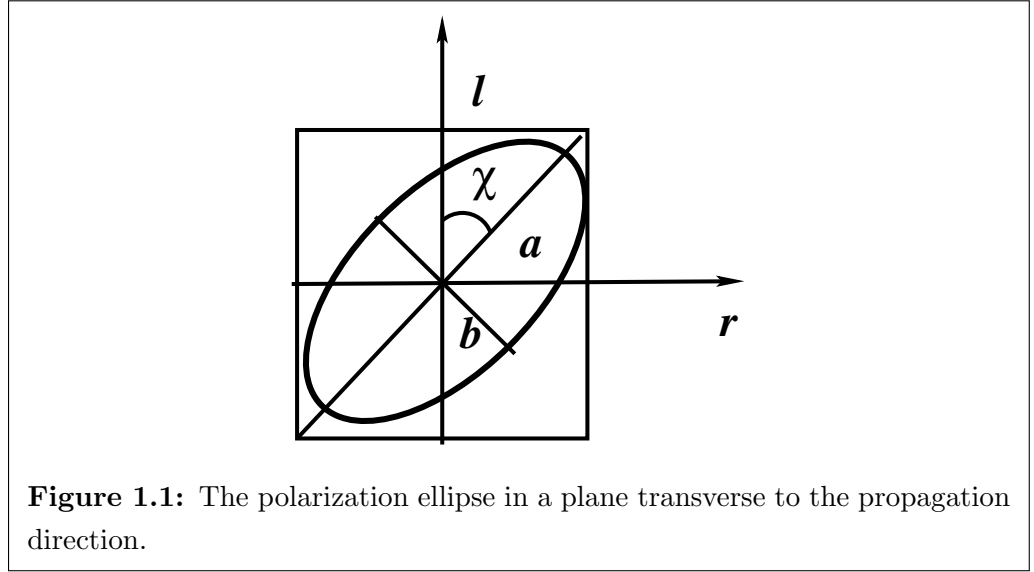
$$E_z(\mathbf{r}, t) = E_{0z} \cos(\omega t - \mathbf{k} \cdot \mathbf{r} + \delta_z), \quad (1.4)$$

where  $E_{0x}$ ,  $E_{0y}$ ,  $E_{0z}$  are the maximum amplitudes,  $\delta_x$ ,  $\delta_y$ ,  $\delta_z$  are arbitrary phases, and  $\mathbf{k}$  is the wave vector. After many experiments it was found that longitudinal component in Equation (1.4) does not exist for light, i.e., light consisted only of the transverse components represented by Equations (1.2) and (1.3). If we take the direction of propagation to be the  $z$ -direction then the radiation field in free space must be

$$E_x(z, t) = E_{0x} \cos(\omega t - k_z z + \delta_x), \quad (1.5)$$

$$E_y(z, t) = E_{0y} \cos(\omega t - k_z z + \delta_y). \quad (1.6)$$

Later, by solution of the Maxwell's equations it was proved that in free space only transverse components arose, there was no longitudinal component. Equations (1.5) and (1.6) are called polarization components of the radiation field.



### 1.1.1 Polarization ellipse

As the electric field propagates  $E_x(z, t)$  and  $E_y(z, t)$  give rise to a resultant vector. This vector describes a locus of points in space and the curve generated by those points is an ellipse. This ellipse is called as the polarization ellipse (see Figure 1.1) and is given by

$$\frac{E_x^2}{E_{0x}^2} + \frac{E_y^2}{E_{0y}^2} - \frac{2E_x E_y \cos \delta}{E_{0x} E_{0y}} = \sin^2 \delta, \quad (1.7)$$

where  $\delta = \delta_y - \delta_x$  is the phase difference.

### 1.1.2 Representation of polarized light

To describe an arbitrarily polarized radiation field four parameters are sufficient, which will give the “intensity”, “degree of polarization”, “plane” of polarization and “ellipticity” of the radiation at each point in any given direction. To include such diverse quantities which represent energy, a ratio, an angle and a pure number in a self-consistent manner into the RT equation, the Stokes parameters were introduced (see Chandrasekhar 1950). Denoting by  $I_l = E_{0x}^2$  and  $I_r = E_{0y}^2$ , which are the components of intensity of a beam of light in two mutually perpendicular directions ( $l$  and  $r$ ) the Stokes parameters  $I$ ,  $Q$ ,  $U$  and

$V$  are defined as

$$I = I_l + I_r = E_{0x}^2 + E_{0y}^2, \quad (1.8)$$

$$Q = I_l - I_r = E_{0x}^2 - E_{0y}^2, \quad (1.9)$$

$$U = (I_l - I_r) \tan 2\chi = 2E_{0x}E_{0y} \cos \delta, \quad (1.10)$$

$$V = (I_l - I_r) \tan 2\beta \sec 2\chi = 2E_{0x}E_{0y} \sin \delta, \quad (1.11)$$

where  $\chi$  is the angle between the direction  $l$  and the semi-major axis ( $a$ ) of the ellipse and  $\tan \beta$  is the ratio of semi-major to semi-minor axis ( $b$ ) of the ellipse. The vector  $\mathbf{I} = (I, Q, U, V)$  is called as the Stokes vector. The polarization ellipse is shown in Figure 1.1.

## 1.2 The polarized light in stellar atmospheres

In general, light gets polarized due to (i) coherent scattering and (ii) the external magnetic fields. An example of scattering polarization is that of Rayleigh's scattering in which the light gets partially polarized in the ratio of intensities  $1 : \cos^2 \Theta$  ( $\Theta$  is the angle between the incident and the scattered beam) in directions perpendicular and parallel to the plane of scattering (the plane containing the incident and scattered beams of light). The diffuse (multiply scattered) radiation field in a scattering atmosphere must therefore be partially polarized (see Chandrasekhar 1950). Magnetic fields produce polarization of light through (a) Zeeman effect and (b) the Hanle effect. In this thesis we emphasize on studies of polarization of light through scattering and Hanle effect which are described below.

### 1.2.1 Resonance scattering in spectral lines

The following events are considered as typical examples of scattering processes. (i) A photon traveling in direction  $\boldsymbol{\Omega}'$  and with frequency  $\nu'$ , is incident on an atom in bound state  $a$  leading to the excitation to a higher energy bound state  $b$ , with the photon's energy being converted to the internal excitation energy of the atom, followed by a radiative decay back to state  $a$  with the emission of a photon, that travels in a different direction  $\boldsymbol{\Omega}$  and has a slightly different frequency  $\nu$ . Further, the lower and upper states  $a$  and  $b$  of the atom will not be perfectly sharp, but have finite energy widths arising due to finite lifetime of each state caused by radiative de-excitation (natural broadening), or the broadening caused by collisions with other particles. The scattering of incident radiation on atoms and molecules, in the vicinity of the energy gap between their bound states, is called resonance scattering. The process involved is nothing but the well known Rayleigh (dipole) scattering, but on the bound states of the atoms and molecules – producing polarized spectral lines.

(ii) scattering of photons involving atomic and molecular bound – free states (and its inverse processes) is also called Rayleigh scattering, producing weakly polarized continuum spectrum. Note that scattering of photons by free electrons (Thompson scattering) has an identical angular distribution as the Rayleigh scattering process and produces a polarized continuous spectrum. In this thesis we consider scattering processes of the type (i) and (ii) mentioned above.

Following Landi Degl’Innocenti & Landolfi (2004, hereafter LL04), here we qualitatively describe the resonance scattering polarization and its magnetic analogue – the Hanle effect. In Figure 1.2 we show a  $90^\circ$  scattering event in the absence of an external magnetic field. We assume that the incident radiation field is unpolarized. The scattering atom is assumed to be consisting of three linear oscillators  $x$ ,  $y$  and  $z$ , oscillating with frequency, say  $\nu_0$ . The electric field of the incident radiation can be decomposed into its  $x$ - and  $z$ -components, which do not have any phase relation between them (incoherence), owing to the unpolarized nature of the incident beam. This in-coherency is transferred to the oscillators of the atom and thus the  $x$ -component of the electric field vector excites  $x$ -oscillator and the  $z$ -component excites the  $z$ -oscillator. We assume that  $y$  is the direction of propagation of the incident radiation beam, and therefore there is no component of the electric field in  $y$ -direction. Thus the  $y$ -oscillator is not excited. All of the oscillators decay with a damped motion as they emit in any given direction, a radiation beam polarized according to the classical dipole scattering (see e.g., Jackson 1962). On viewing the beam scattered along the  $z$ -direction, one cannot see the oscillation that is along the  $z$ -direction. There is no oscillation excited along  $y$ -direction as well, and therefore  $I_r = 0$ . The  $x$ -oscillator produces a radiation beam that is linearly polarized along the  $x$ -direction, which we denote by  $I_l$ . This means that  $Q/I = (I_l/I_l) \times 100 = 100\%$  (see Figure 1.2). Thus the radiation scattered along  $z$ -direction is 100% linearly polarized perpendicular to the scattering plane. The same scattering event can be understood by considering the atom to be consisting of a linear  $z$ -oscillator and two circular oscillators denoted by  $\sigma_+$  and  $\sigma_-$  laying in the  $xy$  plane (equivalent to the linear  $x$ -oscillator). In this picture, the  $z$ -component of the electric field of the incident beam still excites the  $z$ -oscillator (oscillations of which cannot however be seen, when viewed along the  $z$ -direction), but the  $x$ -oscillator excites the  $\sigma_+$  and  $\sigma_-$  circular oscillators. These two circular oscillators are in a well-defined phase relation, so as to produce the resulting motion of the electric charge in the  $x$ -direction.

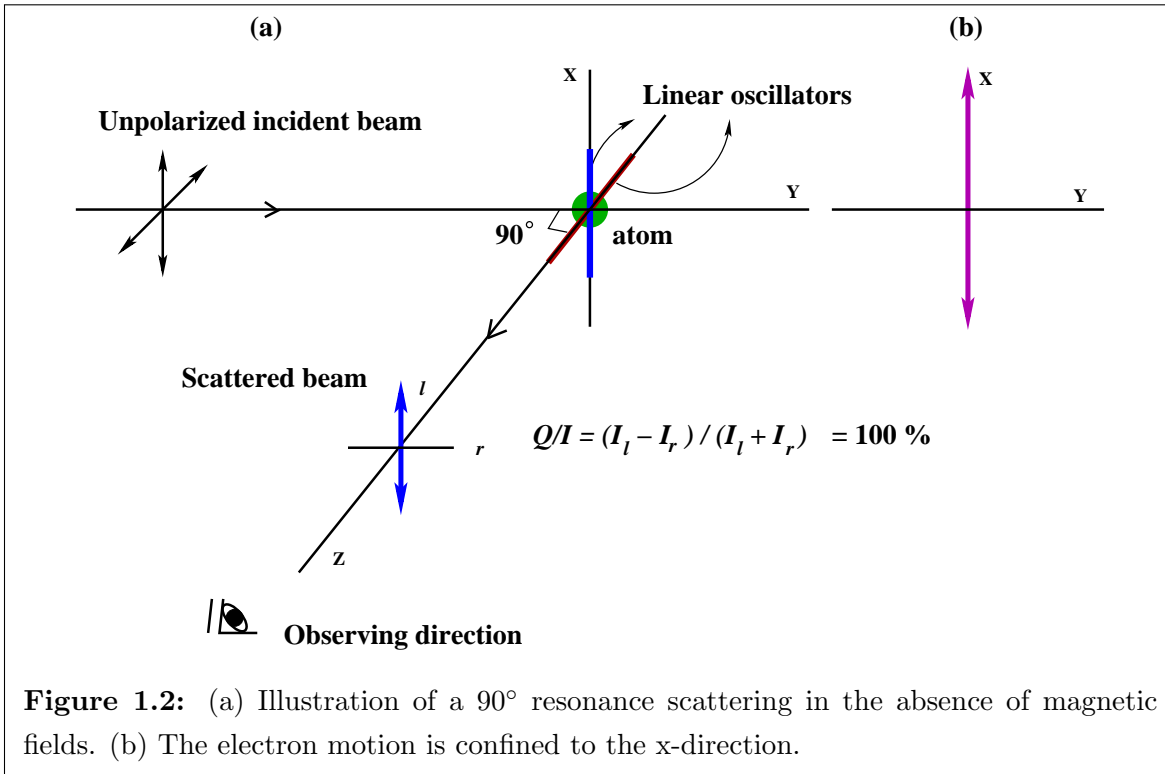


**Figure 1.2:** (a) Illustration of a  $90^\circ$  resonance scattering in the absence of magnetic fields. (b) The electron motion is confined to the x-direction.

### 1.2.2 The Hanle effect

The Hanle effect is the magnetic field modification of the resonance scattering polarization described above. We schematically illustrate this in Figure 1.3. We now assume that we have a weak magnetic field oriented along the z-direction. While the linear z-oscillator continues to oscillate with the frequency  $\nu_0$ , the frequencies of the  $\sigma_+$  and  $\sigma_-$  circular oscillators get modified as  $\nu_0 + \nu_L$  and  $\nu_0 - \nu_L$  respectively, with  $\nu_L$  being the Larmour frequency. This causes the loss of the phase relation produced by the exciting electric field, during the damped decay process. Therefore the electric charge describes a so-called “rossett” pattern in the xy plane. Thus, the linear polarization of the scattered beam – which actually represents the weighted time average of this rossett pattern – is decreased and rotated with respect to the direction of the non-magnetic regime. This effect on the resonance scattered linear polarization caused by the weak magnetic field, which relaxes the phase relations or the coherences between the  $\sigma_+$  and  $\sigma_-$  oscillators of the resonance scattering, is called as the Hanle effect. The Hanle effect was discovered in Göttingen in 1923 by Wilhelm Hanle (see Hanle 1923, 1924). The diagnostic potential of the Hanle effect to estimate weak solar magnetic fields was pioneered by Stenflo (1982).



### 1.2.3 The second solar spectrum

The linearly polarized spectrum of the Sun formed due to coherent scattering processes is called the second solar spectrum. Because of its enormous structural difference when compared to the intensity spectrum (first solar spectrum), it was named as the second solar spectrum by Ivanov (1991). The first investigation of the second solar spectrum was carried out by Stenflo et al. (1983a, 1983b). The invention of high precision polarimeters such as ZIMPOL (Povel 1995, 2001) made the faint structural details in the linearly polarized spectrum possible to be detected and explored. A comprehensive atlas of the second solar spectrum in the wavelength regime 3160–6995 Å was recorded in three volumes by Gandorfer (2000, 2002, 2005).

### 1.2.4 Polarization phase matrices

A polarization phase matrix  $\hat{P}(\boldsymbol{\Omega}, \boldsymbol{\Omega}')$  is a matrix that describes the probability that a photon incident from direction  $\boldsymbol{\Omega}'$  will be scattered into direction  $\boldsymbol{\Omega}$ . The phase matrix is a  $4 \times 4$  matrix because it transforms the polarization state  $(I', Q', U', V')$  of the incident photon, which is a 4-component vector into another 4-component vector  $(I, Q, U, V)$  that represents the polarization state of the scattered photon. Each element of the phase matrix depends on  $\boldsymbol{\Omega}'$  and  $\boldsymbol{\Omega}$ . The expressions for the phase matrix elements can be found in Chandrasekhar (1950) for resonance scattering and in Stenflo (1994) for the Hanle effect.

### 1.2.5 Irreducible spherical tensors $\mathcal{T}_Q^K$

The irreducible spherical tensors  $\mathcal{T}_Q^K(i, \boldsymbol{\Omega})$  are mathematical entities introduced to polarimetry by Landi Degl'Innocenti (1984). The index  $i = 0, 1, 2, 3$  refers to four Stokes parameters  $I, Q, U$  and  $V$  and  $\boldsymbol{\Omega}$  is the direction of the scattered photon. The indices  $K$  and  $Q$  arise from the multi-polar expansion of the density matrix elements in terms of irreducible spherical tensors.  $K$  takes values 0, 1, and 2. For each value of  $K$ , we have  $-K \leq Q \leq +K$ . The values  $K = 0$  and 2 correspond to the terms generating linear polarization components and  $K = 1$  to the circular polarization components. The tensors  $\mathcal{T}_Q^K(i, \boldsymbol{\Omega})$  are purely geometrical quantities which enable factorization of the elements of the phase matrix  $\hat{P}(\boldsymbol{\Omega}, \boldsymbol{\Omega}')$ . In other words we can express the elements of the phase matrix as a sum of the product of terms which depend separately on  $\boldsymbol{\Omega}$  and  $\boldsymbol{\Omega}'$ . This is an important property that helps to simplify the polarized RT problems to a great extent. A major part of this thesis is built upon the idea of decomposing the Stokes parameters in terms of these irreducible spherical tensors. A complete description of properties of these

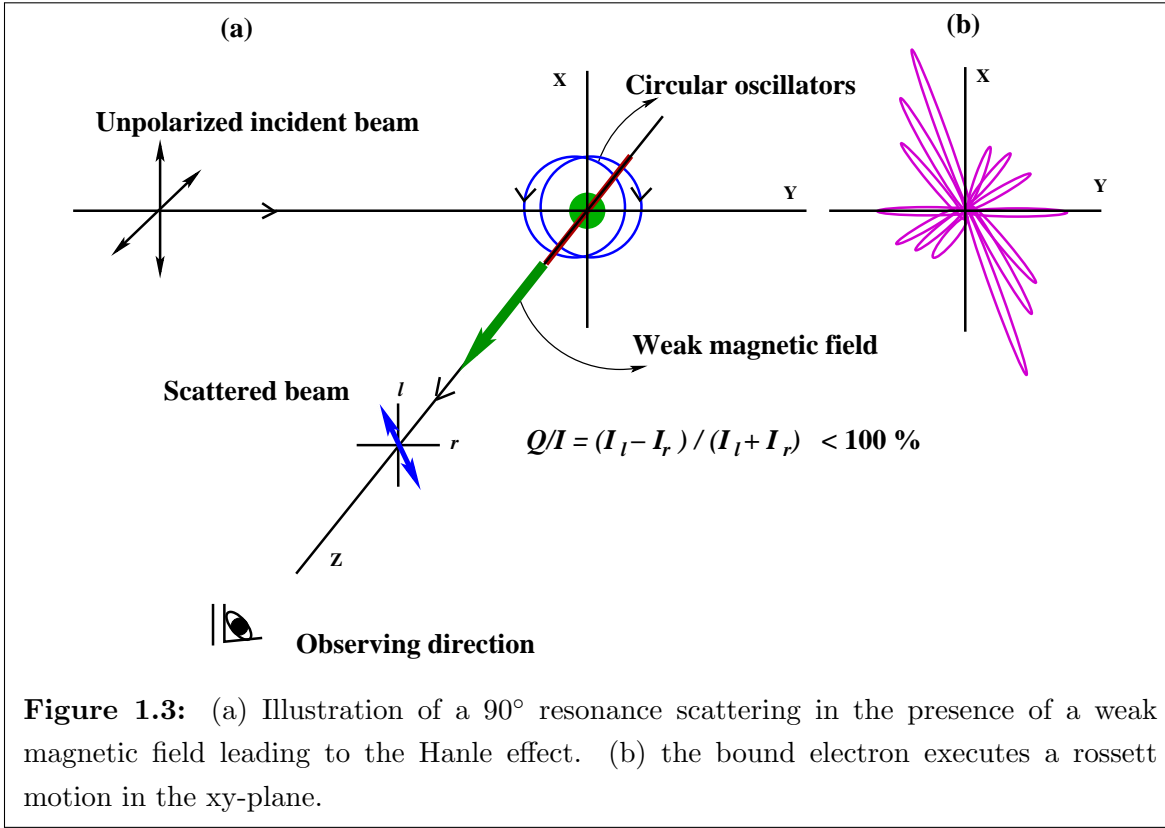


**Figure 1.3:** (a) Illustration of a  $90^\circ$  resonance scattering in the presence of a weak magnetic field leading to the Hanle effect. (b) the bound electron executes a rosette motion in the  $xy$ -plane.

tensors is given in LL04.

### 1.3 Partial frequency redistribution in line scattering

As discussed above, the process of scattering which leads to polarized spectral lines is the one in which an atom is excited from a bound state to another by absorbing a photon, immediately followed by a radiative de-excitation to the original state by emitting a photon. Often the frequency and direction of the scattered photon is different from those of the incident photon. In other words there is a “redistribution” of the angle and frequency of the incident photon. This redistribution process is represented by elegant mathematical functions called redistribution functions, derived originally by Hummer (1962). Specifically, a redistribution function

$$R(\nu, \nu', \Omega, \Omega') d\nu d\nu' (d\Omega/4\pi) (d\Omega'/4\pi), \quad (1.12)$$

gives the *joint probability* that a photon will be scattered from incident direction  $\Omega'$  within a solid angle  $d\Omega'$  and in the frequency interval  $(\nu', \nu' + d\nu')$  into a solid angle  $d\Omega$  around the direction  $\Omega$  and in the frequency interval  $(\nu, \nu + d\nu)$ . The functional form of this

redistribution function in two important categories are widely used. These functions are derived with the assumption that the transition is represented by only two energy levels with no coupling to other levels. In both the cases discussed below, it is assumed that in the atomic rest frame the lower state is perfectly sharp. (i) In the first case, the upper state is assumed to have a finite width arising due to finite life time of the excited state of the atom, against radiative decay back to the lower state. Further, it is assumed that no additional perturbations occur while the atom is in the upper state. (ii) In the second case, the upper state is assumed to be broadened because frequent collisions in the medium cause a random reshuffling of the atom in the upper state, before the emission of a photon. Note that in this case the width of the upper state is due to radiative plus collisional processes. The redistribution functions are derived first in the atom's rest frame. Then Doppler redistribution in frequency produced by atom's random motion are considered, recognizing that what is actually observed in a stellar atmosphere is an ensemble of atoms moving with a thermal velocity distribution (assumed to be Maxwellian).

The functional form of type-II redistribution function that describes the case (i) is

$$r_{\text{II}}(x, x', \boldsymbol{\Omega}, \boldsymbol{\Omega}') = \frac{1}{\pi \sin \Theta} \exp \left[ -\frac{1}{2}(x - x')^2 \csc^2 \frac{1}{2}\Theta \right] \\ \times H \left( a \sec \frac{1}{2}\Theta, \frac{1}{2}(x + x') \sec \frac{1}{2}\Theta \right). \quad (1.13)$$

Here frequencies are measured in units of the Doppler width. The incident and scattered frequencies are respectively  $x'$  and  $x$ . The scattering angle (angle between incident and scattered beams) is given by

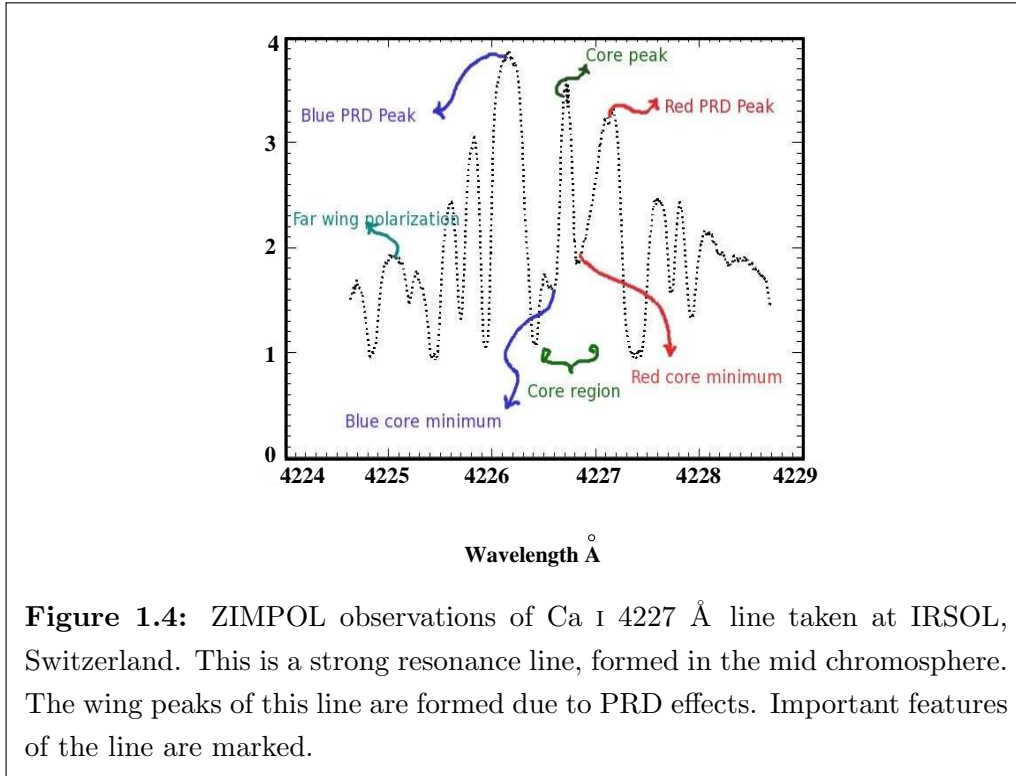
$$\Theta = \cos^{-1} \{ \boldsymbol{\Omega} \cdot \boldsymbol{\Omega}' \}. \quad (1.14)$$

$H$  is the well known Voigt profile function and  $a$  is the total width of the upper state is expressed in terms of line the Doppler width.

The functional form of type-III redistribution function that describes the case (ii) is

$$r_{\text{III}}(x, x', \boldsymbol{\Omega}, \boldsymbol{\Omega}') = \frac{1}{\pi^2 \sin \Theta} \int_{-\infty}^{+\infty} du e^{-u^2} \frac{a}{a^2 + (x' - u)^2} \\ \times H \left( \frac{a}{\sin \Theta}, \frac{x - u \cos \Theta}{\sin \Theta} \right). \quad (1.15)$$

The functions given in Equations (1.13) and (1.15) contain the full information on the ‘‘correlation’’ between incident and scattered angles and frequencies. They are known as ‘‘angle-dependent’’ partial frequency redistribution (PRD) functions in the laboratory frame. They form the mathematical basis functions in terms of which more complex (for instance polarized) ‘redistribution matrices’ are constructed.



### 1.3.1 Angle-averaged redistribution functions

It is often difficult to treat RT problems in the degree of generality contained in the angle-dependent redistribution functions. A level of simplification is achieved, yet retaining the information on frequency correlations, by averaging over the entire range of incident and scattered directions. This approximation is useful when one is primarily interested in correlations in frequency, not in angles. The angle-averaged type-II and type-III redistribution functions are given by

$$r_{\text{II}}(x, x') = \frac{1}{2} \int_0^\pi r_{\text{II}}(x, x', \boldsymbol{\Omega}, \boldsymbol{\Omega}') \sin \Theta d\Theta, \quad (1.16)$$

and

$$r_{\text{III}}(x, x') = \frac{1}{2} \int_0^\pi r_{\text{III}}(x, x', \boldsymbol{\Omega}, \boldsymbol{\Omega}') \sin \Theta d\Theta. \quad (1.17)$$

For detailed discussions on redistribution theory in line scattering one can refer to Hummer (1962) and Mihalas (1978).

### 1.3.2 Complete frequency redistribution function

When there is a complete reshuffling of atoms in their excited state in such a way that there is no correlation between the frequencies of incoming and scattered photons, then both have frequencies independently distributed over the absorption profile. This situation is referred to as “complete frequency redistribution (CRD)” and is represented mathematically by  $\phi(x)\phi(x')$ , where  $\phi$  is the absorption profile function.

## 1.4 The polarized redistribution matrices

As we have seen in previous sections, (i) phase matrices represent the probability distribution of angularly anisotropic scattering which determines the polarization state of the scattered photon, and (ii) redistribution functions represent the probability distributions of angular and frequency correlations, which determine the frequency and direction of the scattered photons. Actually to understand the polarization observed in spectral lines we must implement in the RT equation, both the effects described above in (i) and (ii). The combined effects constitute the scattering redistribution matrices denoted by  $\hat{R}(x, x', \mathbf{\Omega}, \mathbf{\Omega}')$ , which are basically linear combination of the unpolarized redistribution functions  $r_{II,III}$  and the polarization phase matrices  $\hat{P}$ .

In this thesis we use two types of redistribution matrices: non-magnetic redistribution matrix with collisions derived for resonance scattering by Domke & Hubeny (1988) and magnetic redistribution matrix derived for the case of Hanle effect by Bommier (1997a, 1997b). In chapters 2 and 3 we use the approximation of CRD in line scattering. In chapters 4, 5 and 9 we use non-magnetic redistribution matrices. In chapters 6 and 10 we use the magnetic redistribution matrices with angle-averaged redistribution functions. In chapters 7 and 8 we consider the magnetic redistribution matrices with angle-dependent redistribution functions. The functional forms of these matrices are given in respective chapters and further details in the appendices.

An example of the PRD scattering in polarized line formation is presented in Figure 1.4 where we show the  $Q/I$  profile in the Ca I 4227 Å line observed near the limb of the Sun. This line is formed in the mid-chromosphere and has maximum linear polarization in the visible region of the spectrum. The two peaks on either sides of the line center are formed due to the PRD scattering mechanism. We have taken up modeling of this line in chapters 9 and 10.

## 1.5 Line radiative transfer equation and its solution

The polarized line transfer equation for a ray traveling along the direction  $\boldsymbol{\Omega}$  is given by

$$\frac{d\mathbf{I}(\mathbf{r}, \boldsymbol{\Omega}, x)}{ds} = -\kappa_{\text{tot}}(\mathbf{r}, x)[\mathbf{I}(\mathbf{r}, \boldsymbol{\Omega}, x) - \mathbf{S}(\mathbf{r}, \boldsymbol{\Omega}, x)], \quad (1.18)$$

where  $s$  is the path length along the ray. Here  $\mathbf{I} = (I, Q, U)$  is the Stokes vector,  $\kappa_{\text{tot}}$  is the total opacity (line plus continuum),  $\mathbf{r} = (x, y, z)$  is the position vector of the ray in the Cartesian co-ordinate system. The Stokes source vector  $\mathbf{S} = (S_I, S_Q, S_U)$  for a two-level atom model with unpolarized ground level takes the form

$$\mathbf{S}(\mathbf{r}, \boldsymbol{\Omega}, x) = \frac{\kappa_l(\mathbf{r})\phi(x)\mathbf{S}_l(\mathbf{r}, \boldsymbol{\Omega}, x) + \kappa_c(\mathbf{r})\mathbf{S}_c(\mathbf{r}, x)}{\kappa_{\text{tot}}(\mathbf{r}, x)}. \quad (1.19)$$

Here  $\mathbf{S}_c$  is the continuum source vector,  $\kappa_l$  and  $\kappa_c$  are the line and continuum opacities,  $\phi$  is the Voigt profile function. The polarized line source vector can be expressed as

$$\begin{aligned} \mathbf{S}_l(\mathbf{r}, \boldsymbol{\Omega}, x) &= \mathbf{G}(\mathbf{r}) + \int_{-\infty}^{+\infty} dx' \\ &\times \oint \frac{d\boldsymbol{\Omega}'}{4\pi} \frac{\hat{R}(x, x', \boldsymbol{\Omega}, \boldsymbol{\Omega}')}{\phi(x)} \mathbf{I}(\mathbf{r}, \boldsymbol{\Omega}', x'), \end{aligned} \quad (1.20)$$

where  $\mathbf{G}(\mathbf{r})$  is the thermal source vector,  $\hat{R}(x, x', \boldsymbol{\Omega}, \boldsymbol{\Omega}')$  is the redistribution matrix. Actual functional form of different quantities appearing in the above equations depend on the problem at hand. Their explicit form and further details specific to the problem will be given in each of the chapters. Therefore we treat them as abstract quantities in this introductory chapter, to avoid repetition and confusion.

The spatial derivative in the left-hand-side of Equation (1.18) takes different forms in different geometries. In this thesis we consider RT in 1D Cartesian geometry in chapters 2, 9 and 10, 1D spherical geometry in chapter 3, and finally multi-D Cartesian geometry in chapters 4–8. As a major part of the thesis is about multi-D line RT, we discuss below some of the concepts and historical developments in this field.

### 1.5.1 Multi-D radiative transfer

With the introduction of high precision spectro-polarimeters such as ZIMPOL, observations of a wealth of structures are now available for exploration. Figure 1.5 shows the Stokes images recorded around the core of the Ca II K line observed in quiet regions of the Sun.

The most striking feature is the “high degree of spatial structuring” along the slit length observed in both  $Q/I$  and  $U/I$  (see Stenflo 2006). A natural explanation of this spatial structuring is in terms of Hanle effect from spatially varying magnetic fields. This effect is entangled with the local departure from axial symmetry which causes spatial distribution of  $Q/I$  and  $U/I$ . In addition, the broad wings of the chromospheric Ca II K line (see Figure 1.6) have their origin in the PRD scattering mechanism. An attempt to model this line using two-component 1D model atmospheres has been made in Holzreuter et al. (2006), Holzreuter & Stenflo (2007a, 2007b). They try to simulate the observed polarization spectrum by using hot, cool, quiet Sun 1D model atmospheres and finally combinations of hot and cool 1D model atmospheres. Their studies reveal that even the use of multi-component 1D model atmospheres are unable to provide a detailed fit to the polarimetric observations for all the center-to-limb distances simultaneously. This is because, in such idealized 1D models the hot and cold components are assumed to be optically independent of each other, which is certainly not the case in realistic geometries of the structures in the solar atmospheres. They indicate that multi-D RT would be needed for a fully self-consistent treatment.

Modeling using a simplified geometry serves a purpose in the historical development of the field, by providing the parameters to be looked for, such as temperature structure, magnetic fields etc. It is always a necessary to achieve as high a degree of realism as possible. Detailed 2D and 3D magnetohydrodynamical models of the solar atmosphere have now become available, with higher sophistication (see Nordlund & Stein 1991 and references therein).

A successful modeling of the Stokes observations of lines such as Ca II K requires multi-D polarized line RT with a proper treatment of PRD and Hanle effect using magnetohydrodynamic simulations of the solar atmospheres. As a first step towards this major effort, we formulate in this thesis multi-D polarized RT, and develop methods to solve them. We explore the effects of both PRD and Hanle effect in isothermal slabs and cubes. We apply these methods in realistic modeling of solar 3D structures in future.

### 1.5.2 Methods to solve radiative transfer equation

#### Formal solution methods

Important contributions in the early history of solving NLTE unpolarized multi-D RT problems are the papers by Cannon (1970) and Cannon & Rees (1971), who considered

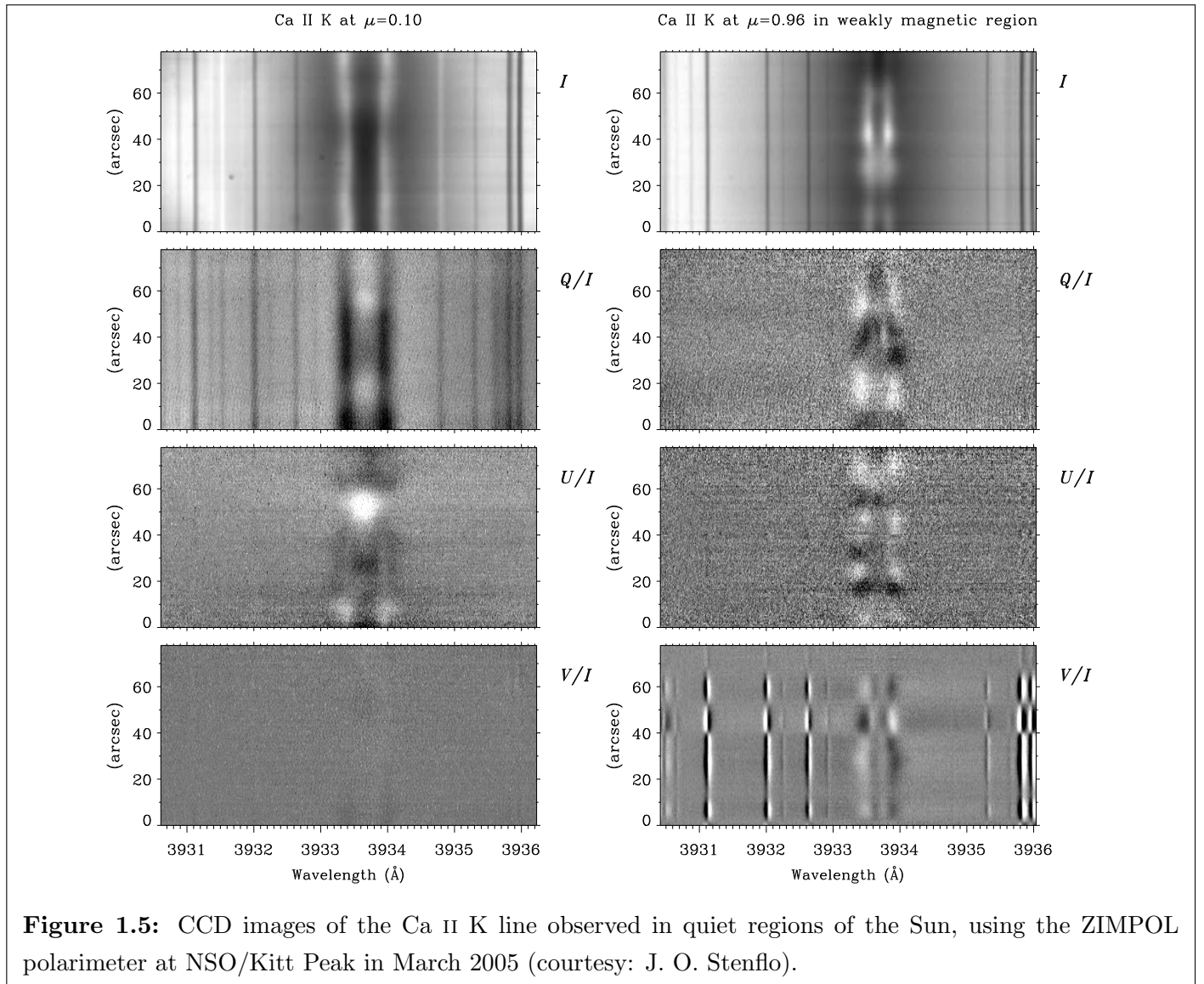


**Figure 1.5:** CCD images of the Ca II K line observed in quiet regions of the Sun, using the ZIMPOL polarimeter at NSO/Kitt Peak in March 2005 (courtesy: J. O. Stenflo).



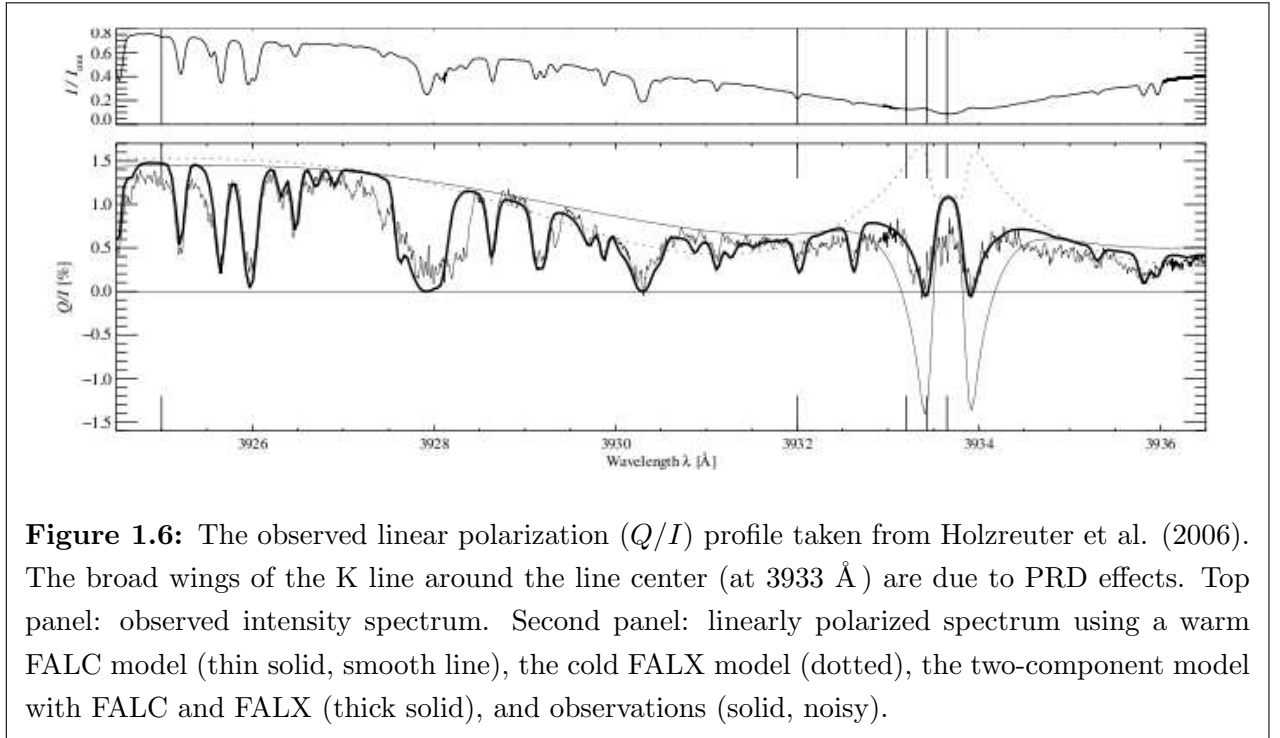
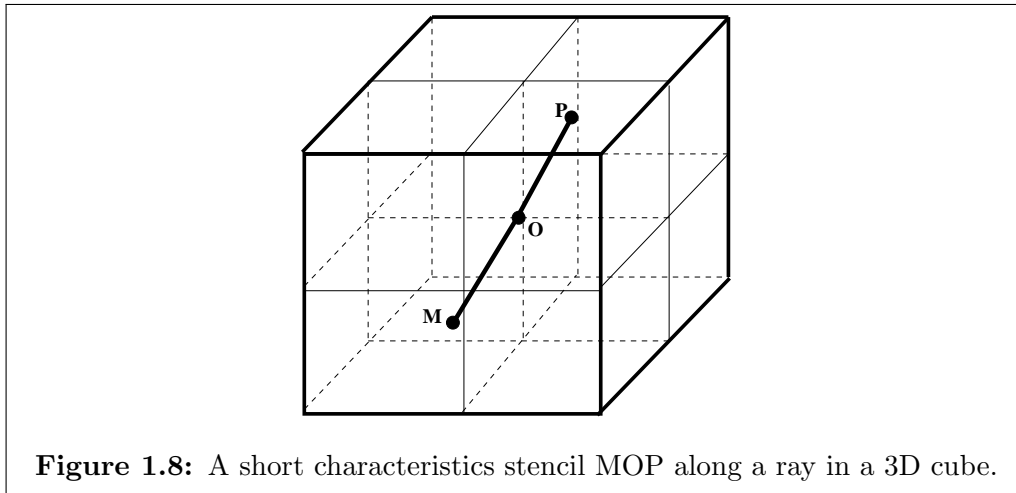
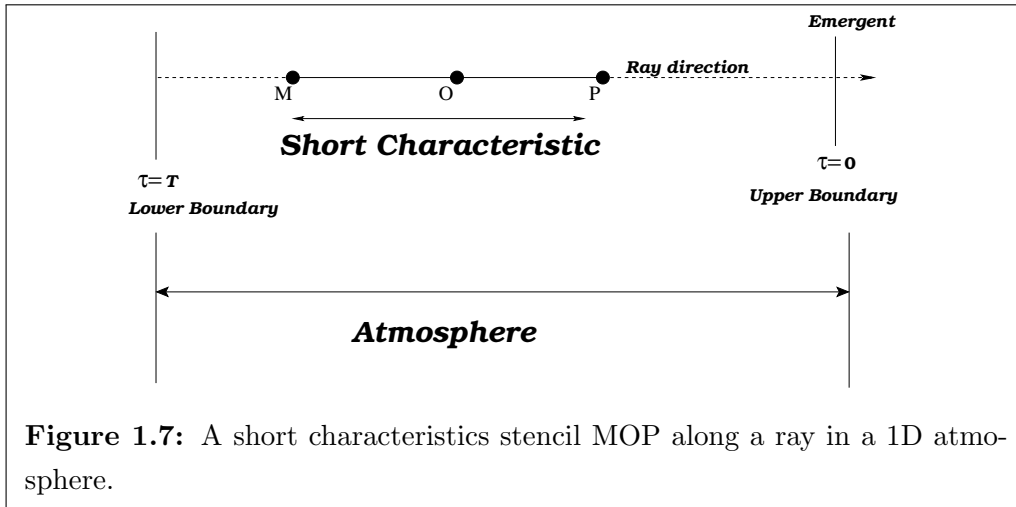


**Figure 1.6:** The observed linear polarization ( $Q/I$ ) profile taken from Holzreuter et al. (2006). The broad wings of the K line around the line center (at  $3933 \text{ \AA}$ ) are due to PRD effects. Top panel: observed intensity spectrum. Second panel: linearly polarized spectrum using a warm FALC model (thin solid, smooth line), the cold FALX model (dotted), the two-component model with FALC and FALX (thick solid), and observations (solid, noisy).

the problem of solving unpolarized 2D RT equation for a two-level atom model. A further step ahead was taken by Mihalas et al. (1978) who introduced the method of “short characteristics” for the formal solution of the multi-D RT equation. Kunasz & Auer (1988) developed an improved short characteristics method where the idea of direct integration of source terms over short stencils along the ray combined with the use of parabolic interpolation of the source terms were introduced. Here the authors considered the formal solution with a known source term. Kunasz & Olson (1988) solved the NLTE unpolarized 2D RT problem for a two-level model atom was solved using the method developed in Kunasz & Auer (1988). An improvement in the numerical stability was achieved by the introduction of monotonic interpolation in Auer & Paletou (1994). Auer et al. (1994) generalized the method to the case of 2D RT with horizontal periodic boundary conditions, including multi-level atoms. This method was generalized to the 3D case by Fabiani Bendicho & Trujillo Bueno (1999). A remarkable contributions to the field is by van Noort et al. (2002) who developed efficient formal solvers for unpolarized multi-D RT problems in Cartesian, cylindrical and spherical co-ordinate systems.

The idea of short characteristics is presented in Figure 1.7. A ray traveling in the atmosphere is shown. *MOP* is a short three-point stencil along the ray. Source terms at these three points are assumed to fit a parabola. A direct analytical integration of



the source terms with exponential attenuation terms is carried out to obtain a formal expression for the solution of RT equation. This solution is expressed in terms the values of source terms at points  $M$ ,  $O$  and  $P$  and the value of intensity (or Stokes vector in general), at the upwind point  $M$ . This process is continued until one reaches the outer boundary (piece wise integration). In the case of multi-D RT the short characteristics stencil has more surrounding points unlike 1D, and the source terms at points  $M$  and  $P$  are in general non-grid points (see Figure 1.8). This requires the source terms at  $M$  and  $P$  and the value of the upwind radiation field (intensity or the Stokes vector) at  $M$  to be interpolated using their respective values at the surrounding points.

The short characteristics method is numerically very efficient and has paved the way for obtaining reliable solutions of the line RT equations.

For simplicity, formal solution methods based on linear differencing techniques were successfully used by few authors in the past (see e.g., Adam 1990 and Folini 1998). Although linear differencing techniques give accurate solutions with the use of sufficiently fine spatial grids to represent the depth integration, the short characteristics method is superior in several aspects.

### Iterative methods

The formal solution of the RT equation requires specification of the source terms along the ray path. In NLTE RT problems (both unpolarized and polarized) the source term implicitly depends on the radiation field, and hence the RT equation is an integro-differential equation. The degree of non-locality enhances in the case of multi-D RT. For this reason, solving multi-D, self-consistent, NLTE radiation hydrodynamics problems was considered to be a formidable task until recent years. The inclusion of polarization increases the level of complexity much more.

A dramatic change in the field of solving line RT equations occurred with the advent of Approximate Lambda Iteration (ALI) methods (see Olson et al. 1986). It involved an application of the operator splitting methods, well known in applied mathematics, to the RT problems. Equation (1.18) is a linear differential equation as long as the source term  $\mathbf{S}$  is known. We can write its solution formally as

$$\mathbf{I}_x(\boldsymbol{\Omega}) = \Lambda_x(\boldsymbol{\Omega})[\mathbf{S}]. \quad (1.21)$$

Here  $\Lambda_x(\boldsymbol{\Omega})$  is an integral operator acting on  $\mathbf{S}$ . The angle integrated  $\Lambda_x$  operator is defined as

$$\mathbf{J}_x = \Lambda_x[\mathbf{S}]; \quad \mathbf{J}_x = \oint \frac{d\boldsymbol{\Omega}'}{4\pi} f \mathbf{I}, \quad (1.22)$$

where  $f$  again represents an abstract quantity which depends on the problem at hand. For the two-level atom system without the lower level polarization considered throughout this thesis, we can transform the RT problem to be a system of linear equations expressed in terms of the  $\Lambda_x$  operator. ALI methods consist of splitting the  $\Lambda_x$  operator as  $\Lambda_x = (\Lambda_x - \Lambda_x^*) + \Lambda_x^*$  (this idea was introduced to the RT theory by Cannon 1973). The  $\Lambda_x^*$  operator helps to accelerate the convergence of the iterative method. A choice that has proven optimum is the diagonal  $\Lambda_x^*$  of the  $\Lambda_x$  matrix. The first application of the ALI methods to multi-D RT was done by Kunasz & Olson (1988). The important feature of ALI methods is that the coupled RT problem is reduced to a set of formal solutions, while the coupling is taken care through iterations. An excellent review on ALI methods can be found

in Hubeny (2003). ALI methods are routinely applied to the line formation problems using the Jacobi iteration scheme. A class of methods that can provide a considerably higher rate of convergence are Gauss-Seidel and Successive Over Relaxation (SOR) introduced to RT by Trujillo Bueno & Fabiani Bendicho (1995). These methods were implemented in the 3D RT by Fabiani Bendicho & Trujillo Bueno (1999).

Another class of iterative methods which are extremely efficient are the projection methods. In this thesis we have systematically developed one of the most efficient projection techniques namely Stabilized Preconditioned Bi-Conjugate Gradient (Pre-BiCG-STAB) method to polarized multi-D RT with PRD and Hanle effect. Here we discuss details of the essential mathematical background based on which the Pre-BiCG-STAB method is developed in the field of applied mathematics. For a comprehensive description of these methods one can refer to the e-book Saad (2000).

We can pose the RT problem for a two-level model atom as a system of linear equations to be solved, symbolically represented as

$$\hat{A}\mathbf{x} = \mathbf{b}, \quad (1.23)$$

where  $\hat{A} = (a_{ij}), i, j = 1, 2, \dots, n$  is an  $n \times n$  matrix,  $\mathbf{x}$  and  $\mathbf{b}$  are the unknown and known vectors of length  $n$ . Iterative methods start with an initial guess, and therefore we have the residual vector  $\mathbf{b} - \hat{A}\mathbf{x}$  for each iterate. One example to improve an iterate is to “annihilate some component” of the residual vector. An ultimate aim of any iterative method is to make the residual vector go to zero, which means that we have obtained the solution of Equation (1.23).

Let  $\mathbf{x}^{(k)} = (\xi_1^{(k)}, \xi_2^{(k)}, \dots, \xi_n^{(k)})$  with  $k$  being the index of iteration and  $\mathbf{b} = (\beta_1, \beta_2, \dots, \beta_n)$ . Assuming an initial guess  $\mathbf{x}^{(0)}$  we get  $\mathbf{x}^{(1)}$  and so on, and after  $k$  steps we get  $\mathbf{x}^{(k+1)}$ . The Jacobi iteration determines  $i$ -th component of the next iterate. That is, at  $k$ -th iteration we determine  $(k+1)$ -th estimate for  $\mathbf{x}$ . But all the components are considered independent. The iteration scheme then determines  $i$ -th component of the next iterate so as to “annihilate” the  $i$ -th component of the residual vector namely

$$(\mathbf{b} - \hat{A}\mathbf{x}^{(k+1)})_i = 0. \quad (1.24)$$

Thus the component form of Jacobi iteration can be written as

$$\xi_i^{(k+1)} = \frac{1}{a_{ii}} \left[ \beta_i - \sum_{j=1; j \neq i}^n a_{ij} \xi_j^{(k)} \right], \quad i = 1, 2, \dots, n, \quad (1.25)$$

which can be written in a matrix form as

$$\mathbf{x}^{(k+1)} = \hat{D}^{-1}[\hat{E} + \hat{F}]\mathbf{x}^{(k)} + \hat{D}^{-1}\mathbf{b}, \quad (1.26)$$

where  $\hat{D}$  is the diagonal of the matrix  $\hat{A}$ ,  $\hat{E}$  is the strict lower part and  $\hat{F}$  is the strict upper part of the matrix  $\hat{A}$ .

Similarly a Gauss-Seidel iteration corrects the  $i$ -th component of the current approximate solution in the order  $i = 1, 2, \dots, n$  again to annihilate the  $i$ -th component of the residual. However this time, approximate solution is updated immediately after the new component is determined. The newly computed components  $\xi_i^{(k)}$ ,  $i = 1, 2, \dots, n$  can be changed within a working vector which is redefined at each relaxation step. The resulting component form of Gauss-Seidel iteration is

$$\xi_i^{(k+1)} = \frac{1}{a_{ii}} \left[ \beta_i - \sum_{j=1}^{i-1} a_{ij} \xi_j^{(k+1)} - \sum_{j=i+1}^n a_{ij} \xi_j^{(k)} \right], \quad i = 1, 2, \dots, n, \quad (1.27)$$

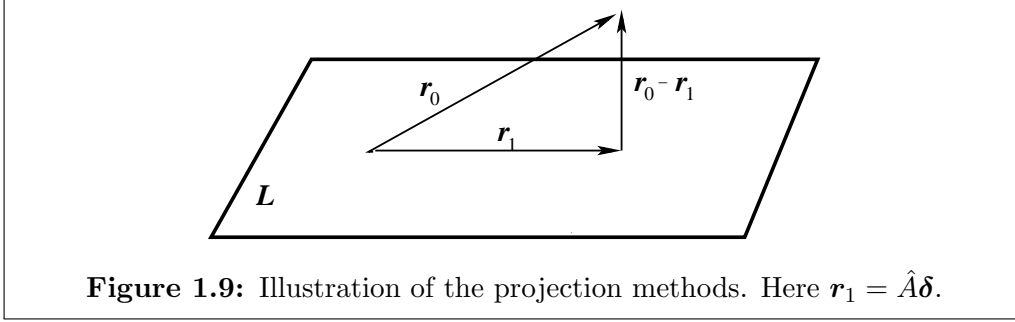
which can be written in a matrix form as

$$\mathbf{x}^{(k+1)} = [\hat{D} - \hat{E}]^{-1}\mathbf{b} + [\hat{D} - \hat{E}]^{-1}\hat{F}\mathbf{x}^{(k)}. \quad (1.28)$$

### The projection methods

The idea of a projection method is to extract an approximate solution to the problem imposed in Equation (1.23) from a subspace of  $\mathbb{R}^n$ . Let  $\mathcal{K}$  be this subspace which is a search space for such approximate solutions. In general,  $m$  constraints must be imposed to be able to extract such an approximation. A typical way of describing these constraints is to impose  $m$  independent orthogonality conditions. Specifically the residual vector  $\mathbf{b} - \hat{A}\tilde{\mathbf{x}}$  is constrained to be orthogonal to  $m$  linearly independent vectors where  $\tilde{\mathbf{x}}$  is an approximate solution. This forms another  $m$ -dimensional subspace  $\mathcal{L}$  which is called as the subspace of constraints. For instance, if the subspaces  $\mathcal{L}$  and  $\mathcal{K}$  are the same or related to each other linearly by  $\mathcal{L} = \hat{A}\mathcal{K}$  then these projections are called orthogonal projections.

In other words, a projection technique onto the subspace  $\mathcal{K}$  and orthogonal to  $\mathcal{L}$  is a process which finds an approximate solution  $\tilde{\mathbf{x}}$  to Equation (1.23) by imposing the condition that the residual vector  $\mathbf{b} - \hat{A}\tilde{\mathbf{x}}$  be orthogonal to  $\mathcal{L}$ . Generally  $\tilde{\mathbf{x}}$  is chosen such that  $\tilde{\mathbf{x}} \in \mathbf{x}_0 + \mathcal{K}$ , with  $\mathbf{x}_0$  being an arbitrary initial guess to the solution. Most standard techniques use a succession of such projections. A *Krylov subspace* method is a projection method for which the subspace  $\mathcal{K}$  is chosen to be  $\mathcal{K}_m(\hat{A}, \mathbf{r}_0) = (\mathbf{r}_0, \hat{A}\mathbf{r}_0, \dots, \hat{A}^{m-1}\mathbf{r}_0)$  where  $\mathbf{r}_0$  is the initial residual vector  $\mathbf{r}_0 = \mathbf{b} - \hat{A}\mathbf{x}_0$ .

**Definition:**

A projector or a projection operator  $P$  is any linear mapping from the  $n$ -dimensional complex space  $\mathbb{C}^n$  to itself such that  $P^2 = P$ . If  $P$  is a projector, then so is  $I - P$ , where  $I$  is the identity operator.

The result of a projection process can be interpreted in terms of actions of orthogonal projection operators on the initial residual vector.

**Proof:**

Let  $\mathcal{L} = \hat{A}\mathcal{K}$ . As above let  $\mathbf{x}_0$  be an arbitrary initial guess.

Now impose the condition  $\mathbf{r}_0 = \mathbf{b} - \hat{A}\mathbf{x}_0 \perp$  (orthogonal to)  $\mathcal{L}$ .

$\implies$  Choose  $\boldsymbol{\delta} \in \mathcal{K}$  such that  $\mathbf{r}_0 \perp \hat{A}\boldsymbol{\delta}$ .

Define the operator  $P$  such that  $P(\mathbf{r}_0) = \hat{A}\boldsymbol{\delta}$ .

$\implies$   $P$  is a projection operator because the quantity  $\hat{A}\boldsymbol{\delta}$  is the orthogonal projection of  $\mathbf{r}_0$  onto the subspace  $\mathcal{L} = \hat{A}\mathcal{K}$ .

Generally in Krylov subspace projection methods, next approximate solution is chosen to be  $\tilde{\mathbf{x}} = \mathbf{x}_0 + \boldsymbol{\delta}$ .

$\implies$  The residual vector  $\tilde{\mathbf{r}} = \mathbf{b} - \hat{A}\tilde{\mathbf{x}} = \mathbf{b} - \hat{A}\mathbf{x}_0 - \hat{A}\boldsymbol{\delta}$ .

Then  $\tilde{\mathbf{r}} = \mathbf{r}_0 - P(\mathbf{r}_0) = (I - P)\mathbf{r}_0$ .

Thus, the following proposition is valid:

If  $\tilde{\mathbf{x}}$  is the approximate solution obtained from a projection process on to  $\mathcal{K}$  (such as the Krylov subspace method), orthogonally to  $\mathcal{L} = \hat{A}\mathcal{K}$ , and if  $\tilde{\mathbf{r}} = \mathbf{b} - \hat{A}\tilde{\mathbf{x}}$  denotes the associated residual, then we have  $\tilde{\mathbf{r}} = (I - P)\mathbf{r}_0$ , with  $P$  being an orthogonal projector of  $\mathbf{r}_0$  onto the subspace  $\hat{A}\mathcal{K}$ . This means that the new residual also is an orthogonal projector of the initial residual  $\mathbf{r}_0$ . A projection method is illustrated in Figure 1.9.

In this thesis we have first developed the Pre-BiCG-STAB method for the unpolarized

RT in spherical geometry (chapter 3). Then we extend this method to polarized multi-D RT with PRD and Hanle effect in chapters 5 and 6 using angle-averaged PRD. In chapter 7 we further extend the method to handle angle-dependent PRD.

### 1.5.3 Applications of multi-D radiative transfer

Radiative flux is a crucial ingredient in the construction of model solar and stellar atmospheres. Due to computational limitations inclusion of full NLTE RT for constructing model atmospheres is not yet possible. With approximate description of the radiation several codes have been developed to construct 3D model atmospheres. Some important contributions in this field of research are by Nordlund (1982), Stein & Nordlund (1998, 2000), Skartlien (2000), Wedemeyer et al. (2004), i Vögler et al. (2005), Hansteen (2004), Hansteen et al. (2007), Leenaarts et al. (2007), Hayek (2008), Gudiksen et al. (2011).

However a legitimate question to be asked is whether these realistic simulations really realistic? Can the results be trusted? The photospheric simulations, there have been some positive answers by the works of Wedemeyer-Bohm & Rouppe van der Voort (2009), Pereira et al. (2009a, 2009b) who compared unpolarized intensity spectrum and the spectrum obtained through the model simulations.

For testing 3D chromospheric models one has to solve 3D NLTE RT equation and the statistical equilibrium equation to obtain the model spectrum and compare with the observations. To do such studies several numerical codes were developed. Some remarkable contributions in this field are due to Botnen (1997) who extended the MULTI code of Carlsson (1986) to 3D, and a general 3D RT solver presented in Hauschildt & Baron (2006, 2008). Further, Uitenbroek (2001) has developed a general multi-level NLTE RT code called the RH-code for 1D, 2D and 3D problems, which also solves the statistical equilibrium equation using the MALI scheme of Rybicki & Hummer (1991, 1992). The above codes are dedicated to the calculation of the unpolarized intensity spectrum.

The code for the solution of 3D NLTE RT equation based on the works in Auer et al. (1994), Trujillo Bueno & Fabiani Bendicho (1995), Fabiani Bendicho et al. (1997), Fabiani Bendicho & Trujillo Bueno (1999) can also compute the linearly polarized profiles in multi-level systems but under the assumption of CRD. They use the density matrix theory of Landi Degl’Innocenti and co-workers described in LL04.

Using the RH code for the solutions of unpolarized RT equation and the statistical equilibrium equations, Fluri et al. (2003a) have developed a code called POLY that solves

the non-magnetic polarized RT equation with angle-averaged PRD. They consider two-level atom model to solve the polarization part of the problem.

The NLTE calculations and the analysis of unpolarized intensity spectra using the unpolarized multi-level RT codes were done by for example, Asplund et al. (2003, 2004), Cayrel et al. (2007) and Uitenbroek & Criscuoli (2011). Linear polarization analysis using 3D NLTE RT codes is addressed rarely. Few important contributions are those by Trujillo Bueno et al. (2004), Asensio Ramos & Trujillo Bueno (2005), Trujillo Bueno & Shchukina (2007, 2009). A detailed review on the hydrodynamics and RT in 3D model atmospheres can be found in Carlsson (2009).

## 1.6 Modeling of the second solar spectrum

Realistic modeling of the second solar spectrum using detailed 1D RT calculations were performed for the first time by Faurobert-Scholl (1991, 1992, 1993, 1994). She used both CRD and PRD in line scattering. The linear polarization was considered in the photospheric line Sr I 4607 Å and the chromospheric line Ca I 4227 Å. Several studies using combinations of RH-code and POLY code were carried out by Fluri et al. (2003a), Holzreuter et al. (2005, 2006, 2007a, 2007b). They considered linear polarization in the chromospheric Ca I 4227 Å, Na I D2 and Ca II K lines. Faurobert et al. (2009) have carried out extensive studies of linear polarization in the chromospheric Ba II D2 line.

Modeling of second solar spectrum using multi-D RT was taken up only very recently (see e.g., Trujillo Bueno et al. 2004; Asensio Ramos & Trujillo Bueno 2005; Trujillo Bueno & Shchukina 2007, 2009). They considered the photospheric Sr I 4607 Å line.

In this thesis we consider modeling the Ca I 4227 Å line observed near the solar limb (chapter 9) and near the disk center (chapter 10) using 1D model atmospheres. We use combinations of RH-code and the POLY code. For the studies in chapter 10 we have extended the POLY code to include the Hanle effect by oriented magnetic fields and a general PRD theory for the Hanle effect developed by Bommier (1997a, 1997b).

Our ultimate goal is to develop methods which can be used to solve 3D NLTE polarized RT equation to compute linear polarization profiles using PRD scattering and realistic 3D model atmospheres. This can be done with an extension of the methods developed in this thesis to handle realistic model atmospheres combined with the RH-code of Uitenbroek (2001).



## 1.7 Outline of the thesis

In this thesis we have developed new and efficient methods to solve the NLTE RT problems (both unpolarized and polarized) in the contexts of astrophysical applications. We have tested these methods by comparing the results with well established benchmarks solutions and limiting cases. In some cases we have formulated the RT problem and provided the first solutions and analyzed the results. We have presented details of the formulations and conducted extensive studies on the solutions to prove their correctness. Finally we have carried out analysis of polarimetric observational data, and model them.

We have divided the thesis into three parts. In Chapter 1 we give a general introduction. Chapters 2 and 3 deal with Part-I of the thesis. Here we develop advanced numerical methods for the solution of RT problems in the case of 1D planar and spherical media. Chapters 4–8 are devoted to the Part-II. In this part we formulate and solve the polarized RT problems for non-magnetic and magnetic multi-D atmospheres with PRD scattering and Hanle effect using elegant and modern mathematical techniques. Chapters 9 and 10 constitute Part-III. In this part we analyze spectro-polarimetric data of the second solar spectrum, and model them using the standard 1D model solar atmospheres. Chapter 11 presents future outlook on the work described in this thesis.

### 1.7.1 Outline on part-I of the thesis

In chapter 2 we consider studies on the turbulent Hanle effect. The Hanle effect is used to determine weak turbulent magnetic fields in the solar atmosphere, usually assuming that the angular distribution is isotropic, the magnetic field strength is constant and that micro-turbulence holds, i.e., that the magnetic field correlation length is much smaller than a photon mean free path. In order to examine the sensitivity of turbulent magnetic field measurements to these assumptions, we study the dependence of Hanle effect on the magnetic field correlation length, its angular and strength distributions. We introduce a fairly general random magnetic field model characterized by a correlation length and a magnetic field vector distribution. Micro-turbulence is recovered when the correlation length goes to zero and macro-turbulence when it goes to infinity. RT equations are established for the calculation of the mean Stokes parameters and they are solved numerically by a Polarized Approximate Lambda Iteration (PALI) method. We show that optically thin spectral lines and optically very thick ones are insensitive to the correlation length of the magnetic field while spectral lines with intermediate optical depths (around 10-100) show some sensitivity to this parameter. The result is interpreted in terms of the mean number of scattering

events needed to create the surface polarization. It is shown that the single-scattering approximation holds good for thin and thick lines, but may fail for lines with intermediate thickness. The dependence of the polarization on the magnetic field vector probability density function (PDF) is examined in the micro-turbulent limit. A few PDFs with different angular and strength distributions, but equal mean value of the magnetic field, are considered. It is found that the polarization is in general quite sensitive to the shape of the magnetic field strength PDF and also somewhat to the angular distribution. The mean field derived from Hanle effect analysis of polarimetric data strongly depends on the choice of the field strength distribution used in the analysis. It is shown that micro-turbulence is in general a safe approximation. Some mathematical details related to chapter 2 are presented in Appendices A and B.

In chapter 3 we embark on developing a new and robust numerical technique called the Pre-BiCG-STAB method for the solution of RT equation in spherically symmetric media. This method is one of the best methods in applied mathematics for the solution of systems of linear equations. This method belongs to the class of iterative methods called projection methods. This method in particular is based on the construction of a set of bi-orthogonal vectors. The application of Pre-BiCG-STAB method in some benchmark tests shows that it is quite versatile, and can handle hard problems that may arise in astrophysical RT theory. The applicability of this method is discussed in the later chapters where we extend it to multi-D RT problems (chapters 5, 6, 7 and 8). In Appendix C we give some additional mathematical details related to chapter 3.

### 1.7.2 Outline on part–II of the thesis

The solution of the polarized line RT equation in multi-D media has been rarely addressed and only under the approximation that the changes of frequencies at each scattering are uncorrelated (the assumption of CRD). With the increase in the resolution power of telescopes, being able to handle RT in multi-D structures becomes absolutely necessary. In chapter 4 our first aim is to formulate the polarized RT equation for resonance scattering in multi-D media, using the elegant technique of irreducible spherical tensors  $\mathcal{T}_Q^K(i, \Omega)$ . Our second aim is to develop a numerical method of solution based on the PALI approach. We consider both CRD as well as PRD in line scattering. In a multi-D medium the radiation field is non-axisymmetrical even in the absence of a symmetry breaking mechanism such as an oriented magnetic field. We generalize here to the 3D case, the decomposition technique developed for the Hanle effect in a 1D medium which allows one to represent the Stokes parameters  $I, Q, U$  by a set of 6 cylindrically symmetrical functions. The scattering phase

matrix is expressed in terms of  $\mathcal{T}_Q^K(i, \boldsymbol{\Omega})$ , ( $i = 0, 1, 2, K = 0, 1, 2, -K \leq Q \leq +K$ ), with  $\boldsymbol{\Omega}$  being the direction of the outgoing ray. Starting from the definition of the source vector, we show that it can be represented in terms of 6 components  $S_Q^K$  independent of  $\boldsymbol{\Omega}$ . The formal solution of the multi-D transfer equation shows that the Stokes parameters can also be expanded in terms of the  $\mathcal{T}_Q^K(i, \boldsymbol{\Omega})$ . Because of the 3D-geometry, the expansion coefficients  $I_Q^K$  remain  $\boldsymbol{\Omega}$ -dependent. We show that each  $I_Q^K$  satisfies a simple transfer equation with a source term  $S_Q^K$  and that this transfer equation provides an efficient approach for handling the polarized transfer in multi-D geometries. A PALI method for 3D, associated to a core-wing separation method for treating PRD is developed. It is tested by comparison with 1D solutions and several benchmark solutions in the 3D case are given. Appendix D is devoted to detailed description of the numerical method of solution presented in chapter 4.

The work in chapter 5 is an up-gradation of the numerical methods developed in chapter 4. In chapter 5, we develop a faster and more efficient Pre-BiCG-STAB method to solve polarized 2D RT with PRD. The formal solution used in chapter 4 was based on a simple finite volume technique. In chapter 5 we use a more accurate formal solver, namely the well known 2D short characteristics method. Using the numerical methods developed in chapter 4, we can consider only simpler cases of finite 2D slabs due to computational limitations. It was a first step towards solving polarized multi-D problems with PRD. Using the superior methods developed in chapter 5, we could compute PRD solutions in 2D media, in the more difficult context of semi-infinite 2D atmospheres as well. We present several solutions which may serve as benchmarks for future studies in this area. In Appendix E we discuss the simplification brought about by the symmetry properties of the polarized radiation field in a 2D medium and in Appendix F we prove these symmetry relations.

In chapters 4 and 5 we assumed Rayleigh scattering as the only source of linear polarization ( $Q/I, U/I$ ). In chapter 6 we extend these previous works to include the effect of weak oriented magnetic fields (Hanle effect) on line scattering. We generalize the technique of Stokes vector decomposition in terms of the irreducible spherical tensors  $\mathcal{T}_Q^K$ , developed in chapter 4, to the case of RT with Hanle effect. A fast iterative Pre-BiCG-STAB method for the solution of polarized 2D RT equation, developed in chapter 5 is now generalized to the case of RT in magnetized 3D media. We use the efficient short-characteristics formal solution method for multi-D media, generalized appropriately to the present context. The main results obtained in chapter 6 are the following: (1) A comparison of emergent ( $I, Q/I, U/I$ ) profiles formed in 1D media with the corresponding emergent, spatially averaged profiles formed in multi-D media shows that in the spatially resolved structures, the assumption of 1D may lead to large errors in linear polarization, especially in the line

wings. (2) The multi-D RT in semi-infinite non-magnetic media causes a strong spatial variation of the emergent  $(Q/I, U/I)$  profiles, which is more pronounced in the line wings. (3) The presence of a weak magnetic field modifies the spatial variation of the emergent  $(Q/I, U/I)$  profiles in the line core, by producing significant changes in their magnitudes. Appendices G–J are devoted to provide the essential mathematical details that are related to the formulations presented in chapter 6.

In the previous three chapters (4, 5 and 6) we have been investigating the nature of Stokes profiles formed in multi-D media including PRD in line scattering. For numerical simplicity, so far we restricted our attention to the particular case of PRD functions which are averaged over all the incident and scattered directions. In chapter 7 we formulate the polarized RT equation in multi-D media that takes into account Hanle effect with angle-dependent PRD functions. We generalize here to the multi-D case, the method of Fourier series expansion of angle-dependent PRD functions originally developed for RT in 1D geometry. We show that the Stokes source vector  $\mathbf{S} = (S_I, S_Q, S_U)^T$  and the Stokes vector  $\mathbf{I} = (I, Q, U)^T$  can be expanded in terms of infinite sets of components  $\tilde{\mathbf{S}}^{(k)}$ ,  $\tilde{\mathbf{I}}^{(k)}$  respectively,  $k \in [0, +\infty)$ . We show that the components  $\tilde{\mathbf{S}}^{(k)}$  become independent of the azimuthal angle ( $\varphi$ ) of the scattered ray, whereas the components  $\tilde{\mathbf{I}}^{(k)}$  remain dependent on  $\varphi$  due to the nature of RT in multi-D geometry. We also establish that  $\tilde{\mathbf{S}}^{(k)}$  and  $\tilde{\mathbf{I}}^{(k)}$  satisfy a simple transfer equation, which can be solved by any iterative method like PALI or a Biconjugate-Gradient type projection method, provided we truncate the Fourier series to have a finite number of terms.

The solution of polarized RT equation with angle-dependent PRD is a challenging problem. Modeling the linear polarization of strong lines in the solar spectrum often requires solving angle-dependent line transfer problems in 1D or multi-D geometries. It is essential to have a clear picture of the relative importance of angle-dependent PRD effects and the multi-D transfer effects and particularly their combined influence on the line polarization. The purpose of chapter 8 is to develop a physical and mathematical understanding of these two effects. This would help in a quantitative analysis of the second solar spectrum (the linearly polarized spectrum of the Sun). In chapter 8 we reduce the Stokes vector transfer equation to a simpler form using a Fourier decomposition technique. A fast numerical method is also devised to solve the concerned multi-D transfer problem. We show that the angle-dependent PRD effects are significant, and can not be ignored in a fine quantitative analysis of the line polarization. These effects are accentuated by the finite dimensionality of the medium (multi-D transfer). The presence of magnetic fields (Hanle effect) modifies the impact of these two effects to a considerable extent. In Appendices K

and L we discuss the mathematical details of the phase matrices used in chapter 8 and the symmetry breaking properties of angle-dependent PRD functions respectively.

### 1.7.3 Outline on part–III of the thesis

To model the second solar spectrum one needs to solve the polarized RT equation. For strong resonance lines PRD effects must be accounted for, which makes the problem computationally demanding. The ‘last scattering approximation’ (LSA) is a concept that has been introduced to make this highly complex problem more tractable. An earlier application of a simple LSA version could successfully model the wings of the strong Ca I 4227 Å resonance line in Stokes  $Q/I$  (fractional linear polarization), but failed completely to reproduce the observed  $Q/I$  peak in the line core. Since the magnetic-field signatures from the Hanle effect only occur in the line core, we need to generalize the existing LSA approach if it is to be useful for diagnostics of chromospheric and turbulent magnetic fields. In chapter 9 we explore three different approximation levels for LSA and compare each of them with the benchmark represented by the solution of the full polarized RT, including PRD effects. The simplest approximation level is LSA-1, which uses the observed center to limb variation of the intensity profile to obtain the anisotropy of the radiation field at the surface, without solving any RT equation. In contrast, the next two approximation levels use the solution of the unpolarized RT equation to derive the anisotropy of the incident radiation field and use it as input. In the case of LSA-2 the anisotropy at level  $\tau_\lambda = \mu$  is used, the atmospheric level from which an observed photon is most likely to originate. LSA-3 on the other hand makes use of the full depth dependence of the radiation anisotropy. The  $Q/I$  formula for LSA-3 is obtained by keeping the first term in a series expansion of the  $Q$ -source function in powers of the mean number of scattering events. Computationally, LSA-1 is 21 times faster than LSA-2, which is 5 times faster than the more general LSA-3, which itself is 8 times faster than the exact polarized RT approach. Comparison of the calculated  $Q/I$  spectra with the RT benchmark shows excellent agreement for LSA-3, including good modeling of the  $Q/I$  core region with its PRD effects. In contrast both LSA-1 and LSA-2 fail to model the core region. The RT and LSA-3 approaches are then applied to model the observed  $Q/I$  profile of the Ca I 4227 Å line in quiet regions of the Sun. Apart from a global scale factor, both give a very good fit to the  $Q/I$  spectra for all the wavelengths, including the core peak and blend line depolarization. We conclude that LSA-3 is an excellent substitute for full polarized RT and can be used to interpret the second solar spectrum, including the Hanle effect with PRD. It also allows the techniques developed for unpolarized 3D RT to be applied to modeling of the second solar spectrum.

In Appendix M we discuss in detail the phase matrices used in the calculations performed in chapter 9.

Coherent scattering of limb darkened radiation is responsible for the generation of the second solar spectrum. This second solar spectrum is usually observed near the limb of the Sun, where the polarization amplitudes are the largest. At the center of the solar disk the linear polarization is zero for an axially symmetric atmosphere. Any mechanism that breaks the axial symmetry (like the presence of an oriented magnetic field, or resolved inhomogeneities in the atmosphere) can generate a non-zero linear polarization. In chapter 10 we study the linear polarization near disk center in a weakly magnetized region, where the axi-symmetry is broken. We present polarimetric ( $I$ ,  $Q/I$ ,  $U/I$ ,  $V/I$ ) observations of the Ca I 4227 Å line recorded around  $\mu = \cos \theta = 0.9$  (where  $\theta$  is the heliocentric angle) and a modeling of these observations. The high sensitivity of the polarimeter (ZIMPOL) makes it possible to measure the weak polarimetric signals with great accuracy. The modeling of these high quality observations requires the solution of polarized RT equation in the presence of a magnetic field. For this we use standard 1D model atmospheres. We show that the linear polarization is mainly produced by the Hanle effect (rather than by the transverse Zeeman effect), while the circular polarization is due to the longitudinal Zeeman effect. A unique determination of the full  $\mathbf{B}$  vector may be achieved when both effects are accounted for. The field strengths required for the simultaneous fitting of ( $Q/I$ ,  $U/I$ ,  $V/I$ ) are in the range 10–50 G. The shapes and signs of the  $Q/I$  and  $U/I$  profiles are highly sensitive to the orientation of the magnetic field. In Appendices N and O we discuss the mathematical details of the phase matrices used in chapter 10 and some additional details related to the calculations in chapter 10.

Chapter 11 constitutes conclusions from the studies undertaken in this thesis and future outlook into possible progress in this field. We give a chapter-wise summary of the thesis presenting the important results obtained in each of the chapters. Finally we discuss the application of the work done in this thesis to realistic modeling of the spectro-polarimetric observations using 3D magnetohydrodynamical model atmospheres of the Sun.

All the mathematical details are presented in the form of a collection of Appendices A–O, which pertain to different chapters of the thesis as discussed above. A detailed bibliography is prepared and included at the end of the thesis.

## Part-I

Advanced numerical methods to  
solve line radiative transfer equation  
in one-dimensional media





## Chapter 2

# The Hanle effect in a random magnetic field

*The contents of this chapter are based on the following publication:*

Frisch, H., Anusha, L. S., Sampoorna, M., Nagendra, K. N., 2009, **A&A**, 501, 335-348

### 2.1 Introduction

As pointed out by Stenflo (1982; see also 1994, 2010), the Hanle effect provides a powerful diagnostic for the detection of a weak turbulent magnetic field. The physical origin of this field, and symmetry properties of the observed linear polarization, suggest that the field scale of variation is small compared to the mean free path of photons and hence that “micro-turbulence” could be assumed. This allows one to replace all the physical parameters depending on the magnetic field by their average over the magnetic field vector probability density function (PDF). All the determinations of solar turbulent magnetic fields have been carried out so far with this approximation (Faurobert-Scholl 1993, 1996; Faurobert et al. 2001; Trujillo Bueno et al. 2004; Bommier et al. 2005; Faurobert et al. 2009). In addition, it is usually assumed that the magnetic field PDF is isotropically distributed, and that its strength has a single value. The Hanle problem reduces then to a resonance polarization problem with a modified polarization parameter that is in general smaller (Stenflo 1982, 1994).

In Frisch 2006 (henceforth referred to as HF06), a model magnetic field has been introduced allowing one to examine the possible effects of a finite magnetic field correlation length (comparable to a typical photon mean free path). Equations have been established for the calculation of the mean Stokes parameters, but no numerical results were given. In this chapter (see also Frisch et al. 2009), the equations given in HF06 are rewritten in a

form easily amenable to a numerical solution. An iterative method of solution of the Approximate Lambda Iteration (ALI) type is used to calculate the mean Stokes parameters. We examine their dependence on the correlation length of the magnetic field and analyze the results in terms of the mean number of scattering events contributing to the formation of the surface polarization. We also investigate the sensitivity of the mean Stokes parameters to the shape of the magnetic field PDF, the objective being to see whether the Hanle effect can provide some clue on the behavior of this quantity.

In Section 2.2, we describe the magnetic field, the atomic and atmospheric models (they are the same as in HF06). We establish the radiative transfer (RT) equations for the calculation of the mean Stokes parameters in Section 2.3. In Section 2.4 we describe an ALI type numerical method of solution. In Section 2.5 we describe different types of PDFs used in our investigation. The finite correlation effects are presented in Section 2.6 and analyzed in Section 2.7. Finally, in Section 2.8, we calculate the mean polarization for various types of magnetic field strength PDFs, in the framework of micro-turbulence. Some technical details about RT equations and calculations of the mean Stokes parameters are presented in Appendices A and B.

## 2.2 Assumptions

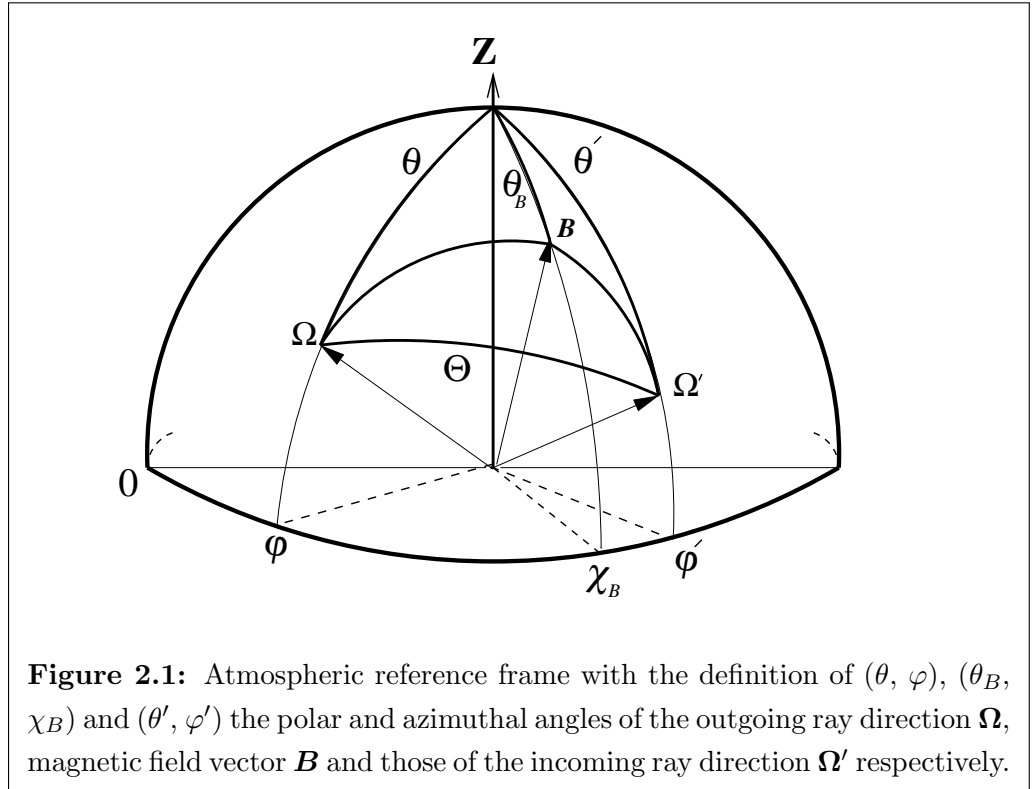
We consider a two-level atom with unpolarized ground level and assume complete frequency redistribution (CRD). The  $4 \times 4$  redistribution matrix is then of the form

$$\hat{R}(x, x', \boldsymbol{\Omega}, \boldsymbol{\Omega}', \mathbf{B}) = \phi(x)\phi(x')\hat{P}_H(\boldsymbol{\Omega}, \boldsymbol{\Omega}', \mathbf{B}), \quad (2.1)$$

where  $x'$  and  $x$  are the frequencies of incident and scattered beams measured in Doppler width units from line center and  $\boldsymbol{\Omega}'$ ,  $\boldsymbol{\Omega}$  their directions. The function  $\phi(x)$  is the line absorption profile normalized to unity. The elements of the polarization matrix can be written in the form

$$[\hat{P}_H(\boldsymbol{\Omega}, \boldsymbol{\Omega}', \mathbf{B})]_{ij} = \sum_{KQ} \mathcal{T}_Q^K(i, \boldsymbol{\Omega}) \sum_{Q'} \mathcal{M}_{QQ'}^K(\mathbf{B})(-1)^{Q'} \mathcal{T}_{-Q'}^K(j, \boldsymbol{\Omega}'), \quad (2.2)$$

where  $\mathcal{T}_Q^K(i, \boldsymbol{\Omega})$  are the irreducible spherical tensors for polarimetry introduced by Landi Degl'Innocenti (1984). The index  $K$  takes the values  $K = 0, 1, 2$ . The index  $Q$  takes  $(2K + 1)$  integer values in the range  $-K \leq Q \leq +K$ . For the lower index, we have followed the usual notation  $Q$ . There should be no confusion with the Stokes  $Q$  parameter that never appears as an index in this chapter. The indices  $i, j$  refer to the Stokes parameters ( $i, j = 0, \dots, 3$ ). The coefficients  $\mathcal{T}_Q^K(i, \boldsymbol{\Omega})$  with  $i = 1, 2$ , associated to linear polarization,



depend also on a reference angle, often denoted  $\gamma$ , needed to define the reference frame of the electric field in a plane perpendicular to  $\Omega$  (see Figure 5.14 in Landi Degl’Innocenti & Landolfi 2004, henceforth LL04). Hanle effect measurements are usually performed close to the solar limb, with the spectrograph slit parallel to the nearest limb. Stokes  $Q$  is negative along the slit (positive in the direction perpendicular to it) for  $\gamma = 0$ . The elements  $\mathcal{M}_{QQ'}^K$  of the magnetic kernel depend on the magnetic field vector, on atomic parameters and collision rates (for details see Appendix A).

In this chapter we consider a one-dimensional (1D) medium (plane-parallel atmosphere). The direction of the magnetic field and of the radiation beams are reckoned in an atmospheric reference frame with the  $Z$ -axis along the outward normal to the medium. The polar angles of the magnetic field direction are denoted by  $\theta_B$  and  $\chi_B$ ; the polar angles of the directions  $\Omega$  and  $\Omega'$  are denoted by  $\theta, \varphi$  and  $\theta', \varphi'$  (see Figure 2.1).

The random magnetic field  $\mathbf{B}$  is modeled by a Kubo–Anderson process (KAP). It is a Markov process, discontinuous, stationary, and piecewise constant (Brissaud & Frisch 1971, 1974). By definition, a random function  $m(t)$  is a KAP, if the jumping times  $t_i$  are uniformly and independently distributed in  $[-\infty, +\infty]$  according to a Poisson distribution.

Further,  $m(t) = m_i$  for  $t_i \leq t \leq t_{i+1}$  where the  $m_i$  are independent random variables with the same probability density  $P(m)$ . A KAP is thus fully characterized by a probability density  $P(m)$  and a correlation time  $t_{\text{cor}} = 1/\nu_t$ , with  $\nu_t$  the density of jumping times on the time axis (Papoulis, 1968, p. 557). For a KAP, the covariance  $\langle m(t)m(t') \rangle$  varies as  $e^{-\nu_t|t-t'|}$ . Hence, the spectrum is algebraic.

For the Hanle effect, polarization is created by a scattering process and this implies that the photons make a random walk inside the medium. If the magnetic field is a Markov process, say along the normal to a plane-parallel atmosphere, the radiation field at a point  $\mathbf{r}$ , depends on magnetic field values below and above the point  $\mathbf{r}$ . To take advantage of the Markov character of the magnetic field, it is necessary to simplify a little and assume that the magnetic field is a random process in time, defined by a density  $\nu_t$  and a probability density  $P(\mathbf{B})$ . This approach was first used for random velocities with a finite correlation length by Frisch & Frisch (1976). Its shortcoming is that it ignores correlations between photons that return to a same turbulent element after having been scattered a number of times (Frisch & Frisch 1975). The radiation field  $\mathbf{I}$  has then to be taken as time dependent. Standard techniques of solutions for stochastic differential equations with Markov coefficients become applicable (Brissaud & Frisch 1974). They rely on the crucial remark that the joint random process in time  $\{\mathbf{B}(t); \mathbf{I}(t)\}$  is also a Markov process. To simplify the notation we have omitted other independent variables on which the radiation field depends. As shown in HF06, the combination of the time-dependent RT equation, with the evolution equation for the probability density of the joint process  $\{\mathbf{B}(t); \mathbf{I}(t)\}$ , provides a time-dependent RT equation for a conditional mean Stokes vector  $\mathbf{I}(t, \mathbf{r}, x, \boldsymbol{\Omega} | \mathbf{B})$ . For this radiation field,  $\mathbf{B}$  plays the role of an additional independent variable with values distributed according to the probability density  $P(\mathbf{B})$  (for the definition of the conditional mean see HF06).

The next step is to consider the stationary solution,  $\mathbf{I}(\mathbf{r}, x, \boldsymbol{\Omega} | \mathbf{B})$ , for  $t \rightarrow \infty$ . It satisfies an RT equation which has the usual advection, scattering and primary source terms, but contains also an additional term describing the action of the magnetic field. Somewhat similar equations (without the scattering term) have been introduced for the Zeeman effect by Carroll & Staude (2005). The mean Stokes parameters that one is looking for are given by

$$\langle \mathbf{I} \rangle(\mathbf{r}, x, \boldsymbol{\Omega}) = \int P(\mathbf{B}) \mathbf{I}(\mathbf{r}, x, \boldsymbol{\Omega} | \mathbf{B}) d^3 \mathbf{B}. \quad (2.3)$$

In the next Section we construct the stationary RT equation for the conditional mean Stokes vector. We work with the irreducible components of the Stokes vector because they

satisfy RT equations that are simpler than the RT equations for the Stokes parameters themselves.

## 2.3 The transfer problem

We specialize now to the case of a 1D slab. We introduce the frequency averaged line optical depth  $\tau$  defined by  $d\tau = -\kappa(z)dz$  with  $z$  the coordinate along the vertical axis (see Figure 2.1) and  $\kappa(z)$  the absorption coefficient per unit length. We denote by  $T$  the total optical thickness of the slab with the surface at  $\tau = 0$  towards the observer. We assume that the incident radiation is zero on both sides of the slab.

For the deterministic Hanle effect with CRD, each component  $S_i(\tau, \boldsymbol{\Omega}; \mathbf{B})$  of the emission term in the RT equation (sum of the scattering and primary source terms) has an expansion of the form

$$S_i(\tau, \boldsymbol{\Omega}; \mathbf{B}) = \sum_{KQ} \mathcal{T}_Q^K(i, \boldsymbol{\Omega}) S_Q^K(\tau; \mathbf{B}), \quad i = 0, \dots, 3. \quad (2.4)$$

Starting from this expression, one can show (Frisch 2007, henceforth HF07) that the Stokes parameters have a similar expansion that can be written as

$$I_i(\tau, x, \boldsymbol{\Omega}; \mathbf{B}) = \sum_{KQ} \mathcal{T}_Q^K(i, \boldsymbol{\Omega}) I_Q^K(\tau, x, \mu; \mathbf{B}), \quad i = 0, \dots, 3, \quad (2.5)$$

where  $\mu = \cos \theta$ . Whereas the four Stokes parameters (three if one considers only linear polarization) depend on the two polar angles  $\theta$  and  $\varphi$  defining  $\boldsymbol{\Omega}$ , the nine irreducible components  $I_Q^K$  (six only for linear polarization) are independent of the azimuthal angle  $\varphi$ . This decomposition holds also for the conditional mean Stokes vector  $\mathbf{I}(\tau, x, \boldsymbol{\Omega}|\mathbf{B})$  and the corresponding source vector  $\mathbf{S}(\tau, \boldsymbol{\Omega}|\mathbf{B})$ . The components  $I_Q^K$  and  $S_Q^K$  can be regrouped into nine (or six) component vectors  $\mathcal{I}(\tau, x, \mu|\mathbf{B})$  and  $\mathcal{S}(\tau|\mathbf{B})$ . We will be using calligraphic letters for the vectors  $\mathcal{I}$  and  $\mathcal{S}$  constructed with the  $KQ$  decomposition and refer to them for simplicity as the ‘‘Stokes vector’’ and ‘‘source vector’’. We now give in Section 2.3.1 the RT equation satisfied by  $\mathcal{I}(\tau, x, \mu|\mathbf{B})$  and construct in Section 2.3.2 an integral equation for  $\mathcal{S}(\tau|\mathbf{B})$ .

### 2.3.1 Transfer equation for the conditional mean Stokes parameters

Proceeding as described in Section 2.2 (see also HF06), we find that  $\mathcal{I}(\tau, x, \mu|\mathbf{B})$  satisfies the RT equation

$$\begin{aligned} \mu \frac{\partial \mathcal{I}(\tau, x, \mu|\mathbf{B})}{\partial \tau} &= \phi(x) [\mathcal{I}(\tau, x, \mu|\mathbf{B}) - \mathcal{S}(\tau|\mathbf{B})] \\ -\nu \int \Pi_1(\mathbf{B}, \mathbf{B}') \mathcal{I}(\tau, x, \mu|\mathbf{B}') d^3 \mathbf{B}', \end{aligned} \quad (2.6)$$

where

$$\mathcal{S}(\tau|\mathbf{B}) = \mathcal{G}(\tau) + \hat{M}(\mathbf{B}) \mathcal{J}(\tau|\mathbf{B}), \quad (2.7)$$

with

$$\mathcal{J}(\tau|\mathbf{B}) = \int_{-\infty}^{+\infty} \frac{1}{2} \int_{-1}^{+1} \phi(x) \hat{\Psi}(\mu) \mathcal{I}(\tau, x, \mu|\mathbf{B}) d\mu dx. \quad (2.8)$$

The operator  $\nu \Pi_1$  describes the effects of the random magnetic field. The factor  $\nu$  is now the mean number of jumping points per unit optical depth. It is related to the density of jumping times  $\nu_t$  by  $\nu = \nu_t / c\kappa(z)$ , with  $c$  the speed of light. For simplicity we assume  $\nu$  independent of  $\tau$ , but a depth-dependent  $\nu$  could be handled (see e.g. Auvergne et al. 1973). Micro-turbulence corresponds to  $\nu = \infty$  and macro-turbulence to  $\nu = 0$ . Macro and micro-turbulence are also referred to as the optically thick and optically thin limits. The operator  $\Pi_1$  is defined by

$$\Pi_1 = - [\delta(\mathbf{B} - \mathbf{B}') - P(\mathbf{B}')]. \quad (2.9)$$

The matrix  $\hat{M}(\mathbf{B})$  describes the Hanle effect. Construction rules for its elements  $\mathcal{M}_{QQ'}^K(\mathbf{B})$  are given in Equation (A.4). When the magnetic field is zero,  $\hat{M}(\mathbf{B})$  reduces to a diagonal matrix with elements depending only on the atomic model and collision rates (see Appendix A). The matrix  $\hat{\Psi}(\mu)$  describes resonance polarization. Its elements  $\Psi_Q^{KK'}$  are real quantities. They can be found in LL04 (Appendix A20) (see also Landi Degl'Innocenti et al. 1990; HF07). The primary source term  $\mathcal{G}(\tau)$  is non-random.

Averaging Equation (2.6) over  $P(\mathbf{B})$ , we see that  $\langle \mathcal{I} \rangle(\tau, x, \mu)$  satisfies the RT equation

$$\mu \frac{\partial \langle \mathcal{I} \rangle(\tau, x, \mu)}{\partial \tau} = \phi(x) [\langle \mathcal{I} \rangle(\tau, x, \mu) - \langle \mathcal{S} \rangle(\tau)], \quad (2.10)$$

where  $\langle \mathcal{I} \rangle$  and  $\langle \mathcal{S} \rangle$  are averages over the magnetic field vector PDF (see Equation (2.3)). It is not possible to write an integral equation for  $\langle \mathcal{S} \rangle(\tau)$  (except in the micro-turbulent limit). One must first calculate  $\mathcal{S}(\tau|\mathbf{B})$  and then average it over  $P(\mathbf{B})$ .

### 2.3.2 Integral equation for $\mathcal{S}(\tau|\mathbf{B})$

With the boundary condition that there is no incident radiation on the outer surfaces of the slab, the formal solution of Equation (2.6) can be written as

$$\mathcal{I}(\tau, x, \mu|\mathbf{B}) = \int_{\tau}^T \exp\left[-\frac{\tau' - \tau}{\mu}(\phi - \nu\Pi_1)\right] \phi(x) \mathcal{S}(\tau'|\cdot) \frac{d\tau'}{\mu}; \quad \mu > 0; \quad (2.11)$$

$$\mathcal{I}(\tau, x, \mu|\mathbf{B}) = - \int_0^{\tau} \exp\left[-\frac{\tau' - \tau}{\mu}(\phi - \nu\Pi_1)\right] \phi(x) \mathcal{S}(\tau'|\cdot) \frac{d\tau'}{\mu}; \quad \mu < 0. \quad (2.12)$$

The operator  $\Pi_1$  acts on the variable denoted “.”. It is standard notation for cases when the variable cannot be written explicitly. The action of  $\Pi_1$  can be calculated by considering the Laplace transform

$$\int_0^{\infty} e^{-pE\varpi} e^{\varpi\nu\Pi_1} d\varpi = (pE - \nu\Pi_1)^{-1}, \quad (2.13)$$

where  $\varpi = |\tau' - \tau|/\mu$  and  $E$  is the identity operator. To ensure convergence  $\Re(p) > 0$ . Solving for  $f(\mathbf{B})$  the equation

$$(pE - \nu\Pi_1)f(\mathbf{B}) = g(\mathbf{B}), \quad (2.14)$$

where  $g(\mathbf{B})$  is known, one finds a simple expression that is easily expressed in terms of elementary Laplace transforms (for details see HF06; also Frisch & Frisch 1976). We thus obtain

$$\begin{aligned} \mathcal{I}(\tau, x, \mu|\mathbf{B}) &= \int_{\tau}^T \phi(x) e^{-\frac{\tau' - \tau}{\mu}\phi(x)} \left\{ e^{-\frac{\tau' - \tau}{\mu}\nu} \mathcal{S}(\tau'|\mathbf{B}) \right. \\ &+ \left. [1 - e^{-\frac{\tau' - \tau}{\mu}\nu}] \int P(\mathbf{B}') \mathcal{S}(\tau'|\mathbf{B}') d^3\mathbf{B}' \right\} \frac{d\tau'}{\mu}; \quad \mu > 0; \end{aligned} \quad (2.15)$$

$$\begin{aligned} \mathcal{I}(\tau, x, \mu|\mathbf{B}) &= - \int_0^{\tau} \phi(x) e^{-\frac{\tau' - \tau}{\mu}\phi(x)} \left\{ e^{-\frac{\tau' - \tau}{\mu}\nu} \mathcal{S}(\tau'|\mathbf{B}) \right. \\ &+ \left. [1 - e^{-\frac{\tau' - \tau}{\mu}\nu}] \int P(\mathbf{B}') \mathcal{S}(\tau'|\mathbf{B}') d^3\mathbf{B}' \right\} \frac{d\tau'}{\mu}; \quad \mu < 0. \end{aligned} \quad (2.16)$$

The combination of Eqs. (2.15) and (2.16) with Equation (2.7) yields the integral equation

$$\mathcal{S}(\tau|\mathbf{B}) = \mathcal{G}(\tau) + \hat{M}(\mathbf{B})\Lambda[\mathcal{S}], \quad (2.17)$$

where

$$\Lambda[\mathcal{S}] = \int_0^T d\tau' \left\{ \hat{\mathcal{L}}(\tau - \tau'; \nu) \mathcal{S}(\tau' | \mathbf{B}) + \left[ \hat{\mathcal{L}}(\tau - \tau'; 0) - \hat{\mathcal{L}}(\tau - \tau'; \nu) \right] \int P(\mathbf{B}') \mathcal{S}(\tau' | \mathbf{B}') d^3 \mathbf{B}' \right\}, \quad (2.18)$$

with

$$\hat{\mathcal{L}}(\tau; \nu) = \int_{-\infty}^{+\infty} \int_0^1 \frac{1}{2\mu} \hat{\Psi}(\mu) e^{-\frac{|\tau|}{\mu}(\phi(x)+\nu)} \phi^2(x) d\mu dx. \quad (2.19)$$

For  $\nu = 0$ , we recover the usual kernel matrix for resonance scattering with CRD, denoted here by  $\hat{K}(\tau)$  (see e.g. Landi Degl'Innocenti et al. 1990; Nagendra et al. 1998), and for  $\nu = \infty$ , we have  $\hat{\mathcal{L}}(\tau; \nu) = 0$ . Thus, in the micro-turbulent limit, the averaging of Equation (2.17) over  $P(\mathbf{B})$  yields a standard integral equation

$$\langle \mathcal{S} \rangle(\tau) = \mathcal{G}(\tau) + \langle \hat{M}(\mathbf{B}) \rangle \int_0^T \hat{K}(\tau - \tau') \langle \mathcal{S} \rangle(\tau') d\tau', \quad (2.20)$$

where  $\langle \hat{M}(\mathbf{B}) \rangle$  is the mean value of  $\hat{M}(\mathbf{B})$ , and  $\hat{K}(\tau) = \hat{\mathcal{L}}(\tau; 0)$ .

## 2.4 A PALI type numerical method of solution

Several numerical methods of solution have been developed to solve integral equations arising in the study of the Hanle effect with deterministic or micro-turbulent magnetic field. In Landi Degl'Innocenti et al. (1990), the system of linear integral equations for the components  $\mathcal{S}_Q^K(\tau)$  is transformed into a system of linear equations for the  $\mathcal{S}_Q^K(\tau_i)$  with  $\tau_i$  the optical depth grid points. In this reference, the unknown functions are actually the density matrix elements  $\rho_Q^K(\tau)$ , but for a two-level atom with CRD,  $\rho_Q^K(\tau)$  and  $\mathcal{S}_Q^K(\tau)$  are proportional (see e.g. Landi Degl'Innocenti & Bommier 1994).

Iterative methods of the ALI type have been developed for the Hanle effect with CRD (Nagendra et al. 1998; Manso Sainz & Trujillo Bueno 1999, 2003) and partial frequency redistribution (PRD) (Nagendra et al. 1999; Fluri et al. 2003b; Sampoorana et al. 2008a). For PRD, the unknown functions depend on two independent variables: optical depth and frequency. Here we have a similar problem, the independent variables being now the optical depth and the magnetic field vector. We have developed a PALI method (P for polarized) described below to solve the integral equation (2.17) for  $\mathcal{S}(\tau | \mathbf{B})$ . The results are presented in Section 2.6.

We have followed a standard approach by which one introduces an approximate  $\Lambda$  operator denoted by  $\Lambda^*$ , choosing for  $\Lambda^*$  the diagonal of  $\Lambda$  with respect to optical depth.



This is the so-called Jacobi scheme (Stoer & Bulirsch, 1983). It is the only one that has been used for PRD (see e.g. the review by Nagendra & Sampoorna 2009 and references therein) and seemed to be an appropriate choice for exploratory work with random magnetic fields. More efficient iteration methods based on the Gauss–Seidel scheme have been developed for CRD (see e.g. Trujillo Bueno & Fabiani Bendicho 1995; Léger et al. 2007).

The Jacobi iteration scheme is

$$\left[ \hat{E} - \hat{M}(\mathbf{B})\Lambda^* \right] \delta\mathcal{S}^{(n)}(\tau|\mathbf{B}) = \mathcal{G}(\tau) + \hat{M}(\mathbf{B})\mathcal{J}^{(n)}(\tau|\mathbf{B}) - \mathcal{S}^{(n)}(\tau|\mathbf{B}), \quad (2.21)$$

with

$$\delta\mathcal{S}^{(n)}(\tau|\mathbf{B}) = \mathcal{S}^{(n+1)}(\tau|\mathbf{B}) - \mathcal{S}^{(n)}(\tau|\mathbf{B}), \quad (2.22)$$

and

$$\mathcal{J}^{(n)}(\tau|\mathbf{B}) = \Lambda[\mathcal{S}^{(n)}]. \quad (2.23)$$

The superscript  $(n)$  refers to the iteration step, and  $\hat{E}$  is the identity matrix.

The right hand side (r.h.s.) in Equation (2.21) is easy to calculate. Knowing  $\mathcal{S}^{(n)}(\tau|\mathbf{B})$ , one can calculate its mean value  $\langle \mathcal{S} \rangle^{(n)}(\tau)$  by averaging over  $P(\mathbf{B})$ . Equations (2.15) and (2.16) are then used to calculate  $\mathcal{I}(\tau, x, \mu|\mathbf{B})$ . A short characteristics method (Kunasz & Auer 1988; Auer & Paletou 1994) is used for this step. Finally  $\mathcal{J}^{(n)}(\tau|\mathbf{B})$  is deduced from Equation (2.8).

Equation (2.18) shows that to construct the operator  $\Lambda^*$  we only need the diagonal operator corresponding to  $\mathcal{L}(\tau; \nu)$ , henceforth denoted  $\mathcal{L}^*(\tau; \nu)$ . As Equation (2.19) shows, it can be calculated by a standard method introduced in Auer & Paletou (1994). At each grid point in space, we solve an RT equation, like Equation (2.10), where  $\phi(x)$  is replaced by  $\phi(x) + \nu$  and the source term replaced by a point source at the grid point under consideration. A short characteristics method is also used for this step. Finally, the elements of  $\hat{\mathcal{L}}^*$  are obtained by performing the integration over  $x$  and  $\mu$  (see Equation (2.19)).

The corrections  $\delta\mathcal{S}^{(n)}(\tau|\mathbf{B})$  are solutions of Equation (2.21). Since the operator  $\Lambda^*$  is diagonal in space, there is no coupling between the different depth points. At each depth point  $\tau_q$ , we have a system of linear equations for  $\delta\mathcal{S}^{(n)}(\tau_q|\mathbf{B})$ . The dimension of this system is  $n_{\mathbf{B}} \times n_p$ , with  $n_p$  the number of irreducible components (6 for linear polarization) and  $n_{\mathbf{B}}$  the number of grid points needed to describe the magnetic field PDF. Since the magnetic field is defined by its strength  $B$ , inclination  $\theta_B$  and azimuth  $\chi_B$  (see Figure 2.1),  $n_{\mathbf{B}} = n_B \times n_{\theta_B} \times n_{\chi_B}$ , with  $n_B$ ,  $n_{\theta_B}$  and  $n_{\chi_B}$  the number of grid points corresponding to the respective variables.

**Table 2.1:** A list of different PDFs used in this chapter :

	$P_S(B)$	$P_A(\theta_B)$
(i)	$P_D(B) = \delta(B - B_0)$	$P_{\text{iso}}(\theta_B) = \sin \theta_B$
(ii)	$P_M(B) = \frac{32}{\pi^2 B_0} (B/B_0)^2 \exp[-\frac{4}{\pi} (B/B_0)^2]$	$P_{\text{pl-c}}(\theta_B) = (p+1)  \cos \theta_B ^p \sin \theta_B$
(iii)	$P_G(B) = \frac{2}{\pi B_0} \exp[-\frac{1}{\pi} (B/B_0)^2]$	$P_{\text{pl-s}}(\theta_B) = (\sin \theta_B)^p \sin \theta_B / C_p$
(iv)	$P_E(B) = \frac{1}{B_0} \exp(-B/B_0)$	

At each depth point  $\tau_q$ , the linear system of equations for the  $\delta \mathcal{S}_j^{(n)}$  can be written as

$$\sum_j \hat{A}_{ij}(\tau_q) \delta \mathcal{S}_j^{(n)}(\tau_q) = \mathbf{r}_i^{(n)}(\tau_q), \quad (2.24)$$

where  $i$  and  $j$  are indices for the magnetic field vector grid points ( $i, j = 1, \dots, n_B$ ). The vectors  $\delta \mathcal{S}_j^{(n)}$  and  $\mathbf{r}_i^{(n)}$  have the dimension  $n_p$ . We use the notation  $\delta \mathcal{S}_j^{(n)}(\tau_q) = \delta \mathcal{S}^{(n)}(\tau_q | \mathbf{B}_j)$ . Similarly,  $\mathbf{r}_i^{(n)}(\tau_q) = \mathbf{r}^{(n)}(\tau_q | \mathbf{B}_i)$ . Each element  $\hat{A}_{ij}$  is a  $n_p \times n_p$  block given by

$$\hat{A}_{ij}(\tau_q) = \delta_{ij} \hat{E} - \delta_{ij} \hat{M}_i \hat{\mathcal{L}}^*(\tau_q; \nu) - \hat{M}_i [\hat{\mathcal{L}}^*(\tau_q; 0) - \hat{\mathcal{L}}^*(\tau_q; \nu)] \varpi_j. \quad (2.25)$$

The  $\varpi_j$  are weights for the integration over the magnetic field PDF. The matrices  $\hat{E}$ ,  $\hat{M}_i = \hat{M}(\mathbf{B}_i)$ , and  $\hat{\mathcal{L}}^*(\tau_q; \nu)$ , corresponding to the operator  $\mathcal{L}^*$ , are of dimension  $n_p \times n_p$ . Explicit expressions for the elements of  $\hat{M}$  and  $\hat{\mathcal{L}}$  are given in the Appendix A. The elements  $\hat{A}_{ij}$  have to be computed only once since they do not change during the iteration cycle.

The convergence properties of this iteration method are similar to those of other PALI methods used for polarized problems (Nagendra et al. 1998, 1999). The new feature here is the discretization of the magnetic field vector. Typically we have been using  $n_B = 40$ . For an isotropic angular distribution,  $n_{\theta_B} = 5 - 7$  points in the interval  $[0, \pi]$ , the integration over  $\theta_B$  being performed with a Gauss-Legendre quadrature. Significantly larger values of  $n_{\theta_B}$  are needed for angular distributions that are peaked along some direction (see

Section 2.5). All the magnetic field PDFs chosen here have a cylindrical symmetry about the normal to the atmosphere, so no integration over  $\chi_B$  is needed. For the integration over  $\tau$ , we are using 5 to 7 points per decade.

In this work, we are considering self-emitting slabs. The primary source is  $G(\tau) = \epsilon' B_\nu / (1 + \epsilon')$  with  $\epsilon'$  the rate of destruction by inelastic collisions (see Appendix A) and  $B_\nu$  the Planck function at line center. The line absorption profile  $\phi(x)$  is a Voigt function with damping parameter  $a$ . The atomic and atmospheric models are thus defined by a set of parameters  $(T, a, \epsilon, B_\nu)$  where  $a$ ,  $\epsilon = \epsilon' / (1 + \epsilon')$  and  $B_\nu$  are assumed to be constant with  $\tau$ . The solution of the RT equation is then symmetrical with respect to  $T/2$ .

The magnetic kernel elements  $\mathcal{M}_{QQ'}^K(\mathbf{B})$  are defined in the Appendix A. In all the calculations we assume a normal Zeeman triplet, an electric-dipole transition and no depolarizing collisions. For the magnetic field, the parameters are the magnetic field strength  $B$ , the polar angles  $\theta_B$  and  $\chi_B$ , the density  $\nu$  of jumping points and the PDF  $P(\mathbf{B})$ . For the Hanle effect, it is convenient to use the Hanle efficiency factor  $\Gamma_B$ , instead of the magnetic field strength itself. The definition of  $\Gamma_B$  is recalled in the Appendix A.

## 2.5 A choice of magnetic field vector PDFs

For the quiet Sun, a few PDFs have been proposed in the literature for the field strength  $B$  and for the inclination  $\theta_B$  of the magnetic field with respect to the vertical direction. They are based on the analysis of magneto-convection simulations, inversion of Stokes parameters, and heuristic considerations (see e.g. Trujillo Bueno et al. 2004; Dominguez Cerdeña et al. 2006; Sánchez Almeida 2007; Sampoorana et al. 2008b). Almost nothing is known about the azimuthal distribution. For our investigation we have chosen PDFs that are cylindrically symmetrical, and of the form

$$P(\mathbf{B})d^3\mathbf{B} = f(B)g(\theta_B)B^2 \sin\theta_B dB d\theta_B \frac{d\chi_B}{4\pi}, \quad (2.26)$$

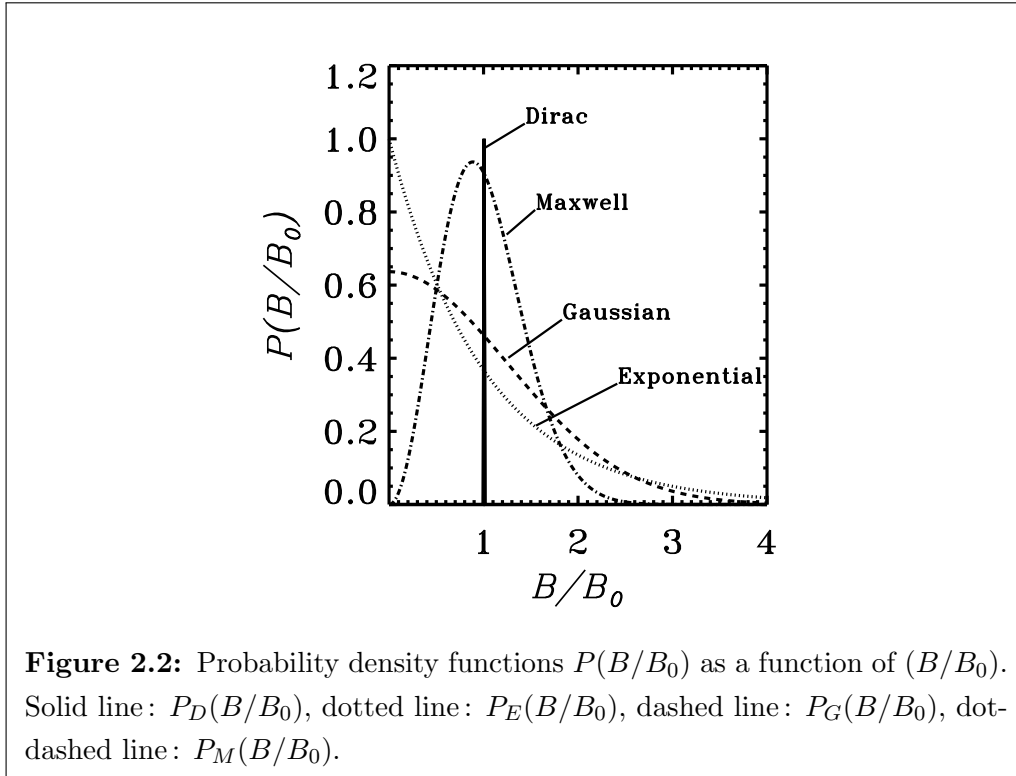
$$0 \leq B < +\infty, \quad \theta_B \in [0, \pi], \quad \chi_B \in [0, 2\pi].$$

For convenience, we rewrite them as

$$P(\mathbf{B})d^3\mathbf{B} = \frac{1}{2}P_S(B)P_A(\theta_B)dB d\theta_B. \quad (2.27)$$

Our choices for the strength and angular distributions are presented in Table 2.1.

For  $P_S(B)$ , we have chosen a Delta function,  $P_D(B)$ , an exponential distribution,  $P_E(B)$ , a Gaussian distribution,  $P_G(B)$ , and a Maxwell Distribution,  $P_M(B)$ . They are

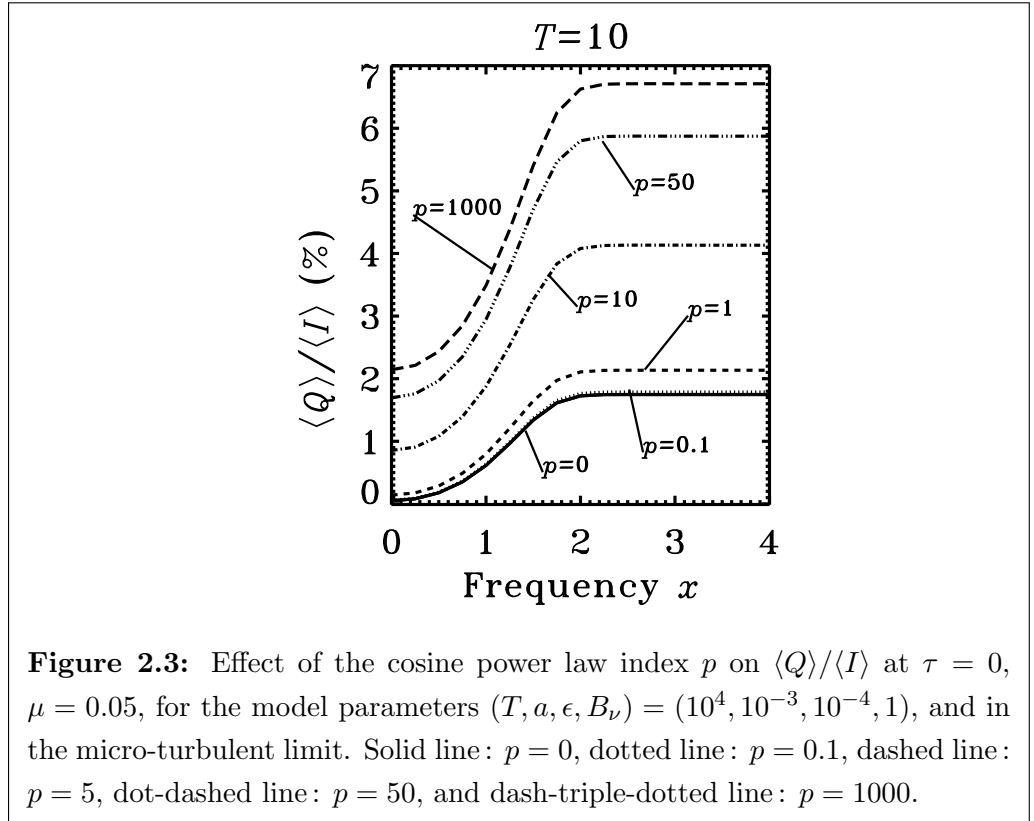


plotted in Figure 2.2 as a function of  $B/B_0$ . These functions are normalized to unity; they have the same mean value,  $\langle B \rangle = B_0$ , but the variance  $\sigma = [\langle B^2 \rangle - \langle B \rangle^2]^{1/2}$  changes: for the exponential distribution,  $\sigma = B_0$ , for the Gaussian distribution,  $\sigma = \sqrt{\pi/2}B_0$ , and for the Maxwell distribution,  $\sigma = [(3\pi/8) - 1]^{1/2}B_0$ .

For the angular distribution (see Table 2.1, second column), we have retained the isotropic distribution  $P_{\text{iso}}$ , frequently used in the analysis of the Hanle effect. It was introduced by Stenflo (1982) to model weak magnetic fields that are passively tangled by the turbulent motions (see also Stenflo, 2010).

Recent Hinode observations suggest a predominantly horizontal magnetic flux in the quiet Sun (Lites et al. 2008). This finding is supported by some numerical simulations (Schüssler & Vögler 2008). This type of distribution can be modeled with the sine power law  $P_{\text{pl-s}}$ , where  $p$  ( $p \geq 0$ ) is an index that can be chosen arbitrarily, and  $C_p$  a normalization constant. When  $p$  goes to zero, one recovers the isotropic distribution, and when  $p$  goes to infinity, a purely horizontal random field, considered in Stenflo (1982). When  $p$  is an integer, the normalization constant  $C_p$  can be calculated explicitly. For even values of  $p$ ,

$$C_p = \frac{p \times (p-2) \times \cdots \times 2}{(p+1) \times (p-1) \times \cdots \times 3}, \quad (2.28)$$



and for odd values of  $p$ ,

$$C_p = \frac{p \times (p-2) \times \cdots \times 1}{(p+1) \times (p-1) \times \cdots \times 2} \frac{\pi}{2}. \quad (2.29)$$

When  $p = 0$ , we have  $C_p = 1$ . When  $p$  goes to infinity,  $C_p$  goes to zero. Setting  $p = 2m$  for even values of  $p$ , and  $p = 2m - 1$  for odd values ( $m \geq 1$ ), one can establish that  $C_p \rightarrow \sqrt{\pi/m}/2$  when  $m \rightarrow \infty$ .

The cosine power law  $P_{\text{pl-c}}$  was introduced in Stenflo (1987) to investigate the Zeeman effect with random magnetic fields that may become predominantly vertical. It was used in Sampoorna et al. (2008b) to construct a composite PDF that mimics a distribution becoming more and more vertical as the field strength increases. When  $p = 0$ , the distribution is isotropic. When  $p$  increases the field becomes more and more vertical. In the limit  $p \rightarrow \infty$ , the Hanle effect disappears because the scattering atoms are illuminated by an unpolarized field, cylindrically symmetrical about the magnetic field direction. This effect is illustrated in Figure 2.3. We see that the ratio  $\langle Q \rangle / \langle I \rangle$  increases with  $p$ . It reaches the Rayleigh limit when  $p = 1000$ . The mean Stokes parameters,  $\langle Q \rangle$  and  $\langle I \rangle$ , have been calculated in the micro-turbulent limit, for a magnetic field with constant strength, corresponding to a

Hanle factor  $\Gamma_{B_0} = 1$ .

## 2.6 Dependence of the polarization on the correlation length

In order to examine the dependence of the polarization on the correlation length  $1/\nu$  (in Doppler width units), we have examined the surface value of the ratio  $\langle Q \rangle / \langle I \rangle$  at the limb ( $\mu = 0.05$ ),  $\langle Q \rangle$  and  $\langle I \rangle$  being the mean values of Stokes  $Q$  and  $I$ , for several values of  $\nu$  and  $T$ .

We have first chosen the most simple PDF, namely an isotropic angular distribution with a Dirac distribution  $\delta(B - B_0)$ . The parameter  $\Gamma_{B_0}$  has been set to unity. We found that the dependence of  $\langle Q \rangle / \langle I \rangle$  on the value of  $\nu$  is quite small for optically thin ( $T \ll 1$ ) lines, and also optically thick ( $T \geq 10^3$ ) ones. For lines with a moderate optical depth ( $T = 10$ ), some dependence could be observed, the maximum variation of the ratio  $\langle Q \rangle / \langle I \rangle$  being about 0.1%.

Keeping the assumption of a single value field strength, we have calculated the ratio  $\langle Q \rangle / \langle I \rangle$  for the sine and cosine power law distributions (see Table 2.1). For the sine power law, we choose  $p = 50$ . For this value of  $p$ , the distribution is strongly peaked in the horizontal direction. For the cosine power law, we retained  $p = 5$ . The distribution is also strongly peaked, but in the vertical direction (see Figure 11 in Sampoorna et al. 2008b) and the diminution of the Hanle effect is significant (see Figure 2.3). For these two distributions, the dependence on the correlation length is also negligible for optically thin and optically thick lines. Some dependence appears for lines with an intermediate optical depth. Figure 2.4, corresponding to the sine power law and  $T = 10$ , shows that the difference  $(\langle Q \rangle / \langle I \rangle)_{\text{macro}} - (\langle Q \rangle / \langle I \rangle)_{\text{micro}} \simeq 0.30\%$  all along the polarization profile. The variation of  $\langle Q \rangle / \langle I \rangle$  is coming almost exclusively from the variation of  $\langle Q \rangle$ , since the dependence of Stokes  $I$  on the magnetic field is very small for the Hanle effect. This figure shows also that the micro-turbulent limit is reached for  $\nu \simeq 10$ . The reason is that  $\nu$  enters only in exponential terms, as can be seen in Equation (2.19). For the cosine power law and  $T = 10$ , we found a behavior very similar to that shown in Figure 2.4, but the polarization is somewhat larger because of the reduction of the Hanle effect.

To understand the dependence on the correlation length, we have examined the dependence on  $\nu$  and  $\theta_B$  of the conditional source function component  $S_0^2(\tau = 0 | B, \theta_B)$ . This function depends strongly on  $\nu$  and  $\theta_B$ , with the micro and macro-turbulent limits showing quite different variation with  $\theta_B$ . The averaging over  $\theta_B$  eliminates most of the variation

with  $\nu$ . Some of it may remain however, in particular when the angular distribution is peaked in the horizontal or vertical direction.

A very small sensitivity to the value of the correlation length is a strong indication that the polarization is created locally. For a line with a very small optical thickness,  $T \ll 1$ , photons will suffer about one scattering and the polarization is well represented by the so-called single scattering approximation. For very thick lines, although photons suffer a very large number of scattering events, the polarization is created near the surface by a few of them. So in these two limits, the polarization cannot feel the correlation length of the magnetic field. For  $T = 10$ , we have an intermediate situation with a clear sensitivity to the correlation length.

For the Hanle effect, the polarization can be evaluated by a perturbation method leading to a series expansion in terms of a mean number of scattering events (see HF06). In the next Section we show how to construct this expansion. We use it to examine how many terms are needed to reproduce the exact solution and thus give a somewhat quantitative content to the above remarks.

## 2.7 A series expansion for the calculation of the polarization

The construction of a series expansion for the calculation of the polarization is possible for the following three reasons: (i) the Hanle polarization is weak, (ii) it is controlled by the anisotropy of the radiation field, (iii) at each scattering a significant amount of polarization is being lost. This last point will be clarified below.

Here, for simplicity we present the perturbation method and discuss its convergence properties for the simple case of a deterministic (or micro-turbulent) magnetic field. We then show how to carry it out for magnetic fields with a finite correlation length and propose a perturbation expansion which is an improved version of the method presented in HF06.

### 2.7.1 Construction of the expansion

We start from the standard integral equation for the Hanle effect with a deterministic magnetic field, namely

$$\mathbf{S}(\tau; \mathbf{B}) = \mathbf{G}(\tau) + \hat{M}(\mathbf{B}) \int_0^T \hat{K}(\tau - \tau') \mathbf{S}(\tau'; \mathbf{B}) d\tau'. \quad (2.30)$$

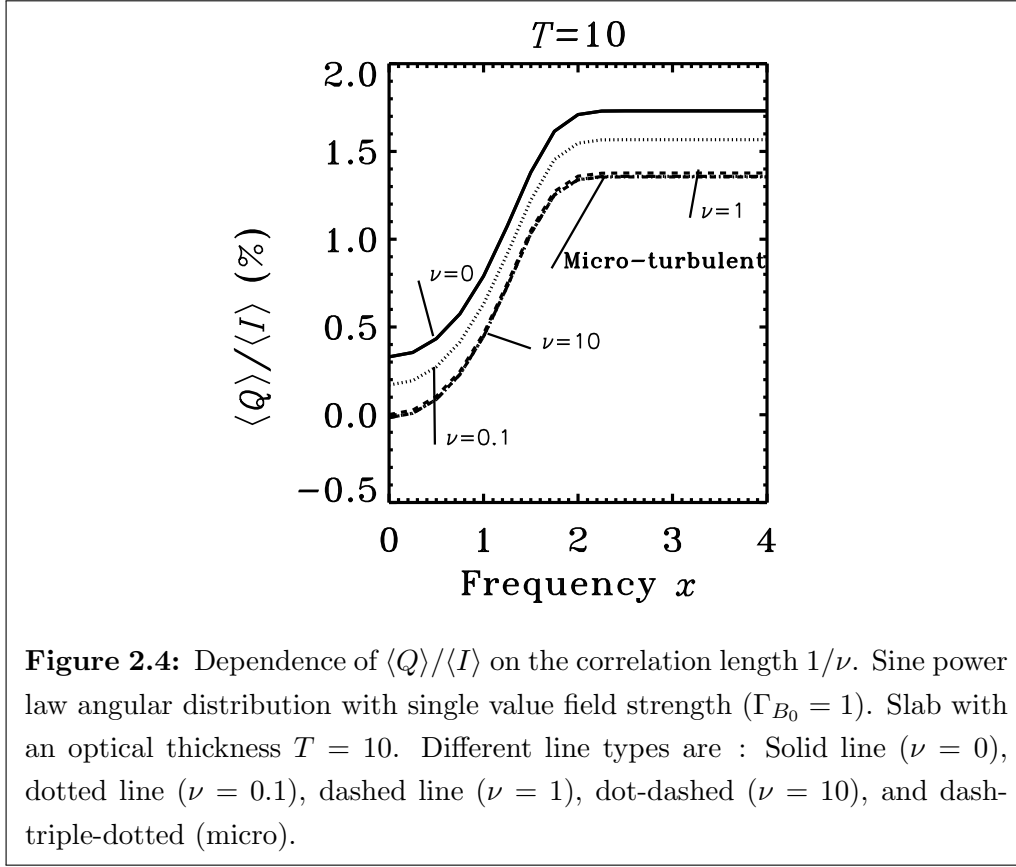


**Figure 2.4:** Dependence of  $\langle Q \rangle / \langle I \rangle$  on the correlation length  $1/\nu$ . Sine power law angular distribution with single value field strength ( $\Gamma_{B_0} = 1$ ). Slab with an optical thickness  $T = 10$ . Different line types are : Solid line ( $\nu = 0$ ), dotted line ( $\nu = 0.1$ ), dashed line ( $\nu = 1$ ), dot-dashed ( $\nu = 10$ ), and dash-triple-dotted (micro).

In the micro-turbulent limit,  $\hat{M}(\mathbf{B})$  should be replaced by its mean value over the magnetic field PDF and  $\mathcal{S}$  will depend only on  $\tau$ . With  $\mathbf{B} = 0$ , this equation describes Rayleigh scattering.

In the deterministic case, if the magnetic field is a constant, the dependence on the azimuthal angle  $\chi_B$  can be factored out as shown in the Appendix A. Henceforth we work with the components  $S_Q^K = e^{iQ\chi_B} \mathcal{S}_Q^K$  and to simplify the notation, the dependence on  $\mathbf{B}$  is omitted. These new components satisfy the set of equations

$$S_Q^K(\tau) = \delta_{K0} \delta_{Q0} G(\tau) + \sum_{K'Q'} \mathcal{M}_{QQ'}^K(\mathbf{B}) \int_0^T K_{Q'K'}^{KK'}(\tau - \tau') S_{Q'}^{K'}(\tau') d\tau', \quad (2.31)$$

with  $K_{Q'K'}^{KK'}(\tau)$  the components of the matrix  $\hat{K}(\tau)$ . The notation  $\mathbf{B}$  stands now for  $(B, \theta_B)$ . The components  $I_Q^K$  of the radiation field satisfy the RT equation

$$\mu \frac{\partial I_Q^K(\tau, x, \mu)}{\partial \tau} = \phi(x) [I_Q^K(\tau, x, \mu) - S_Q^K(\tau)]. \quad (2.32)$$

We first consider the equation for  $S_0^0$ . Only  $S_0^2$  appears in the r.h.s. since  $K = 0$  implies



$Q = Q' = 0$ . For the Hanle effect, the polarization is always weak and its effect on Stokes  $I$  may be neglected, at least in first approximation. Neglecting the contribution from  $S_0^2$ , we obtain

$$\tilde{S}_0^0(\tau) = G(\tau) + \mathcal{M}_{00}^0 \int_0^T K_0^{00}(\tau - \tau') \tilde{S}_0^0(\tau') d\tau'. \quad (2.33)$$

The notation  $\tilde{S}_Q^K$  is used to denote approximate values. Equation (2.33) is the usual unpolarized integral equation for the source function where  $\mathcal{M}_{00}^0 = 1/(1 + \epsilon')$ .

We now replace  $S_0^0$  by  $\tilde{S}_0^0$  in the equation for  $S_Q^2$  and obtain

$$\tilde{S}_Q^2(\tau) = \mathcal{M}_{Q0}^2(\mathbf{B})C_0^2(\tau) + \sum_{Q'} \mathcal{M}_{QQ'}^2(\mathbf{B}) \int_0^T K_{Q'}^{22}(\tau - \tau') \tilde{S}_{Q'}^2(\tau') d\tau', \quad (2.34)$$

where

$$C_0^2(\tau) = \int_0^T K_0^{20}(\tau - \tau') \tilde{S}_0^0(\tau') d\tau'. \quad (2.35)$$

The kernel  $K_0^{20}(\tau)$  is sometimes denoted  $K_{12}(\tau)$  (e.g. Landi Degl'Innocenti et al. 1990; Nagendra et al. 1998). Its integral over  $\tau$  in the interval  $[0, +\infty]$  is zero. The function  $C_0^2(\tau)$ , can also be written as

$$C_0^2(\tau) = \int_{-\infty}^{+\infty} \frac{1}{2} \int_{-1}^{+1} \Psi_0^{20}(\mu) \phi(x) \tilde{I}_0^0(\tau, x, \mu) d\mu dx, \quad (2.36)$$

with  $\Psi_0^{20}(\mu) = \frac{3}{2\sqrt{2}}(3\mu^2 - 1)$ . In this form we recognize the dominant term in the radiation spherical tensor  $\tilde{J}_0^2(\tau)$ . This function, which is zero for an isotropic radiation field, serves to measure the anisotropy of the field (see e.g. Trujillo Bueno 2001; LL04).

Equation (2.34) shows that  $\mathcal{M}_{Q0}^2(\mathbf{B})C_0^2(\tau)$  is the driving term for the polarization. This suggests to solve this equation by the standard method of successive iterations for Fredholm integral equations of the second type (Iyanaga & Kawada 1970). For RT problems, this method is usually referred to as  $\Lambda$ -iteration. The zeroth-order solution in this iteration scheme is given by  $\mathcal{M}_{Q0}^2(\mathbf{B})C_0^2(\tau)$ . The recurrence scheme may be written as

$$[\tilde{S}_Q^2]^{(k)} = \mathcal{M}_{Q0}^2(\mathbf{B})C_0^2(\tau) + \sum_{Q'} \mathcal{M}_{QQ'}^2(\mathbf{B}) \int_0^T K_{Q'}^{22}(\tau - \tau') [\tilde{S}_{Q'}^2(\tau')]^{(k-1)} d\tau', \quad (2.37)$$

with  $[\tilde{S}_Q^2]^{(0)} = \mathcal{M}_{Q0}^2(\mathbf{B})C_0^2(\tau)$ .

It is well known that the  $\Lambda$ -iteration applied to Equation (2.33) has a very poor convergence rate when  $T$  is large and  $\epsilon'$  very small, because the kernel  $K_0^{00}$  is normalized to unity and the coefficient  $\mathcal{M}_{00}^0$  almost equal to unity. In Equation (2.34) the situation is radically

different because the kernels  $K_Q^{22}(\tau)$  have integrals over  $[-\infty, +\infty]$  which are smaller than unity, actually they are all equal to  $7/10$  (see e.g. HF06), and the coefficients  $\mathcal{M}_{Q_0}^2(\mathbf{B})$  are also significantly smaller than unity when  $\mathbf{B}$  is not zero. For Rayleigh scattering, the only non zero coefficient is  $\mathcal{M}_{00}^2$ , which is of the order of the depolarization parameter  $W_K(J_l, J_u)$  (see AppendixA).

In order to examine the convergence properties of this iteration scheme, we can consider a simplified version of Equation (2.34). The r.h.s. of this equation contains a driving term, a transport term corresponding to  $Q' = Q$ , and terms coupling  $\tilde{S}_Q^2$  with the  $\tilde{S}_{Q'}^2$ ,  $Q' \neq Q$ . Neglecting these last terms, we see that the solution at step ( $k$ ) can be written as a series expansion of the form

$$\begin{aligned} [\tilde{S}_Q^2]^{(k)} &= \mathcal{M}_{Q_0}^2(\mathbf{B})C_0^2(\tau) + \sum_{m=1}^{m=k} \left[ \frac{7}{10} \mathcal{M}_{QQ}^2 \right]^m \int_0^T \bar{K}_Q^{22}(\tau - \tau_1) d\tau_1 \\ &\times \int_0^T \bar{K}_Q^{22}(\tau_1 - \tau_2) d\tau_2 \dots \int_0^T \bar{K}_Q^{22}(\tau_{k-1} - \tau_k) \mathcal{M}_{Q_0}^2(\mathbf{B})C_0^2(\tau_k) d\tau_k. \end{aligned} \quad (2.38)$$

Here the kernels  $\bar{K}_Q^{22}$ , defined by  $\bar{K}_Q^{22} = \frac{10}{7} K_Q^{22}$ , are normalized to unity. The term of order  $m$  contains the contribution of all the photons that have been scattered  $(m+1)$  times, the first scattering corresponding to the creation of the primary source  $\mathcal{M}_{Q_0}^2(\mathbf{B})C_0^2(\tau)$ . Since the kernels  $\bar{K}_Q^{22}$  are positive and normalized to unity, the ratio of the term of order  $(m+1)$  over the term of order  $m$  scales as  $0.7 \mathcal{M}_{QQ}^2(\mathbf{B})$ . Since the  $\mathcal{M}_{QQ}^2(\mathbf{B})$  are smaller than unity, one can expect that a few terms in the series will suffice to provide a good approximation to the exact solution. Somewhat more accurate predictions can be made for optically thin and optically thick lines.

For optically thin lines ( $T \ll 1$ ), one can approximate  $[\tilde{S}_Q^2]^{(k)}(\tau)$  by

$$[\tilde{S}_Q^2]^{(k)}(\tau) \simeq \mathcal{M}_{Q_0}^2(\mathbf{B})C_0^2(\tau) \left[ 1 + \sum_{m=1}^k \left[ \frac{7}{10} \mathcal{M}_{QQ}^2(\mathbf{B}) \right]^m T^m \right]. \quad (2.39)$$

The driving term is dominant and suffices to correctly evaluate the polarization. This is the so-called single scattering approximation.

To examine the case of optically thick lines, we can let  $T \rightarrow \infty$ . If we approximate  $\bar{K}_Q^{22}(\tau)$  by a delta function, we obtain

$$[\tilde{S}_Q^2]^{(k)}(\tau) \simeq \mathcal{M}_{Q_0}^2(\mathbf{B})C_0^2(\tau) \left[ 1 + \sum_{m=1}^k \left[ \frac{7}{10} \mathcal{M}_{QQ}^2(\mathbf{B}) \right]^m \right]. \quad (2.40)$$

This expression shows that a single scattering can provide a reasonable approximation for optically thick lines also. We also see that the smaller  $\mathcal{M}_{QQ}^2(\mathbf{B})$ , the better the single scattering approximation and the faster the speed of convergence of the series expansion. We note also that the  $\mathcal{M}_{QQ}^2(\mathbf{B})$  are positive, hence the sum inside the square brackets increases with the value of  $k$ .

For lines with very large optical thicknesses, the value of Stokes  $Q$  at the surface can be easily related to  $S_0^2(\tau)$ . For these lines,  $Q$  is controlled by the component  $I_0^2$ . Using  $\mathcal{T}_0^2(1, \Omega) = -3(1 - \mu^2)/(2\sqrt{2})$  for  $\gamma = 0$ , and the Eddington–Barbier relation, we obtain

$$Q(0, x, \mu) \simeq -\frac{3}{2\sqrt{2}}(1 - \mu^2)\tilde{S}_0^2\left(\frac{\mu}{\phi(x)}\right). \quad (2.41)$$

We have performed a few numerical experiments described below to give a quantitative proof to these predictions.

**Table 2.2:** Number of iterations needed to reproduce the exact solution with a relative error about  $10^{-3}$  at line center. The parameters of the magnetic field in columns 2 and 3 are the same as in Figures 2.6 and 2.7

	Rayleigh		deterministic	micro-turbulent
$T$	$n_k$	$n_k$	$n_k$	$n_k$
$10^{-2}$	3	3	3	3
$10^{-1}$	4	4	4	4
1	7	7	5	5
10	16	16	9	9
$10^2$	12	11	4	4
$10^3$	7	6	5	5
$10^4$	7	7	5	5
$10^6$	8	7	5	5
$10^8$	8	7	5	5

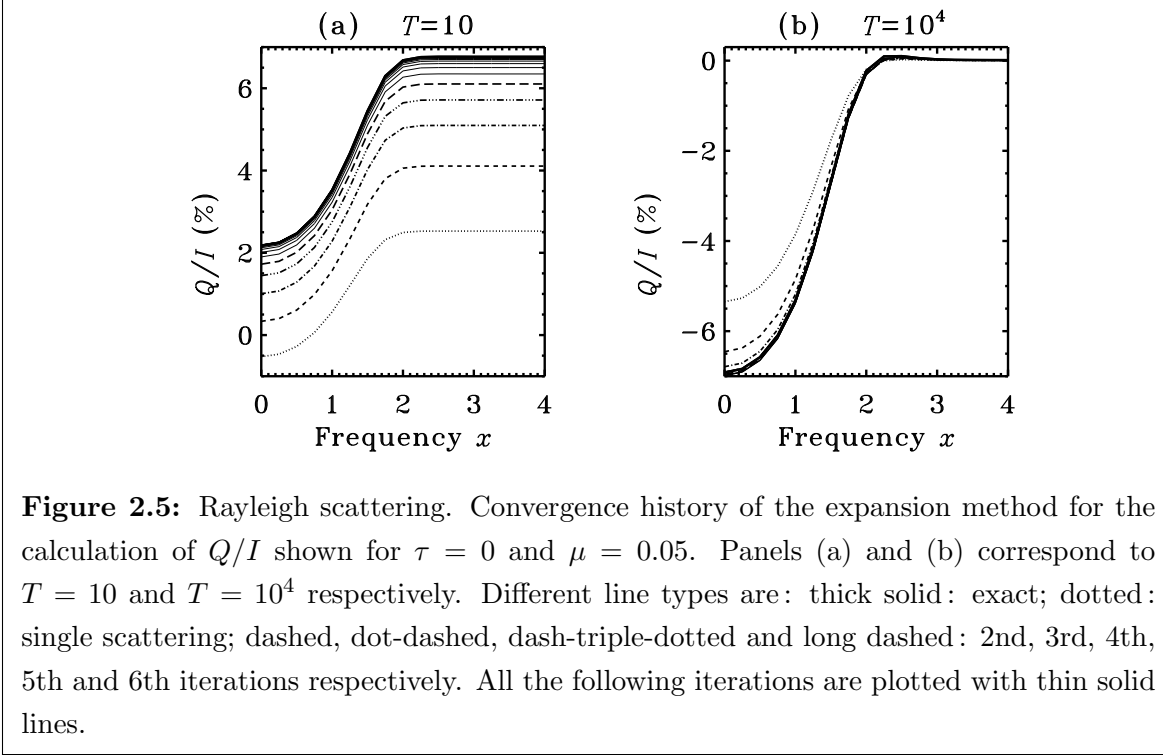


**Figure 2.5:** Rayleigh scattering. Convergence history of the expansion method for the calculation of  $Q/I$  shown for  $\tau = 0$  and  $\mu = 0.05$ . Panels (a) and (b) correspond to  $T = 10$  and  $T = 10^4$  respectively. Different line types are: thick solid: exact; dotted: single scattering; dashed, dot-dashed, dash-triple-dotted and long dashed: 2nd, 3rd, 4th, 5th and 6th iterations respectively. All the following iterations are plotted with thin solid lines.

### 2.7.2 Numerical results

The computation of the polarization by the series expansion method involves the following steps:

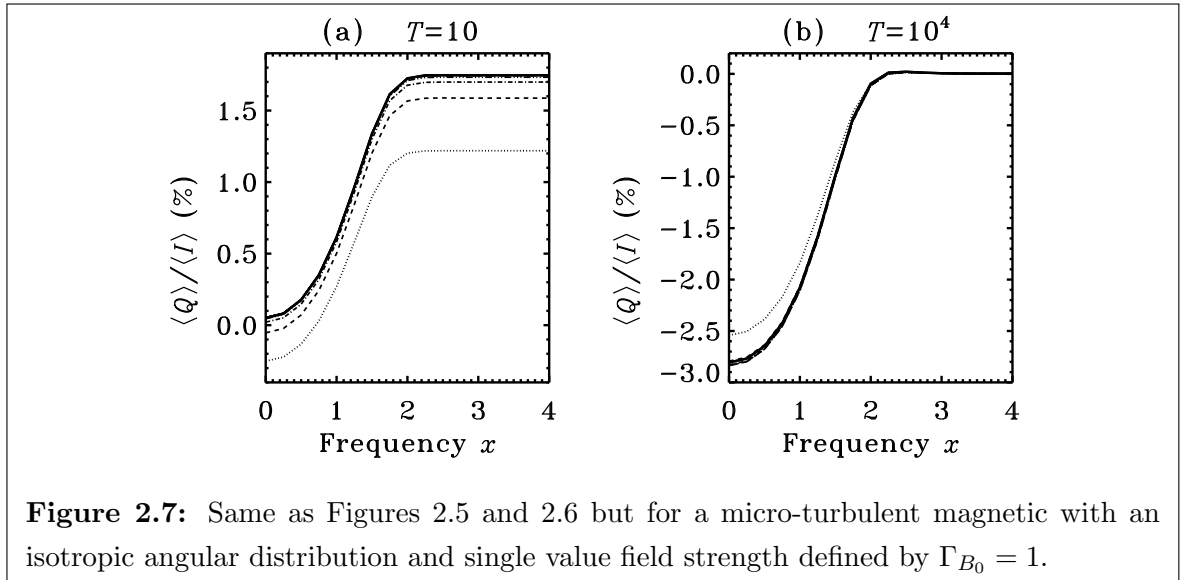
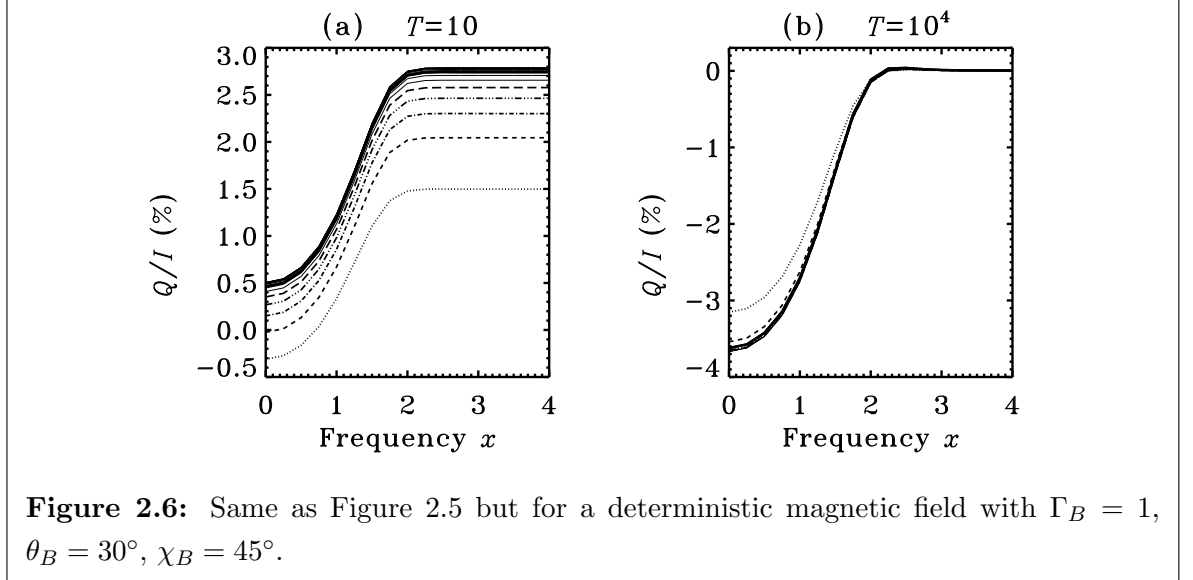
- (i) Solution of Equation (2.33) for  $\tilde{S}_0^0$  by an ALI method and calculation of the corresponding scalar radiation field  $\tilde{I}_0^0$ .
- (ii) Computation of  $C_0^2(\tau)$  with Equation (2.36).
- (iii) Calculation of the source terms  $[\tilde{S}_Q^2]^{(k)}$ , with the iterative scheme in Equation (2.37), starting from  $\mathcal{M}_{Q_0}^2(\mathbf{B})C_0^2(\tau)$ .
- (iv) At each step ( $k$ ), solution of Equation (2.32) by a short characteristics method, calculation of the Stokes parameters with Equation (2.5), and of the ratio

$$r^{(k)} = [|p^{(k)} - p^{(k-1)}|] / p^{(k)}, \quad (2.42)$$

at  $\tau = 0, x = 0, \mu = 0.05$ . Here  $p = \{[Q/I]^2 + [U/I]^2\}^{1/2}$ .

The iterations are stopped when  $r^{(k)} < 10^{-3}$ .

The polarization has been calculated by this expansion method for several values of the slab optical thickness  $T$  varying between  $10^{-2}$  and  $10^8$ . For each value of  $T$ , we have considered Rayleigh scattering, a deterministic magnetic field and a micro-turbulent



magnetic field. For the deterministic case we chose  $\Gamma_B = 1$ ,  $\theta_B = 30^\circ$  and  $\chi_B = 45^\circ$ . For the micro-turbulent case, the magnetic field has an isotropic angular distribution and takes a single value  $B_0$ , with  $\Gamma_{B_0} = 1$ . The coefficients  $\mathcal{M}_{QQ'}^2$  are replaced by their mean values over the isotropic distribution. In each case, the exact solution has been calculated with a PALI method applied to Equation (2.31). For Rayleigh scattering and the micro-turbulent magnetic field, Stokes  $U$  is zero and Stokes  $Q$  depends only on the inclination angle  $\theta$  of the line of sight (see Figure 2.1). For a deterministic magnetic field, the Stokes parameters  $Q$  and  $U$  depend also on the azimuthal angle  $\varphi$ . In the calculations presented here  $\varphi = 0$ .

We show in Table 2.2 the number  $n_k$  of iterations defined by the criterion  $r^{(k)} < 10^{-3}$ . We stress that the value of  $n_k$  has nothing to do with the number of iterations of the PALI method, the latter being controlled by the choice of the approximate  $\Lambda^*$ - operator. In Figures 2.5 to 2.7 we show the results of our calculations for  $T = 10$  and  $T = 10^4$ , Figure 2.5 being devoted to Rayleigh scattering, Figure 2.6 to the deterministic Hanle effect, and Figure 2.7 to the micro-turbulent case. In each panel we have plotted the exact values of  $Q/I$  and a few iteration steps. For the micro-turbulent case,  $Q$  and  $I$  are replaced by  $\langle Q \rangle$  and  $\langle I \rangle$ .

We observe that the series expansion properly converges to the exact solution, that single scattering provides an approximation which is much better for  $T = 10^4$  than for  $T = 10$ , and that the accuracy of this approximation improves from Rayleigh scattering to deterministic and micro-turbulent Hanle effect. These last two points are illustrated in Figure 2.8 where we show the difference

$$e_{\text{ss}} = (Q_{\text{exact}} - Q_{\text{ss}})/I, \quad (2.43)$$

calculated at  $\tau = 0$ ,  $x = 0$ ,  $\mu = 0.05$ , as a function of the slab optical thickness  $T$ . Here,  $Q_{\text{exact}}$  is the solution of Equation (2.30),  $Q_{\text{ss}}$  is given by the single scattering approximation, and  $I$  is the exact value of Stokes  $I$ . We see that for  $T$  small,  $e_{\text{ss}}$  increases with  $T$  in agreement with Equation (2.39). For  $T$  large, it becomes essentially independent of  $T$  as predicted by Equation (2.40). It goes through a maximum around  $T = 10$ .

The decrease of  $e_{\text{ss}}$  from Rayleigh scattering to micro-turbulent Hanle effect, is directly related to the value of the elements  $\mathcal{M}_{QQ}^2$ . For Rayleigh scattering, the index  $Q$  takes only the value  $Q = 0$  and  $\mathcal{M}_{00}^2 = 1/(1 + \epsilon')$  (assuming  $W_K = 1$ ). For the Hanle effect, the  $\mathcal{M}_{QQ}^2$  and  $\langle \mathcal{M}_{QQ}^2 \rangle$  are significantly smaller than unity. Experiments with different angular distributions clearly show that a decrease of  $\langle \mathcal{M}_{00}^2 \rangle$  induces a decrease of  $e_{\text{ss}}$ .

Table 2.2 shows also clearly that the single scattering approximation is better for opti-

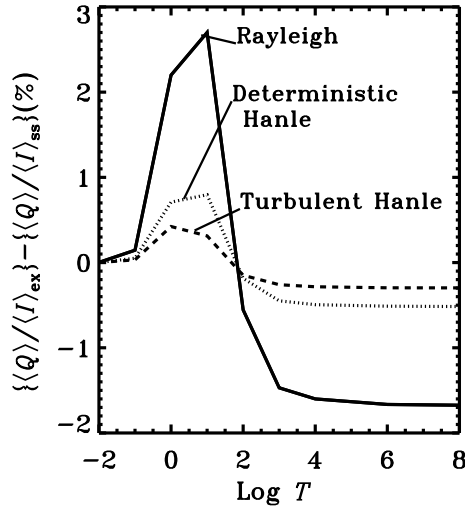


**Figure 2.8:** Difference between single scattering (ss) and exact (ex) solution as a function of the optical thickness  $T$  for  $\tau = 0$ ,  $x = 0$ , and  $\mu = 0.05$ . Rayleigh scattering (solid line), deterministic Hanle (dotted line), micro-turbulent Hanle (dashed line). Magnetic field parameters are the same as in Figures 2.6 and 2.7.

cally thin and optically thick lines, than for lines with intermediate optical thicknesses. It also shows that this approximation is better for a micro-turbulent magnetic field, than for a deterministic one or Rayleigh scattering. We have examined the values of  $n_k$  at different frequency points along the line profile, and found that in the wings they are in general a bit larger than at line center.

Our last comment is on the fact that the exact value of Stokes  $Q$  is reached from below in the case of thin to moderately thick slabs and from above in the case of thick slabs (see Figures 2.5 to 2.8). The transition is occurring around  $T = 10^2$  as shown in Figure 2.8. This change of behavior is directly related to the sign of  $C_0^2(\tau)$ , determined by a competition between a limb-darkened outgoing radiation and a limb-brightened incoming one (see e.g. Trujillo Bueno 2001). For  $T = 10^4$ ,  $C_0^2(\tau)$  is positive as long as  $\tau$  is smaller than unity and then becomes negative ( $\tau$  is assumed to be in the range  $0 < \tau < T/2$ ). Since the sum inside the square bracket in Equation (2.40) increases with  $k$ , the value of  $[\tilde{S}_0^{21}]^{(k)}$  near the surface will also increase with the value of  $k$ . We can then deduce from Equation (2.41) that  $Q$  is negative and decreases (increases in absolute value) when  $k$  increases.

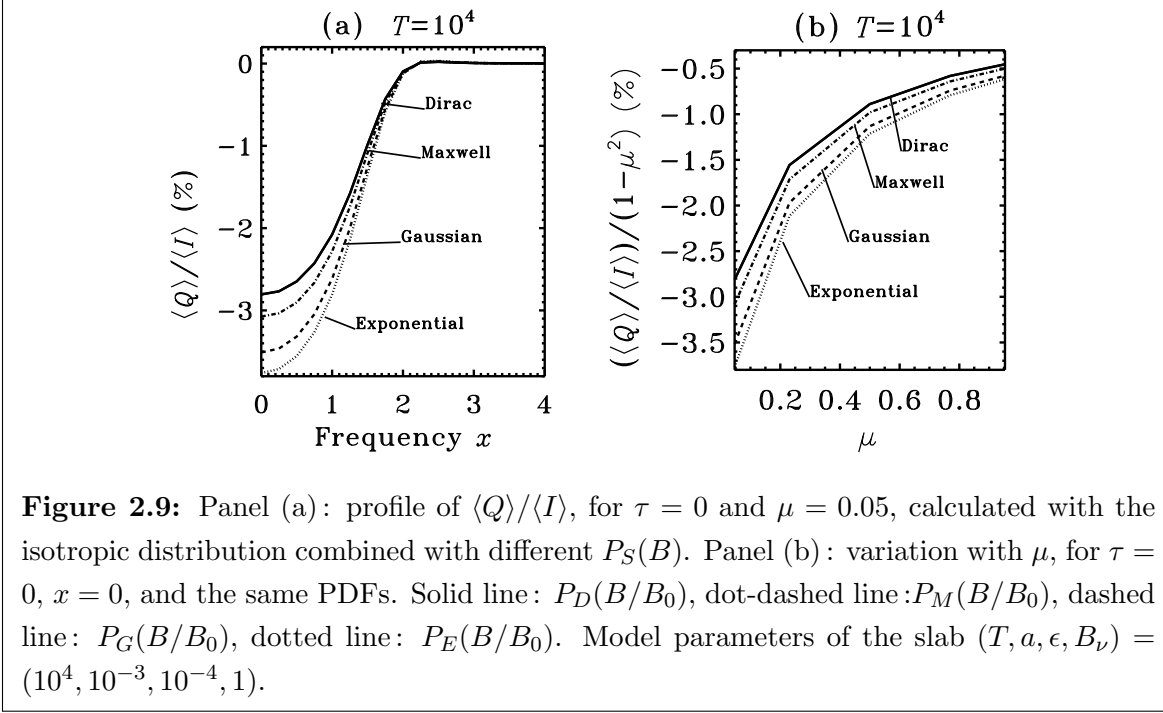


**Figure 2.9:** Panel (a): profile of  $\langle Q \rangle / \langle I \rangle$ , for  $\tau = 0$  and  $\mu = 0.05$ , calculated with the isotropic distribution combined with different  $P_S(B)$ . Panel (b): variation with  $\mu$ , for  $\tau = 0$ ,  $x = 0$ , and the same PDFs. Solid line:  $P_D(B/B_0)$ , dot-dashed line:  $P_M(B/B_0)$ , dashed line:  $P_G(B/B_0)$ , dotted line:  $P_E(B/B_0)$ . Model parameters of the slab  $(T, a, \epsilon, B_\nu) = (10^4, 10^{-3}, 10^{-4}, 1)$ .

For  $T < 1$ ,  $C_0^2(\tau)$  is negative, and we have the opposite behavior. Apparently this behavior holds until  $T$  becomes around  $10^2$  (see Figures 2.5 to 2.8) but we have no simple approximation for Stokes  $Q$ , nor for  $[\tilde{S}_0^2]^{(k)}(\tau)$ , in this intermediate range of optical thicknesses.

What should be remembered is that the single scattering approximation can lead to very large errors for Rayleigh scattering, but may be sufficient for the micro-turbulent Hanle effect, especially when the line optical thickness is small or large enough.

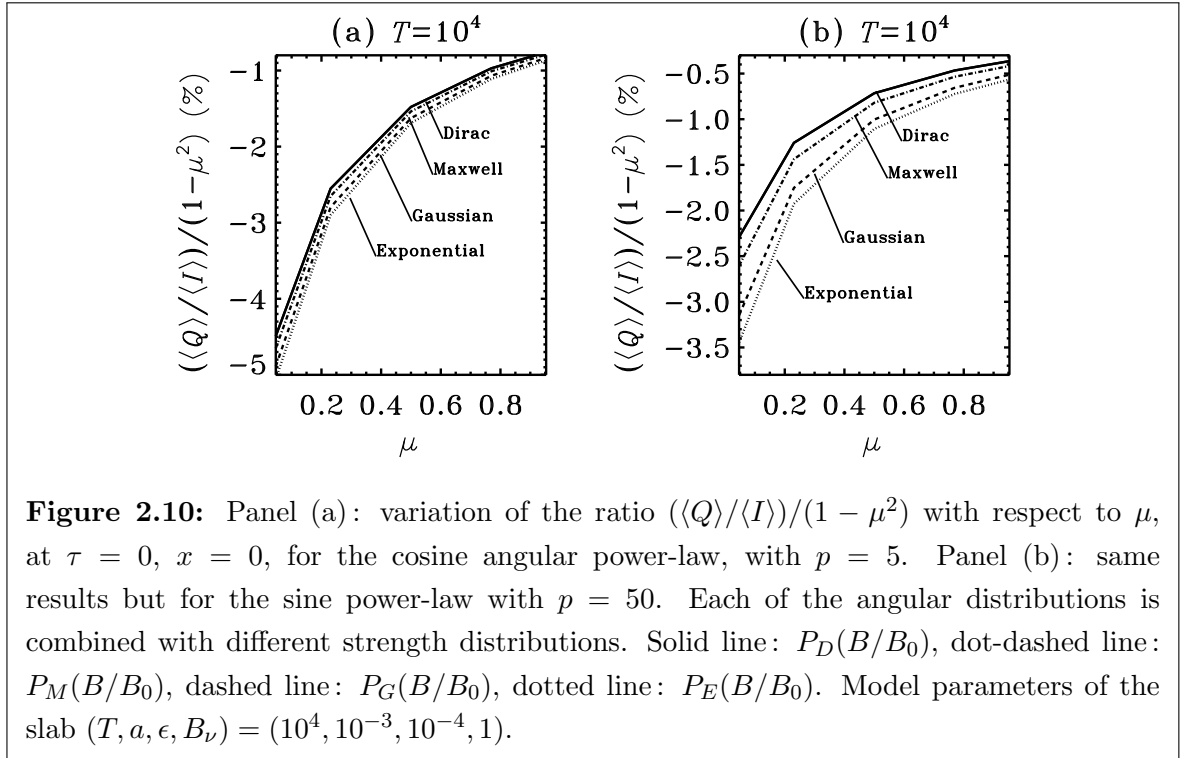
### 2.7.3 Magnetic field with a finite correlation length

Assuming, as above, that  $S_0^0$  is independent of the polarization and given by the solution of Equation (2.33), the equation for  $\tilde{S}_Q^2(\tau|\mathbf{B})$  can be written as (see Equation (A.1))

$$\begin{aligned} \tilde{S}_Q^2(\tau|\mathbf{B}) &= \mathcal{M}_{Q0}^2(\mathbf{B})C_0^2(\tau) + \sum_{Q'} \mathcal{M}_{QQ'}^2(\mathbf{B}) \left\{ \int_0^T L_{Q'}^{22}(\tau - \tau'; \nu) \tilde{S}_{Q'}^2(\tau'|\mathbf{B}) d\tau' \right. \\ &+ \left. \int_0^T [K_{Q'}^{22}(\tau - \tau') - L_{Q'}^{22}(\tau - \tau'; \nu)] \int P(\mathbf{B}') \tilde{S}_{Q'}^2(\tau'|\mathbf{B}') d^3 \mathbf{B}' d\tau' \right\}. \end{aligned} \quad (2.44)$$

The iteration scheme defined in Equation (2.37) can be carried out on this equation. If, at step  $(k - 1)$ , one knows  $[\tilde{S}_{Q'}^2(\tau'|\mathbf{B})]^{(k-1)}$ , one knows also its average over the magnetic field





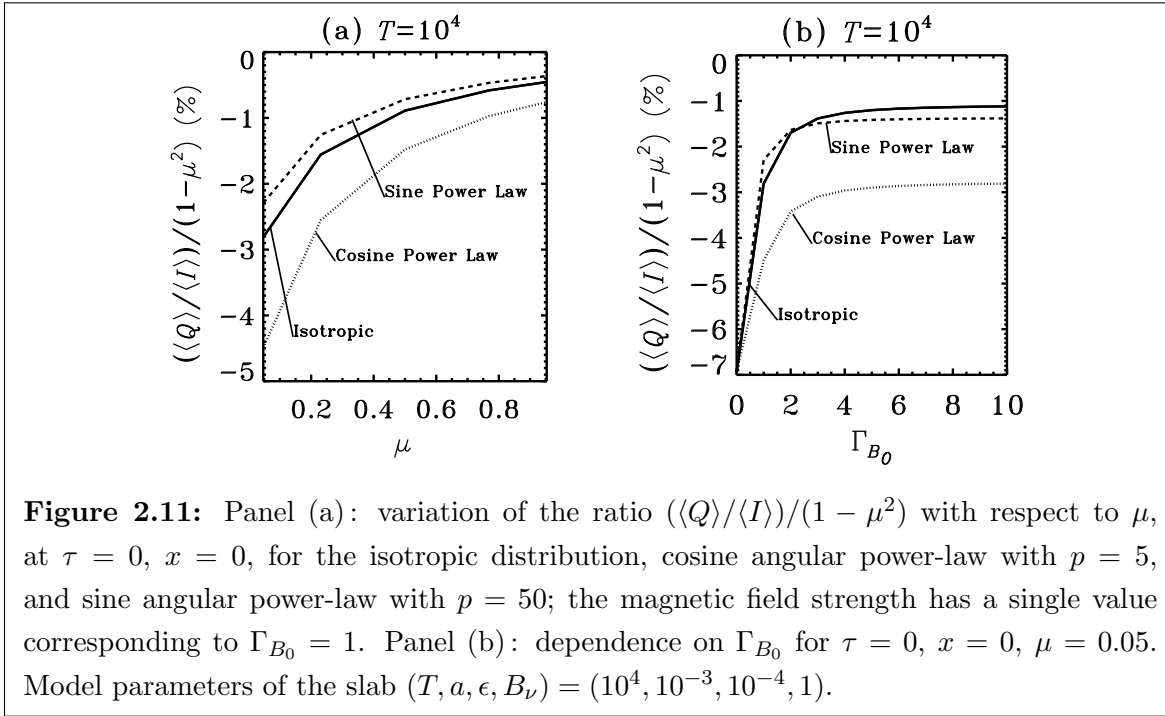
PDF which appears in the r.h.s. of Equation (2.44). The iteration scheme for a finite value of  $\nu$  will have the same convergence properties as the simpler case of Equation (2.37).

## 2.8 Dependence of the polarization on the magnetic field vector PDF

This study is carried out for the micro-turbulent limit, because one can expect, from our previous results, that the dependence of the polarization on the shape of the magnetic field PDF will be essentially independent of the value of the correlation length.

In the micro-turbulent limit, the mean source vector satisfies Equation (2.20). Here we are dealing with magnetic field distributions that are cylindrically symmetric about the vertical axis and a primary source term which is unpolarized. Hence, the matrix  $\hat{M}(\mathbf{B})$  is diagonal and the only source vector components that are not zero are  $\langle S_0^0 \rangle$  and  $\langle S_0^2 \rangle$ . For their calculation, carried out here with a standard PALI method, we only need  $\mathcal{M}_{00}^0$  and  $\langle \mathcal{M}_{00}^2 \rangle$ . The solution of Equation (2.10), with  $\langle S_0^2 \rangle(\tau)$  as source term, yields  $\langle I_0^2 \rangle$ . The mean value of Stokes  $Q$  is then given by  $\langle Q \rangle = -3(1 - \mu^2) / (2\sqrt{2}) \langle I_0^2 \rangle$ .

The element  $\langle \mathcal{M}_{00}^2 \rangle$  can be calculated explicitly for all the angular distributions given



in Table 2.1, when they are associated to the Delta and Gaussian strength distributions. The expressions are given in the Appendix B. In the other cases,  $\langle \mathcal{M}_{00}^2 \rangle$  is calculated by numerical averaging with Gauss–Legendre quadratures. We have also considered a log-normal distribution, but it yields essentially the same results as the Gaussian distribution.

The calculations have been performed for slabs with different optical thickness  $T$  and we found that the main conclusions are essentially independent of the value of  $T$ . The results shown in this Section correspond to a slab with parameters  $(T, a, \epsilon, B_\nu) = (10^4, 10^{-3}, 10^{-4}, 1)$ .

Figure 2.9 is devoted to the isotropic distribution. The Panel (a) shows that  $\langle Q \rangle / \langle I \rangle$  increases (in absolute value) as we go from a Dirac distribution (single field strength value), to a Maxwell distribution, then a Gaussian distribution and finally an exponential distribution, i.e., from case (i) to case (iv) (see Table 2.1). All these curves lie well above the Rayleigh scattering limit in which  $Q/I(\tau = 0, x = 0, \mu = 0.05) = -0.07$ . The variation of  $\langle Q \rangle / \langle I \rangle$  is due to the fact that the value of  $\langle \mathcal{M}_{00}^2 \rangle$  increases as we go from case (i) to case (iv), because the probability of having weak magnetic fields increases. The maximum value of  $\langle \mathcal{M}_{00}^2 \rangle$  is reached for Rayleigh scattering.

In Figure 2.9(b) we show the center-to-limb variation of  $(\langle Q \rangle / \langle I \rangle) / (1 - \mu^2)$ . A striking feature is that the variation with  $\mu$  is almost insensitive to the field strength distribution.

We have even found that the full line curve, corresponding to a Dirac PDF with  $B = B_0$ , exactly coincides with the center-to-limb variation given by an exponential distribution with a mean value  $\langle B \rangle = 2B_0$ . This result is fully in agreement with calculations of Trujillo Bueno et al. (2004), showing that observed center-to-limb variations can be fitted by an isotropic field with a strength of 60 G, or by an exponential distribution with a mean value of 130G.

Somewhat more insight on the behavior of  $\langle Q \rangle$  can be obtained by considering  $\langle S_0^2 \rangle(\tau)$ . The dependence on optical depth is controlled by the propagation kernel  $K_0^{22}(\tau)$  (see Section 2.7). Hence changing the shape of  $P_S(B)$  will have a very small effect on the  $\mu$ -dependence of  $\langle Q \rangle$  (see Equation (2.41)). In contrast, a change in the shape of  $P_S(B)$  will modify the value of  $\langle \mathcal{M}_{00}^2 \rangle$  and hence the degree of polarization.

In Figure 2.10, devoted to the cosine and sine angular power-laws, we see that the ratio  $(\langle Q \rangle / \langle I \rangle) / (1 - \mu^2)$  also increases from case (i) to case (iv). The dependence on the shape of  $P_S(B)$  is quite large for the sine power-law with  $p = 50$  (even a bit larger than with the isotropic distribution), but very small for the cosine power-law with  $p = 5$ . This is due to the reduction of the Hanle effect when the field becomes strongly peaked in the vertical direction.

In Figure 2.11, we show the ratio  $(\langle Q \rangle / \langle I \rangle) / (1 - \mu^2)$  for magnetic fields with different angular distributions, the field strength being kept equal to a single value  $B_0$ . In Figure 2.11(a), we see that the choice of the angular distribution has a strong effect on the amplitude of this ratio, but not on its center-to-limb variation, for the reason given above. Figure 2.11(b) shows the variation of this ratio with the Hanle efficiency parameter  $\Gamma_{B_0}$  for  $\tau = 0$ ,  $x = 0$ , and  $\mu = 0.05$ . We observe the standard Hanle saturation for large field strengths. An isotropic distribution, and a sine power-law with a fairly horizontally peaked distribution, yield similar polarizations, as already been pointed out in Stenflo (1982). There are however observable differences around  $\Gamma_{B_0} = 1$ . The polarization is larger for the cosine power-law because the distribution is strongly peaked in the vertical direction.

These numerical experiments with different magnetic field PDFs indicate a clear sensitivity of the polarization to the magnetic field strength and angular distributions. Hence, any information on mean magnetic field strengths, extracted from Hanle depolarization measurements, may depend critically on the choice of the magnetic field PDF that has been made a priori for the analysis of the observations.

## 2.9 Concluding remarks

In this chapter, we have studied the Hanle effect due to a random magnetic field with a finite correlation length, in order to assess limitations to the usual micro-turbulent approximation. The modeling of the magnetic field by a Markovian random process, piecewise constant, characterized by a correlation length and a magnetic field vector PDF, has enabled us to construct a RT equation for a mean radiation field, that still depends on the random values of the magnetic field (Section 2.3). A simple averaging of the solution of this equation over the PDF yields the mean Stokes parameters. The RT equation is solved numerically by an PALI method, generalized to the problem at hand (Section 2.4).

We have found that optically thin lines (lines with optical thickness  $T \ll 1$ ), and very optically thick ones ( $T \gg 100$ ) can be treated with the micro-turbulent approximation. For these lines, the polarization is created locally by a small number of scattering events. For optically thick lines they are located near the surface. To evaluate this number of events, the polarization has been calculated by a method of successive iterations leading to a series expansion in the mean number of scattering events (Section 2.7). For optically thin and thick lines, this number is around 5; for lines with intermediate optical thicknesses ( $T \simeq 10 - 100$ ), it is significantly larger (10–15) and these lines show some sensitivity to the magnetic field correlation length (see Figure 2.4).

We have also found that for a random magnetic field, the single scattering approximation can be safely used to evaluate the Hanle depolarization. For a deterministic magnetic field, it may also provide a reasonable approximation. In contrast, for the Rayleigh scattering, it may lead to large errors, except for optically thin lines (see Figure 2.8).

Numerical experiments carried out in the micro-turbulent limit with different types of magnetic field PDF, indicate that the polarization is quite sensitive to the shape of the PDF (Section 2.8). However, our results suggest that it may not be easy to retrieve a quiet Sun magnetic field PDF from the Hanle effect depolarization measurements, since the same degree of linear polarization can be created by PDFs that have rather different shapes. Also the center-to-limb variation of the linear polarization depends very little on the PDF shape. Several laws for the solar magnetic field PDF have been proposed in recent years. They have been deduced from Zeeman effect measurements and may contain some uncertainty in the weak field domain involved in the Hanle effect. Numerical simulations such as those carried out in Schüssler & Vögler (2008) may clarify the situation.

In this chapter, we have assumed CRD at each scattering. This assumption is certainly

not valid to analyze the Hanle depolarization of strong resonance lines showing significant PRD effects. An example is the Ba II D2 line considered in Faurobert et al. (2009) to evaluate the turbulent magnetic field in the low chromosphere. However, our conclusions concerning the applicability of the micro-turbulent approximation remain most probably valid, since the polarization is still created in a small region close to the surface. The RT equations given here, and their method of solution, can be easily generalized to handle PRD and to verify this prediction, but this generalization will be accompanied by a significant increase in computing time.

### New Results

For the first time, an exact theory of turbulent magnetic fields for the Hanle effect is developed in this chapter. The following important results were achieved.

1. RT equations are established for the calculation of the mean Stokes parameters and they are solved numerically by a Polarized Approximate Lambda Iteration (PALI) method.
2. We show that optically thin spectral lines and optically very thick ones are insensitive to the correlation length of the magnetic field, while spectral lines with intermediate optical depths (around 10-100) show some sensitivity to this parameter.
3. The result is interpreted in terms of the mean number of scattering events needed to create the surface polarization. It is shown that the single-scattering approximation holds good for optically thin and thick lines, but may fail for lines with intermediate thickness.
4. The dependence of the polarization on the magnetic field vector probability density function (PDF) is examined in the micro-turbulent limit. A few PDFs with different angular and strength distributions, but equal mean value of the magnetic field, are considered. It is found that the polarization is in general quite sensitive to the shape of the magnetic field strength PDF and also to the angular distribution.
5. The mean field derived from Hanle effect analysis of polarimetric data strongly depends

on the choice of the field strength distribution used in the analysis. It is shown that micro-turbulence is in general a safe approximation.

*Further studies related to the work presented in this chapter are published in:*

1. Anusha, L. S., Sampoorna, M., Frisch, H., & Nagendra, K. N., 2010b, in **Astrophysics and Space Science Proceedings: Magnetic Coupling between the Interior and the Atmosphere of the Sun**, eds. S. S. Hasan, & R. J. Rutten (Heidelberg, Berlin:Springer-Verlag), 390–394
2. Nagendra, K. N., Sampoorna, M., & **Anusha, L. S.**, 2010, in **Recent advances in Spectroscopy; Astrophysical, Theoretical and Experimental Perspective**, eds. R. Chaudhary, M. V. Mekkaden, A. V. Raveendran, A. Satyanarayanan (Heidelberg, Berlin: Springer-Verlag), 139–153

## Chapter 3

# Bi-Conjugate Gradient methods for radiative transfer

*The contents of this chapter are based on the following publication:*

Anusha, L. S., Nagendra, K. N., Paletou, F., and Léger, L. 2009, **ApJ**, 704, 661-671

### 3.1 Introduction

The solution of radiative transfer (RT) equation in spherical geometry remains a classic problem even 75 years after the first attempts by Chandrasekhar (1934) and Kosirev (1934) who used Eddington approximation. In later decades more accurate methods were given (see Mihalas 1978; Peraiah 2002 for historical reviews). Hummer & Rybicki (1971) and Kunasz & Hummer (1974a, 1974b) developed a variable Eddington factor method, and computed the solution on rays of constant impact parameter (tangents to the discrete shells and parallel to line of sight) in one-dimensional (1D) spherical geometry. This is a very efficient differential equation based technique which uses Feautrier solution along rays of constant impact parameter. An integral equation method was developed by Schmid-Burgk (1974) to solve the problem, again based on tangent rays approach. Peraiah & Grant (1973) presented a highly accurate finite difference method based on the first order form of the RT equation. All these methods were later extended to expanding, and highly extended atmospheres. However, in this chapter we confine our attention to static, 1D spherical atmospheres.

In a next epoch in the development of spherical RT, the integral operator techniques were proposed. The idea of operator splitting and the use of approximate operators in

iterative methods was brought to the astrophysical RT in planar media by Cannon (1973). Scharmer (1981) extended his work with a new definition of the approximate operator. The application of integral operator technique to the spherical RT problems started with the work of Hamann (1985) and Werner & Husfeld (1985). They used approximate operators that are diagonal, constructed from core saturation approach. The  $\Lambda$  operator contains the non-local coupling between all the spatial points. Olson et al. (1986) showed that the diagonal part (local coupling) of the actual  $\Lambda$  operator itself is an optimum choice for the ‘approximate operator’. These methods are known as Approximate Lambda Iteration (ALI) methods. The ALI methods which are based on the concept of operator splitting and the use of Jacobi iterative technique, were widely used in the later decades in RT theory (see Hubeny 2003; Hamann 2003, for historical reviews).

Gros et al. (1997) used an implicit integral method to solve static spherical line RT problems. The most recent and interesting work on spherical RT are the papers by Asensio Ramos & Trujillo Bueno (2006) and Daniel & Cernicharo (2008) both of which are based on Gauss-Seidel (GS) and Successive Over Relaxation (SOR) iterative techniques.

Klein et al. (1989) were the first to use Bi-Conjugate Gradient (BiCG) technique in astrophysics. They use BiCG with incomplete LU decomposition technique in their double splitting iterative scheme along with Orthomin acceleration. They applied it to multi-dimensional line RT problem. Auer (1991) describes a variant of Orthomin acceleration which uses ‘Minimization with respect to a set of Conjugate vectors’. He uses a set of  $n$  (usually  $n=2$  or  $n=4$ ) conjugate direction vectors which are orthogonal to each other, constructed using the residual vectors with a purpose to accelerate the convergence sequence.

Hubeny & Burrows (2007) developed GMRES (actually its variant called Generalized Conjugate Residuals GCR) method to solve the spherical RT problem. It is based on an application of the idea of Krylov subspace techniques. They applied it to a more general time-dependent transport with velocity fields in a medium which scatters anisotropically. They apply GMRES method to the neutrino transfer. It can also be used for RT problem, including the simple problem of two-level atom line RT discussed in this chapter.

The Preconditioned Bi-Conjugate Gradient method (hereafter Pre-BiCG, see eg., Saad 2000) was first introduced to the line RT in planar media, by Paletou & Anterrieu (2009) who describe the method and compare it with other prevalent iterative methods, namely GS/SOR. In this chapter (see also Anusha et al. 2009) we adopt the Pre-BiCG method to the case of spherical media. We also show that the ‘Stabilized Preconditioned Bi-Conjugate Gradient (Pre-BiCG-STAB)’ is even more advantageous in terms of memory requirements



but with similar convergence rate as Pre-BiCG method.

It is well known that the spherical RT in highly extended systems, despite being a straight forward problem, has two inherent numerical difficulties namely (i) peaking of the radiation field towards the radial direction, and (ii) the  $(1/r^2)$  dilution of radiation in spherical geometry. To handle these, it becomes essential to take a very large number of angle ( $\mu$ ) points and spatial ( $\tau$ ) points respectively. The existing ALI methods clearly slow down when extreme angular and spatial resolutions are demanded (for example see Table 3.1). Therefore there is a need to look for a method that is as efficient as ALI methods, but faster, and is relatively less sensitive to the grid resolution. The Pre-BiCG method and Pre-BiCG-STAB provide such an alternative as we show in this chapter.

Governing equations are presented in Section 3.2.1. In Section 3.2.2, we define the geometry of the problem and the specific details of gridding. In Section 3.2.3, the benchmark models are defined. We briefly recall the Jacobi, and GS/SOR methods in Section 3.2.4. In Section 3.3 we describe the Pre-BiCG method. The computing algorithm is presented in Section 3.3.1. In Section 3.4 we describe the Pre-BiCG-STAB method briefly, and we give the computing algorithm in Section 3.4.1. In Section 3.5 we compare the performance of Pre-BiCG with the Jacobi, and GS/SOR methods. In Section 3.6 we validate this new method, by comparing with the existing well known benchmark solutions in spherical line RT theory. Concluding remarks are presented in Section 3.7.

## 3.2 Radiative transfer in a spherical medium

### 3.2.1 The transfer equation

In this chapter we restrict ourselves to the case of a two-level atom model. Further, we assume complete frequency redistribution. The RT equation in divergence form is written as

$$\mu \frac{\partial \mathbf{I}(r, \mu, x)}{\partial r} + \frac{1 - \mu^2}{r} \frac{\partial \mathbf{I}(r, \mu, x)}{\partial \mu} = [\kappa_l(r)\phi(x) + \kappa_c(r)][\mathbf{S}(x, r) - \mathbf{I}(r, \mu, x)]. \quad (3.1)$$

Here,  $\mathbf{I}$  is the specific intensity of radiation,  $\mathbf{S}$  - the source function,  $r$  - the radial distance,  $\mu$  - the direction cosine,  $x$  - the frequency measured in Doppler width units from line center,  $\phi(x)$  - the line profile function, and  $\kappa_l(r)$ ,  $\kappa_c(r)$  - line center and continuum opacities respectively. The differential optical depth element is given by

$$d\tau(r) = -\kappa_l(r)dr. \quad (3.2)$$

There are several methods which use the above form of the RT equation (see Peraiah 2002). In this chapter we solve the RT equation on a set of rays tangent to the spherical shells. It is written as

$$\pm \frac{\partial \mathbf{I}^\pm(z, p, x)}{\partial z} = [\kappa_l(r)\phi(x) + \kappa_c(r)][\mathbf{S}(x, r) - \mathbf{I}^\pm(z, p, x)], \quad (3.3)$$

for the outgoing (+) and incoming (-) rays respectively. Here  $z$  is the distance along the tangent rays and  $p$  is the distance from the center to the points on the vertical axis (the mid-line), where the tangent rays intersect it (see Figure 3.1). The direction cosines  $\mu$  ( $0 \leq \mu \leq 1$ ) are related to  $p$  by  $\mu = \sqrt{1 - (p^2/r^2)}$  for a shell of radius  $r$ . The optical depth scale along the tangent rays are now computed using  $d\tau(z) = d\tau(r)/\mu$ . In practical work, due to the symmetry of the problem, it is sufficient to perform the computations on a quadrant only. The source function is defined as

$$\mathbf{S}(x, r) = \frac{\kappa_l(r)\phi(x)\mathbf{S}_l(r) + \kappa_c(r)\mathbf{S}_c(r)}{\kappa_l(r)\phi(x) + \kappa_c(r)}. \quad (3.4)$$

$\mathbf{S}_c(r)$  is the continuum source function taken as the Planck function  $B_\nu(r)$  throughout this chapter. The monochromatic optical depth scale  $\Delta\tau_x = \Delta\tau_z[\phi(x) + \beta_c]$ , with  $\beta_c = \kappa_c(r)/\kappa_l(r)$  along the tangent rays. For simplicity, hereafter we omit the subscript  $z$  from  $\tau_z$  and write  $\tau$  to denote  $\tau_z$ . The line source function is given by

$$\mathbf{S}_l(r) = (1 - \epsilon) \int_{-1}^1 \frac{d\mu'}{2} \int_{-\infty}^{\infty} dx' \phi(x') \mathbf{I}(\tau, \mu', x') + \epsilon B_\nu(r), \quad (3.5)$$

with the thermalization parameter defined in the conventional manner as  $\epsilon = C_{ul}/(A_{ul} + C_{ul})$ , where  $C_{ul}$  and  $A_{ul}$  are collisional and radiative de-excitation rates. The intensity along the rays is computed using the formal solution integral

$$\mathbf{I}^+(\tau, p, x) = \mathbf{I}_0^+(\tau, p, x) \exp[-\Delta\tau_x] + \int_{\tau}^T \exp[-\Delta\tau'_x] \mathbf{S}(\tau') [\phi(x) + \beta_c] d\tau'. \quad (3.6)$$

The corresponding integral for the incoming rays is

$$\mathbf{I}^-(\tau, p, x) = \mathbf{I}_0^-(\tau, p, x) \exp[-\Delta\tau_x] + \int_0^{\tau} \exp[-\Delta\tau'_x] \mathbf{S}(\tau') [\phi(x) + \beta_c] d\tau'. \quad (3.7)$$

Here,  $\mathbf{I}_0^+(\tau, p, x)$  represents the inner boundary condition imposed at the core and along the mid-vertical line (see Figure 3.1).  $\mathbf{I}_0^-(\tau, p, x)$  is the outer boundary condition specified at the surface of the spherical atmosphere. When the above formal integral is applied to a stencil of short characteristics (MOP) along a tangent ray, it takes a simple algebraic form

$$\mathbf{I}^\pm(\tau, p, x) = \mathbf{I}_0^\pm(\tau, p, x) \exp[-\Delta\tau_M] + \psi_M^\pm(\tau, p, x) \mathbf{S}_M + \psi_O^\pm(\tau, p, x) \mathbf{S}_O + \psi_P^\pm(\tau, p, x) \mathbf{S}_P, \quad (3.8)$$

where  $\mathbf{S}_{M,O,P}$  are the source function values at M, O and P points on a short characteristics. The coefficients  $\psi$  are calculated following the method described in Kunasz & Auer (1988).

### 3.2.2 The constant impact parameter approach

In Figure 3.1, we show the geometry used for computing the specific intensity  $\mathbf{I}(\tau, p, x)$  along rays of constant impact parameter.

In a spherically symmetric medium, we first discretize the radial co-ordinate  $r$  ( $R_{\text{core}} \leq r \leq R$ ), where  $R_{\text{core}}$  is the core radius, and  $R$  is the outer radius of the atmosphere. The radial grid is given by  $r_k, k = 1, 2, \dots, n_d$ , where  $r_1$  is the radius of the outer most shell, and  $r_{n_d}$  is that of the inner most shell.  $d\Omega/4\pi$  is the probability that the direction of propagation of an emitted photon lies within an element of solid angle  $d\Omega$ . In the azimuthally symmetric case, it is  $d\mu/2$ . To calculate the mean intensity  $\bar{\mathbf{J}}$  in plane parallel geometry, we integrate the intensity over the angular variable  $\mu$  itself. In spherical medium, we have one to one correspondence between the  $(\mu, r)$  and the  $(p, r)$  system. In  $(p, r)$  system, the probability that a photon is emitted with its impact parameter between  $p$  and  $p+dp$ , propagating in either positive  $\mu$  or negative  $\mu$  direction is  $pdp/2r\sqrt{r^2 - p^2}$ . The direction cosines made by the rays in the  $(\mu, r)$  space, with a tangent ray of constant  $p$  value, are given by  $\mu_i = \sqrt{1 - (p^2/r_i^2)}$  at different radii  $r_i$ . Therefore the angular integration factor  $d\mu/2$  can be changed to  $pdp/2r\sqrt{r^2 - p^2}$  (see Kunasz & Hummer 1974b).

*The  $p$  - grid construction:* If  $n_c$  is the number of core rays, then the  $p$ -grid for the core rays is computed using:

```

do  $i = 1, n_c$ 
 $p(i) = R_{\text{core}} * (\sqrt{1 - (i/n_c)^2})$ 
 $0 < p < R_{\text{core}}$ 
end do

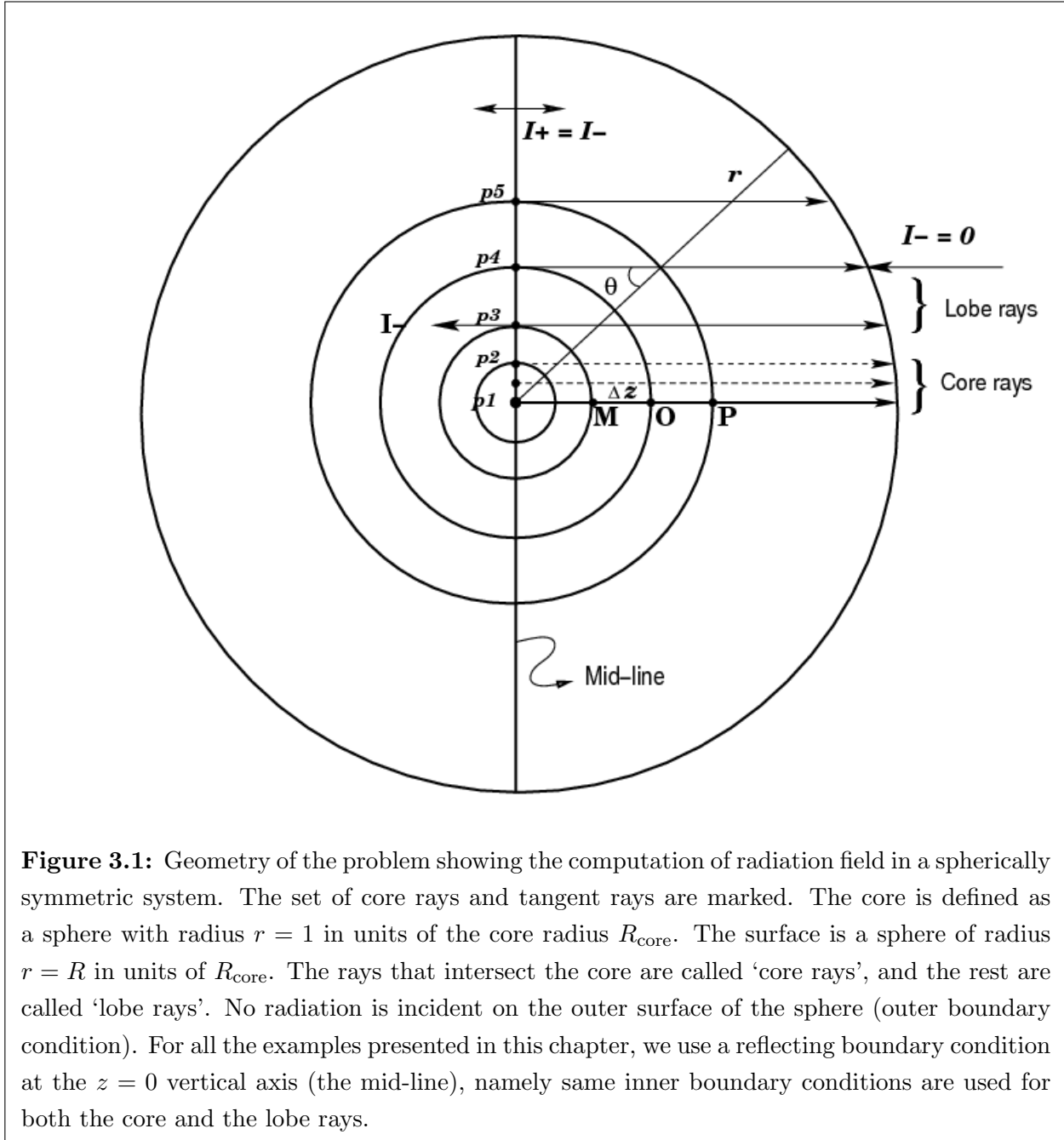
```

The number of lobe rays equals the number of radial points. For lobe rays, the  $p$ -grid is same as radial  $r$ -grid. It is constructed using:

```

do  $i = 1, n_d$ 
 $p(n_c + i) = r(i)$ 
end do

```



where  $n_d$  = the number of radial points. Thus, the total number of impact parameters is  $n_p = n_c + n_d$ . We have followed Auer (1984) in defining the  $p$ -grid in this manner.

### 3.2.3 Benchmark models

Geometrical distances along the rays of constant impact parameter are constructed as follows:

$$z(p, r) = \sqrt{r^2 - p^2}. \quad (3.9)$$

For spherical shells we perform several tests using power-law type variation of density. For such atmospheres, the line and continuum opacities also vary as a power law given by

$$\kappa_{l,c}(r) \propto r^{-\tilde{n}}. \quad (3.10)$$

Let  $C$  and  $\bar{C}$  denote the proportionality constants for  $\kappa_l(r)$  and  $\kappa_c(r)$  respectively. The constant  $C$  can be determined using the optical depth at line center  $T$ . For a power law with index  $\tilde{n}$ ,

$$C = \frac{T(1 - \tilde{n})}{R^{(1-\tilde{n})} - R_{\text{core}}^{(1-\tilde{n})}}. \quad (3.11)$$

Using the given input value of  $\beta_c = \bar{C}/C$  we can compute the constant  $\bar{C}$ .

We use Voigt profile with damping parameter  $a$  or the Doppler profile for the results presented in this chapter. The spherical shell atmosphere is characterized by the following parameters:  $(R, \tilde{n}, T, a, \epsilon, \beta_c, B_\nu)$ . We recall that  $R$  is the outer radius of the spherical atmosphere surrounding a hollow central cavity of radius  $R_{\text{core}}$ . When  $R = R_{\text{core}}$  we recover the plane parallel limit. For the spherical shell atmospheres, we take  $R_{\text{core}} = 1$  as the unit of length to express the radial co-ordinate. The boundary conditions are specified at the outer boundary ( $\mathbf{I}^-(\tau = 0, p, x) = 0$ ) and the inner boundary. There are two types of inner boundary conditions:

(a) *Emitting Core:*

Core rays:

$$\mathbf{I}^+(\tau = T, p \leq R_{\text{core}}, x) = B_\nu. \quad (3.12)$$

Lobe rays:

$$\mathbf{I}^+(\tau = T, p = r_i, x) = \mathbf{I}^-(\tau = T, p = r_i, x), \quad (3.13)$$

$i = 1, 2, \dots, n_d$  along the mid-vertical.

(b) *Hollow Core:*

For both the core and the lobe rays:

$$\mathbf{I}^+(\tau = T, p, x) = \mathbf{I}^-(\tau = T, p, x). \quad (3.14)$$

The hollow core boundary condition is also called ‘planetary nebula boundary condition’ (see Mihalas 1978). It is clear that a spherical shell with a hollow core is equivalent to a plane parallel slab of optical thickness  $2T$  with symmetry about the mid-plane at  $\tau = T$ . We use spherical shell atmospheres for most of our studies.

### 3.2.4 Iterative methods of ALI type for a spherical medium

The ALI methods have been successfully used for the solution of RT equation in spherical shell atmospheres (see eg., Hamann 2003 and references therein). These authors use the Jacobi iterative methods (first introduced by Olson et al. 1986) for computing the source function corrections. Recently the GS method has been proposed to solve the same problem (see eg., Asensio Ramos & Trujillo Bueno 2006; Daniel & Cernicharo 2008). Hubeny & Burrows (2007) proposed the GMRES method for solving spherical RT problem. GMRES and Pre-BiCG both belong to Krylov subspace technique. In this chapter we compute the spherical RT solutions by Jacobi and GS/SOR methods, and compare with the solutions computed using the Pre-BiCG method. For the sake of clarity, we recall briefly the steps of Jacobi and GS/SOR methods.

*Jacobi Iteration Cycle:* The source function corrections are given by

$$\delta \mathbf{S}_k^n = \mathbf{S}_k^{n+1} - \mathbf{S}_k^n = \frac{(1 - \epsilon) \bar{\mathbf{J}}_k^n + \epsilon B_\nu - \mathbf{S}_k^n}{[1 - (1 - \epsilon) \Lambda_{k,k}^*]}, \quad (3.15)$$

for the  $n$ th iterate. Here  $k$  is the depth index. The  $\Lambda^*$  is the approximate operator which is simply taken as the diagonal of the actual  $\Lambda$  operator defined through

$$\Lambda[\mathbf{S}] = \bar{\mathbf{J}}; \quad (3.16)$$

$$\bar{\mathbf{J}}(\tau) = \int_{-1}^{+1} \frac{d\mu'}{2} \int_{-\infty}^{\infty} dx' \phi(x') \mathbf{I}(\tau, \mu', x'). \quad (3.17)$$

*GS/SOR Iteration Cycle:* The essential difference between the Jacobi and GS/SOR methods is the following:

$$\mathbf{S}_k^{n+1} = \mathbf{S}_k^n + \omega \delta \mathbf{S}_k^n.$$

**Table 3.1:** The sensitivity of different iterative methods to the convergence criteria  $\bar{\omega}$ . Tables 3.1(a), 3.1(b), 3.1(c) correspond respectively to  $\bar{\omega}=10^{-6}$ ,  $10^{-8}$ , and  $10^{-10}$ . Number of points per decade in the logarithmic  $\tau$  scale is denoted by  $[n_{\text{pts}}/D]$ . The SOR parameter used is 1.5. The entries under each method indicate the number of iterations required for convergence.

(a)  $\bar{\omega}=10^{-6}$ 

$[n_{\text{pts}}/D]$	Jacobi	GS	SOR	Pre-BiCG	Pre-BiCG-STAB
5	81	40	24	16	12
8	136	69	22	19	15
30	444	230	74	33	23

(b)  $\bar{\omega}=10^{-8}$ 

$[n_{\text{pts}}/D]$	Jacobi	GS	SOR	Pre-BiCG	Pre-BiCG-STAB
5	110	54	30	18	13
8	186	94	30	22	15
30	635	325	103	39	30

(c)  $\bar{\omega}=10^{-10}$ 

$[n_{\text{pts}}/D]$	Jacobi	GS	SOR	Pre-BiCG	Pre-BiCG-STAB
5	138	68	37	20	14
8	236	118	40	25	18
30	827	419	132	45	30

Here the parameter  $\omega$  is called the relaxation parameter which is unity for the GS technique.

The SOR method is derived from the GS method by simply taking  $1 < \omega < 2$  (see Trujillo Bueno & Fabiani Bendicho 1995 for details). The source function correction for the GS method is given by

$$\delta \mathbf{S}_k^n = \frac{(1 - \epsilon) \bar{\mathbf{J}}_k^{n(\text{old}+\text{new})} + \epsilon B_\nu - \mathbf{S}_k^n}{[1 - (1 - \epsilon) \Lambda_{k,k}^*]}, \quad (3.18)$$

where the quantity  $\bar{\mathbf{J}}_k^{n(\text{old}+\text{new})}$  denotes the mean intensity computed using new values of the source function as soon as they become available. For those depth points for which the source function correction is not yet complete, GS method uses the values of the source function corresponding to the previous iteration (see Trujillo Bueno & Fabiani Bendicho(1995)). For clarity we explain how the GS algorithm works in spherical geometry, on

rays of constant impact parameter.

Begin loop over iterations

Begin loop over radial shells with index  $k$

Begin loop over impact parameters (or directions) with increasing  $p$

For the  $n$ th iteration:

**For the incoming rays ( $\mu < 0$ ):**  
**(Reverse sweep along radial shells)**

- (a) This part of the calculations start at the outer boundary for all impact parameter rays.
- (b)  $\mathbf{I}_k$  are first calculated for a given radial shell  $k$  using  $\mathbf{S}_k^n$ ,  $\mathbf{S}_{k-1}^n$  and  $\mathbf{S}_{k+1}^n$ .
- (c) The partial integral  $\bar{\mathbf{J}}_k(\mu < 0)$  are calculated before proceeding to the next shell. This part of the calculations is stopped when the core (for the core rays) and the mid-vertical line (for the lobe rays) are reached.

**For outgoing rays ( $\mu > 0$ ):**  
**(Forward sweep along radial shells)**

- (d) This part of the calculations start at the inner boundary. First, for the radial shell with  $k = n_d$   $\bar{\mathbf{J}}_{n_d}$  is calculated, using boundary conditions  $\mathbf{I}_{n_d}$ .
- (e)  $\delta\mathbf{S}_{n_d}^n$  is computed and the source function is updated using  $\mathbf{S}_{n_d}^{n+1} = \mathbf{S}_{n_d}^n + \delta\mathbf{S}_{n_d}^n$ .
- (f) For the next radial shell  $k = n_d - 1$ :  
to calculate  $\mathbf{I}_{n_d-1}$  by applying the short characteristics formula,  $\mathbf{S}_{n_d}$ ,  $\mathbf{S}_{n_d-1}$  and  $\mathbf{S}_{n_d-2}$  are needed. Already  $\mathbf{S}_{n_d}^{n+1}$ ,  $\mathbf{S}_{n_d-1}^n$  and  $\mathbf{S}_{n_d-2}^n$  are available. GS takes advantage of the available new source function at  $k = n_d$ .  $\mathbf{I}_{n_d-1}$  is calculated with this set of source functions.



(g) Then  $\bar{\mathbf{J}}_{n_d-1}(\mu > 0)$  are calculated using  $\mathbf{I}_{n_d-1}$ .

(h) Note that,  $\bar{\mathbf{J}}_{n_d-1}(\mu < 0)$  was calculated using  $\mathbf{S}_{n_d}^n$ ,  $\mathbf{S}_{n_d-1}^n$ , and  $\mathbf{S}_{n_d-2}^n$  whereas  $\bar{\mathbf{J}}_{n_d-1}(\mu > 0)$  used the “updated” source function  $\mathbf{S}_{n_d}^{n+1}$ . Therefore  $\bar{\mathbf{J}}_{n_d-1}$  is corrected by adding the following correction:

$$\Delta \bar{\mathbf{J}}_{n_d-1} = \delta \mathbf{S}_{n_d}^n \int_{-1}^0 \psi_{n_d}(\mu < 0) d\mu.$$

(i)  $\delta \mathbf{S}_{n_d-1}^n$  and  $\mathbf{S}_{n_d-1}^{n+1} = \mathbf{S}_{n_d-1}^n + \delta \mathbf{S}_{n_d-1}^n$  are now calculated.

(j) Since “updated”  $\mathbf{S}_{n_d-1}^{n+1}$  at  $k = n_d - 1$  is also available now, before going to the next radial shell it is appropriate to correct the intensity at the present radial shell by adding to it, the following correction term

$$\Delta \mathbf{I}_{n_d-1}(\mu) = \delta \mathbf{S}_{n_d-1}^n \psi_{n_d-1}.$$

End loop over impact parameters (or directions)

End loop over radial shells

End loop over iterations.

### 3.3 Preconditioned BiCG method for a spherical medium

In this section we first describe the essential ideas of the Pre-BiCG method. The complete theory of the method is described in Saad (2000). We recall that the two-level atom source function with a background continuum is given by

$$\mathbf{S}(x, r) = \frac{\kappa_l(r)\phi(x)\mathbf{S}_l(r) + \kappa_c(r)\mathbf{S}_c(r)}{\kappa_l(r)\phi(x) + \kappa_c(r)}. \quad (3.19)$$

It can be re-written as

$$\mathbf{S}(x, r) = \tilde{p}(x, r)\mathbf{S}_l(r) + [1 - \tilde{p}(x, r)]\mathbf{S}_c(r), \quad (3.20)$$

where

$$\tilde{p}(x, r) = \frac{\kappa_l(r)\phi(x)}{\kappa_l(r)\phi(x) + \kappa_c(r)}. \quad (3.21)$$

From Equations (3.5), (3.16) and (3.17), we get

$$\mathbf{S}(x, r) = \tilde{p}(x, r)\{(1 - \epsilon)\Lambda[\mathbf{S}(x, r)] + \epsilon B_\nu(r)\} + [1 - \tilde{p}(x, r)]\mathbf{S}_c(r). \quad (3.22)$$

Therefore the system of equations to be solved becomes

$$[\hat{I} - (1 - \epsilon)\tilde{p}(x, r)\Lambda]\mathbf{S}(x, r) = \tilde{p}(x, r)\epsilon B_\nu(r) + [1 - \tilde{p}(x, r)]\mathbf{S}_c(r), \quad (3.23)$$

which can be expressed in a symbolic form as

$$\hat{A}\mathbf{y} = \mathbf{b}; \quad \text{with} \quad \hat{A} = [\hat{I} - (1 - \epsilon)\tilde{p}(x, r)\Lambda]; \quad \mathbf{y} = \mathbf{S}(x, r). \quad (3.24)$$

The vector  $\mathbf{b}$  represents quantities on the RHS of Equation (3.23). Now we describe briefly, how the Pre-BiCG method differs from ALI based methods.

Let  $\mathbb{R}^n$  denote the  $n$ -dimensional Euclidean space of real numbers.

**Definition:** The Pre-BiCG algorithm is a process involving projections onto the  $m$ -dimensional subspace ( $m \leq n$ ) of  $\mathbb{R}^n$

$$\mathcal{K}_m = \text{span}\{\mathbf{v}_1, \hat{A}\mathbf{v}_1, \dots, \hat{A}^{m-1}\mathbf{v}_1\}, \quad (3.25)$$

and also being orthogonal to another  $m$ -dimensional subspace of  $\mathbb{R}^n$

$$\mathcal{L}_m = \text{span}\{\mathbf{w}_1, \hat{A}^T\mathbf{w}_1, \dots, \hat{A}^{T(m-1)}\mathbf{w}_1\}. \quad (3.26)$$

Here  $\mathbf{v}_1$  is taken as the initial residual vector  $\mathbf{r}_0 = \mathbf{b} - \hat{A}\mathbf{y}_0$  with  $\mathbf{y}_0$  the initial guess for the solution of Equation (3.24). The vector  $\mathbf{w}_1$  is taken as arbitrary such that the inner product  $\langle \mathbf{v}_1, \mathbf{w}_1 \rangle \neq 0$ . The method recursively constructs a pair of bi-orthogonal bases  $\{\mathbf{v}_i; i = 1, 2, \dots, m\}$  and  $\{\mathbf{w}_i; i = 1, 2, \dots, m\}$  for  $\mathcal{K}_m$  and  $\mathcal{L}_m$  respectively, such that they satisfy the bi-orthogonality condition  $\langle \mathbf{v}_i, \mathbf{w}_j \rangle = \delta_{ij}$ . For the purpose of application to the RT theory it is convenient to write the Pre-BiCG steps in the form of an algorithm. For simplicity we drop the explicit dependence on variables.

### 3.3.1 The Preconditioned BiCG Algorithm

Our goal is to solve Equation (3.24). In this section the symbols  $\mathbf{r}_i$  and  $\mathbf{p}_i$  are used to be in conformity with the standard notation of residual and conjugate direction vectors. They should not be confused with the radius vector  $r_i$  and impact parameter  $p_i$  which appear in spherical RT theory.

(a) The very first step is to construct and store the matrix  $\hat{A}^T$  (which does not change with iterations, for the cases considered here, namely two-level atom model). Details of computing  $\hat{A}^T$  efficiently is described in Appendix C.

We follow the preconditioned version of the BiCG method. Preconditioning is a process in which the original system of equations is transformed into a new system, which has faster rate of convergence. For example, this can be done by solving the new system  $\hat{M}^{-1}\hat{A}\mathbf{y} = \hat{M}^{-1}\mathbf{b}$  where  $\hat{M}$  is an appropriately chosen matrix, called the ‘‘preconditioner’’ (see also equation 2 of Auer 1991). This preconditioner is chosen in such a way that,

- (i) the new system should be easier to solve,
- (ii)  $\hat{M}^{-1}$  itself should be inexpensive to operate on an arbitrary vector,
- (iii) the preconditioning is expected to increase the convergence rate.

The choice of the preconditioner depends on the problem at hand. When an appropriate  $\Lambda^*$  is chosen such that the amplification matrix  $[\hat{I} - (1 - \epsilon)\Lambda^*]$  has as small a maximum eigen value as possible (see Olson et al. 1986), the convergence rate is enhanced. What enables the convergence of ALI, that satisfies the above property, and simplest to manipulate, is the diagonal of the  $\Lambda$  itself. Therefore the amplification matrix  $[\hat{I} - (1 - \epsilon)\Lambda^*]$  with a diagonal form for  $\Lambda^*$  is a simple and natural choice as a ‘preconditioner’. We construct the preconditioner matrix  $\hat{M}$  by taking it as the diagonal of  $\hat{A}$ .

(b) An initial guess for the source function is

$$\mathbf{y}_0 = \tilde{p}\epsilon\mathbf{B} + (1 - \tilde{p})\mathbf{S}_c, \quad (3.27)$$

where the thermal part  $\epsilon\mathbf{B}$  is taken as an initial guess for  $\mathbf{S}_l$ .

(c) The formal solver is used with  $\mathbf{y}_0$  as input to calculate  $\bar{\mathbf{J}}(\mathbf{y}_0)$ .

(d) The initial residual vector is computed using

$$\mathbf{r}_0 = \mathbf{b} - \hat{A}\mathbf{y}_0.$$

(e) The initial bi-orthogonal counterpart  $\mathbf{r}_0^*$  for  $\mathbf{r}_0$  is chosen such that we have  $\langle \mathbf{r}_0, \mathbf{r}_0^* \rangle \neq 0$ . One can choose  $\mathbf{r}_0^* = \mathbf{r}_0$  itself.

Such an initial choice of  $\mathbf{r}_0^*$  vector is necessary, as the method is based on the construction of bi-orthogonal residual vectors  $\mathbf{r}_i$  and  $\mathbf{r}_i^*$  recursively, for  $i = 1, 2, \dots, m$ , where

$m$  is the number of iterations required for convergence. The process of constructing the bi-orthogonal vectors gets completed, once we reach the convergence. In other words, the number of bi-orthogonal vectors necessary to guarantee a converged solution represents the actual number of iterations itself. It is useful to remember that when we refer to ‘bi-orthogonality’ hereafter, say eg., of the residual vectors  $\mathbf{r}_i, \mathbf{r}_i^*$  we simply mean that  $\langle \mathbf{r}_i, \mathbf{r}_j^* \rangle = 0$  for  $i \neq j$ , but  $\langle \mathbf{r}_i, \mathbf{r}_i^* \rangle$  need not be unity.

(f) The bi-orthogonalization process makes use of conjugate direction vectors  $\mathbf{p}$  and  $\mathbf{p}^*$  for each iteration. They can be constructed during the iterative process, again through recursive relations. An initial guess to these vectors is made as  $\mathbf{p}_0 = \mathbf{r}_0$  and  $\mathbf{p}_0^* = \mathbf{r}_0^*$ .

(g) The preconditioned initial residual vectors  $\boldsymbol{\zeta}_0^*$  are computed using

$$\boldsymbol{\zeta}_0^* = \hat{M}^{-1} \mathbf{r}_0^*. \quad (3.28)$$

(h) For  $i = 1, 2, \dots$ , the following steps are carried out until convergence:

(i) Using the formal solver with  $\mathbf{p}_i$  as input (instead of actual source vector  $\mathbf{y}$ ),  $\bar{\mathbf{J}}[\mathbf{p}_i]$  is obtained.

(j)  $\hat{A}[\mathbf{p}_i]$  is computed using

$$\hat{A}[\mathbf{p}_i] = \mathbf{p}_i - (1 - \epsilon) \tilde{p} \bar{\mathbf{J}}[\mathbf{p}_i].$$

(k) The inner products

$$\langle \hat{A}[\mathbf{p}_i], \mathbf{p}_i^* \rangle \quad \text{and} \quad \langle \mathbf{r}_i, \boldsymbol{\zeta}_i^* \rangle, \quad (3.29)$$

are computed and used to estimate the quantity

$$\alpha_i = \frac{\langle \mathbf{r}_i, \boldsymbol{\zeta}_i^* \rangle}{\langle \hat{A}[\mathbf{p}_i], \mathbf{p}_i^* \rangle}. \quad (3.30)$$

(l) The new source function is obtained through

$$\mathbf{y}_{i+1} = \mathbf{y}_i + \alpha_i \mathbf{p}_i. \quad (3.31)$$

*Test for Convergence:* Let  $\bar{\omega}$  denote the convergence criteria. If

$$\max_{\tau} \{ \delta \mathbf{y} / \mathbf{y} \} \leq \bar{\omega}, \quad (3.32)$$

then iteration sequence is terminated. Otherwise it is continued from step (m) onwards. The convergence criteria  $\bar{\omega}$  is chosen depending on the problem.

(m) Following recursive relations are used to compute the new set of vectors to be used in the  $(i + 1)$ th iteration:

$$\mathbf{r}_{i+1} = \mathbf{r}_i - \alpha_i \hat{A}[\mathbf{p}_i], \quad (3.33)$$

$$\mathbf{r}_{i+1}^* = \mathbf{r}_i^* - \alpha_i \hat{A}^T[\mathbf{p}_i^*], \quad (3.34)$$

$$\boldsymbol{\zeta}_{i+1}^* = \hat{M}^{-1} \mathbf{r}_{i+1}^*. \quad (3.35)$$

(n) The quantity  $\beta_i$  is computed using

$$\beta_i = \frac{\langle \mathbf{r}_{i+1}, \boldsymbol{\zeta}_{i+1}^* \rangle}{\langle \mathbf{r}_i, \boldsymbol{\zeta}_i^* \rangle}. \quad (3.36)$$

(o) The conjugate direction vectors for the  $(i + 1)$ th iteration are computed through

$$\begin{aligned} \mathbf{p}_{i+1} &= \mathbf{r}_{i+1} + \beta_i \mathbf{p}_i, \\ \mathbf{p}_{i+1}^* &= \mathbf{r}_{i+1}^* + \beta_i \mathbf{p}_i^*. \end{aligned} \quad (3.37)$$

(p) The control is transferred to step (g).

The converged source function  $\mathbf{y}$  is finally used to compute the specific intensity everywhere within the spherical medium.

### 3.4 Transpose free variant - Pre-BiCG-STAB

In spite of higher convergence rate, computation and storage of the  $\hat{A}^T$  matrix is a main disadvantage of the Pre-BiCG method. To avoid this, and to make use of only the ‘action’ of  $\hat{A}$  matrix on an arbitrary vector, a method called ‘BiCG-squared’ was developed (see Saad 2000, for references and details), which is based on squaring the residual polynomials. Later it was improved by re-defining the residual polynomial as a product of two polynomials and obtaining a recursive relation for the new residual polynomial. This product involves residual polynomial of the Pre-BiCG method and a new polynomial which ‘smoothens’ the iterative process. In this section we give the computing algorithm of the Pre-BiCG-STAB method as applied to a RT problem. As described below, we can avoid computing and storing of the  $\hat{A}^T$  matrix in the Pre-BiCG-STAB method. However we would now need

to call the formal solver twice per iteration unlike in Pre-BiCG method, where it is called only once. This results in an increase in number of operations per iteration when compared to Pre-BiCG method, causing a slight increase in the CPU time per iteration. In spite of these the Pre-BiCG-STAB method turns out to be always faster than the regular Pre-BiCG method in terms of convergence rate (lesser number of iterations for convergence).

### 3.4.1 Pre-BiCG-STAB algorithm

Now we give the algorithm of Pre-BiCG-STAB method to solve the system  $\hat{M}^{-1}\hat{A}\mathbf{S} = \hat{M}^{-1}\mathbf{b}$ . Here  $\hat{M}$  is a suitably chosen preconditioner matrix. The computing algorithm is organized as follows:

(a) First initial preconditioned residual vectors and conjugate direction vectors are defined through

$$\mathbf{z}_0 = \hat{M}^{-1}\mathbf{b} - \hat{M}^{-1}\hat{A}\mathbf{S}, \quad (3.38)$$

$$\mathbf{z}_0^* = \mathbf{z}_0, \quad \mathbf{P}_0 = \mathbf{z}_0. \quad (3.39)$$

(b) For  $j = 1, 2, \dots$  the following steps are carried out until convergence.

(c) Using  $\mathbf{P}_j$  instead of the source function a call to the formal solver is made to compute  $\hat{A}\mathbf{P}_j$ .

(d) The coefficient  $\alpha_j$  can be evaluated now as

$$\alpha_j = \frac{\langle \mathbf{z}_j, \mathbf{z}_0^* \rangle}{\langle \hat{M}^{-1}\hat{A}\mathbf{P}_j, \mathbf{z}_0^* \rangle}. \quad (3.40)$$

(e) Another vector  $\mathbf{q}_j$  is calculated as

$$\mathbf{q}_j = \mathbf{z}_j - \alpha_j \hat{M}^{-1}\hat{A}\mathbf{P}_j. \quad (3.41)$$

(f) Using  $\mathbf{q}_j$  in place of the source function a call to the formal solver is made to obtain  $\hat{A}\mathbf{q}_j$ .

(g) The coefficient  $\omega_j$  is estimated as

$$\omega_j = \frac{\langle \hat{M}^{-1}\hat{A}\mathbf{q}_j, \mathbf{q}_j \rangle}{\langle \hat{M}^{-1}\hat{A}\mathbf{q}_j, \hat{M}^{-1}\hat{A}\mathbf{q}_j \rangle}. \quad (3.42)$$

(h) The updated new source function is calculated as

$$\mathbf{S}_{j+1} = \mathbf{S}_j + \alpha_j \mathbf{P}_j + \omega_j \mathbf{q}_j. \quad (3.43)$$

(i) Test for convergence is made as in the Pre-BiCG algorithm.

(j) Before going to the next iteration a set of recursive relations are used to compute residual vectors

$$\mathbf{z}_{j+1} = \mathbf{q}_j - \omega_j \hat{M}^{-1} \hat{A} \mathbf{q}_j, \quad (3.44)$$

and conjugate direction vectors

$$\mathbf{P}_{j+1} = \mathbf{z}_{j+1} + \beta_j (\mathbf{P}_j - \omega_j \hat{M}^{-1} \hat{A} \mathbf{P}_j). \quad (3.45)$$

for the next iteration, where the coefficient  $\beta_j$  is

$$\beta_j = \frac{\langle \mathbf{z}_{j+1}, \mathbf{z}_0^* \rangle \alpha_j}{\langle \mathbf{z}_j, \mathbf{z}_0^* \rangle \omega_j}, \quad (3.46)$$

(k) The control is now transferred to the step (b).

### 3.5 Comparison of ALI and Pre-BiCG methods

There are two characteristic quantities that define iterative techniques. They are (a) convergence rate, which is nothing but the maximum relative change (MRC) defined as

$$R_c = \max_{\tau} \left\{ \frac{\delta \mathbf{S}^n}{\mathbf{S}^n} \right\}, \quad (3.47)$$

and (b) the total CPU time  $T_{\text{total}}$  required for convergence.  $T_{\text{total}}$  is the time taken to reach a given level of convergence, taking account only of the arithmetic manipulations within the iteration cycle. We also define a quantity called the true error  $T_e$  and use it to evaluate these methods.

#### 3.5.1 The behaviour of the maximum relative change (MRC)

In this section we compare  $R_c$  and  $T_{\text{total}}$  for the Jacobi, GS, SOR, Pre-BiCG and the Pre-BiCG-STAB methods. The SOR parameter used is 1.5. It is worth noting that the

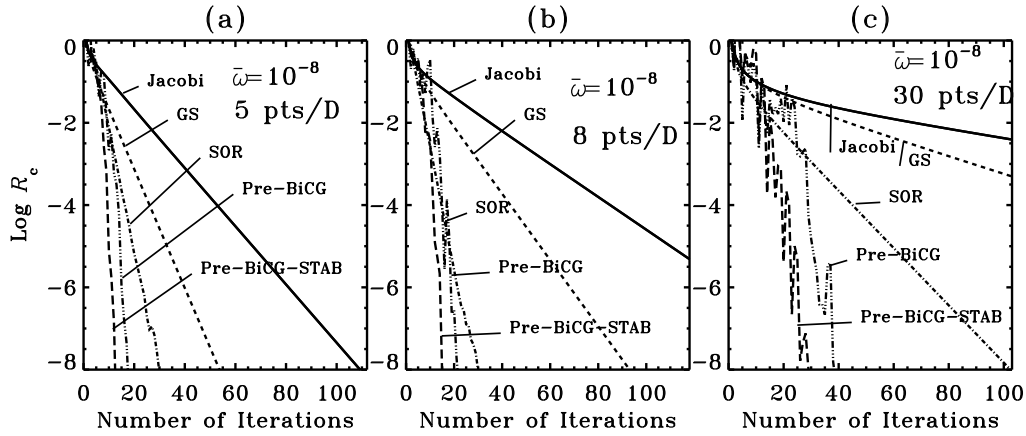


**Figure 3.2:** Dependence of the Maximum Relative Change  $R_c$  on the iterative progress for different methods. Panels (a), (b), and (c) represent models with low, medium and high spatial resolution respectively. The model parameters are  $(\tilde{n}, R, T, a, \epsilon, \beta_c, B_\nu) = (0, 10, 10^3, 10^{-3}, 10^{-4}, 0, 1)$ . The convergence criteria is chosen arbitrarily as  $\bar{\omega} = 10^{-8}$ . The SOR parameter  $\omega = 1.5$ . The figures show clearly that Jacobi method has the smallest convergence rate, which progressively increases for GS and SOR methods. Pre-BiCG and Pre-BiCG-STAB methods generally have the largest convergence rate compared to the other three.

**Table 3.2:** Timing efficiency of the iterative methods. The “CPU time” refers to the time taken for convergence, “Overrates” to the extra time excluding the time needed for the iteration sequence to converge and the “Total time” to the total computing time.

	Jacobi	GS	SOR	Pre-BiCG	Pre-BiCG-STAB
CPU time	7 min 49 sec	4 min 4 sec	1 min 18 sec	27 sec	42 sec
Overrates	6 sec	6 sec	6 sec	9 sec	6 sec
Total time	7 min 55 sec	4 min 10 sec	1 min 24 sec	36 sec	48 sec



overrates (the time taken to prepare the necessary set up, before initiating the iterative cycle) are expected to be different for different methods. For instance, in Jacobi and GS/SOR this is essentially the CPU time required to set up the  $\Lambda^*$  matrix. In the Pre-BiCG method this involves the time taken to construct the  $\hat{A}^T$  matrix, which is a critical quantity of this method. The Pre-BiCG method is described in this chapter in the context of a two-level atom model, because of which, we do not need to update the  $\hat{A}^T$  matrix at each iteration. For the Pre-BiCG-STAB method it is the time taken to construct the preconditioner matrix  $\hat{M}$ .

Figure 3.2 shows a plot of  $R_c$  for different methods. We can take  $R_c$  as a measure of the convergence rate. Chevallier et al.(2003) show that it always becomes necessary to use high resolution grids, to achieve high accuracy of the solution (see also Section 3.1 of this chapter). This is especially true in the case of spherical RT where a spatial grid with a large number of points per decade becomes necessary to achieve reasonable accuracy. In the following we discuss how different methods respond to the grid refinement. It is a well known fact with the ALI methods, that the convergence rate is small when the resolution of the depth grid is very high. In contrast they have a high convergence rate in low resolution grids. On the other hand the  $R_c$  of Pre-BiCG and Pre-BiCG-STAB methods have higher convergence rate even in a high resolution grid. Figure 3.2(a) shows  $R_c$  for different methods when a low resolution spatial grid is used (5pts/D in the logarithmic scale for  $\tau$  grid). The Jacobi method has a low convergence rate. In comparison, GS has a convergence rate which is twice that of Jacobi. SOR has a rate that is even better than that of GS. However Pre-BiCG and the Pre-BiCG-STAB methods have the higher convergence rate. Figure 3.2(b) and 3.2(c) are shown for intermediate (8 pts/D) and high (30 pts/D) grid resolutions. The essential point to note is that, as the grid resolution increases, the convergence rate decreases drastically and monotonically for the Jacobi and the GS methods. It is not so drastic for the SOR method which shows non-monotonic dependence on grid resolution. The Pre-BiCG and Pre-BiCG-STAB methods exhibit again a monotonic behaviour apart from being relatively less sensitive to the grid resolution.

In Table 3.1 we show what happens when we set convergence criteria to progressively smaller values ( $\bar{\omega} = 10^{-6}$ ,  $10^{-8}$ , and  $10^{-10}$  for Tables 3.1(a), 3.1(b) and 3.1(c) respectively) for various grid resolutions. The model used to compute these results is  $(\tilde{n}, R, T, a, \epsilon, \beta_c, B_\nu) = (0, 10, 10^3, 10^{-3}, 10^{-4}, 0, 1)$ . The idea is to demonstrate that for a given grid resolution (corresponding rows of the Tables 3.1(a), 3.1(b) and 3.1(c)), all the methods show a monotonic increase in the number of iterations for convergence, as we decrease the  $\bar{\omega}$ . On the other hand Pre-BiCG and Pre-BiCG-STAB require much less number of

iterations to reach the same level of accuracy.

*CPU time considerations:* Table 3.2 shows the CPU time requirements for the methods discussed in this chapter. The model used to compute these test cases is  $(\tilde{n}, R, T, \epsilon, \beta_c, B_\nu, \bar{\omega}) = (0, 300, 10^3, 10^{-4}, 0, 1, 10^{-8})$ . The grid resolution considered is 30 pts/D. The CPU time for convergence can be defined as the computing time required to complete the convergence cycle and reach a fixed level of accuracy. We recall that the overrates in computing time is the time taken to prepare the necessary set up before initiating the iterative cycle. Total computing time is the sum of these two. In Appendix C we discuss in detail how to construct  $\Lambda^*$  matrix for Jacobi, GS/SOR methods and  $\hat{A}$  and  $\hat{M}$  matrices for Pre-BiCG and Pre-BiCG-STAB methods respectively with an optimum effort. Construction of these matrices constitutes the overrates in computing time of each method. The first row of Table 3.2 shows that Pre-BiCG is the fastest to complete the convergence cycle. The reason why Pre-BiCG-STAB takes slightly longer time than Pre-BiCG is explained at the end of Section 3.4.

The second row of Table 3.2 shows that all methods except Pre-BiCG take nearly 8 seconds as overrates for the chosen model. Pre-BiCG takes additional 3-4 seconds as explicit integrals are performed for computing off-diagonal elements also (Unlike the other methods where such integrals are performed only for diagonal elements).

The last row of Table 3.2 shows that in terms of total CPU time requirement, the other methods fall behind the Pre-BiCG and the Pre-BiCG-STAB. Pre-BiCG seems to be a bit faster compared to Pre-BiCG-STAB for the particular model chosen. However it is model dependent. For instance, as the contribution towards overrates increases, Pre-BiCG-STAB clearly stands out as the fastest method of all, discussed in this chapter.

### 3.5.2 A study of the True Error

We now study the true errors in these methods (see Figure 3.3). The model parameters are  $(\tilde{n}, R, T, \epsilon, \beta_c, B_\nu) = (0, 10, 10^3, 10^{-4}, 0, 1)$ . A coherent scattering limit is used. To define a true error, we need a so called ‘exact solution’. Except for highly idealized cases, exact solutions do not exist. For practical purposes, the exact solution can be defined as a solution obtained on a spatial grid of resolution that is three times larger than the grid resolution of the model that we are interested in. Also, we extend the iteration until  $R_c$  reaches an extremely small value of  $10^{-12}$ . The source function computed in this way can be called  $\mathbf{S}(\infty, \infty)$  (fully converged solution on an infinite resolution) (see Auer et al. 1994). The source function at the  $n$ th iterate is denoted by  $\mathbf{S}^n$ . We define the true error

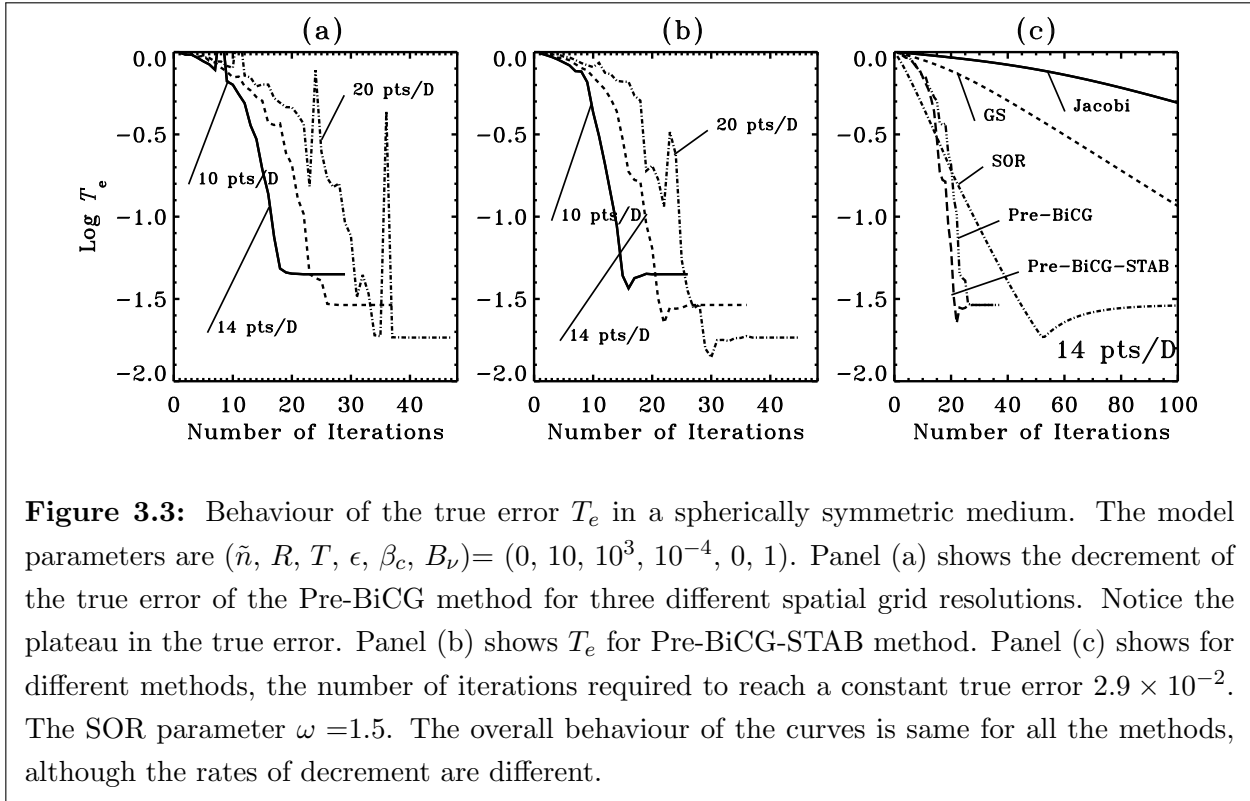
as

$$T_e = \max_{\tau} \left| \frac{\mathbf{S}^n - \mathbf{S}_{\text{exact}}}{\mathbf{S}_{\text{exact}}} \right|, \quad (3.48)$$

following Trujillo Bueno & Fabiani Bendicho (1995). In Figure 3.3(a) we show  $T_e$  computed for the Pre-BiCG method using three grid resolutions, namely 10 pts/D, 14 pts/D and 20 pts/D. The plateau of each curve represents the minimum value of the true error reached for a given grid resolution. We notice that as the resolution increases,  $T_e$  gradually decreases in magnitude as expected. In Figure 3.3(b) we show  $T_e$  computed for the Pre-BiCG-STAB method. The model parameters are same as in Figure 3.3(a). Clearly, Pre-BiCG-STAB shows a smooth decrement of true error compared to Pre-BiCG, because of the smoothing polynomial used to define the residual vectors. In Figure 3.3(c) we compare the decrement of true errors for different iterative methods. The grid resolution chosen is 14 pts/D with other model parameters being same as in Figures 3.3(a), (b). The decrease of the true errors follows the same pattern in all the iterative methods, although the number of iterations required for  $T_e$  to reach a constant value (plateau) depends on the method. To reach the same level of true error, the Pre-BiCG and Pre-BiCG-STAB methods require considerably less number of iterations, when compared to the other three.

### 3.5.3 A theoretical upper bound on the number of iterations for convergence in the Pre-BiCG method

Suppose that  $\hat{A}$  is an  $n_d \times n_d$  matrix. The solution to the problem  $\hat{A}\mathbf{y} = \mathbf{b}$  is a vector of length  $n_d$ . In an  $n_d$ -dimensional vector space  $V_{n_d}$  the maximum number of linearly independent vectors is  $n_d$ . Hence, there can at the most be  $n_d$  orthogonal vectors in  $V_{n_d}$ . The Pre-BiCG method seeks a solution by constructing orthogonal vectors. We recall that the residual counterpart vectors  $\{\mathbf{r}_1^*, \mathbf{r}_2^*, \dots, \mathbf{r}_m^*\}$  constructed during the iteration process are orthogonal to the initial residual vector  $\mathbf{r}_0$ . Thus, when we reach convergence after  $m$  iterations, we will have a set of  $m + 1$  orthogonal vectors  $\{\mathbf{r}_0, \mathbf{r}_1^*, \mathbf{r}_2^*, \dots, \mathbf{r}_m^*\}$ . From the arguments given above, it is clear that  $m + 1 \leq n_d$ , namely in the Pre-BiCG method, ‘the convergence must be reached theoretically in at the most  $n_d$  steps (or iterations)’. This sets an upper limit to the number of iterations to reach convergence (see also Hestenes & Stiefel 1952). For example when the dimensionality of a problem is high (very large value of  $n_d$ ), the Pre-BiCG method ensures convergence in at the most  $n_d$  iterations. A theoretical upper bound on the number of iterations also exists for the Pre-BiCG-STAB method, whereas the other methods do not have such a theoretical upper bound. In practice we find that Pre-BiCG and Pre-BiCG-STAB methods actually require much less number of iterations than  $n_d$ , even when  $n_d$  is large.



### 3.6 Results and discussions

The main purpose of this chapter is to propose a new method to solve the line RT problems in spherically symmetric media. In this section we show some illustrative examples in order to compare with the famous benchmarks for spherical RT solutions presented in the papers by Kunasz & Hummer (1974a). In Figure 3.4 we show source functions for different test cases. Figure 3.4(a) shows the source functions for  $\epsilon = 10^{-2}$  and  $\epsilon = 10^{-4}$  for  $R = 300$  and  $T = 10^3$ . Other model parameters are  $(\tilde{n}, \beta_c, B_\nu) = (2, 0, 1)$ . We use a Doppler profile to compare with the results of Kunasz & Hummer (1974a). Plane parallel result is also shown for comparison. When  $\epsilon = 10^{-2}$  we observe that the thermalization is reached at the thermalization length for the Doppler profile namely  $1/\epsilon = 100$ . When  $\epsilon = 10^{-4}$  thermalization does not occur. Clearly the minimum value of the source function is  $\epsilon B_\nu$ . For the large values of  $R = 300$  and opacity index  $\tilde{n} = 2$ , as  $r$  increases the opacity decreases steadily and the source function indeed approaches this minimum value near the surface layers. For this case, the departure of the source function from planar limit is severe near the surface. It can be shown (dashed line of Figure 3.4(b), see also Figure 3 of Kunasz & Hummer 1974a) that this departure is not so acute when  $\tilde{n} = 0$ , but is more

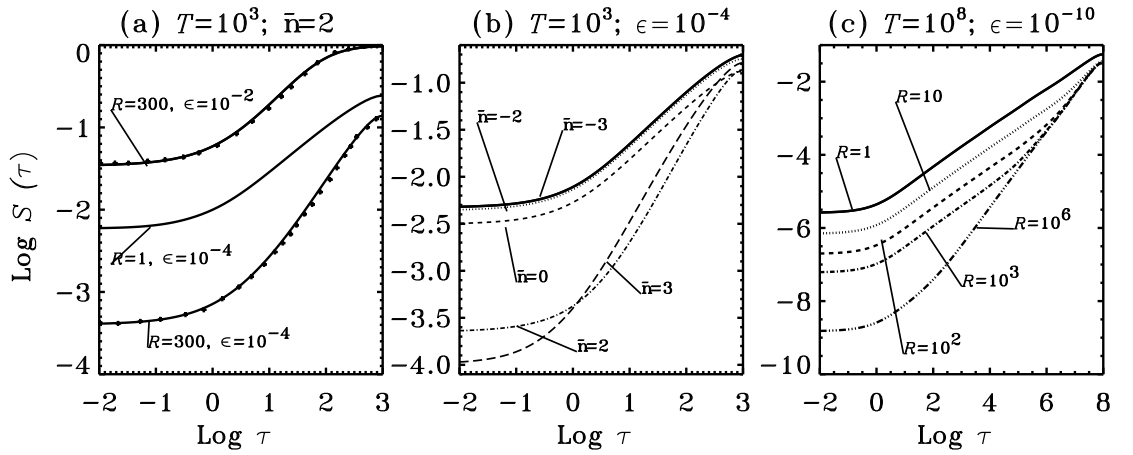


**Figure 3.4:** In panel (a) the source function variation with optical depth is shown for a spherical media with inverse square opacity variation for two different values of  $\epsilon$ . The symbols show the benchmark solution read from Kunasz & Hummer (1974a), which compare well with the solution by our method (Pre-BiCG - full lines). The plane parallel solution ( $R = 1$ ) is shown for comparison. Panel (b) shows the effect of power law opacity indices  $\tilde{n}$  on the source function variation with  $\tau$ . In panel (c) the effects of spherical extension  $R$  are shown by taking a difficult case of highly scattering, effectively optically thin medium.

acute when  $\tilde{n} = 3$  (dash triple-dotted line in Figure 3.4(b)). In Figure 3.4(b) we plot source function for the same model as Figure 3.4(a) but for various values of  $\tilde{n}$ . For negative  $\tilde{n}$ , the distinction between  $\mathcal{S}(\tau)$  vs.  $\tau$  curves for different  $\tilde{n}$  is small. For positive  $\tilde{n}$ , the effects are relatively larger (see dot-dashed and long dashed curves in Figure 3.4(b)). In Figure 3.4(c), we show source function variation for a range of spherical extensions  $R$ . We have chosen an effectively optically thin model  $(T, \epsilon) = (10^8, 10^{-10})$  because in such a medium, thermalization effects do not completely dominate over the effects of sphericity. Other parameters are same as in Figure 3.4(b). Clearly, the decrease in the value of source function throughout the atmosphere is monotonic, with an increase in the value of  $R$  from 1 to  $10^6$ . In Figure 3.5, we show effects of limb darkening in spherical atmospheres for  $R = 10^3$  and  $R = 10^6$ . The other model parameters for Figure 3.5(a) are  $(\tilde{n}, T, \epsilon, \beta_c, B_\nu) = (2, 10^8, 10^{-4}, 0, 1)$ . A Doppler line profile is used. From the Figure, we notice absorption in the line core and emission in the near line wings ( $x \approx 4$ ) for  $\theta = 0^\circ$  and  $10^\circ$ . This is the characteristic self reversal observed in spectral lines formed in extended spherical atmospheres. The self reversal decreases gradually as  $\theta$  increases, and finally vanishes for large values of  $\theta$ . Indeed for extreme value of  $\theta = 90^\circ$ , we observe a pure emission line.

In Figure 3.5(b) we show line profiles formed in a semi-infinite spherical medium. The

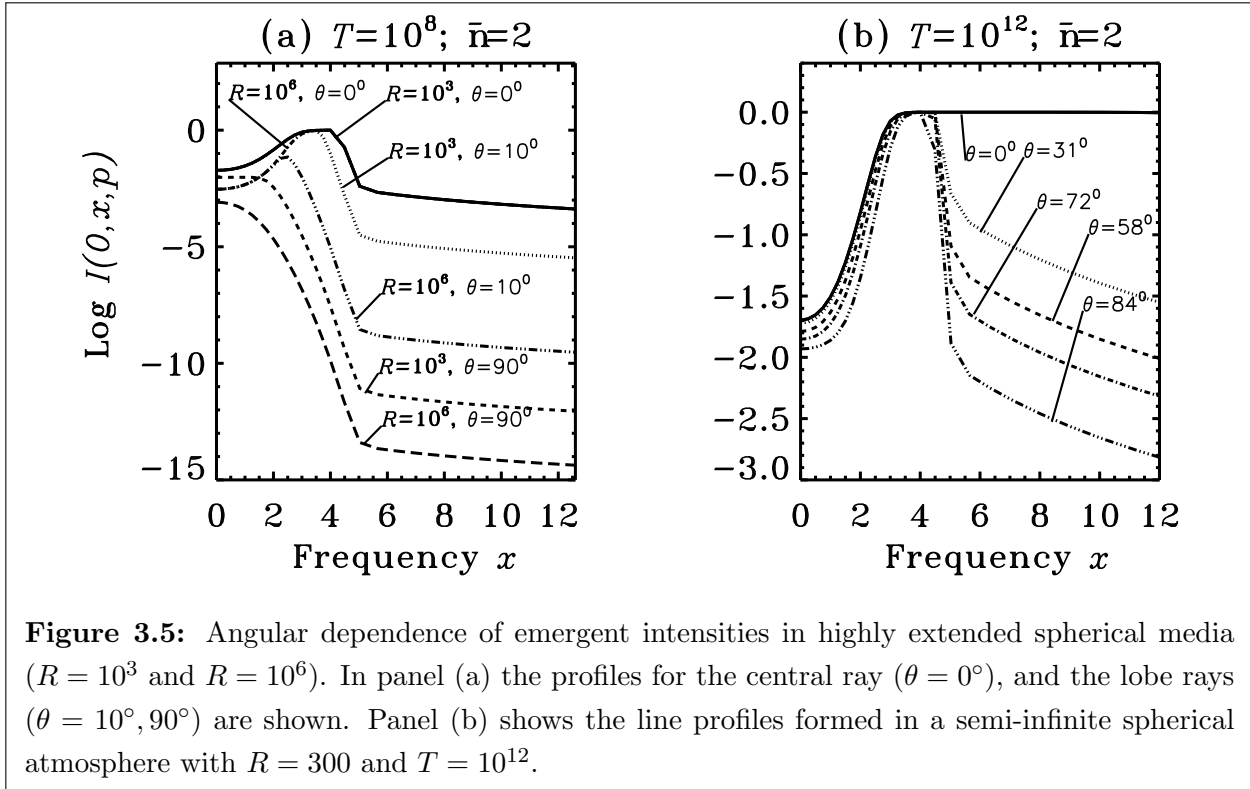


**Figure 3.5:** Angular dependence of emergent intensities in highly extended spherical media ( $R = 10^3$  and  $R = 10^6$ ). In panel (a) the profiles for the central ray ( $\theta = 0^\circ$ ), and the lobe rays ( $\theta = 10^\circ, 90^\circ$ ) are shown. Panel (b) shows the line profiles formed in a semi-infinite spherical atmosphere with  $R = 300$  and  $T = 10^{12}$ .

model parameters are same as in Figure 3.5(a) except for  $(R, T)=(300, 10^{12})$ . The profiles for a range of  $\theta = 0^\circ, 31^\circ, 54^\circ, 72^\circ, 84^\circ$  are shown. For the core rays ( $\theta = 0^\circ$ ) we see a pure absorption line due to thermalization of source function. For other angles, as expected we see chromospheric type self-reversed emission lines, formed in the lobe part of the spherical medium.

### 3.7 Concluding remarks

In this chapter we propose a robust method called Pre-BiCG method to solve the classical problem of line RT in spherical media. This method belongs to a class of iterative methods based on the projection techniques. We briefly present the method, and the computing algorithm. We also present a transpose-free variant called the Pre-BiCG-STAB method which is more advantageous in some of its features. The Pre-BiCG and Pre-BiCG-STAB methods are validated in terms of its efficiency and accuracy, by comparing with the contemporary iterative methods like Jacobi, GS and SOR. To calculate the benchmark solutions we use spherical shell atmospheres. Few difficult test cases are also presented to show that the Pre-BiCG and Pre-BiCG-STAB are efficient numerical methods for spherical line RT.

## New Results

For the first time, the projection methods were introduced to spherical RT in this chapter. Further, it is for the first time that Pre-BiCG-STAB method is applied to RT in any context. The following are the results obtained in chapter 3.

1. The Pre-BiCG and Pre-BiCG-STAB show highest speed of convergence when compared with all other contemporary iterative methods.
2. The application of Pre-BiCG and Pre-BiCG-STAB methods in some benchmark tests shows that it is quite versatile, and can handle hard problems that may arise in astrophysical RT theory.
3. The applicability of this method is discussed in the later chapters where we extend it to multi-D RT problems (chapters 5, 6, 7 and 8). Therefore the development in this chapter is a basis for the work in the later chapters.

*Further studies related to the work presented in this chapter are published in:*

1. Anusha, L. S., & Nagendra, K. N., 2009, **Mem.S.A.It**, 80, 631–634
2. Nagendra, K. N., Anusha, L. S., & Sampoorana, M. 2009, **Mem.S.A.It**, 80, 678–689





## **Part-II**

# **Polarized line formation in multi-dimensional media**



## Chapter 4

# Decomposition of Stokes parameters in multi-D media

*The contents of this chapter are based on the following publication:*

Anusha, L. S., and Nagendra, K. N. 2011a, **ApJ**, 726, 6-19

### 4.1 Introduction

The solution of the polarized line radiative transfer (RT) equation in multi-dimensional (multi-D) media is necessary to model the solar atmospheric features. This requirement stems from the non-axisymmetry of the radiation field arising purely due to inhomogeneous structures in the solar atmosphere. An idealization to simplify this problem, is to represent the inhomogeneities as computational cubes, characterized by their shape and the physical parameters. This approach has proved useful in the hydrodynamics as well as the theory of RT applied to the solar atmosphere (see below). In this chapter we focus on the RT aspects only. Our goal is to set up the polarized RT equation suitable for a given geometry, and to develop numerical techniques to solve them.

Extensive work has been done in *unpolarized multi-D RT* in recent years. Here we mention only a few important developments on this subject. A classic paper on multi-D unpolarized RT is by Mihalas et al. (1978), who undertook an extensive analysis of the nature of two-dimensional (2D) RT solutions and presented illustrative examples that helped later developments. They used a formal solver based on short characteristics but solved the problem using a second order RT equation. A faster and more efficient formal solution based on short characteristics method for 2D was developed by Kunasz & Auer (1988). An

Approximate Lambda Iteration (ALI) method for unpolarized line RT was formulated by Auer & Paletou (1994) who used partial frequency redistribution (PRD) in the line scattering. Auer et al. (1994) formulated an ALI method for line RT in a three-dimensional (3D) medium for a multi-level atom model, under the complete frequency redistribution (CRD) approximation. Vath (1994) and Papkalla (1995) also proposed efficient 3D RT codes based on the short characteristics formal solvers. Folini (1998) has done extensive work on the numerical techniques to solve the multi-D RT equation, and applied them to few astrophysical problems of practical interest. van Noort et al. (2002) have developed a general multi-D RT code applicable to a variety of astronomical problems. This list of papers to the unpolarized RT in 3D does not pretend to be complete. Indeed 3D RT techniques and applications have been the subject of keen interest in other branches of astrophysics (see e.g., Nagendra et al. 2009).

There are two formalisms to write the RT equation for line polarization. The density matrix formalism (see for e.g., Landi Degl’Innocenti & Landolfi 2004, hereafter LL04), and the scattering phase matrix formalism (see e.g., Stenflo 1994). The density matrix formalism may handle polarized scattering in multi-level atoms, while it is not the case for the scattering formalism, but with the advantage that it is well adapted to handle the polarized line scattering with PRD. Again there are two streams in the scattering phase matrix formalism. The first one used the Stokes vector RT equation (see e.g., Stenflo 1976; Dumont et al. 1977; Rees & Saliba 1982; Faurobert 1987; Nagendra 1988; Nagendra 1994; Nagendra et al. 2002; Sampoorna et al. 2008c). The second stream worked with the polarized RT equation for a reduced intensity vector (see e.g., Faurobert-Scholl 1991; Nagendra et al. 1998; Fluri et al. 2003b; Sampoorna et al. 2008a; Frisch et al. 2009; Sampoorna & Trujillo Bueno 2010; Nagendra et al. 2010; Anusha et al. 2010b).

The solution of *multi-D polarized line RT equation* formulated in the Stokes vector basis is rather complicated to solve. The reason for this is the explicit dependence of the physical quantities on the spatial variables  $(x, y, z)$ , angular variables  $(\theta, \varphi)$  and frequency  $x$ , in the standard notation. Therefore it is advantageous to write the RT equation in a basis where it takes a simpler form. For example Chandrasekhar (1950) showed that in a one-dimensional (1D) geometry, the monochromatic polarized RT equation in the Stokes vector  $(I, Q, U)^T$  basis can be transformed to a Fourier basis, where the physical quantities no longer depend on the azimuthal angle  $\varphi$ . An RT equation can be written for the Fourier components of the Stokes vector and the solution is transformed back to the original  $(I, Q, U)^T$  basis. This technique was later extended by Faurobert-Scholl (1991), (see also Nagendra et al. 1998) to the case of polarized line RT in the presence of a magnetic

field (Hanle effect). (Frisch 2007, hereafter HF07) decomposed the Stokes vector  $(I, Q, U)^T$  in terms of irreducible spherical tensors for polarimetry (see LL04 and the references cited therein). In HF07 it is shown that the Fourier expansion approach and the irreducible spherical tensor approach are somewhat equivalent, the latter being more compact and convenient to use in the scattering theory.

Dittmann (1997) formulated the solution of the polarized RT equation for continuum scattering in 3D media. Later he (Dittmann 1999) proposed an approach of factorizing the Hanle phase matrix into a form which is suitable for the solution of the line RT equation in 3D geometries, under the assumption of CRD. The Hanle line RT equation in 2D and 3D media with CRD using the density matrix formalism was solved by Manso Sainz & Trujillo Bueno (1999). Paletou et al. (1999) solved the non-magnetic polarized resonance scattering with CRD using a perturbative approach, in a 2D geometry. Trujillo Bueno et al. 2004 and Trujillo Bueno & Shchukina (2007, 2009, and references cited therein) have applied their multi-level 3D polarized RT code to a variety of problems to understand the nature of the line RT in the second solar spectrum. An escape probability method to compute the polarized line profiles in non-spherical winds was developed by Jeffrey (1989). In all the works mentioned above, the authors used the CRD in line scattering. Hillier (1996) solved the problem of Rayleigh scattering polarization in a 2D-spherical geometry based on the Sobolov-P approach (polarized line RT in high speed winds) using the angle-averaged partial frequency redistribution functions.

In this chapter (see also Anusha & Nagendra 2011a) we solve the 3D polarized line RT equation in a non-magnetic medium under the assumption of PRD. For this purpose we use the traditional scattering phase matrix approach. We follow the decomposition technique of HF07 all through this chapter. Basically we start from the decomposition of Stokes parameters in terms of the irreducible spherical tensors for 1D media, developed by HF07, and extend it to handle the case of RT in multi-D media. For the PRD we consider the collisional redistribution matrix (Domke & Hubeny 1988; Bomnier 1997a, 1997b) for a two-level atom model with unpolarized ground level.

A polarized RT equation in Stokes vector formalism is presented in Section 4.2. A general multipolar expansion of the Stokes source vector and Stokes parameters in terms of the irreducible spherical tensors and the corresponding RT equation is presented in Section 4.3. For the formal solution of the RT equation we use the finite volume element method formulated by Adam (1990), extended here to include polarization and PRD. We briefly explain in Section 4.4 the numerical method that we have developed in this chapter.

**Table 4.1:** The optical depth information for the spatial points 1–9 on the top surface ( $\tau_Z = 0$ ) in Figure 4.2.

Spatial point	$\tau_X$	$\tau_Y$	$\tau_Z$
1	$T_X/2$	$T_Y/2$	0
2	$T_X$	$T_Y/2$	0
3	0	$T_Y/2$	0
4	$T_X/2$	$T_Y$	0
5	$T_X/2$	0	0
6	0	$T_Y$	0
7	$T_X$	0	0
8	0	0	0
9	$T_X$	$T_Y$	0

Details of the numerical method are presented in Appendix D. In Section 4.5 we present some solutions to understand the nature of polarization in a 3D scattering medium. They may serve as benchmarks for further exploration. In Section 4.6 we present our concluding remarks.

## 4.2 Polarized radiative transfer in a 3D medium – Stokes vector basis

The RT equation in divergence form in the atmospheric reference frame (see Figure 4.2) is written as

$$\boldsymbol{\Omega} \cdot \nabla \mathbf{I}(\mathbf{r}, \boldsymbol{\Omega}, x) = -[\kappa_l(\mathbf{r})\phi(x) + \kappa_c(\mathbf{r})][\mathbf{I}(\mathbf{r}, \boldsymbol{\Omega}, x) - \mathbf{S}(\mathbf{r}, \boldsymbol{\Omega}, x)], \quad (4.1)$$

where  $\mathbf{I} = (I, Q, U)^T$  is the Stokes vector, with  $I$ ,  $Q$  and  $U$  the Stokes parameters defined below. Following Chandrasekhar (1950), we consider an elliptically polarized beam of light, the vibrations of the electric vector of which describe an ellipse. If  $I_l$  and  $I_r$  denote the components of the specific intensity of this beam of light along two mutually perpendicular

directions  $l$  and  $r$ , in a plane transverse to the propagation direction, then we define

$$\begin{aligned} I &= I_l + I_r, \\ Q &= I_l - I_r, \\ U &= (I_l - I_r) \tan 2\chi, \end{aligned} \quad (4.2)$$

where  $\chi$  is the angle between the direction  $l$  and the semi major axis of the ellipse. Positive value of  $Q$  is defined to be in a direction perpendicular to the surface, and negative  $Q$  in the directions parallel to it. The quantity  $\mathbf{r} = (x, y, z)$  is the position vector of the ray in the Cartesian co-ordinate system. The unit vector  $\boldsymbol{\Omega} = (\eta, \gamma, \mu) = (\sin \theta \cos \varphi, \sin \theta \sin \varphi, \cos \theta)$  describes the direction cosines of the ray in the atmosphere with respect to the atmospheric normal, with  $\theta, \varphi$  being polar and azimuthal angles of the ray. The quantity  $\kappa_l$  is the frequency averaged line opacity,  $\phi$  is the Voigt profile function and  $\kappa_c$  is the continuum opacity. Frequency is measured in reduced units, namely  $x = (\nu - \nu_0)/\Delta\nu_D$ , where  $\Delta\nu_D$  is the Doppler width. The total source vector  $\mathbf{S}$  is given by

$$\mathbf{S}(\mathbf{r}, \boldsymbol{\Omega}, x) = \frac{\kappa_l(\mathbf{r})\phi(x)\mathbf{S}_l(\mathbf{r}, \boldsymbol{\Omega}, x) + \kappa_c(\mathbf{r})\mathbf{S}_c(\mathbf{r}, x)}{\kappa_l(\mathbf{r})\phi(x) + \kappa_c(\mathbf{r})}. \quad (4.3)$$

Here  $\mathbf{S}_c$  is the continuum source vector namely  $(B_\nu(\mathbf{r}), 0, 0)^T$  with  $B_\nu(\mathbf{r})$  being the Planck function at the line center frequency. The line source vector can be expressed as

$$\mathbf{S}_l(\mathbf{r}, \boldsymbol{\Omega}, x) = \mathbf{G}(\mathbf{r}) + \int_{-\infty}^{+\infty} dx' \oint \frac{d\boldsymbol{\Omega}'}{4\pi} \frac{\hat{R}(x, x', \boldsymbol{\Omega}, \boldsymbol{\Omega}')}{\phi(x)} \mathbf{I}(\mathbf{r}, \boldsymbol{\Omega}', x'), \quad (4.4)$$

where  $\mathbf{G} = (\epsilon B_\nu(\mathbf{r}), 0, 0)^T$  is the thermal source.  $\epsilon = \Gamma_I/(\Gamma_R + \Gamma_I)$  with  $\Gamma_I$  and  $\Gamma_R$  being the inelastic collision rate and the radiative de-excitation rate respectively, so that  $\epsilon$  is the rate of destruction by inelastic collisions, also known as the thermalization parameter. The damping parameter is computed using  $a = a_R[1 + (\Gamma_E + \Gamma_I)/\Gamma_R]$  where  $a_R = \Gamma_R/4\pi\Delta\nu_D$  and  $\Gamma_E$  is the elastic collision rate.  $\hat{R}$  is the redistribution matrix. The solid angle element  $d\boldsymbol{\Omega}' = \sin \theta' d\theta' d\varphi'$   $\theta \in [0, \pi]$  and  $\varphi \in [0, 2\pi]$ . To construct the decomposition in multipolar components, it is convenient to work with the RT equation written along a ray path. It has the form

$$\frac{d\mathbf{I}(\mathbf{r}, \boldsymbol{\Omega}, x)}{ds} = -\kappa_{\text{tot}}(\mathbf{r}, x)[\mathbf{I}(\mathbf{r}, \boldsymbol{\Omega}, x) - \mathbf{S}(\mathbf{r}, \boldsymbol{\Omega}, x)], \quad (4.5)$$

where  $s$  is the path length along the ray (see Figure 4.1) and  $\kappa_{\text{tot}}(\mathbf{r}, x)$  is the total opacity given by

$$\kappa_{\text{tot}}(\mathbf{r}, x) = \kappa_l(\mathbf{r})\phi(x) + \kappa_c(\mathbf{r}). \quad (4.6)$$

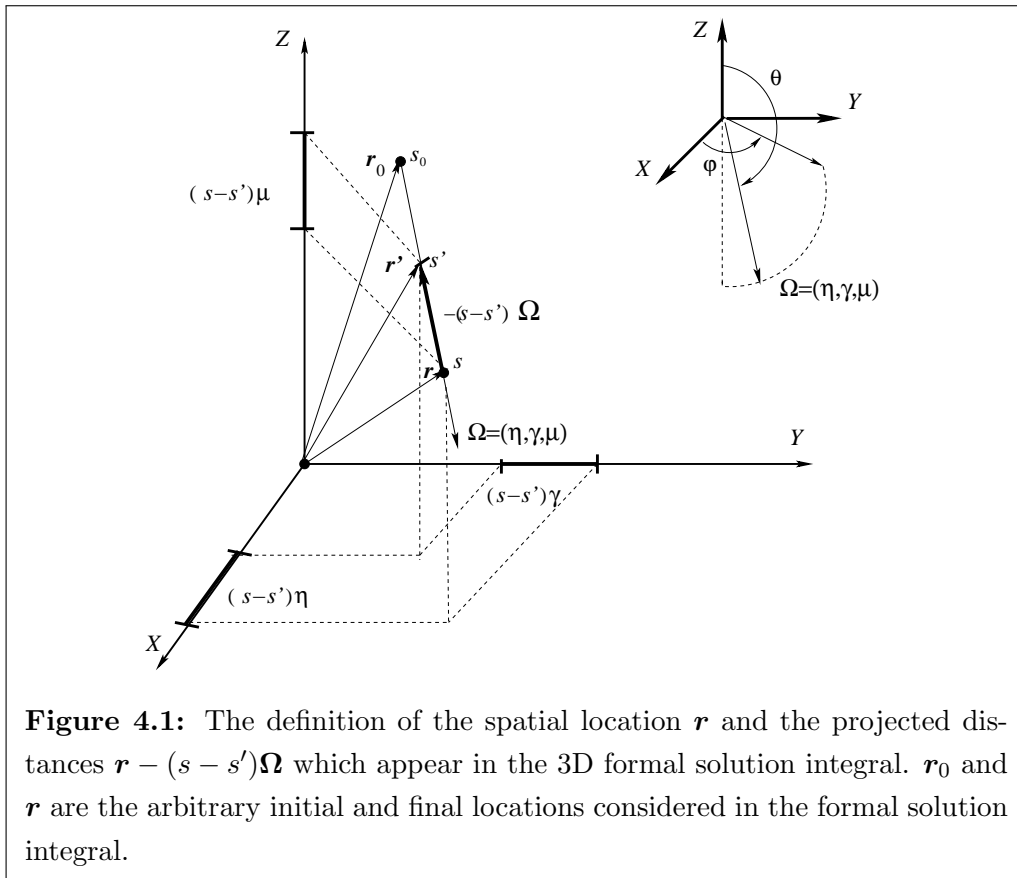


**Figure 4.1:** The definition of the spatial location  $\mathbf{r}$  and the projected distances  $\mathbf{r} - (s - s')\mathbf{\Omega}$  which appear in the 3D formal solution integral.  $\mathbf{r}_0$  and  $\mathbf{r}$  are the arbitrary initial and final locations considered in the formal solution integral.



**Table 4.2:** The values of the free parameters corresponding to different models shown in Figure 4.8.

Model	Scat. mechanism	$\alpha$	$\beta^{(0)}$	$\beta^{(2)}$	$(\beta^{(0)} - \alpha)$	$(\beta^{(2)} - \alpha)$
1	CRD	0.00	1.00	1.00	1.00	1.00
2	$\Gamma_E/\Gamma_R = 10^{-4}$	0.99	0.99	0.99	0.00	0.00
3	$\Gamma_E/\Gamma_R = 0.1$	0.90	0.99	0.96	0.09	0.06
4	$\Gamma_E/\Gamma_R = 1$	0.49	0.99	0.72	0.50	0.23
5	$\Gamma_E/\Gamma_R = 10$	0.09	0.99	0.21	0.89	0.12

The formal solution of Equation (4.5) is given by

$$\begin{aligned}
\mathbf{I}(\mathbf{r}, \boldsymbol{\Omega}, x) = & \mathbf{I}(\mathbf{r}_0, \boldsymbol{\Omega}, x) e^{-\int_{s_0}^s \kappa_{\text{tot}}(\mathbf{r} - (s - s')\boldsymbol{\Omega}, x) ds'} \\
& + \int_{s_0}^s \mathbf{S}(\mathbf{r} - (s - s')\boldsymbol{\Omega}, \boldsymbol{\Omega}, x) e^{-\int_{s'}^s \kappa_{\text{tot}}(\mathbf{r} - (s - s'')\boldsymbol{\Omega}, x) ds''} \kappa_{\text{tot}}(\mathbf{r} - (s - s')\boldsymbol{\Omega}, x) ds'.
\end{aligned} \tag{4.7}$$

$\mathbf{I}(\mathbf{r}_0, \boldsymbol{\Omega}, x)$  is the boundary condition imposed at  $\mathbf{r}_0 = (x_0, y_0, z_0)$ .

### 4.3 Decomposition of Stokes vectors for multi-D transfer

In this section we show how to generalize to a multi-D geometry the Stokes parameters decomposition method developed for the Hanle effect in 1D geometry.

#### 4.3.1 A multipolar expansion of the Stokes source vector and the Stokes intensity vector in a 3D medium

We derive the required decomposition starting from the polarized RT equation in  $(I, Q, U)^T$  basis. For simplicity, we assume that the redistribution matrix can be written as a product of angle-averaged redistribution functions and an explicit angle  $(\theta, \varphi)$  dependent phase matrix. The scattering phase matrix can be expressed in terms of the irreducible spherical tensors introduced in LL04. The  $ij$ -th element of the redistribution matrix in the

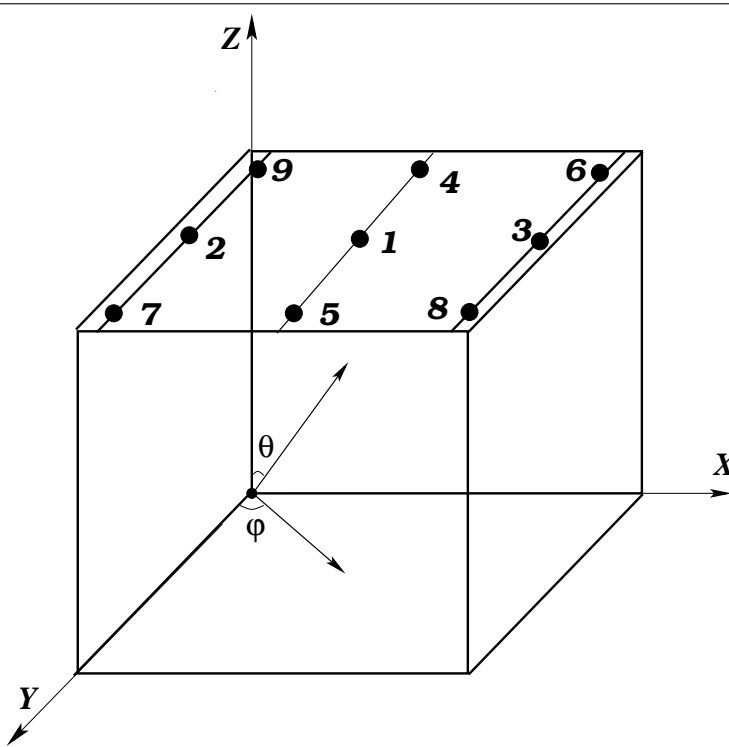


**Figure 4.2:** The geometry of the problem. The angle pair  $(\theta, \varphi)$  defines the ray direction. The optical depth information of the spatial points 1–9 on the top surface ( $\tau_Z = 0$ ) of the computational cube are given in Table 4.1. The results are shown at the points marked on grid lines which are just inside the outermost boundaries. The  $Z$ -axis is along the atmospheric normal.

atmospheric reference frame (Bommier 1997b) is given by

$$R_{ij}(x, x', \boldsymbol{\Omega}, \boldsymbol{\Omega}') = \sum_{KQ} W_K \mathcal{T}_Q^K(i, \boldsymbol{\Omega}) (-1)^Q \mathcal{T}_{-Q}^K(j, \boldsymbol{\Omega}') R^K(x, x'), \quad (4.8)$$

where  $(i, j) = (1, 2, 3)$  and

$$R^K(x, x') = \{\alpha r_{\text{II}}(x, x') + [\beta^{(K)} - \alpha] r_{\text{III}}(x, x')\}. \quad (4.9)$$

In this chapter, we consider only the linear polarization. Therefore,  $K = 0, 2$  and  $Q \in [-K, +K]$ . The weights  $W_K$  depend on the line under consideration (see LL04). Here  $r_{\text{II}}(x, x')$  and  $r_{\text{III}}(x, x')$  are the angle-averaged versions of redistribution functions (see Hummer 1962). The branching ratios are given by

$$\alpha = \frac{\Gamma_R}{\Gamma_R + \Gamma_E + \Gamma_I}, \quad (4.10)$$

$$\beta^{(K)} = \frac{\Gamma_R}{\Gamma_R + D^{(K)} + \Gamma_I}, \quad (4.11)$$

with  $D^{(0)} = 0$  and  $D^{(2)} = c\Gamma_E$ , where  $c$  is a constant, taken to be 0.379 (see Faurobert-Scholl 1992). Substituting Equations (4.8) and (4.9) in Equation (4.4), we can write the  $i$ -th component of the line source vector as

$$\begin{aligned} S_{i,l}(\mathbf{r}, \boldsymbol{\Omega}, x) &= G_i(\mathbf{r}) + \frac{1}{\phi(x)} \int_{-\infty}^{+\infty} dx' \oint \frac{d\boldsymbol{\Omega}'}{4\pi} \\ &\times \sum_{j=0}^3 \sum_{KQ} \mathcal{T}_Q^K(i, \boldsymbol{\Omega}) (-1)^Q \mathcal{T}_{-Q}^K(j, \boldsymbol{\Omega}') R^K(x, x') I_j(\mathbf{r}, \boldsymbol{\Omega}', x'). \end{aligned} \quad (4.12)$$

Denoting  $G_Q^K = \delta_{K0} \delta_{Q0} G(\mathbf{r})$ , where  $G(\mathbf{r}) = \epsilon B_\nu(\mathbf{r})$  we can write the  $i$ -th component of the thermal source vector as

$$G_i(\mathbf{r}) = \sum_{KQ} \mathcal{T}_Q^K(i, \boldsymbol{\Omega}) G_Q^K(\mathbf{r}). \quad (4.13)$$

Substituting Equation (4.13) in Equation (4.12) we can write the line source vector as

$$S_{i,l}(\mathbf{r}, \boldsymbol{\Omega}, x) = \sum_{KQ} \mathcal{T}_Q^K(i, \boldsymbol{\Omega}) S_{Q,l}^K(\mathbf{r}, x), \quad (4.14)$$

where

$$\begin{aligned} S_{Q,l}^K(\mathbf{r}, x) &= G_Q^K(\mathbf{r}) + \frac{1}{\phi(x)} \int_{-\infty}^{+\infty} dx' \oint \frac{d\boldsymbol{\Omega}'}{4\pi} \\ &\times R^K(x, x') \sum_{j=0}^3 (-1)^Q \mathcal{T}_{-Q}^K(j, \boldsymbol{\Omega}') I_j(\mathbf{r}, \boldsymbol{\Omega}', x'). \end{aligned} \quad (4.15)$$

Notice that the components  $S_{Q,l}^K(\mathbf{r}, x)$  now depend only on the spatial variables  $(x, y, z)$  and frequency  $x$ . The  $(\theta, \varphi)$  dependence is fully contained in  $\mathcal{T}_Q^K(i, \mathbf{\Omega})$ . These quantities are listed in LL04 (chapter 5, Table 5.6, p. 211, see also Table 2 of HF07). We can define the monochromatic optical depth scale as

$$\tau_x(\mathbf{r}, \mathbf{\Omega}) = \tau_x(x, y, z, \mathbf{\Omega}) = \int_{s_0}^s \kappa_{tot}(\mathbf{r} - (s - s')\mathbf{\Omega}, x) ds', \quad (4.16)$$

where  $\tau_x$  is measured along a given ray determined by the direction  $\mathbf{\Omega}$ . We use the notation  $\tau_X, \tau_Y$  and  $\tau_Z$  to denote the optical depths along the  $X, Y$  and  $Z$  axes respectively at line center. Substituting Equation (4.14) in Equation (4.7), the components of  $\mathbf{I}$  can be written as

$$I_i(\mathbf{r}, \mathbf{\Omega}, x) = \sum_{KQ} \mathcal{T}_Q^K(i, \mathbf{\Omega}) I_Q^K(\mathbf{r}, \mathbf{\Omega}, x), \quad (4.17)$$

where

$$\begin{aligned} I_Q^K(\mathbf{r}, \mathbf{\Omega}, x) &= I_{Q,0}^K(\mathbf{r}_0, \mathbf{\Omega}, x) e^{-\int_{s_0}^s \kappa_{tot}(\mathbf{r} - (s - s')\mathbf{\Omega}, x) ds'} \\ &+ \int_{s_0}^s e^{-\int_{s'}^s \kappa_{tot}(\mathbf{r} - (s - s'')\mathbf{\Omega}, x) ds''} \left[ p_x S_{Q,l}^K(\mathbf{r} - (s - s')\mathbf{\Omega}, x) \right. \\ &\left. + (1 - p_x) S_{Q,c}^K(\mathbf{r} - (s - s')\mathbf{\Omega}, x) \right] \kappa_{tot}(\mathbf{r} - (s - s')\mathbf{\Omega}, x) ds'. \end{aligned} \quad (4.18)$$

$I_{Q,0}^K = I_0(\mathbf{r}_0, \mathbf{\Omega}, x) \delta_{K0} \delta_{Q0}$  are the intensity components at the lower boundary. The quantities  $S_{Q,c}^K = S_c(\mathbf{r}, x) \delta_{K0} \delta_{Q0}$  denote the continuum source vector components. We assume that  $S_c(\mathbf{r}, x) = B_\nu(\mathbf{r})$ . The ratio of the line opacity to the total opacity is given by

$$p_x = \kappa_l(\mathbf{r}) \phi(x) / \kappa_{tot}(\mathbf{r}, x). \quad (4.19)$$

Expressed in terms of optical depth along the ray, Equation (4.18) can be written as

$$\begin{aligned} I_Q^K(\mathbf{r}, \mathbf{\Omega}, x) &= I_{Q,0}^K(\mathbf{r}_0, \mathbf{\Omega}, x) e^{-\tau_x(\mathbf{r}, \mathbf{\Omega})} \\ &+ \int_0^{\tau_x(\mathbf{r}, \mathbf{\Omega})} e^{-\tau'_x(\mathbf{r}', \mathbf{\Omega})} \left[ p_x S_{Q,l}^K(\mathbf{r}', x) + (1 - p_x) S_{Q,c}^K(\mathbf{r}', x) \right] d\tau'_x(\mathbf{r}', \mathbf{\Omega}). \end{aligned} \quad (4.20)$$

In Equation (4.20)  $\tau_x(\mathbf{r}, \mathbf{\Omega})$  is the maximum optical depth when measured along the ray. Let  $S_Q^K = p_x S_{Q,l}^K + (1 - p_x) S_{Q,c}^K$ . Using the expansions in Equations (4.14) and (4.17), it

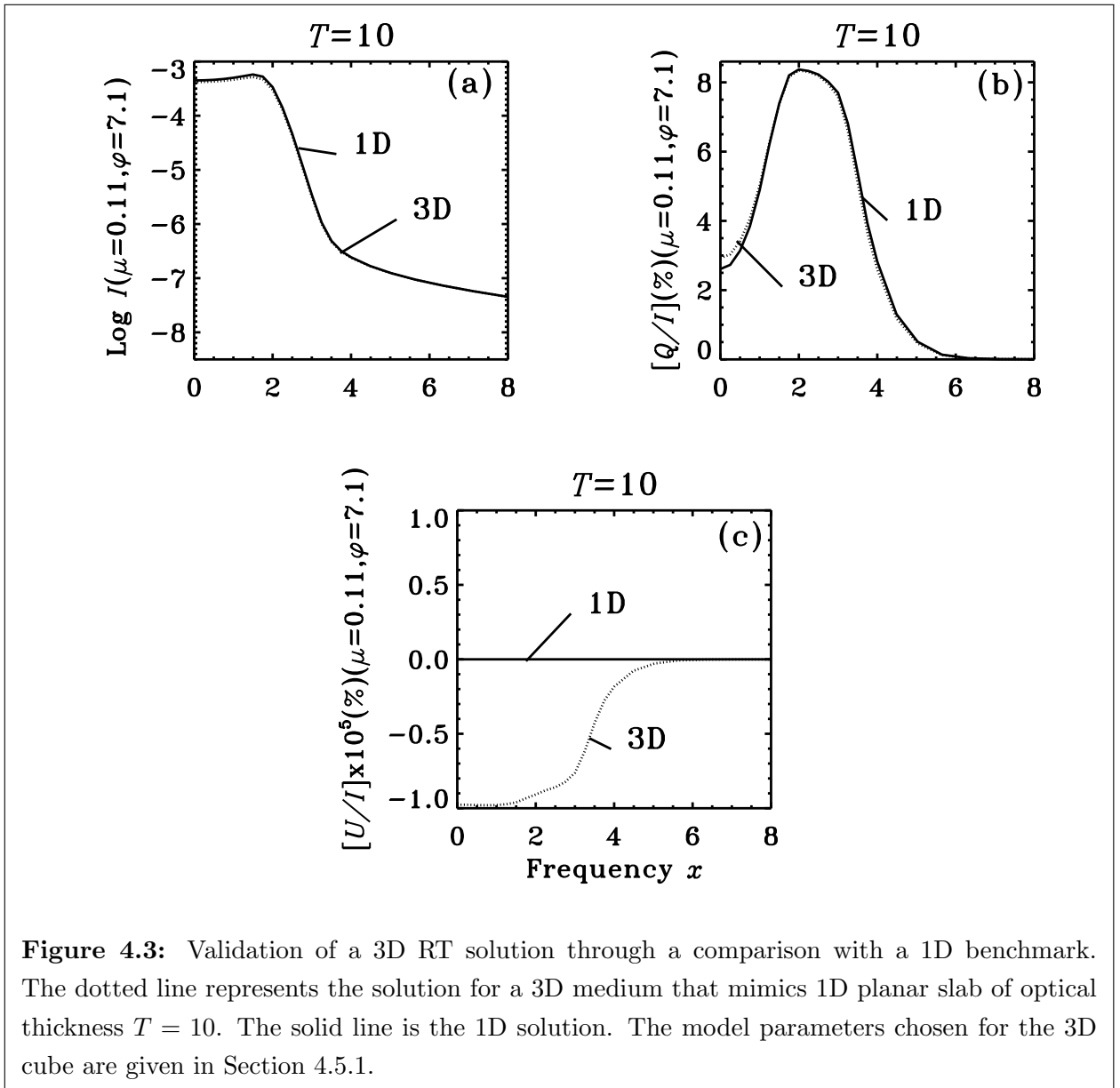


**Figure 4.3:** Validation of a 3D RT solution through a comparison with a 1D benchmark. The dotted line represents the solution for a 3D medium that mimics 1D planar slab of optical thickness  $T = 10$ . The solid line is the 1D solution. The model parameters chosen for the 3D cube are given in Section 4.5.1.

can be shown that  $S_Q^K$  and  $I_Q^K$  satisfy a RT equation of the form

$$-\frac{1}{\kappa_{\text{tot}}(\mathbf{r}, x)} \boldsymbol{\Omega} \cdot \nabla I_Q^K(\mathbf{r}, \boldsymbol{\Omega}, x) = [I_Q^K(\mathbf{r}, \boldsymbol{\Omega}, x) - S_Q^K(\mathbf{r}, x)]. \quad (4.21)$$

The great advantage of working with the irreducible intensity components  $I_Q^K$  is that the corresponding source terms  $S_Q^K$  become independent of the direction  $\boldsymbol{\Omega}$  of the ray.

Substituting Equation (4.17) in Equation (4.15) we obtain

$$S_{Q,l}^K(\mathbf{r}, x) = G_Q^K(\mathbf{r}) + \bar{J}_Q^K(\mathbf{r}, x), \quad (4.22)$$

where

$$\begin{aligned} \bar{J}_Q^K(\mathbf{r}, x) &= \frac{1}{\phi(x)} \int_{-\infty}^{+\infty} dx' \oint \frac{d\boldsymbol{\Omega}'}{4\pi} R^K(x, x') \\ &\times \sum_{j=0}^3 \sum_{K'Q'} (\mathcal{T}_Q^K)^*(j, \boldsymbol{\Omega}') \mathcal{T}_{Q'}^{K'}(j, \boldsymbol{\Omega}') I_{Q'}^{K'}(\mathbf{r}, \boldsymbol{\Omega}', x'). \end{aligned} \quad (4.23)$$

The symbol  $*$  represents the conjugation.  $\mathcal{T}_Q^K$  satisfy the conjugation property

$$(\mathcal{T}_Q^K)^*(j, \boldsymbol{\Omega}) = (-1)^Q \mathcal{T}_{-Q}^K(j, \boldsymbol{\Omega}). \quad (4.24)$$

Equation (4.23) can be expressed in a matrix form as

$$\bar{\mathcal{J}}(\mathbf{r}, x) = \frac{1}{\phi(x)} \int_{-\infty}^{+\infty} dx' \oint \frac{d\boldsymbol{\Omega}'}{4\pi} \hat{R}(x, x') \hat{\Psi}(\boldsymbol{\Omega}') \mathcal{I}(\mathbf{r}, \boldsymbol{\Omega}', x'), \quad (4.25)$$

where the components of the vectors  $\bar{\mathcal{J}}$  and  $\mathcal{I}$  are  $\bar{J}_Q^K$  and  $I_Q^K$  respectively. The matrix  $\hat{R}$  is given by

$$\hat{R}(x, x') = \hat{W}[\hat{\alpha} r_{\text{II}}(x, x') + (\hat{\beta} - \hat{\alpha}) r_{\text{III}}(x, x')], \quad (4.26)$$

where

$$\hat{W} = \text{diag}\{W_0, W_2, W_2, W_2, W_2, W_2\}, \quad (4.27)$$

$$\hat{\alpha} = \text{diag}\{\alpha, \alpha, \alpha, \alpha, \alpha, \alpha\}, \quad (4.28)$$

$$\hat{\beta} = \text{diag}\{\beta^{(0)}, \beta^{(2)}, \beta^{(2)}, \beta^{(2)}, \beta^{(2)}, \beta^{(2)}\}. \quad (4.29)$$

The elements of the matrix  $\hat{\Psi}(\boldsymbol{\Omega})$  are

$$\Psi_{QQ'}^{KK'}(\boldsymbol{\Omega}) = \sum_{j=0}^3 (\mathcal{T}_Q^K)^*(j, \boldsymbol{\Omega}) \mathcal{T}_{Q'}^{K'}(j, \boldsymbol{\Omega}). \quad (4.30)$$

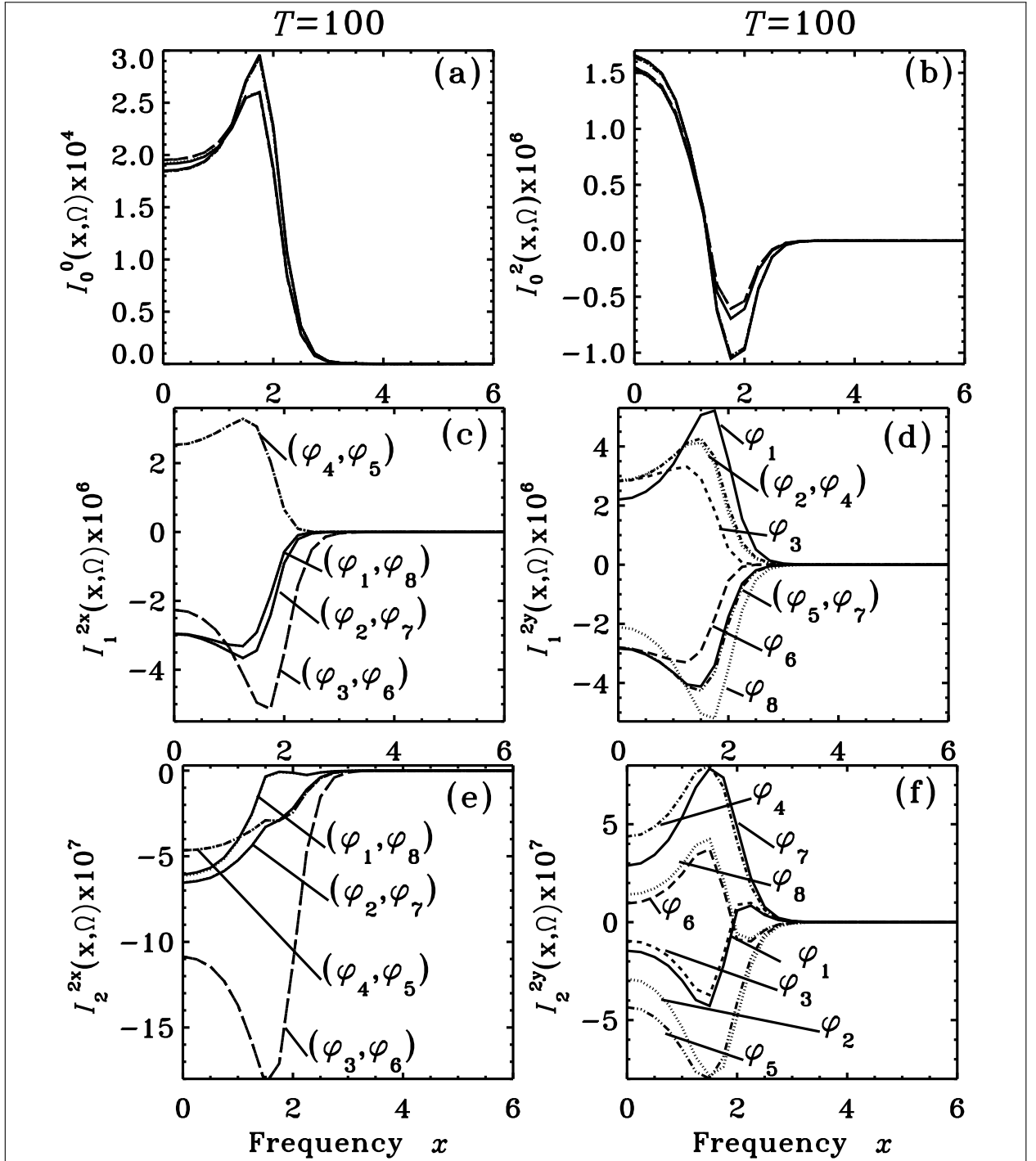


**Figure 4.4:** The azimuth angle ( $\varphi$ ) dependence of the spatially averaged irreducible intensity components of polarization at  $\tau_Z = 0$  in a 3D medium. The model parameters used are the same as those in Figure 4.3 except for  $T_X = T_Y = T_Z = T = 100$ . The values of the azimuth are  $\varphi_{1,8} = 7^\circ, 36^\circ, 85^\circ, 146^\circ, 213^\circ, 274^\circ, 323^\circ, 352^\circ$ . The intensity components approach a constant small value, or tend to zero in the wings ( $x \geq 3$ ).

$\Psi_{QQ'}^{KK'}$  are exactly the same as  $\Gamma_{KK',QQ'}(\boldsymbol{\Omega})$  given in LL04 (Appendix A.20). We stress here that the phase matrix  $\hat{\Psi}(\boldsymbol{\Omega}')$  in Equation (4.25) depends only on the directions  $\boldsymbol{\Omega}'$  of the incident rays. The dependence on  $\boldsymbol{\Omega}$ , present in the phase matrix when one works with the  $(I, Q, U)$  basis, disappears when the polarized radiation field is represented with the six  $I_Q^K$  components. For short we refer to this representation as the “reduced basis”. The matrix  $\hat{\Psi}(\boldsymbol{\Omega}')$  differs from the  $\hat{\Psi}(\mu')$  matrix that appears in 1D RT problems (see HF07; Nagendra et al. 1998), since it now depends on the azimuthal angle  $\varphi'$  of the incident ray.

### 4.3.2 Polarized radiative transfer equation for the real irreducible intensity vector in a 3D medium

The irreducible components  $I_Q^K$  and  $S_Q^K$  and the phase matrix elements  $\Psi_{QQ'}^{KK'}$  introduced in Section 4.3.1 are complex quantities. For practical computations, we prefer working with the real quantities. In this section we transform those quantities into the real space. For this purpose we follow the procedure given in HF07. We define

$$\begin{aligned} I_Q^{K,x}(\mathbf{r}, \boldsymbol{\Omega}, x) &= \text{Re}\{I_Q^K(\mathbf{r}, \boldsymbol{\Omega}, x)\}, \\ I_Q^{K,y}(\mathbf{r}, \boldsymbol{\Omega}, x) &= \text{Im}\{I_Q^K(\mathbf{r}, \boldsymbol{\Omega}, x)\}. \end{aligned} \quad (4.31)$$

We denote the the real vectors also by  $\mathcal{I}$  and  $\mathcal{S}$  for brevity. it can be shown that  $\mathcal{I} = (I_0^0, I_0^2, I_1^{2,x}, I_1^{2,y}, I_2^{2,x}, I_2^{2,y})^T$  and the corresponding source vector  $\mathcal{S}$  satisfy an RT equation of the form

$$-\frac{1}{\kappa_{\text{tot}}(\mathbf{r}, x)} \boldsymbol{\Omega} \cdot \nabla \mathcal{I}(\mathbf{r}, \boldsymbol{\Omega}, x) = [\mathcal{I}(\mathbf{r}, \boldsymbol{\Omega}, x) - \mathcal{S}(\mathbf{r}, x)], \quad (4.32)$$

where  $\mathcal{S}(\mathbf{r}, x) = p_x \mathcal{S}_l(\mathbf{r}, x) + (1 - p_x) \mathcal{S}_c(\mathbf{r}, x)$  with

$$\mathcal{S}_l(\mathbf{r}, x) = \epsilon \mathcal{B}(\mathbf{r}) + \frac{1}{\phi(x)} \int_{-\infty}^{+\infty} dx' \oint \frac{d\boldsymbol{\Omega}'}{4\pi} \hat{R}(x, x') \hat{\Psi}^r(\boldsymbol{\Omega}') \mathcal{I}(\mathbf{r}, \boldsymbol{\Omega}', x'). \quad (4.33)$$

Here  $\mathcal{S}_c(\mathbf{r}, x) = (B_\nu(\mathbf{r}), 0, 0, 0, 0, 0)^T$  is the continuum source vector and  $\mathcal{B} = (B_\nu(\mathbf{r}), 0, 0, 0, 0, 0)^T$  is the Planck vector. In the above equation, the real part of the scattering phase matrix  $\hat{\Psi}^r(\boldsymbol{\Omega})$  has the form

$$\hat{\Psi}^r(\boldsymbol{\Omega}) = \hat{T}^{-1} \hat{\Psi}(\boldsymbol{\Omega}) \hat{T} \quad (4.34)$$



where the matrix  $\hat{T}$  is given by

$$\hat{T} = \begin{pmatrix} 1 & 0 & 0 & 0 & 0 & 0 \\ 0 & 1 & 0 & 0 & 0 & 0 \\ 0 & 0 & 1 & i & 0 & 0 \\ 0 & 0 & -1 & i & 0 & 0 \\ 0 & 0 & 0 & 0 & 1 & i \\ 0 & 0 & 0 & 0 & 1 & -i \end{pmatrix}. \quad (4.35)$$

Hereafter we denote the real matrix  $\hat{\Psi}^r(\boldsymbol{\Omega})$  also by  $\hat{\Psi}(\boldsymbol{\Omega})$  for brevity. The elements of the scattering phase matrix  $\hat{\Psi}(\boldsymbol{\Omega})$  are given in the Appendix J. The matrix  $\hat{\Psi}(\boldsymbol{\Omega})$  has only 21 distinct coefficients due to symmetry reasons. We remark that  $\hat{\Psi}(\boldsymbol{\Omega})$  is a full matrix to be used in Multi-D case, unlike the  $\hat{\Psi}(\mu)$  that is used in the 1D case, which has a sparse structure. After solving the RT problem in the real, reduced basis, one has to transform back to the Stokes  $(I, Q, U)^T$  basis. This can be done using the following equations (see also Appendix B of HF07).

$$\begin{aligned} I(\mathbf{r}, \boldsymbol{\Omega}, x) &= I_0^0 + \frac{1}{2\sqrt{2}}(3 \cos^2 \theta - 1)I_0^2 \\ &\quad - \sqrt{3} \cos \theta \sin \theta (I_1^{2,x} \cos \varphi - I_1^{2,y} \sin \varphi) \\ &\quad + \frac{\sqrt{3}}{2}(1 - \cos^2 \theta)(I_2^{2,x} \cos 2\varphi - I_2^{2,y} \sin 2\varphi), \end{aligned} \quad (4.36)$$

$$\begin{aligned} Q(\mathbf{r}, \boldsymbol{\Omega}, x) &= -\frac{3}{2\sqrt{2}}(1 - \cos^2 \theta)I_0^2 \\ &\quad - \sqrt{3} \cos \theta \sin \theta (I_1^{2,x} \cos \varphi - I_1^{2,y} \sin \varphi) \\ &\quad - \frac{\sqrt{3}}{2}(1 + \cos^2 \theta)(I_2^{2,x} \cos 2\varphi - I_2^{2,y} \sin 2\varphi), \end{aligned} \quad (4.37)$$

$$\begin{aligned} U(\mathbf{r}, \boldsymbol{\Omega}, x) &= \sqrt{3} \sin \theta (I_1^{2,x} \sin \varphi + I_1^{2,y} \cos \varphi) \\ &\quad + \sqrt{3} \cos \theta (I_2^{2,x} \sin 2\varphi + I_2^{2,y} \cos 2\varphi). \end{aligned} \quad (4.38)$$

The irreducible components in the above equations also depend on  $\mathbf{r}$ ,  $\boldsymbol{\Omega}$  and  $x$ .

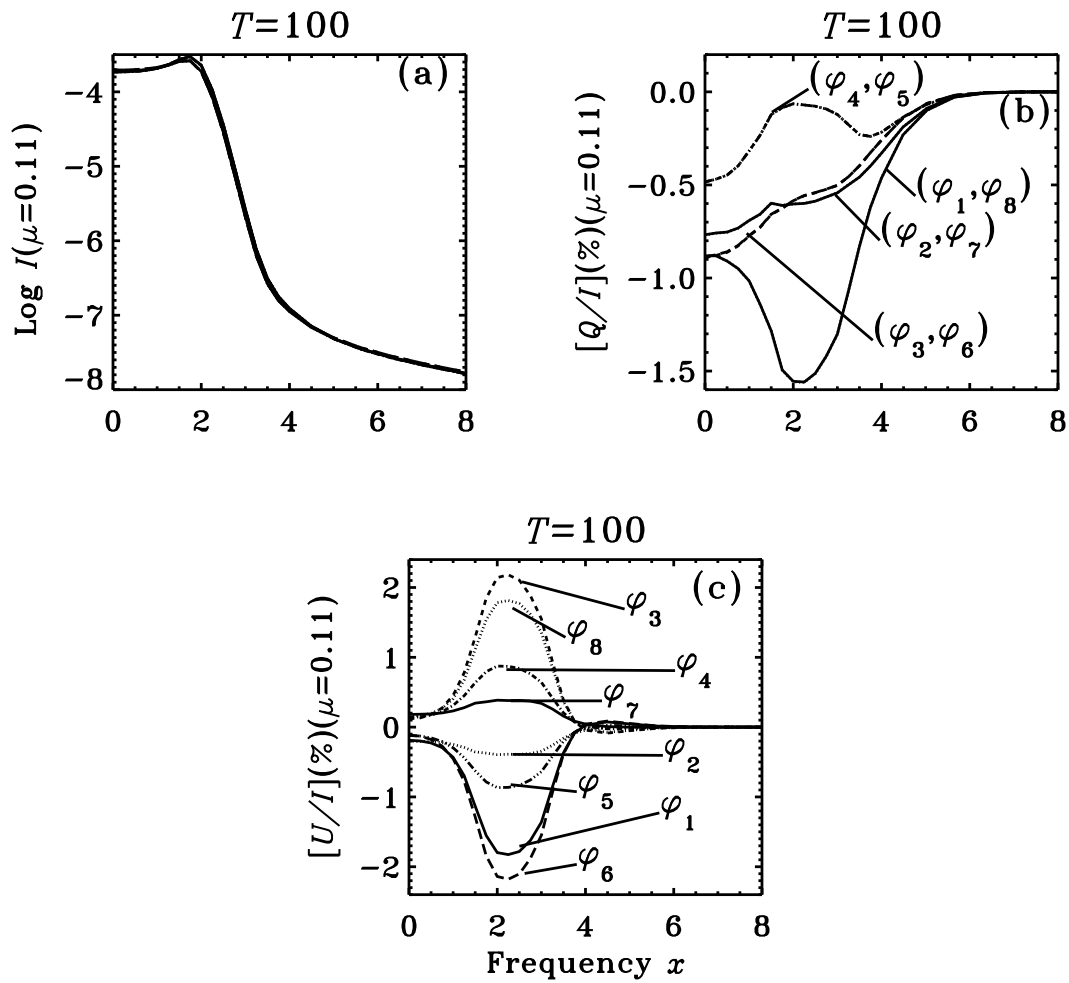


**Figure 4.5:** Spatially averaged emergent ( $I, Q/I, U/I$ ) in a 3D medium. The model parameters are the same as those in Figure 4.4.

## 4.4 The Numerical Method of Solution

For the numerical solution of the 3D RT problem (Equation (4.32)), we use a polarized approximate lambda iteration (PALI) method, associated to a core-wing separation method to handle PRD. The 6 component scattering integral can be expressed as

$$\overline{\mathcal{J}}(\mathbf{r}, x) = \int_{-\infty}^{+\infty} dx' \frac{\hat{R}(x, x')}{\phi(x)} \mathcal{J}(\mathbf{r}, x'), \quad (4.39)$$

with

$$\mathcal{J}(\mathbf{r}, x) = \oint \frac{d\Omega'}{4\pi} \hat{\Psi}(\Omega') \mathcal{I}(\mathbf{r}, \Omega', x). \quad (4.40)$$

The formal solution for  $\mathcal{I}(\mathbf{r}, \Omega', x)$  allows us to define the operator  $\Lambda_x$  as

$$\mathcal{J}(\mathbf{r}, x) = \Lambda_x[\mathcal{S}(\mathbf{r}, x)]. \quad (4.41)$$

Applying the operator splitting technique, the scattering integral at the  $(n+1)$ -th iteration can be written as

$$\overline{\mathcal{J}}^{r,n+1}(\mathbf{r}, x) = \int_{-\infty}^{+\infty} dx' \frac{\hat{R}(x, x')}{\phi(x)} [\Lambda_{x'}^* + (\Lambda_{x'} - \Lambda_{x'}^*)] \mathcal{S}^{r,n+1}(\mathbf{r}, x'). \quad (4.42)$$

We can re-write the scattering integral as

$$\overline{\mathcal{J}}^{r,n+1}(\mathbf{r}, x) = \overline{\mathcal{J}}^{r,n}(\mathbf{r}, x) + \int_{-\infty}^{+\infty} dx' \frac{\hat{R}(x, x')}{\phi(x)} \Lambda_{x'}^* p_{x'} \delta \mathcal{S}_l^{r,n}(\mathbf{r}, x'). \quad (4.43)$$

It is useful to notice here that  $\delta \mathcal{S}_l^{r,n}(\mathbf{r}, x) = p_x \delta \mathcal{S}_l^{r,n}(\mathbf{r}, x)$ . The correction to the line source vector in the  $n$ -th iteration is given by

$$\delta \mathcal{S}_l^{r,n}(\mathbf{r}, x) = \overline{\mathcal{J}}^{r,n+1}(\mathbf{r}, x) + \epsilon \mathbf{B}(\mathbf{r}) - \mathcal{S}_l^{r,n}. \quad (4.44)$$

Further details of the numerical method of solution to solve the 3D RT equation is given in Appendix D.

### 4.4.1 The formal solution in 3D geometry

In this section we generalize the method of Adam (1990) for 3D RT to include the polarization and PRD. For the sake of brevity we drop the explicit dependence of the physical quantities on the arguments. To start with, we divide the computational domain (a cube) into a 3 dimensional mesh of grid points  $(x_i, y_j, z_k)$  with  $i = 1, 2, \dots, n_X; j = 1, 2, \dots, n_Y; k = 1, 2, \dots, n_Z$ . A discretization of Equation (4.32) on this mesh can be written as

$$-\frac{1}{\kappa_{\text{tot}}} \left[ \eta \frac{\mathcal{I}_{ijk} - \mathcal{I}_{i-a,j,k}}{x_i - x_{i-a}} + \gamma \frac{\mathcal{I}_{ijk} - \mathcal{I}_{i,j-b,k}}{y_j - y_{j-b}} + \mu \frac{\mathcal{I}_{ijk} - \mathcal{I}_{i,j,k-c}}{z_k - z_{k-c}} \right] = [\mathcal{I}_{ijk} - \mathcal{S}_{ijk}], \quad (4.45)$$

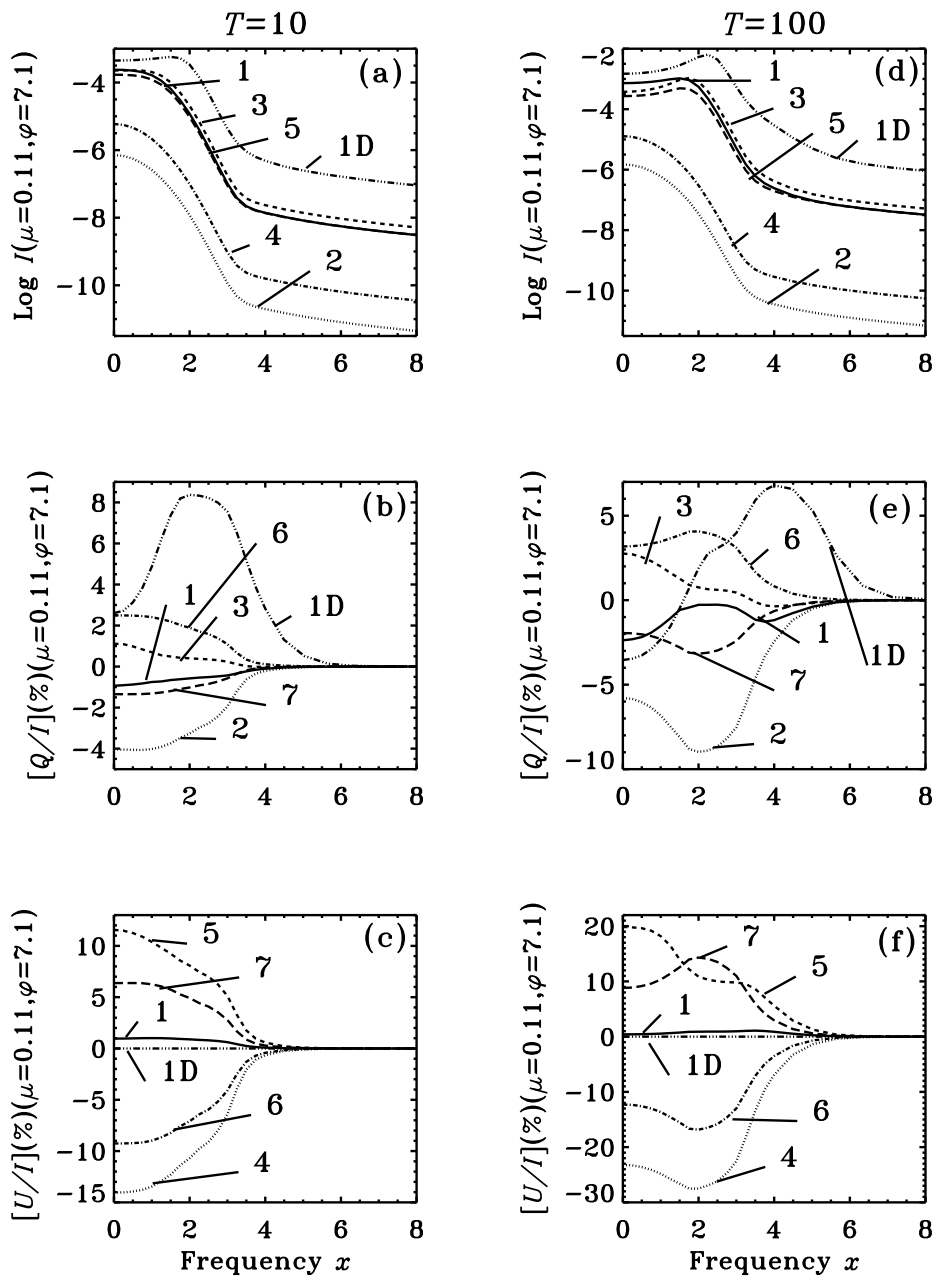


**Figure 4.6:** Optical depth effects on emergent ( $I, Q/I, U/I$ ) in a 3D medium. The computations are done using a cube with optical depths  $T_X = T_Y = T_Z = T$ , for a given value of  $T$ . Other model parameters are the same as in the Figure 4.3. The solution for a planar slab of vertical optical depth  $T = T_Z$  is also shown as dash-triple-dotted line, for comparison. The labels on the curves correspond to the points in Figure 4.2.

where  $a, b, c$  are the increments, taking values  $+1$  or  $-1$  depending on the choice of the direction vector  $\boldsymbol{\Omega}$ . In deriving Equation (4.45) we have used a finite difference method where the differential operator is represented to the linear order. Equation (4.45) can be simplified to get

$$\mathcal{I}_{ijk} = \left\{ \mathcal{S}_{ijk} + \frac{1}{\kappa_{\text{tot}}} \left[ \eta \frac{\mathcal{I}_{i-a,j,k}}{x_i - x_{i-a}} + \gamma \frac{\mathcal{I}_{i,j-b,k}}{y_j - y_{j-b}} + \mu \frac{\mathcal{I}_{i,j,k-c}}{z_k - z_{k-c}} \right] \right\} / \left\{ 1 + \frac{1}{\kappa_{\text{tot}}} \left( \frac{\eta}{x_i - x_{i-a}} + \frac{\gamma}{y_j - y_{j-b}} + \frac{\mu}{z_k - z_{k-c}} \right) \right\}. \quad (4.46)$$

Equation (4.46) is solved recursively, namely the intensity at any spatial point  $(ijk)$  depends only on the intensity at 3 previous neighboring points  $(i-a, j, k)$ ,  $(i, j-b, k)$ ,  $(i, j, k-c)$ .

It is shown by Adam (1990) that this numerical approach is unconditionally stable. The linear differencing is relatively less accurate compared to the short characteristic method, as a formal solver. However, we can overcome this problem of accuracy by taking sufficiently small step sizes in the  $(x, y, z)$  co-ordinates. The main emphasis of this chapter is to understand the nature of 3D solutions for the problem at hand, instead of devising highly accurate and rapid methods. These issues would be addressed in another chapter. In Section 4.5 we present few benchmark solutions computed by the method presented in Appendix D.

*Computational details:* We consider a self-emitting cube (or a slab) for the results presented in this chapter. A Gaussian angle grid of 6 inclination ( $\theta=83.5^\circ, 60^\circ, 27.4^\circ, 96.5^\circ, 120^\circ, 152.6^\circ$ ) and 8 azimuths ( $\varphi=7^\circ, 36^\circ, 85^\circ, 146^\circ, 213^\circ, 274^\circ, 323^\circ, 352^\circ$ ) are used. We have numerically tested that this kind of angular resolution is quite reasonable and gives stable solutions. A spatial grid resolution of 15 points per decade or 20 points per decade in  $X, Y$  and  $Z$  directions are used. The spatial grid is logarithmic, with fine gridding near the boundaries. A logarithmic frequency grid of 31 points covering 20 Doppler widths ( $0 \leq x \leq x_{\text{max}} = 20$ ) is sufficient for the examples shown in this chapter. The standard model parameters are listed in Section 4.5.1. The specific model parameters for each figure are given on the figures and the respective figure captions.

## 4.5 Results and Discussions

In this section we present sample results to show the correctness of the Stokes decomposition procedure, as applied to the 3D case. Further we show some results to validate the numerical method that computes the 3D solution. The departure of the radiation field from axi-symmetry is discussed in some detail. A study of the PRD effects in 3D media is also presented along with the role of collisional redistribution.

### 4.5.1 A validation test for the 3D polarized radiative transfer solution

It is possible to test the correctness of a 3D solution by going to a geometric situation where the 3D cube mimics an 1D slab. For  $T_X \gg T_Z$  and  $T_Y \gg T_Z$ , with a finite value of  $T_Z = T$ , the computational box looks like a planar slab of optical thickness  $T$ . We can expect the emergent solution  $(I, Q/I, U/I)^T$  at the center of the upper surface  $(T_X/2, T_Y/2, \tau_Z = 0)$  of such a cube to approach the emergent 1D solution  $(I, Q/I, U/I)^T$  at  $\tau_Z = 0$ . Figure 4.3 presents this validation test. The 1D benchmark solution is computed using a PALI method (see e.g., Nagendra et al. 1999; Fluri et al. 2003b). The model parameters are  $T_X = T_Y = 10^7$ , and  $T_Z = T = 10$ ; the elastic and inelastic collision rates are respectively  $\Gamma_E/\Gamma_R = 10^{-4}$ ,  $\Gamma_I/\Gamma_R = 10^{-4}$ . The damping parameter of the Voigt profile is  $a = 2 \times 10^{-3}$ . The branching ratios for this choice of model parameters are  $(\alpha, \beta^{(0)}, \beta^{(2)}) \approx (1, 1, 1)$  (see the exact values in Table 4.2). We consider the pure line case ( $\kappa_c = 0$ ), and scattering according to PRD (see Equation (4.8)). The internal thermal sources are taken as constant (the Planck function  $B = 1$ ). The medium is assumed to be self-emitting (no incident radiation on the boundaries). The emergent  $(I, Q/I, U/I)$  profiles are shown for a choice of angles  $(\mu, \varphi) = (0.11, 7^\circ)$ . From Figures 4.3(a) and 4.3(b), we see that there is a good agreement between the two solutions. In the planar case  $U/I \equiv 0$ . The  $U/I$  in the 3D case approaches this value to a high accuracy ( $10^{-5}$  percent). This figure shows the correctness of the Stokes decomposition expressions, and also the numerical method that computes the 3D solution.

### 4.5.2 The nature of irreducible intensity components $\mathcal{I}$ in a 3D medium

In Section 4.3 we showed how to express the Stokes parameters in terms of the irreducible intensity components. These components are more fundamental than the Stokes parameters themselves. Their study is useful to understand the behavior of Stokes parameters - which are actually the measurable quantities. If we choose optical thickness in the  $X$ ,  $Y$ , and  $Z$  directions as  $T_X = T_Y = T_Z = T$ , then we encounter a situation where the

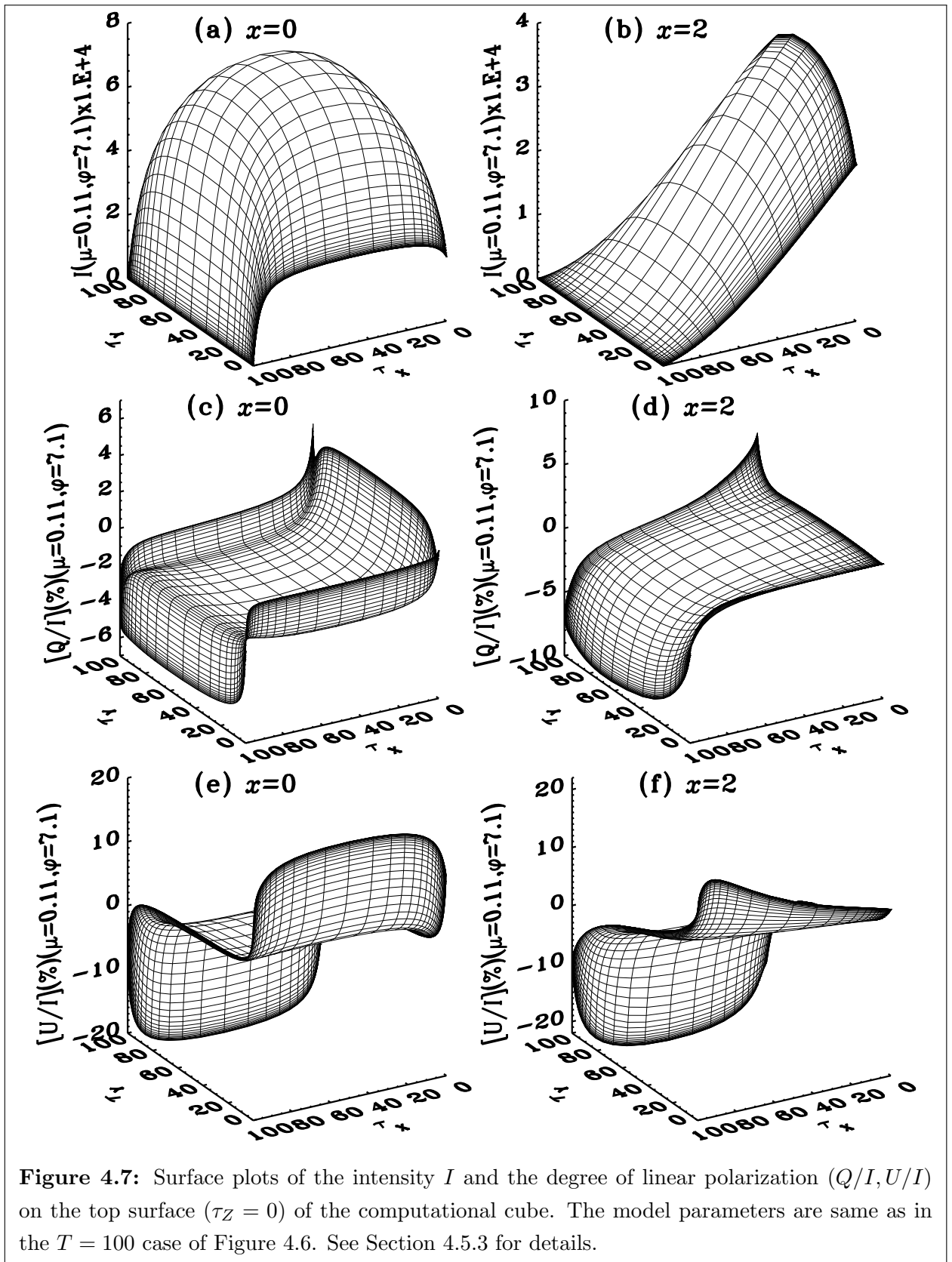


**Figure 4.7:** Surface plots of the intensity  $I$  and the degree of linear polarization ( $Q/I, U/I$ ) on the top surface ( $\tau_Z = 0$ ) of the computational cube. The model parameters are same as in the  $T = 100$  case of Figure 4.6. See Section 4.5.3 for details.

3D nature of the RT problem is clearly exhibited. Figure 4.4 shows the spatially averaged emergent  $\mathcal{I}$  at the top surface ( $\tau_Z = 0$ ). We prefer to show the spatially averaged  $\mathcal{I}$  because the components themselves sensitively depend on the spatial location on the surface. It is useful to note that the spatially averaged  $\mathcal{I}$  retain the original symmetries even after averaging. The results are shown for  $\mu = 0.11$  and for all the 8 values of the azimuth angle  $\varphi$  (namely  $7^\circ, 36^\circ, 85^\circ, 146^\circ, 213^\circ, 274^\circ, 323^\circ, 352^\circ$ ). The model parameters and the physical conditions chosen for Figure 4.4 are the same as in Figure 4.3, except for  $T_X = T_Y = T_Z = T = 100$ .

The  $I_0^0$  component is the driving term. It is also the largest in magnitude. The  $I_0^2$  component is two orders of magnitude smaller than  $I_0^0$ . In a corresponding 1D medium the last 4 components of  $\mathcal{I}$  become zero because of the cylindrical symmetry of the radiation field. In a 3D medium, these components are non-zero. Specifically for our chosen model the components  $I_1^{2,x}$  and  $I_1^{2,y}$  are nearly one order of magnitude larger than  $I_0^2$  itself. The components  $I_2^{2,x}$  and  $I_2^{2,y}$  are of the same order as  $I_0^2$ .

Because  $I_0^0$  is the largest of all the components, the behavior of the  $\mathcal{I}$  can be understood by considering the action of the first column elements of the  $\hat{\Psi}$  matrix on  $I_0^0$ . The quantities  $I_0^0$  in panel (a) and  $I_0^2$  in panel (b) are nearly independent of the azimuthal angle  $\varphi$ . This comes from the  $\varphi$ -independence of the elements  $\Psi_{11}$  and  $\Psi_{21}$  of the scattering phase matrix in the reduced basis.  $\Psi_{31}$  and  $\Psi_{51}$  elements contain  $\cos \varphi$  and  $\cos 2\varphi$  functions respectively. The  $\varphi$  values are chosen in such a way that  $\varphi_i = 2\pi - \varphi_{n_\varphi - i + 1}$  with  $i = 1, 2, 3, 4$  and  $n_\varphi = 8$ . Due to symmetry of  $\cos \varphi$  and  $\cos 2\varphi$  functions with respect to  $\varphi = 2\pi$  and  $4\pi$  respectively, only 4 curves are distinguishable among the 8 in Figures 4.4(c) and 4.4(e). The elements  $\Psi_{41}$  and  $\Psi_{61}$  contain  $\sin \varphi$  and  $\sin 2\varphi$  functions respectively. Due to antisymmetry of  $\sin \varphi$  and  $\sin 2\varphi$  functions with respect to  $\varphi = 2\pi$  and  $4\pi$  respectively, in Figures 4.4(d) and 4.4(f) the curves for  $\varphi_i$ ,  $i = 1, 2, 3, 4$  have opposite signs with respect to the curves for  $\varphi_{n_\varphi - i + 1}$ ,  $n_\varphi = 8$ . Moreover,  $\varphi_2$  and  $\pi - \varphi_4$  are close, and  $\varphi_5$  and  $3\pi - \varphi_7$  are also close. Due to symmetry of  $\sin \varphi$  with respect to  $\varphi = \pi$  and  $3\pi$ , in Figure 4.4(d) curves for  $\varphi_2$  and  $\varphi_5$  nearly coincide with those for  $\varphi_4$  and  $\varphi_7$  respectively. On the other hand,  $2\varphi_2$  is close to  $2\pi - 2\varphi_4$  and  $2\varphi_5$  is close to  $6\pi - 2\varphi_7$ , which in turn lead to the  $\varphi_2$  and  $\varphi_4$  curves and  $\varphi_5$  and  $\varphi_7$  curves to have opposite signs in Figure 4.4(f) due to the anti symmetry of  $\sin 2\varphi$  function about  $\varphi = 2\pi$  and  $6\pi$  respectively. Therefore, all the curves are clearly resolved.

In Figure 4.5 we present the spatially averaged emergent  $(I, Q/I, U/I)$  corresponding to the irreducible intensity components shown in Figure 4.4. The Stokes  $I$  profile has dominant contribution from  $I_0^0$  (see Equation (4.36)). The  $Q/I$  profile on the other hand has



significant contributions from  $I_0^2$ ,  $I_1^{2,x}$  and  $I_1^{2,y}$ . The component  $I_0^2$  is nearly  $\varphi$ -independent, however  $I_1^{2,x}$  and  $I_1^{2,y}$  are strongly  $\varphi$ -dependent. This dependence is responsible for a strong variation of  $Q/I$  with respect to the azimuthal angle  $\varphi$  (see Equation (4.37)). On the other hand, in a 1D medium  $I_0^2$  is the only component that is responsible for the generation of Stokes  $Q$ . Because of this,  $Q/I$  in 1D medium becomes  $\varphi$ -independent. The dominant contribution to  $U/I$  comes from  $I_1^{2,x}$  and  $I_1^{2,y}$ . The magnitude of  $U/I$  is quite significant, and could become larger than  $Q/I$ , unlike the corresponding 1D situation, where  $U/I \equiv 0$  always.

### 4.5.3 Linear polarization in 3D medium of finite optical depths

In this section we show  $(I, Q/I, U/I)$  profiles at chosen spatial points on the top surface ( $\tau_Z = 0$ ). Our purpose is to understand the spatial dependence of the solution. In Figure 4.6 we show the solutions for a cube defined by  $T_X = T_Y = T_Z = T$  with  $T = 10$ , and 100. All the other model parameters and physical conditions are taken to be the same as in Figure 4.3. The curves in Figure 4.6 represent the emergent  $(I, Q/I, U/I)$  at the spatial locations marked as points 1–9 on the top surface of the computational cube as shown in Figure 4.2 (see Table 4.1 for optical depth information). The corresponding 1D solution is shown for comparison as dash-triple-dotted lines in all the panels.

*Stokes I:* In Figures 4.6(a) and 4.6(d) we plot the Stokes  $I$  in 1D and 3D media. The 3D solutions are shown at spatial points 1, 2, 3, 4, 5 as solid, dotted, dashed, dot-dashed, long dashed lines respectively. The results are shown for  $\mu = 0.11$  and  $\varphi = 7^\circ$ . In all the cases, Stokes  $I$  shows an emission line spectra, and the  $[I]_{3D}$  is less in magnitude than the  $[I]_{1D}$ . This indicates the leaking in the 3D case, of the radiation through the surface boundaries perpendicular to  $X$  and  $Y$  directions in contrast to the 1D case characterized by  $T_X, T_Y \rightarrow \infty$ . As we are showing Stokes  $I$  for  $\mu = 0.11$  (positive  $\mu$  direction), the Stokes  $I$  for points 2 and 4 are much smaller in magnitude than those at points 3 and 5. This is because the incident intensity is zero at the boundaries adjacent to the points 2 and 4. At points 3 and 5 Stokes  $I$  emergent in the direction  $\mu = 0.11$  is larger in magnitude due to the contribution of scattering in the medium. Stokes  $I$  shows a larger spatial gradient in the regions covered by  $[T_X, T_X/2]$  and  $[T_Y, T_Y/2]$ , when compared to the region covered by  $[T_X/2, 0]$  and  $[T_Y/2, 0]$ . This can be seen clearly by looking at the surface plots, namely Figure 4.7(a) and 4.7(b).

*Stokes Q:* In Figures 4.6(b) and 4.6(e) we plot the  $Q/I$  in 1D and 3D medium. The 3D solutions are shown at spatial points 1, 2, 3, 6, 7 as solid, dotted, dashed, dot-dashed, long dashed lines respectively. There exist significant differences between  $[Q/I]_{1D}$  and  $[Q/I]_{3D}$ . For  $T = 10$ , the maximum value of  $[Q/I]_{3D}$  is for the spatial location 2. At this point,  $[Q/I]_{3D}$  is about 4 percent and  $[Q/I]_{1D}$  is 3 percent at line center. However in the near wings ( $x \leq 6$ ),  $[Q/I]_{1D}$  reaches a maximum of around 8 percent at  $x = 2$  and the corresponding  $[Q/I]_{3D}$  is around 3 percent. For  $T = 100$ , the  $[Q/I]_{3D}$  reaches a maximum of 10 percent for the spatial point 2 at  $x = 2$  and  $[Q/I]_{1D}$  reaches maximum of 7 percent at  $x = 4$ . For the points 2 and 6,  $[Q/I]_{3D}$  takes largest values for both  $T = 10$  and  $T = 100$ . The dominant quantity that dictates the emergent  $Q/I$  is the radiation anisotropy within the cube. The above results show the existence of a sharp variation of anisotropy within the cube than within a slab which has only one degree of freedom for RT in the spatial domain. Also from the surface plots Figures 4.7(c) and 4.7(d) we see a sharp variation of  $[Q/I]_{3D}$  at the edges of the top surface. However, the polarization remains nearly constant ( $\approx 2$  percent) at  $x = 0$  in the inner parts of the top surface. The spatial variation of  $[Q/I]_{3D}$  at  $x = 2$  is quite different from that at  $x = 0$ . There is a sharp increase in  $[Q/I]_{3D}$  near the edge region ( $\tau_X = 0$  or  $\tau_X = T_X$ ), reaching a maximum value of around 10 percent.

*Stokes U:* In Figures 4.6(c) and 4.6(f) we show  $U/I$  in 1D and 3D medium. The 3D solutions are shown at spatial points 1, 4, 5, 6, 7 as solid, dotted, dashed, dot-dashed, long dashed lines respectively.  $[U/I]_{1D} \equiv 0$ , whereas  $[U/I]_{3D}$  has a significant value. The variation of  $[U/I]_{3D}$  with an increase in  $T$  is analogous to the behavior of  $[Q/I]_{3D}$ . For the points 4 and 5,  $[U/I]_{3D}$  takes largest values for both  $T = 10$  and  $T = 100$ . It reaches a maximum of 15 percent at the spatial point 4, for  $x = 0$  and  $T=10$  (see Figure 4.6(c)) and 25 percent at the spatial point 4, for  $x = 2$  and  $T=100$  (see Figure 4.6(f)). This shows that  $U/I$  is much more sensitive to the anisotropy of the radiation field within a 3D medium. At the spatial point 1,  $[U/I]_{3D} \approx 0$  as expected, namely the axi-symmetry of the emergent radiation at the central point. From the surface plots Figures 4.7(e) and 4.7(f) we can see a large variation of  $[U/I]_{3D}$  again at the edges of the cube, where non-axisymmetry reaches maximum. As in  $[Q/I]_{3D}$  the behavior of  $[U/I]_{3D}$  at  $x = 2$  is quite different from that at  $x = 0$ . However its maximum is now reached near the edge region ( $\tau_Y = 0$  or  $\tau_Y = T_Y$ ), which is oriented at  $90^\circ$  with respect to the regions where  $[Q/I]_{3D}$  shows a maximum variation ( $\tau_X = 0$  or  $\tau_X = T_X$ ). In general, the run of anisotropy in the 3D case depends on the optical depths in  $X$ ,  $Y$  and  $Z$  directions simultaneously. This is

clearly seen in the complicated frequency dependence of  $(Q/I, U/I)$  profiles in the 3D case unlike the 1D case. Although the linear polarization  $(Q/I, U/I)$  may take large values at different spatial points (for e.g., points 1–9), the spatially averaged values of  $(Q/I, U/I)$  are usually less, in the self-emitting cubes that we have considered in this chapter. The effect of spatial averaging can be seen in Figure 4.5. The fact that 1D values of  $(Q/I, U/I)$  differ considerably from the 3D situation shows that realistic modeling of the observed linear polarization using 3D model atmospheres is not as straight forward as the use of 1D model atmospheres.

#### 4.5.4 The effect of collisional redistribution on the Stokes parameters in a 3D medium

Figure 4.8 shows spatially averaged  $(I, Q/I, U/I)^T$  results computed for a  $T = 100$  model with a range of elastic collision rate parameters  $\Gamma_E/\Gamma_R = (10^{-4}, 0.1, 1, 10)$ . The models corresponding to the curves shown in Figure 4.8 are given in Table 4.2. Models 2 and 3 can be termed as radiative de-excitation models (dominated by  $r_{\text{II}}$ -type PRD). Model 4 has a mixture of  $r_{\text{II}}$  and  $r_{\text{III}}$  type PRD scattering mechanisms. The collisions dominate ( $r_{\text{III}}$ -type PRD) in the model 5. Model 1, corresponding to CRD, is presented for comparisons.

*Stokes I:* The Stokes  $I$  is controlled by  $\alpha$  and  $\beta^{(0)} - \alpha$ . The line core ( $x \leq 1$ ) of the Stokes  $I$  profile is unaffected by collisions. In the line core, the  $r_{\text{II}}$  and  $r_{\text{III}}$  type functions both behave like CRD function, and hence the PRD and CRD profiles are similar. As we go from models 2 to 5, the relative contribution of  $r_{\text{III}}$  progressively increases throughout the line profile. However its effect is felt only in the wings ( $x \geq 2$ ).

*Stokes Q:* The ratio  $Q/I$  is controlled by  $\alpha$  and  $\beta^{(2)} - \alpha$ . The models 1 to 3 yield nearly the same magnitude for  $[[Q/I]]_{3\text{D}}$  at line center again because of the CRD-type behavior of  $r_{\text{II}}$  and  $r_{\text{III}}$  in the line core. In model 4, both  $r_{\text{II}}$  and  $r_{\text{III}}$  are weighted by smaller values of  $\alpha$  and  $\beta^{(2)} - \alpha$ . This causes a large depolarization in the line core. In the near line wings,  $r_{\text{II}}$  dominated models 2 and 3 show largest polarization ( $\approx 1.5$  percent). In the CRD case (model 1), the scattering integral becomes constant in the optically thin wings. This is because the contribution of the wing frequencies to the scattering integral becomes smaller and smaller, in comparison to the contribution from the core frequencies. For this reason, the anisotropy and hence the wing polarization takes a constant value. In models 2 and 3  $r_{\text{II}}$  type scattering dominates throughout the profile. For these cases, the scattering

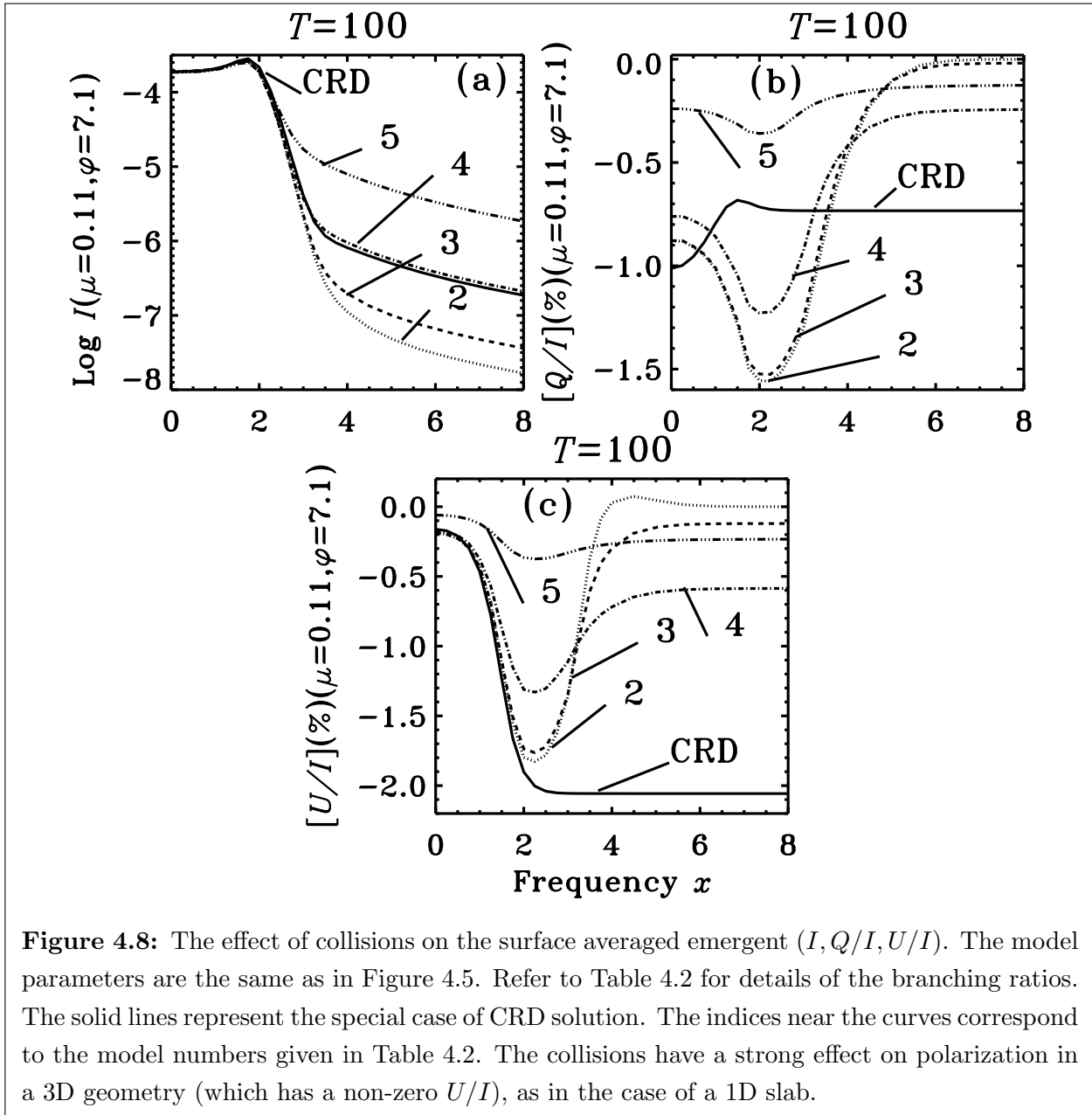


**Figure 4.8:** The effect of collisions on the surface averaged emergent ( $I, Q/I, U/I$ ). The model parameters are the same as in Figure 4.5. Refer to Table 4.2 for details of the branching ratios. The solid lines represent the special case of CRD solution. The indices near the curves correspond to the model numbers given in Table 4.2. The collisions have a strong effect on polarization in a 3D geometry (which has a non-zero  $U/I$ ), as in the case of a 1D slab.

integral approaches zero and hence only the thermal (isotropic) part contributes to the line source function. As a consequence, polarization goes to zero in these optically thin wings (see Faurobert 1987). The other two models are a combination of these two extreme conditions and therefore the corresponding  $Q/I$  curves lie in between the two extreme situations.

*Stokes U:* As discussed before, generation of Stokes  $U$  is a characteristic of multi-D RT (through a large non-axisymmetry). The qualitative behavior of  $U/I$  profile is similar to that of  $Q/I$  for all the models. In the CRD case the magnitude of  $U/I$  in the wings is much larger ( $\approx 2$  percent) than that of  $Q/I$  ( $\approx 0.72$  percent).

## 4.6 Concluding remarks

In this chapter we formulate the polarized RT equation in 3D geometry using the technique of irreducible spherical tensors  $\mathcal{T}_Q^K(i, \boldsymbol{\Omega})$ . The polarized RT equation for the irreducible components of the Stokes parameters lends itself for solution by the standard PALI methods, extended appropriately to handle the RT of the rays in a 3D geometry. We present 3D solution on some test cases, which may serve as benchmarks. The nature of line RT in 3D geometry, as compared to the 1D case is discussed in some detail.

We show that the 3D PALI method gives correct results in the limit of 1D geometry. The 3D RT is characterized by the anisotropy of the radiation field within the computational cube. The 3D anisotropy is characteristically different from the 1D anisotropy of the radiation field. The difference arises due to the finite optical depths in the horizontal directions ( $X, Y$ ). This causes large differences between the 3D and 1D values of the degree of linear polarization ( $Q/I, U/I$ ). In fact, in 3D geometry the radiation field is non-axisymmetric (even in the absence of magnetic fields) because the finite optical depths in  $X, Y, Z$  directions break the azimuthal symmetry of the radiation field. In a 1D geometry, the radiation field is axisymmetric about the  $Z$ -axis. Due to these reasons, the shapes and magnitude of the ( $Q/I, U/I$ ) spectra differ significantly from the corresponding 1D cases. We compare the spatially averaged ( $I, Q/I, U/I$ ) spectra computed under the CRD and PRD assumptions. The nature of differences between CRD and PRD profiles in 3D geometry remain the same as that for the 1D geometry. We notice that  $[[U/I]]_{3D}$  is in general larger in magnitude, than  $[[Q/I]]_{3D}$  in the 3D models. This is because the radiation field in a 3D medium is highly non-axisymmetrical in nature. The degree of linear polarization in the spatially resolved ( $Q/I, U/I$ ) spectra are generally larger in magnitude when compared to the corresponding spatially averaged values, clearly due to the fact that

a spatial averaging over sign changing quantities leads to smaller values of  $Q/I$  and  $U/I$ . Another reason for this is the fact that linear polarization is largest in the very narrow regions close to the boundaries (see Figure 4.7). When a spatial averaging is performed, the relative contributions from these highly polarized narrow regions are dominated over by the inner regions, where the linear polarization is considerably smaller.

We show that the advantage of solving the RT equation in the irreducible components basis, is that the irreducible source vector  $S_Q^K$  becomes completely independent of the angle variables, making it easier to extend the existing 1D PALI methods to the 3D case. However the irreducible intensity components  $I_Q^K$  remain dependent on the inclination and also on the azimuthal angle of the ray. It is important to recognize the fact that the multipolar expansion for Stokes intensity and Stokes source vectors presented in this chapter allows us to write a RT equation in terms of  $I_Q^K$  and  $S_Q^K$ . A further advantage is that this formalism allows to efficiently use the scattering phase matrix approach to different problems in multi-D geometry. We have demonstrated this by taking the example of polarized line RT with PRD. In future we try to apply the solution method presented in this chapter, to model the polarimetric observations of the resolved structures like solar filaments and prominences.

## New Results

It is for the first time that a multi-D polarized RT is solved ever, with PRD as the line scattering mechanism. In chapter 4 we have achieved the following important results.

1. We have formulated the polarized RT equation for resonance scattering in multi-D media, using the elegant technique of irreducible spherical tensors  $\mathcal{T}_Q^K(i, \Omega)$ , where  $i = 0, 1, 2, K = 0, 1, 2, -K \leq Q \leq +K$ .
2. We have developed a numerical method of solution based on the PALI approach.
3. For the first time, PRD in line scattering is considered for multi-D polarized RT and the corresponding polarized RT equation is solved using the new PALI method that we have developed.

4. In a multi-D medium the radiation field is non-axisymmetrical even in the absence of a symmetry breaking mechanism such as an oriented magnetic field. We have generalized to the 3D case, the decomposition technique developed for the Hanle effect in a 1D medium which allows one to represent the Stokes parameters  $I, Q, U$  by a set of 6 cylindrically symmetrical functions. The scattering phase matrix is expressed in terms of  $\mathcal{T}_Q^K(i, \mathbf{\Omega})$ , with  $\mathbf{\Omega}$  being the direction of the outgoing ray.
5. Starting from the definition of the source vector, we have shown that it can be represented in terms of 6 components  $S_Q^K$  independent of  $\mathbf{\Omega}$ .
6. The formal solution of the multi-D transfer equation shows that the Stokes parameters can also be expanded in terms of the  $\mathcal{T}_Q^K(i, \mathbf{\Omega})$ . Because of the 3D-geometry, the expansion coefficients  $I_Q^K$  remain  $\mathbf{\Omega}$ -dependent.
7. We have shown that each  $I_Q^K$  satisfies a simple transfer equation with a source term  $S_Q^K$  and that this transfer equation provides an efficient approach for handling the polarized transfer in multi-D geometries.
8. A PALI method for 3D, associated to a core-wing separation method for treating PRD is developed. It is tested by comparison with 1D solutions and several benchmark solutions in the 3D case are given.





## Chapter 5

# Solution of partial redistribution problems in multi-D media

*The contents of this chapter are based on the following publication:*

Anusha, L. S., Nagendra, K. N. Paletou, F. 2011a, **ApJ**, 726, 96–109

### 5.1 Introduction

The observations of the solar atmosphere indicate the existence of small scale structures, which break the spatial homogeneity of the atmosphere. Since these structures have different physical properties, one can expect the effect of lateral transport of radiation to be rather important. Extensive studies on radiative transfer (RT) in two-dimensional (2D) and three-dimensional (3D) geometries have been made to understand the intensity profiles in spectroscopic observations. As the polarization of the radiation field is more sensitive to the breaking of axisymmetry occurring in 2D and 3D geometries than the intensity (Stokes  $I$  parameter), the solution of polarized RT equation in 2D and 3D geometries is very much needed for the understanding of the spectropolarimetric observations. Polarized RT problems have been addressed in the past decade, but only for complete frequency redistribution (CRD). A first investigation with partial frequency redistribution (PRD), for 3D geometry, is described in chapter 4 (see also Anusha & Nagendra 2011a). Solving polarized RT equation with PRD in multi-dimensional (multi-D) geometries is numerically expensive, both in terms of computing time and the computer memory. To address this problem, in this chapter (see also Anusha et al. 2011a) we develop a numerical method for 2D geometry which is faster than the Jacobi iteration method used in chapter 4. The method developed here can be easily extended to 3D geometries. For reviews on iterative

methods see Trujillo Bueno (2003), Nagendra & Sampurna (2009), and references cited therein. For a detailed historical account of the developments in the area of multi-D RT we refer to chapter 4.

For 2D geometry, Paletou et al. (1999) solve the polarized line RT equation for the Stokes  $I, Q, U$  parameters, with CRD, using a perturbation technique combined with a short characteristics formal solution method. We generalize their work in following respects. We include PRD, and solve the RT problem using a decomposition of the Stokes parameters into a set of irreducible components. This Stokes vector decomposition for multi-D geometries was developed in chapter 4. Its main advantage is that the mean intensity components (averaged over all frequencies and directions of the incident radiation) become independent of the outgoing direction ( $\Omega$ ) and also the scattering phase matrix. These properties have allowed us to set up an iterative method which is faster and more accurate than the previous methods.

First, instead of the perturbation method used in Paletou et al. (1999) and the Jacobi method used in chapter 4, we have implemented a new iterative method called the Stabilized Preconditioned Bi-Conjugate Gradient (Pre-BiCG-STAB) algorithm introduced in chapter 3 (see also Anusha et al. 2009; Anusha & Nagendra 2009; Nagendra et al. 2009). The Pre-BiCG and Pre-BiCG-STAB methods belong to a class of iterative methods known as projection techniques. Projection methods have already proved their usefulness for unpolarized RT problems with the CRD approximation in different geometries (see e.g., Klein et al. 1989; Folini 1998; Papkalla 1995; Meinkhon 2009; Hubeny & Burrows 2007; Paletou & Anterrieu 2009; Anusha et al. 2009). Polarization was considered in Nagendra et al. (2009) for planar geometry. Second, we have generalized the 2D short characteristics formal solver of Paletou et al. (1999) to PRD. This 2D formal solver is more accurate than the formal solver used in chapter 4.

The organization of the chapter is as follows. In Section 5.2 we present the governing equations. In Section 5.3 we describe the 2D short characteristics formal solution method. In Section 5.4 we give some details of the computations. In Section 5.5 we discuss the Pre-BiCG-STAB algorithm. Section 5.6 is devoted to results and discussions. Concluding remarks are presented in Section 5.7.

## 5.2 The Polarized transfer equation in a 2D medium

We consider RT in a 2D slab in Cartesian geometry. We assume that the medium is infinite in  $X$  direction and finite in  $Y$  and  $Z$  directions (see Figure 5.1). This means that any two  $YZ$  planes at two different points on the  $X$  axis are identical. As a result, all the physical quantities like the Stokes vector  $\mathbf{I}$ , the source vector  $\mathbf{S}$  remain independent of the  $X$  coordinate. We assume that our 2D slab is situated at  $x = x_0$ . For a given ray with direction  $\boldsymbol{\Omega}$ , the RT equation in divergence form in the atmospheric reference frame may be written as

$$\boldsymbol{\Omega} \cdot \nabla \mathbf{I}(\mathbf{r}, \boldsymbol{\Omega}, x) = -[\kappa_l(\mathbf{r})\phi(x) + \kappa_c(\mathbf{r})][\mathbf{I}(\mathbf{r}, \boldsymbol{\Omega}, x) - \mathbf{S}(\mathbf{r}, \boldsymbol{\Omega}, x)], \quad (5.1)$$

where  $\mathbf{I} = (I, Q, U)^T$  is the Stokes vector. We choose positive Stokes  $Q$  to be in the direction perpendicular to the surface defined by  $z = Z_{\max}$ . Here  $\mathbf{r} = (x, y, z)$  is the position vector of the ray.  $\boldsymbol{\Omega} = (\eta, \gamma, \mu) = (\sin \theta \cos \varphi, \sin \theta \sin \varphi, \cos \theta)$  describes the direction cosines of the ray with respect to the atmospheric normal  $Z$ , with  $\theta, \varphi$  being the polar and azimuthal angles of the ray (see Figure 5.3(b)). The Stokes  $V$  parameter decouples from the other three. We confine our attention in this chapter to the polarized RT equation for  $(I, Q, U)^T$ . We represent the frequency averaged line opacity and continuum opacity by  $\kappa_l$  and  $\kappa_c$  respectively, and the profile function by  $\phi$ . Frequency is measured in Doppler width units from the line center and is denoted by  $x$ , with the Doppler width being constant in the atmosphere. It is convenient to work with the RT equation written along a ray path. It has the form

$$\frac{d\mathbf{I}(\mathbf{r}, \boldsymbol{\Omega}, x)}{ds} = -\kappa_{\text{tot}}(\mathbf{r}, x)[\mathbf{I}(\mathbf{r}, \boldsymbol{\Omega}, x) - \mathbf{S}(\mathbf{r}, \boldsymbol{\Omega}, x)], \quad (5.2)$$

where  $s = \sqrt{x^2 + y^2 + z^2}$  is the path length along the ray. The total opacity  $\kappa_{\text{tot}}(\mathbf{r}, x)$  is given by

$$\kappa_{\text{tot}}(\mathbf{r}, x) = \kappa_l(\mathbf{r})\phi(x) + \kappa_c(\mathbf{r}). \quad (5.3)$$

The formal solution of Equation (5.2) is given by

$$\begin{aligned} \mathbf{I}(\mathbf{r}, \boldsymbol{\Omega}, x) = & \mathbf{I}(\mathbf{r}_0, \boldsymbol{\Omega}, x) e^{-\int_{s_0}^s \kappa_{\text{tot}}(\mathbf{r} - (s-s')\boldsymbol{\Omega}, x) ds'} \\ & + \int_{s_0}^s \mathbf{S}(\mathbf{r} - (s-s')\boldsymbol{\Omega}, \boldsymbol{\Omega}, x) e^{-\int_{s'}^s \kappa_{\text{tot}}(\mathbf{r} - (s-s'')\boldsymbol{\Omega}, x) ds''} \kappa_{\text{tot}}(\mathbf{r} - (s-s')\boldsymbol{\Omega}, x) ds'. \end{aligned} \quad (5.4)$$

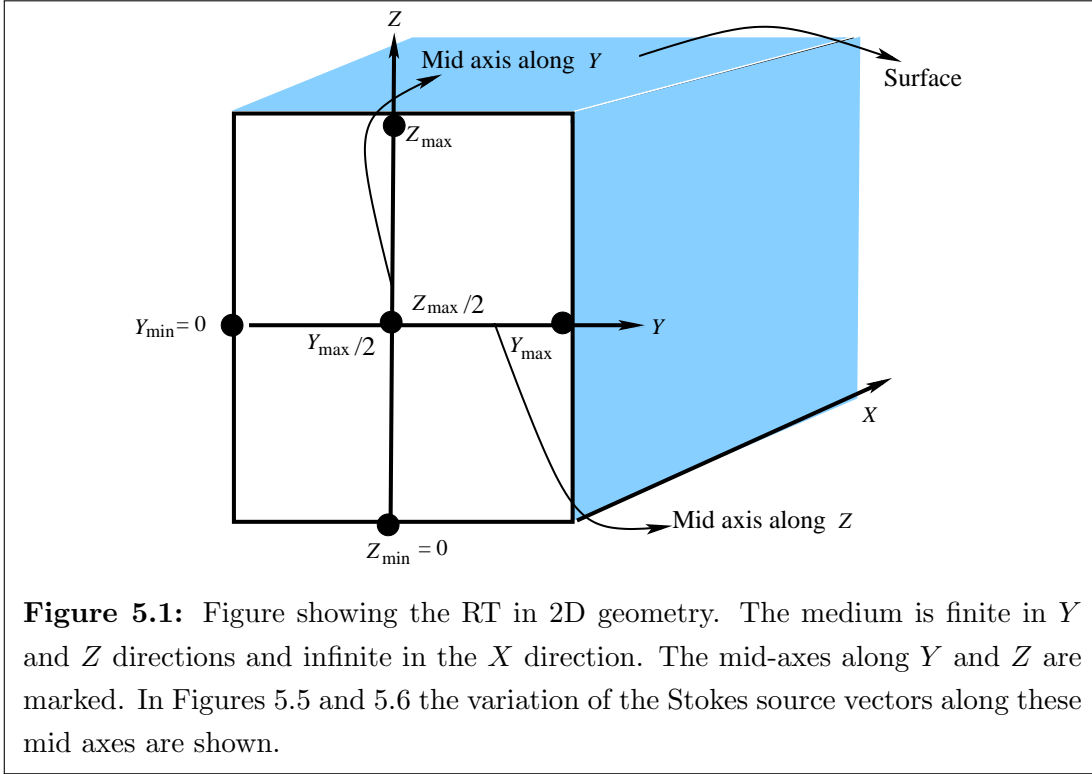


**Figure 5.1:** Figure showing the RT in 2D geometry. The medium is finite in  $Y$  and  $Z$  directions and infinite in the  $X$  direction. The mid-axes along  $Y$  and  $Z$  are marked. In Figures 5.5 and 5.6 the variation of the Stokes source vectors along these mid axes are shown.

$\mathbf{I}(\mathbf{r}_0, \boldsymbol{\Omega}, x)$  is the boundary condition imposed at  $\mathbf{r}_0 = (x_0, y_0, z_0)$  (see Figure 5.2).

In a two-level atom model with unpolarized ground level, the total source vector  $\mathbf{S}$  is given by

$$\mathbf{S}(\mathbf{r}, \boldsymbol{\Omega}, x) = \frac{\kappa_l(\mathbf{r})\phi(x)\mathbf{S}_l(\mathbf{r}, \boldsymbol{\Omega}, x) + \kappa_c(\mathbf{r})\mathbf{S}_c(\mathbf{r}, x)}{\kappa_l(\mathbf{r})\phi(x) + \kappa_c(\mathbf{r})}. \quad (5.5)$$

Here  $\mathbf{S}_c$  is the continuum source vector given by  $(B_\nu(\mathbf{r}), 0, 0)^T$  with  $B_\nu(\mathbf{r})$  the Planck function at the line center frequency. The line source vector can be expressed as

$$\mathbf{S}_l(\mathbf{r}, \boldsymbol{\Omega}, x) = \mathbf{G}(\mathbf{r}) + \int_{-\infty}^{+\infty} dx' \oint \frac{d\boldsymbol{\Omega}'}{4\pi} \frac{\hat{R}(x, x', \boldsymbol{\Omega}, \boldsymbol{\Omega}')}{\phi(x)} \mathbf{I}(\mathbf{r}, \boldsymbol{\Omega}', x'), \quad (5.6)$$

where  $\mathbf{G} = (\epsilon B_\nu(\mathbf{r}), 0, 0)^T$  is the thermal source.  $\epsilon = \Gamma_I / (\Gamma_R + \Gamma_I)$  with  $\Gamma_I$  and  $\Gamma_R$  the inelastic collisional de-excitation rate and the radiative de-excitation rate respectively, so that  $\epsilon$  represents the rate of photon destruction by inelastic collisions, also known as the thermalization parameter. We assume that  $\phi$  is a Voigt function. It depends on the damping parameter  $a$ , given by  $a = a_R [1 + (\Gamma_E + \Gamma_I) / \Gamma_R]$  where  $a_R = \Gamma_R / 4\pi \Delta\nu_D$  and  $\Gamma_E$  is the elastic collision rate. As the lower level is assumed to be infinitely sharp,

the radiative, and collisional rates refer only to the upper level.  $\hat{R}$  is the redistribution matrix given in Domke & Hubeny (1988) and Bommier (1997b). The solid angle element  $d\Omega' = \sin\theta' d\theta' d\varphi'$ ,  $\theta \in [0, \pi]$  and  $\varphi \in [0, 2\pi]$  (see Figure 5.3(b)). After decomposition of the vectors  $\mathbf{I}$  and  $\mathbf{S}$  into irreducible components following the method described in chapter 4, the redistribution matrix  $\hat{R}(x, x', \Omega, \Omega')$  can be factorized into the product of a matrix  $\hat{R}(x, x')$  and a phase matrix  $\hat{\Psi}(\Omega)$ . Its elements are given by

$$\Psi_{QQ'}^{KK'}(\Omega) = \sum_{j=0}^3 (\mathcal{T}_Q^K)^*(j, \Omega) \mathcal{T}_{Q'}^{K'}(j, \Omega). \quad (5.7)$$

Here  $\mathcal{T}_Q^{K'}(j, \Omega)$  are irreducible spherical tensors for polarimetry with  $K = 0, 1, 2, -K \leq Q \leq +K$  (see Landi Degl'Innocenti & Landolfi 2004). In this chapter, we consider only the linear polarization. Therefore,  $K = 0, 2$  and  $Q \in [-K, +K]$ . The matrix  $\hat{\Psi}(\Omega)$  is a  $6 \times 6$  matrix. Its elements and the irreducible components of  $\mathbf{I}$  and  $\mathbf{S}$  are complex quantities. We apply the transformation described in Frisch (2007) to transform these components and the elements of  $\hat{\Psi}(\Omega)$  matrix into real quantities. Hereafter we work with only real quantities. We keep the notation  $\hat{\Psi}(\Omega)$  for the phase matrix. We introduce the irreducible Stokes vector  $\mathcal{I} = (I_0^0, I_0^2, I_1^{2,x}, I_1^{2,y}, I_2^{2,x}, I_2^{2,y})^T$  and irreducible source vector  $\mathcal{S} = (S_0^0, S_0^2, S_1^{2,x}, S_1^{2,y}, S_2^{2,x}, S_2^{2,y})^T$ . The components of  $\mathcal{I}$  and  $\mathcal{S}$  are all real. The RT equation for the vector  $\mathcal{I}$  is given by

$$-\frac{1}{\kappa_{\text{tot}}(\mathbf{r}, x)} \Omega \cdot \nabla \mathcal{I}(\mathbf{r}, \Omega, x) = [\mathcal{I}(\mathbf{r}, \Omega, x) - \mathcal{S}(\mathbf{r}, x)]. \quad (5.8)$$

Here  $\mathcal{S}(\mathbf{r}, x) = p_x \mathcal{S}_l(\mathbf{r}, x) + (1 - p_x) \mathcal{S}_c(\mathbf{r}, x)$  with

$$\mathcal{S}_l(\mathbf{r}, x) = \epsilon \mathcal{B}(\mathbf{r}) + \mathcal{J}(\mathbf{r}, x), \quad (5.9)$$

where the mean intensity vector is

$$\mathcal{J}(\mathbf{r}, x) = \frac{1}{\phi(x)} \int_{-\infty}^{+\infty} dx' \oint \frac{d\Omega}{4\pi} \hat{R}(x, x') \hat{\Psi}(\Omega) \mathcal{I}(\mathbf{r}, \Omega, x'). \quad (5.10)$$

$\mathcal{S}_c(\mathbf{r}, x) = (B_\nu(\mathbf{r}), 0, 0, 0, 0, 0)^T$  is the continuum source vector and  $\mathcal{B} = (B_\nu(\mathbf{r}), 0, 0, 0, 0, 0)^T$  is the Planck vector. We assume that the ratio  $\kappa_c(\mathbf{r})/\kappa_l(\mathbf{r})$  is independent of  $\mathbf{r}$ . The parameter  $p_x$  is defined by

$$p_x = \kappa_l(\mathbf{r}) \phi(x) / \kappa_{\text{tot}}(\mathbf{r}, x). \quad (5.11)$$

The 2D Cartesian geometry used here implies some symmetries which simplify the problem. The radiation field has a symmetry with respect to the  $X$  axis which leads to

$$\begin{aligned} I(\mathbf{r}, \theta, \varphi, x) &= I(\mathbf{r}, \theta, \pi - \varphi, x), \\ I(\mathbf{r}, \theta, \pi + \varphi, x) &= I(\mathbf{r}, \theta, 2\pi - \varphi, x), \quad \theta \in [0, \pi], \varphi \in [0, \pi/2]. \end{aligned} \quad (5.12)$$

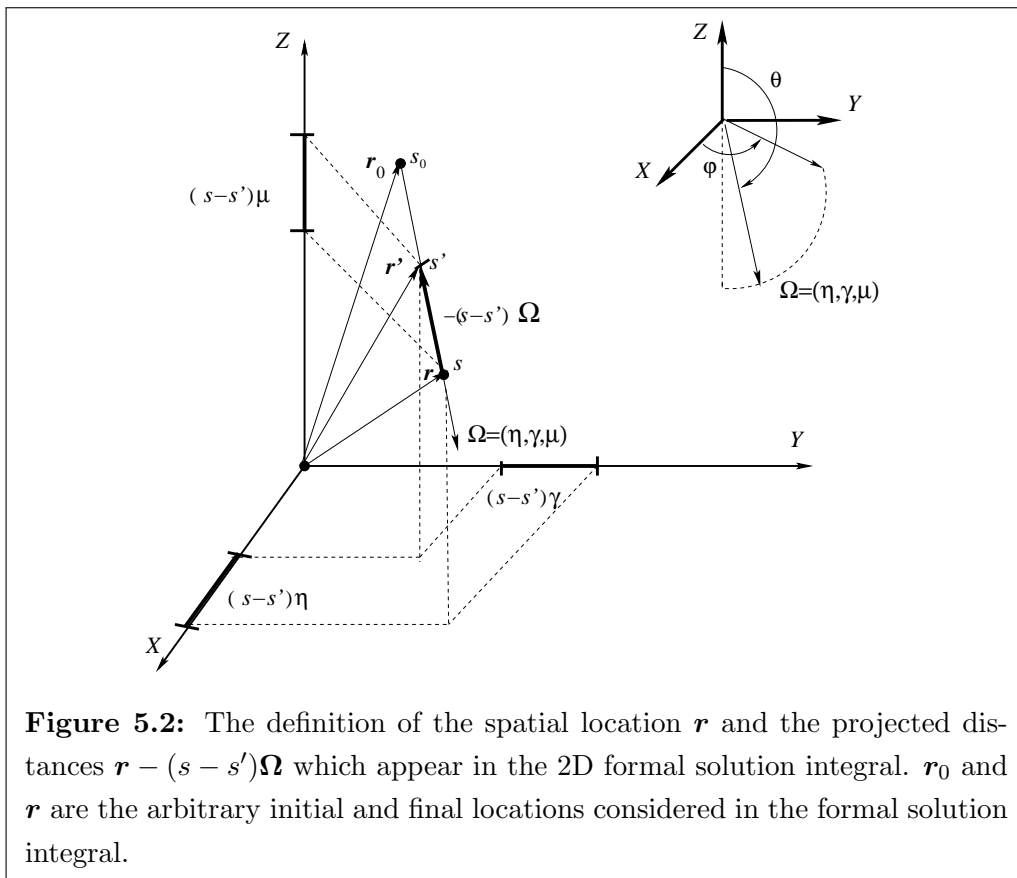


**Figure 5.2:** The definition of the spatial location  $\mathbf{r}$  and the projected distances  $\mathbf{r} - (s - s')\mathbf{\Omega}$  which appear in the 2D formal solution integral.  $\mathbf{r}_0$  and  $\mathbf{r}$  are the arbitrary initial and final locations considered in the formal solution integral.

Because the thermal source vector is unpolarized, the above symmetry relation leads to the symmetry of Stokes  $Q$  and anti-symmetry of Stokes  $U$  (see Appendix F) namely

$$\begin{aligned} Q(\mathbf{r}, \theta, \varphi, x) &= Q(\mathbf{r}, \theta, \pi - \varphi, x), \\ Q(\mathbf{r}, \theta, \pi + \varphi, x) &= Q(\mathbf{r}, \theta, 2\pi - \varphi, x), \\ U(\mathbf{r}, \theta, \varphi, x) &= -U(\mathbf{r}, \theta, \pi - \varphi, x), \\ U(\mathbf{r}, \theta, \pi + \varphi, x) &= -U(\mathbf{r}, \theta, 2\pi - \varphi, x), \quad \theta \in [0, \pi], \varphi \in [0, \pi/2]. \end{aligned} \quad (5.13)$$

Using Equations (5.12) and (5.13) we can prove that

$$J_1^{2,x} = 0, \quad J_2^{2,y} = 0. \quad (5.14)$$

Thus we have  $S_1^{2,x} = 0$  and  $S_2^{2,y} = 0$  and  $I_1^{2,x} = 0$  and  $I_2^{2,y} = 0$ . Thus in a 2D geometry, one needs to only 4 out of the 6 irreducible components to describe the linearly polarized radiation field. We recall that in a 3D geometry all the 6 irreducible components are non-zero (see chapter 4).

The matrix  $\hat{R}$  is diagonal. It is given by

$$\hat{R}(x, x') = \hat{W}[\hat{\alpha}r_{\text{II}}(x, x') + (\hat{\beta} - \hat{\alpha})r_{\text{III}}(x, x')], \quad (5.15)$$

where

$$\hat{W} = \text{diag}\{W_0, W_2, W_2, W_2\}, \quad (5.16)$$

$$\hat{\alpha} = \text{diag}\{\alpha, \alpha, \alpha, \alpha\}, \quad (5.17)$$

$$\hat{\beta} = \text{diag}\{\beta^{(0)}, \beta^{(2)}, \beta^{(2)}, \beta^{(2)}\}. \quad (5.18)$$

The weight  $W_0 = 1$  and the weights  $W_2$  depend on the line under consideration (see Landi Degl'Innocenti & Landolfi 2004). Here  $r_{\text{II}}(x, x')$  and  $r_{\text{III}}(x, x')$  are the angle-averaged redistribution functions introduced by Hummer (1962). The branching ratios (Bommier 1997b) are given by

$$\alpha = \frac{\Gamma_R}{\Gamma_R + \Gamma_E + \Gamma_I}, \quad (5.19)$$

$$\beta^{(K)} = \frac{\Gamma_R}{\Gamma_R + D^{(K)} + \Gamma_I}, \quad (5.20)$$

with  $D^{(0)} = 0$  and  $D^{(2)} = c\Gamma_E$ , where  $c$  is a constant, taken to be 0.379 (see Faurobert-Scholl 1992).

### 5.3 A short characteristics method for 2D radiative transfer

In this section we discuss the short characteristics formal solver used here. The first 2D short characteristics formal solver was introduced by Mihalas et al. (1978) for scalar RT and an improved version was given in Kunasz & Auer (1988). A further improvement with the introduction of monotonic interpolation was proposed by Auer & Paletou (1994). Then Auer et al. (1994) generalized it to the case of 3D geometry. The extension to include polarization in 2D geometries was done by Paletou et al. (1999) for Rayleigh scattering and by Manso Sainz & Trujillo Bueno (1999) and Dittmann (1999) for the Hanle effect in 2D and 3D geometries. All the above papers use CRD as the scattering mechanism. PRD was introduced for the scalar case by Auer & Paletou (1994). In this chapter we generalize to the PRD scattering, the method of Paletou et al. (1999).

A short characteristics stencil MOP of a ray passing through the point O, projected on to the 2D plane is shown in Figure 5.3(a). The point O is always chosen to coincide with a grid point along the ray path. The points M and P intersect the boundaries of the 2D cells either on a horizontal line or on a vertical line, depending on the direction cosines of the given ray. The length  $\Delta s$  of the line segment MO or OP is simply,

$$\Delta s = \Delta z / \mu, \quad \text{if the ray hits the horizontal line,} \quad (5.21)$$

and

$$\Delta s = \Delta y / \gamma, \quad \text{if the ray hits the vertical line.} \quad (5.22)$$

Here  $\Delta z$  and  $\Delta y$  are increments (positive or negative) between two successive grid points in  $Z$  and  $Y$  directions respectively. Figure 5.3(b) shows the angles  $\theta$  and  $\varphi$  that define the orientation of a ray that passes through the point O. Figure 5.3(b) also shows all the 8 octants contributing to the radiation field at O. The cone of rays above the point O corresponds to  $\mu < 0$ , and the one below the point O corresponds to  $\mu > 0$ . Each of these cones is further divided into 4 regions, which are defined by  $\varphi \in [0, \pi/2], [\pi/2, \pi], [\pi, 3\pi/2], [3\pi/2, 2\pi]$ . In the short characteristics method, the irreducible Stokes vector  $\mathcal{I}$  at O is given by

$$\begin{aligned} \mathcal{I}_O(\mathbf{r}, \boldsymbol{\Omega}, x) &= \mathcal{I}_M(\mathbf{r}, \boldsymbol{\Omega}, x) \exp[-\Delta\tau_M] \\ &+ \psi_M(\mathbf{r}, \boldsymbol{\Omega}, x) \mathcal{S}_M(\mathbf{r}, x) + \psi_O(\mathbf{r}, \boldsymbol{\Omega}, x) \mathcal{S}_O(\mathbf{r}, x) + \psi_P(\mathbf{r}, \boldsymbol{\Omega}, x) \mathcal{S}_P(\mathbf{r}, x), \end{aligned} \quad (5.23)$$

where  $\mathcal{S}_{M,O,P}$  are the irreducible source vectors at M, O and P. The quantity  $\mathcal{I}_M$  is the upwind irreducible Stokes vector at the point O. If M and P are non-grid points, then,



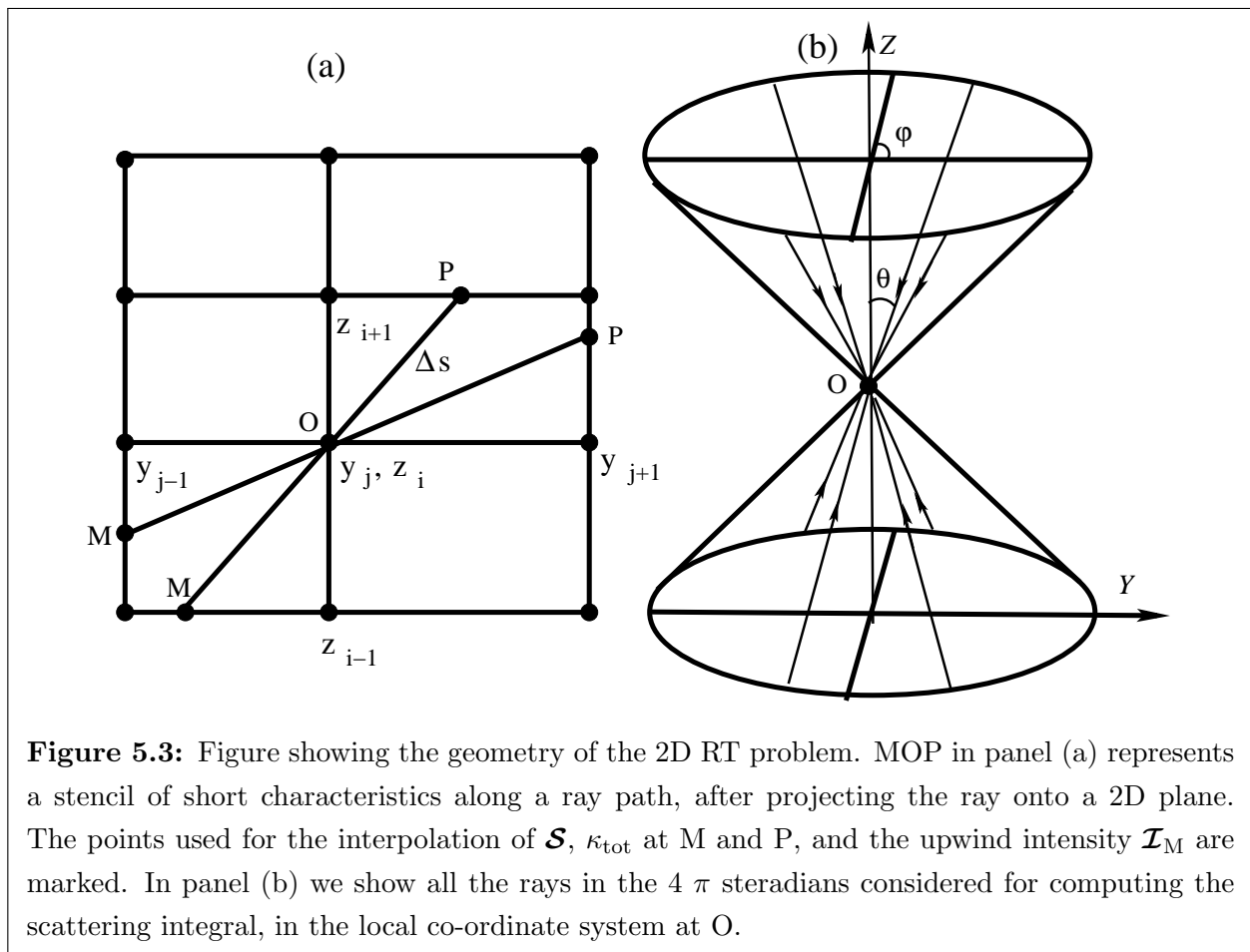
**Table 5.1:** The 12-point Carlsson type B angle points and weights for a quadrature of order  $n = 8$ . See Figure 5.3(b) for the definition of  $\theta$  and  $\varphi$ .

(a)

i	$\mu_i$	$\eta_i$	$\gamma_i$	$w_i$
1	0.857080E+00	0.111044E+00	0.503073E+00	0.142935E-01
2	0.702734E+00	0.111044E+00	0.702734E+00	0.992212E-02
3	0.503073E+00	0.111044E+00	0.857080E+00	0.142935E-01
4	0.857080E+00	0.503073E+00	0.111044E+00	0.142935E-01
5	0.702734E+00	0.503073E+00	0.503073E+00	0.315749E-02
6	0.503073E+00	0.503073E+00	0.702734E+00	0.315749E-02
7	0.111044E+00	0.503073E+00	0.857080E+00	0.142935E-01
8	0.702734E+00	0.702734E+00	0.111044E+00	0.992212E-02
9	0.503073E+00	0.702734E+00	0.503073E+00	0.315749E-02
10	0.111044E+00	0.702734E+00	0.702734E+00	0.992212E-02
11	0.503073E+00	0.857080E+00	0.111044E+00	0.142935E-01
12	0.111044E+00	0.857080E+00	0.503073E+00	0.142935E-01

(b)

i	$\theta_i$	$\varphi_i$
1	0.310097E+02	0.775526E+02
2	0.453533E+02	0.810205E+02
3	0.597965E+02	0.826178E+02
4	0.310097E+02	0.124474E+02
5	0.453533E+02	0.450000E+02
6	0.597965E+02	0.544019E+02
7	0.836245E+02	0.595887E+02
8	0.453533E+02	0.897951E+01
9	0.597965E+02	0.355981E+02
10	0.836245E+02	0.450000E+02
11	0.597965E+02	0.738219E+01
12	0.836245E+02	0.304113E+02



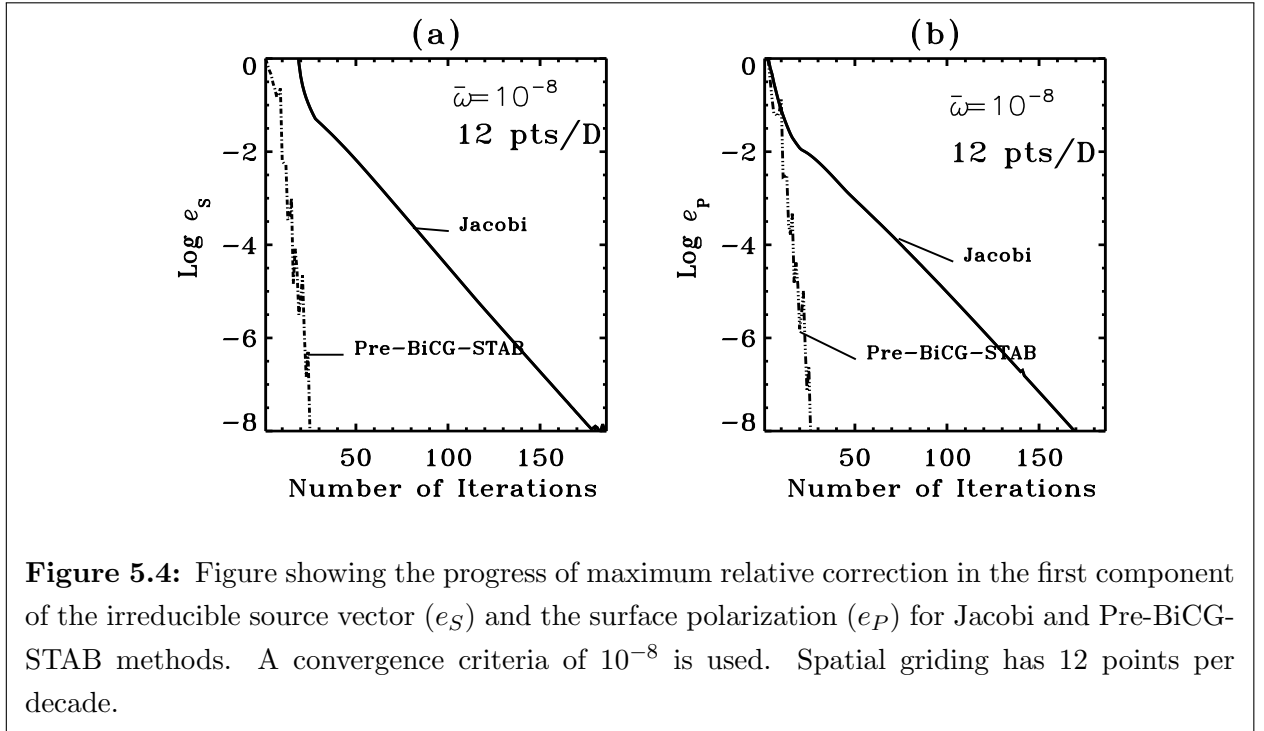


**Figure 5.4:** Figure showing the progress of maximum relative correction in the first component of the irreducible source vector ( $e_s$ ) and the surface polarization ( $e_p$ ) for Jacobi and Pre-BiCG-STAB methods. A convergence criteria of  $10^{-8}$  is used. Spatial gridding has 12 points per decade.

$\mathcal{S}_{M,P}$  and  $\mathcal{I}_M$  are computed using a parabolic interpolation formula. While computing them, one has to ensure the monotonicity of all the 4 components of these vectors, by appropriate logical tests (see Auer & Paletou 1994). The coefficients  $\psi$  depend on the optical depth increments in  $Y$  and  $Z$  directions and are given in Auer & Paletou (1994).

## 5.4 Computational details

To calculate the integral in Equation (5.9) and the formal solution in Equation (5.23), we need to define quadratures for angles, frequencies and depths.

### 5.4.1 The angle quadrature in 2D/3D geometries

Performing angle integrations in 2D or 3D geometries is not a trivial task. We have to consider the distribution of the rays in the 3D angular space namely,  $\Omega = (\eta, \gamma, \mu)$ . This is important because a correct representation of the incident and scattered radiation field from all the octants surrounding the point of interest  $O$  is essential. A Gaussian quadrature, because it tends to distribute more points near the limits of integration, is not appropriate to correctly represent the radiation field in all the 8 octants.

The special quadrature method developed by Carlsson (1963) for neutron transport is

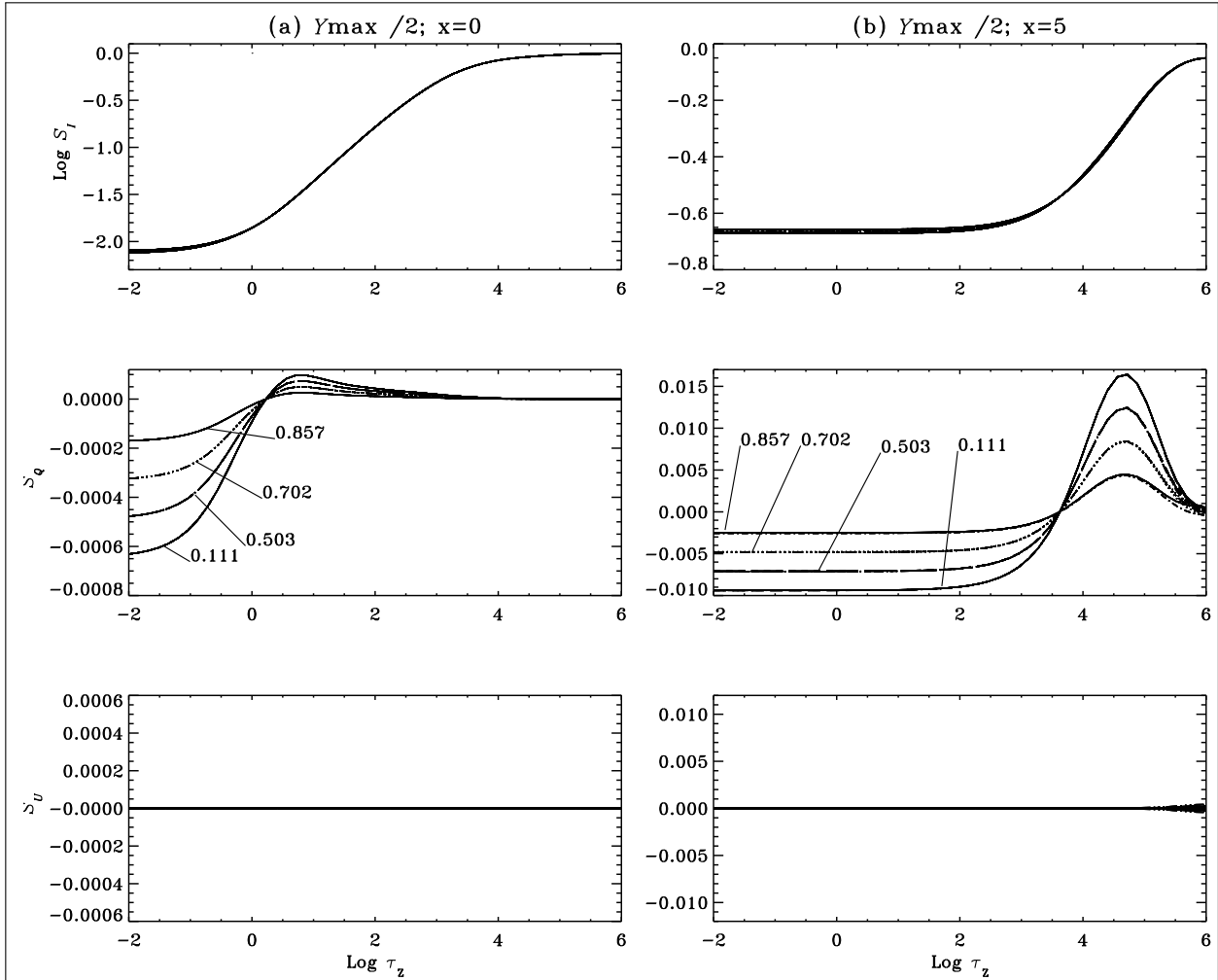


**Figure 5.5:** Variation of the Stokes source vectors as a function of optical depth. The model parameters are  $(T_Z, T_Y, a, \epsilon, \kappa_c, \Gamma_E/\Gamma_R) = (2 \times 10^6, 2 \times 10^6, 10^{-3}, 10^{-4}, 0, 10^{-4})$ . Panels (a) and (b) show variations of the source vectors along the  $Z$ -axis at  $Y_{\max}/2$  for frequencies  $x = 0$  and  $x = 5$  respectively. The mid  $Y$ -axis is marked in Figure 5.1. The results are shown for a half slab only due to symmetry about the mid axes. The curves are labeled by the values of  $\mu$ .

much superior in this respect. For all the computations presented in this chapter, Carlsson type B quadrature with the order  $n = 8$  is used. In the first octant, the  $\theta$  and  $\varphi$  grid points are computed using

$$\theta = \arccos |\mu|, \quad (5.24)$$

and

$$\varphi = \arctan |\gamma/\eta|. \quad (5.25)$$

The values of the quadrature points  $(\eta_i, \gamma_i, \mu_i)$  in the first octant ( $\theta \in [0, \pi/2]$ ,  $\varphi \in [0, \pi/2]$ ) and the respective weights  $w_i$  are given in Table 5.1. The values of corresponding  $\theta_i$  and  $\varphi_i$  are also listed.

The angle points in the other octants can be easily computed using simple trigonometric formulas. We have found that the order  $n = 8$  provides a good accuracy for the solution. These quadrature points can be used in 2D as well as 3D RT computations.

#### 5.4.2 The spatial and frequency gridding

In this chapter, we use a logarithmic spacing in  $Y$  and  $Z$  directions, with a fine gridding near the boundaries. The  $X$  direction is taken to be infinitely extended. We recall that the polarized radiation field depends on  $Y$  and  $Z$  co-ordinates, but is independent of the  $X$  co-ordinate.

For most of the results presented in this chapter, a damping parameter of the Voigt profile function,  $a = 10^{-3}$  is used. The number of frequency points required for a problem depends on the value of  $a$  and the optical thickness in  $Y$  and  $Z$  directions (denoted by  $T_Y$  and  $T_Z$ ). A frequency bandwidth satisfying the conditions  $\phi(x_{\max})T_Y \ll 1$  and  $\phi(x_{\max})T_Z \ll 1$  at the largest frequency point denoted by  $x_{\max}$  has been used. We have used a logarithmic frequency grid with a fine spacing in the line core region and the near wings where the PRD effects are important.

### 5.5 A Preconditioned BiCG-STAB method

The Pre-BiCG and Pre-BiCG-STAB are iterative methods based on projections of residual vectors on Krylov subspaces (see Saad 2000). We recall that a great advantage of the Pre-BiCG-STAB method is that, unlike the Pre-BiCG method, it does not require the construction and storage of the transpose of  $\hat{A}$  matrix, where  $\hat{A}$  is the matrix of the system of equations to be solved (see below). The Pre-BiCG and Pre-BiCG-STAB methods have been applied up to now to RT problems with CRD (see Introduction for references). In

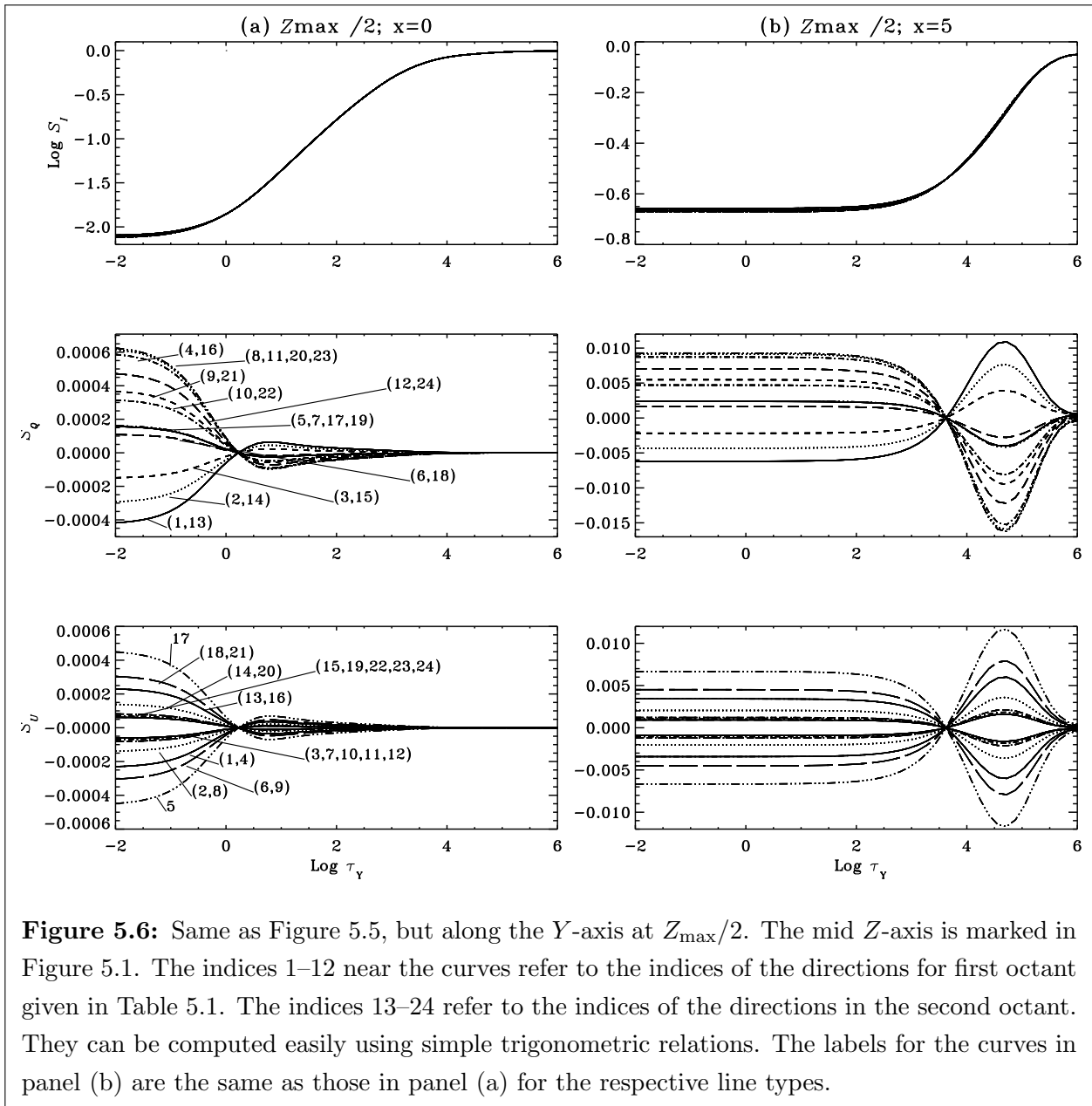


**Figure 5.6:** Same as Figure 5.5, but along the  $Y$ -axis at  $Z_{\max}/2$ . The mid  $Z$ -axis is marked in Figure 5.1. The indices 1–12 near the curves refer to the indices of the directions for first octant given in Table 5.1. The indices 13–24 refer to the indices of the directions in the second octant. They can be computed easily using simple trigonometric relations. The labels for the curves in panel (b) are the same as those in panel (a) for the respective line types.

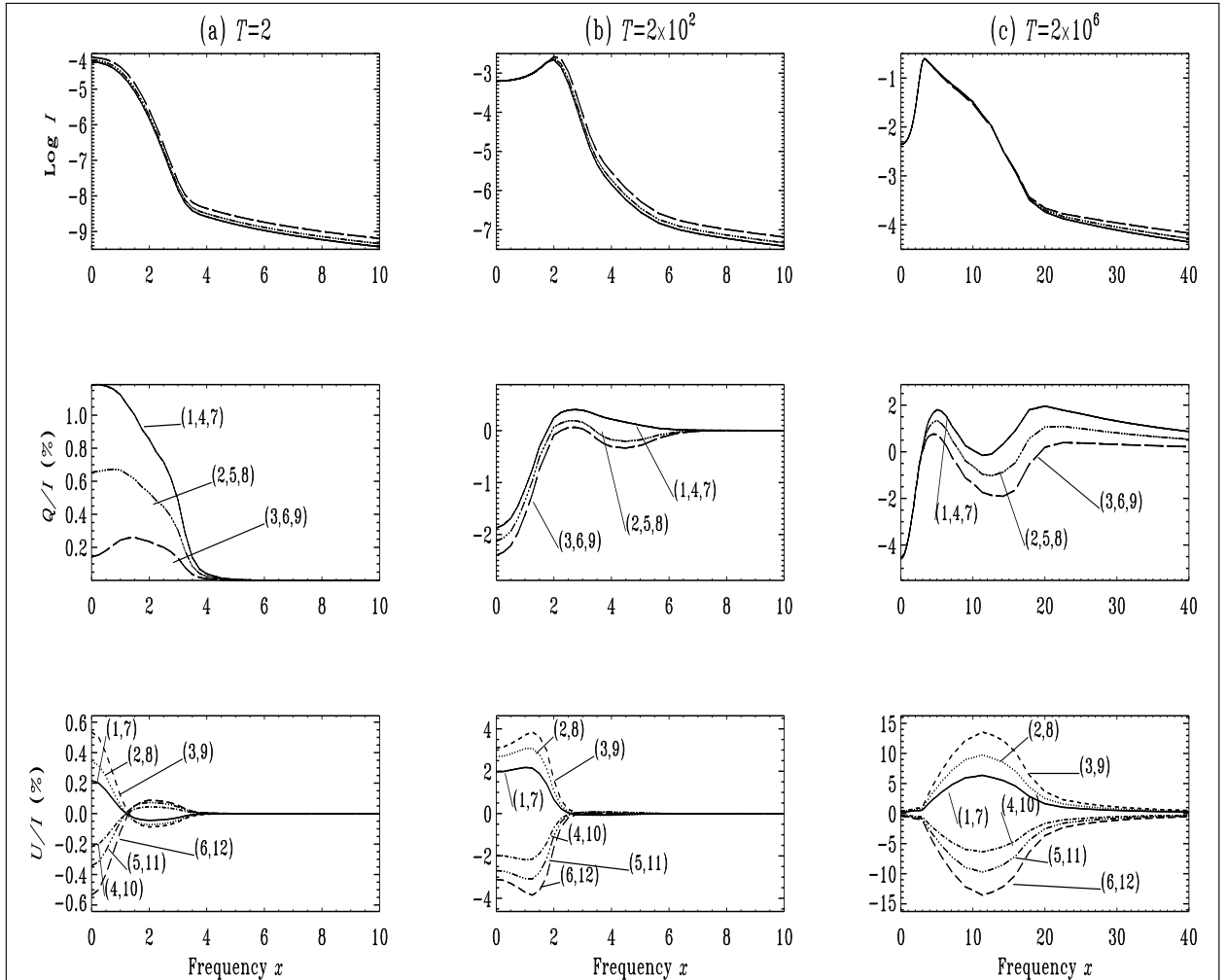


**Figure 5.7:** Optical depth effects on 2D polarized radiation field. The spatially averaged emergent Stokes profiles are presented for  $T_Y = T_Z = T = 2, 200, 2 \times 10^6$ . The other model parameters are same as those in Figure 5.5. The results are plotted for 12 directions with  $\mu = 0.11$  and 12  $\varphi$  values given by  $\varphi_i (i = 1, 12) = 60, 45, 30, 300, 315, 329, 120, 135, 150, 240, 225, 210$ . First 3  $\varphi$  values correspond to first octant and are given in Table 5.1. The curves are labeled by the indices of  $\varphi$ . Due to symmetry reasons, only some of them are distinct.

this chapter we generalize the computing algorithm of the Pre-BiCG-STAB method to polarized RT with PRD in a 2D medium and show that this method is quite efficient.

Using the formal solution expression for  $\mathcal{I}$ , the vector  $\mathcal{J}$  defined in Equation (5.10) can be written as we can write

$$\mathcal{J}(\mathbf{r}, x) = \Lambda[\mathcal{S}(\mathbf{r}, x)]. \quad (5.26)$$

The source vector is given by

$$\mathcal{S}(\mathbf{r}, x) = p_x[\epsilon\mathcal{B}(\mathbf{r}) + \mathcal{J}(\mathbf{r}, x)] + (1 - p_x)\mathcal{S}_c(\mathbf{r}, x). \quad (5.27)$$

Substituting Equation (5.26) in Equation (5.27), we obtain a system of equations

$$[\hat{I} - p_x\Lambda]\mathcal{S}(\mathbf{r}, x) = p_x\epsilon\mathcal{B}(\mathbf{r}) + (1 - p_x)\mathcal{S}_c(\mathbf{r}, x), \quad (5.28)$$

which can be expressed in a symbolic form as

$$\hat{A}\mathcal{S} = \mathbf{b}. \quad (5.29)$$

The computing algorithm is given below:

Step (a): Let  $\hat{M}$  denote a preconditioner matrix (defined below). We introduce the 4-component initial preconditioned residual vectors  $\zeta_0$ ,  $\zeta_0^*$  and conjugate direction vectors  $\mathbf{p}_0$ . We define  $\zeta_0$  by

$$\zeta_0 = \hat{M}^{-1}\mathbf{b} - \hat{M}^{-1}\hat{A}\mathcal{S}_0, \quad (5.30)$$

and impose

$$\zeta_0^* = \zeta_0, \quad \mathbf{p}_0 = \zeta_0. \quad (5.31)$$

Here  $\mathcal{S}_0$  is an initial guess for the source vector defined by  $\mathcal{S}_0 = p_x\epsilon\mathcal{B} + (1 - p_x)\mathcal{S}_c$ . As we discretize the frequency and depths, the 4-component irreducible source vector and all the auxiliary vectors introduced in this algorithm can be treated as vectors of length  $4 \times n_x \times n_Y \times n_Z$ , where  $n_x$ ,  $n_Y$  and  $n_Z$  are the number of grid points in frequency,  $Y$  and  $Z$  co-ordinates respectively. The iterations are referred to by an index  $j$ , with  $j = 0, 1, 2, \dots$  *niter*, where *niter* is the number of iterations needed for convergence. For the  $j$ th iteration, the following steps are carried out.

Step (b): We use the formal solver to compute  $\hat{A}\mathbf{p}_j$ .



Step (c): We introduce a coefficient  $\alpha_j$  defined by

$$\alpha_j = \frac{\langle \zeta_j, \zeta_0^* \rangle}{\langle \hat{M}^{-1} \hat{A} \mathbf{p}_j, \zeta_0^* \rangle}. \quad (5.32)$$

where the angle brackets  $\langle \cdot, \cdot \rangle$  represent the inner product in the Euclidian space of real numbers  $\mathbb{R}^n$ , where  $n = 4 \times n_x \times n_Y \times n_Z$ .

Step (d): We introduce a new vector  $\mathbf{q}_j$  defined as

$$\mathbf{q}_j = \zeta_j - \alpha_j \hat{M}^{-1} \hat{A} \mathbf{p}_j. \quad (5.33)$$

Step (e): We use the formal solver to compute  $\hat{A} \mathbf{q}_j$ .

Step (f): We introduce a coefficient  $\omega_j$  defined by

$$\omega_j = \frac{\langle \hat{M}^{-1} \hat{A} \mathbf{q}_j, \mathbf{q}_j \rangle}{\langle \hat{M}^{-1} \hat{A} \mathbf{q}_j, \hat{M}^{-1} \hat{A} \mathbf{q}_j \rangle}. \quad (5.34)$$

Step (g): The value of the new irreducible source vector is derived from the recursive relation

$$\mathbf{S}_{j+1} = \mathbf{S}_j + \alpha_j \mathbf{p}_j + \omega_j \mathbf{q}_j. \quad (5.35)$$

Step (h): New values for the residual vectors  $\zeta_j$  and conjugate direction vectors  $\mathbf{p}_j$  are calculated with the recursive relations

$$\zeta_{j+1} = \mathbf{q}_j - \omega_j \hat{M}^{-1} \hat{A} \mathbf{q}_j, \quad (5.36)$$

$$\mathbf{p}_{j+1} = \zeta_{j+1} + \beta_j (\mathbf{p}_j - \omega_j \hat{M}^{-1} \hat{A} \mathbf{p}_j). \quad (5.37)$$

Here, the coefficient  $\beta_j$  is defined as

$$\beta_j = \frac{\langle \zeta_{j+1}, \zeta_0^* \rangle}{\langle \zeta_j, \zeta_0^* \rangle} \frac{\alpha_j}{\omega_j}. \quad (5.38)$$

Step (i): If the test for convergence described below is satisfied, we terminate the iteration sequence. Otherwise, we go to the Step (b).

*Test for Convergence:* At each iteration, we calculate the quantities

$$e_S = \max_{\tau_Y, \tau_Z, x=0} \{|\delta S_0^0/S_0^0|\} \quad (5.39)$$

which denotes the maximum relative change (MRC) on the first component  $S_0^0$  of the irreducible source vector and

$$e_P = \max_{\tau_Y, x=0, \theta_1, \varphi_1} \{|\delta P/P|\} (\tau_Z = 0) \quad (5.40)$$

$$\text{with } P = \sqrt{(Q/I)^2 + (U/I)^2}, \quad (5.41)$$

which defines a maximum relative change on the surface polarization. The values of  $\theta_1$  and  $\varphi_1$  are given in Table 5.1. The test for convergence is defined as  $e \equiv \max[e_S, e_P] \leq \bar{\omega}$ , with  $\bar{\omega}$ , a given number. In this chapter we use  $\bar{\omega} = 10^{-8}$ .

### *The Preconditioner matrix*

The preconditioner matrix  $\hat{M}$  is any form of implicit or explicit modification of the matrix  $\hat{A}$ , that helps to solve the given system of equations more efficiently (see Saad 2000). In a way, construction of the preconditioner matrix is similar to the construction of  $\Lambda^*$  matrix in ALI methods. For problems with CRD, the  $\hat{M}$  matrix is nothing but the diagonal matrix  $[\hat{I} - (1 - \epsilon)\Lambda^*]$ , with  $\Lambda^*$  being the diagonal of the  $\Lambda$  matrix. For problems with PRD, the kernel in the scattering integral has dependence on both  $x$  and  $x'$  and a diagonal preconditioner is not sufficient to represent this  $x, x'$  dependence. Therefore, we construct a preconditioner matrix  $\hat{M}$  given by

$$\hat{M} = [\hat{I} - (\hat{R}(x, x')/\phi(x))\Lambda_{x'}^*]. \quad (5.42)$$

It is a block diagonal matrix. Each block is a full matrix with respect to  $x$  and  $x'$ . The matrix  $\hat{M}$  is diagonal with respect to other variables. The  $\Lambda_x^*$  matrix in Equation (5.42) is constructed following the method of constructing the  $\Lambda_x^*$  matrix in the frequency by frequency (FBF) method of Paletou & Auer (1995).

Figure 5.4 demonstrates the performance of Pre-BiCG-STAB method in comparison to the Jacobi method. The model parameters chosen are same as those in Figure 5.5. We show progress of the maximum relative corrections  $e_S$  and  $e_P$  as a function of iteration number for these two methods. While the Jacobi method takes 186 iterations, Pre-BiCG-STAB takes only 26 iterations to reach the same level of accuracy ( $\bar{\omega} = 10^{-8}$ ). In terms of CPU time taken for the computations, the Pre-BiCG-STAB is much faster than the Jacobi method.

## 5.6 Results and Discussions

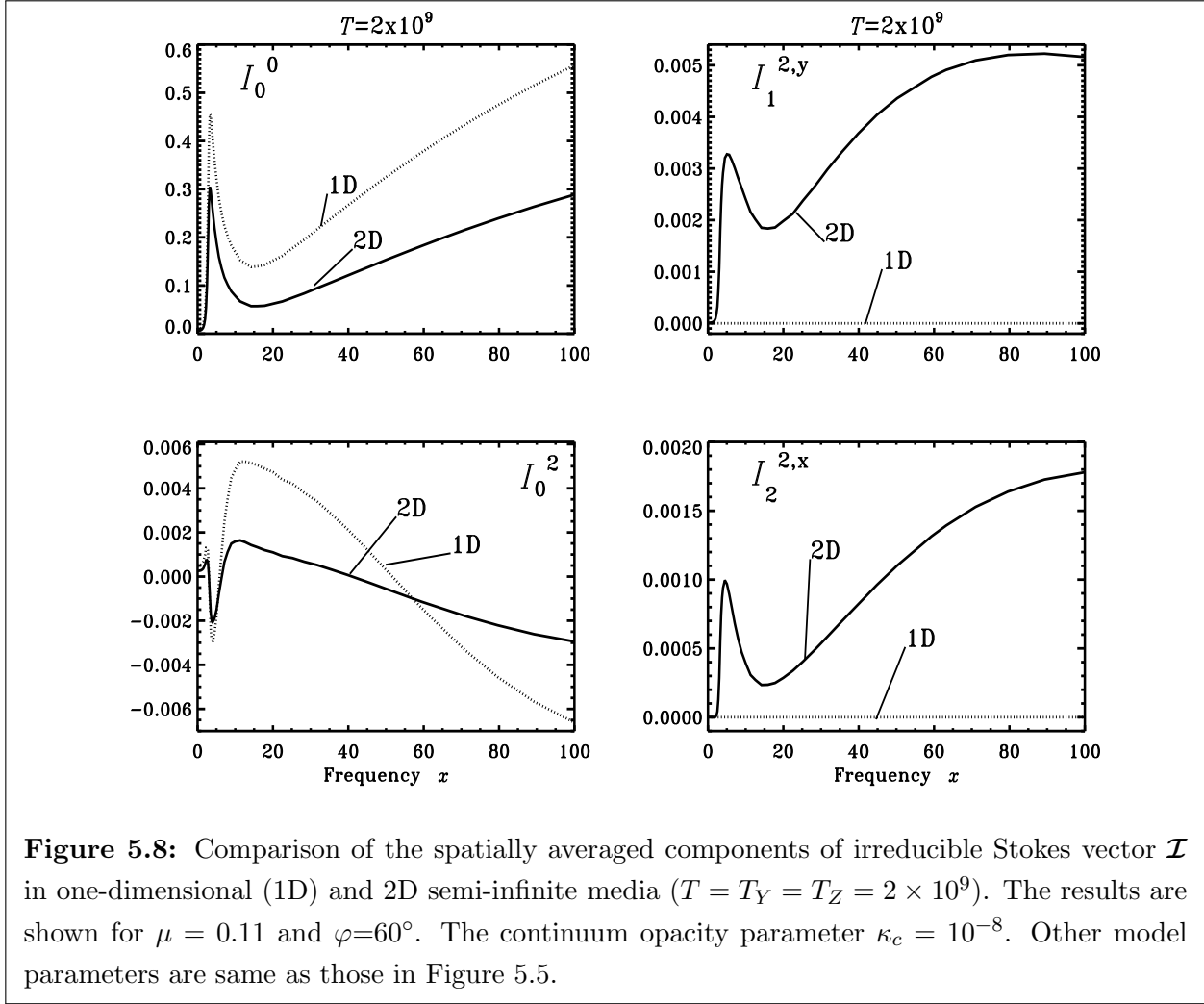
The numerical calculations have been performed with the irreducible Stokes and the source vectors. Most of the results presented in this section are for the Stokes parameters  $I$ ,  $Q$ ,  $U$  and the Stokes source vector components  $S_I$ ,  $S_Q$ ,  $S_U$  which are related to the irreducible components by Equations (E.1), (E.2), and (E.3).

Figures 5.5 and 5.6 show the optical depth dependence of  $S_I$ ,  $S_Q$  and  $S_U$  along the mid-axes in the  $Y$  and  $Z$  directions respectively, for two different frequencies namely  $x = 0$  and  $x = 5$ . The optical thickness in  $Y$  and  $Z$  directions are  $T_Y = T_Z = 2 \times 10^6$ . The damping parameter of the Voigt profile is  $a = 10^{-3}$ . We consider the pure line case ( $\kappa_c = 0$ ), with scattering according to PRD. The elastic and inelastic collision rates are respectively  $\Gamma_E/\Gamma_R = 10^{-4}$ ,  $\Gamma_I/\Gamma_R = 10^{-4}$ . The corresponding branching ratios are  $(\alpha, \beta^{(0)}, \beta^{(2)}) \approx (1, 1, 1)$ . This PRD model is dominated by the  $r_{II}$  redistribution function. The internal thermal sources are taken as constant (the Planck function  $B_\nu(\mathbf{r}) = 1$ ). The medium is assumed to be self-emitting (no incident radiation on the boundaries). We have plotted the results for all the 96 ( $= 12 \times 8$ ) directions that we have considered, which cover all the octants, with 12 directions per octant. For the first octant, they are listed in Table 5.1.

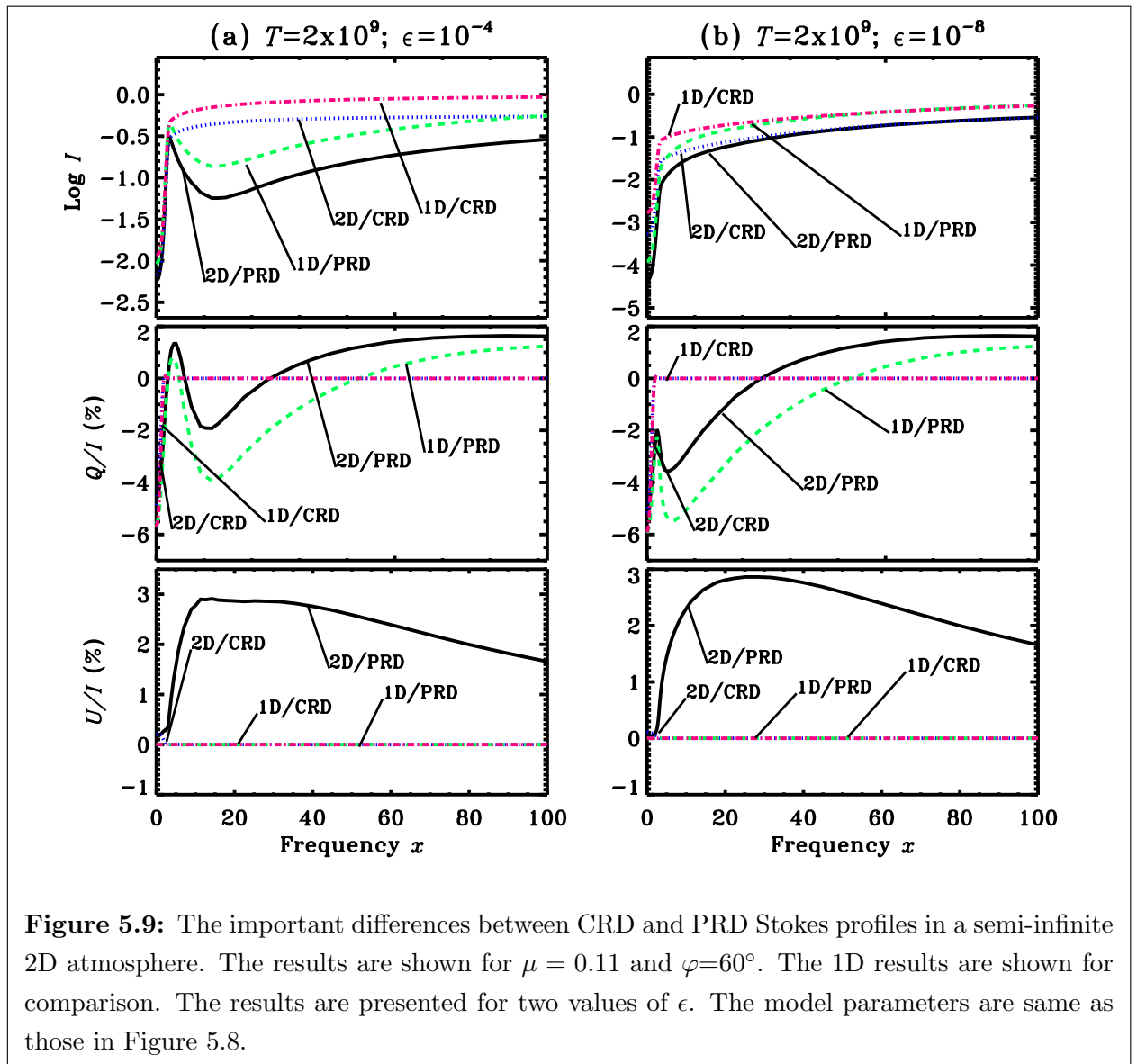
Figures 5.5(a) and (b) show the variation of source vectors along the mid  $Z$ -axis for  $x = 0$  and  $x = 5$  respectively. Because the  $Z$ -axis is the axis of symmetry,  $S_Q$  depends only on  $|\mu|$ , and hence only 4 out of 96 curves are distinguishable. For the same reason,  $S_U = 0$ .

Depth variation of the source vectors along the mid  $Y$ -axis is shown in Figures 5.6(a) and (b). Along the  $Y$ -axis,  $S_Q$  and  $S_U$  are sensitive to both  $\mu$  and  $\varphi$ . They show some symmetries which follow from the symmetry of the angle-gridding. For  $S_Q$ , the distinguishable curves correspond to the directions of the first octant. For  $S_U$ , the distinguishable curves correspond to all the directions in the first and second octants (second octant is defined by  $\theta \in [0, \pi/2]$ ,  $\varphi \in [\pi/2, \pi]$ ). Curves for the remaining directions coincide with these curves.

In Figures 5.5(b) and 5.6(b),  $S_Q$  and  $S_U$  are independent of the optical depth on the surface up to  $\tau = 10^4$  because, the monochromatic optical depth at  $x = 5$  is so small that the RT effects become negligible. The magnitudes of  $S_Q$  and  $S_U$  profiles are larger for  $x = 5$  because of the frequency coherent nature of  $r_{II}$  in the wings. When the thermalization has taken place,  $S_I \rightarrow B_\nu(\mathbf{r})$  and  $S_Q$  and  $S_U$  vanish. For  $x = 0$  this occurs at  $\tau \approx 10^4$  and for  $x = 5$  at  $\tau \approx 10^6$  (see Figures 5.5 and 5.6).



The angular behavior and sign changes of  $S_Q$  and  $S_U$  depend on the nature of the mean intensity components  $J_0^0$ ,  $J_0^2$ ,  $J_1^{2,y}$  and  $J_2^{2,x}$ . The behaviors of all these 4 components are controlled by the angular dependence of the intensity component  $I_0^0$ . Considering only the action of first column of the  $\hat{\Psi}$  matrix on  $I_0^0$ , these 4 components can be written as shown in Equation (F.1). For example,  $J_0^2$  changes its sign roughly at the depth point where  $I_0^0$  changes its angular dependence from limb darkening (at the surface) to limb brightening (at the interior) (see Nagendra et al. 1998). The signs of other components depend on the  $\theta$  and  $\varphi$  dependence of  $I_0^0$  and on the signs of the trigonometric weights in each octant. For instance,  $J_1^{2,y}$  can be split into 8 terms, each representing the contribution from one octant. It can be easily seen that the trigonometric weights coming from four of these terms are positive ( $\theta \in [0, \pi/2]$  with  $\varphi \in [0, \pi/2], [\pi/2, \pi]$  and  $\theta \in [\pi/2, \pi]$  with  $\varphi \in [\pi, 3\pi/2], [3\pi/2, 2\pi]$ ). The weights for the remaining four terms are negative. If the sum of the



positive terms dominates over the sum of the negative terms, then  $J_1^{2,y}$  will be positive, and vice-versa. This clearly shows that the signs of  $S_Q$  and  $S_U$  in a 2D medium depend strongly on the combined effects of  $\theta$  and  $\varphi$  dependence of the  $I_0^0$  component, unlike the 1D case, where  $I_0^0$  being independent of the azimuth, the sign of  $S_Q$  depends only on the  $\theta$  dependence of  $I_0^0$ .

In Figure 5.7 we show spatially averaged emergent Stokes profiles for  $T = 2, 200$  and  $2 \times 10^6$ . By spatial averaging, we mean that we integrate the values of the Stokes profiles in the  $Y$  direction at the surface ( $\tau_Z = 0$ ), by taking an arithmetic average. The other model parameters are same as in Figure 5.5. For both  $T = 2$  and  $200$ , the medium is effectively thin because  $\epsilon = 10^{-4}$ , and hence we see an emission line in the Stokes  $I$  profile. For  $T = 2 \times 10^6$  the medium is effectively thick, hence we see an emission line with self absorption in the core. Here the line core means that  $x \lesssim 4$ . Due to symmetries in the distribution of the angular quadrature points there are only 3 different curves for  $Q/I$  and only 6 different ones for  $U/I$ , out of the 12 azimuths. For effectively thin cases ( $T = 2, 200$ ), the product  $aT$  is smaller than unity and therefore the RT effects are restricted to the line core (see Nagendra et al. 1998). Therefore the source functions  $S_Q$  and  $S_U$  depend on the ray direction only in the line core. They tend to zero in the line wings. The same behavior is seen of course for emergent  $Q/I$  and  $U/I$ . For  $T = 2 \times 10^6$ ,  $S_Q$  and  $S_U$  are almost independent of the ray direction in the line core but show significant variation in the wings. This is because of the larger monochromatic optical depth in the line core leading to an increased number of scattering. For wing frequencies, the angular dependence of  $Q/I$  and  $U/I$  is significant because,  $S_Q$  and  $S_U$  show variation throughout the atmosphere as the thermalization is reached only near the mid slab (see Figures 5.5(b) and 5.6(b)).

The magnitudes of  $Q/I$  and  $U/I$  increase with  $T$ . For  $|Q/I|$  the largest values are always at the line center. Further, for  $T = 2 \times 10^6$ , we see a dip at  $x \approx 12$  and a second peak at  $x \approx 20$ . For  $|U/I|$  the situation is a bit more complicated. For  $T = 2, 200$  the values of  $|U/I|$  are largest in the line core. For  $T = 2 \times 10^6$ ,  $|U/I|$  is very small in the line core and reaches up to 15 % in the wings around  $x \approx 12$ . These results are not easy to interpret, as they represent the case of an unsaturated radiation field that prevails in 2D slabs with intermediate optical thickness.

In Figure 5.8, we compare the spatially averaged components of  $\mathcal{I}$  for 1D and 2D geometries in a semi-infinite media ( $T_Y = T_Z = T = 2 \times 10^9$ ). The continuum opacity parameter is  $\kappa_c = 10^{-8}$ . We have shown the results for  $\mu = 0.11$  and  $\varphi = 60^\circ$ . The other model parameters are same as in Figure 5.5. The  $I_0^0$  component is larger for 1D than 2D

due to the leaking of the radiation from the boundaries of the 2D slab. The component  $|I_0^2|_{1D}$  is larger than  $|I_0^2|_{2D}$  because of the spatial averaging. It acts in 2 different ways. (1) The signs of  $I_0^2$  change along the  $Y$  direction (2) the largest values of  $I_0^2$  occurs in narrow regions near the boundaries of the 2D slab (see chapter 4). The components with the index  $Q = 1, 2$  are zero for 1D. For 2D geometry,  $I_1^{2,x}$  and  $I_2^{2,y}$  are zero. The components  $I_2^{2,x}$  and  $I_1^{2,y}$  have significant values which contribute to the differences between the  $Q/I$  and  $U/I$  in 1D and 2D geometries.

In Figure 5.9 we show spatially averaged emergent Stokes profiles for CRD and PRD in a semi-infinite 2D medium ( $T_Y = T_Z = T = 2 \times 10^9$ ). We choose the same PRD model as in Figure 5.5. This PRD model is dominated by  $r_{II}$ . The other model parameters are same as in Figure 5.8. We show the corresponding 1D results for comparison. Figures 5.9(a) and (b) correspond to  $\epsilon = 10^{-4}$  and  $\epsilon = 10^{-8}$  respectively. The global behaviors of  $I$  and  $Q/I$  for CRD and PRD in a 2D semi-infinite medium, are similar to those of 1D. As expected, intensity and polarization profiles for CRD and PRD are identical in the line core. In the wings, the Stokes  $I$  for CRD reaches a constant value and becomes independent of frequency whereas for PRD it varies sharply with frequency and reaches the CRD value only in the far wings. Further details of the behavior of Stokes profiles in semi-infinite 1D media can be found in Faurobert (1988). Now we focus on the essential differences between 1D and 2D results.  $[I]_{2D}$  is smaller than  $[I]_{1D}$  throughout the line profile due to leaking of the radiation field near the boundaries of the 2D slab for both CRD and PRD. For CRD,  $Q/I$  approaches zero in the wings while PRD profiles are non-zero ( $Q/I$  can take both positive and negative values). For CRD, the effects of 2D geometry are not as significant as for PRD.

We remark that for both CRD and PRD, the curves for  $[Q/I]_{1D}$  remain below the curves for  $[Q/I]_{2D}$ . This can be understood by looking at the components of the irreducible Stokes vector  $\mathcal{I}$  plotted in Figure 5.8. Equation (E.2) can be re-written as

$$\begin{aligned} [Q(\mathbf{r}, \boldsymbol{\Omega}, x)]_{1D} &\simeq -a_1 \times [I_0^2]_{1D}, \\ [Q(\mathbf{r}, \boldsymbol{\Omega}, x)]_{2D} &\simeq -a_1 \times [I_0^2]_{2D} + a_c, \end{aligned} \quad (5.43)$$

where  $a_1$  depends on  $\mu$  and is same for both 1D and 2D cases. The quantity  $a_c$  depends on  $\mu$ ,  $\varphi$  and the components  $I_1^{2,y}$  and  $I_2^{2,x}$ . For  $\mu = 0.11$  and  $\varphi = 60^\circ$  considered for Figure 5.8,  $a_1$  and  $a_c$  are positive. As discussed above,  $|I_0^2|_{1D}$  is larger than  $|I_0^2|_{2D}$ . When  $[I_0^2]_{2D} > 0$ ,  $-a_1 \times [I_0^2]_{2D} > -a_1 \times [I_0^2]_{1D}$  and therefore the addition of  $a_c$  to  $-a_1 \times [I_0^2]_{2D}$  leads to  $|Q/I|_{2D} < |Q/I|_{1D}$ . When  $[I_0^2]_{2D} < 0$ ,  $-a_1 \times [I_0^2]_{2D} < -a_1 \times [I_0^2]_{1D}$ . In this case, the addition of  $a_c$  to  $-a_1 \times [I_0^2]_{2D}$  may lead to  $|Q/I|_{2D} > |Q/I|_{1D}$  or  $|Q/I|_{2D} < |Q/I|_{1D}$ .

But the contribution from  $a_c$  is sufficiently large that we have  $|Q/I|_{2D} > |Q/I|_{1D}$ . The differences between the  $[Q/I]_{2D}$  for other  $\varphi$  values and  $[Q/I]_{1D}$  are similar.

Finally, as pointed out in chapter 4,  $[U/I]_{2D}$  is non-zero and can become significantly large in the wings for the PRD case. In the CRD case  $[U/I]_{2D}$  is non-zero only very close to the line center and goes to zero in the rest of the frequency domain. As is well known,  $[U/I]_{1D} \equiv 0$  due to axial symmetry.

## 5.7 Concluding remarks

In this chapter we develop an efficient method to solve polarized RT equation with PRD in a 2D slab. We assume a two-level atom model with unpolarized ground level. We assume that the medium is finite in two directions ( $Y$  and  $Z$ ) and infinite in the third direction ( $X$ ). First we apply the Stokes vector decomposition technique developed in chapter 4 to 2D geometry. We show that due to symmetry of the Stokes  $I$  parameter with respect to the  $\varphi = \pi/2$  axis, the Stokes  $Q$  becomes symmetric and the Stokes  $U$  becomes anti-symmetric about this axis ( $\varphi$  is measured from the infinite  $X$  direction anti-clockwise). Using this property we can represent the polarized radiation field by 4 irreducible components  $I_0^0$ ,  $I_0^2$ ,  $I_1^{2,y}$  and  $I_2^{2,x}$ . The Stokes source vectors are also decomposed into 4 irreducible components which are independent of the ray direction. Due to axi-symmetry  $I_1^{2,y}$  and  $I_2^{2,x}$  are zero in 1D geometry.

This decomposition technique is interesting for the development of iterative methods. Here we describe a numerical method called the Pre-BiCG-STAB and show that it is much faster than the Jacobi iteration method used in chapter 4. This method can be easily generalized to 3D geometries.

Further, in this chapter we generalize to PRD, the 2D short characteristics method developed in Paletou et al. (1999) for CRD. This formal solver is much more efficient than the one used in chapter 4.

With these two new features it is possible to compute the solutions for a wide range of model parameters. With the method of chapter 4 only media with small optical depths can be considered.

In Figure 5.5 and 5.6 we show the optical depth dependence of the source vectors along the mid axes in the  $Y$  and  $Z$  directions. We recover similar angular dependence of  $S_Q$  and  $S_U$  at line center as in Paletou et al. (1999). Contrary to CRD, one can observe the increase in the values of  $S_Q$  and  $S_U$  at  $x = 5$ . This is a PRD effect on the polarization



caused by the coherence nature of  $r_{\Pi}$  redistribution function in the wings.

In Figure 5.7 we study the spatially averaged emergent Stokes profiles for different optical thicknesses. We show that the polarization is restricted to the line core for small values of  $T$ . As  $T$  increases,  $Q/I, U/I$  take larger values in the line wings as well. This is also a PRD effect. In the line core  $Q/I$  becomes independent of the ray directions and  $U/I \rightarrow 0$  due to an increased number of scattering for the line core photons.

In Figures 5.8 and 5.9 we consider the case of semi-infinite atmospheres with  $T_Z = T_Y = T = 2 \times 10^9$ . In Figure 5.8 we compare the behaviors of the emergent spatially averaged irreducible components, for 2D geometry and the corresponding components in 1D geometry. For 1D geometry only non-zero components are  $I_0^0$  and  $I_0^2$ . The  $I_0^0$  component is larger for 1D than 2D due to the leaking of the radiation from the boundaries of the 2D slab. The component  $|I_0^2|_{1D}$  is larger than  $|I_0^2|_{2D}$  due to spatial averaging. The contribution from the components  $I_2^{2,x}$  and  $I_1^{2,y}$  is mainly responsible for the deviation of  $Q/I$  and  $U/I$  in 2D geometry from their 1D values.

In Figure 5.9 we compare the spatially averaged emergent Stokes profiles in 2D geometry, and the corresponding 1D solutions for CRD and PRD. We show that the deviation of polarized radiation field in 2D geometry from the one in 1D geometry exists both for CRD and PRD, but is more severe in the line wings of the PRD solutions. In Figure 5.9(a), at  $x \approx 12$ , we see a near wing maxima in  $-[Q/I]$ . At this frequency  $||Q/I|_{2D} - |Q/I|_{1D}| \approx 2\%$ . At this wing frequency we have  $|U/I|_{2D} \approx 3\%$  and  $|U/I|_{1D} \equiv 0$ .

We thus propose our numerical method as an efficient and fast method to solve the polarized RT problems with PRD in multi-D media.

## New Results

The high efficiency of Pre-BiCG-STAB method was established in chapter 3. In this chapter the method is extended to handle polarized multi-D RT. The important results of chapter 5 are as follows.

1. We have developed faster and more efficient Pre-BiCG-STAB method to solve polarized two-dimensional (2D) RT with PRD.

**2.** The formal solution used in chapter 4 was based on a simple finite volume technique. In chapter 5 we use a more accurate formal solver, namely the well known 2D short characteristics method.

**3.** Using the numerical methods developed in chapter 4, we can consider only simpler cases of finite 2D slabs due to computational limitations. It was a first step towards solving polarized multi-D problems with PRD. Using the superior methods developed in chapter 5, we could compute PRD solutions in 2D media, in the more difficult context of semi-infinite 2D atmospheres as well. We present several solutions which may serve as benchmarks for future studies in this area.

## Chapter 6

# Hanle effect with partial redistribution in multi-D media

*The contents of this chapter are based on the following publication:*  
Anusha, L. S., and Nagendra, K. N. 2011b, **ApJ**, 738, 116-135

### 6.1 Introduction

Multi-dimensional (multi-D) radiative transfer (RT) is important to advance our understanding of the solar atmosphere. With the increase in the resolving power of modern telescopes, and the computing power of supercomputers, multi-D polarized line RT is becoming a necessity, and practically feasible. The multi-D effects manifest themselves in the resolved structures on the Sun. The finite dimensional structures on the solar surface lead to inhomogeneity in the atmosphere, which is then no longer axis-symmetric. The presence of magnetic fields adds to the non-axisymmetry, in the microscopic scales through the Hanle effect. The purpose of this chapter is to address the relative importance of non-axisymmetry caused by geometry, and oriented magnetic fields.

In the past decades extensive studies on line RT in multi-D media are done. A historical account on these developments is given in chapter 4 (see also Anusha & Nagendra 2011a). In chapter 4 we presented a method of Stokes vector decomposition, which helped to formulate an ‘irreducible form’ of the polarized line RT equation in a 3D Cartesian geometry. Such a formulation is advantageous because, the source vector and the mean intensity vector become angle independent in the reduced basis. Also the scattering phase matrix becomes independent of the outgoing directions ( $\Omega$ ). This property leads to several

advantages in numerical work. It also provides a framework in which the transfer equation can be solved more conveniently, because the decomposition is applied to both the Stokes source vector, and the Stokes intensity vector. In chapter 5 (see also Anusha et al. 2011a), we focused our attention on devising fast numerical methods to solve polarized RT equation with partial frequency redistribution (PRD) in a two-dimensional (2D) geometry. In chapters 4 and 5 we considered the case of non-magnetic resonance scattering polarization. Manso Sainz & Trujillo Bueno (1999) and Dittmann (1999) solved the polarized RT equation in the presence of a magnetic field (Hanle effect), in multi-D media. Their calculations used the assumption of complete frequency redistribution (CRD) in line scattering. In this chapter (see also Anusha & Nagendra 2011b) we solve the same problem, but for the more difficult and more realistic case of Hanle scattering with PRD. The physics of PRD scattering is treated using the frequency-domain based approach developed by Bommier (1997a, 1997b). The RT calculations in one-dimensional (1D) geometry, using this approach are described in Nagendra et al. (2002). We extend their work to 2D and 3D geometries. For simplicity we restrict to the case of angle-averaged PRD functions.

This chapter represents a generalization to the magnetic case, the decomposition technique developed in chapter 4. It also represents the generalizations to the 3D case, the Stabilized Pre-conditioned Bi-Conjugate Gradient (Pre-BiCG-STAB) method developed in chapter 5. Another generalization is the use of 3D short characteristics formal solver in this chapter, for the case of PRD.

In Section 6.2 we describe the multi-D transfer equation in the Stokes vector basis. The decomposition technique as applied to the case of a magnetic multi-D media is described in Section 6.3. In Section 6.4 we briefly describe the 3D short characteristics formal solution method. Section 6.5 is devoted to a brief description of the numerical method of solution. Results and discussions are presented in Section 6.6. Concluding remarks are given in Section 6.7.

## 6.2 The polarized radiative transfer in a magnetized multi-D media

In this chapter we consider polarized RT in 1D, 2D and 3D media in Cartesian geometry (see Figure 6.1). We assume that the 1D medium is infinite in the  $X$  and  $Y$  directions but finite in the  $Z$  direction. For 2D, we assume that the medium is infinite in the  $X$  direction, but finite in the  $Y$  and  $Z$  directions. The 3D medium is assumed to be finite in all the  $X$ ,  $Y$  and  $Z$  directions. We define the “top surface” for a 1D medium to be the infinite

$XY$  plane passing through the point  $Z_{\max}$ . For a 2D medium, the top surface is defined to be the plane passing through the line  $(Y, Z_{\max})$ , which is infinite in  $X$  direction. For a 3D medium, the top surface is the plane  $(X, Y, Z_{\max})$  which is finite in  $X$  and  $Y$  directions. For a given ray with direction  $\boldsymbol{\Omega}$ , the polarized transfer equation in a multi-D medium with an oriented magnetic field is given by

$$\boldsymbol{\Omega} \cdot \nabla \mathbf{I}(\mathbf{r}, \boldsymbol{\Omega}, x) = -[\kappa_l(\mathbf{r})\phi(x) + \kappa_c(\mathbf{r})][\mathbf{I}(\mathbf{r}, \boldsymbol{\Omega}, x) - \mathbf{S}(\mathbf{r}, \boldsymbol{\Omega}, x)], \quad (6.1)$$

where  $\mathbf{I} = (I, Q, U)^T$  is the Stokes vector, with  $I$ ,  $Q$  and  $U$  the Stokes parameters defined below. Following Chandrasekhar (1950), we consider an elliptically polarized beam of light, the vibrations of the electric vector of which describe an ellipse. If  $I_l$  and  $I_r$  denote the components of the specific intensity of this beam of light along two mutually perpendicular directions  $l$  and  $r$ , in a plane (see Figure 6.2) transverse to the propagation direction, then we define

$$\begin{aligned} I &= I_l + I_r, \\ Q &= I_l - I_r, \\ U &= (I_l - I_r) \tan 2\chi, \end{aligned} \quad (6.2)$$

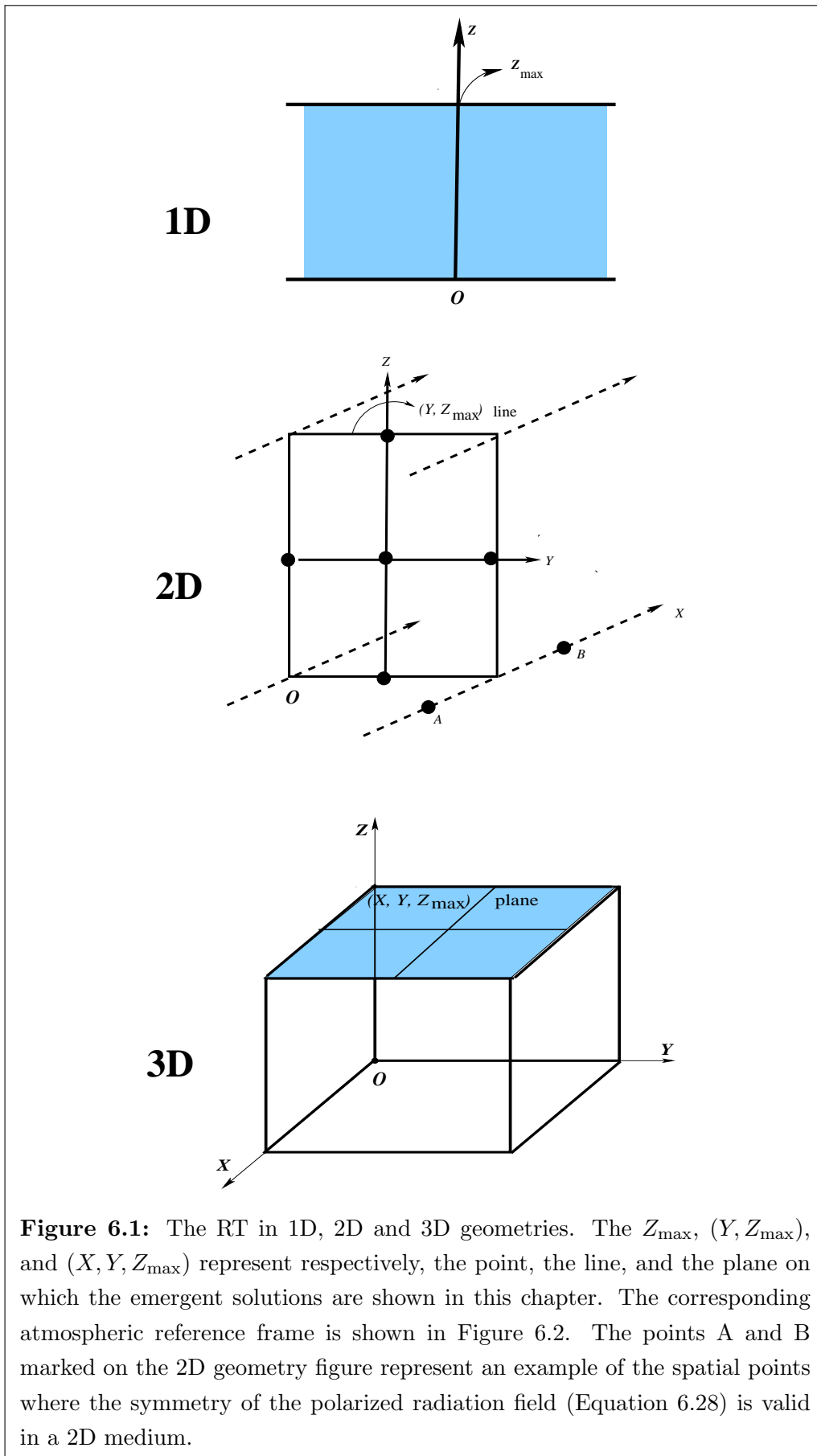
where  $\chi$  is the angle between the direction  $l$  and the semi-major axis of the ellipse. Positive value of  $Q$  is defined to be a direction parallel to  $l$  and negative  $Q$  to be in a direction parallel to  $r$ . The quantity  $\mathbf{r} = (x, y, z)$  is the position vector of the ray in the Cartesian coordinate system. The unit vector  $\boldsymbol{\Omega} = (\eta, \gamma, \mu) = (\sin \theta \cos \varphi, \sin \theta \sin \varphi, \cos \theta)$  describes the direction cosines of the ray in the atmosphere, with respect to the atmospheric normal (the  $Z$ -axis), where  $\theta$  and  $\varphi$  are the polar and azimuthal angles of the ray (see Figure 6.2). The quantity  $\kappa_l$  is the frequency averaged line opacity,  $\phi$  is the Voigt profile function and  $\kappa_c$  is the continuum opacity. Frequency is measured in reduced units, namely  $x = (\nu - \nu_0)/\Delta\nu_D$ , where  $\Delta\nu_D$  is the Doppler width.

The Stokes source vector in a two-level atom model with unpolarized ground level is

$$\mathbf{S}(\mathbf{r}, \boldsymbol{\Omega}, x) = \frac{\kappa_l(\mathbf{r})\phi(x)\mathbf{S}_l(\mathbf{r}, \boldsymbol{\Omega}, x) + \kappa_c(\mathbf{r})\mathbf{S}_c(\mathbf{r}, x)}{\kappa_l(\mathbf{r})\phi(x) + \kappa_c(\mathbf{r})}. \quad (6.3)$$

Here  $\mathbf{S}_c$  is the continuum source vector given by  $(B_\nu(\mathbf{r}), 0, 0)^T$  with  $B_\nu(\mathbf{r})$  being the Planck function. The line source vector is written as

$$\mathbf{S}_l(\mathbf{r}, \boldsymbol{\Omega}, x) = \mathbf{G}(\mathbf{r}) + \int_{-\infty}^{+\infty} dx' \times \oint \frac{d\boldsymbol{\Omega}'}{4\pi} \frac{\hat{R}(x, x', \boldsymbol{\Omega}, \boldsymbol{\Omega}', \mathbf{B})}{\phi(x)} \mathbf{I}(\mathbf{r}, \boldsymbol{\Omega}', x'). \quad (6.4)$$



Here  $\hat{R}$  is the Hanle redistribution matrix and  $\mathbf{B}$  represents an oriented vector magnetic field.  $\epsilon = \Gamma_I/(\Gamma_R + \Gamma_I)$  with  $\Gamma_I$  and  $\Gamma_R$  being the inelastic collision rate and the radiative de-excitation rate respectively. The thermalization parameter  $\epsilon$  is the rate of photon destruction by inelastic collisions. The damping parameter is computed using  $a = a_R[1 + (\Gamma_E + \Gamma_I)/\Gamma_R]$  where  $a_R = \Gamma_R/4\pi\Delta\nu_D$  and  $\Gamma_E$  is the elastic collision rate. We denote the thermal source vector by  $\mathbf{G}(\mathbf{r}) = \epsilon\mathbf{B}_\nu(\mathbf{r})$  with  $\mathbf{B}_\nu(\mathbf{r}) = (B_\nu(\mathbf{r}), 0, 0)^T$ . The solid angle element  $d\Omega' = \sin\theta' d\theta' d\varphi'$ , where  $\theta \in [0, \pi]$  and  $\varphi \in [0, 2\pi]$ . The transfer equation along the ray path takes the form

$$\frac{d\mathbf{I}(\mathbf{r}, \boldsymbol{\Omega}, x)}{ds} = -\kappa_{\text{tot}}(\mathbf{r}, x)[\mathbf{I}(\mathbf{r}, \boldsymbol{\Omega}, x) - \mathbf{S}(\mathbf{r}, \boldsymbol{\Omega}, x)], \quad (6.5)$$

where  $s$  is the path length along the ray and  $\kappa_{\text{tot}}(\mathbf{r}, x)$  is the total opacity given by

$$\kappa_{\text{tot}}(\mathbf{r}, x) = \kappa_l(\mathbf{r})\phi(x) + \kappa_c(\mathbf{r}). \quad (6.6)$$

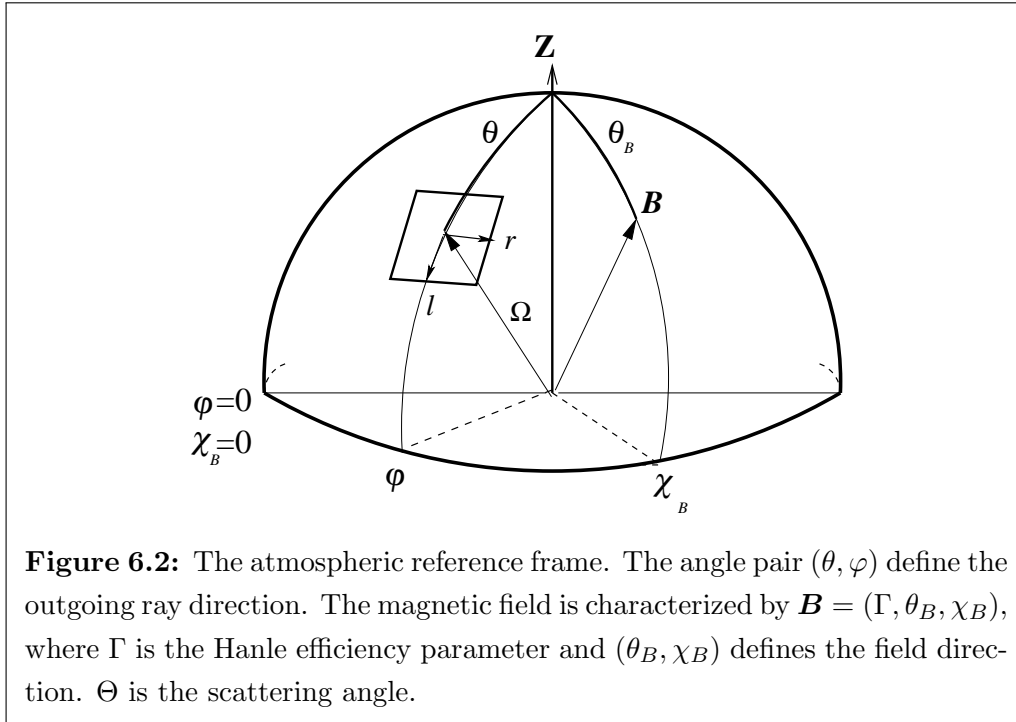
The formal solution of Equation (6.5) is given by

$$\begin{aligned} \mathbf{I}(\mathbf{r}, \boldsymbol{\Omega}, x) = & \mathbf{I}(\mathbf{r}_0, \boldsymbol{\Omega}, x) \exp \left\{ - \int_{s_0}^s \kappa_{\text{tot}}(\mathbf{r} - (s - s')\boldsymbol{\Omega}, x) ds' \right\} \\ & + \int_{s_0}^s \mathbf{S}(\mathbf{r} - (s - s')\boldsymbol{\Omega}, \boldsymbol{\Omega}, x) \kappa_{\text{tot}}(\mathbf{r} - (s - s')\boldsymbol{\Omega}, x) \exp \left\{ - \int_{s'}^s \kappa_{\text{tot}}(\mathbf{r} - (s - s'')\boldsymbol{\Omega}, x) ds'' \right\} ds'. \end{aligned} \quad (6.7)$$

$\mathbf{I}(\mathbf{r}_0, \boldsymbol{\Omega}, x)$  is the boundary condition imposed at  $\mathbf{r}_0 = (x_0, y_0, z_0)$ . The ray path on which the formal solution is defined is shown in Figure 6.3.

### 6.3 Decomposition of $\mathbf{S}$ and $\mathbf{I}$ in a magnetized multi-D media

As already discussed in chapter 4, a decomposition of the Stokes source vector  $\mathbf{S}$  and the intensity vector  $\mathbf{I}$  in terms of the irreducible spherical tensors is necessary to simplify the problem. In chapter 4, it was a generalization to the 3D non-magnetic case, of the decomposition technique for the 1D transfer problems, developed by Frisch (2007, hereafter HF07). Here we extend our work presented in chapter 4 to include the magnetic fields. A similar technique, but in the Fourier space was presented in Faurobert-Scholl (1991) and Nagendra et al. (1998), who solved the Hanle scattering RT problem in 1D geometry. The solution of polarized Hanle scattering transfer equation using the angle-averaged and angle-dependent redistribution matrices was presented in Nagendra et al. (2002), where



a perturbation method of solution was used. A Polarized Approximate Lambda Iteration method to solve similar problems, using the Fourier decomposition technique was presented in Fluri et al. (2003b), but only for the case of angle-averaged PRD.

A general theory of PRD for the two-level atom problem with Hanle scattering was developed by Bommier(1997a, 1997b). It involves the construction of PRD matrices that describe radiative plus collisional frequency redistribution in scattering. It is rather difficult to use the exact redistribution matrix  $\hat{R}$  in the polarized transfer equation. For convenience of applications in line transfer theories, Bommier(1997b) proposed 3 levels of approximations, to handle the  $\hat{R}$  matrices. In approximation levels II and III, the  $\hat{R}$  matrices were factorized into products of redistribution functions of Hummer (1962), and the multi-polar components of the Hanle phase matrix. The collisions enter naturally in this formalism. It is shown that such a factorization of  $\hat{R}$  can be achieved only in certain frequency domains in the 2D  $(x, x')$  frequency space. In this chapter we refer to this way of writing the PRD Hanle  $\hat{R}$  matrix, as the ‘domain based PRD’. The definition of the domains are given in Bommier(1997b, see also Nagendra et al. 2002; Nagendra et al. 2003; Fluri et al. 2003b). We use the domain based PRD, but write the relevant equations in a form suitable for our present context (multi-D transfer). We recall that in the special case of non-magnetic scattering, the domain based PRD equations for  $\hat{R}$  matrix naturally go to



the Domke-Hubeny redistribution matrix (Domke & Hubeny 1988). We start by writing Hanle phase matrix in the atmospheric reference frame in terms of the irreducible spherical tensors for polarimetry, introduced by Landi Degl’Innocenti & Landolfi (2004, hereafter LL04). In this formalism the  $(i, j)$ -th element of the Hanle phase matrix is given by

$$[\hat{P}_H(\boldsymbol{\Omega}, \boldsymbol{\Omega}', \mathbf{B})]_{ij} = \sum_{KQ} \mathcal{T}_Q^K(i, \boldsymbol{\Omega}) \sum_{Q'} \mathcal{M}_{QQ'}^K(\mathbf{B}) (-1)^{Q'} \mathcal{T}_{-Q'}^K(j, \boldsymbol{\Omega}'), \quad (6.8)$$

where  $(i, j) = (1, 2, 3)$  and

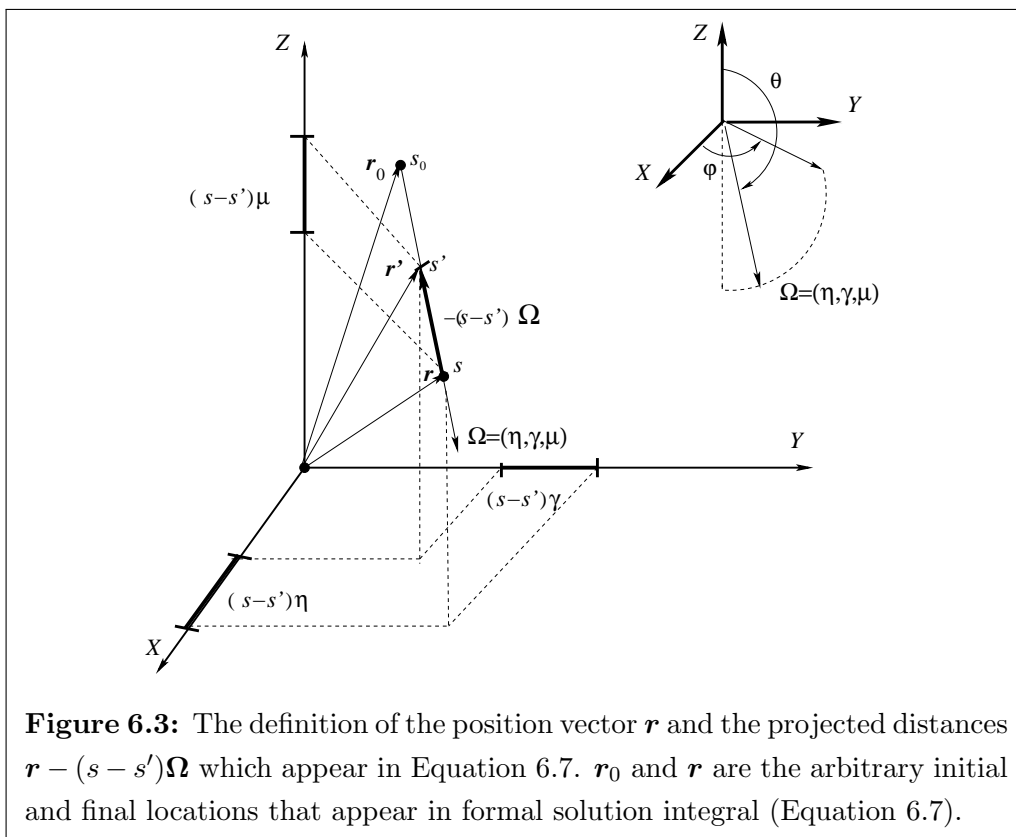
$$\mathcal{M}_{QQ'}^K(\mathbf{B}) = e^{i(Q'-Q)\chi_B} \sum_{Q''} d_{QQ''}^K(\theta_B) d_{Q''Q'}^K(-\theta_B) \frac{1}{1 + iQ''\Gamma_B}, \quad (6.9)$$

where the  $d_{MM'}^J$  are the reduced rotation matrices given in LL04. The magnetic Hanle  $\Gamma_B$  parameter takes different values in different frequency domains (see Appendix H).  $\mathcal{T}_Q^K(i, \boldsymbol{\Omega})$  are the irreducible spherical tensors for polarimetry with  $K = 0, 1, 2$ ,  $-K \leq Q \leq +K$  (see Landi Degl’Innocenti & Landolfi 2004). In this chapter, we consider only the linear polarization. Therefore,  $K = 0, 2$  and  $Q \in [-K, +K]$ . For the practical use, we need to further expand the  $\hat{P}_H$  matrix in each of the domains in terms of  $\mathcal{T}_Q^K$ . The required domain based expansions of the PRD matrices in terms of  $\mathcal{T}_Q^K$  were already given in HF07, applicable there to the case of 1D Hanle transfer. We present here the corresponding equations that are applicable to the multi-D transfer, which now become  $\varphi$  dependent (in the 1D case, those phase matrix components were  $\varphi$  independent). We restrict our attention in this chapter to the particular case of angle-averaged redistribution functions (approximation level III of Bommier 1997b).

The  $ij$ -th element of the redistribution matrix in the atmospheric reference frame (Bommier 1997b) can be written as

$$R_{ij}(x, x', \boldsymbol{\Omega}, \boldsymbol{\Omega}', \mathbf{B}) = \sum_{KQ} W_K \mathcal{T}_Q^K(i, \boldsymbol{\Omega}) \left\{ r_{\text{II}}(x, x') P_{Q,\text{II}}^K(j, \boldsymbol{\Omega}', \mathbf{B}) + r_{\text{III}}(x, x') P_{Q,\text{III}}^K(j, \boldsymbol{\Omega}', \mathbf{B}) \right\}. \quad (6.10)$$

The weights  $W_K$  depend on the line under consideration (see LL04). Here  $r_{\text{II}}(x, x')$  and  $r_{\text{III}}(x, x')$  are the angle-averaged versions of redistribution functions (see Hummer 1962). The quantities  $P_{Q,\text{II}}^K(j, \boldsymbol{\Omega}', \mathbf{B})$  and  $P_{Q,\text{III}}^K(j, \boldsymbol{\Omega}', \mathbf{B})$  take different forms in different frequency domains. They are described in Appendix H.



Denoting  $G_Q^K = \delta_{K0}\delta_{Q0}G(\mathbf{r})$ , where  $G(\mathbf{r}) = \epsilon B_\nu(\mathbf{r})$ , we can write the  $i$ -th component of the thermal source vector as

$$G_i(\mathbf{r}) = \sum_{KQ} \mathcal{T}_Q^K(i, \boldsymbol{\Omega}) G_Q^K(\mathbf{r}). \quad (6.11)$$

The line source vector can be decomposed as

$$S_{i,l}(\mathbf{r}, \boldsymbol{\Omega}, x) = \sum_{KQ} \mathcal{T}_Q^K(i, \boldsymbol{\Omega}) S_{Q,l}^K(\mathbf{r}, x), \quad (6.12)$$

where

$$S_{Q,l}^K(\mathbf{r}, x) = G_Q^K(\mathbf{r}) + \frac{1}{\phi(x)} \int_{-\infty}^{+\infty} dx' \oint \frac{d\boldsymbol{\Omega}'}{4\pi} \sum_{j=0}^3 W_K \left\{ r_{\text{II}}(x, x') P_{Q,\text{II}}^K(j, \boldsymbol{\Omega}', \mathbf{B}) \right. \\ \left. + r_{\text{III}}(x, x') P_{Q,\text{III}}^K(j, \boldsymbol{\Omega}', \mathbf{B}) \right\} I_j(\mathbf{r}, \boldsymbol{\Omega}', x'). \quad (6.13)$$

Note that the components  $S_{Q,l}^K(\mathbf{r}, x)$  now depend only on the spatial variables ( $x, y, z$ ), frequency  $x$ . The  $(\theta, \varphi)$  dependence is fully contained in  $\mathcal{T}_Q^K(i, \boldsymbol{\Omega})$ . These quantities are listed in LL04 (chapter 5, Table 5.6, p. 211). Substituting Equation (6.12) in Equation (6.7), the components of  $\mathbf{I}$  can be written as

$$I_i(\mathbf{r}, \boldsymbol{\Omega}, x) = \sum_{KQ} \mathcal{T}_Q^K(i, \boldsymbol{\Omega}) I_Q^K(\mathbf{r}, \boldsymbol{\Omega}, x), \quad (6.14)$$

where

$$I_Q^K(\mathbf{r}, \boldsymbol{\Omega}, x) = I_{Q,0}^K(\mathbf{r}_0, \boldsymbol{\Omega}, x) e^{-\tau_x(\mathbf{r}, \boldsymbol{\Omega})} \\ + \int_0^{\tau_x(\mathbf{r}, \boldsymbol{\Omega})} e^{-\tau'_x(\mathbf{r}', \boldsymbol{\Omega})} \left[ p_x S_{Q,l}^K(\mathbf{r}', x) + (1 - p_x) S_{Q,c}^K(\mathbf{r}', x) \right] d\tau'_x(\mathbf{r}', \boldsymbol{\Omega}). \quad (6.15)$$

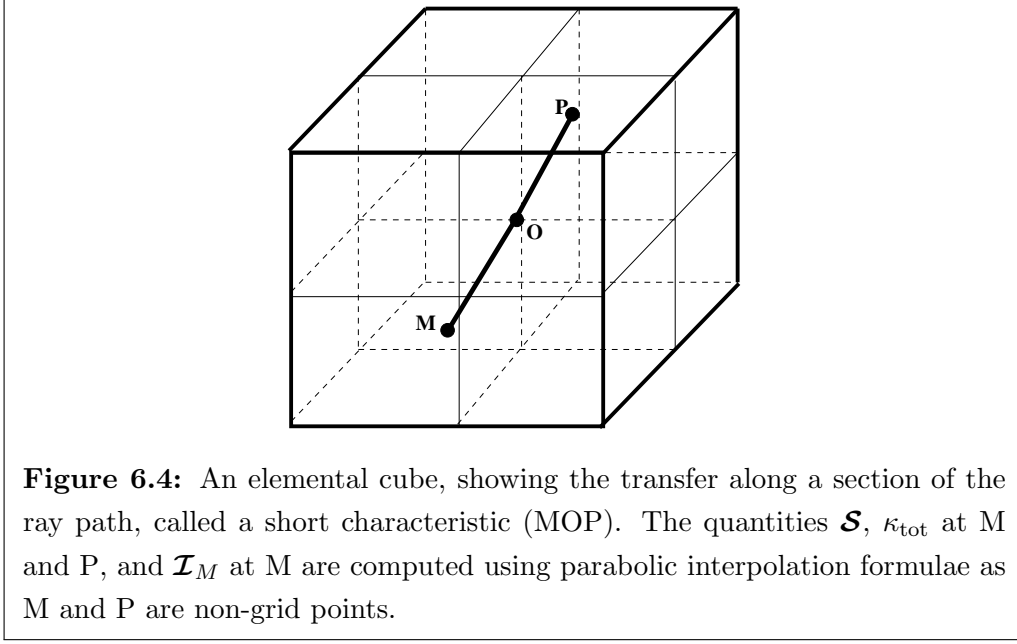
Here  $I_{Q,0}^K = I_0(\mathbf{r}_0, \boldsymbol{\Omega}, x) \delta_{K0} \delta_{Q0}$  are the intensity components at the lower boundary. The quantities  $S_{Q,c}^K = S_c(\mathbf{r}, x) \delta_{K0} \delta_{Q0}$  denote the continuum source vector components. We assume that  $S_c(\mathbf{r}, x) = B_\nu(\mathbf{r})$ . The ratio of the line opacity to the total opacity is given by

$$p_x = \kappa_l(\mathbf{r}) \phi(x) / \kappa_{\text{tot}}(\mathbf{r}, x). \quad (6.16)$$

The monochromatic optical depth scale is defined as

$$\tau_x(\mathbf{r}, \boldsymbol{\Omega}) = \tau_x(x, y, z, \boldsymbol{\Omega}) = \int_{s_0}^s \kappa_{\text{tot}}(\mathbf{r} - (s - s')\boldsymbol{\Omega}, x) ds', \quad (6.17)$$

where  $\tau_x$  is measured along a given ray determined by the direction  $\boldsymbol{\Omega}$ .



### 6.3.1 The irreducible transfer equation in multi-D geometry for the Hanle scattering problem

Let  $S_Q^K = p_x S_{Q,l}^K + (1 - p_x) S_{Q,c}^K$ .  $I_Q^K$  and  $S_Q^K$  as well as the phase matrix elements  $P_{Q,\text{II}}^K(j, \Omega', \mathbf{B})$  and  $P_{Q,\text{III}}^K(j, \Omega', \mathbf{B})$  are all complex quantities. Following the method of transformation from complex to the real quantities given in HF07, we define the real irreducible Stokes vector  $\mathcal{I} = (I_0^0, I_0^2, I_1^{2,x}, I_1^{2,y}, I_2^{2,x}, I_2^{2,y})^T$  and the real irreducible source vector  $\mathcal{S} = (S_0^0, S_0^2, S_1^{2,x}, S_1^{2,y}, S_2^{2,x}, S_2^{2,y})^T$ . It can be shown that the  $\mathcal{I}$  and  $\mathcal{S}$  satisfy a transfer equation of the form

$$-\frac{1}{\kappa_{\text{tot}}(\mathbf{r}, x)} \boldsymbol{\Omega} \cdot \nabla \mathcal{I}(\mathbf{r}, \boldsymbol{\Omega}, x) = [\mathcal{I}(\mathbf{r}, \boldsymbol{\Omega}, x) - \mathcal{S}(\mathbf{r}, x)], \quad (6.18)$$

where  $\mathcal{S}(\mathbf{r}, x) = p_x \mathcal{S}_l(\mathbf{r}, x) + (1 - p_x) \mathcal{S}_c(\mathbf{r}, x)$  with  $\mathcal{S}_c(\mathbf{r}, x) = (B_\nu(\mathbf{r}), 0, 0, 0, 0, 0)^T$  and

$$\mathcal{S}_l(\mathbf{r}, x) = \epsilon \mathbf{B}_\nu(\mathbf{r}) + \mathcal{J}(\mathbf{r}, x). \quad (6.19)$$

Here the polarized mean intensity vector is

$$\begin{aligned} \mathcal{J}(\mathbf{r}, x) = & \frac{1}{\phi(x)} \int_{-\infty}^{+\infty} dx' \oint \frac{d\Omega'}{4\pi} \hat{W} \left\{ \hat{M}_{\text{II}}^{(i)}(\mathbf{B}) r_{\text{II}}(x, x') \right. \\ & \left. + \hat{M}_{\text{III}}^{(i)}(\mathbf{B}) r_{\text{III}}(x, x') \right\} \hat{\Psi}(\Omega') \mathcal{I}(\mathbf{r}, \Omega', x'), \end{aligned} \quad (6.20)$$

and  $\mathbf{B} = (B_\nu(\mathbf{r}), 0, 0, 0, 0, 0)^T$  is the Planck vector.  $\hat{W}$  is a diagonal matrix given by

$$\hat{W} = \text{diag}\{W_0, W_2, W_2, W_2, W_2, W_2\}. \quad (6.21)$$

The matrix  $\hat{\Psi}$  represents the phase matrix for the Rayleigh scattering, to be used in multi-D geometries. Its elements are listed in Appendix J. The matrices  $\hat{M}_{\text{II,III}}^{(i)}(\mathbf{B})$  in different domains are given in Appendix I. The formal solution now takes the form

$$\mathcal{I}(\mathbf{r}, \boldsymbol{\Omega}, x) = \mathcal{I}(\mathbf{r}_0, \boldsymbol{\Omega}, x)e^{-\tau_x(\mathbf{r}, \boldsymbol{\Omega})} + \int_0^{\tau_x(\mathbf{r}, \boldsymbol{\Omega})} e^{-\tau'_x(\mathbf{r}', \boldsymbol{\Omega})} \mathcal{S}(\mathbf{r}', x) d\tau'_x(\mathbf{r}', \boldsymbol{\Omega}). \quad (6.22)$$

Here  $\mathcal{I}(\mathbf{r}_0, \boldsymbol{\Omega}, x)$  is the boundary condition imposed at  $\mathbf{r}_0$ .

## 6.4 A 3D formal solver based on the short characteristics approach

This section is devoted to a discussion of 3D short characteristics formal solver. Here we generalize to the 3D case, the 2D short characteristics formal solver that we had used in chapter 5. A short characteristic stencil MOP of a ray passing through the point O, in a

**Table 6.1:** The 12-point Carlsson type B quadrature for the azimuth angle  $\varphi$ . The corresponding values of  $\sin \varphi$ ,  $\cos \varphi$ ,  $\sin 2\varphi$  and  $\cos 2\varphi$  are given for the purpose of discussion.

$\varphi_i$ (in degrees)	$\sin \varphi$	$\cos \varphi$	$\sin 2\varphi$	$\cos 2\varphi$
30	0.5	0.866	0.866	0.5
45	0.707	0.707	1	0
60	0.866	0.5	0.866	-0.5
120	0.866	-0.5	-0.866	-0.5
135	0.707	-0.707	-1	0
150	0.5	-0.866	-0.866	0.5
210	-0.5	-0.866	0.866	0.5
225	-0.707	-0.707	1	0
240	-0.866	-0.5	0.866	-0.5
300	-0.866	0.5	-0.866	-0.5
315	-0.707	0.707	-1	0
330	-0.5	0.866	-0.866	0.5

3D cube is shown in Figure 6.4. The point O represents a grid point along the ray path. The point M (or P) represents an intersection of the ray with one of the boundary planes

of a 3D cell. The plane of intersection is determined by the direction cosines of the ray. The length  $\Delta s$  of the line segment MO (or OP) is given by

$$\begin{aligned}\Delta s &= \Delta z/\mu, & \text{if the ray hits the } XY \text{ plane,} \\ \Delta s &= \Delta y/\gamma, & \text{if the ray hits the } XZ \text{ plane,} \\ \Delta s &= \Delta x/\eta, & \text{if the ray hits the } YZ \text{ plane.}\end{aligned}\tag{6.23}$$

Here  $\Delta x$ ,  $\Delta y$  and  $\Delta z$  are incremental lengths (positive or negative) between two successive grid points on the  $X$ ,  $Y$  and  $Z$  directions respectively. In the short characteristics method, the irreducible Stokes vector  $\mathcal{I}$  at O is given by

$$\begin{aligned}\mathcal{I}_O(\mathbf{r}, \boldsymbol{\Omega}, x) &= \mathcal{I}_M(\mathbf{r}, \boldsymbol{\Omega}, x) \exp[-\Delta\tau_M] \\ &+ \psi_M(\mathbf{r}, \boldsymbol{\Omega}, x)\mathcal{S}_M(\mathbf{r}, x) + \psi_O(\mathbf{r}, \boldsymbol{\Omega}, x)\mathcal{S}_O(\mathbf{r}, x) + \psi_P(\mathbf{r}, \boldsymbol{\Omega}, x)\mathcal{S}_P(\mathbf{r}, x),\end{aligned}\tag{6.24}$$

where  $\mathcal{S}_{M,O,P}$  are the irreducible source vectors at M, O and P. The quantity  $\mathcal{I}_M$  is the upwind irreducible Stokes vector for the point O. If M and P are non-grid points, then  $\mathcal{S}_{M,P}$  and  $\mathcal{I}_M$  are computed using a two-dimensional parabolic interpolation formula. While computing them, one has to ensure the monotonicity of all the 6 components of these vectors, through appropriate logical tests (see Auer & Paletou 1994). The coefficients  $\psi$  depend on the optical depth increments in  $X$ ,  $Y$  and  $Z$  directions. For a 2D geometry, these coefficients are given in Auer & Paletou (1994). Here we have used a generalized version of these coefficients, that are applicable to a 3D geometry.

## 6.5 Numerical method of solution

In this chapter we generalize the Pre-BiCG-STAB method described in chapter 5 to the case of a 3D geometry. The present work represents also an extension of this technique to the case of polarized RT in the presence of an oriented magnetic field. The essential difference between the 2D and 3D algorithms is in terms of the lengths of the vectors. In a 2D geometry it is  $n_p \times n_x \times n_Y \times n_Z$  whereas in a 3D geometry it is  $n_p \times n_x \times n_X \times n_Y \times n_Z$ , where  $n_{X,Y,Z}$  are the number of grid points in the  $X$ ,  $Y$  and  $Z$  directions, and  $n_x$  refers to the number of frequency points.  $n_p$  is the number of polarization components of the irreducible vectors. In the presence of a magnetic field,  $n_p = 6$  in both 2D and 3D geometries. In non-magnetic problems,  $n_p = 4, 6$  for 2D and 3D geometries respectively.

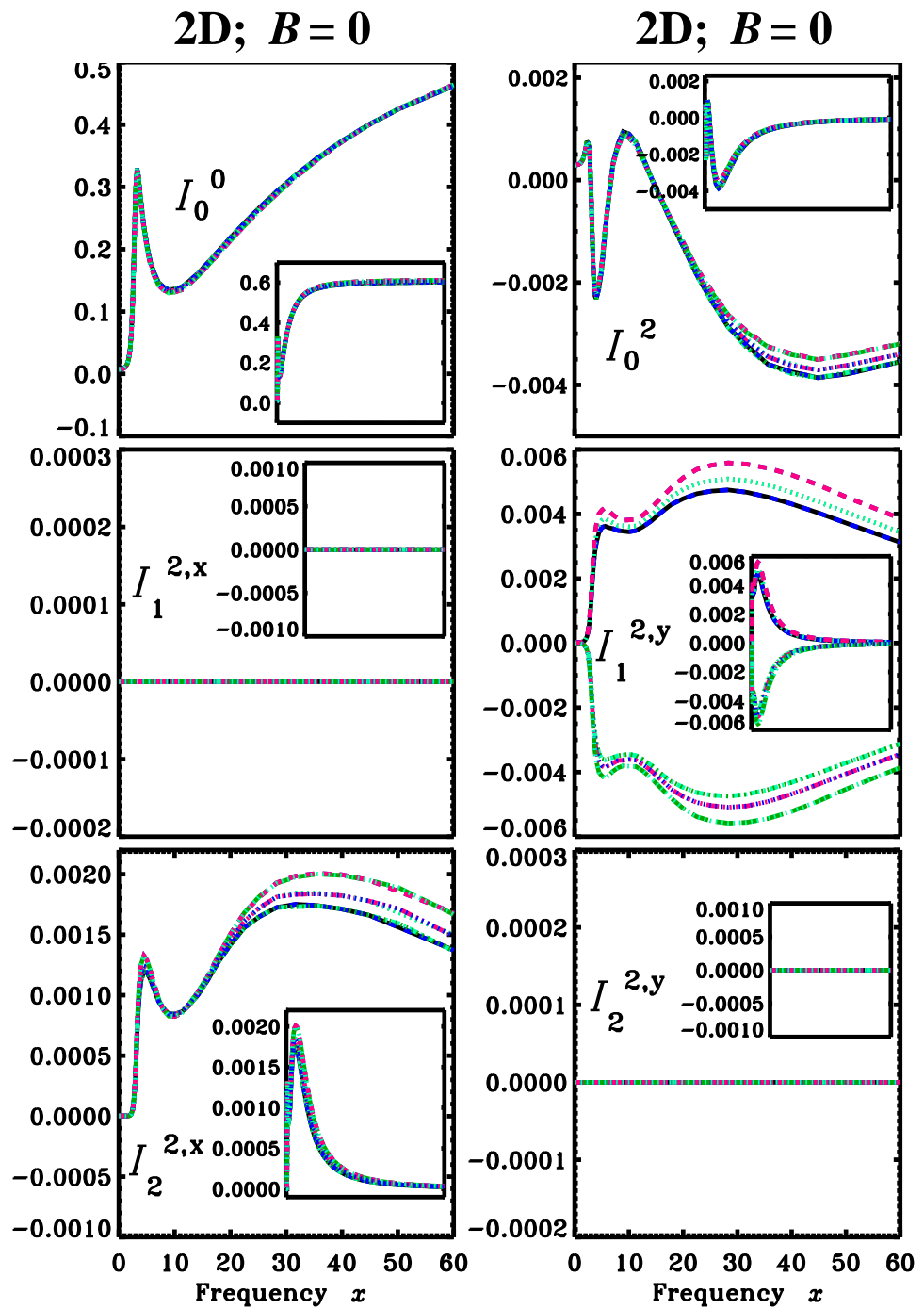


**Figure 6.5:** The emergent, spatially averaged irreducible Stokes vector components formed in a non-magnetic 2D medium. Different curves represent different values of the radiation azimuth  $\varphi$ . The value of  $\mu = 0.11$ . The other model parameters are given in Section 6.6.1. The inset panels show the far wing behavior of  $\mathcal{I}$ . The  $x$  grid for these inset panels is  $0 \leq x \leq 600$ .

### 6.5.1 The Preconditioner matrix

A description of the preconditioner matrix that appears in the Pre-BiCG-STAB method, is already given in chapter 5. Here we give its functional form applicable to the problems considered in this chapter. In chapter 5 a single preconditioner matrix was sufficient to handle the non-magnetic line transfer problem with PRD. The presence of magnetic field requires the use of domain based PRD matrices, for a better description of the PRD in line scattering. The method requires preconditioner matrices to be defined, that are suitable for each of the frequency domains. We denote the preconditioner matrices by  $\hat{\mathcal{M}}^{(i)}$ .

$$\hat{\mathcal{M}}^{(i)} = \hat{I} - p_x \frac{1}{\phi(x)} \left\{ \Lambda_{x',\text{II}}^{\star(i)} r_{\text{II}}(x, x') + \Lambda_{x',\text{III}}^{\star(i)} r_{\text{III}}(x, x') \right\}, \quad (6.25)$$

where

$$\Lambda_{x',\text{II}}^{\star(i)} = \oint \frac{d\Omega'}{4\pi} \hat{W} \hat{M}_{\text{II}}^{(i)}(\mathbf{B}) \hat{\Psi}(\Omega') \mathcal{I}(\mathbf{r}, \Omega', x'), \quad (6.26)$$

and

$$\Lambda_{x',\text{III}}^{\star(i)} = \oint \frac{d\Omega'}{4\pi} \hat{W} \hat{M}_{\text{III}}^{(i)}(\mathbf{B}) \hat{\Psi}(\Omega') \mathcal{I}(\mathbf{r}, \Omega', x'). \quad (6.27)$$

Here  $\mathcal{I}(\mathbf{r}, \Omega', x')$  is computed using a delta source vector as input. The expressions for the matrices  $\hat{M}_{\text{II}}^{(i)}$  and  $\hat{M}_{\text{III}}^{(i)}$  in different domains are given in Appendix I. The matrices  $\hat{\mathcal{M}}^{(i)}$  are block diagonal. Each block is a full matrix with respect to  $x$  and  $x'$ . The matrices  $\hat{\mathcal{M}}^{(i)}$  are diagonal with respect to other variables.

### 6.5.2 Computational details

To calculate the integral in Equation (6.19) and the formal solution in Equation (6.24), we need to define quadratures for angles, frequencies and depths. For all the computations presented in this chapter, Carlsson type B angular quadrature with an order  $n = 8$  is used. All the results are presented in this chapter for damping parameter  $a = 10^{-3}$ . The number of frequency points required for a given problem depends on the value of  $a$  and the optical thickness in the  $X$ ,  $Y$  and  $Z$  directions (denoted by  $T_X$ ,  $T_Y$  and  $T_Z$ ). A frequency bandwidth satisfying the conditions  $\phi(x_{\text{max}})T_X \ll 1$ ,  $\phi(x_{\text{max}})T_Y \ll 1$  and  $\phi(x_{\text{max}})T_Z \ll 1$  at the largest frequency point denoted by  $x_{\text{max}}$  has been used. We have used a logarithmic frequency grid with a fine spacing in the line core region, and the near wings where the PRD effects are important. We use a logarithmic spacing in the  $X$ ,  $Y$  and  $Z$  directions, with a fine gridding near the boundaries. We find that with the modern



solution methods used in the calculations give sufficiently accurate solutions for 5 spatial points per decade.

Computing time depends on the number of angle, frequency and depth points considered in the calculations and also the machine used for computations. We use the Intel(R) Core(TM) i5 CPU 760 at 2.8 GHz processor running an un-parallelized code. For the difficult test case of a semi-infinite 3D atmosphere the computing time is approximately an hour for one iteration. Even for this difficult test case the Pre-BiCG-STAB method needs just 18 iterations to reach a convergence criteria of  $10^{-8}$ .

## 6.6 Results and discussions

In this section we present the results of computations to illustrate broader aspects of the polarized transfer in 1D, 2D and 3D media. We present simple test cases (which can be treated as benchmarks), to show the nature of these solutions. In all the calculations we assume the atmosphere to be isothermal.

We organize our discussions in terms of two effects. One is macroscopic in nature—namely the effect of RT on the Stokes profiles formed in 2D and 3D media. Another is microscopic in nature—namely the effect of an oriented weak magnetic field on line scattering (Hanle effect). We discuss how these two effects act together on the polarized line formation.

### 6.6.1 The Stokes profiles formed due to resonance scattering in 2D and 3D media

A discussion on the behavior of Stokes profiles formed in 1D media with PRD scattering can be found in Faurobert (1988) and Nagendra et al. (1999). In chapter 5, the nature of profiles in a 2D semi-infinite medium is compared with those formed in 1D semi-infinite medium for CRD and PRD scattering (see Figures 5.8 and 5.9 in chapter 5). Here we discuss the emergent, spatially averaged  $\mathcal{I}$  and  $(I, Q/I, U/I)$  in 2D and 3D media for PRD scattering.

Figures 6.5 and 6.6 show the frequency dependence of the components of emergent, spatially averaged  $\mathcal{I}$  in 2D and 3D media respectively. The model parameters are,  $T_X = T_Y = T_Z = T = 2 \times 10^9$ ,  $a = 10^{-3}$ ,  $\Gamma_E/\Gamma_R = 10^{-4}$ ,  $\Gamma_I/\Gamma_R = 10^{-4}$ ,  $\kappa_c/\kappa_l = 10^{-7}$ , and  $\mu = 0.11$ . Our choice of collisional parameters represent a situation in which  $r_{II}$  type scattering dominates. Different curves in each panel represent different radiation azimuths

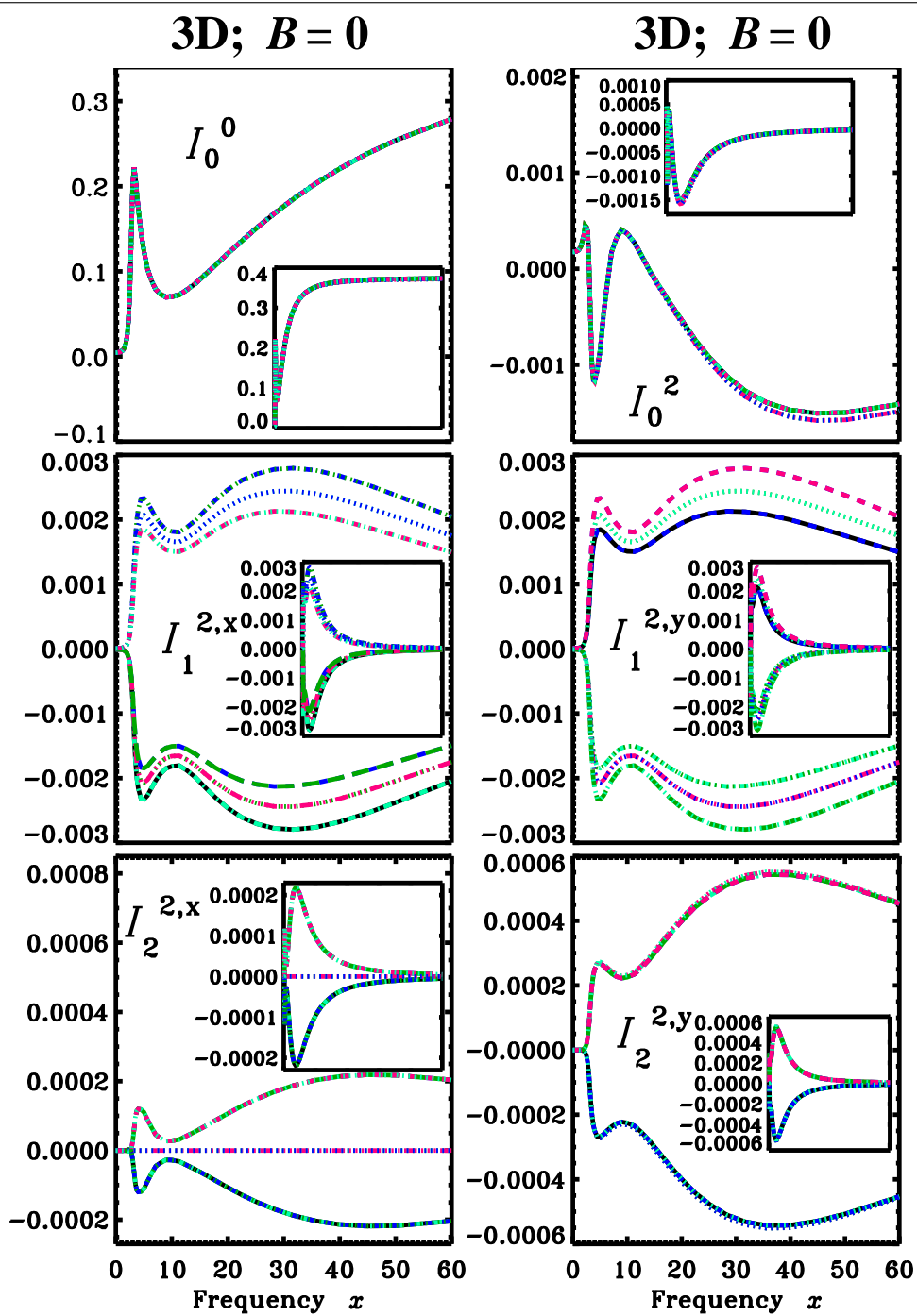
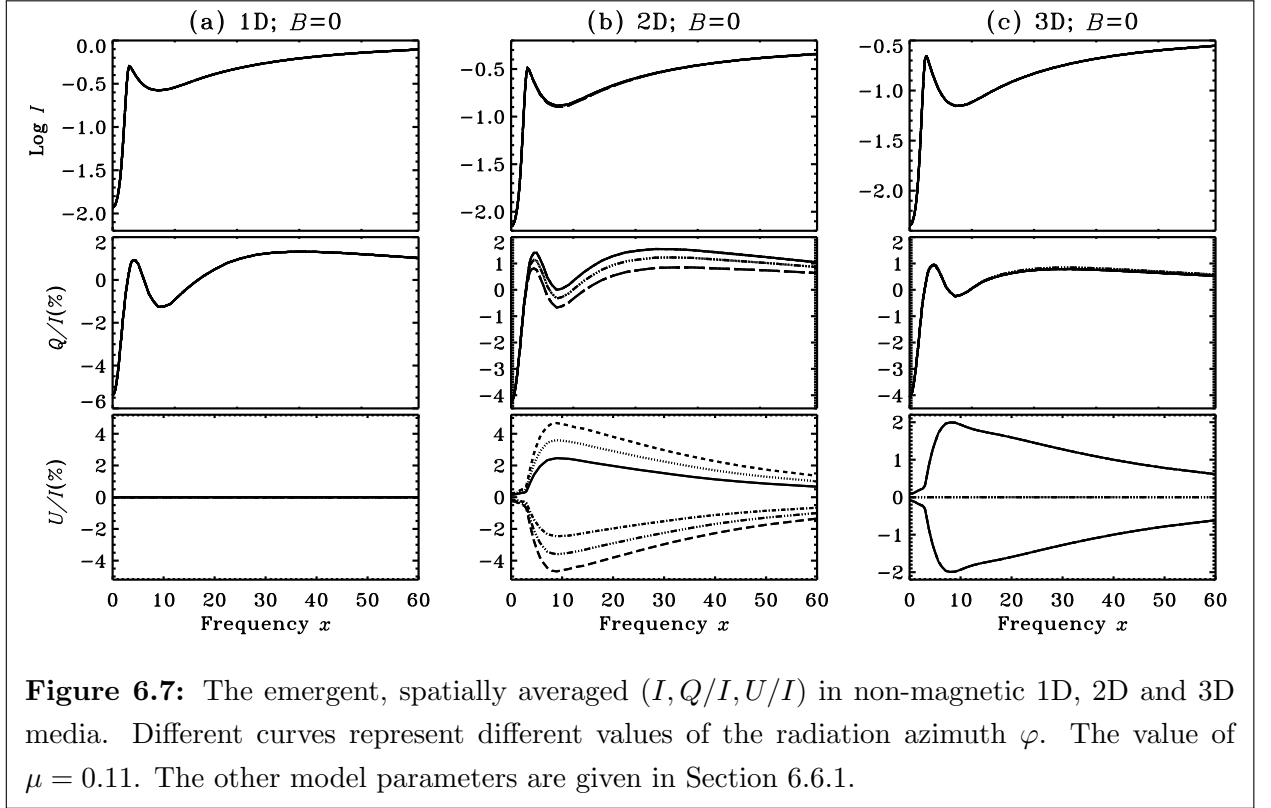


Figure 6.6: Same as Figure 6.5 but for a 3D medium.



$\varphi_i (i = 1, 12) = 60, 45, 30^\circ, 300^\circ, 315^\circ, 330^\circ, 120^\circ, 135^\circ, 150^\circ, 240^\circ, 225^\circ, 210^\circ$ .

$I_0^0$  is the largest of all the components. For the chosen model parameters, all the other non-zero components are of the same order of magnitude. The components  $I_1^{2,x}$  and  $I_2^{2,y}$  are zero in a 2D geometry due to symmetry reasons (see Appendix F for a proof).

The  $\varphi$  dependence of the  $\mathcal{I}$  comes from the  $\varphi$  dependence of the scattering phase matrix ( $\hat{\Psi}$ ) elements. The spatial distribution of  $\mathcal{I}$ , on the top surface depends sensitively on the monochromatic optical depths for the ray at these spatial points. This is a transfer effect within the medium, for the chosen ray direction. In the line core frequencies ( $x \leq 3$ ), the monochromatic optical depths are larger, resulting in a relatively uniform spatial distribution of  $\mathcal{I}$  on the top surface. The  $\varphi$  dependence appears as either symmetric or anti-symmetric with respect to the  $X$ -axis from which  $\varphi$  is measured. Thus the spatial averaging leads to a weak dependence of  $\mathcal{I}$  on the azimuth angle  $\varphi$ . When the averaging is performed over sign changing quantities like the polarization components, it leads to cancellation, resulting in vanishing of these components.

The  $\varphi$  dependence of  $\mathcal{I}$  in the line wings can be understood by considering the action of the first column elements of the  $\hat{\Psi}$  matrix on  $I_0^0$ , which is the largest among all the

components. The elements of  $\hat{\Psi}$  matrix are listed in Appendix J.  $I_0^0$  is independent of  $\varphi$  because it is controlled by the element  $\Psi_{11}$  which takes a constant value unity. Similarly  $I_0^2$  is controlled by  $\Psi_{21}$  which is also independent of  $\varphi$ . However we see a weak  $\varphi$  dependence of  $I_0^2$  in the wings, which is due to the coupling of the last 4 components to  $I_0^2$ , which are of equal order of magnitude as  $I_0^2$ , and are sensitive to the values of  $\varphi$ . The  $\varphi$  dependence of  $I_1^{2,y}$  and  $I_2^{2,x}$  elements in both 2D and 3D geometries is controlled by  $\sin \varphi$  and  $\cos 2\varphi$  functions appearing in  $\Psi_{41}$  and  $\Psi_{51}$  elements respectively. The distribution of angle points  $\varphi$  in Carlson B quadrature is such that among the 12  $\varphi$  values in the grid,  $\sin \varphi$  takes only 6 distinct values, and  $\cos 2\varphi$  takes only 3 distinct values (see Table 6.1). The components  $I_1^{2,x}$  and  $I_2^{2,y}$  are non-zero in 3D geometry unlike the 2D case. Their magnitudes are comparable to those of  $I_1^{2,y}$  and  $I_2^{2,x}$ . The  $\varphi$  dependence of these components are controlled by  $\cos \varphi$  and  $\sin 2\varphi$  functions appearing in  $\Psi_{31}$  and  $\Psi_{61}$  elements. In the far wings, all the components of  $\mathcal{I}$  go to their continuum values, as shown in the inset panels of Figures 6.5 and 6.6. In a 1D geometry  $I_0^0$  reaches the value of  $B_\nu$  (parameterized as 1 here) in the far wings where the source function is dominated by  $B_\nu$ . This is because of the fact that the formal solution with  $B_\nu$  as source function along a given ray leads to terms of the form  $B_\nu[1 - \exp(-\tau_x(\mathbf{r}, \boldsymbol{\Omega}))]$ . In 1D medium  $\tau_x(\mathbf{r}, \boldsymbol{\Omega}) = T\kappa_{\text{tot}}/\mu$ . This implies that for semi-infinite 1D medium,  $\exp(-\tau_x(\mathbf{r}, \boldsymbol{\Omega})) = 0$  so that  $I_0^0 = B_\nu$  in the far wings. However in semi-infinite 2D and 3D media the distances traveled by the rays in a given direction at different spatial points on the top surface are not always the same and therefore  $\exp(-\tau_x(\mathbf{r}, \boldsymbol{\Omega}))$  is not always zero unlike the 1D case. Further the radiation drops sharply near the edges due to finiteness of the boundaries. Therefore when we perform spatial averaging of emergent  $I_0^0$  over such different spatial points on the top surface of a 2D medium (which is actually a line),  $I_0^0$  will take a value smaller than  $B_\nu$ . For a similar reason (averaging over a plane) the value of  $I_0^0$  in the far wings in a 3D medium becomes even smaller than the value in a 2D medium. All other components reach zero in the far wings because the radiation is unpolarized in the far wings (because of an unpolarized continuum).

The way in which the components of  $\mathcal{I}$  depend on  $\varphi$  is different in 2D and 3D geometries (compare Figures 6.5 and 6.6). This is a direct effect of spatial averaging. In a 2D medium, spatial averaging of the profiles is performed over the line  $(Y, Z_{\text{max}})$  marked in Figure 6.1, whereas in a 3D medium the averaging is performed over the plane  $(X, Y, Z_{\text{max}})$  marked in Figure 6.1. The 2D spatial averaging actually samples only a part of the plane considered for averaging in a 3D medium. Also, 2D geometry has an implicit assumption of front-back symmetry of the polarized radiation field with respect to the infinite  $X$  axis in the

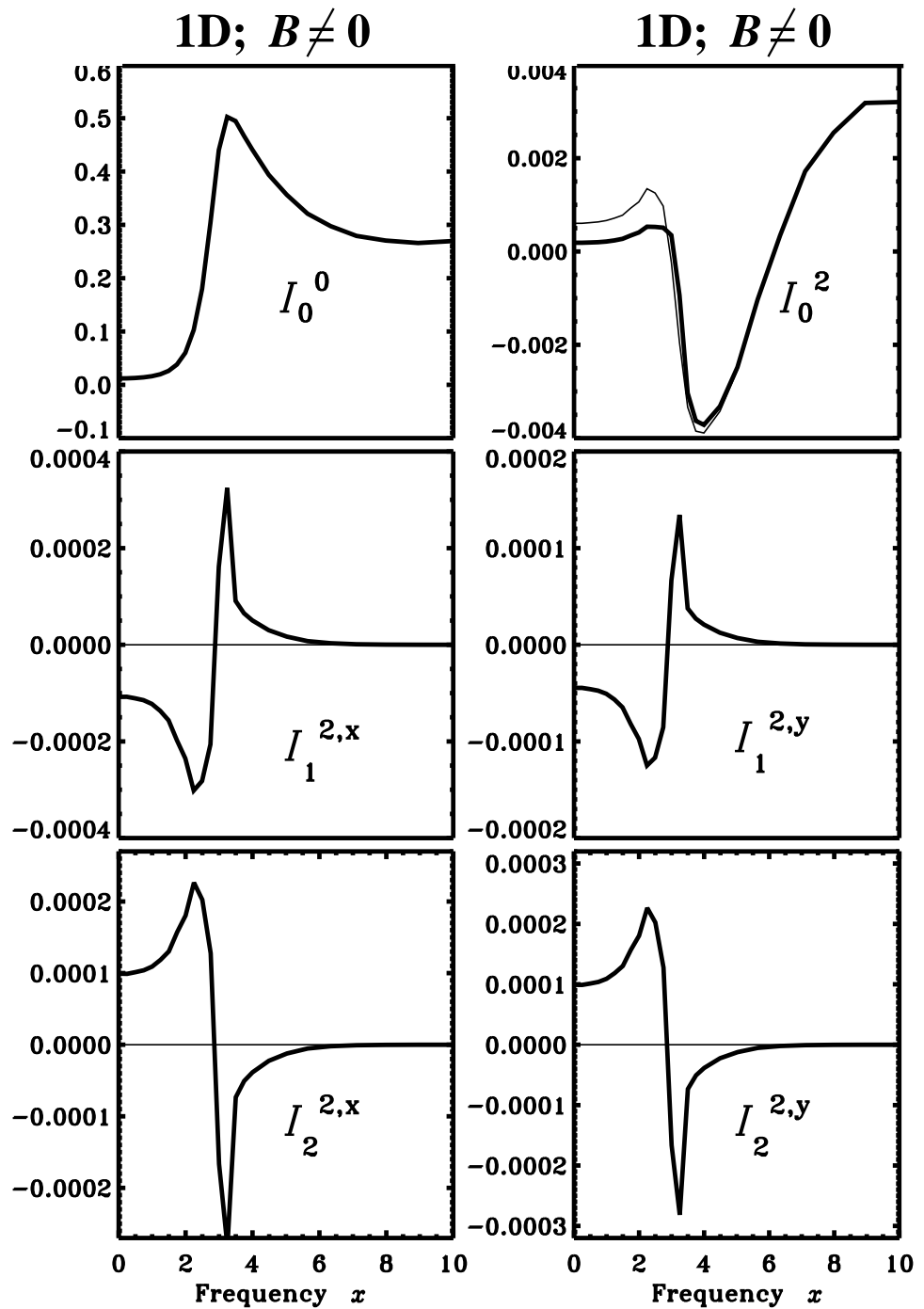


**Figure 6.8:** Same as Figure 6.5 but for a magnetic 1D medium. The vector magnetic field is represented by  $(\Gamma, \theta_B, \chi_B) = (1, 90^\circ, 68^\circ)$ . The thin solid lines show the corresponding non-magnetic components.

non-magnetic case, namely

$$\begin{aligned}
I(\mathbf{r}, \theta, \varphi, x) &= I(\mathbf{r}, \theta, \pi - \varphi, x), \\
I(\mathbf{r}, \theta, \pi + \varphi, x) &= I(\mathbf{r}, \theta, 2\pi - \varphi, x), \\
Q(\mathbf{r}, \theta, \varphi, x) &= Q(\mathbf{r}, \theta, \pi - \varphi, x), \\
Q(\mathbf{r}, \theta, \pi + \varphi, x) &= Q(\mathbf{r}, \theta, 2\pi - \varphi, x), \\
U(\mathbf{r}, \theta, \varphi, x) &= -U(\mathbf{r}, \theta, \pi - \varphi, x), \\
U(\mathbf{r}, \theta, \pi + \varphi, x) &= -U(\mathbf{r}, \theta, 2\pi - \varphi, x), \theta \in [0, \pi], \varphi \in [0, \pi/2].
\end{aligned} \tag{6.28}$$

See Appendix F for a proof of Equation (6.28). However no such assumptions are involved in 3D geometry.

Figures 6.7(a), (b) and (c) show  $I, Q/I, U/I$  profiles in non-magnetic 1D, 2D and 3D media. Intensity  $I$  decreases monotonically from 1D to the 3D case, because of the leaking of radiation through the finite boundaries in the lateral directions which is specific to RT in 2D and 3D geometries. In panels (b) and (c), different curves represent different  $\varphi$  values. Only one curve is shown in panel (a), because of the axi-symmetry of the radiation field in the 1D medium. For the same reason,  $|U/I|_{1D} = 0$ . The  $\varphi$  dependence of  $|Q/I|_{2D,3D}$  and  $|U/I|_{2D,3D}$  directly follow from those of the components of  $\mathcal{I}$  shown in Figures 6.5 and 6.6, and their combinations (see Appendix G in this chapter where we list the formulae used to construct the Stokes vector  $(I, Q, U)^T$  from the irreducible components of  $\mathcal{I}$ ). At the line center,  $[U/I]_{2D,3D} \sim 0$ . This is because  $U/I$  is zero in large parts of the top surface and the positive and negative values of  $U/I$  at  $x = 0$  are nearly equally distributed in a narrow region near the edges. A spatial averaging of such a distribution leads to cancellation giving a net value of  $U/I$  approaching zero. This is not the case in wing frequencies of the  $U/I$  profile (see discussions in Section 6.6.3 for spatial distribution of  $Q/I$  and  $U/I$ ).

### 6.6.2 The Stokes profiles in 2D and 3D media in the presence of a magnetic field

Figures 6.8, 6.9 and 6.10 show all the 6 components of  $\mathcal{I}$  in magnetized 1D, 2D and 3D media respectively. The vector magnetic field  $\mathbf{B}$  is represented by  $(\Gamma, \theta_B, \chi_B) = (1, 90^\circ, 68^\circ)$ . The corresponding non-magnetic components are shown as thin solid lines. Different line types in Figures 6.9 and 6.10 correspond to different  $\varphi$ . The irreducible components in 1D geometry are cylindrically symmetrical, even when there is an oriented magnetic field. Therefore there is only one curve in each panel in Figure 6.8. When  $\mathbf{B} = 0$  the 4 components  $I_{1,2}^{2,x,y}$  become zero due to axi-symmetry in 1D geometry (Figure 6.8). These

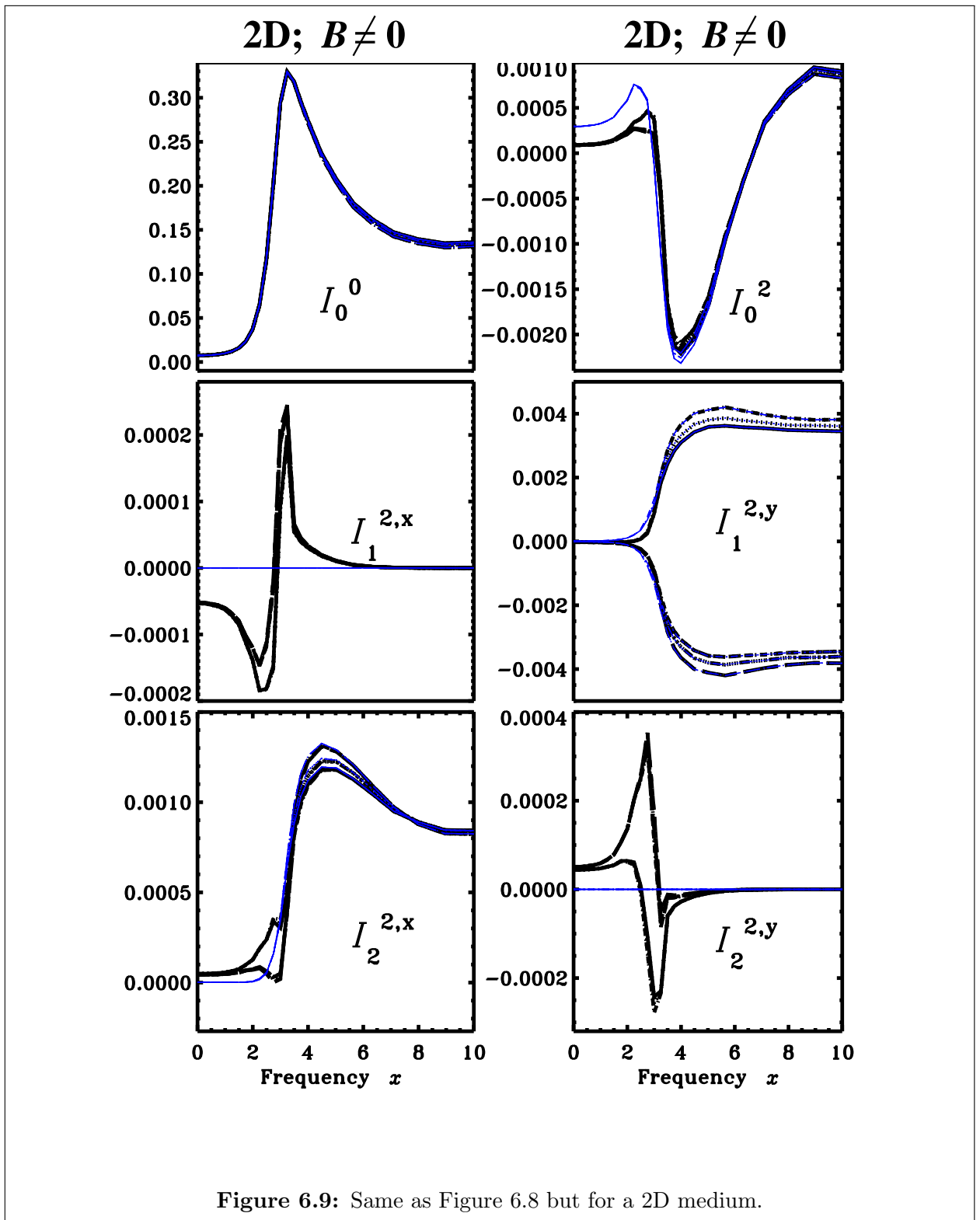


Figure 6.9: Same as Figure 6.8 but for a 2D medium.

components take non-zero values in the line core when  $\mathbf{B} \neq 0$ . The magnitudes of  $I_0^0$  and  $I_0^2$  monotonically decrease from 1D to 3D. In the 2D case, the 2 components which were zero when  $\mathbf{B} = 0$ , take non-zero values in the line core, when  $\mathbf{B} \neq 0$ . Unlike 1D geometry in 2D and 3D geometries, a non-zero  $\mathbf{B}$  causes the last 4 components to become sensitive to  $\varphi$ . The components  $I_1^{2,y}$  in 2D and  $I_1^{2,x}$  and  $I_1^{2,y}$  in 3D remain almost unaffected by  $\mathbf{B}$ . This behavior is particular to the present choice of  $\mathbf{B}$ . For a different choice of  $\mathbf{B}$ , the behavior of the 6 components may differ from what is shown in these figures. In all the geometries, the components go to their non-magnetic (Rayleigh scattering) values in the wings, because the Hanle effect operates only in the line core region.

Figures 6.11(a), (b) and (c) show spatially averaged  $I$ ,  $Q/I$ ,  $U/I$  in 1D, 2D and 3D geometries respectively. Due to the finiteness of the boundaries in 2D and 3D media the value of spatially averaged  $I$  decreases monotonically from 1D to 3D. The dependence of  $Q/I$  and  $U/I$  on  $\varphi$  in 1D medium is purely due to the  $\varphi$  dependence coming from the formulae used to convert  $\mathcal{I}$  to  $I$ ,  $Q$  and  $U$  (see Appendix G). In 2D and 3D media, the  $\varphi$  dependence comes from both, the  $\varphi$  dependence of the respective components of  $\mathcal{I}$ , and also the above mentioned conversion formulae. The magnitudes of  $Q/I$  and  $U/I$  decrease in 2D and 3D geometries due to the spatial averaging process. The wings of  $Q/I$  and  $U/I$  in 1D are insensitive to  $\varphi$  due to the inherent axi-symmetry. In 2D they become more sensitive to  $\varphi$  values. Again they become weakly sensitive to  $\varphi$  in 3D geometry. These differences in sensitivities of  $Q/I$ ,  $U/I$  to the azimuth angle  $\varphi$  in 2D and 3D geometries is due to the way in which the spatial averaging is performed in these geometries (see discussions above Equation (6.28)).

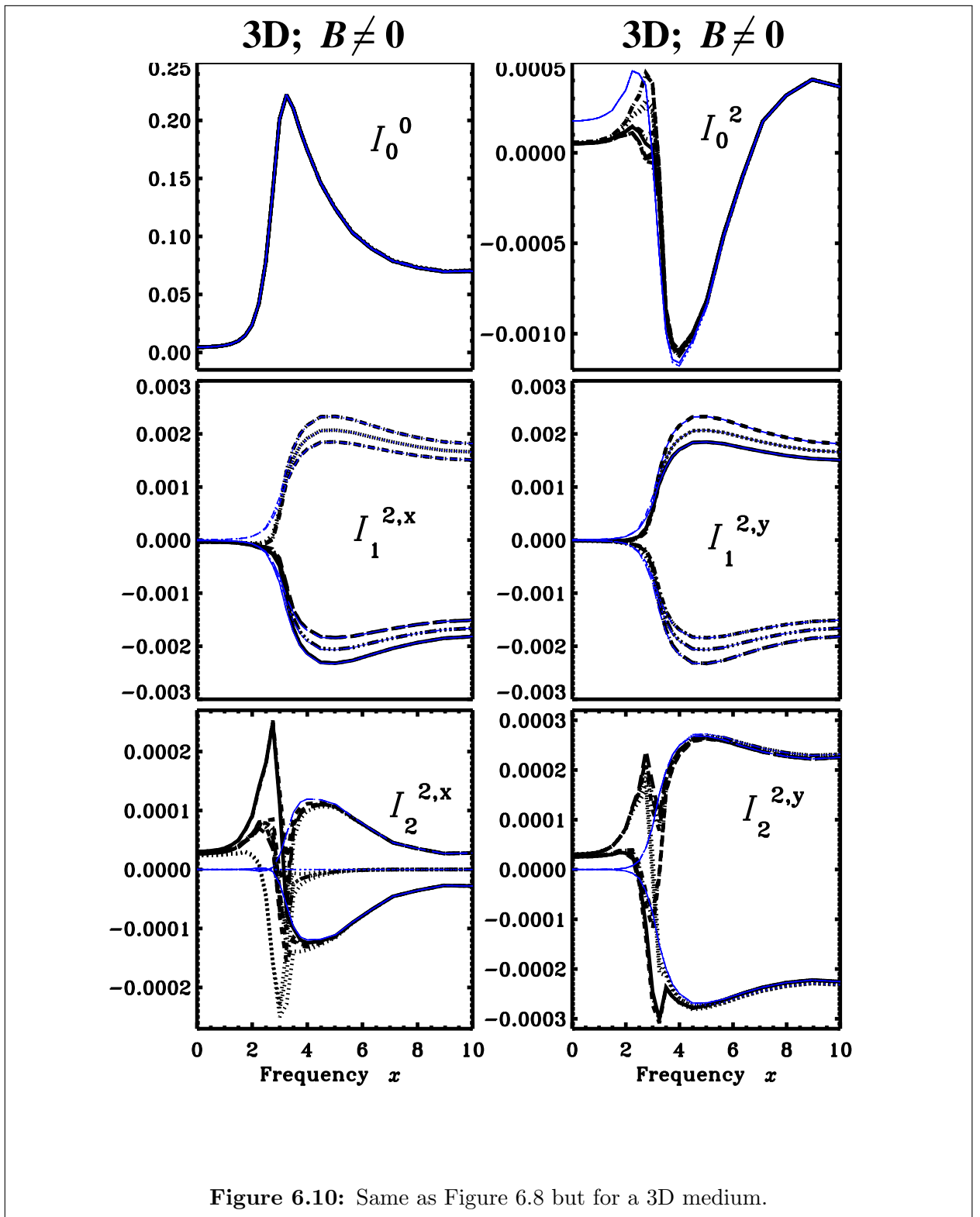
### Polarization diagrams in 1D and 2D media

In Figure 6.12 we show polarization diagrams (see e.g., Stenflo 1994), which are plots of  $Q/I$  versus  $U/I$  for a given value of frequency  $x$ , ray direction  $(\mu, \varphi)$ , and varying the field parameters two out of three at a time. We take  $\Gamma = 1$ , and vary  $\theta_B$  and  $\chi_B$  values. For the 2D case we show spatially averaged quantities.

For  $x = 0$ , the shapes of closed curves (loops) in the polarization diagrams are the same in both 1D and 2D cases. When compared to the loops in 1D, the sizes of the loops in 2D are smaller by about 1% in the magnitudes of  $Q/I$  and  $U/I$ , which is due to spatial averaging.

For  $x = 2.5$ , the shapes of the the loops in 2D are quite different from those for 1D. For e.g., the solid curve in panel (d) is narrower than the one in panel (b) which correspond





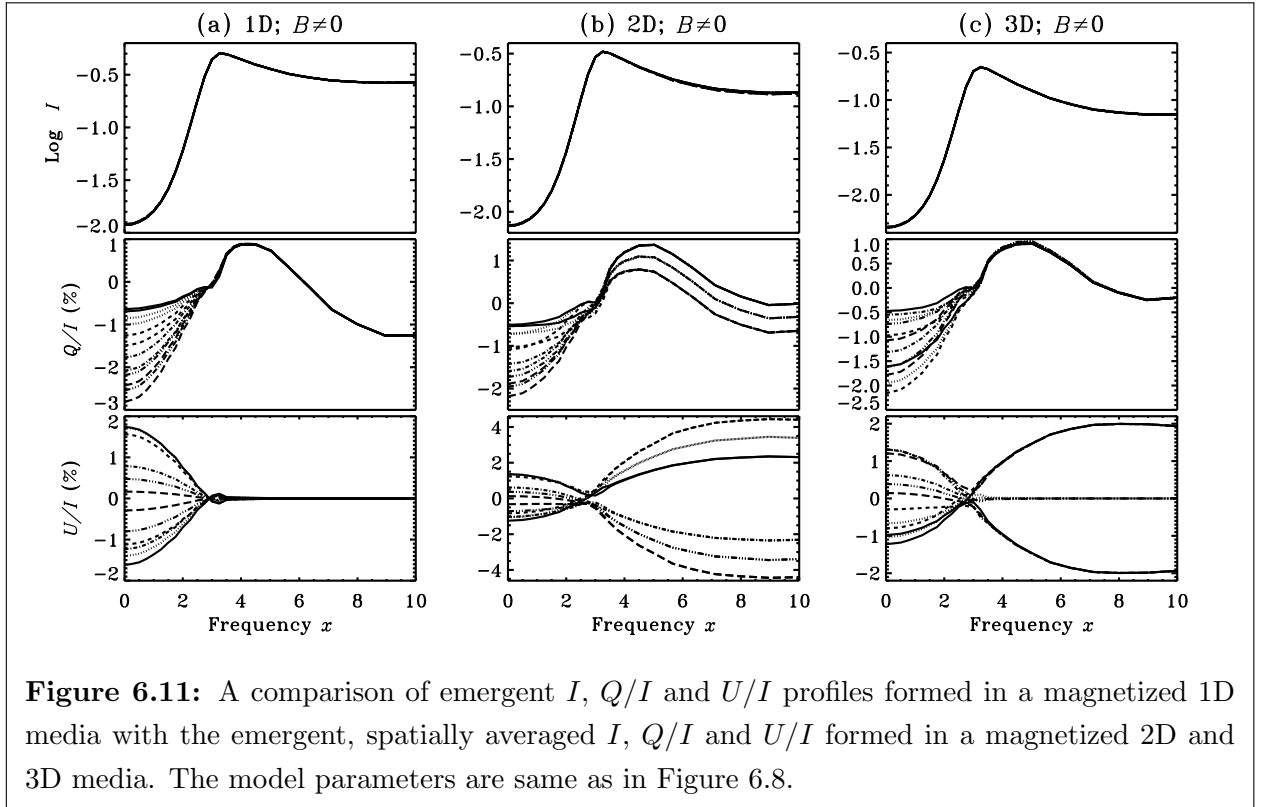
to  $\theta_B = 30^\circ$ . On the other hand, the dash-triple-dotted curve in panel (d) is broader than the one in panel (b), which correspond to  $\theta_B = 120^\circ$ . The orientation of a given loop with respect to the vertical line ( $Q/I = 0$ ) is a measure of the sensitivity of  $(Q/I, U/I)$  to the field orientation  $\theta_B$ . The size of a loop is a measure of the sensitivity of  $(Q/I, U/I)$  to the field azimuth  $\chi_B$ . The values of  $|Q/I|_{2D}$  and  $|U/I|_{2D}$  can be larger or smaller than  $|Q/I|_{1D}$  and  $|U/I|_{1D}$  for  $x = 2.5$ . The sensitivity of the line wing ( $x = 2.5$ ) polarization to  $(\theta_B, \chi_B)$  is different in 1D and 2D geometries, when compared to the sensitivity of line center ( $x = 0$ ) polarization. This is because at  $x = 0$  we sample mainly the outermost layers of the semi-infinite media. At  $x = 2.5$  we actually sample internal inhomogeneities of the radiation field in  $(Y, Z)$  directions in the 2D case, and only those in the  $Z$  direction, in the 1D case. We have noticed that the spatial distribution of  $Q/I, U/I$  at  $x = 0$  is relatively more homogeneous, than at  $x = 2.5$  (see figures and discussions in Section 6.6.3 for spatial distribution of  $Q/I$  and  $U/I$ ).

### 6.6.3 The spatial variation of emergent $(Q/I, U/I)$ in a 3D medium

In Figure 6.13 we show surface plots of  $Q/I$  and  $U/I$  formed in a 3D media. The region chosen for showing the spatial distribution is the top surface plane  $(X, Y, Z_{\max})$ .

Figures 6.13(a), (b) demonstrate purely the effects of multi-D geometry on the  $(Q/I, U/I)$  profiles. In Figure 6.13(a)  $Q/I$  shows a homogeneous distribution at the interiors of the top surface (away from the boundaries) approaching a constant value ( $\sim -3.6\%$ ). Large parts of the top surface contribute to the negative values of  $Q/I$  and only a narrow region near the edges contribute to positive values. The magnitudes of  $Q/I$  sharply raise near the edges. This is due to the finite boundaries of the 3D medium. Maximum value of  $|Q/I|$  in these figures is  $\sim 6\%$ . In Figure 6.13(b)  $U/I$  is nearly zero at the interiors of the top surface. Near the edges, the values of  $U/I$  sharply raise and  $|U/I|$  takes a maximum value of  $\sim 20\%$ .

Figures 6.13(c), (d) demonstrate the effects of magnetic field on the  $(Q/I, U/I)$  profiles. The magnetic field vector is represented by  $\mathbf{B}=(\Gamma, \theta_B, \chi_B)=(1, 30^\circ, 68^\circ)$ . The nature of homogeneity at the interior and sharp raise near the edges of the 3D surface, in the values of  $Q/I$  and  $U/I$  remain similar in both the magnetic and non-magnetic cases. An important effect of  $\mathbf{B}$  is to significantly change the values of  $Q/I$  and  $U/I$  with respect to their non-magnetic values.  $|Q/I|$  values are slightly reduced at the interior and  $Q/I$  now becomes  $-2.3\%$ . Near the edges  $|Q/I|$  is significantly enhanced and takes a maximum value of  $15\%$ . The interior values of  $|U/I|$  continue to be nearly zero. The  $|U/I|$  is reduced at different



rates near different edges. Now the maximum value of  $|U/I|$  is 17%. We note that in 1D geometry, for  $\mu = 0.11$ , any magnetic field configuration always causes a decrease in  $|Q/I|$  and a fresh generation of  $|U/I|$  with respect to the non-magnetic values.

Figures 6.13(e), (f) demonstrate the effects of PRD on the  $(Q/I, U/I)$  profiles. For this purpose we have chosen a wing frequency  $x = 5$ . The spatial distribution of  $Q/I$  and  $U/I$  is highly inhomogeneous at the wing frequencies. This effect can be easily seen by comparing Figure 6.13(a) which exhibits large spatial homogeneity for  $x = 0$ , with Figure 6.13(e) which exhibits large spatial inhomogeneity for  $x = 5$ . For  $x = 0$ , the optical depth of the medium is large and therefore the radiation field in the line core becomes homogeneous over large volumes of the cube. The spatial inhomogeneity of the  $Q/I$  at  $x = 5$  is actually caused by the the nature of PRD function used in our computations (which is dominated by the  $r_{II}$  function). Due to the frequency coherent nature of  $r_{II}$ , the photons scattered in the wings get decoupled from the line core radiation field. As the optical depth of the medium in the line wings is smaller than in the line core, the wing radiation field becomes more inhomogeneous and more polarized. Same arguments are valid for the inhomogeneous distribution of  $U/I$  on the top surface of the 3D cube. This

can be seen by comparing Figure 6.13(b) with Figure 6.13(f). We recall that under the assumption of CRD, the values of  $Q/I$  and  $U/I$  are zero in the line wings (see Figure 5.9 of chapter 5 for a comparison of emergent, spatially averaged  $Q/I$ ,  $U/I$  profiles for CRD and PRD in a multi-D medium). The sharp increase in magnitudes of  $Q/I$  and  $U/I$  near the edges is larger for  $x = 5$  when compared to those for  $x = 0$ . Maximum value of  $|Q/I|$  is now 10% and that of  $|U/I|$  is 40%.

In Figure 6.14 we show spatial distribution of  $I$ ,  $Q/I$  and  $U/I$  on the top surface of two different kinds of 3D media. Here we have chosen  $\mathbf{B} = 0$  which is equivalent to the choice of a vertical magnetic field parallel to the  $Z$  axis (because, for this field geometry the Hanle effect goes to its non-magnetic Rayleigh scattering limit). In view of the possible applications, we consider a cuboid with  $T_X = T_Y = 2 \times 10^6$ ,  $T_Z = 20$  in the left panels (a, b, c) and a cuboid with  $T_X = T_Y = 20$ ,  $T_Z = 2 \times 10^6$  in the right panels (d, e, f). They represent respectively a sheet and a rod like structure. For the chosen optical thickness configurations, the radiative transfer effects are mainly restricted to the line core ( $x \leq 3$ ) for the ray emerging from the top surface. We show the results for  $x = 3$  (in the left panels) and  $x = 1$  (in the right panels), the frequencies for which the magnitudes of  $Q/I$  and  $U/I$  reach their maximum values.

In Figures 6.14(a) and (d) the intensities reach saturation values in the interiors of the top surface and drop to zero at two of the visible boundaries (where a boundary condition of zero intensity is imposed for our chosen ray emerging at the top surface).

In Figures 6.14(b) and (c) we see that  $Q/I$  and  $U/I$  take values  $\leq 1\%$  everywhere on the top surface. The magnitude of  $Q/I$  and  $U/I$  for this case are relatively less than those for the semi-infinite 3D atmospheres (compare with Figure 6.13). This can be understood using the following arguments. We are showing the results for a ray with  $(\mu, \varphi) = (0.11, 60^\circ)$  emerging from the top surface. The top surface for this figure refers to  $\tau_Z = 0$  where  $\tau_Z$  is the optical depth measured inwards in the  $Z$  direction. Using equations given in Appendix G we can write approximate expressions for  $Q$  and  $U$  at the top surface as

$$Q(\mu = 0.11, \varphi = 60^\circ, x) \approx \frac{-3}{2\sqrt{2}} I_0^2(\mu = 0.11, \varphi = 60^\circ, x), \quad (6.29)$$

$$U(\mu = 0.11, \varphi = 60^\circ, x) \approx \frac{3}{2} I_1^{2,x}(\mu = 0.11, \varphi = 60^\circ, x) + \frac{\sqrt{3}}{2} I_1^{2,y}(\mu = 0.11, \varphi = 60^\circ, x). \quad (6.30)$$

$I_0^2$  is controlled by the element  $\Psi_{21} = 3 \cos^2 \theta - 1$  (see Appendix J) which appears in

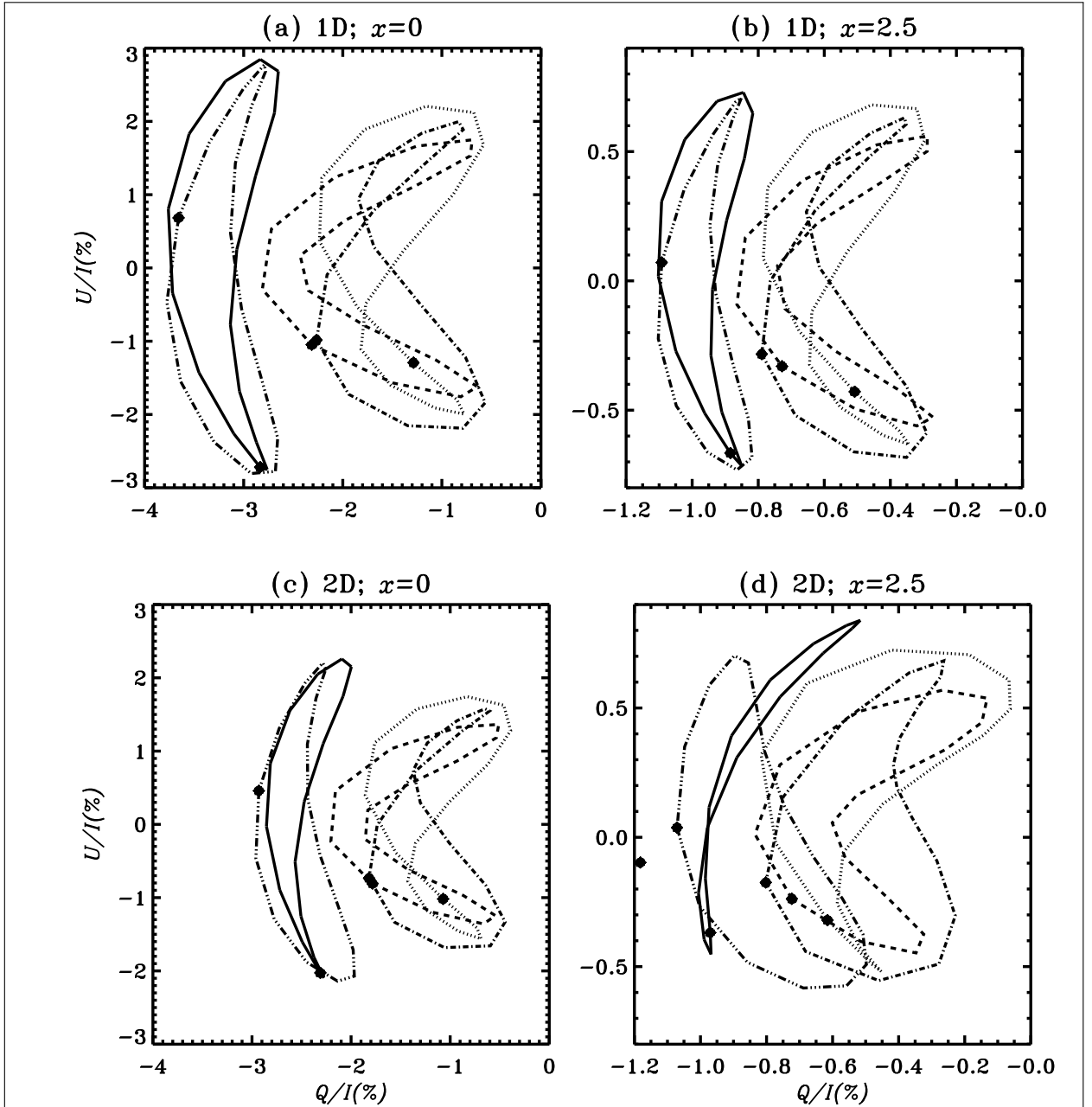


**Figure 6.12:** A comparison of the polarization diagrams in 1D and 2D media for two different values of frequency  $x$ . In 2D, the spatially averaged quantities are shown. The magnetic field parameters are given by  $\Gamma = 1$ , five values of  $\theta_B$  in the range  $30^\circ$  to  $150^\circ$  in steps of  $30^\circ$ , seventeen values of  $\chi_B$  in the range  $0^\circ$  to  $360^\circ$  in steps of  $22^\circ.5$ . Different line types correspond to different values of  $\theta_B$ . Heavy square symbol represents  $\chi_B = 0$ , and as we move in the counter-clockwise direction,  $\chi_B$  takes increasingly larger values. The ray direction is specified by  $(\mu, \varphi) = (0.11, 60^\circ)$ . The line types represent different  $\theta_B$ , namely (solid, dotted, dashed, dot-dashed, dash-triple-dotted) =  $(30^\circ, 60^\circ, 90^\circ, 120^\circ, 150^\circ)$ .

the scattering integral for  $S_0^2$ . The factor  $\Psi_{21} = 3 \cos^2 \theta - 1$  represents the probability of scattering of photons incident from the direction  $\theta$ . For  $\theta = 0^\circ$  or  $\theta = 180^\circ$  (vertical incidence)  $\Psi_{21}$  is larger in magnitude compared to the cases  $\theta = 90^\circ$  or  $\theta = 270^\circ$  (lateral incidence). For  $T_Z = 20$  the medium is effectively optically thin (because  $\epsilon T_Z \ll 1$ ) in the  $Z$  direction, and therefore photons easily escape in this direction. Thus there are smaller number of photons for incidence along the vertical direction when compared to the effectively thick case. For  $T_Z = 2 \times 10^6$  or  $T_Z = 2 \times 10^9$  the medium is effectively optically thick (because  $\epsilon T_Z \gg 1$ ) in the  $Z$  direction and therefore leaking of photons in this direction is reduced when compared to the case of  $T_Z = 20$ . In this way, for large values of  $T_Z$  the probability of photons to be incident in the vertical direction is large. Therefore, as  $T_Z$  increases the values of  $I_0^2$  and hence  $Q/I$  increase.

For the chosen line of sight, Stokes  $U$  is generated mainly by  $I_1^{2,x}$  and  $I_1^{2,y}$ . They are controlled by  $\Psi_{31}$  and  $\Psi_{41}$  elements (see Appendix J) both of which depend on the factor  $\sin 2\theta$ . This implies that  $\Psi_{31}$  and  $\Psi_{41}$  are zero for both vertical and lateral incidence of photons. These elements become larger when the incidence is predominant in the direction of  $\theta = 45^\circ$  or  $\theta = 135^\circ$ . Using similar arguments as above we can understand the increase in the values of  $U/I$  with increasing values of  $T_Z$ .

The spatial distribution of  $Q/I$  and  $U/I$  is inhomogeneous in both left and right panels for the chosen core frequencies, in contrast to the homogeneous distribution observed for semi-infinite 3D atmospheres. The extent of inhomogeneity is larger for the left panels which correspond to smaller  $T_Z$  value than for the right panels. The spatial inhomogeneity could also occur due to different optical thicknesses along the 3 spatial directions leading to different number of scatterings in the 3 directions (unlike the case of Figure 6.13 where  $T_X = T_Y = T_Z$ ). In other words, the inhomogeneities in  $Q/I$  and  $U/I$  can also be caused by a differential leaking of radiation in the  $X$ ,  $Y$  and  $Z$  directions.

## 6.7 Concluding remarks

This chapter is dedicated to certain extensions of our previous works (chapters 4 and 5) on polarized RT in multi-D media with PRD.

First, we present a generalization of the Stokes vector decomposition technique developed in chapter 4, to include the magnetic fields (Hanle effect).

Secondly, we generalize to the magnetic 3D RT, the efficient iterative method called the Pre-BiCG-STAB developed in chapter 5 for the non-magnetic 2D RT.

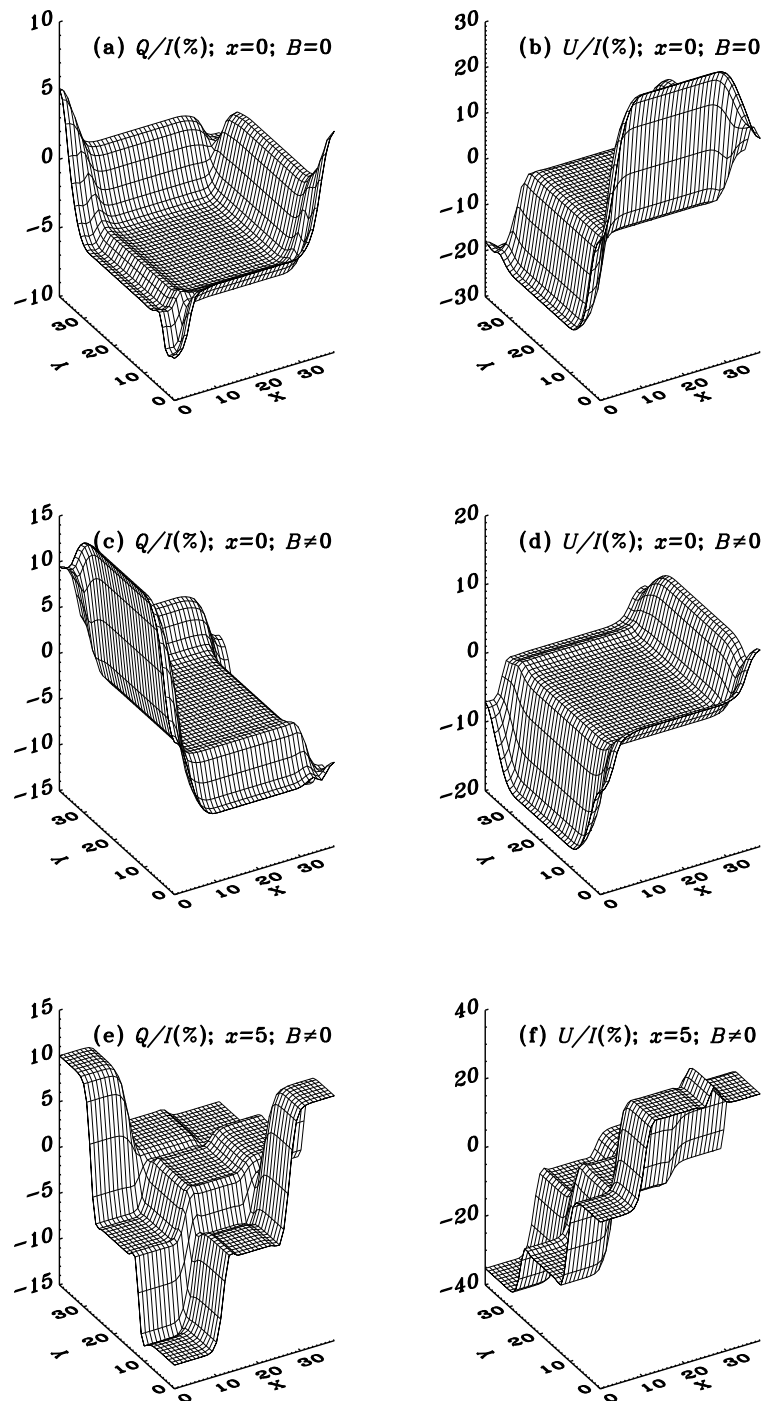


**Figure 6.13:** The spatial distribution of  $(Q/I, U/I)$  on the top surface of a 3D medium. The  $Q/I$  and  $U/I$  are plotted as a function of the grid indices of  $\tau_X$  and  $\tau_Y$ . The ray direction is specified by  $(\mu, \varphi) = (0.11, 60^\circ)$ . Panels (a) and (b) demonstrate purely the multi-D effects. Panels (c) and (d) demonstrate the magnetic field effects. Panels (e) and (f) demonstrate the PRD effects. See Section 6.6.3 for details.

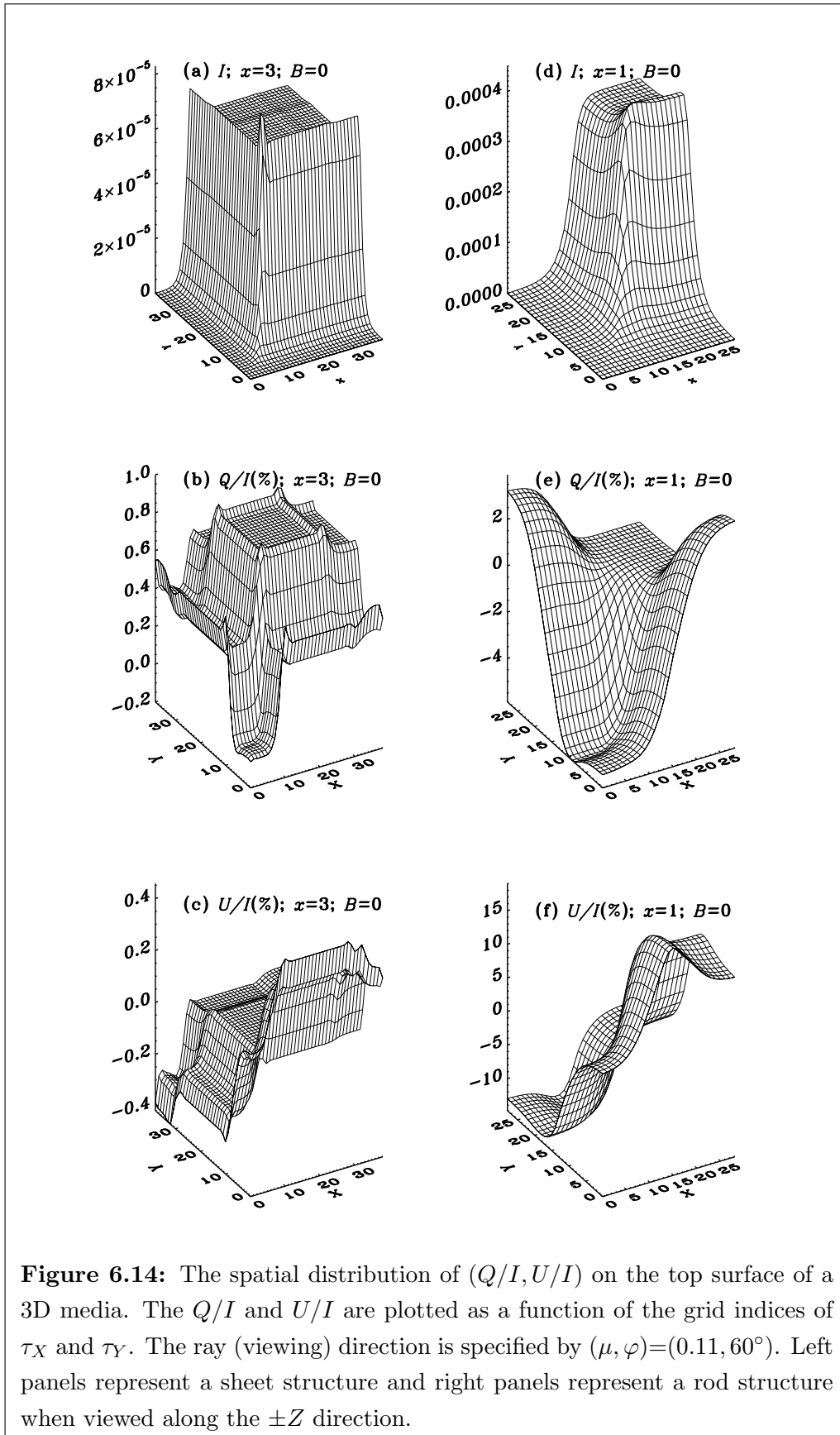


**Figure 6.14:** The spatial distribution of  $(Q/I, U/I)$  on the top surface of a 3D media. The  $Q/I$  and  $U/I$  are plotted as a function of the grid indices of  $\tau_X$  and  $\tau_Y$ . The ray (viewing) direction is specified by  $(\mu, \varphi) = (0.11, 60^\circ)$ . Left panels represent a sheet structure and right panels represent a rod structure when viewed along the  $\pm Z$  direction.



Thirdly, we use the more efficient 2D and 3D short characteristics formal solutions, with appropriate generalizations to the present context. With the linear formal solver used in chapter 4, practically it is difficult to compute the solutions in semi-infinite media. It is not the case with the short characteristics former solution method. Indeed, the solutions presented in this chapter for the difficult case of semi-infinite media, prove this fact.

We present several benchmark solutions computed using the code, with all the above mentioned generalizations. The main results of these solutions are the following.

The emergent  $(Q/I, U/I)$  profiles in 1D media and the emergent, spatially averaged  $(Q/I, U/I)$  profiles in 2D and 3D media differ significantly, both in non-magnetic and magnetic cases. The differences are more pronounced in the wings of the  $(Q/I, U/I)$  profiles. The differences between the emergent, spatially averaged  $(Q/I, U/I)$  profiles in 2D and 3D media are negligible in  $Q/I$ , but noticeable in  $U/I$ .

In the non-magnetic case, at line center, the spatial distribution of  $Q/I$  and  $U/I$  is homogeneous in the interior of the top surface, but sharply raise near the edges. This is purely a multi-D geometric effect. The presence of a magnetic field modifies this distribution by causing a depolarization (decrease in the magnitude) or re-polarization (increase in the magnitude) of  $Q/I$  and  $U/I$ . This is a natural consequence of the Hanle effect. In the line wing frequencies, magnetic and non-magnetic spatial distributions look the same, as Hanle effect is confined to the line core. However, the spatial distribution in the line wing frequency is more inhomogeneous, and the sharp raise of  $Q/I$  and  $U/I$  near the edges is more enhanced, as compared to those at the line center. This behavior at line wings is mainly due to the PRD effects. These characteristics are not noticeable if the CRD assumption is used in line formation studies.

We have developed efficient techniques to solve polarized RT in multi-D media with PRD as the scattering mechanism. In future, we try to apply these methods to understand the linear polarization observed in the spatially resolved structures on the Sun.

## New Results

This chapter concerns the effect of weak magnetic fields on line scattering. We obtain and study the first ever solution to polarized RT in magnetized multi-D atmospheres. The important results in this chapter are listed below.

1. We generalize the technique of Stokes vector decomposition in terms of the irreducible spherical tensors  $\mathcal{T}_Q^K$ , developed in chapter 4, to the case of RT with Hanle effect.
2. The fast iterative Pre-BiCG-STAB method for the solution of polarized 2D RT equation, developed in chapter 5 is now generalized to the case of RT in magnetized 3D media.
3. We use the efficient short-characteristics formal solution method for multi-D geometries, generalized appropriately to the present context.
4. A comparison of emergent  $(I, Q/I, U/I)$  profiles formed in 1D media with the corresponding emergent, spatially averaged profiles formed in multi-D media shows that in the spatially resolved structures, the assumption of 1D may lead to large errors in linear polarization, especially in the line wings.
5. The multi-D RT in semi-infinite non-magnetic media causes a strong spatial variation of the emergent  $(Q/I, U/I)$  profiles, which is more pronounced in the line wings.
6. The presence of a weak magnetic field modifies the spatial variation of the emergent  $(Q/I, U/I)$  profiles in the line core, by producing significant changes in their magnitudes.

## Chapter 7

# Angle-dependent PRD in multi-D media: Formulation

*The contents of this chapter are based on the following publication:*  
Anusha, L. S., and Nagendra, K. N. 2011c, **ApJ**, 739, 40–48

### 7.1 Introduction

The observations of the solar atmospheres reveal a wealth of information about the spatially inhomogeneous structures. Modern spectro-polarimeters with high spatial and polarimetric resolution are able to distinguish the changes in the linearly polarized spectrum caused by such structures. To model the spectro-polarimetric observations of such spatially resolved structures, one has to solve a three-dimensional (3D) polarized line radiative transfer (RT) equation. A historical account of the developments of RT in multi-dimensional (multi-D) media is presented in detail in chapter 4 (see also Anusha & Nagendra 2011a). In the previous three chapters we have been investigating the nature of linearly polarized profiles formed in multi-D media taking account of the partial frequency redistribution (PRD) in line scattering. In chapter 4 we developed a method of ‘Stokes vector decomposition’ in multi-D geometry in terms of ‘irreducible spherical tensors’  $\mathcal{T}_Q^K$  (see Landi Degl’Innocenti & Landolfi 2004). It was a generalization to the multi-D case, of the decomposition technique developed in Frisch (2007, hereafter HF07) for the one-dimensional (1D) case. In chapter 5 (see also Anusha et al. 2011a), we developed a fast numerical method called the Stabilized preconditioned Bi-Conjugate Gradient (Pre-BiCG-STAB), to solve the polarized RT problems in two-dimensional (2D) media. In chapter 6 (see also Anusha & Nagendra 2011b), we generalized the works in chapters 4 and 5 to include scattering in the presence

of weak magnetic fields (Hanle effect) in a 3D geometry. In all these chapters we considered only angle-averaged PRD functions.

The polarized Stokes line RT problems with angle-dependent PRD in 1D planar geometries were solved by several authors (see Dumont et al. 1977; McKenna 1985; Faurobert 1987, 1988; Nagendra et al. 2002; Nagendra et al. 2003; Sampoorna et al. 2011). In this formalism, a strong coupling of incident and scattered ray directions ( $\Omega'$  and  $\Omega$  respectively) prevails in the scattering phase matrices as well as the angle-dependent PRD functions, which brings in unmitigated numerical difficulties. To simplify the problem, a method based on ‘decomposition of the phase matrices’ in terms of  $\mathcal{T}_Q^K$  combined with a ‘Fourier series expansion’ of the angle-dependent redistribution functions  $r_{\text{II,III}}(x, x', \Omega, \Omega')$  of Hummer (1962) was proposed for Hanle and Rayleigh scattering by Frisch (2009, hereafter HF09) and Frisch (2010) respectively. Sampoorna et al. (2011) developed efficient numerical methods to solve angle-dependent RT problems for the case of Rayleigh scattering, based on the decomposition technique developed in Frisch (2010). Sampoorna (2011) proposed a single scattering approximation to solve the more difficult problem of RT with angle-dependent PRD including Hanle effect. However all these works are confined to the limit of 1D planar geometry.

In this chapter (see also Anusha & Nagendra 2011c) we generalize to the multi-D case, the Fourier decomposition technique developed in HF09 for the 1D case. In the first step we decompose the phase matrices in terms of  $\mathcal{T}_Q^K$  as done in chapters 4 and 6. However we now formulate a polarized RT equation for multi-D that also includes angle-dependent PRD functions. We set up an RT equation in terms of a new set of 6-dimensional vectors called as ‘irreducible source and the irreducible Stokes vectors’. In the second step, we expand the  $r_{\text{II,III}}(x, x', \Omega, \Omega')$  redistribution functions in terms of a Fourier series with respect to the azimuthal angle ( $\varphi$ ) of the scattered ray. Then we transform the original RT equation into a new RT equation which is simpler to solve because the latter has smaller number of independent variables. This simplified (reduced) RT equation can be solved by any iterative method like the Approximate Lambda Iteration (ALI) or a Bi-Conjugate Gradient type projection method.

In Table 7.1 we list the important milestones in the specific area of ‘formulation and solution of polarized RT equation’ with resonance scattering and/or Hanle effect in 1D and multi-D media in different formalisms. The emphasis is on showing how the complexity of the problem is reduced to manageable levels, by the concerted efforts of several authors. It includes a brief historical account of the formulation and decomposition of po-

larized phase matrices and the redistribution matrices for spectral lines. In the literature on this topic, the term ‘phase matrix’ refers only to the angular correlations in the polarized light scattering (see e.g., the Rayleigh scattering polarized phase matrix described in Chandrasekhar 1950). The phase matrices are in general frequency independent. The ‘redistribution matrix’ on the other hand, contains both frequency and angle correlations between the incident and scattered photons. The formulation of the redistribution matrices in the astrophysical literature (in the modern analytic form), dates back to the pioneering work of Omont et al.(1972, 1973). The references given here serve only to mark the milestones. No pretension is made to give a full list of references.

In Section 7.2 we describe the multi-D RT equation in the Stokes vector formalism. An irreducible RT equation for angle-dependent PRD functions in multi-D media is presented in Section 7.3. In Section 7.4 an RT equation in multi-D geometry for the irreducible Fourier coefficients of the Stokes source vector and the Stokes vector is established. Concluding remarks are given in Section 7.6.

## 7.2 Transfer equation in terms of Stokes parameters

For a given ray defined by the direction  $\boldsymbol{\Omega}$ , the polarized RT equation in a multi-D medium for a two-level model atom with unpolarized ground level is given by

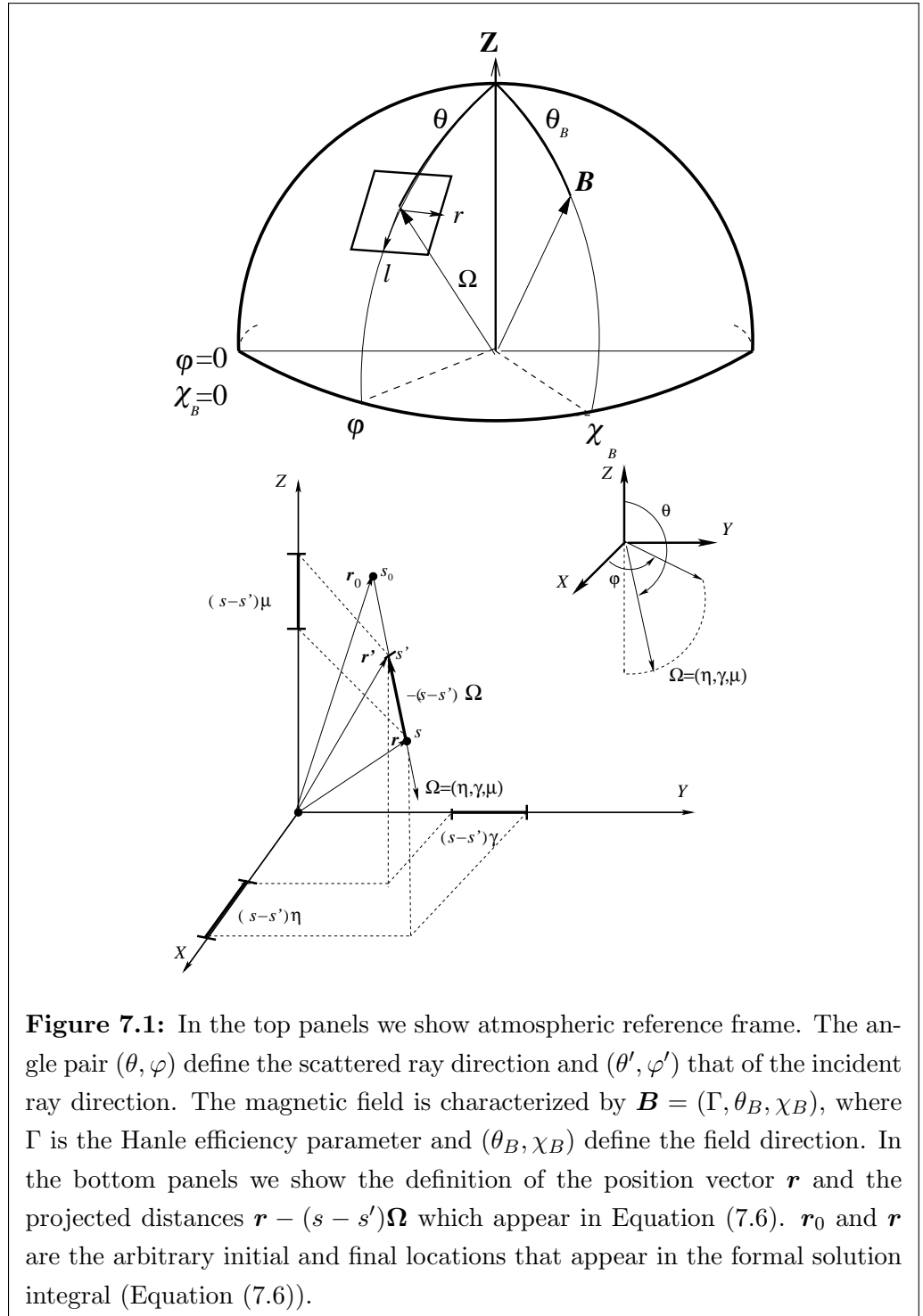
$$\boldsymbol{\Omega} \cdot \nabla \mathbf{I}(\mathbf{r}, \boldsymbol{\Omega}, x) = -[\kappa_l(\mathbf{r})\phi(x) + \kappa_c(\mathbf{r})][\mathbf{I}(\mathbf{r}, \boldsymbol{\Omega}, x) - \mathbf{S}(\mathbf{r}, \boldsymbol{\Omega}, x)]. \quad (7.1)$$

Analogous equations such as Equation (7.1) for the unpolarized case can be found in several references (see e.g., Adam 1990; Mihalas et al. 1978; Pomraning 1973). For the polarized case with PRD, the RT equations are given in chapters 4, 5 and 6. Here  $\mathbf{I} = (I, Q, U)^T$  is the Stokes vector with  $I$ ,  $Q$  and  $U$  the Stokes parameters defined as in Chandrasekhar (1950). The reference directions  $l$  and  $r$  are marked in the top panels of Figure 7.1. Positive value of  $Q$  is defined to be in a direction parallel to  $l$  and negative  $Q$  in a direction parallel to  $r$ . The quantity  $\mathbf{r} = (x, y, z)$  is the position vector of the ray in the Cartesian co-ordinate system (see bottom panels of Figure 7.1). The unit vector  $\boldsymbol{\Omega} = (\eta, \gamma, \mu) = (\sin \theta \cos \varphi, \sin \theta \sin \varphi, \cos \theta)$  defines the direction cosines of the ray in the atmosphere with respect to the atmospheric normal (the  $Z$ -axis), where  $\theta$  and  $\varphi$  are the polar and azimuthal angles of the ray (see Figure 7.1).

The quantity  $\kappa_l$  is the frequency averaged line opacity,  $\phi$  is the Voigt profile function and  $\kappa_c$  is the continuum opacity. Frequency is measured in reduced units, namely  $x = (\nu - \nu_0)/\Delta\nu_D$  where  $\Delta\nu_D$  is the Doppler width. The Stokes source vector in a two-level

**Table 7.1:** Table describing the evolution of ideas in the past three decades to simplify the difficult problem of formulating/solving the polarized line RT equation. In the text of the table, we use the following abbreviations. RTE: radiative transfer equation; AA: angle-averaged; AD: angle-dependent; PM: phase matrix; RM: redistribution matrix, CRD: complete frequency redistribution; PRD: partial frequency redistribution.

Milestones	$B = 0$ (Rayleigh scattering)	$B \neq 0$ (Hanle effect)
(1) Formulation of PM in Stokes vector formulation	Chandrasekhar (1946) Hamilton (1947)	Stenflo (1978)
(2) Stokes vector RTE : 1D/CRD	Rees (1978)	Faurobert-Scholl (1991) Nagendra et al. (2002)
(3) Stokes vector RTE : multi-D/CRD	Paletou et al. (1999)	
(4) Stokes vector RTE : 1D/PRD	Rees & Saliba (1982) : AA Dumont et al. (1977) : AD Nagendra (1986) : AA Faurobert (1987) : AA/AD	Faurobert-Scholl (1991) : AA Nagendra et al. (2002) : AA/AD
(5) PM decomposition in terms of $\mathcal{T}_Q^K$	Landi Degl'Innocenti & Landi Degl'Innocenti (1988)	Landi Degl'Innocenti & Landi Degl'Innocenti (1988)
(6) Irreducible Stokes source vector in Stokes vector RTE: 1D/CRD	Landi Degl'Innocenti et al. (1987)	Landi Degl'Innocenti et al. (1987)
(7) Irreducible Stokes source vector in Stokes vector RTE: multi-D/CRD	Manso Sainz & Trujillo Bueno (1999) Dittmann (1999)	Manso Sainz & Trujillo Bueno (1999) Dittmann (1999)
(8) Irreducible Stokes vector RTE: 1D/CRD	Frisch (2007)	Frisch (2007)
(9) Formulation of polarized RM :	Omont et al. (1972) Domke & Hubeny (1988)	Omont et al. (1973) Bommier (1997a, 1997b)
(10) RTE with RM : 1D/AA	Faurobert-Scholl (1991) Nagendra (1994)	Nagendra et al. (2002)
(11) RTE with RM : multi-D/AA	Anusha & Nagendra (2011a) Anusha et al. (2011a)	Anusha & Nagendra (2011b)
(12) RTE with RM : 1D/AD	Faurobert (1987) Nagendra et al. (2002)	Nagendra et al. (2002) Sampoorna et al. (2008c)
(13) Fourier decomposition of AD PRD functions: 1D	Frisch (2009, 2010)	Frisch (2009)
(14) RTE with RM based on Fourier expansions of AD PRD functions : 1D	Sampoorna et al. (2011)	Sampoorna (2011) Nagendra & Sampoorna (2011)
(15) a. RTE with RM : multi-D/AD b. Fourier expansion of AD PRD functions: multi-D c. RTE with RM based on Fourier expansions of AD PRD functions : multi-D	Anusha & Nagendra (2011c) and Anusha & Nagendra (2011d)	Anusha & Nagendra (2011c) and Anusha & Nagendra (2011d)



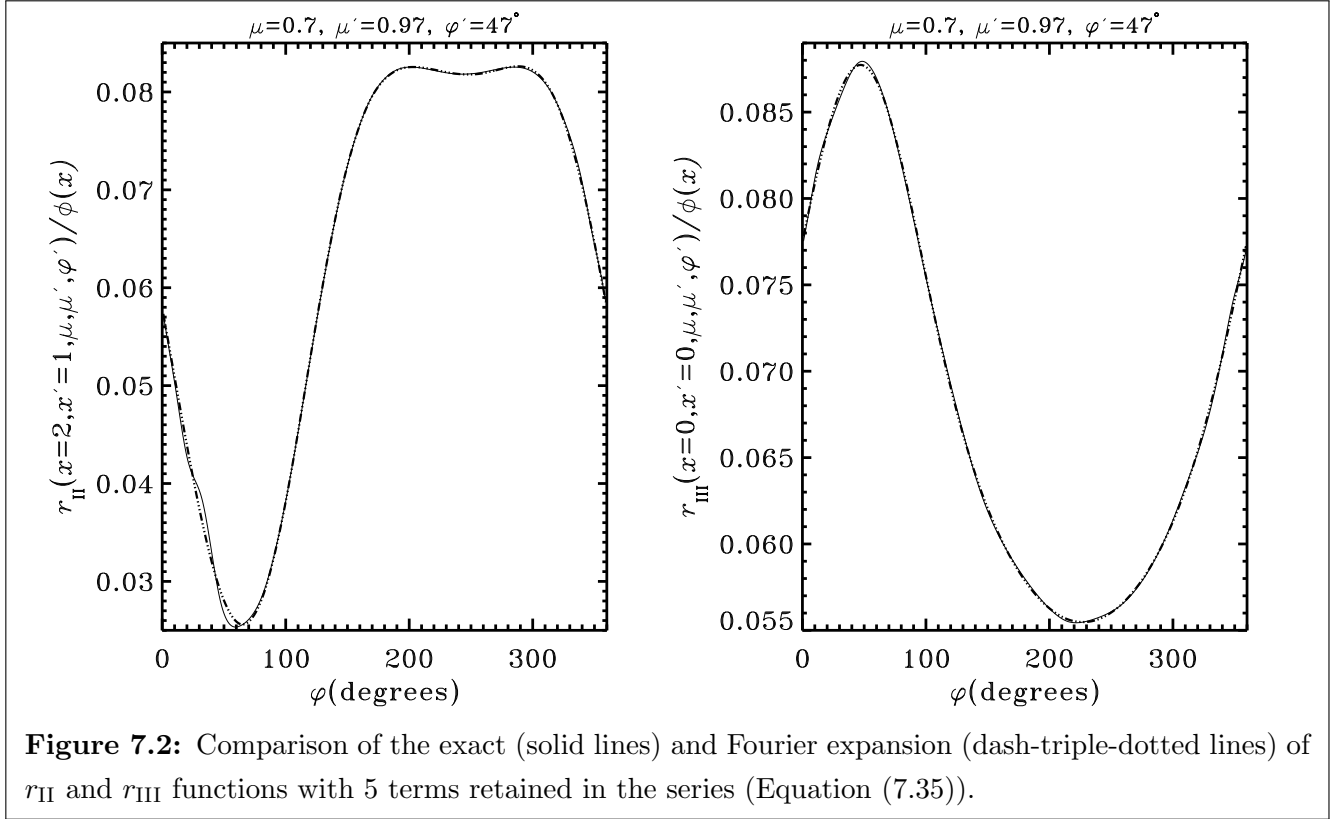


**Figure 7.2:** Comparison of the exact (solid lines) and Fourier expansion (dash-triple-dotted lines) of  $r_{II}$  and  $r_{III}$  functions with 5 terms retained in the series (Equation (7.35)).

model atom with unpolarized ground level (see e.g., Faurobert 1987; Nagendra et al. 2002) is

$$\mathbf{S}(\mathbf{r}, \boldsymbol{\Omega}, x) = \frac{\kappa_l(\mathbf{r})\phi(x)\mathbf{S}_l(\mathbf{r}, \boldsymbol{\Omega}, x) + \kappa_c(\mathbf{r})\mathbf{S}_c(\mathbf{r}, x)}{\kappa_l(\mathbf{r})\phi(x) + \kappa_c(\mathbf{r})}. \quad (7.2)$$

$\mathbf{S}_c$  is the unpolarized continuum source vector given by  $(B_\nu(\mathbf{r}), 0, 0)^T$  with  $B_\nu(\mathbf{r})$  being the Planck function. The line source vector (see e.g., Faurobert 1987; Nagendra et al. 2002) is written as

$$\mathbf{S}_l(\mathbf{r}, \boldsymbol{\Omega}, x) = \mathbf{G}(\mathbf{r}) + \int_{-\infty}^{+\infty} dx' \times \oint \frac{d\boldsymbol{\Omega}'}{4\pi} \frac{\hat{R}(x, x', \boldsymbol{\Omega}, \boldsymbol{\Omega}', \mathbf{B})}{\phi(x)} \mathbf{I}(\mathbf{r}, \boldsymbol{\Omega}', x'). \quad (7.3)$$

$\hat{R}$  is the Hanle redistribution matrix with angle dependent PRD (see Section 4.2, approximation level II of Bommier 1997b).  $\mathbf{B}$  represents an oriented vector magnetic field. The thermalization parameter  $\epsilon = \Gamma_I / (\Gamma_R + \Gamma_I)$  with  $\Gamma_I$  and  $\Gamma_R$  being the inelastic collision rate and the radiative de-excitation rate respectively. The damping parameter is computed using  $a = a_R [1 + (\Gamma_E + \Gamma_I) / \Gamma_R]$  where  $a_R = \Gamma_R / 4\pi \Delta\nu_D$  and  $\Gamma_E$  is the elastic collision rate. We denote the thermal source vector by  $\mathbf{G}(\mathbf{r}) = \epsilon \mathbf{B}_\nu(\mathbf{r})$  with  $\mathbf{B}_\nu(\mathbf{r}) = (B_\nu(\mathbf{r}), 0, 0)^T$ . The



solid angle element  $d\Omega' = \sin \theta' d\theta' d\varphi'$  where  $\theta \in [0, \pi]$  and  $\varphi \in [0, 2\pi]$ . The RT equation along the ray path takes the form

$$\frac{d\mathbf{I}(\mathbf{r}, \boldsymbol{\Omega}, x)}{ds} = -\kappa_{\text{tot}}(\mathbf{r}, x)[\mathbf{I}(\mathbf{r}, \boldsymbol{\Omega}, x) - \mathbf{S}(\mathbf{r}, \boldsymbol{\Omega}, x)], \quad (7.4)$$

where  $s$  is the path length along the ray and  $\kappa_{\text{tot}}(\mathbf{r}, x)$  is the total opacity given by

$$\kappa_{\text{tot}}(\mathbf{r}, x) = \kappa_l(\mathbf{r})\phi(x) + \kappa_c(\mathbf{r}). \quad (7.5)$$

The formal solution of Equation (7.4) is given by

$$\begin{aligned} \mathbf{I}(\mathbf{r}, \boldsymbol{\Omega}, x) = & \mathbf{I}(\mathbf{r}_0, \boldsymbol{\Omega}, x) \exp \left\{ - \int_{s_0}^s \kappa_{\text{tot}}(\mathbf{r} - (s - s')\boldsymbol{\Omega}, x) ds' \right\} \\ & + \int_{s_0}^s \mathbf{S}(\mathbf{r} - (s - s')\boldsymbol{\Omega}, \boldsymbol{\Omega}, x) \kappa_{\text{tot}}(\mathbf{r} - (s - s')\boldsymbol{\Omega}, x) \exp \left\{ - \int_{s'}^s \kappa_{\text{tot}}(\mathbf{r} - (s - s'')\boldsymbol{\Omega}, x) ds'' \right\} ds'. \end{aligned} \quad (7.6)$$

$\mathbf{I}(\mathbf{r}_0, \boldsymbol{\Omega}, x)$  is the boundary condition imposed at  $\mathbf{r}_0 = (x_0, y_0, z_0)$ . Here  $s$  is the distance measured along the ray path (see bottom panels of Figure 7.1). Equations (7.1)–(7.6) can be solved using a perturbation method (see for the corresponding 1D case, Nagendra et al. 2002). However the perturbation method involves an approximation that the degree of linear polarization is small (few % only). Under the situations where the degree of polarization becomes large the perturbation method cannot be expected to guarantee a stable solution. A numerical disadvantage of working in Stokes vector formalism is that the physical quantities depend on all the angular variables  $(\boldsymbol{\Omega}, \boldsymbol{\Omega}')$ . Added to this, the angle-dependent polarized RT problem demands high angular grid resolution thereby requiring enormous memory and CPU time.

### 7.3 Transfer equation in terms of irreducible spherical tensors

As shown in HF07,  $\mathbf{S}$  and  $\mathbf{I}$  can be decomposed into 6-dimensional cylindrically symmetrical vectors  $\boldsymbol{\mathcal{S}}$  and  $\boldsymbol{\mathcal{I}}$  defined for a 1D geometry as

$$\begin{aligned} \boldsymbol{\mathcal{S}} &= (S_0^0, S_0^2, S_1^{2,x}, S_1^{2,y}, S_2^{2,x}, S_2^{2,y})^T, \\ \boldsymbol{\mathcal{I}} &= (I_0^0, I_0^2, I_1^{2,x}, I_1^{2,y}, I_2^{2,x}, I_2^{2,y})^T. \end{aligned} \quad (7.7)$$

In chapters 4 and 6 generalizations of the technique of HF07 to the multi-D case are discussed, for the case of angle-averaged PRD. We show here that the same decomposition

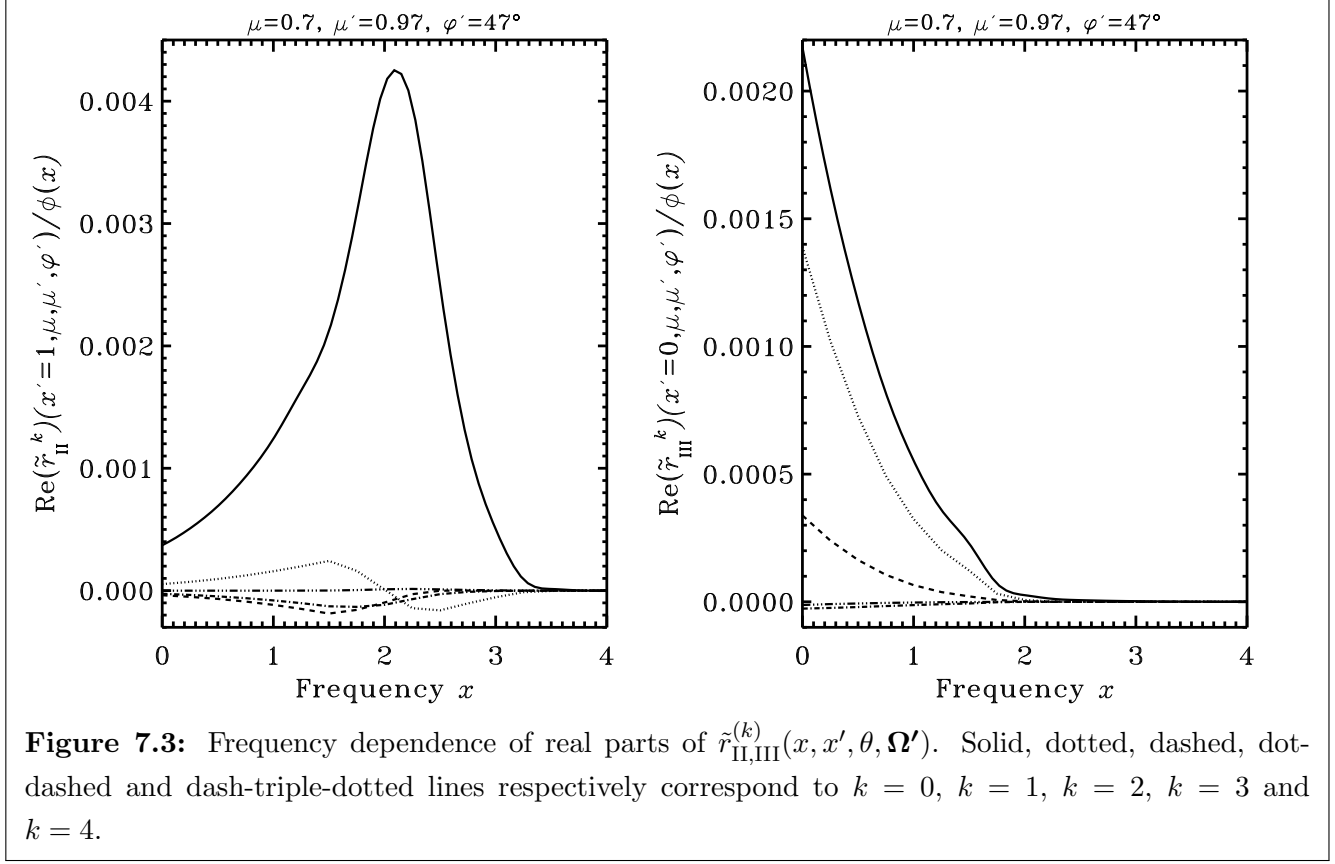


**Figure 7.3:** Frequency dependence of real parts of  $\tilde{r}_{\text{II,III}}^{(k)}(x, x', \theta, \boldsymbol{\Omega}')$ . Solid, dotted, dashed, dot-dashed and dash-triple-dotted lines respectively correspond to  $k = 0, k = 1, k = 2, k = 3$  and  $k = 4$ .

method can be applied to the corresponding angle-dependent PRD case, by replacing the angle-averaged PRD functions with angle-dependent PRD functions. This leads to an additional dependence of  $\boldsymbol{S}$  on the scattered ray direction  $\boldsymbol{\Omega}$ . The vectors  $\boldsymbol{I}$  and  $\boldsymbol{S}$  satisfy an RT equation of the form

$$-\frac{1}{\kappa_{\text{tot}}(\boldsymbol{r}, x)} \boldsymbol{\Omega} \cdot \nabla \boldsymbol{I}(\boldsymbol{r}, \boldsymbol{\Omega}, x) = [\boldsymbol{I}(\boldsymbol{r}, \boldsymbol{\Omega}, x) - \boldsymbol{S}(\boldsymbol{r}, \boldsymbol{\Omega}, x)], \quad (7.8)$$

where

$$\boldsymbol{S}(\boldsymbol{r}, \boldsymbol{\Omega}, x) = p_x \boldsymbol{S}_l(\boldsymbol{r}, \boldsymbol{\Omega}, x) + (1 - p_x) \boldsymbol{S}_c(\boldsymbol{r}, x), \quad (7.9)$$

with  $\boldsymbol{S}_c(\boldsymbol{r}, x) = (B_\nu(\boldsymbol{r}), 0, 0, 0, 0, 0)^T$  and

$$p_x = \kappa_l(\boldsymbol{r}) \phi(x) / \kappa_{\text{tot}}(\boldsymbol{r}, x). \quad (7.10)$$

The irreducible line source vector is given by

$$\begin{aligned} \boldsymbol{S}_l(\boldsymbol{r}, \boldsymbol{\Omega}, x) = \epsilon \boldsymbol{B}(\boldsymbol{r}) + \frac{1}{\phi(x)} \int_{-\infty}^{+\infty} dx' \oint \frac{d\boldsymbol{\Omega}'}{4\pi} \hat{W} \left\{ \hat{M}_{\text{II}}(\boldsymbol{B}, x, x') r_{\text{II}}(x, x', \boldsymbol{\Omega}, \boldsymbol{\Omega}') \right. \\ \left. + \hat{M}_{\text{III}}(\boldsymbol{B}, x, x') r_{\text{III}}(x, x', \boldsymbol{\Omega}, \boldsymbol{\Omega}') \right\} \hat{\Psi}(\boldsymbol{\Omega}') \boldsymbol{I}(\boldsymbol{r}, \boldsymbol{\Omega}', x'), \end{aligned} \quad (7.11)$$

with  $\mathbf{B}(\mathbf{r}) = (B_\nu(\mathbf{r}), 0, 0, 0, 0, 0)^T$  being the Planck vector. For brevity of notation hereafter we denote  $\mathcal{G}(\mathbf{r}) = \epsilon \mathbf{B}(\mathbf{r})$ .  $\hat{W}$  is a diagonal matrix written as

$$\hat{W} = \text{diag}\{W_0, W_2, W_2, W_2, W_2, W_2\}. \quad (7.12)$$

$r_{\text{II,III}}$  are the well known angle-dependent PRD functions of Hummer (1962) which depend explicitly on the scattering angle  $\Theta$ , defined through  $\cos \Theta = \boldsymbol{\Omega} \cdot \boldsymbol{\Omega}'$  computed using

$$\cos \Theta = \mu\mu' + \sqrt{(1 - \mu^2)(1 - \mu'^2)} \cos(\varphi' - \varphi). \quad (7.13)$$

The matrix  $\hat{\Psi}$  represents the reduced phase matrix for the Rayleigh scattering. Its elements are listed in Appendix J. The elements of the matrices  $\hat{M}_{\text{II,III}}(\mathbf{B}, x, x')$  can be found in Bommier (1997b, see also Appendix K). The formal solution now takes the form

$$\mathcal{I}(\mathbf{r}, \boldsymbol{\Omega}, x) = \mathcal{I}(\mathbf{r}_0, \boldsymbol{\Omega}, x) e^{-\tau_x(\mathbf{r}, \boldsymbol{\Omega})} + \int_0^{\tau_x(\mathbf{r}, \boldsymbol{\Omega})} e^{-\tau'_x(\mathbf{r}', \boldsymbol{\Omega})} \mathcal{S}(\mathbf{r}', \boldsymbol{\Omega}, x) d\tau'_x(\mathbf{r}', \boldsymbol{\Omega}). \quad (7.14)$$

Here  $\mathcal{I}(\mathbf{r}_0, \boldsymbol{\Omega}, x)$  is the boundary condition imposed at  $\mathbf{r}_0$ . The monochromatic optical depth scale is defined as

$$\tau_x(\mathbf{r}, \boldsymbol{\Omega}) = \tau_x(x, y, z, \boldsymbol{\Omega}) = \int_{s_0}^s \kappa_{\text{tot}}(\mathbf{r} - (s - s')\boldsymbol{\Omega}, x) ds', \quad (7.15)$$

where  $\tau_x$  is measured along a given ray determined by the direction  $\boldsymbol{\Omega}$ .

One can develop iterative methods to solve Equations (7.8)–(7.14). Because the physical quantities (like  $\mathcal{S}$ ) still depend on  $\boldsymbol{\Omega}$ , it is not numerically very efficient. In the next section we present a method to transform the Equation (7.8) into a new RT equation, which is simpler to solve.

## 7.4 Transfer equation in terms of irreducible Fourier coefficients

HF09 introduced a method of Fourier series expansion of the angle-dependent PRD functions  $r_{\text{II,III}}(x, x', \boldsymbol{\Omega}, \boldsymbol{\Omega}')$ . Here we present a generalization to the multi-D case, the formulation given in HF09.

**Theorem:** In a multi-D polarized RT including angle-dependent PRD and Hanle effect, the irreducible source vector  $\mathcal{S}$  and the irreducible Stokes vector  $\mathcal{I}$  exhibit Fourier expansion

sions of the form

$$\begin{aligned}\mathcal{S}(\mathbf{r}, \boldsymbol{\Omega}, x) &= \sum_{k=-\infty}^{k=\infty} e^{ik\varphi} \tilde{\mathcal{S}}^{(k)}(\mathbf{r}, \theta, x), \\ \mathcal{I}(\mathbf{r}, \boldsymbol{\Omega}, x) &= \sum_{k=-\infty}^{k=\infty} e^{ik\varphi} \tilde{\mathcal{I}}^{(k)}(\mathbf{r}, \boldsymbol{\Omega}, x),\end{aligned}\tag{7.16}$$

and that the Fourier coefficients  $\tilde{\mathcal{S}}^{(k)}$  and  $\tilde{\mathcal{I}}^{(k)}$  satisfy an RT equation of the form

$$-\frac{1}{\kappa_{\text{tot}}(\mathbf{r}, x)} \boldsymbol{\Omega} \cdot \nabla \tilde{\mathcal{I}}^{(k)}(\mathbf{r}, \boldsymbol{\Omega}, x) = [\tilde{\mathcal{I}}^{(k)}(\mathbf{r}, \boldsymbol{\Omega}, x) - \tilde{\mathcal{S}}^{(k)}(\mathbf{r}, \theta, x)].\tag{7.17}$$

**Proof:** The proof is given for the general case of a frequency domain based PRD (approximation level II) that was derived by Bommier (1997a, 1997b). Since the angle-dependent PRD functions  $r_{\text{II,III}}(x, x', \boldsymbol{\Omega}, \boldsymbol{\Omega}')$  are periodic functions of  $\varphi$  with a period  $2\pi$ , we can express them in terms of a Fourier series

$$r_{\text{II,III}}(x, x', \boldsymbol{\Omega}, \boldsymbol{\Omega}') = \sum_{k=-\infty}^{k=\infty} e^{ik\varphi} \tilde{r}_{\text{II,III}}^{(k)}(x, x', \theta, \boldsymbol{\Omega}'),\tag{7.18}$$

where the Fourier coefficients  $\tilde{r}_{\text{II,III}}^{(k)}$  are given by

$$\tilde{r}_{\text{II,III}}^{(k)}(x, x', \theta, \boldsymbol{\Omega}') = \int_0^{2\pi} \frac{d\varphi}{2\pi} e^{-ik\varphi} r_{\text{II,III}}(x, x', \boldsymbol{\Omega}, \boldsymbol{\Omega}').\tag{7.19}$$

We let

$$\mathcal{G}(\mathbf{r}) = \sum_{k=-\infty}^{k=\infty} e^{ik\varphi} \tilde{\mathcal{G}}^{(k)}(\mathbf{r}),\tag{7.20}$$

where

$$\tilde{\mathcal{G}}^{(k)}(\mathbf{r}) = \int_0^{2\pi} \frac{d\varphi}{2\pi} e^{-ik\varphi} \mathcal{G}(\mathbf{r}).\tag{7.21}$$

Note that

$$\tilde{\mathcal{G}}^{(k)}(\mathbf{r}) = \begin{cases} \mathcal{G}(\mathbf{r}) & \text{if } k = 0, \\ 0 & \text{if } k \neq 0. \end{cases}\tag{7.22}$$

We can write

$$\mathcal{S}_c(\mathbf{r}, x) = \sum_{k=-\infty}^{k=\infty} e^{ik\varphi} \tilde{\mathcal{S}}_c^{(k)}(\mathbf{r}, x),\tag{7.23}$$

where

$$\tilde{\mathcal{S}}_c^{(k)}(\mathbf{r}, x) = \delta_{k0} \mathcal{S}_c(\mathbf{r}, x) \quad (7.24)$$

Substituting Equation (7.18) in Equation (7.11) and using Equations (7.24) and (7.9) we get

$$\mathcal{S}(\mathbf{r}, \Omega, x) = \sum_{k=-\infty}^{k=\infty} e^{ik\varphi} \tilde{\mathcal{S}}^{(k)}(\mathbf{r}, \theta, x), \quad (7.25)$$

where

$$\tilde{\mathcal{S}}^{(k)}(\mathbf{r}, \theta, x) = p_x \tilde{\mathcal{S}}_l^{(k)}(\mathbf{r}, \theta, x) + (1 - p_x) \tilde{\mathcal{S}}_c^{(k)}(\mathbf{r}, x), \quad (7.26)$$

with

$$\begin{aligned} \tilde{\mathcal{S}}_l^{(k)}(\mathbf{r}, \theta, x) = & \tilde{\mathcal{G}}^{(k)}(\mathbf{r}) + \frac{1}{\phi(x)} \int_{-\infty}^{+\infty} dx' \oint \frac{d\Omega'}{4\pi} \hat{W} \left\{ \hat{M}_{\text{II}}(\mathbf{B}, x, x') \tilde{r}_{\text{II}}^{(k)}(x, x', \theta, \Omega') \right. \\ & \left. + \hat{M}_{\text{III}}(\mathbf{B}, x, x') \tilde{r}_{\text{III}}^{(k)}(x, x', \theta, \Omega') \right\} \hat{\Psi}(\Omega') \mathcal{I}(\mathbf{r}, \Omega', x'). \end{aligned} \quad (7.27)$$

Substituting Equation (7.27) in Equation (7.14) we get

$$\mathcal{I}(\mathbf{r}, \Omega, x) = \sum_{k=-\infty}^{k=\infty} e^{ik\varphi} \tilde{\mathcal{I}}^{(k)}(\mathbf{r}, \Omega, x), \quad (7.28)$$

where

$$\tilde{\mathcal{I}}^{(k)}(\mathbf{r}, \Omega, x) = \tilde{\mathcal{I}}^{(k)}(\mathbf{r}_0, \Omega, x) e^{-\tau_x(\mathbf{r}, \Omega)} + \int_0^{\tau_x(\mathbf{r}, \Omega)} e^{-\tau'_x(\mathbf{r}', \Omega)} \tilde{\mathcal{S}}^{(k)}(\mathbf{r}', \theta, x) d\tau'_x(\mathbf{r}', \Omega), \quad (7.29)$$

with

$$\tilde{\mathcal{I}}^{(k)}(\mathbf{r}_0, \Omega, x) = \delta_{k0} \mathcal{I}(\mathbf{r}_0, \Omega, x). \quad (7.30)$$

Here  $\tilde{\mathcal{S}}^{(k)}$  depends only on  $\mathbf{r}'$  but not the variable of integration  $\tau'_x(\mathbf{r}', \Omega)$  which is measured along a given ray determined by the direction  $\Omega$ . Substituting Equation (7.29) in Equation (7.27) we obtain

$$\begin{aligned} \tilde{\mathcal{S}}_l^{(k)}(\mathbf{r}, \theta, x) = & \tilde{\mathcal{G}}^{(k)}(\mathbf{r}) + \frac{1}{\phi(x)} \int_{-\infty}^{+\infty} dx' \oint \frac{d\Omega'}{4\pi} \hat{W} \left\{ \hat{M}_{\text{II}}(\mathbf{B}, x, x') \tilde{r}_{\text{II}}^{(k)}(x, x', \theta, \Omega') \right. \\ & \left. + \hat{M}_{\text{III}}(\mathbf{B}, x, x') \tilde{r}_{\text{III}}^{(k)}(x, x', \theta, \Omega') \right\} \hat{\Psi}(\Omega') \sum_{k'=-\infty}^{k'=+\infty} e^{ik'\varphi'} \tilde{\mathcal{I}}^{(k')}(\mathbf{r}, \Omega', x'). \end{aligned} \quad (7.31)$$

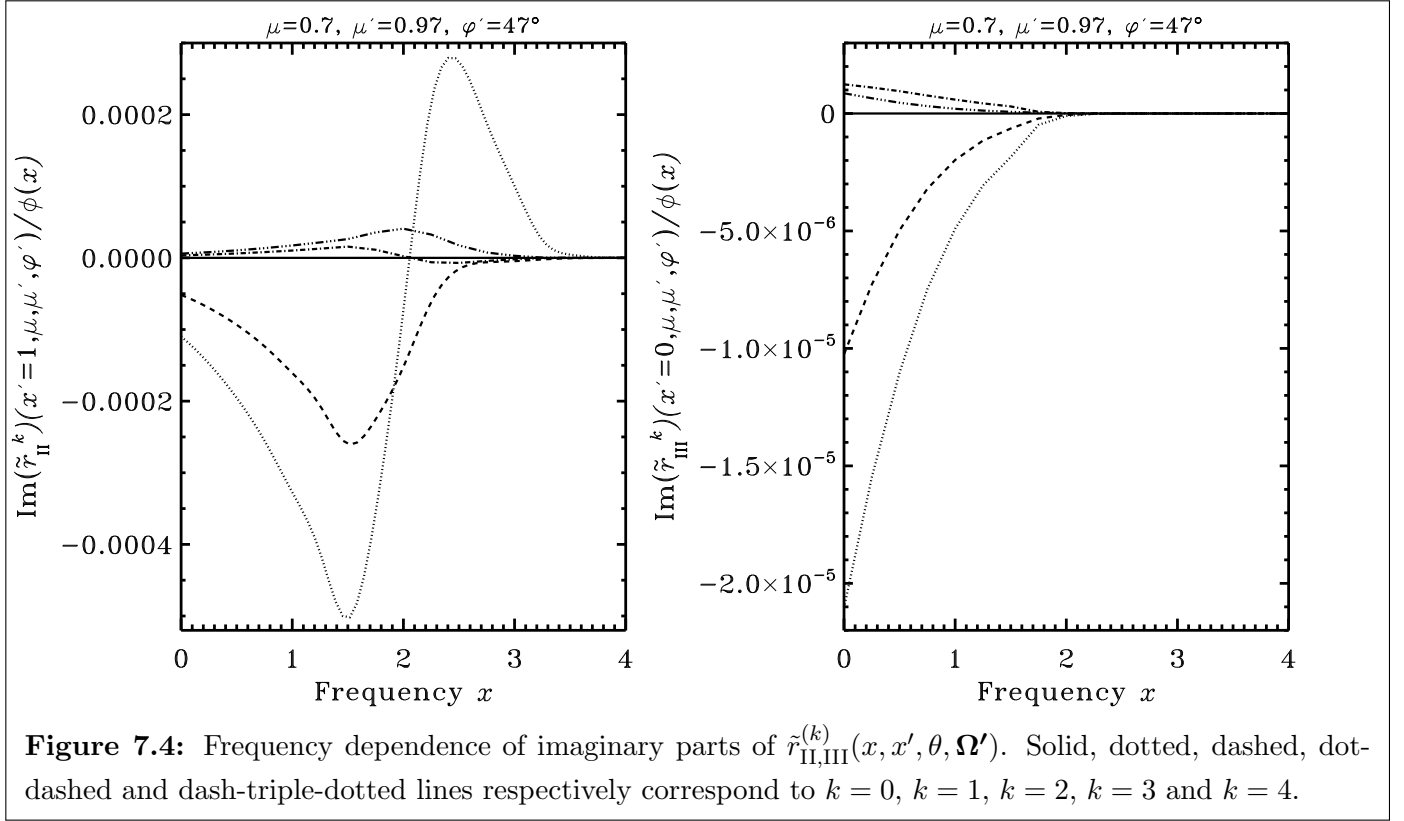


**Figure 7.4:** Frequency dependence of imaginary parts of  $\tilde{r}_{\text{II,III}}^{(k)}(x, x', \theta, \boldsymbol{\Omega}')$ . Solid, dotted, dashed, dot-dashed and dash-triple-dotted lines respectively correspond to  $k = 0, k = 1, k = 2, k = 3$  and  $k = 4$ .

Now from Equations (7.25) and (7.28) and Equation (7.8) it is straight forward to show that the Fourier coefficients  $\tilde{\mathcal{S}}^{(k)}$  and  $\tilde{\mathcal{I}}^{(k)}$  satisfy an RT equation of the form

$$-\frac{1}{\kappa_{\text{tot}}(\mathbf{r}, x)} \boldsymbol{\Omega} \cdot \nabla \tilde{\mathcal{I}}^{(k)}(\mathbf{r}, \boldsymbol{\Omega}, x) = [\tilde{\mathcal{I}}^{(k)}(\mathbf{r}, \boldsymbol{\Omega}, x) - \tilde{\mathcal{S}}^{(k)}(\mathbf{r}, \theta, x)]. \quad (7.32)$$

This proves the theorem. Equation (7.18) represents the Fourier series expansion of the angle-dependent redistribution functions  $r_{\text{II,III}}(x, x', \boldsymbol{\Omega}, \boldsymbol{\Omega}')$ . The expansion is with respect to the azimuth  $\varphi$  of the scattered ray. In this respect our expansion method differs from those used in Domke & Hubeny (1988), HF09, HF10 and Sampoorna et al. (2011), all of whom perform expansion with respect to  $\varphi - \varphi'$ , where  $\varphi'$  is the incident ray azimuth. The expansion used by these authors naturally leads to axisymmetry of the Fourier components  $\tilde{\mathcal{I}}^{(k)}$ , because of the 1D planar geometry assumed by them. In a multi-D geometry the expansion with respect to  $\varphi - \varphi'$  does not provide any advantage. In fact  $\tilde{\mathcal{I}}^{(k)}$  continue to depend on  $\varphi$  due to finiteness of the co-ordinate axes  $X$  and/or  $Y$  in multi-D geometry, under expansions either with respect to  $\varphi$  or  $\varphi - \varphi'$ . The Fourier expansion of the  $\mathcal{S}$  in terms of  $\varphi$  (or  $\varphi - \varphi'$ ) leads to axisymmetric  $\tilde{\mathcal{S}}^{(k)}$  in 1D as well as multi-D geometries. Thus both the approaches are equivalent.

### 7.4.1 Symmetry properties of the irreducible Fourier coefficients

From Equation (7.19) it is easy to show that the components  $\tilde{r}_{\text{II,III}}^{(k)}$  satisfy the conjugation property

$$\tilde{r}_{\text{II,III}}^{(k)} = \left( \tilde{r}_{\text{II,III}}^{(-k)} \right)^*. \quad (7.33)$$

In other words the real and imaginary parts of  $\tilde{r}_{\text{II,III}}^{(k)}$  are respectively symmetric and anti-symmetric about  $k = 0$ .

Using Equation (7.33) we can re-write Equation (7.18) as

$$\begin{aligned} r_{\text{II,III}}(x, x', \boldsymbol{\Omega}, \boldsymbol{\Omega}') &= \tilde{r}_{\text{II,III}}^{(0)}(x, x', \theta, \boldsymbol{\Omega}') \\ &+ \sum_{k=1}^{k=\infty} \{ e^{-ik\varphi} \tilde{r}_{\text{II,III}}^{(-k)}(x, x', \theta, \boldsymbol{\Omega}') + e^{ik\varphi} \tilde{r}_{\text{II,III}}^{(k)}(x, x', \theta, \boldsymbol{\Omega}') \}, \end{aligned} \quad (7.34)$$

or

$$r_{\text{II,III}}(x, x', \boldsymbol{\Omega}, \boldsymbol{\Omega}') = \sum_{k=0}^{k=\infty} (2 - \delta_{k0}) \mathcal{R}e \{ e^{ik\varphi} \tilde{r}_{\text{II,III}}^{(k)}(x, x', \theta, \boldsymbol{\Omega}') \}. \quad (7.35)$$

In Equation (7.35) the Fourier series constitutes only the terms with  $k \geq 0$ . This is useful in practical applications. With this simplification we can show, following the steps similar to those given in Section 7.4, that Equation (7.16) now becomes

$$\begin{aligned} \mathcal{S}(\mathbf{r}, \boldsymbol{\Omega}, x) &= \sum_{k=0}^{k=\infty} (2 - \delta_{k0}) \mathcal{R}e \{ e^{ik\varphi} \tilde{\mathcal{S}}^{(k)}(\mathbf{r}, \theta, x) \}, \\ \mathcal{I}(\mathbf{r}, \boldsymbol{\Omega}, x) &= \sum_{k=0}^{k=\infty} (2 - \delta_{k0}) \mathcal{R}e \{ e^{ik\varphi} \tilde{\mathcal{I}}^{(k)}(\mathbf{r}, \boldsymbol{\Omega}, x) \}, \end{aligned} \quad (7.36)$$

where

$$\tilde{\mathcal{S}}^{(k)}(\mathbf{r}, \theta, x) = p_x \tilde{\mathcal{S}}_l^{(k)}(\mathbf{r}, \theta, x) + (1 - p_x) \tilde{\mathcal{S}}_c^{(k)}(\mathbf{r}, x), \quad (7.37)$$

with

$$\tilde{\mathcal{S}}_c^{(k)}(\mathbf{r}, x) = \delta_{k0} \mathcal{S}_c(\mathbf{r}, x) \quad (7.38)$$

and

$$\begin{aligned} \tilde{\mathcal{S}}_l^{(k)}(\mathbf{r}, \theta, x) &= \tilde{\mathcal{G}}^{(k)}(\mathbf{r}) + \frac{1}{\phi(x)} \int_{-\infty}^{+\infty} dx' \times \oint \frac{d\boldsymbol{\Omega}'}{4\pi} \hat{W} \left\{ \hat{M}_{\text{II}}(\mathbf{B}, x, x') \tilde{r}_{\text{II}}^{(k)}(x, x', \theta, \boldsymbol{\Omega}') \right. \\ &+ \left. \hat{M}_{\text{III}}(\mathbf{B}, x, x') \tilde{r}_{\text{III}}^{(k)}(x, x', \theta, \boldsymbol{\Omega}') \right\} \hat{\Psi}(\boldsymbol{\Omega}') \sum_{k'=0}^{k'=+\infty} (2 - \delta_{k'0}) \mathcal{R}e \{ e^{ik'\varphi'} \tilde{\mathcal{I}}^{(k')}(\mathbf{r}, \boldsymbol{\Omega}', x') \}. \end{aligned} \quad (7.39)$$

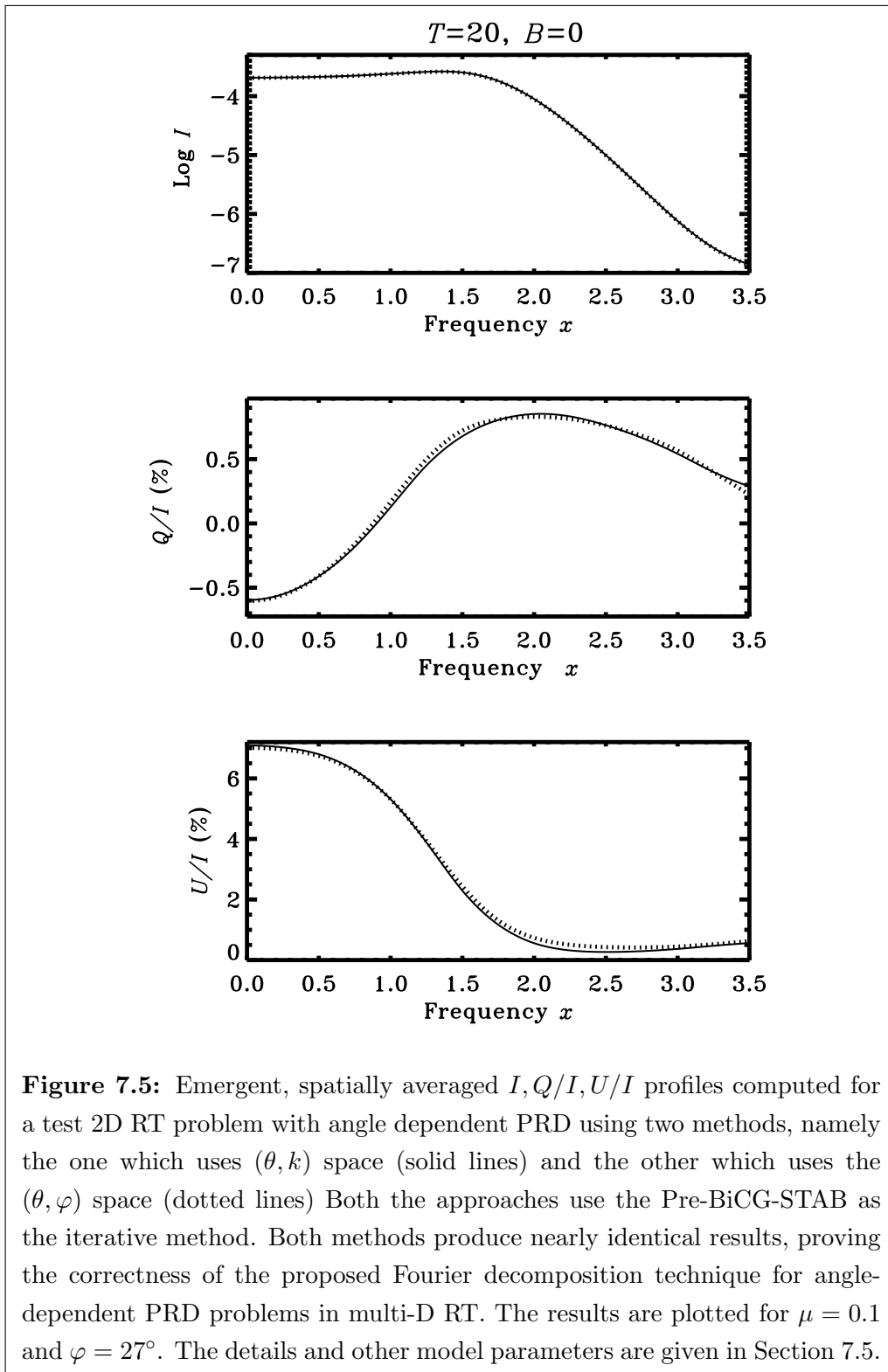


**Figure 7.5:** Emergent, spatially averaged  $I, Q/I, U/I$  profiles computed for a test 2D RT problem with angle dependent PRD using two methods, namely the one which uses  $(\theta, k)$  space (solid lines) and the other which uses the  $(\theta, \varphi)$  space (dotted lines) Both the approaches use the Pre-BiCG-STAB as the iterative method. Both methods produce nearly identical results, proving the correctness of the proposed Fourier decomposition technique for angle-dependent PRD problems in multi-D RT. The results are plotted for  $\mu = 0.1$  and  $\varphi = 27^\circ$ . The details and other model parameters are given in Section 7.5.



The components of  $\tilde{\mathcal{S}}^{(k)}$  and  $\tilde{\mathcal{I}}^{(k)}$  in general form countably infinite sets<sup>1</sup>. We have verified that for practical applications it is sufficient to work with five terms in the Fourier series ( $k \in [0, +4]$ ). Figure 7.2 shows a plot of the  $r_{\text{II,III}}$  functions computed using an exact method (as in Nagendra et al. 2002), and those computed using Equation (7.35) with  $k \in [0, +4]$ , namely keeping only the 5 dominant components in the series expansion. A similar comparison of the exact and series expansion methods for  $r_{\text{II}}$  is presented in Domke & Hubeny (1988), who also show that 5 dominant components are sufficient to accurately represent angle dependent  $r_{\text{II}}$  function.

In Figures 7.3 and 7.4 we study the frequency dependence of the real and imaginary parts of  $\tilde{r}_{\text{II,III}}^{(k)}(x, x', \theta, \boldsymbol{\Omega}')$  for a given incident frequency point ( $x' = 1$  for  $\tilde{r}_{\text{II}}^{(k)}$  and  $x' = 0$  for  $\tilde{r}_{\text{III}}^{(k)}$ ). We show the behaviour of five ( $k = 0, 1, 2, 3, 4$ ) Fourier components. Note that  $\tilde{r}_{\text{II,III}}^{(0)}$  are real quantities.

Equations (7.32) and (7.29) together with Equations (7.39), (7.38) and (7.37) can be solved using an iterative method. In the next chapter (see also Anusha & Nagendra 2011d) we develop a fast iterative method (Pre-BiCG-STAB) and present the solutions of polarized RT in multi-D geometry including Hanle effect with angle-dependent PRD.

After solving for  $\tilde{\mathcal{S}}^{(k)}$  and  $\tilde{\mathcal{I}}^{(k)}$  we can construct  $\mathcal{S}$  and  $\mathcal{I}$  using the Equation (7.36). Since  $\mathcal{S}$  and  $\mathcal{I}$  are real quantities these expansions reduce to the following simpler forms.

$$\begin{aligned} \mathcal{S}(\mathbf{r}, \boldsymbol{\Omega}, x) &= \sum_{k=0}^{k=\infty} (2 - \delta_{k0}) \\ &\times \left\{ \cos(k\varphi) \mathcal{R}e\{\tilde{\mathcal{S}}^{(k)}(\mathbf{r}, \theta, x)\} - \sin(k\varphi) \mathcal{I}m\{\tilde{\mathcal{S}}^{(k)}(\mathbf{r}, \theta, x)\} \right\}, \end{aligned} \quad (7.40)$$

and

$$\begin{aligned} \mathcal{I}(\mathbf{r}, \boldsymbol{\Omega}, x) &= \sum_{k=0}^{k=\infty} (2 - \delta_{k0}) \\ &\times \left\{ \cos(k\varphi) \mathcal{R}e\{\tilde{\mathcal{I}}^{(k)}(\mathbf{r}, \boldsymbol{\Omega}, x)\} - \sin(k\varphi) \mathcal{I}m\{\tilde{\mathcal{I}}^{(k)}(\mathbf{r}, \boldsymbol{\Omega}, x)\} \right\}, \end{aligned} \quad (7.41)$$

where  $\mathcal{S} = (S_0^0, S_0^2, S_1^{2,x}, S_1^{2,y}, S_2^{2,x}, S_2^{2,y})^T$  and  $\mathcal{I} = (I_0^0, I_0^2, I_1^{2,x}, I_1^{2,y}, I_2^{2,x}, I_2^{2,y})^T$ .

Once we obtain  $\mathcal{S}$  and  $\mathcal{I}$ , the Stokes source vector and Stokes intensity vector can be

---

<sup>1</sup>If a set has an one-to-one correspondence with the set of integers, it is called as a countably infinite set.

deduced using the following formulae (see Appendix B of HF07 and also chapter 4).

$$\begin{aligned}
I(\mathbf{r}, \boldsymbol{\Omega}, x) &= I_0^0 + \frac{1}{2\sqrt{2}}(3 \cos^2 \theta - 1)I_0^2 \\
&\quad - \sqrt{3} \cos \theta \sin \theta (I_1^{2,x} \cos \varphi - I_1^{2,y} \sin \varphi) \\
&\quad + \frac{\sqrt{3}}{2}(1 - \cos^2 \theta)(I_2^{2,x} \cos 2\varphi - I_2^{2,y} \sin 2\varphi),
\end{aligned} \tag{7.42}$$

$$\begin{aligned}
Q(\mathbf{r}, \boldsymbol{\Omega}, x) &= -\frac{3}{2\sqrt{2}}(1 - \cos^2 \theta)I_0^2 \\
&\quad - \sqrt{3} \cos \theta \sin \theta (I_1^{2,x} \cos \varphi - I_1^{2,y} \sin \varphi) \\
&\quad - \frac{\sqrt{3}}{2}(1 + \cos^2 \theta)(I_2^{2,x} \cos 2\varphi - I_2^{2,y} \sin 2\varphi),
\end{aligned} \tag{7.43}$$

$$\begin{aligned}
U(\mathbf{r}, \boldsymbol{\Omega}, x) &= \sqrt{3} \sin \theta (I_1^{2,x} \sin \varphi + I_1^{2,y} \cos \varphi) \\
&\quad + \sqrt{3} \cos \theta (I_2^{2,x} \sin 2\varphi + I_2^{2,y} \cos 2\varphi).
\end{aligned} \tag{7.44}$$

The quantities  $I_0^0$ ,  $I_0^2$ ,  $I_1^{2,x}$ ,  $I_1^{2,y}$ ,  $I_2^{2,x}$ ,  $I_2^{2,y}$  also depend on  $\mathbf{r}, \boldsymbol{\Omega}, x$ . Similar formulae can also be used to deduced  $\mathbf{S}$  from  $\mathbf{S}$ .

## 7.5 Numerical considerations

The proposed Fourier series expansion (or Fourier decomposition) technique to solve multi-D RT problems with angle-dependent PRD functions essentially transforms the given problem in  $(\theta, \varphi)$  space (see Section 7.3) into  $(\theta, k)$  space (see Section 7.4). Let  $n_\varphi$  denote the number of azimuths ( $\varphi$ ) used in the computations and  $n_k$  the maximum number of terms retained in the Fourier series expansions. In  $(\theta, \varphi)$  space the source terms  $\mathbf{S}$  depend on  $n_\varphi$  whereas in  $(\theta, k)$  space the source terms  $\tilde{\mathbf{S}}^{(k)}$  depend on  $n_k$ . In Figure 7.2 we have demonstrated that it is sufficient to work with  $n_k = 5$  (i.e.,  $k \in [0, 4]$ ), whereas for 2D RT problems it is necessary to use  $n_\varphi=8, 16, 24$  or  $32$  depending upon the accuracy requirements of the problem. Since  $n_k$  is always smaller than  $n_\varphi$ , the computational cost is reduced when we work in the  $(\theta, k)$  space.

In addition to the computation of  $r_{\text{II,III}}(x, x', \boldsymbol{\Omega}, \boldsymbol{\Omega}')$  functions, we need to compute  $\tilde{r}_{\text{II,III}}^{(k)}(x, x', \theta, \boldsymbol{\Omega}')$  in the  $(\theta, k)$  space. This additional computation does not require much of

CPU time. Moreover, if we can fix the number of angles and frequency points to be used in the computations, it is sufficient to compute these functions only once, which can be written to a file. In subsequent transfer computations this data can be simply read from the archival file.

To demonstrate these advantages, we have compared the CPU time requirements for the two methods, namely the one which uses  $(\theta, \varphi)$  space and the other which uses the  $(\theta, k)$  space. Both the approaches use the Pre-BiCG-STAB as the iterative method to solve the 2D RT problem. We find that with  $n_\varphi = 32$ , the CPU time required to solve a given problem in  $(\theta, k)$  space is 7 times lesser than that required to solve the same problem in  $(\theta, \varphi)$  space. For practical problems requiring more number of azimuthal angles, the advantages of using Fourier decomposition technique is much larger.

To demonstrate the correctness of the proposed Fourier decomposition technique for multi-D RT, we consider a test RT problem in 2D medium. A complete study of the solutions of 2D RT problems with angle-dependent PRD will be taken up in the next chapter. Figure 7.5 shows the emergent, spatially averaged Stokes profiles formed in a 2D media, computed using the two methods mentioned above. The model parameters are: the total optical thickness in two directions namely  $T_Y = T_Z = T = 20$ , the elastic and inelastic collision rates respectively are  $\Gamma_E/\Gamma_R = 10^{-4}$ ,  $\Gamma_I/\Gamma_R = 10^{-4}$ , the damping parameter of the Voigt profile is  $a = 2 \times 10^{-3}$ . We consider the pure line case ( $\kappa_c = 0$ ). The internal thermal sources are taken as constant (the Planck function  $B_\nu = 1$ ). The medium is assumed to be self-emitting (no incident radiation on the boundaries). We consider the case of zero magnetic field. The branching ratios for this choice of model parameters are  $(\alpha, \beta^{(0)}, \beta^{(2)}) = (1, 1, 1)$ . These branching ratios correspond to a PRD scattering that uses only  $\tilde{r}_{\text{II}}^{(k)}(x, x', \theta, \boldsymbol{\Omega}')$  function. We use a logarithmic frequency grid with  $x_{\text{max}} = 3.5$  and a logarithmic depth grid in  $Y$  and  $Z$  directions of the 2D medium. We have used a 3-point Gaussian  $\mu$ -quadrature and a 32-point Gaussian  $\varphi$ -quadrature. In Figure 7.5 we show the results computed at  $\mu = 0.1$  and  $\varphi = 27^\circ$ . The fact that both the methods give nearly identical results proves the correctness of the proposed Fourier decomposition technique for multi-D RT.

## 7.6 Concluding remarks

In this chapter we formulate polarized RT equation in multi-D media that includes angle-dependent PRD and Hanle effect. We propose a method of decomposition of the Stokes source vector and Stokes intensity vector in terms of irreducible Fourier components  $\tilde{\mathcal{S}}^{(k)}$

and  $\tilde{\mathcal{I}}^{(k)}$ , using a combination of the decomposition of the scattering phase matrices in terms of irreducible spherical tensors  $\mathcal{T}_Q^K$  and the Fourier series expansions of angle-dependent PRD functions. We also establish that the irreducible Fourier components  $\tilde{\mathcal{S}}^{(k)}$  and  $\tilde{\mathcal{I}}^{(k)}$  satisfy a simple RT equation, which can be solved by any iterative method like an Approximate Lambda Iteration (ALI) or a Biconjugate-Gradient type projection method.

### New Results

The AD PRD in line scattering is considered to be a challenging problem in astrophysics. Inclusion of AD PRD in multi-D RT is a formidable problem which we have solved in this chapter. The important results of this study are as follows.

1. We have formulated the polarized RT equation in multi-D media that takes into account Hanle effect with AD PRD functions.
2. We have generalized here to the multi-D case, the method of Fourier series expansion of AD PRD functions originally developed for RT in 1D geometry.
3. We show that the Stokes source vector  $\mathbf{S} = (S_I, S_Q, S_U)^T$  and the Stokes vector  $\mathbf{I} = (I, Q, U)^T$  can be expanded in terms of infinite sets of components  $\tilde{\mathcal{S}}^{(k)}$ ,  $\tilde{\mathcal{I}}^{(k)}$  respectively,  $k \in [0, +\infty]$ .
4. We show that the components  $\tilde{\mathcal{S}}^{(k)}$  become independent of the azimuthal angle ( $\varphi$ ) of the scattered ray, whereas the components  $\tilde{\mathcal{I}}^{(k)}$  remain dependent on  $\varphi$  due to the nature of RT in multi-D geometry.
5. We also establish that  $\tilde{\mathcal{S}}^{(k)}$  and  $\tilde{\mathcal{I}}^{(k)}$  satisfy a simple transfer equation, which can be solved by any iterative method like PALI or a Biconjugate-Gradient type projection method, provided we truncate the Fourier series to have a finite number of terms.

## Chapter 8

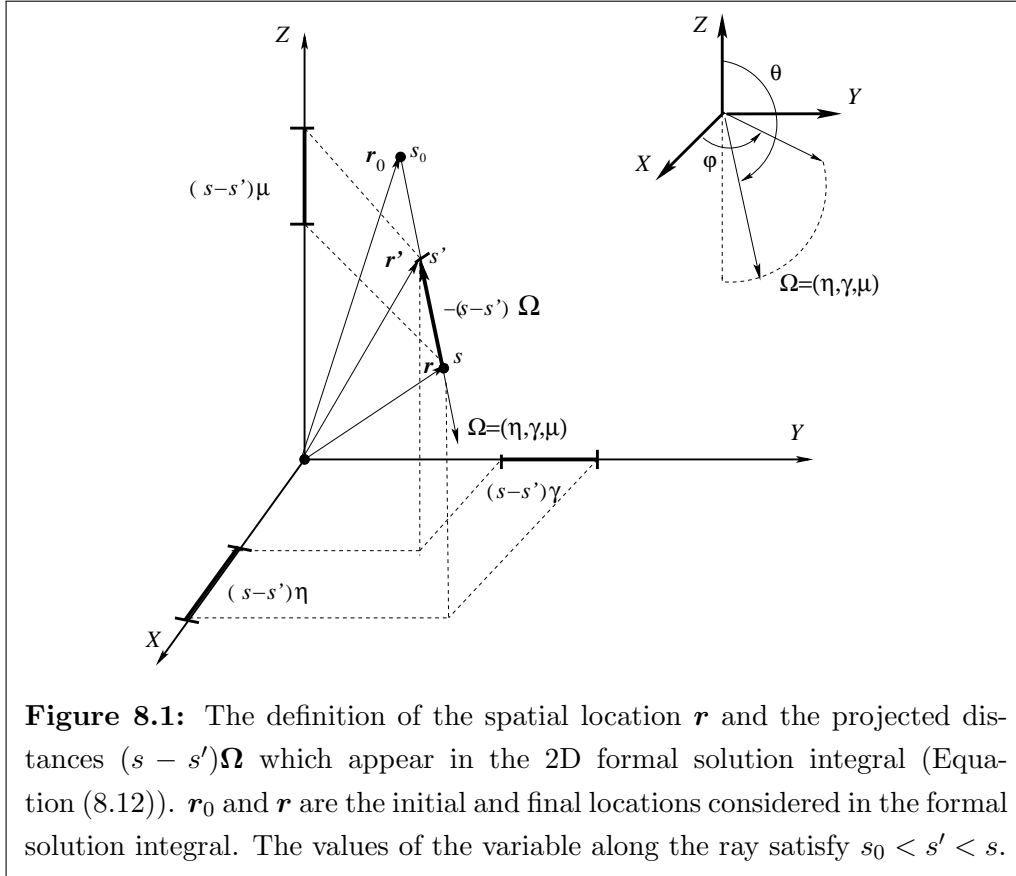
# Angle-dependent PRD in multi-D media: Radiative transfer

*The contents of this chapter are based on the following publication:*  
Anusha, L. S., & Nagendra, K. N., 2012, **ApJ**, 746, 84–99

### 8.1 Introduction

The solution of polarized line transfer equation with angle-dependent (AD) partial frequency redistribution (PRD) has always remained as one of the difficult areas in the astrophysical line formation theory. The problem stems from the inextricable coupling between frequency and angle variables, which are hard to be represented using finite resolution grids. Equally challenging is the solution of polarized line radiative transfer (RT) equation in multi-dimensional (multi-D) media. There existed lack of formulations that reduce the complexity of multi-D transfer, when PRD is taken into account. In previous three chapters namely chapter 4, 5 and 6 (see also Anusha & Nagendra 2011a; Anusha et al 2011a; Anusha & Nagendra 2011b), we formulated and solved the transfer problem using angle-averaged (AA) PRD. In chapter 7 (see also Anusha & Nagendra 2011c), we formulated a Fourier decomposition technique which cleverly simplifies the problem of ‘multi-D RT with AD PRD’. The Fourier decomposition technique for transfer in one-dimensional (1D) media including Hanle effect and AD PRD was formulated by Frisch (2009). This technique was extended to handle multi-D transfer in chapter 7. In this chapter we apply the technique presented in chapter 7 to establish several benchmark solutions of the corresponding line transfer problem. A historical account of the work on polarized RT with AD PRD in 1D planar media, and the related topics is given in detail, in Table 7.1. Therefore we do not

repeat here.

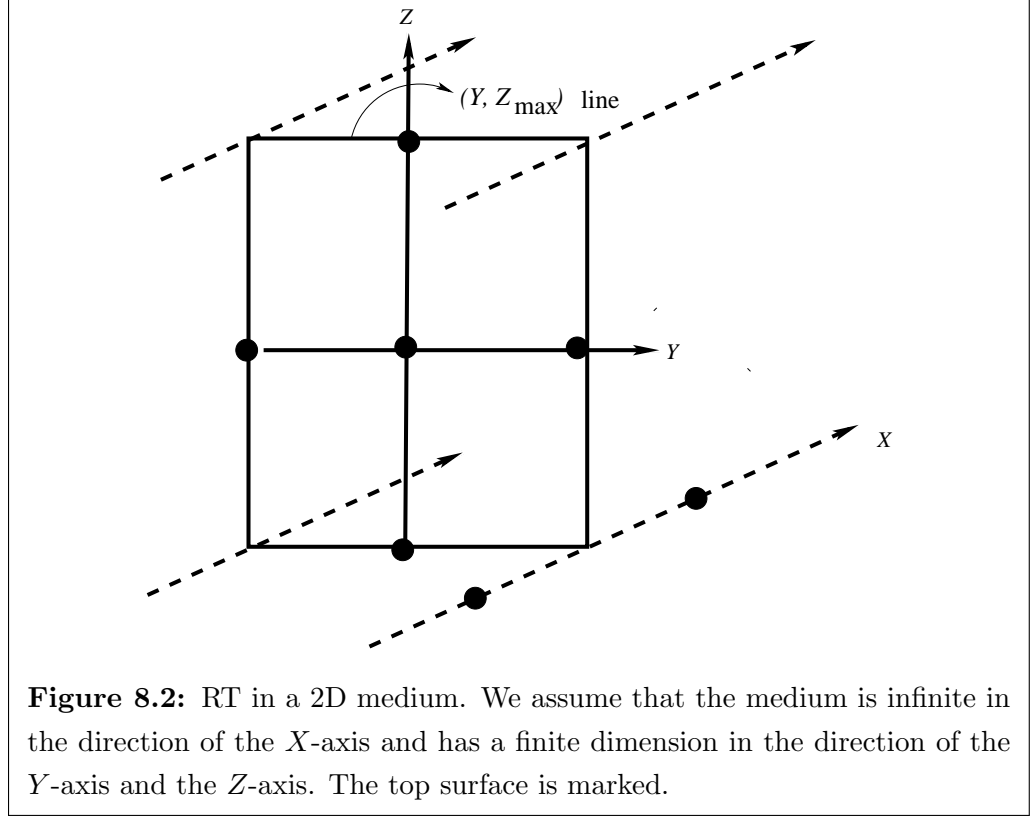


In Section 8.2 we present the multi-D polarized RT equation in a two-dimensional (2D) medium, expressed in terms of irreducible Fourier coefficients, denoted by  $\tilde{\mathcal{I}}^{(k)}$  and  $\tilde{\mathcal{S}}^{(k)}$ , where  $k$  is the index of the terms in the Fourier series expansion of the Stokes vector  $\mathbf{I}$  and the Stokes source vector  $\mathcal{S}$ . Section 8.3 describes the numerical method of solving the concerned transfer equation. Section 8.4 is devoted to a discussion of the results. Concluding remarks are presented in Section 8.5.

## 8.2 Polarized transfer equation in a multi-D medium

The multi-D transfer equation written in terms of the Stokes parameters and the relevant expressions for the Stokes source vectors (for line and continuum) in a two-level atom model with unpolarized ground level, involving the AD PRD matrices is well explained in Section 7.2. All these equations can be expressed in terms of ‘irreducible spherical tensors’ (see Section 7.3). Further, in Section 7.4 we developed a decomposition technique

to simplify this RT equation using Fourier series expansions of the AD PRD functions.



Here we describe a variant of the method presented in chapter 7, which is more useful in practical applications involving polarized RT in magnetized two-dimensional (2D) and three-dimensional (3D) atmospheres.

### 8.2.1 The radiative transfer equation in terms of irreducible spherical tensors

Let  $\mathbf{I} = (I, Q, U)^T$  be the Stokes vector and  $\mathbf{S} = (S_I, S_Q, S_U)^T$  denote the Stokes source vector (see Chandrasekhar 1950). We introduce vectors  $\mathbf{S}$  and  $\mathcal{I}$  given by

$$\begin{aligned}\mathbf{S} &= (S_0^0, S_0^2, S_1^{2,x}, S_1^{2,y}, S_2^{2,x}, S_2^{2,y})^T, \\ \mathcal{I} &= (I_0^0, I_0^2, I_1^{2,x}, I_1^{2,y}, I_2^{2,x}, I_2^{2,y})^T.\end{aligned}\tag{8.1}$$

These quantities are related to the Stokes parameters (see e.g., Frisch 2007) through

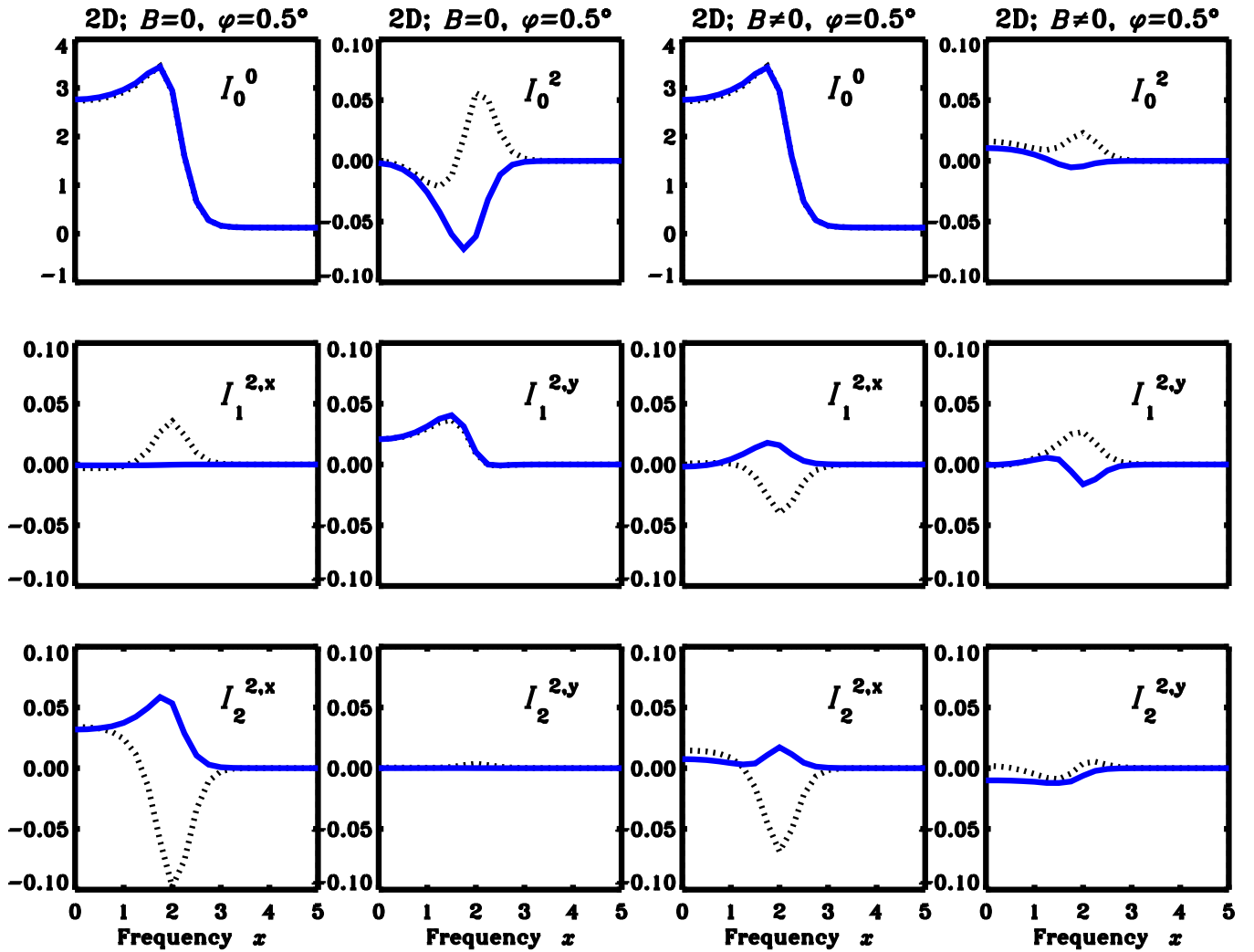


**Figure 8.3:** The emergent, surface averaged components of  $\mathcal{I}$  in non-magnetic (the first two columns) and magnetic (the last two columns) 2D media for  $\mu = 0.11$  and  $\varphi = 0.5^\circ$ . The actual values of the components are scaled up by a factor of  $10^4$ . Solid and dotted lines represent respectively the AA and the AD PRD. In the first two columns (for  $B = 0$ ),  $I_1^{2,x}$  and  $I_2^{2,y}$  are zero for the AA PRD (solid lines) and the other 10 components are non-zero (four AA components and six AD components). In the last two columns, the magnetic field parameters are  $(\Gamma_B, \theta_B, \chi_B) = (1, 90^\circ, 60^\circ)$ . All the components are important for  $B \neq 0$ .



$$\begin{aligned}
I(\mathbf{r}, \boldsymbol{\Omega}, x) &= I_0^0 + \frac{1}{2\sqrt{2}}(3 \cos^2 \theta - 1)I_0^2 \\
&\quad - \sqrt{3} \cos \theta \sin \theta (I_1^{2,x} \cos \varphi - I_1^{2,y} \sin \varphi) \\
&\quad + \frac{\sqrt{3}}{2}(1 - \cos^2 \theta)(I_2^{2,x} \cos 2\varphi - I_2^{2,y} \sin 2\varphi),
\end{aligned} \tag{8.2}$$

$$\begin{aligned}
Q(\mathbf{r}, \boldsymbol{\Omega}, x) &= -\frac{3}{2\sqrt{2}}(1 - \cos^2 \theta)I_0^2 \\
&\quad - \sqrt{3} \cos \theta \sin \theta (I_1^{2,x} \cos \varphi - I_1^{2,y} \sin \varphi) \\
&\quad - \frac{\sqrt{3}}{2}(1 + \cos^2 \theta)(I_2^{2,x} \cos 2\varphi - I_2^{2,y} \sin 2\varphi),
\end{aligned} \tag{8.3}$$

$$\begin{aligned}
U(\mathbf{r}, \boldsymbol{\Omega}, x) &= \sqrt{3} \sin \theta (I_1^{2,x} \sin \varphi + I_1^{2,y} \cos \varphi) \\
&\quad + \sqrt{3} \cos \theta (I_2^{2,x} \sin 2\varphi + I_2^{2,y} \cos 2\varphi).
\end{aligned} \tag{8.4}$$

We note here that the quantities  $I_0^0$ ,  $I_0^2$ ,  $I_1^{2,x}$ ,  $I_1^{2,y}$ ,  $I_2^{2,x}$  and  $I_2^{2,y}$  also depend on the variables  $\mathbf{r}$ ,  $\boldsymbol{\Omega}$  and  $x$  (defined below).

For a given ray defined by the direction  $\boldsymbol{\Omega}$ , the vectors  $\boldsymbol{\mathcal{S}}$  and  $\boldsymbol{\mathcal{I}}$  satisfy the RT equation (see Section 7.3)

$$-\frac{1}{\kappa_{\text{tot}}(\mathbf{r}, x)} \boldsymbol{\Omega} \cdot \nabla \boldsymbol{\mathcal{I}}(\mathbf{r}, \boldsymbol{\Omega}, x) = [\boldsymbol{\mathcal{I}}(\mathbf{r}, \boldsymbol{\Omega}, x) - \boldsymbol{\mathcal{S}}(\mathbf{r}, \boldsymbol{\Omega}, x)]. \tag{8.5}$$

It is useful to note that the above equation was referred to as ‘irreducible RT equation’ in chapter 7. Indeed, for the AA PRD problems, the quantities  $\boldsymbol{\mathcal{I}}$  and  $\boldsymbol{\mathcal{S}}$  are already in the irreducible form. But for the AD PRD problems,  $\boldsymbol{\mathcal{I}}$  and  $\boldsymbol{\mathcal{S}}$  can further be reduced to  $\tilde{\boldsymbol{\mathcal{I}}}^{(k)}$  and  $\tilde{\boldsymbol{\mathcal{S}}}^{(k)}$  using Fourier series expansions. Here  $\mathbf{r}$  is the position vector of the point in the medium with coordinates  $(x, y, z)$ . The unit vector  $\boldsymbol{\Omega} = (\eta, \gamma, \mu) = (\sin \theta \cos \varphi, \sin \theta \sin \varphi, \cos \theta)$  defines the direction cosines of the ray with respect to the atmospheric normal (the  $Z$ -axis), where  $\theta$  and  $\varphi$  are the polar and azimuthal angles of the ray. Total opacity  $\kappa_{\text{tot}}(\mathbf{r}, x)$  is given by

$$\kappa_{\text{tot}}(\mathbf{r}, x) = \kappa_l(\mathbf{r})\phi(x) + \kappa_c(\mathbf{r}), \tag{8.6}$$

where  $\kappa_l$  is the frequency averaged line opacity,  $\phi$  is the Voigt profile function and  $\kappa_c$  is

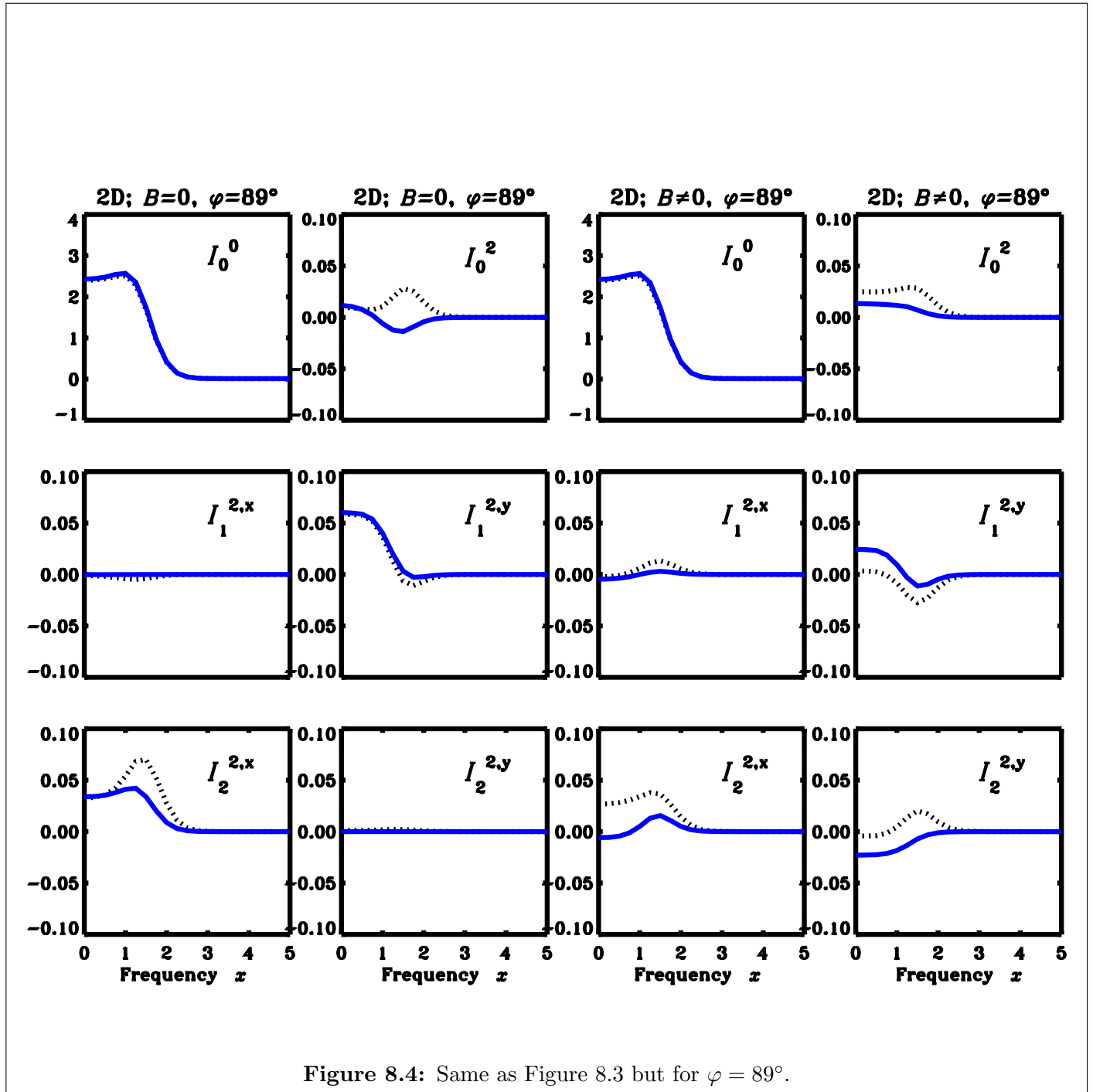


Figure 8.4: Same as Figure 8.3 but for  $\varphi = 89^\circ$ .

the continuum opacity. Frequency is measured in reduced units, namely  $x = (\nu - \nu_0)/\Delta\nu_D$  where  $\Delta\nu_D$  is the Doppler width.

For a two-level atom model with unpolarized ground level,  $\mathcal{S}(\mathbf{r}, \boldsymbol{\Omega}, x)$  has contributions from the line and the continuum sources. It takes the form

$$\mathcal{S}(\mathbf{r}, \boldsymbol{\Omega}, x) = p_x \mathcal{S}_l(\mathbf{r}, \boldsymbol{\Omega}, x) + (1 - p_x) \mathcal{S}_c(\mathbf{r}, x), \quad (8.7)$$

with

$$p_x = \kappa_l(\mathbf{r})\phi(x)/\kappa_{\text{tot}}(\mathbf{r}, x). \quad (8.8)$$

The line source vector is written as

$$\begin{aligned} \mathcal{S}_l(\mathbf{r}, \boldsymbol{\Omega}, x) = & \mathcal{G}(\mathbf{r}) + \frac{1}{\phi(x)} \int_{-\infty}^{+\infty} dx' \oint \frac{d\boldsymbol{\Omega}'}{4\pi} \hat{W} \left\{ \hat{M}_{\text{II}}(\mathbf{B}, x, x') r_{\text{II}}(x, x', \boldsymbol{\Omega}, \boldsymbol{\Omega}') \right. \\ & \left. + \hat{M}_{\text{III}}(\mathbf{B}, x, x') r_{\text{III}}(x, x', \boldsymbol{\Omega}, \boldsymbol{\Omega}') \right\} \hat{\Psi}(\boldsymbol{\Omega}') \mathcal{I}(\mathbf{r}, \boldsymbol{\Omega}', x'), \end{aligned} \quad (8.9)$$

with  $\mathcal{G}(\mathbf{r}) = (\epsilon B_\nu(\mathbf{r}), 0, 0, 0, 0, 0)^T$  and the unpolarized continuum source vector  $\mathcal{S}_c(\mathbf{r}, x) = (S_c(\mathbf{r}, x), 0, 0, 0, 0, 0)^T$ . We assume that  $S_c(\mathbf{r}, x) = B_\nu(\mathbf{r})$  with  $B_\nu(\mathbf{r})$  being the Planck function. The thermalization parameter  $\epsilon = \Gamma_I/(\Gamma_R + \Gamma_I)$  with  $\Gamma_I$  and  $\Gamma_R$  being the inelastic collision rate and the radiative de-excitation rate respectively. The damping parameter is computed using  $a = a_R[1 + (\Gamma_E + \Gamma_I)/\Gamma_R]$  where  $a_R = \Gamma_R/4\pi\Delta\nu_D$  and  $\Gamma_E$  is the elastic collision rate. The matrix  $\hat{\Psi}$  represents the reduced phase matrix for the Rayleigh scattering. Its elements are listed in Appendix J. The elements of the matrices  $\hat{M}_{\text{II,III}}(\mathbf{B}, x, x')$  for the Hanle effect are derived in Bommier (1997a, 1997b). In Appendix K we write them in a form suitable for our calculations.  $\hat{W}$  is a diagonal matrix written as

$$\hat{W} = \text{diag}\{W_0, W_2, W_2, W_2, W_2, W_2\}. \quad (8.10)$$

Here the weight  $W_0 = 1$  and the weight  $W_2$  depends on the line under consideration (see Landi Degl'Innocenti & Landolfi 2004). Here we take  $W_2 = 1$ .  $r_{\text{II,III}}$  are the AD PRD functions of Hummer (1962) which depend explicitly on the scattering angle  $\Theta$ , defined through  $\cos \Theta = \boldsymbol{\Omega} \cdot \boldsymbol{\Omega}'$  computed using

$$\cos \Theta = \mu\mu' + \sqrt{(1 - \mu^2)(1 - \mu'^2)} \cos(\varphi' - \varphi). \quad (8.11)$$

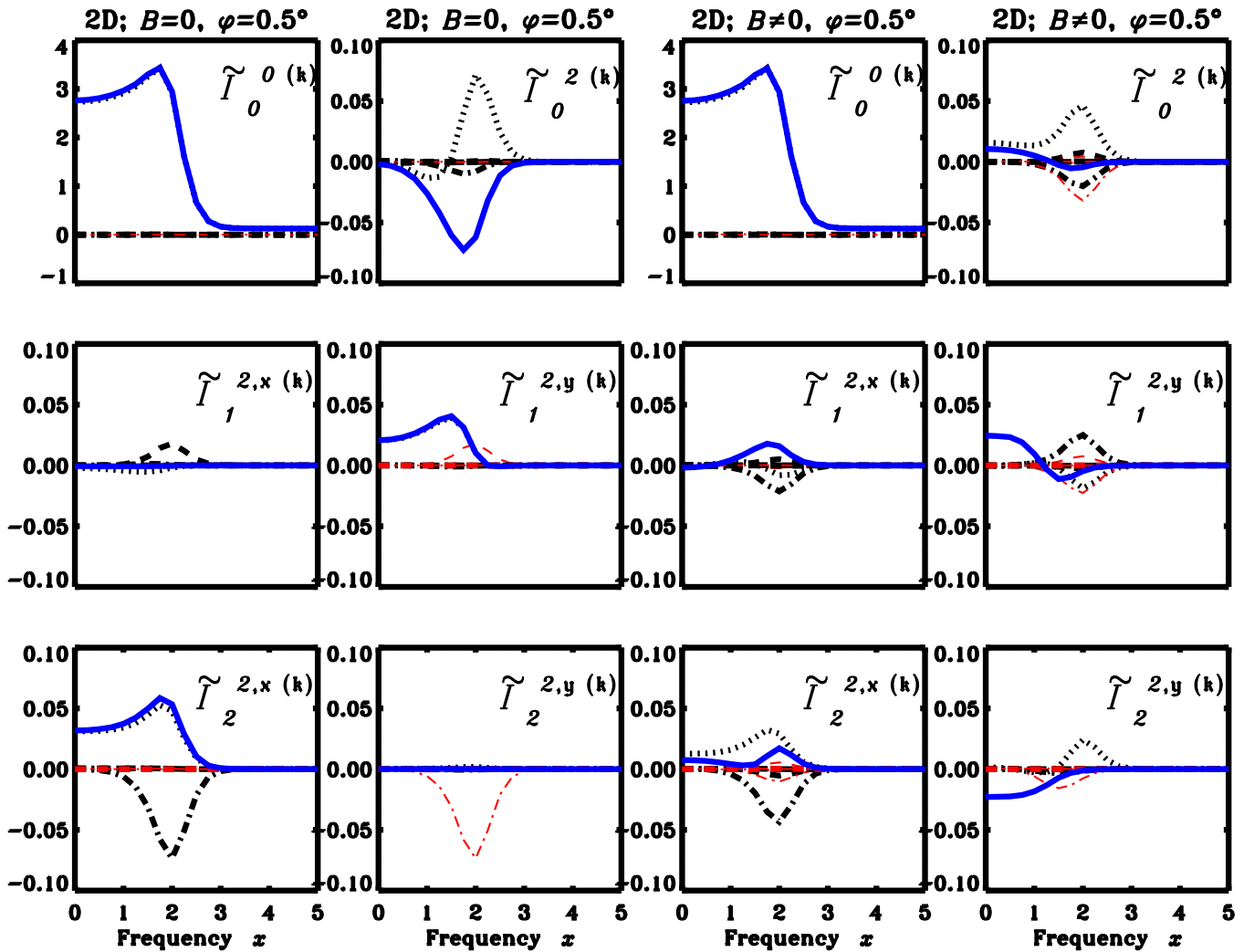


**Figure 8.5:** The emergent, spatially averaged components of  $\tilde{\mathcal{I}}^{(k)}$  in non-magnetic (the first two columns) and magnetic (the last two columns) 2D media for  $\mu = 0.11$  and  $\varphi = 89^\circ$ . The actual values of the components are scaled up by a factor of  $10^4$ . Solid lines represent the components of  $\mathcal{I}$  for the AA PRD, plotted here for comparison. The dotted curves represent the components  $\tilde{\mathcal{I}}^{(0)}$ . The thick curves with dashed, dot-dashed, dash-triple-dotted and long-dashed line types respectively represent  $\mathcal{Re}[\tilde{\mathcal{I}}^{(1)}]$ ,  $\mathcal{Re}[\tilde{\mathcal{I}}^{(2)}]$ ,  $\mathcal{Re}[\tilde{\mathcal{I}}^{(3)}]$  and  $\mathcal{Re}[\tilde{\mathcal{I}}^{(4)}]$ . Similarly the thin curves with dashed, dot-dashed, dash-triple-dotted and long-dashed line types respectively represent  $\mathcal{Im}[\tilde{\mathcal{I}}^{(1)}]$ ,  $\mathcal{Im}[\tilde{\mathcal{I}}^{(2)}]$ ,  $\mathcal{Im}[\tilde{\mathcal{I}}^{(3)}]$  and  $\mathcal{Im}[\tilde{\mathcal{I}}^{(4)}]$ . In the last two columns, the magnetic field parameters are  $(\Gamma_B, \theta_B, \chi_B) = (1, 90^\circ, 60^\circ)$ .

The formal solution of Equation (8.5) is given by

$$\begin{aligned} \mathcal{I}(\mathbf{r}, \boldsymbol{\Omega}, x) &= \mathcal{I}(\mathbf{r}_0, \boldsymbol{\Omega}, x) \exp \left\{ - \int_{s_0}^s \kappa_{\text{tot}}(\mathbf{r} - (s - s')\boldsymbol{\Omega}, x) ds' \right\} \\ &+ \int_{s_0}^s \mathcal{S}(\mathbf{r} - (s - s')\boldsymbol{\Omega}, \boldsymbol{\Omega}, x) \kappa_{\text{tot}}(\mathbf{r} - (s - s')\boldsymbol{\Omega}, x) \exp \left\{ - \int_{s'}^s \kappa_{\text{tot}}(\mathbf{r} - (s - s'')\boldsymbol{\Omega}, x) ds'' \right\} ds'. \end{aligned} \quad (8.12)$$

The formal solution can also be expressed as

$$\mathcal{I}(\mathbf{r}, \boldsymbol{\Omega}, x) = \mathcal{I}(\mathbf{r}_0, \boldsymbol{\Omega}, x) e^{-\tau_x(\mathbf{r}, \boldsymbol{\Omega})} + \int_0^{\tau_x(\mathbf{r}, \boldsymbol{\Omega})} e^{-\tau'_x(\mathbf{r}', \boldsymbol{\Omega})} \mathcal{S}(\mathbf{r}', \boldsymbol{\Omega}, x) d\tau'_x(\mathbf{r}', \boldsymbol{\Omega}). \quad (8.13)$$

Here  $\mathcal{I}(\mathbf{r}_0, \boldsymbol{\Omega}, x)$  is the boundary condition imposed at the boundary point  $\mathbf{r}_0 = (x_0, y_0, z_0)$ . The monochromatic optical depth scale is defined as

$$\tau_x(\mathbf{r}, \boldsymbol{\Omega}) = \tau_x(x, y, z, \boldsymbol{\Omega}) = \int_{s_0}^s \kappa_{\text{tot}}(\mathbf{r} - (s - s')\boldsymbol{\Omega}, x) ds', \quad (8.14)$$

$\tau_x(\mathbf{r}, \boldsymbol{\Omega})$  is the optical thickness from the point  $\mathbf{r}_0$  to the point  $\mathbf{r}$  measured along the ray. In Figure 8.1 we show the construction of the vector  $\mathbf{r}' = \mathbf{r} - (s - s')\boldsymbol{\Omega}$ . The point  $\mathbf{r}'$ , tip of the vector  $\mathbf{r}'$ , runs along the ray from the point  $\mathbf{r}_0$  to the point  $\mathbf{r}$  as the variable along the ray varies from  $s_0$  to  $s$ . In chapters 4–7, the figure corresponding to Figure 8.1 was drawn for a ray passing through the origin of the coordinate system.

In chapter 7 we have shown that using Fourier series expansions of the AD PRD functions  $r_{\text{II,III}}(x, x', \boldsymbol{\Omega}, \boldsymbol{\Omega}')$  with respect to the azimuth ( $\varphi$ ) of the scattered ray, we can transform Equations (8.5)–(8.13) into a simplified set of equations. In the non-magnetic case, the method described in chapter 7 can be implemented numerically, without any modifications. In the magnetic case, it becomes necessary to slightly modify that method to avoid making certain approximations which otherwise would have to be used (see Section 8.2.2 for details).

### 8.2.2 A Fourier decomposition technique for domain based PRD

In the presence of a weak magnetic field  $\mathbf{B}$  defined by its strength  $B$  and the orientation  $(\theta_B, \chi_B)$ , the scattering polarization is modified through the Hanle effect. A general PRD theory including the Hanle effect was developed in Bommier (1997a, 1997b). A description of the Hanle effect with the AD PRD functions is given by the approximation level II described in Bommier (1997b). In this approximation the frequency space  $(x, x')$  is divided

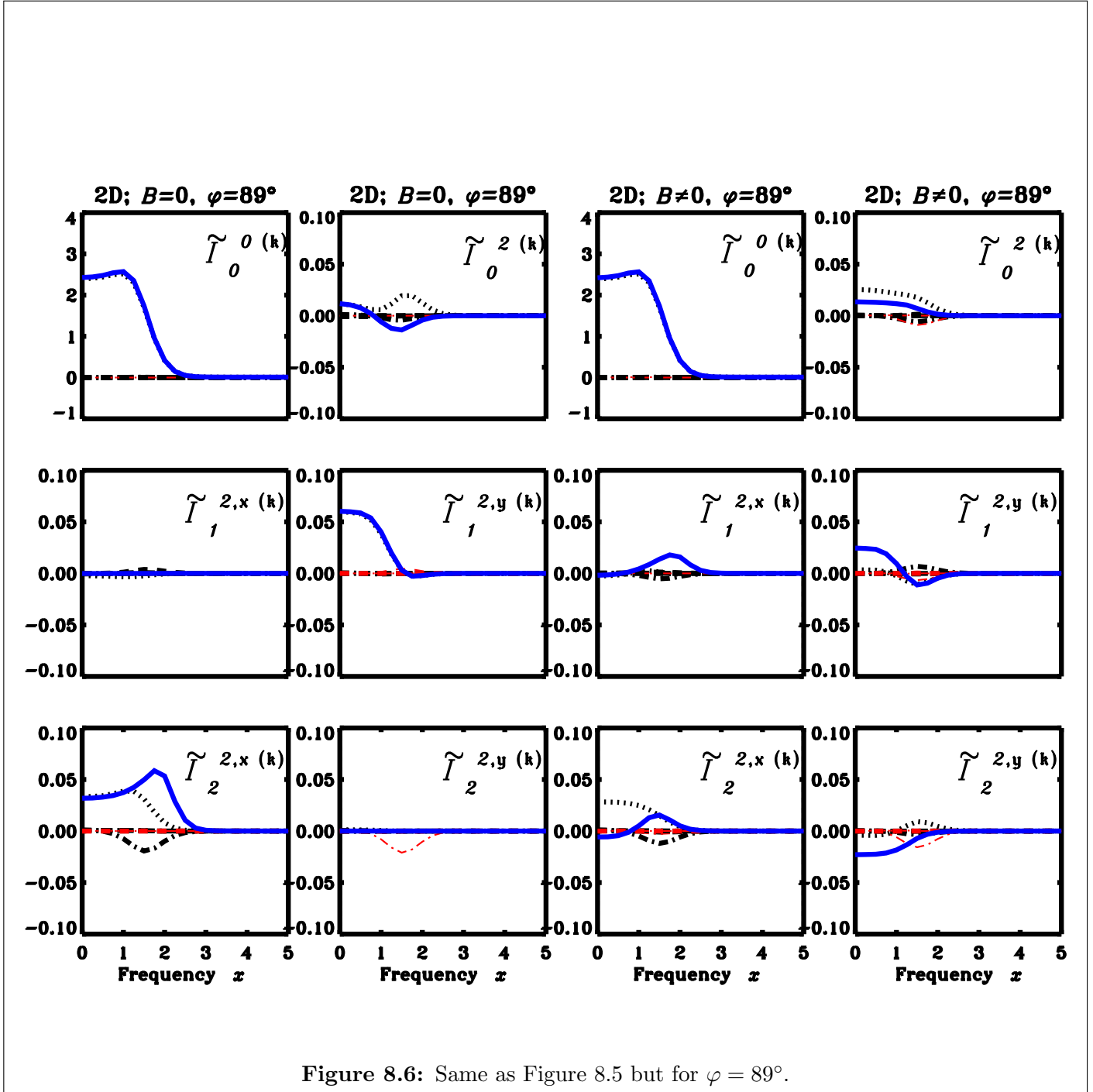


Figure 8.6: Same as Figure 8.5 but for  $\varphi = 89^\circ$ .

into five domains and the functional forms of the redistribution matrices is different in each of these domains. We start with the AD redistribution matrix including Hanle effect namely

$$\begin{aligned} \hat{R}(x, x', \boldsymbol{\Omega}, \boldsymbol{\Omega}', \mathbf{B}) &= \hat{W} \left\{ \hat{M}_{\text{II}}(\mathbf{B}, x, x') r_{\text{II}}(x, x', \boldsymbol{\Omega}, \boldsymbol{\Omega}') \right. \\ &\left. + \hat{M}_{\text{III}}(\mathbf{B}, x, x') r_{\text{III}}(x, x', \boldsymbol{\Omega}, \boldsymbol{\Omega}') \right\} \hat{\Psi}(\boldsymbol{\Omega}'). \end{aligned} \quad (8.15)$$

We recall here that the dependence of the matrices  $\hat{M}_{\text{II,III}}$  on  $x$  and  $x'$  is related to the definition of the frequency domains. Here  $\hat{R}$  is a  $6 \times 6$  matrix. The Fourier series expansions of the functions  $r_{\text{II,III}}(x, x', \boldsymbol{\Omega}, \boldsymbol{\Omega}')$  is written as

$$r_{\text{II,III}}(x, x', \boldsymbol{\Omega}, \boldsymbol{\Omega}') = \sum_{k=0}^{k=\infty} (2 - \delta_{k0}) \mathcal{R}e \{ e^{ik\varphi} \tilde{r}_{\text{II,III}}^{(k)}(x, x', \theta, \boldsymbol{\Omega}') \}, \quad (8.16)$$

with

$$\tilde{r}_{\text{II,III}}^{(k)}(x, x', \theta, \boldsymbol{\Omega}') = \int_0^{2\pi} \frac{d\varphi}{2\pi} e^{-ik\varphi} r_{\text{II,III}}(x, x', \boldsymbol{\Omega}, \boldsymbol{\Omega}'). \quad (8.17)$$

Applying this expansion we can derive a polarized RT equation in terms of the Fourier coefficients  $\tilde{\mathcal{I}}^{(k)}$  and  $\tilde{\mathcal{S}}^{(k)}$  (see Section 7.4 for details) namely

$$-\frac{1}{\kappa_{\text{tot}}(\mathbf{r}, x)} \boldsymbol{\Omega} \cdot \nabla \tilde{\mathcal{I}}^{(k)}(\mathbf{r}, \boldsymbol{\Omega}, x) = [\tilde{\mathcal{I}}^{(k)}(\mathbf{r}, \boldsymbol{\Omega}, x) - \tilde{\mathcal{S}}^{(k)}(\mathbf{r}, \theta, x)], \quad (8.18)$$

where

$$\mathcal{S}(\mathbf{r}, \boldsymbol{\Omega}, x) = \sum_{k=0}^{k=\infty} (2 - \delta_{k0}) \left\{ \cos(k\varphi) \mathcal{R}e \left[ \tilde{\mathcal{S}}^{(k)}(\mathbf{r}, \theta, x) \right] - \sin(k\varphi) \mathcal{I}m \left[ \tilde{\mathcal{S}}^{(k)}(\mathbf{r}, \theta, x) \right] \right\}, \quad (8.19)$$

and

$$\mathcal{I}(\mathbf{r}, \boldsymbol{\Omega}, x) = \sum_{k=0}^{k=\infty} (2 - \delta_{k0}) \left\{ \cos(k\varphi) \mathcal{R}e \left[ \tilde{\mathcal{I}}^{(k)}(\mathbf{r}, \boldsymbol{\Omega}, x) \right] - \sin(k\varphi) \mathcal{I}m \left[ \tilde{\mathcal{I}}^{(k)}(\mathbf{r}, \boldsymbol{\Omega}, x) \right] \right\}. \quad (8.20)$$

Equation (8.18) represents the most reduced form of polarized RT equation in multi-D geometry with the AD PRD. Hereafter we refer to  $\tilde{\mathcal{I}}^{(k)}$  and  $\tilde{\mathcal{S}}^{(k)}$  as ‘irreducible Fourier coefficients’.  $\tilde{\mathcal{I}}^{(k)}$  and  $\tilde{\mathcal{S}}^{(k)}$  are 6-dimensional complex vectors for each value of  $k$ . Here

$$\tilde{\mathcal{S}}^{(k)}(\mathbf{r}, \theta, x) = p_x \tilde{\mathcal{S}}_l^{(k)}(\mathbf{r}, \theta, x) + (1 - p_x) \tilde{\mathcal{S}}_c^{(k)}(\mathbf{r}, x), \quad (8.21)$$

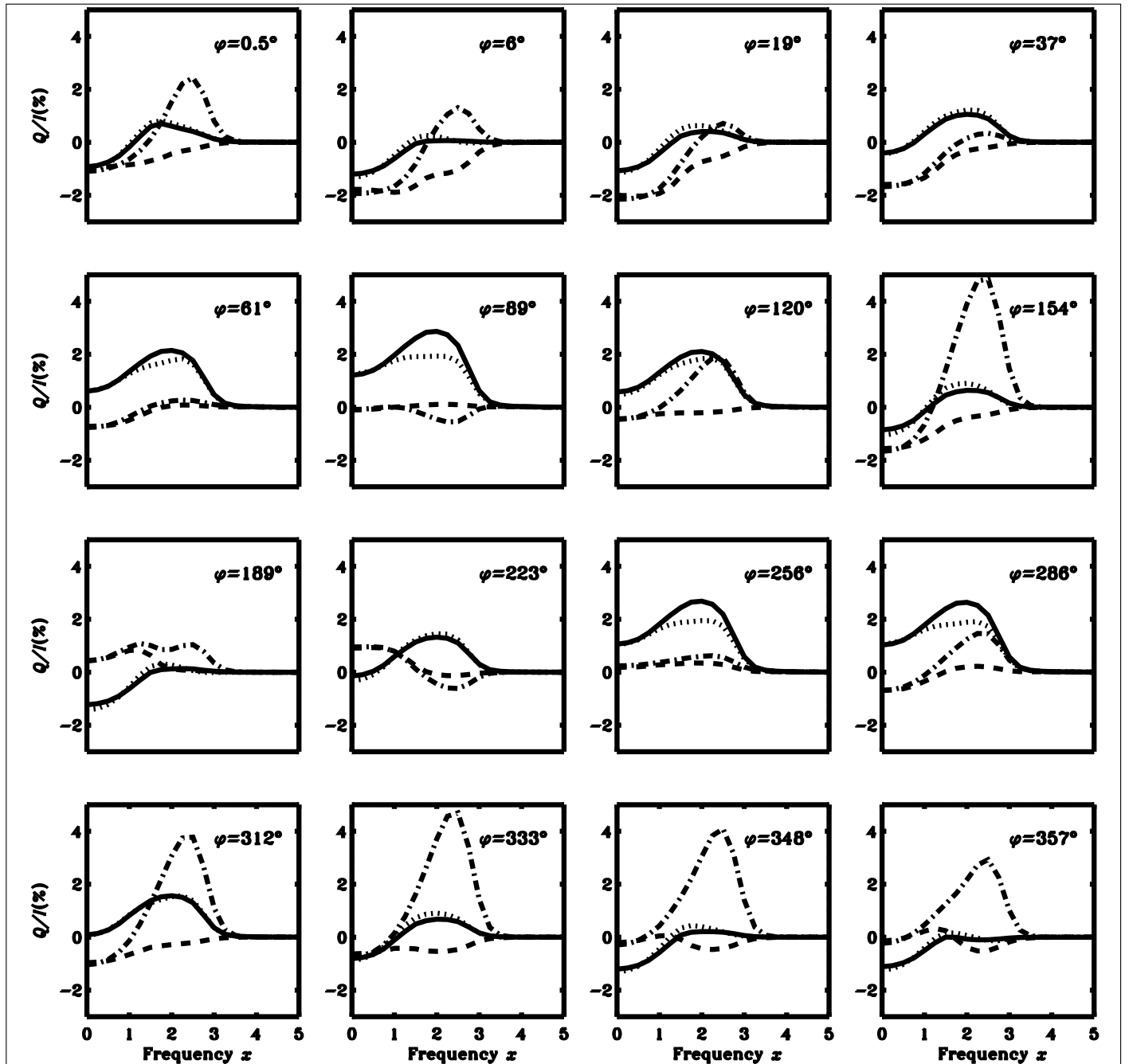


Figure 8.7: Emergent, spatially averaged  $Q/I$  profiles for a 2D medium with  $T_Y = T_Z = 20$ , for a line of sight  $\mu = 0.11$ . Different panels correspond to different values of  $\varphi$  marked in the panels. Solid and dotted lines correspond to the AA and the AD profiles for  $B = 0$ . Dashed and dot-dashed lines correspond to the AA and the AD profiles in a magnetic medium with magnetic field parameter  $(\Gamma, \theta_B, \chi_B) = (1, 90^\circ, 60^\circ)$ .



with

$$\tilde{\mathcal{S}}_c^{(k)}(\mathbf{r}, x) = \delta_{k0} \mathcal{S}_c(\mathbf{r}, x), \quad (8.22)$$

and

$$\begin{aligned} \tilde{\mathcal{S}}_l^{(k)}(\mathbf{r}, \theta, x) &= \tilde{\mathcal{G}}^{(k)}(\mathbf{r}) + \frac{1}{\phi(x)} \int_{-\infty}^{+\infty} dx' \oint \frac{d\Omega'}{4\pi} \\ &\times \hat{R}^{(k)}(x, x', \theta, \Omega', \mathbf{B}) \sum_{k'=0}^{k'=\infty} (2 - \delta_{k'0}) \mathcal{R}e\{e^{ik'\varphi'} \tilde{\mathcal{I}}^{(k')}(\mathbf{r}, \Omega', x')\}. \end{aligned} \quad (8.23)$$

Here  $\tilde{\mathcal{G}}^{(k)}(\mathbf{r}) = \epsilon \delta_{k0} B_\nu(\mathbf{r})$  and

$$\begin{aligned} \hat{R}^{(k)}(x, x', \theta, \Omega', \mathbf{B}) &= \hat{W} \left\{ \hat{M}_{\text{II}}(\mathbf{B}, x, x') \tilde{r}_{\text{II}}^{(k)}(x, x', \theta, \Omega') \right. \\ &\left. + \hat{M}_{\text{III}}(\mathbf{B}, x, x') \tilde{r}_{\text{III}}^{(k)}(x, x', \theta, \Omega') \right\} \hat{\Psi}(\Omega'). \end{aligned} \quad (8.24)$$

Clearly, in the above equation the matrix  $\hat{R}^{(k)}$  is independent of the azimuth ( $\varphi$ ) of the scattered ray. We recall that  $\hat{M}_{\text{II,III}}$  matrices have different forms in different frequency domains (see Bommier 1997b, Nagendra et al. 2002 and Appendix K in this thesis). In the approximation level-II of Bommier (1997b) the expressions for the frequency domains depend on the scattering angle  $\Theta$ , and hence on  $\Omega$  and  $\Omega'$  (because  $\cos \Theta = \Omega \cdot \Omega'$ ). Therefore to be consistent, we must apply the Fourier series expansions to the functions involving  $\Theta$  which appear in the statements defining the AD frequency domains of Bommier (1997b). This leads to complicated mathematical forms of the domain statements. To a first approximation one can keep only the dominant term in the Fourier series (corresponding to the term with  $k = 0$ ). This amounts to replacing the AD frequency domain expressions by their azimuth ( $\varphi$ )-averages. A similar averaging of the domains over the variable ( $\varphi - \varphi'$ ) is done in Nagendra & Sampoorana (2011), where the authors solve the Hanle RT problem with the AD PRD in 1D planar geometry. These kinds of averaging can lead to loss of some information on the azimuth ( $\varphi$ ) dependence of the scattered ray in the domain expressions. A better and alternative approach which avoids any averaging of the domains is the following.

Substituting Equation (8.16) in Equation (8.15) we can write the  $ij$ -th element of the  $\hat{R}$  matrix as

$$R_{ij}(x, x', \Omega, \Omega', \mathbf{B}) = \sum_{k=0}^{k=\infty} (2 - \delta_{k0}) \mathcal{R}e\{e^{ik\varphi} \tilde{R}_{ij}^{(k)}(x, x', \theta, \Omega', \mathbf{B})\}, \quad i, j = 1, 2, \dots, 6, \quad (8.25)$$

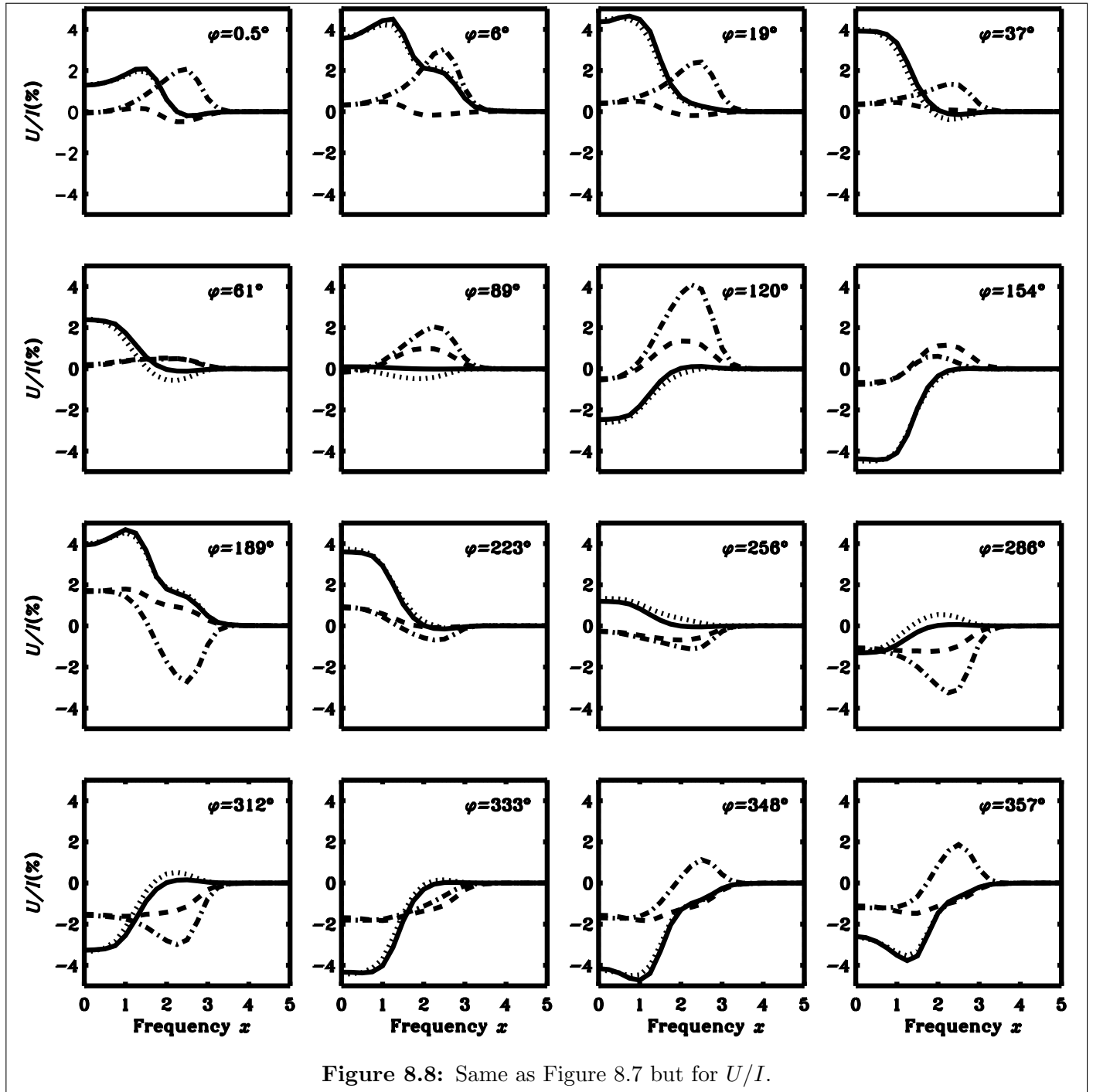


Figure 8.8: Same as Figure 8.7 but for  $U/I$ .

with  $\tilde{R}_{ij}^{(k)}$  being the elements of the matrix  $\hat{R}^{(k)}$  given by Equation (8.24). Through the  $2\pi$ -periodicity of the redistribution functions  $r_{\text{II,III}}(x, x', \boldsymbol{\Omega}, \boldsymbol{\Omega}')$  each element of the  $\hat{R}$  matrix becomes  $2\pi$ -periodic. Therefore we can identify that Equation (8.25) represents the Fourier series expansion of the elements  $R_{ij}$  of the  $\hat{R}$  matrix, with  $\tilde{R}_{ij}^{(k)}$  being the Fourier coefficients. Thus, instead of computing  $\hat{R}^{(k)}$  using Equation (8.24) it is advantageous to compute its elements through the definition of the Fourier coefficients, namely

$$\begin{aligned} \tilde{R}_{ij}^{(k)}(x, x', \theta, \boldsymbol{\Omega}') &= \int_0^{2\pi} \frac{d\varphi}{2\pi} e^{-ik\varphi} W_{ij} \\ &\times \left\{ (M_{\text{II}})_{ij}(\mathbf{B}, x, x') r_{\text{II}}(x, x', \boldsymbol{\Omega}, \boldsymbol{\Omega}') + (M_{\text{III}})_{ij}(\mathbf{B}, x, x') r_{\text{III}}(x, x', \boldsymbol{\Omega}, \boldsymbol{\Omega}') \right\}. \end{aligned} \quad (8.26)$$

Here  $W_{ij}$  are the elements of the  $\hat{W}$  matrix and the matrix elements  $(\hat{M}_{\text{II,III}})_{ij}$  are computed using the AD expressions for the frequency domains as done in Nagendra et al. (2002), without performing azimuth averaging of the domains.

### 8.3 Numerical method of solution

A fast iterative method called the preconditioned Stabilized Bi-Conjugate Gradient (Pre-BiCG-STAB) was introduced in chapter 3. It was developed for 2D transfer with PRD in chapter 5. An AA PRD in the absence of a magnetic field was considered. An extension to a magnetized 3D medium with the AA PRD was taken up in chapter 6. In all these chapters, the computing algorithm was written in the  $n$ -dimensional Euclidean space of real numbers  $\mathbb{R}^n$ . In this chapter, we extend the method to handle the AD PRD for a magnetized 2D media. In this case, it is advantageous to formulate the computing algorithm in the  $n$ -dimensional complex space  $\mathbb{C}^n$ . Here  $n = n_k \times n_p \times n_\theta \times n_x \times n_Y \times n_Z$ , where  $n_{Y,Z}$  are the number of grid points in the  $Y$  and  $Z$  directions, and  $n_x$  refers to the number of frequency points.  $n_\theta$  is the number of polar angles ( $\theta$ ) considered in the problem.  $n_p$  is the number of polarization components of the irreducible vectors.  $n_p = 6$  for both non-magnetic and magnetic AD PRD cases.  $n_k$  is the number of components retained in the Fourier series expansions of the AD PRD functions. Based on the studies in chapter 7 we take  $n_k = 5$ . Clearly the dimensionality of the problem increases when we handle the AD PRD in line scattering in comparison with the AA PRD (see chapters 4 and 5). The numerical results presented in this chapter correspond to 2D media. For 3D RT, the dimensionality escalates, and it is more computationally demanding than the 2D RT. The computing algorithm is similar to the one given in chapter 5, with straightforward extensions to handle the AD PRD. The essential difference is that we now use the vectors

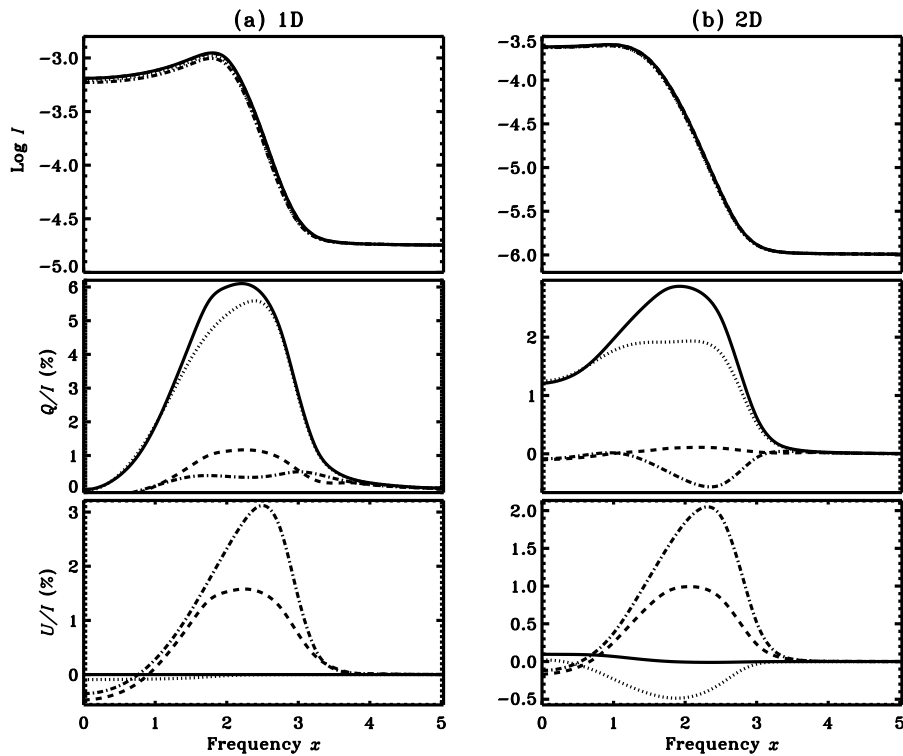


**Figure 8.9:** Panel (a) shows emergent  $(I, Q/I, U/I)$  profiles formed in an 1D medium and the panel (b) shows the emergent, spatially averaged  $(I, Q/I, U/I)$  profiles formed in a 2D medium. The solid and dotted lines represent respectively the AA and the AD profiles for  $\mathbf{B} = 0$ . The dashed and dash-triple-dotted lines represent respectively the AA and the AD profiles for  $\mathbf{B} \neq 0$ , with the magnetic field parameterized by  $(\Gamma, \theta_B, \chi_B) = (1, 90^\circ, 60^\circ)$ . The results are shown for  $\mu = 0.11$  and  $\varphi = 89^\circ$ . For the panel (a) we take  $T_Z = T = 20$  and for the panel (b),  $T_Z = T_Y = T = 20$ .

in the complex space  $\mathbb{C}^n$ . The algorithm contains operations involving the inner product  $\langle \cdot, \cdot \rangle$ . In  $\mathbb{C}^n$  the inner product of two vectors  $\mathbf{u} = (u_1, u_2, \dots, u_n)^T$  and  $\mathbf{v} = (v_1, v_2, \dots, v_n)^T$  is defined as

$$\langle \mathbf{u}, \mathbf{v} \rangle = \sum_{i=1}^n u_i v_i^*, \quad (8.27)$$

where  $*$  represents complex conjugation.

#### *The Preconditioner matrix*

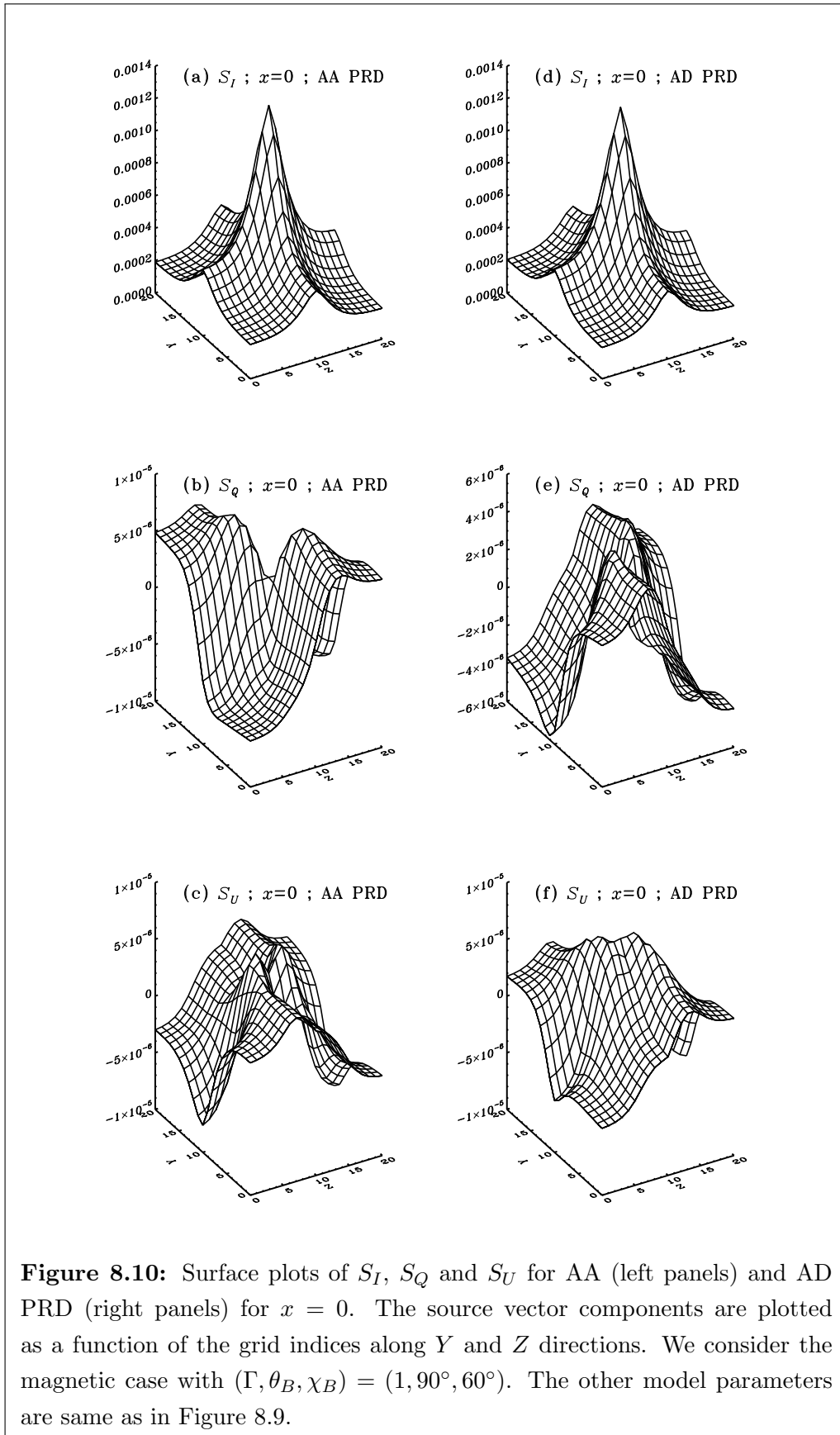
The preconditioner matrices are any form of implicit or explicit modification of the original matrix in the system of equations to be solved, which accelerate the rate of convergence of the problem (see Saad 2000). As explained in chapter 6, the magnetic case requires the use of domain based PRD, where it becomes necessary to use different preconditioner matrices in different frequency domains. In the problem under consideration the preconditioner matrices are complex block diagonal matrices. The dimension of each block is  $n_x \times n_x$ , and the total number of such blocks is  $n/n_x$ . The construction of the preconditioner matrices is analogous to that described in chapter 6, with the appropriate modifications to handle the Fourier decomposed AD PRD matrices.

## 8.4 Results and Discussions

In this section we study some of the benchmark results obtained using the method proposed in this chapter (Sections 8.2.2 and 8.3) which is based on the Fourier decomposition technique developed in chapter 7. In all the results, we consider the following global model parameters. The damping parameter of the Voigt profile is  $a = 2 \times 10^{-3}$  and the continuum to the line opacity  $\kappa_c/\kappa_l = 10^{-7}$ . The internal thermal sources are taken as constant (the Planck function  $B_\nu(\mathbf{r}) = 1$ ). The medium is assumed to be isothermal and self-emitting (no incident radiation on the boundaries). The ratios of elastic and inelastic collision rates to the radiative de-excitation rate are respectively  $\Gamma_E/\Gamma_R = 10^{-4}$ ,  $\Gamma_I/\Gamma_R = 10^{-4}$ . The expressions for the redistribution matrices contain the parameters  $\alpha$  and  $\beta^{(K)}$  and are called as branching ratios (see Bommier 1997b). They are defined as

$$\alpha = \frac{\Gamma_R}{\Gamma_R + \Gamma_E + \Gamma_I}, \quad (8.28)$$

$$\beta^{(K)} = \frac{\Gamma_R}{\Gamma_R + D^{(K)} + \Gamma_I}, \quad (8.29)$$



with  $D^{(0)} = 0$  and  $D^{(2)} = c\Gamma_E$ , where  $c$  is a constant, taken to be 0.379 (see Faurobert-Scholl 1992). The branching ratios for the chosen values of  $\Gamma_E/\Gamma_R$ ,  $\Gamma_I/\Gamma_R$  and  $D^{(K)}$  are  $(\alpha, \beta^{(0)}, \beta^{(2)}) = (1, 1, 1)$ . They correspond to a PRD scattering matrix that uses only  $\tilde{r}_{\text{II}}^{(k)}(x, x', \theta, \boldsymbol{\Omega}')$  function. In other words we consider only the collisionless redistribution processes. We parameterize the magnetic field by  $(\Gamma_B, \theta_B, \chi_B)$ . The Hanle  $\Gamma_B$  coefficient (see Bommier 1997b) takes two different forms, namely

$$\Gamma_B = \Gamma'_K = \beta^{(K)}\Gamma, \quad \Gamma_B = \Gamma'' = \alpha\Gamma, \quad (8.30)$$

with

$$\Gamma = g_J \frac{2\pi eB}{2m_e\Gamma_R}, \quad (8.31)$$

where  $eB/2m_e$  is the Larmor frequency of the electron in the magnetic field (with  $e$  and  $m_e$  being the charge and mass of the electron). We take  $\Gamma_B = 1$  for computing all the results presented in Section 8.4. In this chapter we restrict our attention to effectively optically thin cases (namely the optical thicknesses  $T_Y = T_Z = 20$ ). They represent formation of weak resonance lines in finite dimensional structures.

We show the relative importance of the AD PRD in comparison with the AA PRD considering (1) non-magnetic case ( $\mathbf{B} = 0$ ), and (2) magnetic case ( $\mathbf{B} \neq 0$ ).

In Figure 8.2 we show the geometry of RT in a 2D medium. We assume that the medium is infinite along the  $X$ -axis, and finite along the  $Y$ - and  $Z$ -axes. The top surface of the 2D medium is defined to be the line  $(Y, Z_{\text{max}})$ , as marked in Figure 8.2. We obtain the emergent, spatially averaged  $(I, Q/I, U/I)$  profiles, by simply performing the arithmetic average of these profiles over this line  $(Y, Z_{\text{max}})$  on the top surface.

#### 8.4.1 Nature of the components of $\mathcal{I}$ and $\tilde{\mathcal{I}}^{(k)}$

Often it is pointed out in the literature that the AD PRD effects are important (see e.g., Nagendra et al. 2002) for polarized line formation. For multi-D polarized RT the AD PRD effects have not been addressed so far. Therefore we would like to quantitatively examine this aspect by taking the example of polarized line formation in 2D media, through explicit computation of Stokes profiles using the AD and the AA PRD mechanisms for both  $\mathbf{B} = 0$  and  $\mathbf{B} \neq 0$  cases. The Stokes parameters  $Q$  and  $U$  contain inherently all the AD PRD informations. In order to understand the actual differences between the AD and the AA solutions one has to study the frequency and angular behaviour of the more fundamental quantities, namely  $\mathcal{I}$  and  $\tilde{\mathcal{I}}^{(k)}$ , which are obtained through multi-polar expansions of the Stokes parameters.

In Figures 8.3 and 8.4, we plot the components of the real vector  $\mathcal{I}=(I_0^0, I_0^2, I_1^{2,x}, I_1^{2,y}, I_2^{2,x}, I_2^{2,y})$  which are constructed using the 6 irreducible components of the nine vectors  $\tilde{\mathcal{I}}^{(0)}$ ,  $\mathcal{R}e[\tilde{\mathcal{I}}^{(1)}]$ ,  $\mathcal{I}m[\tilde{\mathcal{I}}^{(1)}]$ ,  $\mathcal{R}e[\tilde{\mathcal{I}}^{(2)}]$ ,  $\mathcal{I}m[\tilde{\mathcal{I}}^{(2)}]$ ,  $\mathcal{R}e[\tilde{\mathcal{I}}^{(3)}]$ ,  $\mathcal{I}m[\tilde{\mathcal{I}}^{(3)}]$ ,  $\mathcal{R}e[\tilde{\mathcal{I}}^{(4)}]$  and  $\mathcal{I}m[\tilde{\mathcal{I}}^{(4)}]$ . For each  $k$ ,  $\tilde{\mathcal{I}}^{(k)}$  is a 6-component complex vector  $(\tilde{I}_0^{0(k)}, \tilde{I}_0^{2(k)}, \tilde{I}_1^{2,x(k)}, \tilde{I}_1^{2,y(k)}, \tilde{I}_2^{2,x(k)}, \tilde{I}_2^{2,y(k)})$ . Thus in Figures 8.5 and 8.6 there are 54 components plotted in 6 panels, with each panel containing 9 curves (see the caption of Figure 8.5 for line identifications). In Figures 8.3– 8.6 the first two columns correspond to the  $\mathbf{B} = 0$  case and the last two columns correspond to the  $\mathbf{B} \neq 0$  case. Here we have chosen  $\mu = 0.11$  and two examples of  $\varphi$  namely  $0.5^\circ$  and  $89^\circ$ .  $\mathcal{I}$  and  $\tilde{\mathcal{I}}^{(k)}$  are related through Equation (8.20) which can be re-written by truncating the Fourier series to five terms, as discussed and validated in chapter 7. Equation (8.20) can be approximated by

$$\mathcal{I} \approx \tilde{\mathcal{I}}^{(0)} + \sum_{k=1}^{k=4} 2 \mathcal{R}e[\tilde{\mathcal{I}}^{(k)}], \quad (8.32)$$

for  $\varphi = 0.5^\circ$  and

$$\mathcal{I} \approx \tilde{\mathcal{I}}^{(0)} - 2 \left\{ \mathcal{I}m[\tilde{\mathcal{I}}^{(1)}] + \mathcal{R}e[\tilde{\mathcal{I}}^{(2)}] - \mathcal{I}m[\tilde{\mathcal{I}}^{(3)}] - \mathcal{R}e[\tilde{\mathcal{I}}^{(4)}] \right\}, \quad (8.33)$$

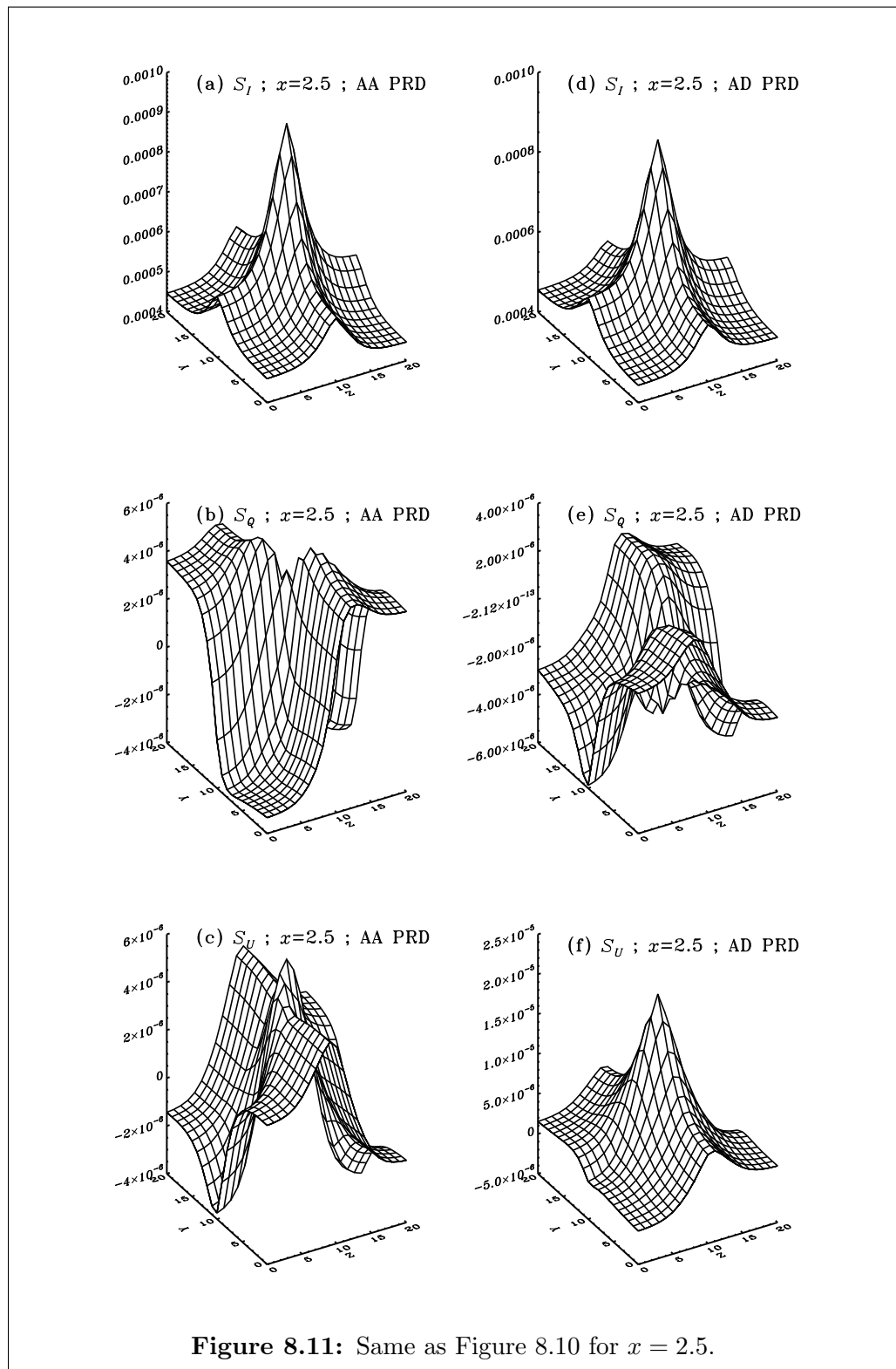
for  $\varphi = 89^\circ$ .

### Non-magnetic case

In general the component  $I_0^0$  (and hence Stokes  $I$  parameter) is less sensitive to the AD nature of PRD functions. Only for certain choices of  $(\theta, \varphi)$ , does  $[I_0^0]_{\text{AD}}$  differ noticeably from  $[I_0^0]_{\text{AA}}$ . The other polarization components exhibit significant sensitivity to the AD PRD. For the present choice of  $(\theta, \varphi)$ , in the second column of Figure 8.3 we see that  $[I_1^{2,y}]_{\text{AD}}$  and  $[I_1^{2,y}]_{\text{AA}}$  are nearly the same. We have verified that they differ very much for other choices of  $(\theta, \varphi)$ . Thus the differences between the AD PRD and the AA PRD are disclosed only when we consider polarization components and not just the  $I_0^0$  component.

In the following we discuss the important symmetry relations of the polarized radiation field for a non-magnetic 2D medium.





## Symmetry relations in non-magnetic 2D media:

In chapter 5 we have shown that  $[I_1^{2,x}]_{AA}$  and  $[I_2^{2,y}]_{AA}$  are identically zero in non-magnetic 2D media (shown as solid lines in the first two columns of Figures 8.3 and 8.4). This property of  $I_1^{2,x}$  and  $I_2^{2,y}$  in a non-magnetic 2D medium arises from the symmetry of the Stokes  $I$  parameter with respect to the infinite axis of the medium ( $X$ -axis in our case), combined with the  $\varphi$ -dependence of the geometrical factors  $\mathcal{T}_Q^K(i, \Omega)$  (see Appendix F, Equations (F.9) and (F.10)). Such a symmetry property is valid if the scattering is according to CRD or the AA PRD where the angular dependence of the source vectors occurs only through the angular dependence of  $(I, Q, U)$  and that of  $\mathcal{T}_Q^K(i, \Omega)$ . For the AD PRD, in addition to these two factors, the angle-dependence of the PRD functions also causes change in the angular behaviour of the source vectors. Thus the AD  $r_{II,III}$  functions depend on  $\varphi$  in such a way that  $[I_1^{2,x}]_{AD}$  and  $[I_2^{2,y}]_{AD}$  are not zero in general (shown as dotted lines in the first two columns of Figures 8.3 and 8.4). Using a Fourier expansion of the AD  $r_{II,III}$  functions we have proved this fact in Appendix L.

**Table 8.1:** The dominant Fourier components contributing to each of the 6 irreducible components of  $\mathcal{I}$  in a non-magnetic 2D medium, shown as cross symbols.

	$k = 0$	$k = 1$	$k = 2$	$k = 3$	$k = 4$
$\tilde{\mathcal{I}}_0^{0(k)}$	x	-	-	-	-
$\tilde{\mathcal{I}}_0^{2(k)}$	x	-	-	-	-
$\mathcal{R}e \left[ \tilde{\mathcal{I}}_1^{2,x(k)} \right]$	x	x	-	-	-
$\mathcal{I}m \left[ \tilde{\mathcal{I}}_1^{2,x(k)} \right]$	-	-	-	-	-
$\mathcal{R}e \left[ \tilde{\mathcal{I}}_1^{2,y(k)} \right]$	x	-	-	-	-
$\mathcal{I}m \left[ \tilde{\mathcal{I}}_1^{2,y(k)} \right]$	-	x	-	-	-
$\mathcal{R}e \left[ \tilde{\mathcal{I}}_2^{2,x(k)} \right]$	x	-	x	-	-
$\mathcal{I}m \left[ \tilde{\mathcal{I}}_2^{2,x(k)} \right]$	-	-	-	-	-
$\mathcal{R}e \left[ \tilde{\mathcal{I}}_2^{2,y(k)} \right]$	-	-	-	-	-
$\mathcal{I}m \left[ \tilde{\mathcal{I}}_2^{2,y(k)} \right]$	-	-	x	-	-

The components of  $\tilde{\mathcal{I}}^{(k)}$  also exhibit some interesting properties. In Table 8.1 we list

the dominant Fourier components contributing to each of the 6 components of  $\mathcal{I}$  in a non-magnetic 2D medium (shown as crosses). In the following we describe the nature of these Fourier components. Of all the components  $\tilde{I}_0^{0(k)}$  and  $\tilde{I}_0^{2(k)}$ , only  $\tilde{I}_0^{0(0)}$  and  $\tilde{I}_0^{2(0)}$  (dotted lines in the first two columns of Figures 8.5 and 8.6) are dominant and they are nearly same as  $[I_0^0]_{\text{AD}}$  and  $[I_0^2]_{\text{AD}}$  respectively (dotted lines in the first two columns of Figures 8.3 and 8.4).  $\tilde{I}_0^{2(0)}$  is an important ingredient for Stokes  $Q$ . The components  $\tilde{I}_{1,2}^{2,x,y(k)}$  are ingredients for both Stokes  $Q$  and  $U$ . It can be seen that except  $\tilde{I}_2^{2,y(0)}$  all other  $\tilde{I}_{1,2}^{2,x,y(0)}$  play an important role in the construction of the vector  $\mathcal{I}$ . For  $\tilde{I}_{1,2}^{2,x(k)}$ ,  $k \neq 0$ , only  $\mathcal{R}e \left[ \tilde{I}_1^{2,x(1)} \right]$  and  $\mathcal{R}e \left[ \tilde{I}_2^{2,x(2)} \right]$  (thick dashed and thick dot-dashed lines respectively) are dominant. For  $\tilde{I}_{1,2}^{2,y(k)}$ ,  $k \neq 0$ , only  $\mathcal{I}m \left[ \tilde{I}_1^{2,y(1)} \right]$  and  $\mathcal{I}m \left[ \tilde{I}_2^{2,y(2)} \right]$  (thin dashed and thin dot-dashed lines respectively) are dominant. This property is true for other choices of  $(\theta, \varphi)$  also. From this property it appears that, in rapid computations involving the AD PRD mechanisms, it may prove useful to approximate the problem by using the truncated, 9-component vector  $(\tilde{I}_0^{0(0)}, \tilde{I}_0^{2(0)}, \tilde{I}_1^{2,x(0)}, \tilde{I}_1^{2,y(0)}, \mathcal{R}e \left[ \tilde{I}_1^{2,x(1)} \right], \mathcal{I}m \left[ \tilde{I}_1^{2,y(1)} \right], \mathcal{R}e \left[ \tilde{I}_2^{2,x(2)} \right], \mathcal{I}m \left[ \tilde{I}_2^{2,y(2)} \right])$  and obtain sufficiently accurate solution with less computational efforts. When the 6-component complex vector  $\tilde{\mathcal{I}}^{(k)}$  for each value of  $k = 0, 1, 2, 3, 4$ , having 54 independent components is used, the computations are expensive.

### Magnetic case

When we introduce a non-zero magnetic field  $\mathbf{B}$ , the shapes, signs and magnitudes of  $\mathcal{I}_{\text{AA,AD}}$  change (see the last two columns of Figures 8.3 and 8.4).  $[I_1^{2,x}]_{\text{AA}}$  and  $[I_2^{2,y}]_{\text{AA}}$  which were zero when  $\mathbf{B} = 0$ , now take non-zero values. With a given  $\mathbf{B} \neq 0$ , except  $I_0^0$ , the behaviors of all the other components for the AD PRD are very different from those for the AA PRD. Because the Hanle effect is operative only in the line core ( $0 \leq x \leq 3.5$ ), all the magnetic effects are confined to the line core.

For  $\mathbf{B} = 0$  only some of the components of  $\tilde{\mathcal{I}}^{(k)}$  play a significant role. For  $\mathbf{B} \neq 0$ , all the components of  $\tilde{\mathcal{I}}^{(k)}$  can become important (see the last two columns of Figures 8.5 and 8.6). This property has a direct impact on the values of  $Q/I$  and  $U/I$ .

#### 8.4.2 Emergent Stokes Profiles

In Figures 8.7 and 8.8 we present the emergent, spatially averaged  $Q/I$  and  $U/I$  profiles computed using the AD and the AA PRD in line scattering for non-magnetic and magnetic 2D media. We show the results for  $\mu = 0.11$  and sixteen different values of  $\varphi$  (marked on the respective panels). For the optically thin cases considered in this chapter the AD PRD

effects are restricted to the frequency domain  $0 \leq x \leq 5$ . To understand these results let us consider two examples ( $\varphi = 0.5^\circ$  and  $89^\circ$ ). For  $\varphi = 0.5^\circ$  we can approximate the emergent  $Q$  and  $U$  using Equations (8.3) and (8.4) as

$$Q(\mu = 0.11, \varphi = 0.5^\circ, x) \approx -\frac{3}{2\sqrt{2}}I_0^2 - \frac{\sqrt{3}}{2}I_2^{2,x}, \quad (8.34)$$

and

$$U(\mu = 0.11, \varphi = 0.5^\circ, x) \approx \sqrt{3}I_1^{2,y}. \quad (8.35)$$

For  $\varphi=89^\circ$  also we can obtain approximate expressions for  $Q$  and  $U$  given by

$$Q(\mu = 0.11, \varphi = 89^\circ, x) \approx -\frac{3}{2\sqrt{2}}I_0^2 + \frac{\sqrt{3}}{2}I_2^{2,x}, \quad (8.36)$$

and

$$U(\mu = 0.11, \varphi = 89^\circ, x) \approx \sqrt{3}I_1^{2,x}. \quad (8.37)$$

### Angle-dependent PRD effects in the non-magnetic case

In both the Figures 8.7 and 8.8, the solid and dotted curves represent the  $\mathbf{B} = 0$  case. It is easy to observe that the differences between these curves depend on the choice of the azimuth angles  $\varphi$  for  $Q/I$ , while for  $U/I$  the differences are marginal.

#### The $Q/I$ profiles:

For  $\varphi = 0.5^\circ$  the  $[Q/I]_{\text{AD}}$  and  $[Q/I]_{\text{AA}}$  nearly coincide. But for  $\varphi = 89^\circ$  they differ by  $\sim 1\%$  (in the degree of linear polarization) around  $x = 2$ , which is very significant. From Equations (8.34) and (8.36) it is clear that  $[Q/I]_{\text{AD}}$  and  $[Q/I]_{\text{AA}}$  are controlled by the combinations of the components  $I_0^2$  and  $I_2^{2,x}$ . We can see from the first two columns of Figure 8.3 that for  $\varphi = 0.5^\circ$ ,  $I_0^2$  and  $I_2^{2,x}$  have comparable magnitudes for both the AA and the AD PRD. Further,  $[I_0^2]_{\text{AA}} < 0$ ,  $[I_2^{2,x}]_{\text{AA}} > 0$ ,  $[I_0^2]_{\text{AD}} > 0$  and  $[I_2^{2,x}]_{\text{AD}} < 0$ . From Equation (8.34) we can see that in spite of their opposite signs, because of their comparable magnitudes, the combinations of  $I_0^2$  and  $I_2^{2,x}$  result in nearly same values of  $[Q/I]_{\text{AD}}$  and  $[Q/I]_{\text{AA}}$ . When  $\varphi = 89^\circ$  the components  $[I_0^2]_{\text{AA}}$ ,  $[I_0^2]_{\text{AD}}$ ,  $[I_2^{2,x}]_{\text{AA}}$  and  $[I_2^{2,x}]_{\text{AD}}$  are of comparable magnitudes. Whereas  $[I_0^2]_{\text{AA}}$  and  $[I_2^{2,x}]_{\text{AA}}$  have opposite signs,  $[I_0^2]_{\text{AD}}$  and

$[I_2^{2,x}]_{\text{AD}}$  have the same sign. Therefore from Equation (8.36) we see that  $[Q/I]_{\text{AD}}$  differs from  $[Q/I]_{\text{AA}}$  for  $\varphi = 89^\circ$ .

To understand the behaviors of the components of  $I_0^2$  and  $I_2^{2,x}$  discussed above, we can refer to Figures 8.5, 8.6 and Table 8.1. The component  $\tilde{I}_0^{2(0)}$  contributes dominantly to  $I_0^2$ , and is almost identical to  $I_0^2$  because the contribution from  $\tilde{I}_0^{2(k)}$  with  $k = 1, 2, 3, 4$  are negligible (for both the values of  $\varphi$ ). When  $\varphi = 0.5^\circ$ , apart from  $\tilde{I}_2^{2,x(0)}$ , the component  $\mathcal{R}e \left[ \tilde{I}_2^{2,x(2)} \right]$  makes a significant contribution to  $I_2^{2,x}$  and  $\tilde{I}_2^{2,x(k)}$  with other values of  $k$  vanish (graphically).  $\mathcal{R}e \left[ \tilde{I}_2^{2,x(2)} \right]$  makes nearly equal and opposite contribution as  $\tilde{I}_2^{2,x(0)}$  when  $\varphi = 0.5^\circ$ . When  $\varphi = 89^\circ$ , the contribution of  $\tilde{I}_2^{2,x(0)}$  is larger than that of  $\mathcal{R}e \left[ \tilde{I}_2^{2,x(2)} \right]$ . Also, the components  $\tilde{I}_0^{2(0)}$  and  $\tilde{I}_2^{2,x(0)}$  have the same sign for both the values of  $\varphi$ . Therefore From Equations (8.32) and (8.33) we can see that  $I_0^2$  and  $I_2^{2,x}$  have opposite signs for  $\varphi = 0.5^\circ$  but have the same signs for  $\varphi = 89^\circ$ .

The AD and the AA values of  $Q/I$  sometimes coincide well and sometimes differ significantly. This is because, the Fourier components of the AD PRD functions  $\tilde{r}_{\text{II,III}}^{(k)}$  with  $k = 0$  essentially represent the azimuthal averages of the AD  $r_{\text{II,III}}$  functions and are not same as the explicit angle-averages of the AD  $r_{\text{II,III}}$  functions. The latter are obtained by averaging over both co-latitudes and azimuths (i.e., over all the scattering angles). The  $\mu$ -dependence of the AD  $r_{\text{II,III}}$  functions are contained dominantly in the  $\tilde{r}_{\text{II,III}}^{(0)}$  terms and the  $\varphi$ -dependence is contained dominantly in the higher order terms in the Fourier expansions of the AD  $r_{\text{II,III}}$  functions. For this reason the AA PRD cannot always be a good representation of the AD PRD, especially in the 2D polarized line transfer. This can be attributed to the strong dependence of the radiation field on the azimuth angle ( $\varphi$ ) in the 2D geometry. As will be shown below, the differences between the AD and the AA solutions get further enhanced in the magnetic case (Hanle effect).

#### The $U/I$ profiles:

When  $\mathbf{B} = 0$ ,  $[U/I]_{\text{AD}}$  and  $[U/I]_{\text{AA}}$  profiles for both values of  $\varphi$  ( $0.5^\circ$  and  $89^\circ$ ) do not differ significantly. Equations (8.35) and (8.37) suggest that  $U$  has dominant contribution from  $I_1^{2,y}$  for  $\varphi=0.5^\circ$  and  $I_1^{2,x}$  for  $89^\circ$ . Looking at the first two columns of Figure 8.5, it can be seen that  $\tilde{I}_1^{2,y(0)}$  nearly coincide with  $[I_1^{2,y}]_{\text{AA}}$  for  $\varphi = 0.5^\circ$ . Except  $\tilde{I}_1^{2,y(0)}$ ,  $\tilde{I}_1^{2,y(k)}$  for  $k \neq 0$  make smaller contribution in the construction of  $[I_1^{2,y}]_{\text{AD}}$ . Thus  $[I_1^{2,y}]_{\text{AA}}$  and  $[I_1^{2,y}]_{\text{AD}}$  nearly coincide for  $\varphi=0.5^\circ$  (see the first two columns of Figure 8.3). Thus  $[U/I]_{\text{AD}}$

and  $[U/I]_{AA}$  are nearly the same for  $\varphi=0.5^\circ$ . When  $\varphi=89^\circ$  (the first two columns of Figure 8.4),  $[I_1^{2,x}]_{AA}$  vanishes. For each  $k$ ,  $\tilde{I}_1^{2,x(k)}$  approach zero, as does  $[I_1^{2,x}]_{AD}$ , which is a combination of  $\tilde{I}_1^{2,x(k)}$ . Thus  $[U/I]_{AD}$  and  $[U/I]_{AA}$  both are nearly zero for  $\varphi=89^\circ$ . We can carry out similar analysis and find out which are the irreducible Fourier components of  $\tilde{\mathcal{I}}^{(k)}$  that contribute to the construction of  $\mathcal{I}$  and which of the components of  $\mathcal{I}$  contribute to generate  $Q$  and  $U$  to interpret their behaviors.

### Angle-dependent PRD effects in the magnetic case

The presence of a weak, oriented magnetic field modifies the values of  $Q/I$  and  $U/I$  in the line core ( $x \leq 3.5$ ) to a considerable extent, due to Hanle effect. Further, it is for  $\mathbf{B} \neq 0$  that the differences between the AA and the AD PRD become more significant. In both the Figures 8.7 and 8.8, the dashed and dot-dashed curves represent  $\mathbf{B} \neq 0$  case. As usual, there is either a depolarization (decrease in the magnitude) or a re-polarization (increase in the magnitude) of both  $Q/I$  and  $U/I$  with respect to those in the  $\mathbf{B} = 0$  case. The AD PRD values of  $Q/I$  and  $U/I$  are larger in magnitude (absolute values) than those of the AA PRD, for the chosen set of model parameters (this is not to be taken as a general conclusion). The differences depend sensitively on the value of  $\mathbf{B}$ .

### Comparison with 1D results:

In Figures 8.9(a) and (b) we present the emergent  $(I, Q/I, U/I)$  profiles for 1D and 2D media for  $\mu = 0.11$  and  $\varphi = 89^\circ$ . For 2D RT, we present the spatially averaged profiles. The effects of a multi-D geometry (2D or 3D) on linear polarization for non-magnetic and magnetic cases are discussed in detail in chapters 4, 5 and 6, where we considered polarized line formation in multi-D media, scattering according to the AA PRD. We recall here that the essential effects are due to the finite boundaries in multi-D media, which cause leaking of radiation and hence a decrease in the values of Stokes  $I$ , and a sharp rise in the values of  $Q/I$  and  $U/I$  near the boundaries. Multi-D geometry naturally breaks the axisymmetry of the medium that prevails in a 1D planar medium. This leads to significant differences in the values of  $Q/I$  and  $U/I$  formed in 1D and multi-D media (compare solid lines in panels (a) and (b) of Figure 8.9). As pointed out in chapters 4, 5 and 6, for non-magnetic case,  $U/I$  is zero in 1D media while in 2D media a non-zero  $U/I$  is generated due to symmetry breaking by the finite boundaries. For the  $(\theta, \varphi)$  values chosen in Figure 8.9(b)  $[U/I]_{AA}$  is nearly zero even for non-magnetic 2D case, which is not generally true for other choices of

$(\theta, \varphi)$  (see solid lines in various panels of Figure 8.8). The effects of the AD PRD in  $Q/I$  and  $U/I$  profiles are already discussed above for non-magnetic and magnetic 2D media. They are similar for both 1D and 2D cases. For the non-magnetic 2D media, we can see the AD PRD effects even in  $U/I$ , which is absent in the corresponding 1D media. In 1D, one has to apply a non-zero magnetic field  $\mathbf{B}$  in order to see the effects of the AD PRD on  $U/I$  profiles.

The magnitudes of  $[Q/I]_{1D}$  in the non-magnetic case and of  $[Q/I]_{1D}$ ,  $[U/I]_{1D}$  in the magnetic case are larger in comparison with the corresponding spatially averaged  $[Q/I]_{2D}$  and  $[U/I]_{2D}$ . This is again due to leaking of photons from the finite boundaries and the effect of spatial averaging (which causes cancellation of positive and negative quantities).

### 8.4.3 Radiation anisotropy in 2D media—Stokes source vectors

In Figures 8.10 and 8.11 we present spatial distribution of  $S_I$ ,  $S_Q$  and  $S_U$  on the plane of the 2D slab for two different frequencies ( $x = 0$  and  $x = 2.5$  respectively). The spatial distribution of source vector components  $S_Q$  and  $S_U$  represent the anisotropy of the radiation field in the 2D medium. It shows how inhomogeneous is the distribution of linear polarization within the 2D medium.

In Figure 8.10 we consider  $x = 0$  (line center). For the chosen values of  $(\theta, \varphi)$  the spatial distribution of  $S_I$  is not very different for the AA and the AD PRD.  $S_Q$  and  $S_U$  for both the AA and the AD PRD have similar magnitudes (Figures 8.10(b),(c) and 8.10(e),(f)), but different spatial distributions. The spatial distribution of  $S_Q$  and  $S_U$  is such that the positive and negative contributions with similar magnitudes of  $S_Q$  and  $S_U$  cancel out in the computation of their formal integrals. Therefore, the average values of  $Q/I$  and  $U/I$  resulting from the formal integrals of  $S_Q$  and  $S_U$  are nearly zero at  $x = 0$  for both the AA and the AD PRD (see dashed and dot-dashed lines at  $x = 0$  in Figure 8.9(b)).

In Figure 8.11 we consider  $x = 2.5$  (near wing frequency). Again,  $S_I$  does not show significant differences between the AA and the AD PRD. For  $S_Q$ , the AA PRD has a distribution with positive and negative values equally distributed in the 2D slab but the AD PRD has more negative contribution. This reflects in the average values of  $Q/I$ , where  $[Q/I]_{AA}$  approach zero due to cancellation, while  $[Q/I]_{AD}$  values are more negative (see dashed and dot-dashed lines at  $x = 2.5$  in Figure 8.9(b)). The positive and negative values of  $S_U$  are distributed in a complicated manner everywhere on the 2D slab for the AA PRD. For the AD PRD, the distribution of  $S_U$  is positive almost everywhere, including the central parts of the 2D slab. Such a spatial distribution reflects again in the average value

of  $U/I$  (shown in Figure 8.9(b)), where  $[U/I]_{AA}$  have smaller positive magnitudes (due to cancellation effects) than the corresponding  $[U/I]_{AD}$ .

## 8.5 Conclusions

In this chapter we have further generalized the Fourier decomposition technique developed in chapter 7 to handle the AD PRD in multi-D polarized RT (see Section 8.2.2). We have applied this technique and developed an efficient iterative method called Pre-BiCG-STAB to solve this problem (see Section 8.3).

We prove in this chapter that the symmetry of the polarized radiation field with respect to the infinite axis, that exists for a non-magnetic 2D medium for the AA PRD (as shown in Appendix F) breaks down for the AD PRD (see Appendix L).

We present results of the very first investigations of the effects of the AD PRD on the polarized line formation in multi-D media. We restrict our attention to freestanding 2D slabs with finite optical thicknesses on the two axes ( $Y$  and  $Z$ ). The optical thicknesses of the isothermal 2D media considered in this chapter are very moderate ( $T = 20$ ). We consider effects of the AD PRD on the scattering polarization in both non-magnetic and magnetic cases. We find that the relative AD PRD effects are prominent in the magnetic case (Hanle effect). They are also present in non-magnetic case for some choices of  $(\theta, \varphi)$ . We conclude that the AD PRD effects are important for interpreting the observations of scattering polarization in multi-D structures on the Sun.

Practically, even with the existing advanced computing facilities, it is extremely difficult to carryout the multi-D polarized RT with the AD PRD in spite of using advanced numerical techniques. Therefore in this chapter we restrict our attention to isothermal 2D slabs. The use of the AD PRD in 3D polarized RT in realistic modeling of the observed scattering polarization on the Sun will be numerically very expensive and can be taken up in future only with highly advanced computing facilities.

### New Results

The important results obtained in chapter 8 are as follows.



1. We reduce the Stokes vector transfer equation to a simpler form using a Fourier decomposition technique for multi-D media developed in chapter 7.
2. A fast numerical method is also devised to solve the concerned multi-D transfer problem.
3. The numerical results are presented for a 2D medium with a moderate optical thickness (effectively thin), and are computed for a collisionless frequency redistribution.
4. We have shown that the AD PRD effects are significant, and can not be ignored in a quantitative fine analysis of the line polarization. These effects are accentuated by the finite dimensionality of the medium (multi-D transfer). The presence of magnetic fields (Hanle effect) modifies the impact of these two effects to a considerable extent.



## Part-III

Realistic modeling of the  
spectropolarimetric observations of  
the second solar spectrum



## Chapter 9

# Last scattering approximation: Case study with Ca I 4227 Å

*The contents of this chapter are based on the following publication:*

Anusha, L. S., Nagendra, K. N., Stenflo, J. O., Bianda, M., Sampoorna, M., Frisch, H., Holzreuter, R., and Ramelli, R., 2010a, **ApJ**, 718, 988-1000

### 9.1 Introduction

The Ca I 4227 Å line shows the largest degree of linear polarization in the Second Solar Spectrum (the linearly polarized spectrum of the Sun that is due to coherent scattering processes). The Hanle effect, a magnetic field modification of this linear polarization, was first observed on the Sun in the core of this line by Stenflo (1982). Enigmatic behaviors of the line wing polarization were observed not only in active regions (see Bianda et al. 2003) but also in the quiet regions of the Sun (see Sampoorna et al. 2009, hereafter S09). These observations motivated a modeling of Ca I 4227 Å line by an extension of the Last Scattering Approximation (LSA) method, originally formulated by Stenflo (1982). It is shown in S09 that the unexpected wing features cannot be interpreted in terms of the Hanle effect, which was thought to become operative in the line wings through a combination of frequency redistribution and elastic collisions (Nagendra et al. 2002; Sampoorna et al. 2007).

The idea behind the LSA introduced in Stenflo (1982) is that the observed polarization  $Q/I$  can be evaluated by considering only one single scattering process in which the observed Stokes  $I$  plays the role of the incident radiation field. Its center to limb variation

provides the angular distribution needed to calculate the anisotropy of the radiation field which is the ultimate source of the linear polarization. The purpose of LSA type methods is to derive the linear polarization from Stokes  $I$ , avoiding the solution of the full scale polarized radiative transfer (RT) equation which is always somewhat computationally expensive and may still be beyond the capabilities of existing computers, for example if one deals with three-dimensional (3D) calculations.

The modeling strategy in S09 is based on an extension of LSA method introduced in Stenflo (1982) for frequency coherent scattering (incident and scattered beams are keeping the same frequency). For the analysis of the Ca I 4227 Å line, frequency changes at each scattering are taken into account. They are described by an angle-dependent Hanle-Zeeman partial frequency redistribution (PRD) matrix. In addition the anisotropy of the radiation field is made frequency dependent. It is deduced from the center to limb variation of Stokes  $I$  at a set of wavelengths along the intensity profile. With this procedure it is possible to model the observed  $Q/I$  profile in the far line wings and the characteristic maxima of  $Q/I$  in the near line wings. However, the other features of the  $Q/I$  profile (the line center peak itself, and the core minima) cannot be reproduced. The PRD matrix used in S09 provides a good representation of frequency redistribution in the line core and the line wings and hence cannot be held responsible for the failure of the modeling at the line center. So we embarked in the construction of new LSA approximations which can take into account RT effects that are neglected when the polarization is deduced from the observed intensity only.

In this chapter (see also Anusha et al. 2010a) we present three different LSA approximations. We refer to them for clarity, as LSA-1, 2 and 3. LSA-3 and LSA-2 take into account RT effects, LSA-2 being a degraded version of LSA-3. LSA-3 is very similar to the single scattering approximation introduced in Frisch et al. (2009). LSA-1 is very similar to the LSA approximation used in S09. All these approximations are computationally much faster than a full polarized RT calculation.

We validate the performance of LSA-1 to LSA-3 by comparing their predictions for the ratio  $Q/I$  of the Ca I 4227 Å line with the solution of a full polarized RT equation, which we refer for brevity as the RT approach. For the RT approach, we use the numerical code developed by D. Fluri (see e.g., Fluri et al. 2003a; Holzreuter et al. 2005), which can take into account multi-level atoms and solar atmospheric models. We also compare the predictions of the LSA-3 and of RT calculations with recent observations of the Ca I 4227 Å line taken at IRSOL in January 2010. With both methods we can fit rather well

the triplet peak structure of the  $Q/I$  profile present around the line center. A qualitative explanation for this triplet structure observed in strong chromospheric lines such as Ca I 4227 Å and Na I D<sub>2</sub> 5890 Å (see Gandorfer 2000; 2002; 2005) can be found in Holzreuter et al. (2005). For the comparison with the observations we have incorporated in the LSA-3 approximation and RT calculation the effect of a micro-turbulent magnetic field. It is a very straightforward generalization (see e.g., Faurobert-Scholl 1993, 1994; Holzreuter et al. 2006). We note that all the approximations presented in this chapter can be generalized to the case of the Hanle effect due to an oriented field (i.e.,  $U \neq 0$ ).

In Section 9.2 we present the polarized RT equations, which serve as starting point for the RT approach and the LSA-3 and LSA-2 approximations. We describe in Section 9.3 the observations and the solar atmospheric models which are used for testing the RT calculation and the LSA-3 approximation. In Section 9.4 we briefly discuss the wavelength and depth dependence of the radiation field anisotropy. The basic equations of LSA-1, 2, and LSA-3 are given in Section 9.5. Section 9.6 is devoted to comparisons between  $Q/I$  profiles calculated with the LSA-3 approximation and a full RT approach and also to comparisons with observations. The concluding remarks are presented in Section 9.7. A brief discussion on PRD matrices is given in the Appendix M.

The mathematical symbols in this part (part - III) of the thesis (chapters 9 and 10) slightly differ from those in other two parts of the thesis. This is because of the fact that in part - I and part - II we deal with isothermal atmospheres and in part - III we use realistic (or standard) model solar atmospheres, model atom etc.

## 9.2 The Radiative Transfer (RT) approach

Throughout this chapter we use the standard notation of line formation theory (Mihalas 1978; Stenflo 1994). As we work with solar model atmospheres, all the physical quantities explicitly depend on the altitude  $z$  in the atmosphere. The polarized RT equation in one-dimensional (1D) planar axisymmetric medium, is written in standard notation as

$$\mu \frac{\partial \mathbf{I}(\lambda, \mu, z)}{\partial z} = -[\kappa_l(z)\phi(\lambda, z) + \kappa_c(\lambda, z) + \sigma_c(\lambda, z)] [\mathbf{I}(\lambda, \mu, z) - \mathbf{S}(\lambda, \mu, z)], \quad (9.1)$$

where the Stokes vector  $\mathbf{I} = (I, Q)^T$ . The Voigt profile function is denoted by  $\phi$ . The dependence on  $\phi$  on  $z$  comes from the damping parameter  $a = \Gamma_{\text{tot}}/4\pi\Delta\nu_D$ . The radiative and collisional broadening are included in  $\Gamma_{\text{tot}}$ . The Doppler width is  $\Delta\nu_D = \sqrt{2k_B T/M_a + v_{\text{turb}}^2}/\lambda_0$  in standard notations. Here,  $\kappa_l$  is the line averaged absorption coefficient,  $\sigma_c$  and  $\kappa_c$  are the continuum scattering and continuum absorption coefficients

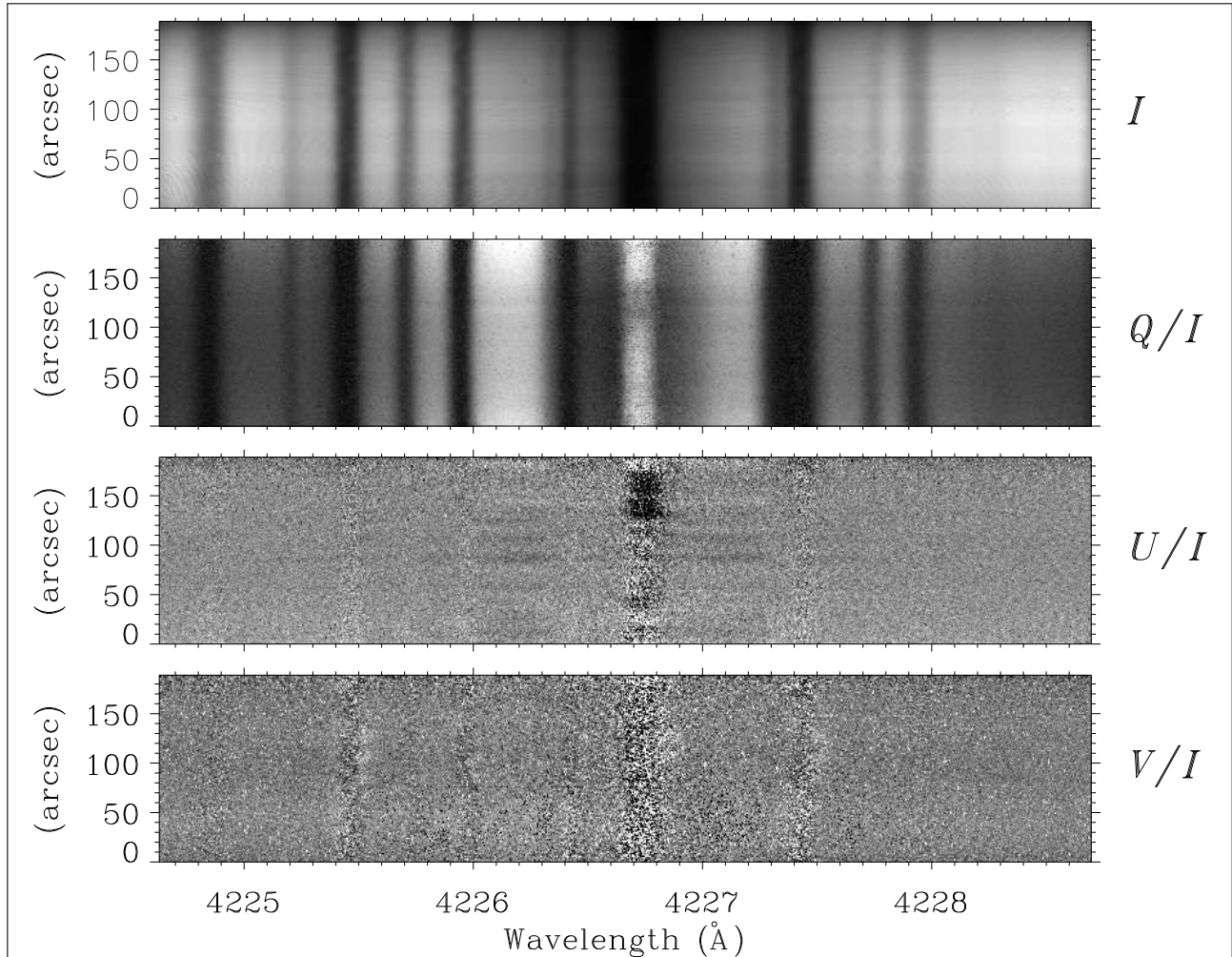


**Figure 9.1:** The CCD image of the Stokes parameters in a spectral window around the Ca I 4227 Å line. The observations are made with the spectrograph slit placed parallel to the north limb (about 6'' inside around the spatial position 60''). Due to the curvature of the solar limb, the end points of the slit are closer to the limb when compared to the center of the slit. This explains the decrease in intensity and increase in the wing amplitude of  $Q/I$  when moving away from the center of the slit. In addition, seeing and guiding cause the image to oscillate and thus the distance of the limb from the spectrograph slit changes continuously. When recording an image, we average the measurements from different  $\mu$  values. In our case the averaged value  $\mu = 0.1$  has a rms of about 0.011 in  $\mu$ .



respectively. The total opacity coefficient is  $\kappa_{\text{tot}}(\lambda, z) = \kappa_l(z)\phi(\lambda, z) + \sigma_c(\lambda, z) + \kappa_c(\lambda, z)$ . In a two-level atom model with unpolarized ground level, the total source vector  $\mathbf{S} = (S_I, S_Q)^T$  is defined as

$$\mathbf{S}(\lambda, \mu, z) = \frac{\kappa_l(z)\phi(\lambda, z)\mathbf{S}_l(\lambda, \mu, z) + \sigma_c(\lambda, z)\mathbf{S}_c(\lambda, \mu, z) + \kappa_c(\lambda, z)\mathbf{B}(\lambda, z)}{\kappa_{\text{tot}}(\lambda, z)}. \quad (9.2)$$

Here  $\mathbf{B} = (B_\lambda, 0)^T$ , with  $B_\lambda$  being the Planck function at the line center wavelength. The line source vector  $\mathbf{S}_l = (S_{I,l}, S_{Q,l})^T$  is given by

$$S_l(\lambda, \mu, z) = \epsilon\mathbf{B}(\lambda, z) + \frac{1 - \epsilon}{\phi(\lambda, z)} \int_{-1}^{+1} \frac{d\mu'}{2} \int_0^\infty d\lambda' \hat{\mathbf{R}}(\lambda, \lambda', \mu, \mu', z) \mathbf{I}(\lambda', \mu', z). \quad (9.3)$$

Here the redistribution matrix  $\hat{\mathbf{R}}(\lambda, \lambda', \mu, \mu', z)$  is the angle-averaged Domke-Hubeny PRD matrix for the non-magnetic scattering, given in Equation (M.7), of the Appendix M. The thermalization parameter  $\epsilon$  is defined by  $\epsilon = \Gamma_I / (\Gamma_R + \Gamma_I)$ , where  $\Gamma_R$  and  $\Gamma_I$  are respectively the radiative and inelastic collision rates. In Equation (9.3),  $(\lambda', \mu')$  refer to the incoming ray, and  $(\lambda, \mu)$  refer to the outgoing ray.

The scattering part of the continuum source vector  $\mathbf{S}_c = (S_{I,c}, S_{Q,c})^T$  is defined by

$$\mathbf{S}_c(\lambda, \mu, z) = \int_{-1}^{+1} \frac{d\mu'}{2} \hat{\mathbf{P}}_R(\mu, \mu') \mathbf{I}(\lambda, \mu', z), \quad (9.4)$$

where  $\hat{\mathbf{P}}_R$  is the Rayleigh phase matrix defined in the Appendix M. For simplicity, frequency coherent scattering is assumed in the continuum. We define the total optical depth scale as  $d\tau_\lambda = -\kappa_{\text{tot}}(\lambda, z)dz$ . The formal solution of Equation (9.1) can be written as

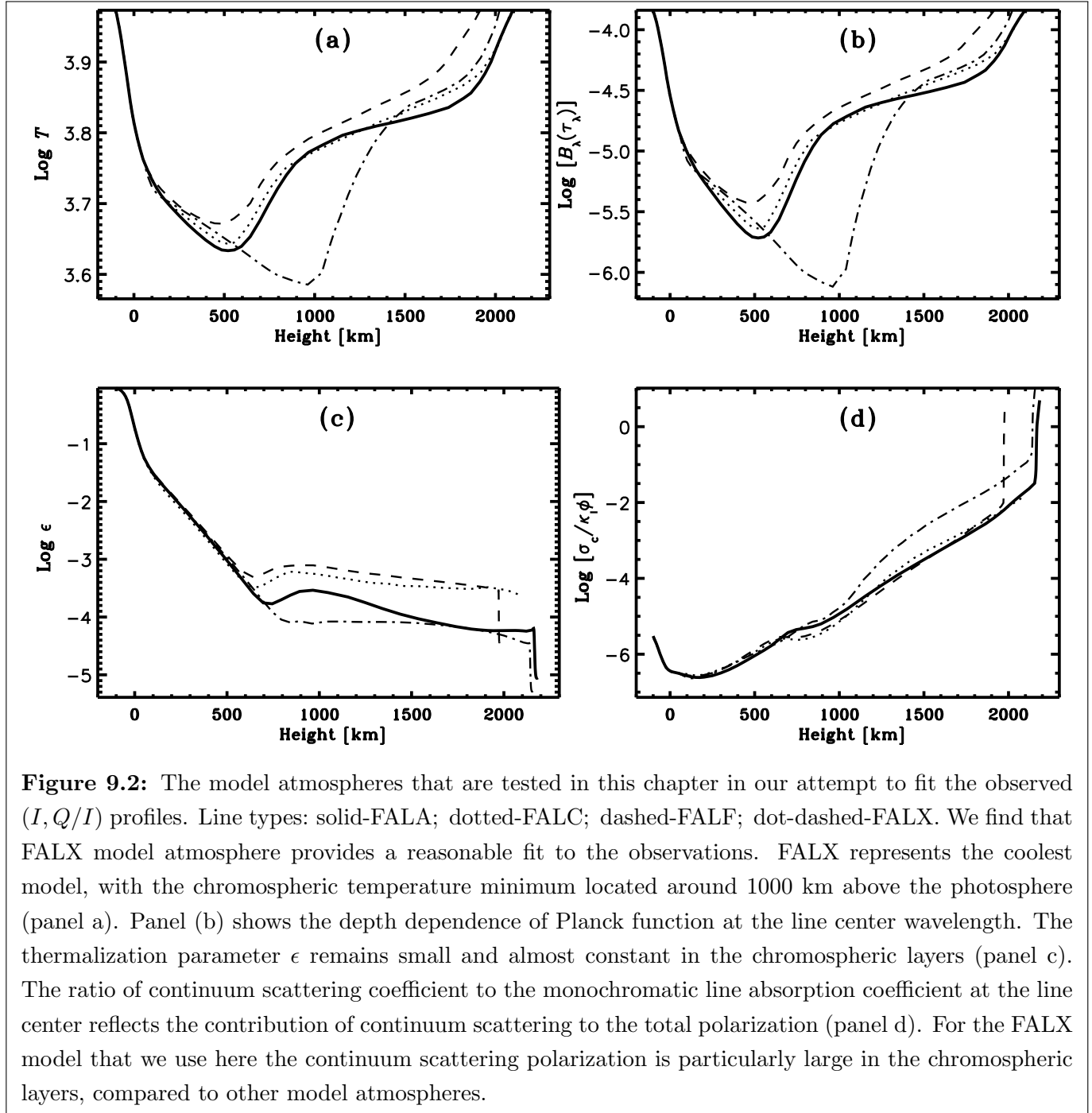
$$\mathbf{I}(\lambda, \mu, \tau_\lambda) = \mathbf{I}_0(\lambda, \mu, T_\lambda) \exp \left[ - \left( \frac{T_\lambda - \tau_\lambda}{\mu} \right) \right] + \int_{\tau_\lambda}^{T_\lambda} \exp \left[ - \left( \frac{\tau'_\lambda - \tau_\lambda}{\mu} \right) \right] \mathbf{S}(\lambda, \mu, \tau'_\lambda) \frac{d\tau'_\lambda}{\mu}, \quad (9.5)$$

for  $\mu > 0$ , and

$$\mathbf{I}(\lambda, \mu, \tau_\lambda) = \mathbf{I}_0(\lambda, \mu, 0) \exp \left( - \frac{\tau_\lambda}{\mu} \right) - \int_0^{\tau_\lambda} \exp \left[ - \left( \frac{\tau'_\lambda - \tau_\lambda}{\mu} \right) \right] \mathbf{S}(\lambda, \mu, \tau'_\lambda) \frac{d\tau'_\lambda}{\mu}, \quad (9.6)$$

for  $\mu < 0$ . In the above equations  $\mathbf{I}_0$  is a radiation field incident on the medium. At the lower boundary  $\mathbf{I}_0(\lambda, \mu, T_\lambda) = (B_\lambda(T_\lambda), 0)^T$ . We assume that no radiation is incident on the upper free boundary ( $\tau_\lambda = 0$ ). Equations (9.1)–(9.6) are used in Section 9.5 to construct three different levels of LSA and to compute the polarized spectrum  $\mathbf{I}(\lambda, \mu, \tau_\lambda)$ .

The polarized spectrum is calculated by a two-stage process described in Holzreuter et al. (2005). In the first-stage, a multi-level PRD-capable MALI (Multi-level Approximate



Lambda Iteration) code of Uitenbroek (2001, hereafter referred to as RH-code), solves the statistical equilibrium equation and the unpolarized RT equation self-consistently, and iteratively. The RH-code is used to compute the intensity, opacities and the collision rates. The angle-averaged redistribution functions of Hummer (1962) are used in the RH-code. In the second stage, the opacities and the collision rates are kept fixed, and the Stokes vector  $(I, Q)^T$  is computed perturbatively by solving the polarized RT equation with the same angle-averaged redistribution functions as in the RH-code. For simplicity, in this stage a two-level atomic model is assumed for the particular transition of interest. Such a two stage approach is justified, when the degree of linear polarization is small, so that it does not affect the population of the levels under consideration. A perturbation technique of this type is used in Faurobert (1987) and Nagendra et al. (2002) for isothermal atmospheres, and is shown to work well. In Section 9.6 we present the theoretical model profiles of  $(I, Q/I)$  computed by the RT approach.

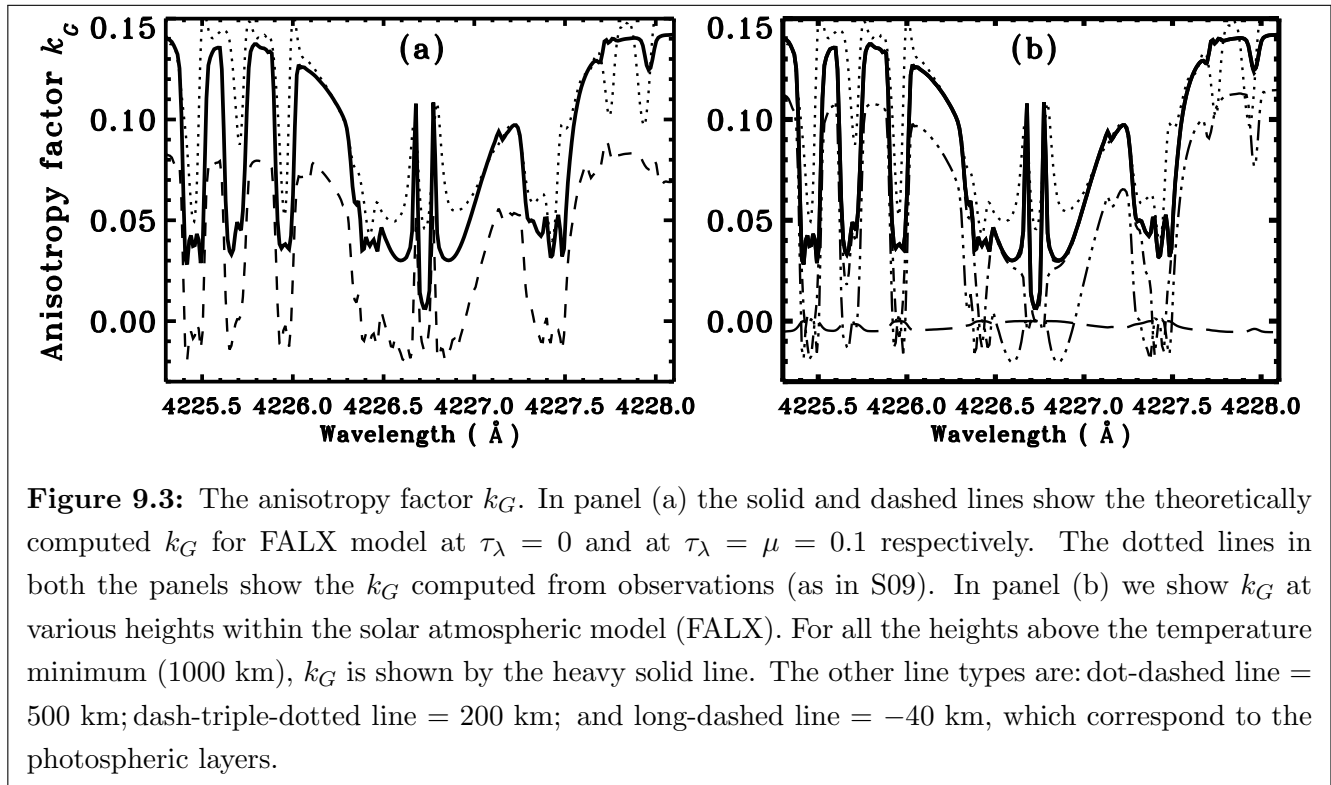
### 9.3 The details of observations and solar model atmospheres

#### 9.3.1 The observation of $(I, Q/I)$ in the Ca I 4227 Å line

The data acquisition was done using the ZIMPOL-2 polarimeter (Gandorfer et al. 2004) at IRSOL in Switzerland. For details of the instrumentation facilities used for obtaining the results shown in this chapter, see Bianda et al. (2003). As several details related to the data acquisition are given in S09, we do not elaborate them here.

Figure 9.1 shows the observations taken during January 2010 near the solar north pole (about  $6''$  inside the limb around spatial position  $60''$ ). The spectrograph slit was  $60 \mu\text{m}$  wide ( $0.5''$  wide on the disk) and  $190''$  long. The resulting CCD images are 140 pixel high in the spatial direction, with a pixel corresponding to  $1.35''$ , and 770 pixel wide in the wavelength direction, with a pixel corresponding to  $5.3 \text{ m}\text{\AA}$ . The total exposure time was 10 minutes (120 single recordings of 5 seconds each).

Figures 9.7(a) and (c) show the intensity and the  $Q/I$  profiles obtained by averaging the Stokes  $I$  and Stokes  $Q/I$  images in Figure 9.1 over the spatial interval  $13''$  to  $41''$  where the average distance from the limb corresponds to  $\mu = 0.1$  value. The limb distance is calculated with the help of slit-jaw images registered during the integration time. Note that due to seeing effects the position of the limb is oscillating with a rms of  $1.1''$  which corresponds to a rms of about 0.011 in  $\mu$ .



The intensity image shows the broad line of Ca I at 4227 Å, which is nearly 90 % saturated at the line center, with broad wings interspersed by the blend lines (see also the dotted line in Figure 9.7(a)). The polarization signatures seen in  $Q/I$  are due to resonance scattering. Especially, worth noting are the PRD peaks (at  $\lambda \approx 4226.2$  Å and  $\lambda \approx 4227.1$  Å) with unequal heights, in the near wings and the depolarization of  $Q/I$  at the wavelength positions of the blend lines. Further, the depth of the core minima (at  $\lambda \approx 4226.6$  Å and  $\lambda \approx 4226.8$  Å) adjacent to the central peak (at  $\lambda_0 = 4226.727$  Å) are significant. The line core is defined as the region between  $\lambda \approx 4226.6$  Å and  $\lambda \approx 4226.8$  Å. The  $Q/I$  in the far wings gradually approaches the continuum polarization (see dotted lines in Figure 9.7(c)).

Although observations are made in the so called quiet regions, Figure 9.1 shows pronounced and spatially varying  $U/I$  signals in the line core, which is due to rotation of the plane of linear polarization by the Hanle effect in the presence of an oriented magnetic field. Some spatial variations in  $(Q/I, U/I)$  along the slit length are seen in the near wings. They were referred to as wing signatures in S09. In this chapter however we focus only on modeling the average  $Q/I$  spectrum corresponding to the interval 13'' to 41''. The  $V/I$  signal in Figure 9.1 is also weak, showing that the longitudinal components of the resolved magnetic field are weak in the observed locations on the solar disk.

### 9.3.2 The smearing effect

The polarimetric observations for this chapter were done with a slit width of  $60 \mu\text{m}$ . To take into account the finite slit width, a convolution of the theoretical  $(I, Q)$  profiles with a slit spectral response function becomes necessary. For simplicity we assume this function to be a Gaussian. The observed profiles are also broadened by macro-turbulent velocity fields. We account for both the broadening effects by using a Gaussian function with a total width at half maximum of  $40 \text{ m}\text{\AA}$ . The main source of smearing is due to the macro-turbulent velocity fields. The smearing due to the instrumental broadening is quite small (about  $10 \text{ m}\text{\AA}$ ) in comparison.

### 9.3.3 The model atmosphere and the model atom

Figure 9.2 shows the run of some physical parameters as a function of height in several model atmospheres of the Sun - namely FALA, FALC, FALF (Fontenla et al. 1993) and FALX (Avrett 1995) that we have tested in our attempts to fit the  $(I, Q/I)$  data. The meaning of the abbreviations, and the nature of the atmospheric models are described in the given references. Basically all these models represent the quiet solar atmosphere. For instance, FALA, FALC and FALF represent respectively the super granular cell center, the average quiet Sun and the bright network region on the solar atmosphere. FALX is a cool model that was proposed by Avrett (1995) to study the CO molecular observations. We have retained the FALX model for our investigation on the LSA approximations because it appeared that it could provide a reasonable fit to the observations.

In the multi-level RH-code, a Ca I model atom consisting of 20 levels, with 17 line transitions and 19 continuum transitions is considered. The main line is treated in PRD. The angle-averaged PRD functions of Hummer (1962) are used for this purpose. All other lines of the multiplet are treated in complete frequency redistribution. However, for computing the polarization, we restrict ourselves to a two-level atom model for the main line transition. The relevant PRD matrix used for computing  $Q/I$  is given in Equation (M.7). All the blend lines are treated in LTE in the RH-code. Therefore, the blend line absorption coefficient is implicitly included in the continuum absorption coefficient  $\kappa_c$ .

## 9.4 The anisotropy factor $k_G(\lambda, \mu, \tau_\lambda)$

It is well known that the key factor which determines the shape of the emergent polarization profile is the anisotropy of the diffuse radiation field within the atmosphere. It is expressed

by the parameter  $k_G$ , introduced in Stenflo (1982).  $k_G$  is the factor by which classical scattering polarization is reduced due to angular averaging over the incident radiation, as compared with the case of unidirectional incident radiation. It is given by

$$k_G(\lambda, \mu, \tau_\lambda) = \frac{3}{2\sqrt{2}}(1 - \mu^2)J_0^2(\lambda, \tau_\lambda)/I(\lambda, \mu, \tau_\lambda), \quad (9.7)$$

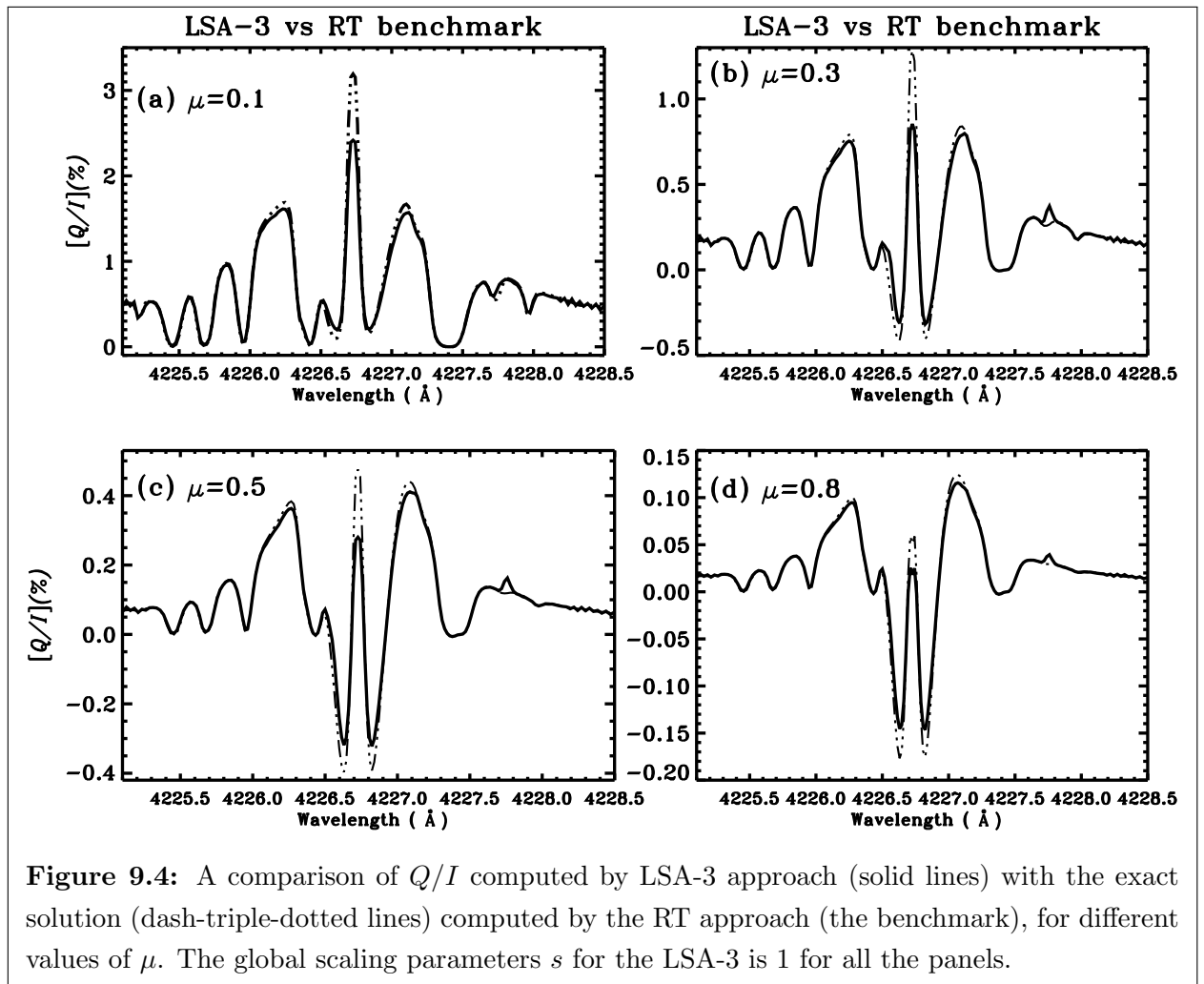
with

$$J_0^2(\lambda, \tau_\lambda) = \frac{1}{4\sqrt{2}} \int_{-1}^{+1} d\mu' (3\mu'^2 - 1)I(\lambda, \mu', \tau_\lambda). \quad (9.8)$$

Here  $\mu'$  is the direction of the incident radiation field and  $\mu$  the direction of the scattered beam. The parameter  $k_G$  thus takes care of actual angular distribution of the radiation field. The integration is over all the incident directions  $\mu'$ . Combining Equations (9.7) and (9.8) one recognizes the factor  $(3/8)(1 - \mu^2)(3\mu'^2 - 1)$  as the (2, 1) element of the Rayleigh phase matrix (see Appendix M).

Figure 9.3 shows the anisotropy factor  $k_G$  for the Ca I 4227 Å line. The dotted lines in both the panels show  $k_G$  computed empirically through a polynomial fit to the observed center to limb variation of the intensity  $I$  (see S09). In this way it represents the observed anisotropy at the surface ( $\tau_\lambda=0$ ). The other line types in Figure 9.3(a) correspond to the  $k_G$  calculated using  $I(\lambda, \mu, \tau_\lambda)$  obtained from the RH-code. Throughout this chapter we use the FALX model atmosphere (Avrett 1995). A good agreement between the theoretically computed  $k_G$  at  $\tau_\lambda=0$  (solid line), and the observationally derived  $k_G$  (also at  $\tau_\lambda=0$ ) is a measure of the realism to which the FALX model mimics the solar atmosphere. The dashed line is the  $k_G$  computed at the monochromatic optical depth  $\tau_\lambda = \mu$  for  $\mu = 0.1$ .

Figure 9.3(b) shows the run of the anisotropy factor  $k_G$  within the solar atmospheric model FALX. The line types correspond to different heights. The long-dashed line represents the deepest layers (−40 km below the photosphere), where the radiation field approaches the Planck function due to thermalization, and therefore  $k_G$  approaches zero. The dot-dashed and dash-triple-dotted lines represent the  $k_G$  in the photospheric layers (500 km and 200 km respectively). In these layers  $k_G$  seems to be most sensitive to the optical depth stratification. For all the heights from the temperature minimum at 1000 km and above, the radiation field saturates to nearly a constant value with respect to the depth, and hence the  $k_G$  plots for all these heights merge into a single curve represented by the heavy solid line (in other words  $k_G$  becomes independent of depth). Holzreuter et al. (2005) have presented a detailed analysis of the correspondence between the depth dependence of the anisotropy and the shape of the emergent  $Q/I$  spectra of this line.



The similar argumentation can be used to understand the anisotropy plots presented in Figure 9.3. Hence we do not elaborate further on this aspect.

## 9.5 The Last Scattering Approximations (LSA)

The concept of LSA implies that one first determines Stokes  $I$ , either through observations or with a numerical calculation in which the polarization is neglected. This is possible for the Second Solar Spectrum because the polarization is a few percent at most. One then assumes that a single scattering of this intensity field suffices to properly evaluate the observed linear polarization. This LSA concept has been used in Stenflo (2005), for the solar continuum polarization, in S09 for the Ca I 4227  $\text{\AA}$  line, in Belluzzi et al. (2007) for the Ba II D<sub>1</sub> and D<sub>2</sub> lines, the ratio  $Q/I$  being deduced from the observed Stokes  $I$ . In

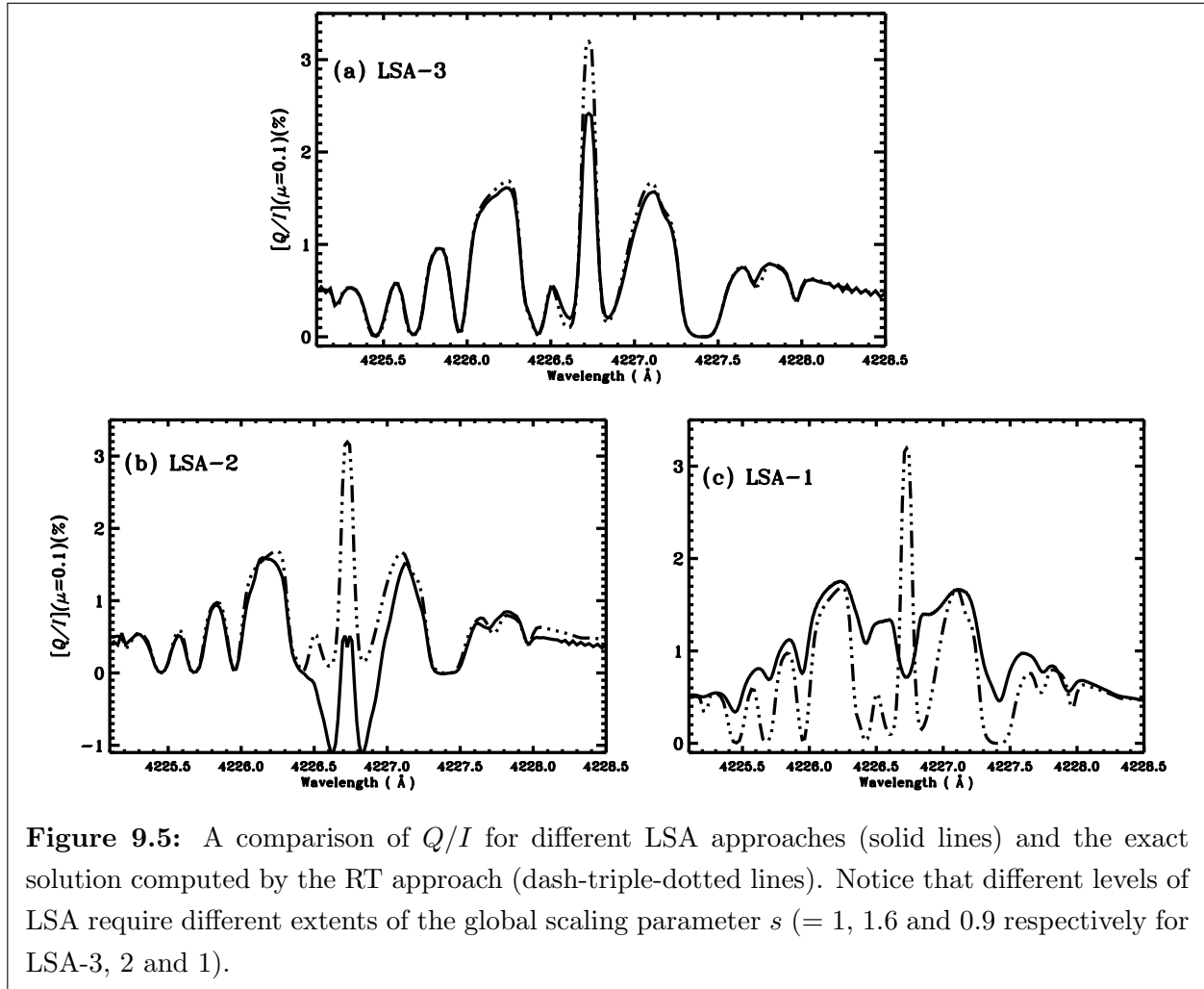


**Figure 9.5:** A comparison of  $Q/I$  for different LSA approaches (solid lines) and the exact solution computed by the RT approach (dash-triple-dotted lines). Notice that different levels of LSA require different extents of the global scaling parameter  $s$  ( $= 1, 1.6$  and  $0.9$  respectively for LSA-3, 2 and 1).

Faurobert & Arnaud (2002) for the scattering polarization of molecular emission lines, the photospheric intensity field used is a solution of an unpolarized RT equation.

In this chapter we present different levels of approximations based on the concept of LSA. From the most sophisticated one to the most simple one they are LSA-3, LSA-2, and LSA-1. A common point to these approximations and what makes them interesting is that they allow one to obtain separately Stokes  $I$  and Stokes  $Q$ . In contrast, in the full RT method,  $I$  and  $Q$  are calculated simultaneously. In LSA-3 and LSA-2 we first calculate Stokes  $I(\lambda, \mu, \tau_\lambda)$  at all the depth points in a solar model atmosphere, ignoring the contribution of Stokes  $Q$  in the source terms  $S_{I,l}$  and  $S_{I,c}$  (see Equations (9.3) and (9.4)). In LSA-1 we use for Stokes  $I$  the observed intensity. To obtain the polarization, we keep only the terms depending on the intensity in the equations for the source terms  $S_{Q,l}$  and  $S_{Q,c}$  (see Equations (9.3) and (9.4)). Once  $S_Q$  has been obtained, one can either solve



a simple RT equation to calculate Stokes  $Q$ , this is the LSA-3 approximation, or evaluate Stokes  $Q$  with an Eddington–Barbier relation, this is the LSA-2 approximation. For LSA-1 we use a somewhat different method for the calculation of Stokes  $Q$  (see below).

The approximations LSA-3 and LSA-2 are directly related to the iterative method introduced in Frisch et al. (2009) for the calculation of the linear polarization. In this method, as done here, one neglects the polarization for the calculation of Stokes  $I$  but the polarization is kept in the  $Q$ -component of the source term and an integral equation is established for this  $S_Q$ . Its solution can be written as a series expansion in the mean number of scattering events. The first term, which gives the value of after a single scattering of the incident radiation field depends only on Stokes  $I$  and is identical to our approximation. The following terms in the expansion take into account additional scattering events. They can be calculated iteratively.

We now describe in details the LSA-3, LSA-2 and LSA-1 approximations.

### 9.5.1 LSA-3

As explained in Section 9.5, we neglect the contribution of  $Q(\lambda, \mu, \tau_\lambda)$  in the right hand side of the equations for  $S_{I,l}(\lambda, \mu, \tau_\lambda)$  and  $S_{Q,l}(\lambda, \mu, \tau_\lambda)$ . Therefore Equation (9.3) can be written as

$$[S_{I,l}(\lambda, \mu, \tau_\lambda)]_{\text{LSA-3}} = \frac{1 - \epsilon}{\phi(\lambda, z)} \int_{-1}^{+1} \frac{d\mu'}{2} \int_0^\infty d\lambda' R_{11}(\lambda, \lambda', \mu, \mu', z) I(\lambda', \mu', \tau_{\lambda'}) + \epsilon B_\lambda(\tau_\lambda), \quad (9.9)$$

for  $S_{I,l}$  and

$$[S_{Q,l}(\lambda, \mu, \tau_\lambda)]_{\text{LSA-3}} = \frac{1 - \epsilon}{\phi(\lambda, z)} \int_{-1}^{+1} \frac{d\mu'}{2} \int_0^\infty d\lambda' R_{21}(\lambda, \lambda', \mu, \mu', z) I(\lambda', \mu', \tau_{\lambda'}). \quad (9.10)$$

for  $S_{Q,l}$ . Here,  $\tau_\lambda$  and  $\tau_{\lambda'}$  stand for  $\tau_\lambda(z)$  and  $\tau_{\lambda'}(z)$ . This remark holds also for Equations (9.15), (9.17), (9.23) and (9.24) below.

### LSA-3 with angle-averaged partial redistribution

In this section we restrict our attention to the use of angle-averaged version of the Domke–Hubeny redistribution matrix (see Equation (M.7)). For this particular choice, the redistribution matrix elements can be written as

$$R_{11}(\lambda, \lambda', \mu, \mu', z) = R^{(0)}(\lambda, \lambda', z) + R^{(2)}(\lambda, \lambda', z) P_{11}^{(2)}(\mu, \mu'), \quad (9.11)$$

and

$$R_{21}(\lambda, \lambda', \mu, \mu', z) = R^{(2)}(\lambda, \lambda', z)P_{21}^{(2)}(\mu, \mu'), \quad (9.12)$$

where

$$R^{(0)}(\lambda, \lambda', z) = \gamma_{\text{coh}} r_{\text{II}}(\lambda, \lambda', z) + (1 - \gamma_{\text{coh}}) r_{\text{III}}(\lambda, \lambda', z), \quad (9.13)$$

$$R^{(2)}(\lambda, \lambda', z) = W_2[\gamma_{\text{coh}} r_{\text{II}}(\lambda, \lambda', z) + (1 - \gamma_{\text{coh}}) k_c r_{\text{III}}(\lambda, \lambda', z)]. \quad (9.14)$$

Substituting Equation (9.11) in Equation (9.9), we obtain

$$[S_{I,l}(\lambda, \tau_\lambda)]_{\text{LSA-3}} = \epsilon B_\lambda(\tau_\lambda) + \frac{1 - \epsilon}{\phi(\lambda, z)} \int_0^\infty d\lambda' R^{(0)}(\lambda, \lambda', z) J(\lambda', \tau_{\lambda'}), \quad (9.15)$$

where

$$J(\lambda', \tau_{\lambda'}) = \int_{-1}^{+1} \frac{d\mu'}{2} I(\lambda', \mu', \tau_{\lambda'}). \quad (9.16)$$

In Equation (9.15), the contribution from  $R^{(2)}P_{11}^{(2)}$  is neglected because it is of the order of the polarization and hence much smaller than the contribution from the term  $R^{(0)}J$ . Substituting Equation (9.12) in Equation (9.10) we get

$$[S_{Q,l}(\lambda, \mu, \tau_\lambda)]_{\text{LSA-3}} = \frac{3}{2\sqrt{2}} \frac{1 - \epsilon}{\phi(\lambda, z)} (1 - \mu^2) \int_0^\infty d\lambda' R^{(2)}(\lambda, \lambda', z) J_0^2(\lambda', \tau_{\lambda'}), \quad (9.17)$$

where  $J_0^2(\lambda', \tau_{\lambda'})$  is defined in Equation (9.8).

So far we considered only the line source functions. Clearly, the continuum is also polarized and needs to be included appropriately. The LSA concept can again be applied to obtain a simpler expression for  $S_{I,c}$  and  $S_{Q,c}$  namely

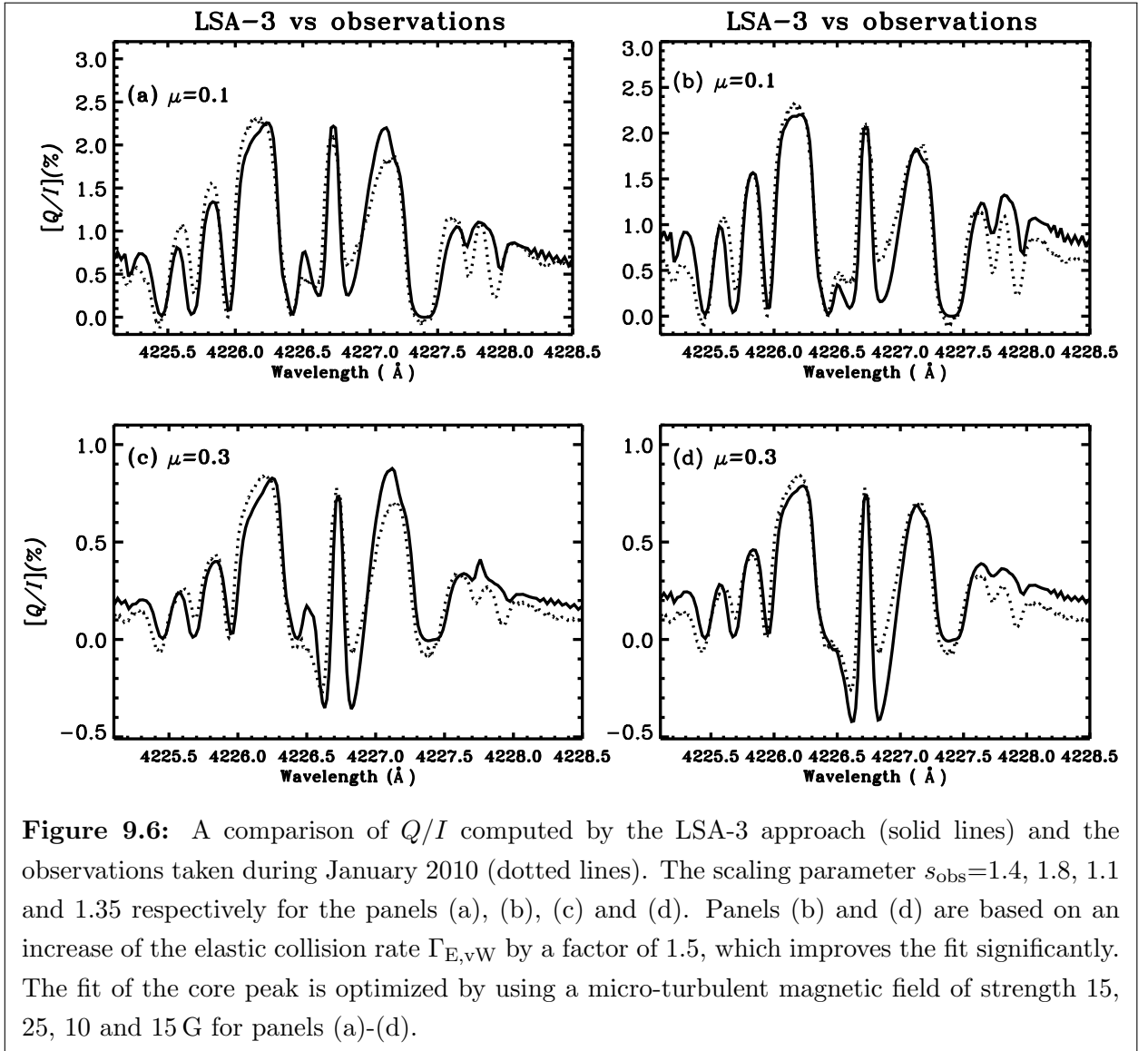
$$[S_{I,c}(\lambda, \tau_\lambda)]_{\text{LSA-3}} = J(\lambda, \tau_\lambda), \quad (9.18)$$

and

$$[S_{Q,c}(\lambda, \mu, \tau_\lambda)]_{\text{LSA-3}} = \frac{3}{2\sqrt{2}} (1 - \mu^2) J_0^2(\lambda, \tau_\lambda). \quad (9.19)$$

The total source functions  $[S_I(\lambda, \tau_\lambda)]_{\text{LSA-3}}$  and  $[S_Q(\lambda, \mu, \tau_\lambda)]_{\text{LSA-3}}$  can be computed by substituting Equations (9.15), (9.17), (9.18) and (9.19) in Equation (9.2). Finally we obtain an approximate formula for the emergent  $Q/I$  by using  $S_I$  and  $S_Q$  computed above in the formal solution expression (Equation (9.5)), namely

$$\begin{aligned} \left[ \frac{Q}{I}(\lambda, \mu) \right]_{\text{LSA-3}} &= s \int_0^{T_\lambda} \frac{d\tau'_\lambda}{\mu} \exp\left(-\frac{\tau'_\lambda}{\mu}\right) [S_Q(\lambda, \mu, \tau'_\lambda)]_{\text{LSA-3}} \\ &\quad / \int_0^{T_\lambda} \frac{d\tau'_\lambda}{\mu} \exp\left(-\frac{\tau'_\lambda}{\mu}\right) \times [S_I(\lambda, \tau'_\lambda)]_{\text{LSA-3}}. \end{aligned} \quad (9.20)$$



In the denominator of the above equation, we have neglected the contribution from incident intensity at the lower boundary. The quantity  $s$  is a global scaling parameter. It is a free parameter which is used to achieve a fit of the  $Q/I$  computed by LSA approach with the  $Q/I$  computed from the RT benchmark. Ideally it should be unity. But in practice it can take values either smaller or slightly larger than unity. It can therefore be used as a measure of the goodness of the last scattering approximations (see Section 9.6.2).

In the RT approach we compute polarization by perturbation. First we give initial unpolarized source vector as input and calculate the Stokes vector using a formal solution. A new source vector is then computed using the improved Stokes vector – and this process is repeated. In LSA-3 we avoid this perturbative loop. For the calculation of Stokes  $I$  we ignore the polarization. The component  $S_Q$  of the source function is deduced from the explicit expressions given in Equations (9.17), and (9.19) which involve only integrations over directions and frequencies of Stokes  $I$ . Stokes  $Q$  can then be calculated by using a formal solver.

### LSA-3 with angle-dependent partial redistribution

In this section we present a formula for  $Q/I$  which can be used in the case of angle ( $\mu$ ) dependent (however azimuthally averaged) redistribution matrices given in Equation (M.6). In this case the redistribution matrix elements can be written as

$$R_{11}(\lambda, \lambda', \mu, \mu', z) = R^{(0)}(\lambda, \lambda', \mu, \mu', z) + R^{(2)}(\lambda, \lambda', \mu, \mu', z)P_{11}^{(2)}(\mu, \mu'), \quad (9.21)$$

$$R_{21}(\lambda, \lambda', \mu, \mu', z) = R^{(2)}(\lambda, \lambda', \mu, \mu', z)P_{21}^{(2)}(\mu, \mu'). \quad (9.22)$$

In the above Equations  $R^{(0)}(\lambda, \lambda', \mu, \mu', z)$  and  $R^{(2)}(\lambda, \lambda', \mu, \mu', z)$  have the same form as the functions  $R^{(0)}(\lambda, \lambda', z)$  and  $R^{(2)}(\lambda, \lambda', z)$  given in Equations (9.13) and (9.14), but with the replacements  $r_{\text{II,III}}(\lambda, \lambda', z) \rightarrow r_{\text{II,III}}(\lambda, \lambda', \mu, \mu', z)$ . We recall that angle-dependent partial redistribution (in the presence of a magnetic field) was used in S09. A simple formula for  $Q/I$  was given in S09 by assuming  $\mu' = 1$  in the expression for the redistribution matrix elements. We can apply the same approximation to the redistribution functions  $R^{(0)}(\lambda, \lambda', \mu, \mu', z)$  and  $R^{(2)}(\lambda, \lambda', \mu, \mu', z)$ . With this approximation we now obtain

$$[S_{I,l}(\lambda, \mu, \tau_\lambda)]_{\text{LSA-3}}^{\text{AD}} = \epsilon B_\lambda(\tau_\lambda) + \frac{1 - \epsilon}{\phi(\lambda, z)} \int_0^\infty d\lambda' R^{(0)}(\lambda, \lambda', \mu, \mu' = 1, z) J(\lambda', \tau_{\lambda'}), \quad (9.23)$$

and

$$[S_{Q,I}(\lambda, \mu, \tau_\lambda)]_{\text{LSA-3}}^{\text{AD}} = \frac{1 - \epsilon}{\phi(\lambda, z)} \frac{3}{2\sqrt{2}} (1 - \mu^2) \int_0^\infty d\lambda' R^{(2)}(\lambda, \lambda', \mu, \mu' = 1, z) J_0^2(\lambda', \tau_{\lambda'}). \quad (9.24)$$

The symbol AD refers to the case of angle ( $\mu$ ) dependent partial redistribution. The above equations along with Equations (9.18) and (9.19) can be used to compute the total source functions  $S_I$  and  $S_Q$ . The  $Q/I$  can be calculated from Equation (9.20) using these  $S_I$  and  $S_Q$ .

### 9.5.2 LSA-2: Eddington-Barbier approximation

We proceed exactly as with LSA-3 but use the Eddington–Barbier approximation to calculate  $Q$  and  $I$  once  $S_Q$  and  $S_I$  have been determined. We also set the thermalization parameter  $\epsilon = 0$ . Equation (9.20) is replaced by

$$\left[ \frac{Q}{I}(\lambda, \mu) \right]_{\text{LSA-2}} = s \frac{S_Q(\lambda, \mu, \tau_\lambda(z_{\lambda, \mu}))}{S_I(\lambda, \tau_\lambda(z_{\lambda, \mu}))}, \quad (9.25)$$

where  $z_{\lambda, \mu}$  denotes the point in space where  $\tau_\lambda = \mu$ , for a given  $\lambda$  and a given  $\mu$ . Equation (9.25) is the polarized analogue of the Eddington-Barbier relation for Stokes  $I$  (see Mihalas 1978, p. 39).

### 9.5.3 LSA-1: semi-empirical approach

In LSA-1 we use the observed center to limb variation (CLV) of the Stokes  $I$  to calculate the anisotropy factor  $k_G$  and, as done in S09, assume that the ratio  $Q/I$  may be written as

$$\left[ \frac{Q}{I}(\lambda, \mu) \right]_{\text{LSA-1}} = s \left[ \frac{\phi(\lambda)}{\phi(\lambda) + C} [Z_{Q,I}(\lambda, \mu, 0)]_{\text{LSA-1}} + \frac{C}{\phi(\lambda) + C} P_C \right], \quad (9.26)$$

with

$$[Z_{Q,I}(\lambda, \mu, 0)]_{\text{LSA-1}} = \frac{3}{2\sqrt{2}} (1 - \mu^2) \int_0^\infty d\lambda' R^{(2)}(\lambda, \lambda') J_0^2(\lambda', 0) / \int_0^\infty d\lambda' R^{(0)}(\lambda, \lambda') I(\lambda', \mu, 0), \quad (9.27)$$

where  $R^{(2)}$  and  $R^{(0)}$  are taken to be independent of depth and are computed for a damping parameter corresponding to a chosen value of  $\Gamma_E/\Gamma_R$  and  $\Gamma_I/\Gamma_R$  set to zero. As in S09,

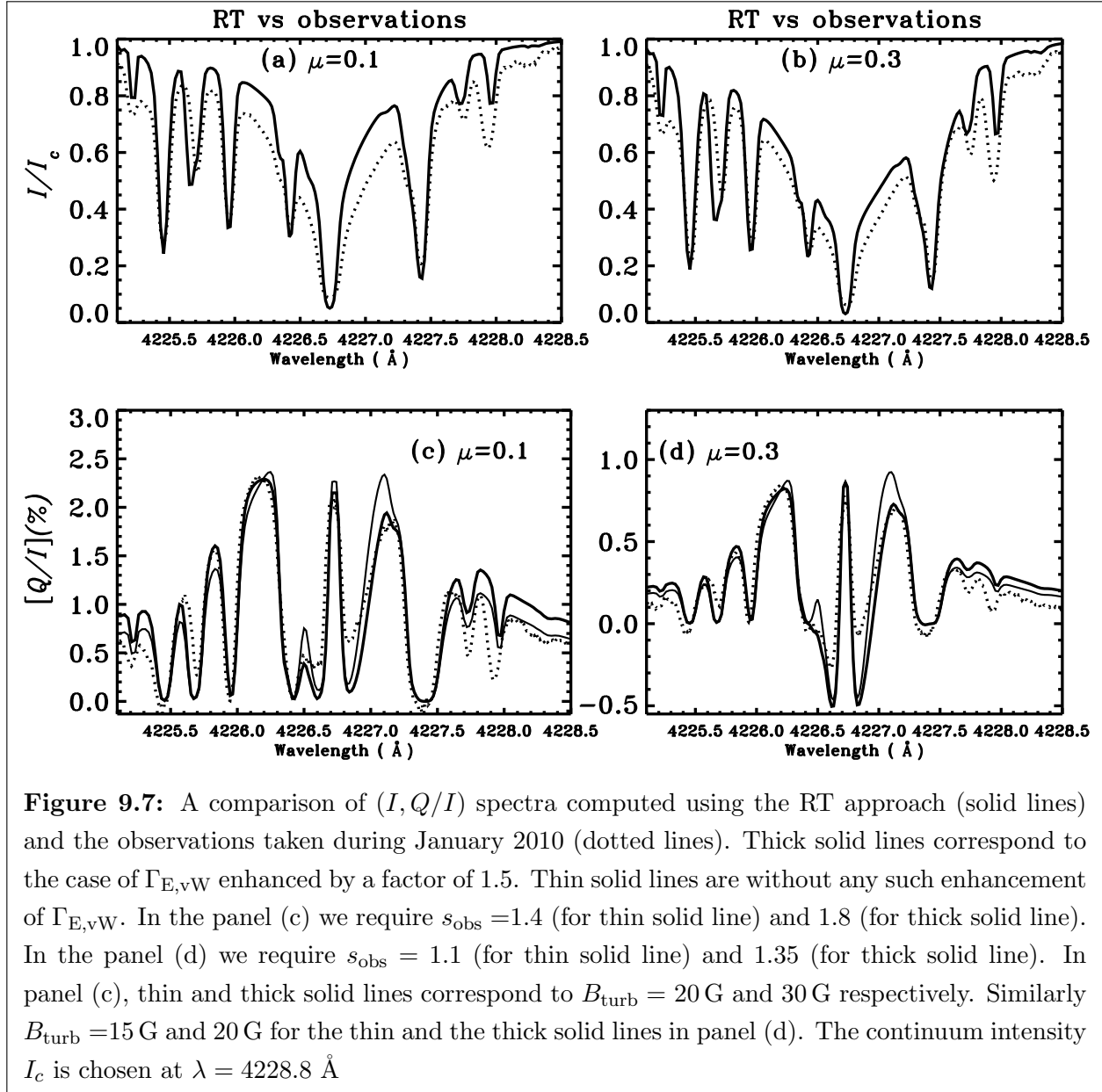


**Figure 9.7:** A comparison of  $(I, Q/I)$  spectra computed using the RT approach (solid lines) and the observations taken during January 2010 (dotted lines). Thick solid lines correspond to the case of  $\Gamma_{E,vW}$  enhanced by a factor of 1.5. Thin solid lines are without any such enhancement of  $\Gamma_{E,vW}$ . In the panel (c) we require  $s_{\text{obs}} = 1.4$  (for thin solid line) and  $1.8$  (for thick solid line). In the panel (d) we require  $s_{\text{obs}} = 1.1$  (for thin solid line) and  $1.35$  (for thick solid line). In panel (c), thin and thick solid lines correspond to  $B_{\text{turb}} = 20$  G and  $30$  G respectively. Similarly  $B_{\text{turb}} = 15$  G and  $20$  G for the thin and the thick solid lines in panel (d). The continuum intensity  $I_c$  is chosen at  $\lambda = 4228.8$  Å

**Table 9.1:** The values of free parameters used in modeling the observed  $Q/I$  spectra.

Approach	Figure	$\mu$	$c$	$s_{\text{obs}}$	$B_{\text{turb}}$
LSA-3	9.6(a)	0.1	1	1.4	15
RT	9.7(c)	0.1	1	1.4	20
LSA-3	9.6(b)	0.1	1.5	1.8	25
RT	9.7(c)	0.1	1.5	1.8	30
LSA-3	9.6(c)	0.3	1	1.1	10
RT	9.7(d)	0.3	1	1.1	15
LSA-3	9.6(d)	0.3	1.5	1.35	15
RT	9.7(d)	0.3	1.5	1.35	20

$\Gamma_E/\Gamma_R$  is treated as a free parameter. In Equation (9.26),  $C$  is the ratio of continuum to the line averaged opacity,  $P_C$  is the continuum polarization. Here,  $s$ ,  $C$  and  $P_C$  are treated as free parameters for a chosen value of  $\Gamma_E/\Gamma_R$ . We refer to S09 for details on the use of LSA-1 to model the Ca I 4227 Å line wings in the  $Q/I$  spectra.

## 9.6 Results and Discussions

In this section we first show how well the approximate solutions introduced above compare with the exact RT solution. Subsequently we also demonstrate how the formulae for  $Q/I$  derived under different levels of LSA approach can be used in a preliminary analysis of the observed  $Q/I$  spectra.

### 9.6.1 Theoretical validation of the LSA approaches

In this section we use the exact RT solution as a theoretical benchmark. In Figure 9.4, we compare LSA-3 solutions with the benchmark RT solution for different values of  $\mu$ . Figure 9.4 shows that the agreement between the LSA-3 approximation and the full RT calculation is excellent, except for the central peak and wing minima. We stress that in this figure the scaling factor is  $s = 1$ . The differences in the line core region are due to the fact that we have neglected the contribution of  $Q$  in the expression of  $S_{Q,I}$ . This contribution plays a significant role in the line core (Frisch et al. 2009). Figure 9.4 shows also that the LSA-3 approach is valid for any value of  $\mu$ .

Figure 9.5 shows a comparison of  $Q/I$  computed by the RT approach (dash-triple dotted lines) and different levels of the LSA approach (solid lines) for  $\mu = 0.1$ . Panel (a) of Figure 9.5 is identical to panel (a) of Figure 9.4. As the LSA-3 approximation has already been discussed above, we concentrate now on LSA-2 and LSA-1. Figure 9.5(b) shows that LSA-2 which makes use of the Eddington–Barbier relation can fit the line wings, including the near wing maxima, rather well, provided one applies a scaling factor  $s = 1.6$ . We note here that we obtain essentially the same  $Q/I$  profile if the Eddington–Barbier approximation is used for the calculation of  $Q$  only.

In the line core, LSA-2 is clearly not an acceptable approximation. We recall that the Eddington–Barbier approximation which amounts to replace an integral of the form  $I(\mu) = \int_0^\infty S(\tau)e^{-\tau/\mu}(d\tau/\mu)$  by  $I(\mu) = S(\mu)$ , provides an exact value of  $I(\mu)$  when  $S$  is a linear function of  $\tau$ . So the accuracy of this approximation will depend on the departures of  $S(\tau)$  from linearity. For the line Ca I 4227 Å  $S_Q(\lambda, \mu, \tau_\lambda)$  has a non-monotonic variation when  $\lambda$  is around the line center. So the failure of Eddington–Barbier approximation in this wavelength range is not surprising. In the line wings  $S_Q(\lambda, \mu, \tau_\lambda)$  increases regularly towards the surface, following the increase in the anisotropy of the radiation field (see Figure 9.3(a)) but the increase is much faster than linear. Therefore the Eddington–Barbier approximation underestimates the value of  $Q$  and a scaling factor  $s = 1.6$  is needed to fit the RT calculation. A comparison between the panels (a) and (b) in Figure 9.5 clearly shows that the depth dependence of the anisotropy factor  $k_G$  has to be taken into account for a proper modeling of the line center peak. For strong chromospheric lines such as Ca I 4227 Å an accurate non-LTE treatment of the line formation is needed to calculate this depth dependence with accuracy.

Figure 9.5(c) shows that LSA-1 can be made to fit the top envelopes of the PRD peaks of Ca I 4227 Å line, blend lines and the far wing continuum polarization, with a proper choice of the free parameters, as it does in S09. The free parameters used in Figure 9.5(c) to compare the LSA-1 and RT solution are:  $s = 0.9$ ,  $C = 2.1 \times 10^{-3}$  and  $P_C = 0.0013$ , for a chosen  $\Gamma_E/\Gamma_R = 10$ . We recall that LSA-1 requires no numerical solution of RT equations and is independent of the atmosphere model.

### 9.6.2 Observational validation of the LSA-3 and the RT approaches

In Figures 9.6 and 9.7 we compare the observations with predictions from the LSA-3 and from the RT calculation for  $\mu = 0.1$  and  $\mu = 0.3$ . Figure 9.6 shows  $Q/I$  computed by the LSA-3 approximation. Figure 9.7 shows the  $Q/I$  profiles and also the intensity profile from



the RT approach.  $I$  is actually computed using the polarized RT approach. However this  $I$  does not differ very much from the intensity computed by the unpolarized RH-code.

Three free parameters are used in the modeling procedure. They are (i) an enhancement parameter  $c$ , associated with the elastic collision rate  $\Gamma_{E,vW}$  (of the van der Waal's type), (ii) a global scaling parameter  $s_{\text{obs}}$ , and (iii) a micro-turbulent magnetic field  $B_{\text{turb}}$ .

With an appropriate choice of these 3 free parameters we can achieve a reasonable fit of the theoretical  $Q/I$  profile with observations for all the wavelengths. We first choose a value of  $c$  not far from unity (here we have chosen  $c = 1$  and  $c = 1.5$ ), then determine  $s_{\text{obs}}$  by a fit to the wings and finally  $B_{\text{turb}}$  by a fit of the core peak. The choice of  $s_{\text{obs}}$  is done by requiring an overall simultaneous fit to the PRD peaks and the blend line minima over the entire  $Q/I$  wings. The values of the 3 free parameters used in Figures 9.6 and 9.7 are listed in Table 9.1.

### The role of global scaling parameter $s_{\text{obs}}$ in modeling the $Q/I$ profile

To compare the theoretical  $Q/I$  with the observed  $Q/I$  profile as the new benchmark, we introduce a new scaling parameter denoted  $s_{\text{obs}}$ , which multiplies both the LSA-3 and RT profiles.  $s_{\text{obs}}$  is different from  $s$ , which was used as the scaling parameter when the RT solution was the benchmark (see Figs. 9.4 and 9.5). It is defined as

$$s_{\text{obs}} = \frac{[(Q/I)_{\text{wing}}]_{\text{observed}}}{[(Q/I)_{\text{wing}}]_{\text{theory}}}. \quad (9.28)$$

While one might expect that  $s_{\text{obs}}$  should be close to unity, Figs. 9.6(a) and 9.6(c) require  $s_{\text{obs}} = 1.4$  and 1.1 respectively. Figures 9.6(b) and 9.6(d) need even larger values of  $s_{\text{obs}}$ , namely 1.8 and 1.35, respectively. Such increased values of  $s_{\text{obs}}$  become necessary to account for the depolarization caused by the enhancement of  $\Gamma_{E,vW}$  (the necessity for an enhancement of the elastic collision rates in our model fitting is discussed below). The values of  $s_{\text{obs}}$  needed for the LSA-3 and the RT approach are the same (see Figs. 9.7(c) and 9.7(d), Table 9.1). Note that for  $\mu = 0.3$  the value of  $s_{\text{obs}}$  is closer to unity than for  $\mu = 0.1$ .

The rationale behind the use of the scaling parameters can be explained as follows: When comparing two  $Q/I$  spectra, either LSA with RT (for which the scaling factor  $s$  is introduced) or LSA and RT with observations (for which the scaling factor  $s_{\text{obs}}$  is introduced), there are two aspects of the comparison: (1) The relative shapes of the  $Q/I$  spectra, and (2) the absolute  $Q/I$  amplitudes. Aspect (1) is much more important than aspect (2), for various reasons: (a) The relative shapes between observations and theory

(RT and LSA) can be brought to good agreement, in contrast to the absolute amplitudes. (b) For magnetic field determinations, one should not use the absolute  $Q/I$  core amplitude, but instead the ratio between core and wing amplitudes (see below). With this differential approach any global scale error divides out, greatly reducing effects of model deficiencies. (c) The absolute  $Q/I$  amplitudes are, in addition to the model deficiencies, directly affected by observational errors in the  $\mu$  value. These observational errors divide out with the differential approach.

The parameter  $s_{\text{obs}}$  is essential for a comparison of the relative shapes of the theoretical  $Q/I$  profiles with the observed ones when  $s_{\text{obs}}$  differs from unity. The circumstance that  $s_{\text{obs}}$  for both RT and LSA-3 differs significantly from unity is an indicator of deficiencies in the modeling of this particular line. Another indicator that there is indeed a modeling problem is the relatively poor fit of the theoretical Stokes  $I$  profiles with the observed Stokes  $I$ . The discrepancies are particularly large for  $\mu = 0.1$ . Possible causes for  $s_{\text{obs}}$  to deviate from unity are

- (i) the choice of the model atmosphere,
- (ii) the use of 1D geometry to represent the solar atmosphere,
- (iii) the use of angle-averaged redistribution functions, and
- (iv) observational uncertainties in the value of  $\mu$ .

The parameter  $s_{\text{obs}}$  absorbs all these as well as possible unknown sources of errors. In addition, the degree of deviation from unity of the scaling factors  $s$  and  $s_{\text{obs}}$  can be used as a measure of the goodness of the model fit.

### The role of elastic collision rate $\Gamma_{\text{E,vW}}$ in modeling the $Q/I$ wings

We have found that in fitting the  $Q/I$  wing shape, an enhanced value of  $\Gamma_{\text{E,vW}}$  becomes necessary. We denote this enhancement parameter by  $c$ . It is used as a source of additional broadening. In Figures 9.6(a) and 9.6(c) we have set  $c = 1$ . In Figures 9.6(b) and 9.6(d), we have used  $c = 1.5$ . One can notice a substantial improvement in fitting the shape of the  $Q/I$  profile, when going from  $c = 1$  to  $c = 1.5$ , in particular in reproducing the asymmetry of the wing maxima. Similar enhancement was also applied by Faurobert-Scholl (1992), to fit the observed  $Q/I$  wing polarization. The justification for this can be found in Derouich et al. (2003) and Barklem & O'Mara (1997) who respectively show that the old theories of  $D^{(2)}$  and elastic collision rate  $\Gamma_{\text{E}}$  actually underestimate  $\Gamma_{\text{E,vW}}$ . An enhanced value of  $\Gamma_{\text{E,vW}}$  causes depolarization (decrease of  $Q/I$  in magnitude) in the line wings which are formed in the deeper layers of the atmosphere, where collision rates are higher. This wing depolarization can be compensated by using an appropriate value of  $s_{\text{obs}}$ , to obtain the

actual magnitude of  $Q/I$  in the wings.

In Figures 9.7(c) and 9.7(d) we show a comparison of the  $Q/I$  computed by the RT approach and the observations. In these two panels also one can notice the improvement in fitting the shape of the  $Q/I$  wings when  $c = 1.5$  (thick solid lines), as compared to the case of  $c = 1$  (thin solid lines).

### The role of micro-turbulent magnetic field $B_{\text{turb}}$ in modeling the $Q/I$ core peak

Once a reasonable fit to the  $Q/I$  wings is achieved, we focus on obtaining a good fit to the  $Q/I$  at the line core. This can be done by using an appropriate value of  $B_{\text{turb}}$  which is the third free parameter.

In other words,  $B_{\text{turb}}$  can be determined by demanding that

$$\frac{[(Q/I)_{\text{core}}]_{\text{observed}}}{[(Q/I)_{\text{wing}}]_{\text{observed}}} = \frac{[(Q/I)_{\text{core}}]_{\text{theory}, B_{\text{turb}} \neq 0}}{[(Q/I)_{\text{wing}}]_{\text{theory}}}, \quad (9.29)$$

should be satisfied. We can rewrite Equation (9.29) as

$$[(Q/I)_{\text{core}}]_{\text{observed}} = s_{\text{obs}} [(Q/I)_{\text{core}}]_{\text{theory}, B_{\text{turb}} \neq 0}, \quad (9.30)$$

where  $s_{\text{obs}}$  is defined in Equation (9.28). In Equation (9.29),  $[(Q/I)_{\text{core}}]_{\text{theory}, B_{\text{turb}} \neq 0}$  is obtained either from LSA-3 or from the RT approach. It depends on  $f_B$  (which is a function of  $B_{\text{turb}}$ ), defined in Equation (M.11) through the modified phase matrix elements. The value of  $B_{\text{turb}}$  is found by solving Equation (9.30). The described procedure is a differential approach to determine  $B_{\text{turb}}$  because we use the ratio of core peak to the wing peak amplitudes, instead of the absolute core peak amplitudes.

The set of values of  $B_{\text{turb}}$  deduced from the LSA-3 approach are systematically smaller than those deduced from the RT approach (see Table 9.1). This is essentially due to the underestimation of the core peak values by the LSA-3 (see Figures 9.4, 9.5(a)). This underestimation of  $B_{\text{turb}}$  when using LSA-3 instead of a full RT calculation is not specific to the Ca I 4227 Å line. It will appear whenever one uses a LSA-3 approximation rather than a full RT approach to evaluate the linear polarization of the strong resonance lines.

## 9.7 Concluding remarks

In this chapter we develop a mathematical framework for the last scattering approximation (LSA) approach, starting from the polarized RT (RT) equation. We derive simple formulae for  $Q/I$  by applying a few approximations to the governing equations of the RT approach.

LSA-1 is the simplest approach, which is based on observationally derived anisotropy at the surface (it was used in S09 to explore the wing signatures observed in Ca I 4227 Å line). It ignores the depth variation of all the physical quantities. For this reason LSA-1 fits only qualitatively the PRD peaks and the envelopes of the wings in the  $Q/I$  spectra. The line core itself as well as the core minima could not be reproduced using LSA-1. In this chapter we aim at modeling various features (including the line core) of the observed  $Q/I$  spectra of this line, in a greater detail. To this end, we generalize the LSA-1 by introducing 2 more levels of LSA, namely LSA-2 and LSA-3. We find that the LSA-2 approach, which takes into account the anisotropy factor at the atmospheric heights where the condition  $\tau_\lambda = \mu$  (for a given  $\mu$  and a given  $\lambda$ ) is satisfied, is insufficient to reproduce the line core region. The only way to adequately model the core region without using the full polarized RT approach is through LSA-3. This is because, unlike LSA-1 and LSA-2, LSA-3 takes into account the run of the anisotropy factor over the optical depth, apart from taking the depth dependence of other concerned physical quantities.

We validate the LSA approaches, by comparing with the exact RT approach. The advantage of LSA-3 (also LSA-2) approach is that it is sufficient to solve the unpolarized RT equation only once to obtain accurate values of  $I(\lambda, \mu, \tau_\lambda)$ , opacities and collision rates throughout the atmosphere. These are subsequently used as inputs to the approximate LSA formulae to evaluate the emergent  $Q/I$  spectra. In this way we avoid solving the exact polarized RT equation – which is computationally more expensive. As for the timing efficiency, LSA-1 is 21 times faster than the LSA-2; 25 times faster than the LSA-3 and 58 times faster than the RT approach. The main advantage of LSA-1 is that it does not need the solution of the unpolarized RT (the inputs from which are needed by LSA-2, LSA-3 and also the polarized RT). LSA-2 is 5 times faster than LSA-3, and 38 times faster than the RT approach. LSA-3 is 8 times faster than the RT approach. Therefore, compared with the full scale polarized RT approach, the LSA approaches are quite efficient.

To illustrate the usefulness of LSA-3 approach in modeling the second solar spectrum, we compare both the LSA-3 and the RT solutions with the recently observed  $Q/I$  spectra of Ca I 4227 Å line. These recent observations are made in the quiet regions on the Sun. In the modeling efforts both the LSA-3 and the RT approaches require three free parameters, namely an enhancement parameter  $c$ , associated with the elastic collision rate  $\Gamma_{E,vW}$ ; a global scaling parameter  $s_{\text{obs}}$  that accounts for all the known and unknown sources of errors; and a micro-turbulent magnetic field strength  $B_{\text{turb}}$ .

LSA-1 can only be useful for certain qualitative studies of wing effects, like what is

done in S09, for exploring the existing of the wing Hanle effect, or a study of quantum interference in the Ca II H and K lines (see Stenflo 1982). Although LSA-2 can be used to perform wing analysis in the same way as LSA-1, it is not computationally as advantageous as LSA-1. As for LSA-3, it gives a reasonable fit to the observed  $Q/I$  throughout the line profile (including the line core). Thus the main advancement of this chapter compared to S09 is that we have improved the fit to the important features of the observed  $Q/I$  spectra like (i) core peak, (ii) asymmetric core minima, (iii) asymmetric PRD peaks in the near wings, (iv) blend line polarization, and (v) far wing polarization.

In this chapter, we have shown that LSA-3 can provide a fit to the observed  $Q/I$  spectra, which is nearly as good as the RT approach itself. As mentioned above, this can be achieved at a much less computational cost. Thus, LSA-3 may be applied

- (i) to interpret the second solar spectrum and the Hanle effect in lines with PRD,
- (ii) to test different theories of the elastic collisions,
- (iii) to explore the formation of the Second Solar Spectrum in media where 3D RT effects have to be taken into account,
- (iv) to estimate the strength of micro-turbulent magnetic fields in the solar chromosphere.

## New Results

This chapter concerns developing three levels of last scattering approximation methods and their comparison with RT solutions and also with observations. The following are the important results obtained in chapter 9.

- 1.** We explore three different approximation levels for LSA and compare each of them with the benchmark represented by the solution of the full polarized RT, including PRD effects.
- 2.** The simplest approximation level is LSA-1, which uses the ‘observed’ center to limb variation of the intensity profile to obtain the anisotropy of the radiation field at the surface, without solving any RT equation.
- 3.** The next two approximation levels use the solution of the unpolarized RT equation to derive the anisotropy of the incident radiation field and use it as input. In the case

of LSA-2 the anisotropy at level  $\tau_\lambda = \mu$  is used, the atmospheric level from which an observed photon is most likely to originate (here  $\tau_\lambda$  is the monochromatic optical depth at wavelength  $\lambda$  and  $\mu = \cos \theta$ , with  $\theta$  being the heliocentric angle). LSA-3 on the other hand makes use of the full depth dependence of the radiation anisotropy.

4. The  $Q/I$  formula for LSA-3 is obtained by keeping the first term in a series expansion of the  $Q$ -source function in powers of the mean number of scattering events.

5. Computationally, LSA-1 is 21 times faster than LSA-2, which is 5 times faster than the more general LSA-3, which itself is 8 times faster than the exact polarized RT approach.

6. Comparison of the calculated  $Q/I$  spectra with the RT benchmark shows excellent agreement for LSA-3, including good modeling of the  $Q/I$  core region with its PRD effects. In contrast both LSA-1 and LSA-2 fail to model the core region.

7. The RT and LSA-3 approaches are then applied to model the observed  $Q/I$  profile of the Ca I 4227 Å line in quiet regions of the Sun.

8. Apart from a global scale factor, both give a very good fit to the  $Q/I$  spectra for all the wavelengths, including the core peak and blend line depolarization.

9. We conclude that LSA-3 is an excellent substitute for full polarized RT and can be used to interpret the second solar spectrum, including the Hanle effect with PRD.

10. It also allows the techniques developed for unpolarized 3D RT to be applied to modeling of the second solar spectrum.

*Further studies related to the work presented in this chapter are published in:*

1. Sampoorna, M., Stenflo, J. O., Nagendra, K. N., Bianda, M., Ramelli, R., & Anusha, L. S., 2009, **ApJ**, 699, 1650–1659
2. Anusha, L. S., Stenflo, J. O., Frisch, H., Bianda, M., Holzreuter, R., Nagendra, K. N., Sampoorna, M., & Ramelli, R., in the proceedings of **Solar Polarization Workshop 6**

(**SPW6**), 2010c, 437, 57

3. Bianda, M., Ramelli, R., Stenflo, J. O., Anusha, L. S., Nagendra, K. N., Sampoorna, M., Holzreuter, R., & Frisch, H. in the proceedings of **Solar Polarization Workshop 6 (SPW6)**, 2010, 437, 67





## Chapter 10

# Forward scattering Hanle effect in the Ca I 4227 Å line

*The contents of this chapter are based on the following publication:*

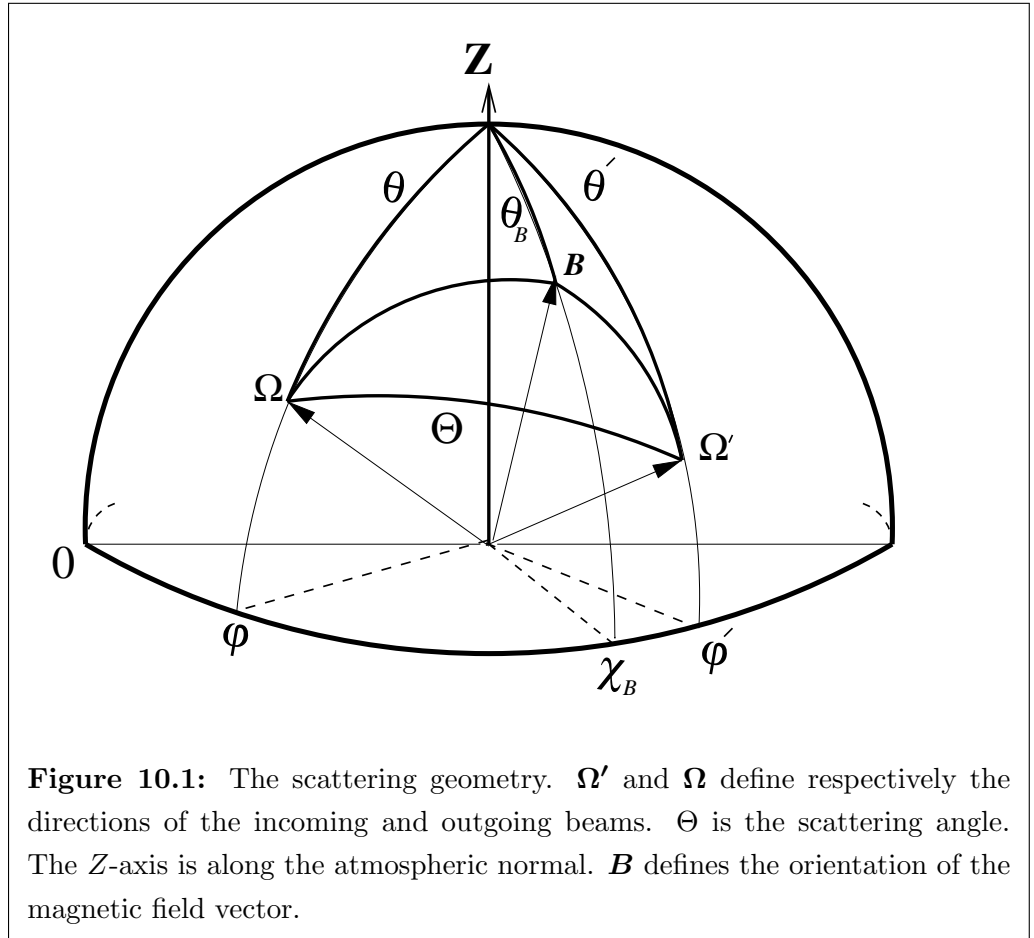
Anusha, L. S., Nagendra, K. N., Bianda, M., Stenflo, J. O., Holzreuter, R., Sampoorna, M., Frisch, H., Ramelli, R. and Smitha, H. N. 2011b, **ApJ**, 737, 95-112

### 10.1 Introduction

Ca I 4227 Å is a preferred line for the exploration of scattering polarization and the determination of the weak magnetic fields in the lower chromosphere (Bianda et al. 1998a, 1998b). This line exhibits the largest degree of linear polarization in the visible spectrum near the limb (Stenflo 1982; Gandorfer 2002; Bianda 2003; Bianda et al. 2003; Sampoorna et al. 2009; Bianda et al. 2010). A detailed modeling of non-magnetic limb observations of this line has been performed recently and are presented in chapter 9 (see also Anusha et al. 2010a, 2010c). The idea of using the Hanle effect near the disk center to measure chromospheric magnetic fields was proposed by Trujillo Bueno (2001). In a one-dimensional (1D) axially symmetric atmosphere with no oriented magnetic fields (meaning fields not parallel to the symmetry axis i.e., the atmospheric normal), the scattering polarization is zero when the line of sight is parallel to the atmospheric normal ( $\mu = \cos\theta = 1$ , where  $\theta$  is the heliocentric angle). However, in the presence of an oriented magnetic field, the Hanle effect produces a non-zero scattering polarization. This is usually referred to as the forward scattering Hanle effect. The first observational evidence for this effect was provided by Trujillo Bueno et al. (2002), who observed it in the He I 10830 Å line. For the Ca I 4227 Å line, Joos (2002) and Stenflo (2003a) showed that the forward scattering

Hanle signatures observed near the disk center ( $\mu = 0.96$ ) can be used for the analysis of weak, horizontal chromospheric magnetic fields. An extensive theoretical study of the linear polarization in the Ca II IR triplet performed by Manso Sainz & Trujillo Bueno (2010) confirms the usefulness of this effect as a diagnostic tool.

We have performed new full Stokes profile observations of the Ca I 4227 Å line near disk center, to explore different regions of varying magnetic activity, from very quiet to moderately active. Details of the observations are given in Bianda et al. 2011. In this chapter (see also Anusha et al. 2011b) we present an analysis of these observations. The observed circular polarization ( $V/I$ ) signals indicate that we are observing a solar region with weak longitudinal magnetic flux, which allows us to apply the “weak field approximation” of the Zeeman effect to model the observed  $V/I$  profiles (see e.g., Stenflo 1994; Landi Degl’Innocenti & Landolfi 2004) and thereby determine the longitudinal component of the magnetic flux density. In the weak field approximation  $V/I$  is proportional to the derivative of the emergent intensity with respect to wavelength, which can be obtained directly from the observed intensity. Thus the longitudinal component of the vector magnetic flux density is uniquely determined by the observed Stokes  $V$  and  $I$ , without any model dependence. Since however only one field component is constrained this way, there are multiple solutions (ambiguities) for the field vector itself. When  $\mu \neq 1$  these ambiguities can be eliminated using the observed linear polarization ( $Q/I$  and  $U/I$ ) profiles as additional constraints. When  $\mu = 1$  (disk center) these ambiguities cannot be eliminated, because all the Stokes parameters remain unchanged under the transformation  $\chi_B \rightarrow \chi_B + \pi$ , where  $\chi_B$  represents the magnetic field azimuth in the atmospheric co-ordinate system (polar  $Z$ -axis along the atmospheric normal). To model the observed  $Q/I$  and  $U/I$  profiles the polarized radiative transfer (RT) equation is solved assuming the presence of an oriented vector magnetic field, taking into account partial frequency redistribution (PRD). A standard model atmosphere and a multi-level model atom are used. The solutions at the line center wavelength are used to construct polarization diagrams (i.e.,  $Q/I$  versus  $U/I$  plots; see e.g., Stenflo 1994). The observed line center data are placed on the polarization diagrams to extract a single vector magnetic field for which the observed and theoretical  $Q/I$  and  $U/I$  amplitudes at line center agree. Thus the magnetic field values extracted from the  $V/I$  profiles with the weak field approximation, together with the Hanle polarization diagrams of  $Q/I$  and  $U/I$  at the line center, allow us to nicely reproduce the entire wavelength dependence of the observed  $Q/I$ ,  $U/I$  and  $V/I$  profiles. The idea of using a combination of the Zeeman and Hanle effects in magnetic field diagnostics has been explored in several papers in the past (see e.g., Bommier et al. 1981; Landi Degl’Innocenti 1982; Ben-Jaffel



et al. 2005).

For modeling the observed  $Q/I$  and  $U/I$  profiles the transverse Zeeman effect can be ruled out for various reasons: (1) the transverse field strengths would have to be more than an order of magnitude stronger than the longitudinal field, implying that all fields would need to “hide” in the transverse plane, which is a very contrived situation. (2) Even then the transverse Zeeman effect is unable to reproduce the  $Q/I$  and  $U/I$  line shapes with the observed strong  $\pi$  component. (3) The forward scattering Hanle effect provides a natural explanation of the observed  $Q/I$  and  $U/I$ , including their profile shapes, with field strengths of the same order as those indicated by the model-independent Stokes  $V/I$  fitting for the line-of-sight component.

In Section 10.2 we briefly describe the theoretical framework of polarized RT used in our calculations. In Section 10.3, details on the observations, the solar atmospheric model, and the model atom are given. Section 10.4 is devoted to a description of the modeling

procedure. The results and discussions are presented in Section 10.5. Concluding remarks are given in Section 10.6.

## 10.2 The Radiative Transfer (RT) formulation

For our modeling procedure, we have solved non-LTE RT equations for the Hanle effect and for the Zeeman effect but under the weak field approximation.

### 10.2.1 Radiative transfer with the Hanle effect

#### Stokes parameters formulation

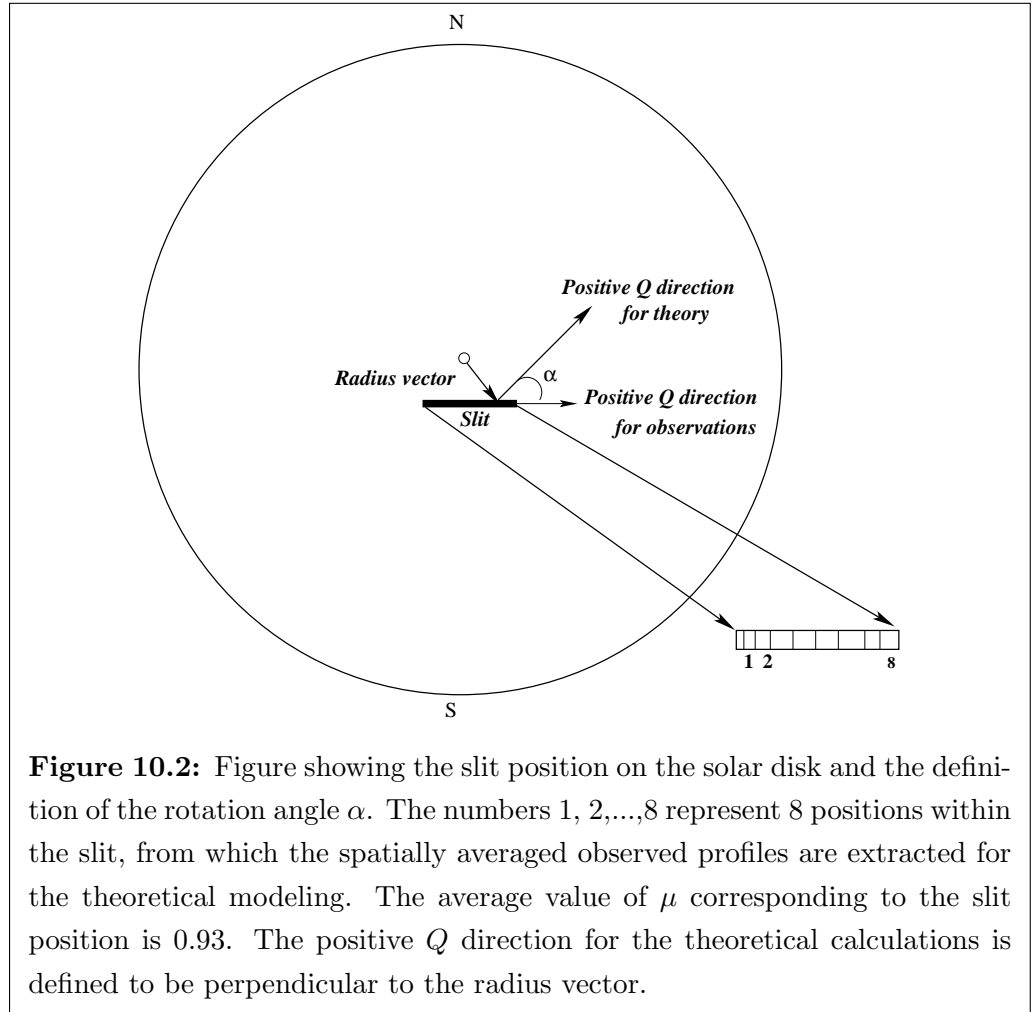
We use the standard notation of line formation theory (Mihalas 1978; Stenflo 1994). The Stokes vector RT equation for a two-level model atom with unpolarized ground level in a 1D planar medium in the presence of weak field Hanle effect may be written as

$$\mu \frac{\partial \mathbf{I}(\lambda, \boldsymbol{\Omega}, z)}{\partial z} = -[\kappa_l(z)\phi(\lambda, z) + \kappa_c(\lambda, z) + \sigma_c(\lambda, z)] [\mathbf{I}(\lambda, \boldsymbol{\Omega}, z) - \mathbf{S}(\lambda, \boldsymbol{\Omega}, z)], \quad (10.1)$$

where  $\mathbf{I} = (I, Q, U)^T$  is the Stokes vector and  $\mathbf{S} = (S_I, S_Q, S_U)^T$  the source vector. Here  $\boldsymbol{\Omega} = (\theta, \varphi)$  defines the ray direction with  $\theta$  and  $\varphi$  being the inclination and azimuth of the scattered ray (see Figure 10.1). The Voigt profile function is denoted by  $\phi$ . The dependence of  $\phi$  on  $z$  comes from the damping parameter  $a = \Gamma_{\text{tot}}/4\pi\Delta\nu_D$ . Here

$$\Gamma_{\text{tot}} = \Gamma_R + \Gamma_E + \Gamma_I, \quad (10.2)$$

with  $\Gamma_R$  being the radiative de-excitation rate. For the Ca I 4227 Å line  $\Gamma_R = 2.18 \times 10^8 \text{ s}^{-1}$ .  $\Gamma_E$  and  $\Gamma_I$  are the elastic and inelastic collision rates respectively.  $\Gamma_E$  is computed taking into account the van der Waal's broadening (arising due to elastic collisions with neutral hydrogen) and Stark broadening (arising due to interactions with free electrons).  $\Gamma_I$  includes the inelastic collision processes like collisional de-excitation by electrons and protons, collisional ionization by electrons, and charge exchange processes (see Uitenbroek 2001, and the multi-level atom computer program provided by him). The Doppler width  $\Delta\nu_D = \sqrt{2k_B T/M_a + v_{\text{turb}}^2}/\lambda_0$ , where  $k_B$  is the Boltzmann constant,  $T$  is the temperature,  $M_a$  is the mass of the atom,  $v_{\text{turb}}$  is the micro-turbulent velocity (taken as 1 km/s) and  $\lambda_0$  is the line center wavelength.  $\kappa_l$  is the wavelength averaged line absorption coefficient, while  $\sigma_c$  and  $\kappa_c$  are the continuum scattering and continuum absorption coefficients, respectively. Other atomic parameters are given in Section 10.4.1 and Appendix N.



The total opacity coefficient is  $\kappa_{\text{tot}}(\lambda, z) = \kappa_l(z)\phi(\lambda, z) + \sigma_c(\lambda, z) + \kappa_c(\lambda, z)$ . In a two-level model atom with unpolarized ground level, the total source vector  $\mathbf{S}$  is defined as

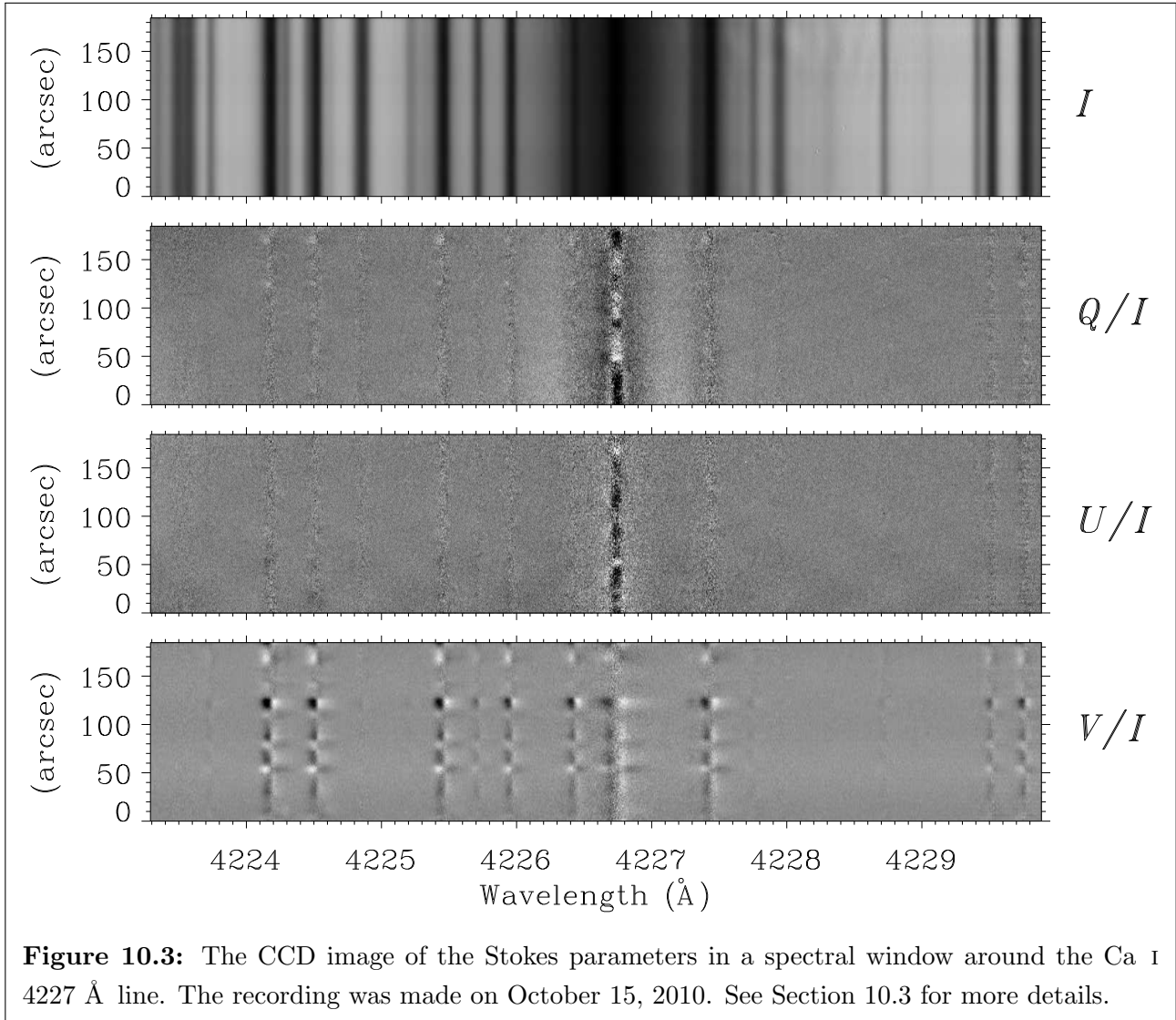
$$\mathbf{S}(\lambda, \boldsymbol{\Omega}, z) = \frac{\kappa_l(z)\phi(\lambda, z)\mathbf{S}_l(\lambda, \boldsymbol{\Omega}, z) + \sigma_c(\lambda, z)\mathbf{S}_c(\lambda, \boldsymbol{\Omega}, z) + \kappa_c(\lambda, z)B_\lambda(z)\mathbf{U}}{\kappa_{\text{tot}}(\lambda, z)}. \quad (10.3)$$

Here  $\mathbf{U} = (1, 0, 0)^T$  and  $B_\lambda$  is the Planck function at the line center. The line source vector is

$$\mathbf{S}_l(\lambda, \boldsymbol{\Omega}, z) = \epsilon B_\lambda(z)\mathbf{U} + \int_{-\infty}^{+\infty} \oint \hat{R}(\lambda, \lambda', \boldsymbol{\Omega}, \boldsymbol{\Omega}', z, \mathbf{B})\mathbf{I}(\lambda', \boldsymbol{\Omega}', z) \frac{d\boldsymbol{\Omega}'}{4\pi} d\lambda'. \quad (10.4)$$

Here  $\hat{R}$  is the Hanle redistribution matrix (Bommier 1997b).  $\mathbf{B}$  is the vector magnetic field taken to be a free parameter. The continuum scattering source vector is

$$\mathbf{S}_c(\lambda, \boldsymbol{\Omega}, z) = \oint \hat{P}(\boldsymbol{\Omega}, \boldsymbol{\Omega}')\mathbf{I}(\lambda, \boldsymbol{\Omega}', z) \frac{d\boldsymbol{\Omega}'}{4\pi}, \quad (10.5)$$



where  $\hat{P}$  is the Rayleigh scattering phase matrix (Chandrasekhar 1950). For simplicity, frequency coherent scattering is assumed for the continuum. The thermalization parameter  $\epsilon$  is defined by  $\epsilon = \Gamma_I/(\Gamma_R + \Gamma_I)$ . In Equation (10.4)  $(\lambda', \boldsymbol{\Omega}')$  and  $(\lambda, \boldsymbol{\Omega})$  refer to the wavelength and direction of the incoming and the outgoing ray, respectively.

### Spherical irreducible tensors decomposition

In general the Stokes source vector  $\boldsymbol{S}$  and the Stokes vector  $\boldsymbol{I}$  in Equation (10.1) depend on  $\boldsymbol{\Omega} = (\theta, \varphi)$ . As shown in Frisch (2007), the vectors  $\boldsymbol{S}$  and  $\boldsymbol{I}$  can be decomposed into 6 cylindrically symmetric components,  $\mathcal{I}_Q^K$  and  $\mathcal{S}_Q^K$ , with  $K = 0, 2$  and  $Q \in [-K, +K]$ , if one represents them in terms of the spherical irreducible tensors for polarimetry defined in,

e.g., Landi Degl'Innocenti & Landolfi (2004). With these components one can construct an irreducible source vector  $\mathcal{S}$  and an irreducible Stokes vector  $\mathcal{I}$ . This decomposition is useful because  $\mathcal{S}$  becomes independent of the ray direction and  $\mathcal{I}$  becomes independent of the azimuthal angle  $\varphi$ . The transfer equation for  $\mathcal{I}$  may be written as

$$\mu \frac{\partial \mathcal{I}(\lambda, \mu, z)}{\partial z} = -\kappa_{\text{tot}}(\lambda, z) [\mathcal{I}(\lambda, \mu, z) - \mathcal{S}(\lambda, z)]. \quad (10.6)$$

In a two-level model atom with unpolarized ground level, the total irreducible source vector  $\mathcal{S}$  is defined as

$$\mathcal{S}(\lambda, z) = \frac{\kappa_l(z)\phi(\lambda, z)\mathcal{S}_l(\lambda, z) + \sigma_c(\lambda, z)\mathcal{S}_c(\lambda, z) + \kappa_c(\lambda, z)B_\lambda(z)\mathbf{u}}{\kappa_{\text{tot}}(\lambda, z)}. \quad (10.7)$$

Here  $\mathbf{u} = (1, 0, 0, 0, 0, 0)^T$ . The irreducible line source vector is

$$\mathcal{S}_l(\lambda, z) = \epsilon B_\lambda(z)\mathbf{u} + \int_{-\infty}^{+\infty} \frac{1}{2} \int_{-1}^{+1} \hat{\mathcal{R}}(\lambda, \lambda', z, \mathbf{B}) \hat{\Psi}(\mu') \mathcal{I}(\lambda', \mu', z) d\mu' d\lambda'. \quad (10.8)$$

Here  $\mu'$  represents the incoming ray directions. The irreducible polarized continuum scattering source vector is

$$\mathcal{S}_c(\lambda, z) = \frac{1}{2} \int_{-1}^{+1} \hat{\Psi}(\mu') \mathcal{I}(\lambda, \mu', z) d\mu'. \quad (10.9)$$

$\hat{\mathcal{R}}$  is the angle-averaged PRD matrix in the irreducible basis for the Hanle effect (see Bomnier 1997a, 1997b) given in Equation (N.1) of Appendix N. The matrix  $\hat{\Psi}$  is the Rayleigh scattering phase matrix in the irreducible basis. Its elements are given in Appendix A of Frisch (2007, see also Faurobert-Scholl 1991). We define the total optical depth scale through  $d\tau_\lambda = -\kappa_{\text{tot}}(\lambda, z)dz$ .

The formal solution of Equation (10.6) can be written as

$$\mathcal{I}(\lambda, \mu, \tau_\lambda) = \mathcal{I}_0(\lambda, \mu, T_\lambda) \exp \left[ - \left( \frac{T_\lambda - \tau_\lambda}{\mu} \right) \right] + \int_{\tau_\lambda}^{T_\lambda} \exp \left[ - \left( \frac{\tau'_\lambda - \tau_\lambda}{\mu} \right) \right] \mathcal{S}(\lambda, \tau'_\lambda) \frac{d\tau'_\lambda}{\mu}, \quad (10.10)$$

for  $\mu > 0$ , and

$$\mathcal{I}(\lambda, \mu, \tau_\lambda) = \mathcal{I}_0(\lambda, \mu, 0) \exp \left( - \frac{\tau_\lambda}{\mu} \right) - \int_0^{\tau_\lambda} \exp \left[ - \left( \frac{\tau'_\lambda - \tau_\lambda}{\mu} \right) \right] \mathcal{S}(\lambda, \tau'_\lambda) \frac{d\tau'_\lambda}{\mu}, \quad (10.11)$$

for  $\mu < 0$ .  $\mathcal{I}_0$  represents a radiation field that is incident on the medium. We assume that no radiation is incident on the upper free boundary ( $\tau_\lambda = 0$ ), while at the lower boundary  $T_\lambda$ ,  $\mathcal{I}_0(\lambda, \mu, T_\lambda) = (B_\lambda(T_\lambda), 0, 0, 0, 0, 0)^T$ .

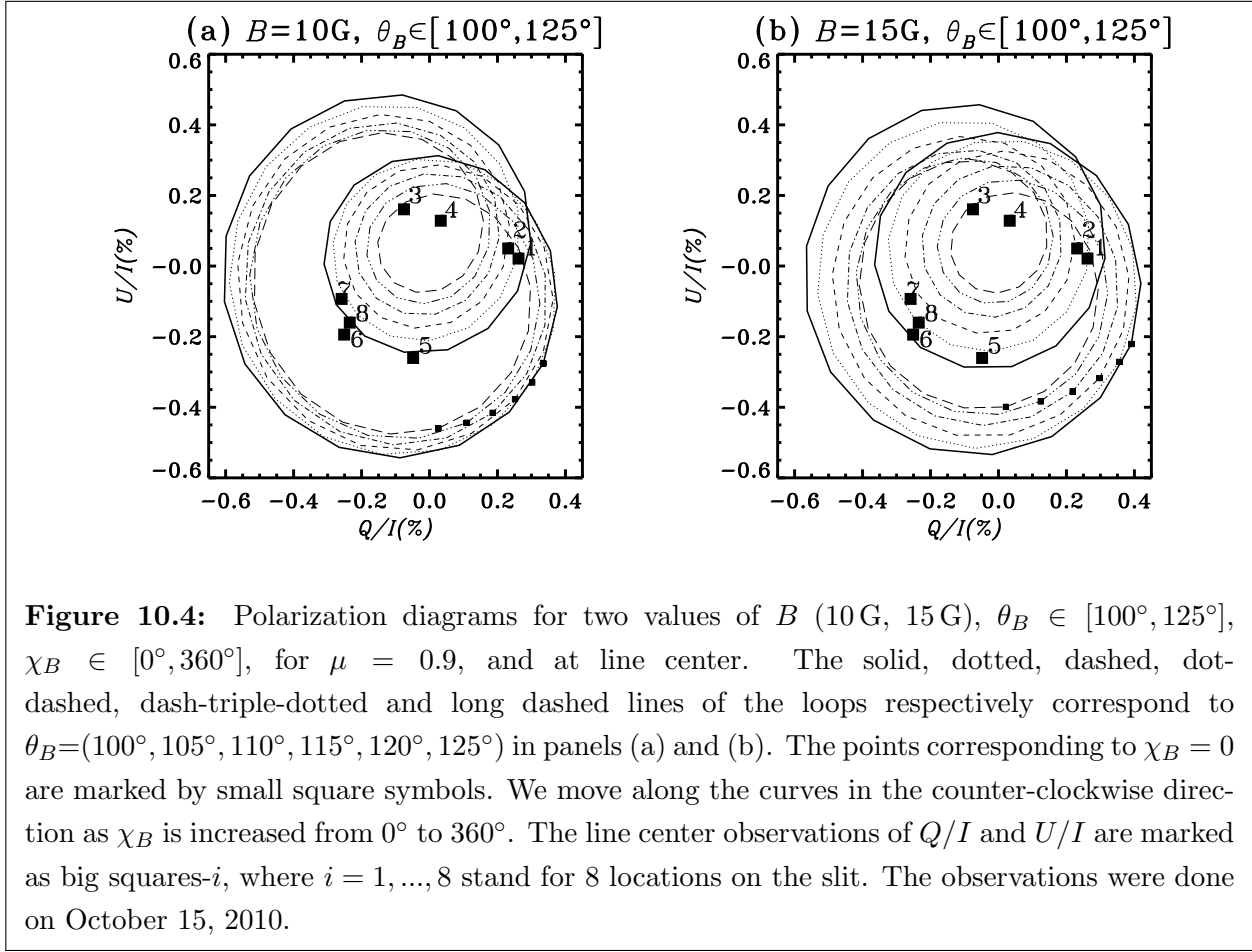
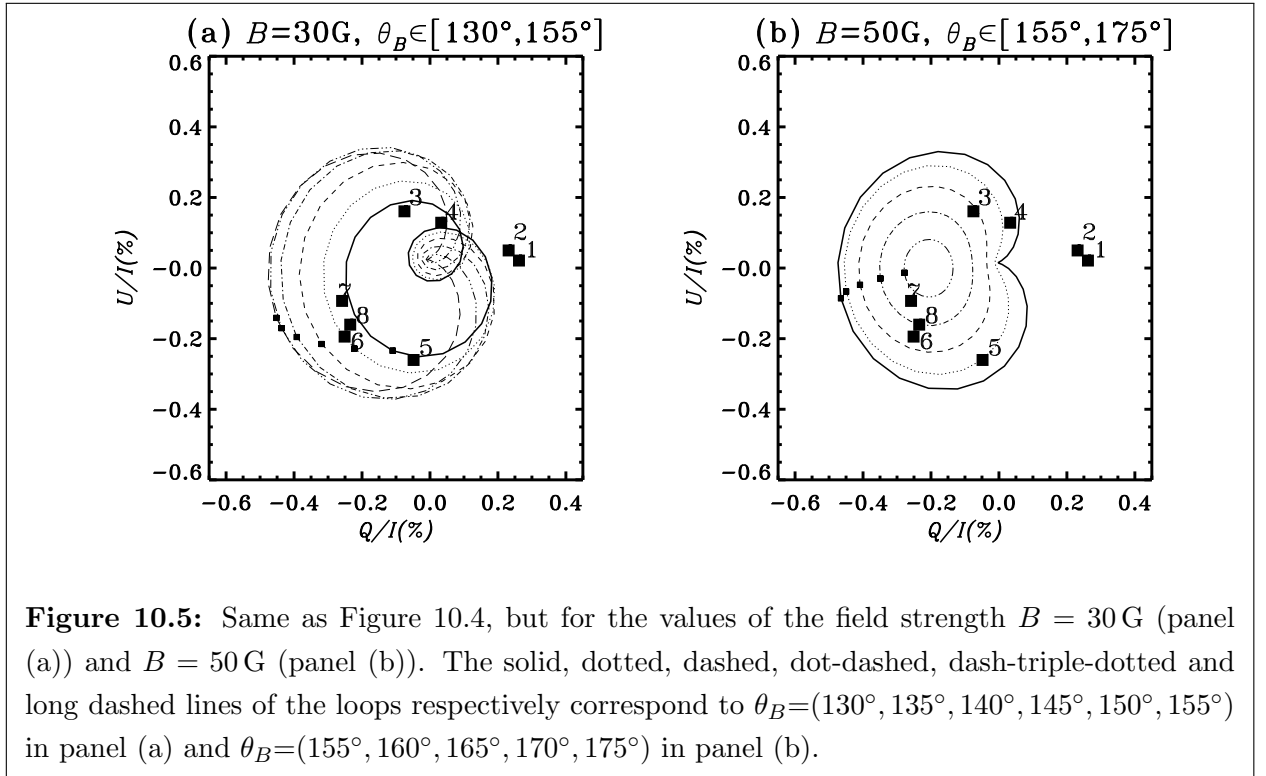


**Figure 10.4:** Polarization diagrams for two values of  $B$  (10 G, 15 G),  $\theta_B \in [100^\circ, 125^\circ]$ ,  $\chi_B \in [0^\circ, 360^\circ]$ , for  $\mu = 0.9$ , and at line center. The solid, dotted, dashed, dot-dashed, dash-triple-dotted and long dashed lines of the loops respectively correspond to  $\theta_B=(100^\circ, 105^\circ, 110^\circ, 115^\circ, 120^\circ, 125^\circ)$  in panels (a) and (b). The points corresponding to  $\chi_B = 0$  are marked by small square symbols. We move along the curves in the counter-clockwise direction as  $\chi_B$  is increased from  $0^\circ$  to  $360^\circ$ . The line center observations of  $Q/I$  and  $U/I$  are marked as big squares- $i$ , where  $i = 1, \dots, 8$  stand for 8 locations on the slit. The observations were done on October 15, 2010.

The redistribution matrices used here are defined under the approximation level III of Bommier (1997b, see our Appendix N) We take into account the depth dependence of the branching ratios that appear in the redistribution matrix  $\hat{\mathcal{R}}$ , in contrast to Nagendra et al. (2002) and Fluri et al. (2003b) where these coefficients were kept independent of depth, because only isothermal atmospheres were considered. The polarized Hanle RT equation is solved for the irreducible Stokes vector  $\mathcal{I}$ . The Stokes vector  $(I, Q, U)^T$  can then be deduced from  $\mathcal{I}$  (see e.g., Frisch 2007; Anusha & Nagendra 2011a). The components of  $\mathcal{I}$  are  $(I_0^0, I_0^2, I_1^{2,x}, I_1^{2,y}, I_2^{2,x}, I_2^{2,y})$ . If the magnetic field is zero, or micro-turbulent, only the two components  $I_0^0$  and  $I_0^2$  are non-zero. It is easy to see on the expression of Stokes  $Q$  that  $Q = 0$  at the disc-center ( $\mu = 1$ ) and maximum at the limb ( $\mu = 0$ ) and that  $U = 0$ . The same argument applies to  $S_0^0$  and  $S_0^2$ . When the magnetic field is non-zero and has some fixed orientation, then all the 6 components are non-zero. Therefore Stokes  $Q$  will be non-zero at disc center and  $U$  will be non-zero with contributions coming from the four components  $I_1^{2,x}, I_1^{2,y}, I_2^{2,x}, I_2^{2,y}$ . This is referred to as forward scattering Hanle effect.





### 10.2.2 Radiative transfer with the Zeeman effect

The non-LTE Zeeman-effect line transfer equation for the Stokes vector  $(I, Q, U, V)^T$  is given by

$$\mu \frac{\partial \mathbf{I}(\lambda, \boldsymbol{\Omega}, z)}{\partial z} = -\hat{K}(\lambda, z, \mathbf{B}) [\mathbf{I}(\lambda, \boldsymbol{\Omega}, z) - \mathbf{S}(\lambda, z)], \quad (10.12)$$

where  $\hat{K}$  is the absorption matrix. In Appendix O we give the relevant trigonometric functions that are required to write the Zeeman absorption matrix in the atmospheric reference frame. The general form of  $\mathbf{S}(\lambda, z)$  for a multi-level model atom can be found in Landi Degl'Innocenti & Landolfi (2004). We recall that Equation (10.1) is the Hanle RT equation written for the Stokes parameters  $(I, Q, U)^T$  (Stokes  $V$  is not included because it is not generated by the weak-field Hanle effect). Stokes  $I$  is not very sensitive to the magnetic field in the weak field limit (see Eq. (10.13) below). Stokes  $Q$  and  $U$  are generated due to scattering in the presence of a weak magnetic field  $\mathbf{B}$ . Equation (10.12) is the Zeeman RT equation written for the Stokes vector  $(I, Q, U, V)^T$ . The Stokes parameters  $Q$  and  $U$  appearing in Equations (10.1) and (10.12) are the same quantities and can therefore have contributions from both the Hanle and Zeeman effects. However, for the range of fields indicated by the observed  $V/I$  amplitudes (see below), Stokes  $Q$  and  $U$  generated

from the transverse Zeeman effect are negligible, and therefore Stokes  $V$  decouples from Stokes  $Q$  and  $U$  in Equation (10.12). In the weak field limit the RT equation for the

**Table 10.1:** List of the ratio  $\Delta\lambda_H/\Delta\lambda_D$  for various  $B$  values

$B$	10	20	30	40	50	60	70	80	90
$\Delta\lambda_H/\Delta\lambda_D$	0.003	0.005	0.008	0.01	0.013	0.016	0.019	0.022	0.024
$B$	100	500	1000	2000	3000				
$\Delta\lambda_H/\Delta\lambda_D$	0.027	0.134	0.269	0.538	0.807				

linear polarization (Equation (10.1)) thus decouples from the RT equation for the circular polarization (Equation (10.12)). With the assumption of height independent magnetic fields the weak field approximation (see e.g., Stenflo 1994; Landi Degl’Innocenti & Landolfi 2004) is defined as

$$\frac{\Delta\lambda_H}{\Delta\lambda_D} \ll 1, \quad (10.13)$$

where

$$\Delta\lambda_H(\text{mÅ}) = 4.67 \times 10^{-10} g_{\text{eff}} \lambda_0^2 B, \quad (10.14)$$

with  $g_{\text{eff}}$  being the effective Landè factor ( $g_{\text{eff}} = 1$  for the Ca I 4227 Å line). The line center wavelength  $\lambda_0$  is given in Å and  $B$  in Gauss.  $\Delta\lambda_D$  is the Doppler width expressed in wavelength units.

For the Ca I atom  $\Delta\lambda_D = 31 \text{ mÅ}$  at the top of the FALC model atmosphere (where  $T = 9257 \text{ K}$ ). We get  $\Delta\lambda_H = 8.33487 \times 10^{-3} B$ . The Zeeman splitting equals the Doppler width for a field strength of about  $B = 3720 \text{ G}$ . In Table 10.1 we list the ratio  $\Delta\lambda_H/\Delta\lambda_D$  for various  $B$  values. For  $B \leq 40\text{G}$ , we have  $\Delta\lambda_H/\Delta\lambda_D \leq 1\%$ , so for  $B \geq 50\text{G}$  the ratio  $\Delta\lambda_H/\Delta\lambda_D$  starts to become significant.

Under the weak field approximation (Equation (10.13))  $V/I$  is simply given by

$$\frac{V(\lambda, \mu)}{I(\lambda, \mu)} = \frac{1}{I(\lambda, \mu)} \left[ -\Delta\lambda_H \cos \gamma \frac{\partial I(\lambda, \mu)}{\partial \lambda} \right], \quad (10.15)$$

where  $I(\lambda, \mu)$  is the emergent Stokes  $I$  profile, and

$$\cos \gamma = \cos \theta_B \cos \theta + \sin \theta_B \sin \theta \cos(\varphi - \chi_B). \quad (10.16)$$

Here  $B$ ,  $\theta_B$  and  $\chi_B$  represent the strength, inclination and azimuth of the magnetic field vector (see Figure 10.1). In all our calculations we set  $\varphi = 0^\circ$  and  $\cos \theta = \mu = 0.9$ . Use of

**Table 10.2:** The values of  $(B, \theta_B, \chi_B)$  derived from the model fits to the observed  $Q/I$ ,  $U/I$  and  $V/I$  data sets.

Observation point	1	2	3	4	5	6	7	8
$B$ (G)	15	15	10	30	50	50	30	30
$\theta_B$ (degrees)	125	110	125	155	160	165	115	135
$\chi_B$ (degrees)	56	191	101	236	68	45	293	360
$B \cos \gamma$	-4.7	-10.6	-5.8	-27.6	-39.4	-39.5	-6.8	-9.8

Equation (10.15) allows us to bypass the numerically expensive task of solving the Zeeman RT equation for a range of  $B$ ,  $\theta_B$  and  $\chi_B$  values.

### 10.3 Polarization observations of Ca I 4227 Å line

The data acquisition was done with the ZIMPOL-3 polarimeter (Ramelli et al. 2010) at IRSOL in Switzerland. More observational details will be given in Bianda et al. (2011). The observations were obtained on 15 October 2010 near the active solar region NOAA 1112 (S19 W5). Figure 10.2 shows the position of the spectrograph slit, which was 60  $\mu\text{m}$  wide (0.5 arcsec on the disk) and subtended 184 arcsec. The slit orientation was parallel to the geographical north limb. The resulting CCD images are 140 pixels high in the spatial direction, with a pixel corresponding to 1.3 arcsec, and 1240 pixels wide in the wavelength direction, with a pixel corresponding to 5.3 mÅ. The total exposure time was about 8 min (500 single recordings of 1 s each). These observations correspond to an average  $\mu$  value of 0.93. Note that  $\mu$  values determined for near disk center observations are more accurate compared to those determined near the limb. Figure 10.3 shows the CCD image of the Ca I 4227 Å line. From the Stokes profiles in Figures 10.7-10.10 we can see that the orders of magnitude of the observed  $Q/I$ ,  $U/I$  and  $V/I$  are in the range 0.1%-1%. This indicates that the observed regions are weakly magnetized. We have selected a set of 8 observed Stokes profiles for analysis. Each of these profiles is a result of averaging over three to four pixels along the slit (to reduce noise). These 8 profiles represent different spatial locations on the solar disk, and therefore are expected to have different magnetic fields. Henceforward these 8 locations are referred to as location (or observation point) 1 to 8. Other near disk center observations have been performed at IRSOL. They can be modeled with the same strategy.

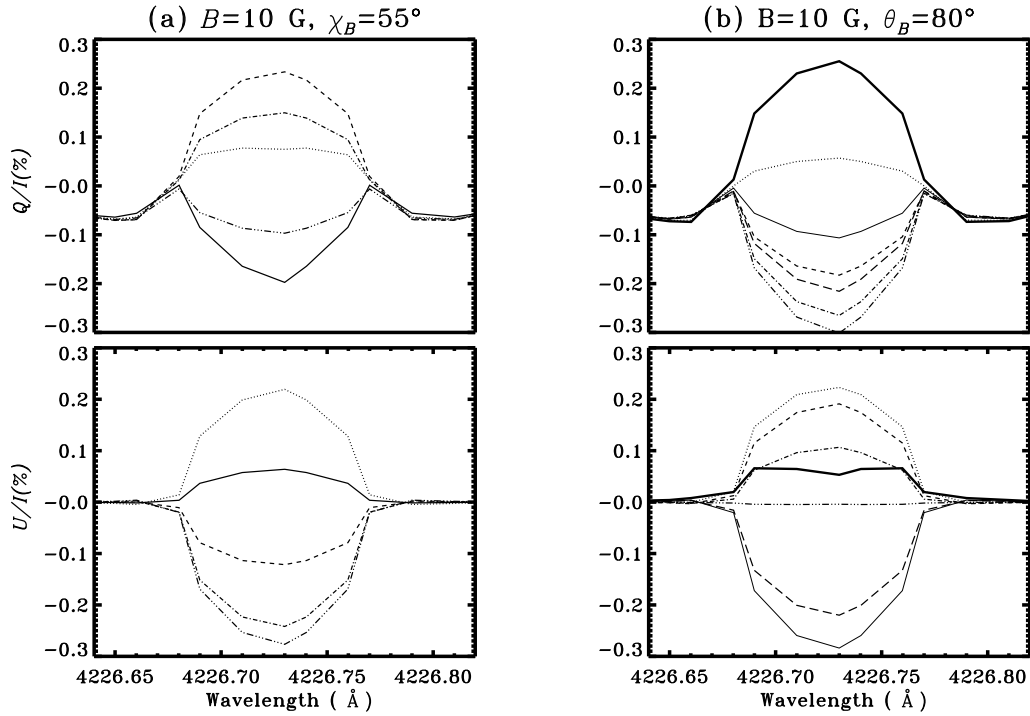


**Figure 10.6:** Illustration of the sensitivity of the  $Q/I$  and  $U/I$  profiles to the magnetic field orientation. Panel (a) shows the dependence of the  $Q/I$  and  $U/I$  profiles on  $\theta_B$  for a fixed value of  $\chi_B = 55^\circ$ . Solid, dotted, dashed, dot-dashed and dash-triple-dotted curves represent  $\theta_B = 5^\circ, 30^\circ, 60^\circ, 70^\circ, 90^\circ$ , respectively. Panel (b) shows the dependence of  $Q/I$  and  $U/I$  profiles on  $\chi_B$  for a fixed value of  $\theta_B = 80^\circ$ . Thick solid, dotted, dashed, dot-dashed, dash-triple-dotted, long-dashed and thin solid curves represent  $\chi_B = 11^\circ, 34^\circ, 56^\circ, 68^\circ, 79^\circ, 101^\circ$  and  $113^\circ$ , respectively.

The positive  $Q/I$  direction for the observations is defined to be parallel to the slit direction (or parallel to the geographical north limb), whereas the positive  $Q/I$  direction for the RT problem is defined to be perpendicular to the radius vector. For each point on the slit, the observational data must therefore be converted to the system where positive  $Q/I$  is oriented perpendicular to the solar radius passing through this point (see Figure 10.2). So for each point, if  $(Q', U')^T$  denotes the original observed data,  $(Q, U)^T$  for a system where positive  $Q/I$  is oriented perpendicular to the solar radius is given by

$$\begin{pmatrix} Q \\ U \end{pmatrix} = \begin{pmatrix} \cos 2\alpha & \sin 2\alpha \\ -\sin 2\alpha & \cos 2\alpha \end{pmatrix} \times \begin{pmatrix} Q' \\ U' \end{pmatrix}, \quad (10.17)$$

where  $\alpha$  is the angle between the slit direction and the vector perpendicular to the radius

vector (see Figure 10.2).

We note that Stokes  $I$  and  $V$  are unaffected by the rotation angle  $\alpha$  (see Equation (13.3) of Stenflo 1994).

Spectropolarimetric observations of the Ca I 4227 Å line at the limb have revealed wing polarization anomalies (see Bianda et al. 2003; Nagendra et al. 2002; Nagendra et al. 2003; Sampoorna et al. 2009), which have been referred to as the “wing Hanle effect enigma”. The work of Sampoorna et al. (2009) has shown that according to the best theoretical approaches now available, it is impossible to explain these wing anomalies in terms of the Hanle effect, and therefore alternative mechanisms have been qualitatively invoked. The wing Hanle effect enigma basically means that the signals that are measured close to the limb are characterized by a faint depolarization in the  $Q/I$  wings, while the  $U/I$  wings exhibit  $Q/I$  like shapes, with amplitudes that are small fractions of the  $Q/I$  amplitudes. Our observations indicate that while the signals can be easily found near the solar limb, they quickly become rare when moving toward the disk center. All the polarization effects that we observe and try to model near disk center for the forward-scattering Hanle effect are concentrated in the inner wings, near the line core, while the wing anomalies observed near the limb would be located significantly further out, in the outer wing region. As we do not observe any polarization effects near disk center in these outer wing regions, neither in  $Q/I$ , nor in  $U/I$ , all that we are dealing with in the forward scattering case has nothing to do with the wing Hanle effect enigma, it is an entirely unrelated phenomenon. This fact further indicates that the wing signatures measured near the limb are not related to the Hanle effect, but have a different physical origin.

## 10.4 Modeling procedure

The theoretical polarized spectrum is calculated with a two-stage process similar to the one described in Holzreuter et al. (2005). In the first stage a multi-level PRD-capable MALI (Multi-level Approximate Lambda Iteration) code of Uitenbroek (2001, hereafter called RH-code), solves the statistical equilibrium equation and the unpolarized RT equation self-consistently and iteratively. The RH-code is used to compute the intensity, opacities, and the collision rates. In the second stage, the opacities and the collision rates are kept fixed, and the vector  $\mathcal{I}$  is computed perturbatively by solving the polarized Hanle transfer equation. The Stokes vector  $\mathbf{I}$  can then be deduced using the irreducible vector  $\mathcal{I}$ . For simplicity, in the second stage a two-level atomic model is assumed for the particular transition of interest.

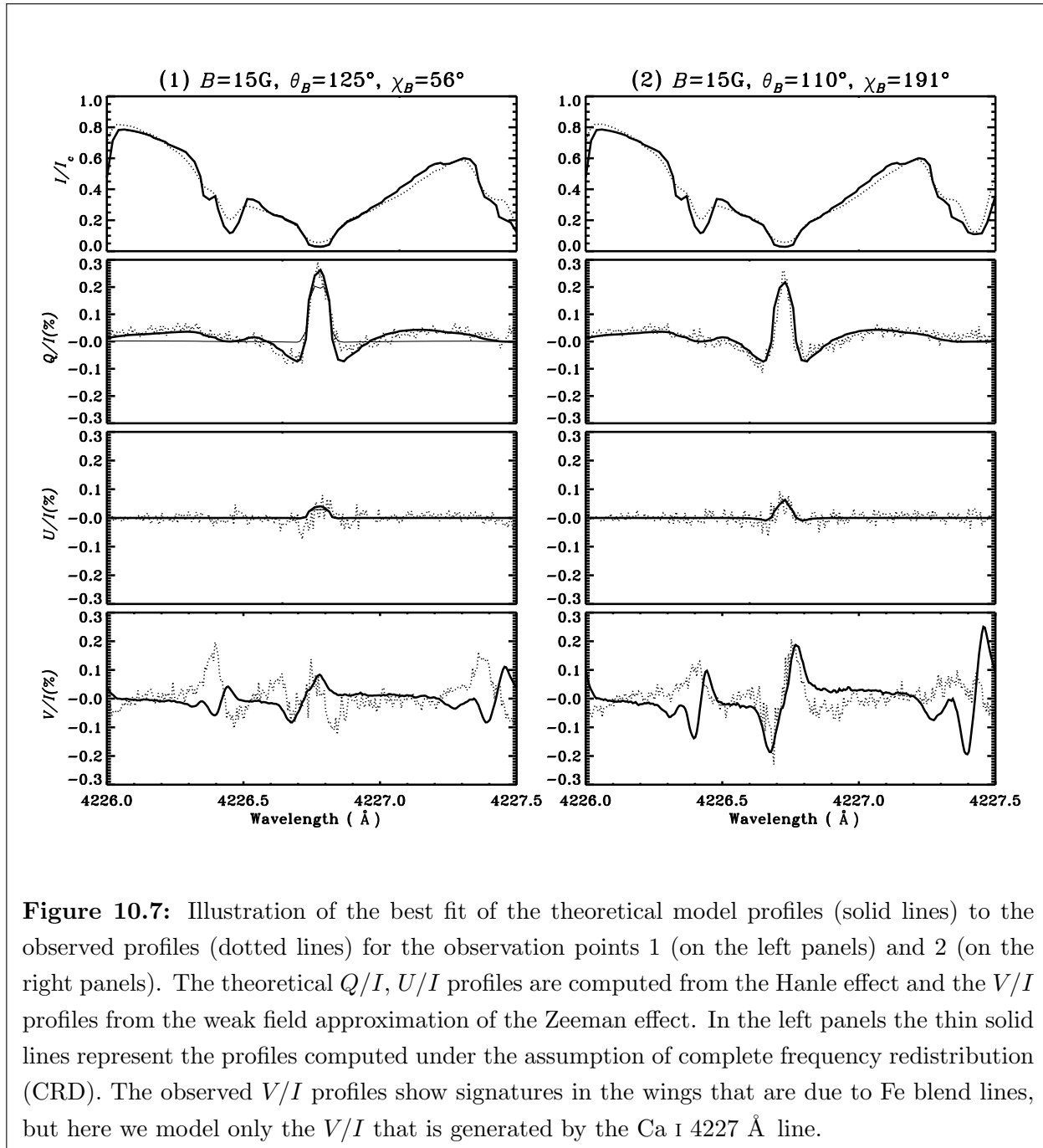
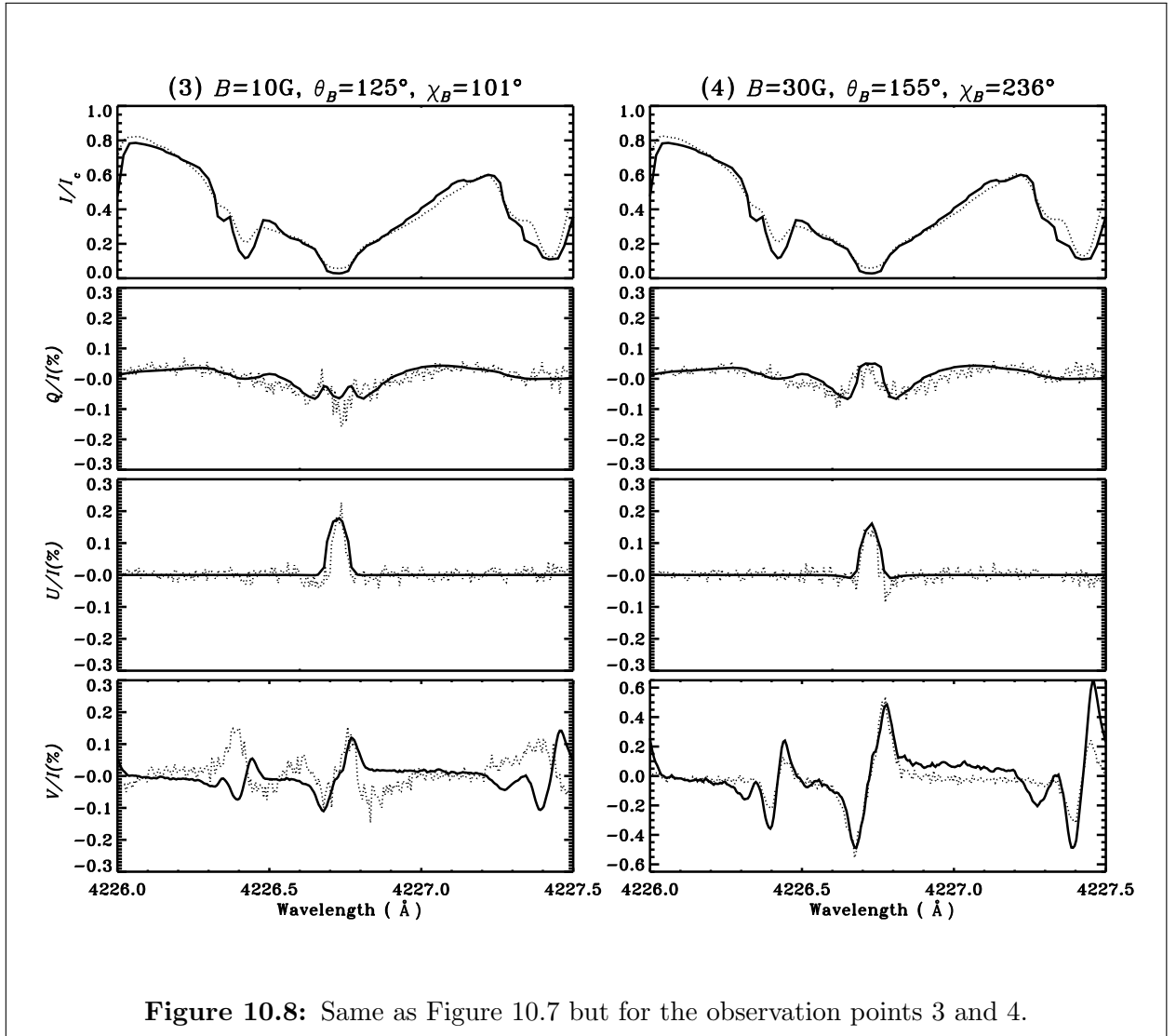


**Figure 10.7:** Illustration of the best fit of the theoretical model profiles (solid lines) to the observed profiles (dotted lines) for the observation points 1 (on the left panels) and 2 (on the right panels). The theoretical  $Q/I$ ,  $U/I$  profiles are computed from the Hanle effect and the  $V/I$  profiles from the weak field approximation of the Zeeman effect. In the left panels the thin solid lines represent the profiles computed under the assumption of complete frequency redistribution (CRD). The observed  $V/I$  profiles show signatures in the wings that are due to Fe blend lines, but here we model only the  $V/I$  that is generated by the Ca I 4227 Å line.



#### 10.4.1 The model atmosphere and the model atom

We use the FALC model atmosphere Fontenla et al. (1993), which we find to be better for reproducing the observed linear polarization profiles from the Hanle effect. For comparison we also show theoretical profiles computed with the FALX model atmosphere Avrett (1995; see our Figure 10.11).

In the multi-level RH-code, the atomic model of CaI is consisting of 20 levels, with 17 line transitions and 19 continuum transitions. The main line is treated in PRD, using the angle-averaged PRD functions of Hummer (1962). All other lines of the multiplet are treated in CRD. However, for computing the polarization we restrict ourselves to a

two-level atom model for the main line transition. All the blend lines are assumed to be depolarizing. They are treated in LTE in the RH-code. Therefore, the blend line absorption coefficient is implicitly included in the continuum absorption coefficient  $\kappa_c$ .

In this chapter the RT equations are solved for  $\mu = 0.9$ . We have verified that one can retain this single  $\mu$  value to analyze all the observation points along the slit. The vector magnetic field  $\mathbf{B} = (B, \theta_B, \chi_B)$  is a free parameter. In all the calculations  $\mathbf{B}$  is assumed to be uniform with height. We also assume that it is filling all the space for reasons that are explained in Section 10.5.6. Our modeling procedure can be described in three steps.

#### 10.4.2 Step 1. Polarization profiles for $V/I$

In this step we first derive the value of  $B \cos \gamma$  (longitudinal component) that is uniquely determined by the observed  $V/I$  profile when compared with the derivative of the observed Stokes  $I$  profile (cf. Equation (10.15)). We then compute ensembles of  $(B, \theta_B, \chi_B)$  values that all reproduce the uniquely determined  $B \cos \gamma$ . These ensembles are model independent because they are directly based on the observed  $V/I$  and  $I$  profiles. For more details see Section 10.5.1.

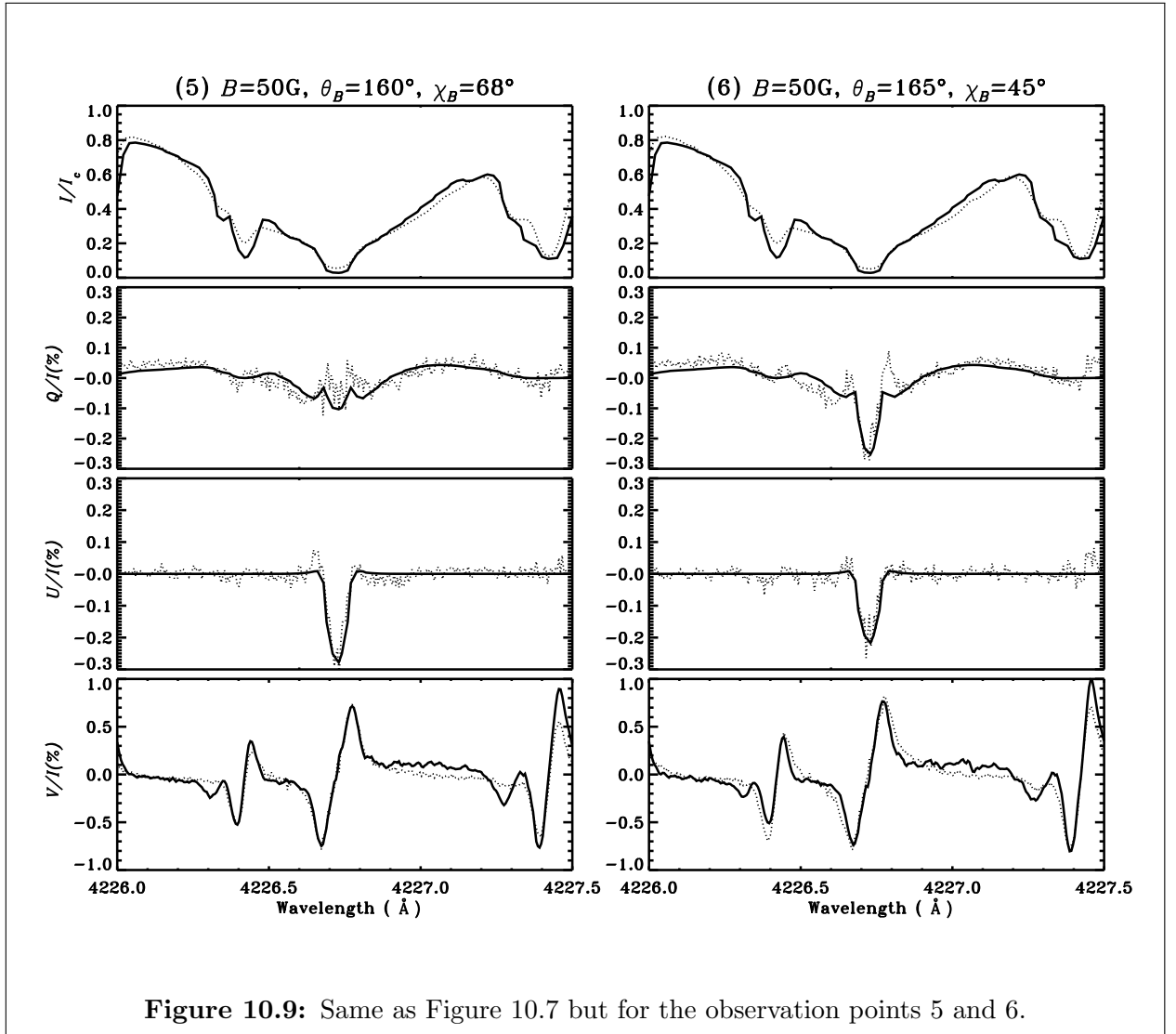
#### 10.4.3 Step 2. Polarization diagrams for $Q/I$ and $U/I$ at line center

While Step 1 fixes the value of the line-of-sight component of  $\mathbf{B}$  by using Stokes  $V$ , the components in the transversal plane are entirely unconstrained. To determine all three components of the field vector we need two additional observables, namely the observed  $Q/I$  and  $U/I$ . We generate theoretical polarization diagrams for  $Q/I$  and  $U/I$  at the line center computed using the RT equation with the Hanle effect (see Equation (10.1)) for the sets of  $\mathbf{B}$  values already extracted in Step 1. The observed line center values of  $Q/I$  and  $U/I$  are marked on these diagrams. With the polarization diagrams we can remove the ambiguities in the  $(B, \theta_B, \chi_B)$  values. For more details see Section 10.5.2.

#### 10.4.4 Step 3. Polarization profiles for $Q/I$ and $U/I$

In this step we compare the observed profiles with the theoretical profiles calculated with the  $(B, \theta_B, \chi_B)$  values extracted from Steps 1 and 2. Although in Step 2 we use the  $Q/I$  and  $U/I$  values only at line center, it turns out that these  $(B, \theta_B, \chi_B)$  values are also able to reproduce the wavelength dependence of the observed  $Q/I$  and  $U/I$  profiles in the line core. For more details see Section 10.5.3.





## 10.5 Results and Discussions

In this section we discuss the results of the modeling procedure described in the previous section.

### 10.5.1 $V/I$ profiles from the Zeeman effect

Here we discuss in more detail how Step 1 is performed (Section 10.4.2). For the computation of the  $V/I$  profiles in Step 1 using Equation (10.15) we consider a grid of magnetic field parameters ( $B, \theta_B, \chi_B$ ), which are in the range  $B \in [0\text{G}, 50\text{G}]$  in steps of 5 G,  $\theta_B \in [0^\circ, 180^\circ]$  in steps of  $5^\circ$ , and  $\chi_B \in [0^\circ, 360^\circ]$  in steps of  $11.25^\circ$ . For the computa-

tion of the derivative of the intensity with respect to the wavelength in Equation (10.15) we use the observed Stokes  $I$  itself. For differentiation we use an in-built subroutine (in the idl programming language) that performs a numerical differentiation using a 3-point Lagrangian interpolation. For a given location and a given field strength, we get several sets of  $(\theta_B, \chi_B)$  values (a minimum of 0 to a maximum of 120 sets) consistent with the observed  $V/I$  profiles.<sup>1</sup> The field strengths derived here always correspond to weak values of  $B$  (10 G–50 G), consistent with the fact that the observed  $V/I$  signals are in the range 0.1% to 0.9%. We have investigated the behavior of the  $V/I$  profiles in the full range of  $B \in [0\text{G}, 50\text{G}]$ ,  $\theta_B \in [0^\circ, 180^\circ]$ . For each observation point the  $V/I$  model fitting restricts the values of  $B$  and  $\theta_B$  to be respectively in the smaller sub-intervals of  $[0\text{G}, 50\text{G}]$  and  $[0^\circ, 180^\circ]$ . No such restriction is imposed on the  $\chi_B$  values.

### 10.5.2 Polarization diagrams from the Hanle effect

The values of  $(B, \theta_B, \chi_B)$  deduced from Stokes  $V$  should also fit the observed  $Q/I$  and  $U/I$  profiles. For field strengths below a few hundred G the transverse Zeeman effect does not produce any significant  $Q/I$  and  $U/I$ . The observed  $Q/I$  and  $U/I$  can however be generated by the Hanle effect and hence provide us with independent constraints. We compute the theoretical Stokes profiles  $(I, Q/I, U/I)$  considering only the Hanle effect (see Equation (10.1)) with  $(B, \theta_B, \chi_B)$  in the range restricted by the  $V/I$  model fitting. Since in the weak field approximation the transfer equation for Stokes  $V$  decouples from the transfer equation for  $(I, Q, U)^T$ , Hanle scattering does not produce any  $V/I$  signal unless there exists an initial source of the circular polarization.

We recall that the polarization diagrams are plots of  $Q/I$  versus  $U/I$  for given values of field strength  $B$ , wavelength  $\lambda$  and line of sight defined by  $\mu, \varphi$  (see e.g., Bommier 1977; Landi Degl’Innocenti 1982; Bommier et al. 1991; Faurobert-Scholl 1992; Stenflo 1994; Nagendra et al. 1998). The values of  $(\theta_B, \chi_B)$  are varied in finite steps. A closed curve (hereafter loop) is produced in the  $(Q/I, U/I)$  plane as  $\chi_B$  is varied from  $0^\circ$  to  $360^\circ$ . Each value of  $\theta_B$  corresponds to a different loop. The size and tilt of the polarization pattern in a loop with respect to the vertical ( $Q/I = 0$  line) depend on the value of  $B$  and  $\theta_B$ . Examples of polarization diagrams are shown in Figures 10.4 and 10.5 for  $B = 10\text{G}$ ,  $B = 15\text{G}$ ,  $B = 30\text{G}$  and  $B = 50\text{G}$ . They are constructed with the theoretical  $Q/I$  and  $U/I$  values at line center calculated with  $\mu = 0.9$  and  $\varphi = 0^\circ$ . Different loops correspond

<sup>1</sup>The values of  $\chi_B$  are actually defined in a local coordinate system attached to each observation point. Corrections for this effect are not taken into account. They are smaller than 10% as the slab is 184 arcsec for a solar diameter of 1920 arcsec.

to different values of  $\theta_B \in [100^\circ, 175^\circ]$ , incremented in steps of  $5^\circ$ . In each of the loops the small square symbol corresponds to the first grid point  $\chi_B = 0$ , and as we proceed in the anti-clockwise direction,  $\chi_B$  takes values between 0 and 360 in steps of 11.25 degrees. The observed  $Q/I$  and  $U/I$  at line center, averaged over three pixels in the wavelength domain (in order to reduce noise) are marked in the diagrams as big squares- $i$ , where  $i = 1, \dots, 8$  stand for the 8 locations on the slit. We recall that we refer to these 8 locations as observation point 1 to 8. We find that among the different solution sets  $(B, \theta_B, \chi_B)$  given by the weak field approximation of the Zeeman effect, there is only one choice which can simultaneously fit the observed line center values of  $Q/I$  and  $U/I$ . Our results strongly suggest that  $Q/I$  and  $U/I$  are signatures of the Hanle effect and  $V/I$  of the Zeeman effect. Whether resolved inhomogeneities in the atmosphere and velocity fields also contribute to the linear and circular polarizations is a question which goes much beyond the scope of this chapter.

In Figure 10.7 we show the  $Q/I$ ,  $U/I$  and  $V/I$  fits for the observation points 1 and 2. The best fit of the vector magnetic field for these points is  $(B, \theta_B, \chi_B) = (15 \text{ G}, 125^\circ, 56^\circ)$  and  $(B, \theta_B, \chi_B) = (15 \text{ G}, 110^\circ, 191^\circ)$ , respectively. Figures 10.8–10.10 are similar to Figure 10.7, but for the observation points 3 to 8.

### 10.5.3 $Q/I$ and $U/I$ profiles from the Hanle effect

It can be observed on the CCD image shown in Figure 10.3 and on the observed spectra shown in Figures 10.7 to 10.10 that the shapes and signs of the  $Q/I$  and  $U/I$  profiles in the line core region vary significantly from point to point along the slit. We think that these variations can be ascribed predominantly to changes in the magnetic field direction. In Figure 10.6 we show how sensitive indeed are the line cores of  $Q/I$  and  $U/I$  to the values of  $\theta_B$  and  $\chi_B$ . In spite of this great sensitivity, the same values of  $(B, \theta_B, \chi_B)$ , which give the best fits to the line center values of the observed  $Q/I$  and  $U/I$ , also give the best fits to the observed  $Q/I$  and  $U/I$  at other wavelengths around the line core. This is so because PRD effects can safely be neglected at these wavelengths. The PRD effects become important further in the line wings where the Hanle effect is not operative. The line core polarization is only controlled by the ‘line center anisotropy’ of the radiation field and by the value of the magnetic field vector.

Outside the core there is no Hanle effect. The wings of  $U/I$  are essentially zero and those of  $Q/I$  are controlled by Rayleigh scattering and PRD effects. In Figure 10.7, left panel, we compare the theoretical profiles of  $Q/I$  calculated with PRD (thick solid lines)

and CRD (thin solid lines) for the observation point 1. This figure clearly shows that the wing shapes and peak values can be nicely fitted with PRD but not with CRD. Also note that the line center values of  $Q/I$  and  $U/I$  computed with CRD are smaller than those computed with PRD (by about 0.5% in  $Q/I$ ). This shows that the magnetic field values extracted using the CRD approximation will lead to significant errors when compared to those extracted using PRD.

We note here that the irreducible components  $\mathcal{I}_Q^2$ ,  $Q \neq 0$ , only contribute to the line cores of  $Q/I$  and  $U/I$ , because they are created by the Hanle effect. The component  $\mathcal{I}_0^2$  on the other hand contributes to both the line core and the wings, but for  $Q/I$  alone.

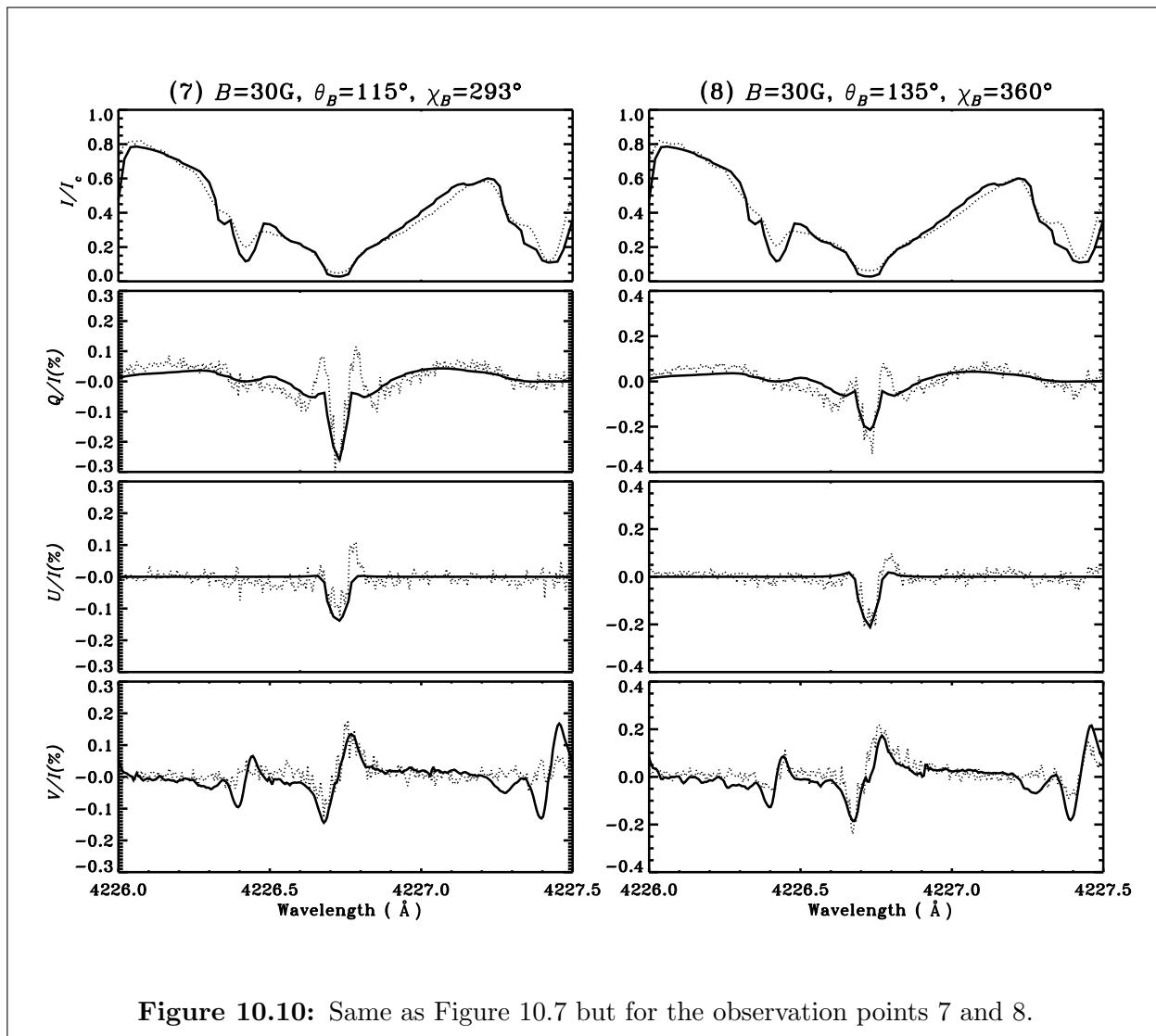


Figure 10.10: Same as Figure 10.7 but for the observation points 7 and 8.

#### 10.5.4 The effect of model atmospheres

In the left panels of Figure 10.10 we see positive peaks in the observed profiles of  $Q/I$  at 4226.65 Å and in both  $Q/I$  and  $U/I$  at 4226.8 Å (region of core minima). We have explored the possibility that these peaks could be due to the transverse Zeeman effect. Although these peaks can well be explained in terms of the  $\sigma$  components of the transverse Zeeman effect (but with fields much stronger than the range indicated by the observed Stokes  $V$ ), it is not possible to fit the core peaks in terms of the  $\pi$  component of the transverse Zeeman effect. Only the Hanle effect can generate core signatures of sufficient amplitude in the linear polarization. This fact can be seen in Figure 10.11(a), where we compare the theoretical Stokes profiles computed using the Zeeman effect (using the RH-code) and the Hanle effect with the observational point 7. The  $\mathbf{B}$  values used for the profiles computed using the Hanle effect are (30 G, 115°, 293°) and those computed using the Zeeman effect are (100 G, 90°, 203°). The curves showing the fit from the Hanle effect are the same as in the left panel of Figure 10.10.

Another explanation of the mentioned peaks could be in terms of a different temperature structure of the atmosphere. To verify this we have tested a cooler model atmosphere (FALX). While the FALX model can generate these peaks, it fails to reproduce the observed line center  $Q/I$  and  $U/I$  amplitudes. The FALC model on the other hand can reproduce the line center peaks but not the peaks near the region of core minima. These results are shown in Figure 10.11(b), where we compare the theoretical Stokes profiles computed with the FALC and FALX model atmospheres, which give the best fit to the observation point 7. The FALC fit is the same as the one in the left panel of Figure 10.10. The  $\mathbf{B}$  values derived from the FALC and FALX model atmospheres are respectively (30 G, 115°, 293°) and (30 G, 115°, 315°). We note that the two model atmospheres give two different azimuths  $\chi_B$ . However, the FALC model gives an overall better fit than the FALX model. For all other observation points we find that FALX cannot reproduce the line center peaks, and that the overall fit is better in terms of the FALC model. Therefore we have chosen the FALC model for all our calculations in this chapter.

We note that the positive red and blue peaks in the left panels of Figure 10.10 are asymmetric in nature. These differences between the red and the blue peaks in the observed  $Q/I$  and  $U/I$  profiles cannot be interpreted in terms of the Hanle effect, the transverse Zeeman effect, or by using a different temperature structure. This is because our theoretical profiles always produce symmetric red and blue peaks. In reality we observe such asymmetries often in Stokes spectra, and it is well known that they are due to spatially

unresolved, correlated gradients of the magnetic and velocity fields in the solar atmosphere (see Stenflo et al. 1984; Stenflo 2010) However we have not taken up such studies in this chapter.

In chapter 9 we had found that the FALX model atmosphere gives a better fit to the observed profiles when modeling the non-magnetic limb observations of the Ca I 4227 Å line, while our present disk-center work favors the FALC model. In Figure 10.12(a) we compare the  $I/I_c$ ,  $Q/I$  profiles computed using FALC and FALX model atmospheres for  $\mu = 0.1$  with the observations. We need three free parameters to model the non-magnetic observations. They are (i) an enhancement parameter  $c$ , associated with the elastic collision rate  $\Gamma_{E,vW}$  (of the van der Waal's type), (ii) a global scaling parameter  $s$ , and (iii) a micro-turbulent magnetic field  $B_{\text{turb}}$  (see chapter 9 for more details). One can notice that with a proper choice of free parameters FALX gives a better fit than the FALC model atmosphere to the non-magnetic limb observations of the  $Q/I$  profiles. This indicates that the actual temperature structure in the solar atmosphere might be better represented by a combination of model atmospheres (two-component models), but such studies are outside the scope of this chapter.

### 10.5.5 The role of collisions

The depolarizing effect of a magnetic fields is often mimicked by a similar effect due to collisions and, in many cases, it is difficult to disentangle the two effects. In this chapter we assume that the main contribution to the elastic collisions come from the van der Waal's type collisions ( $\Gamma_{E,vW}$ ). In chapter 9 we had found that in fitting the limb observations, particularly in reproducing asymmetric  $Q/I$  wing shapes, an enhancement of  $\Gamma_{E,vW}$  by a factor of  $c = 1.5$  became necessary. A similar enhancement was also applied by Faurobert-Scholl (1992), to fit the observed  $Q/I$  wing polarization. The justification for this can be found in Derouich et al. (2003) and Barklem & O'Mara (1997), who respectively show that the old theories for the depolarizing elastic collision rate  $D^{(2)}$  and line broadening elastic collision rate  $\Gamma_E$  actually underestimate  $\Gamma_{E,vW}$ .

However, in this chapter in fitting the near disk center observations we are able to reproduce the wing shapes of  $Q/I$  without any enhancement of  $\Gamma_{E,vW}$ . We examine the effect of such an enhancement of  $\Gamma_{E,vW}$  by taking  $c = 1.5$  in Figure 10.12(b). It is clear that the differences arising due to this effect are small and the effect is mainly in the wings of the  $Q/I$  profiles, which are insensitive to the magnetic fields. The line core is unaffected by this modification of  $\Gamma_{E,vW}$ , because the line core is formed higher in the atmosphere where

elastic collisions do not play any significant role. Thus our magnetic field determinations are unaffected by the inconsistencies in the theories for the elastic collision rates.

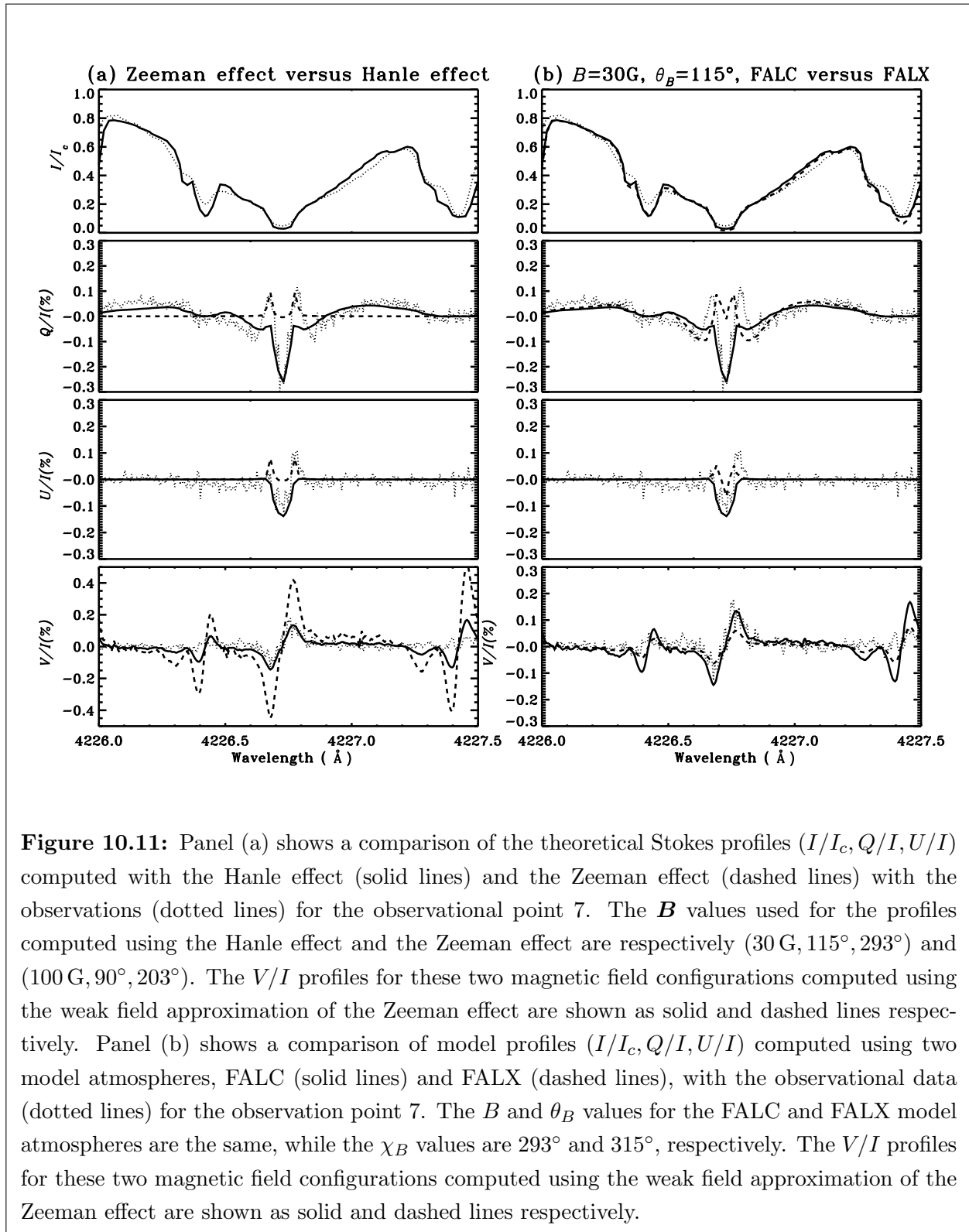
### 10.5.6 The role of a filling factor

When interpreting Zeeman-effect observations of photospheric magnetic fields it is generally necessary to introduce a filling factor as a free parameter, since photospheric fields are extremely intermittent, with most of the flux in the form of strong (kG) elements occupying typically only 1% of the quiet photosphere (Stenflo 1973). The introduction of a filling factor as an additional free model parameter opens up a family of new solutions, which is destructive of the uniqueness of the solution unless some appropriate additional observational constraint is brought in. In the case of the photospheric Zeeman effect, the crucial additional constraint has been the introduction of the Stokes  $V$  line ratio, using simultaneous observations in two spectral lines that are formed in the same way but differ in their Landé factors.

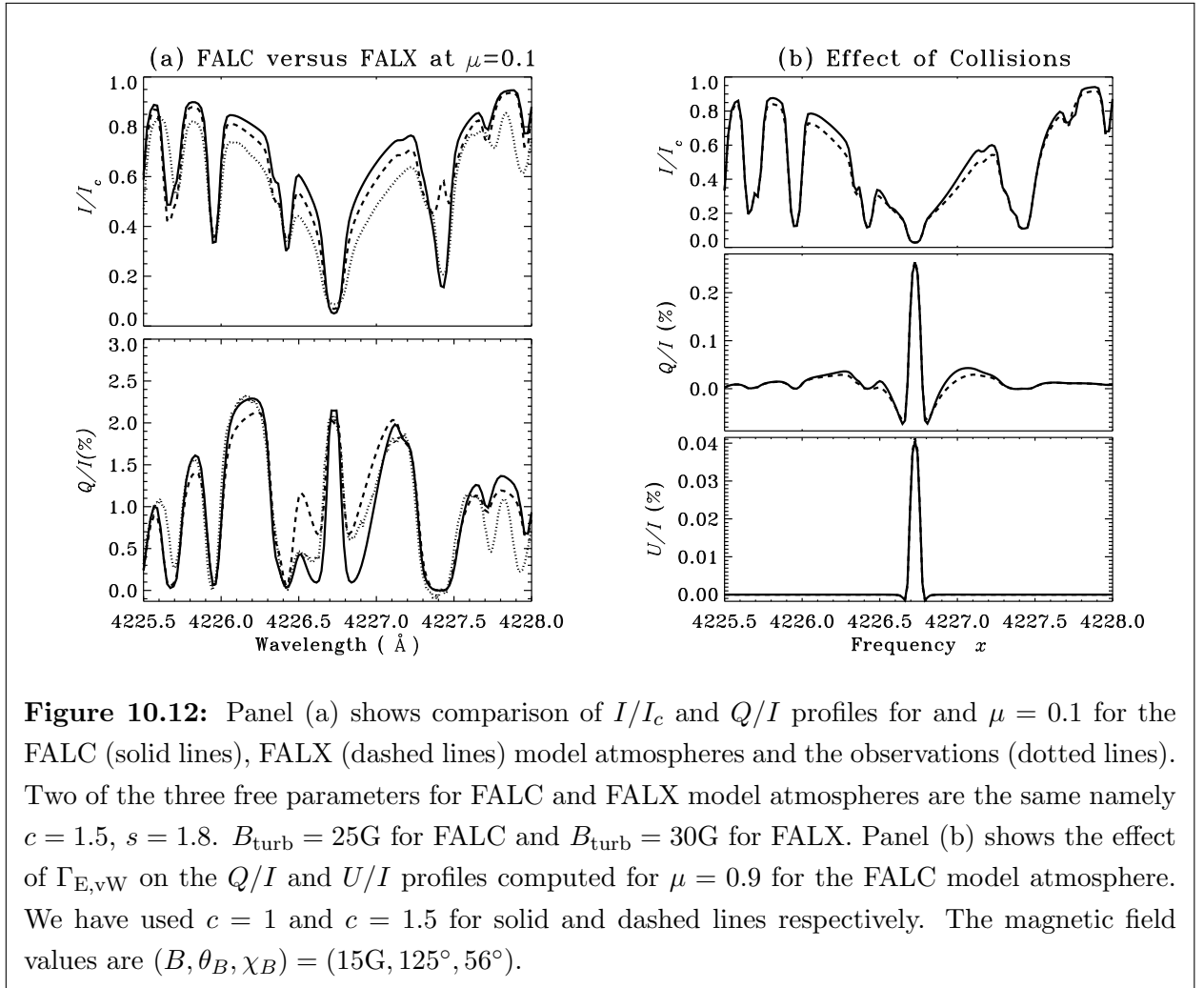
Adding a magnetic filling factor as an additional degree of freedom in our interpretations of the Hanle forward scattering observations might therefore seem to open up a Pandora's box of new possibilities, for which we, with our single-line observations, have no useful constraint. The actual situation is however not at all as unconstrained as it may seem at first, since there are good reasons to believe that the filling factor is close to unity in our case, and therefore does not play the role that it does in photospheric Zeeman-effect observations.

The argument for this is as follows: Many of our observed polarization amplitudes in the core of the 4227 Å line are so large, that theoretical modeling with the FALX atmosphere is unable to produce sufficient polarization, although the implicitly assumed filling factor is the maximum of 100%. Only with a hot atmosphere like FALC a fit becomes possible. With any other filling factor the theoretically predicted polarization amplitudes will be smaller, in proportion to the assumed filling factor. This simply brings the observed amplitudes out of reach for a fit. Only with a filling factor close to unity is a fit at all possible in many of the observed cases.

In the case of the photospheric Zeeman-effect observations the situation is very different. The observed polarization amplitudes are mostly very small (on the quiet Sun). Since there is proportionality between circular polarization and field strength over a very wide range, from zero to typically about 500 G, where saturation gradually begins to set in, a tiny filling factor can easily be compensated for by a large field strength to fit the observed







polarizations. With the line ratio (determining the differential Zeeman-effect non-linearity between the two lines) the value of the field strength can be fixed. In contrast to the Zeeman-effect case, however, the Hanle polarization effects do not scale in proportion to the field strength. A small filling factor can therefore not be compensated for by a large field strength or by any other field parameter, both because the field dependence is very non-linear, and saturation takes place already for rather weak fields.

The question may then arise why we here conclude that the filling factor must be close to unity, while with Zeeman-effect observations we are used to filling factors that are a couple of orders of magnitude smaller. There are two reasons for this:

The first reason is that our  $4227\text{\AA}$  observations refer to the chromosphere, and it is well known that the behavior of the Hanle effect in photospheric lines (like Sr I  $4607\text{\AA}$ )

and chromospheric lines (like Ca I 4227 Å) is entirely different Stenflo (2003b). While the photospheric lines do not show much of any spatial structure and rarely any trace of a Stokes  $U$  signal, the chromospheric lines are full of spatial structures along the slit in both  $Q$  and  $U$ . The absence of  $U$  signals in the photospheric lines can be understood in terms of tangled fields on scales much smaller than the spatial resolution element, causing cancellation of the positive and negative contributions to Stokes  $U$  over each resolution element. The circumstance that we see substantial polarization signals in Stokes  $U$  with no evidence for cancellation effects in the chromospheric lines is evidence for resolved fields (filling factor near unity).

The second reason is that the 4227 Å observations that we are trying to fit here do not represent entirely quiet regions on the Sun, but were recorded in the outskirts of active regions, where we found an abundance of clear forward-scattering polarization signatures. In contrast, much less polarization is found far from active regions. The filling-factor concept may be more applicable in such truly quiet regions, but there the signals are so small that they are hard to measure with any acceptable S/N ratio. Application of the forward-scattering Hanle effect to quiet regions are therefore presently out of reach for two reasons: insufficient S/N ratio of the observations, and insufficient observational constraints (with single-line observations) when the fields are not spatially resolved.

## 10.6 Concluding remarks

We have analyzed spectropolarimetric observations of the Ca I 4227 Å line obtained near the center of the solar disk ( $\mu = 0.93$ ). The use of ZIMPOL-3 allows us to reach the needed polarimetric precision. We analyze 8 positions along the slit, which represent different magnetic fields. These high quality observations are modeled in three steps.

In the first step we use the weak field approximation of the Zeeman effect as applied to the  $V/I$  profiles. We use Equation (10.15) to compute the  $V/I$  profiles with  $(B, \theta_B, \chi_B)$  as a free parameter. We extract the values of  $(B, \theta_B, \chi_B)$ , all of which represent the identical value of  $B \cos \gamma$  (the longitudinal component of  $\mathbf{B}$ ) that has been fixed by the observed  $V/I$ . For each observation data point we obtain a large set of  $(B, \theta_B, \chi_B)$  values, which give equally good fits. In the second step we solve the polarized Hanle RT equation (Equation (10.1)) for the Stokes parameters  $(I, Q, U)^T$ . The parametric space covered in this step is restricted to the values of  $(B, \theta_B, \chi_B)$  already extracted from the  $V/I$  model fitting. We construct polarization diagrams of  $Q/I$  versus  $U/I$  at line center and mark the ‘observed’ line center data points on these diagrams. With the polarization diagrams

we find that only one among the set of  $(B, \theta_B, \chi_B)$  values obtained from the  $V/I$  model fitting is able to reproduce the observed  $Q/I$  and  $U/I$  at line center. In the third step we analyze the shapes of the  $Q/I$  and  $U/I$  profiles in the line core region. It turns out that the  $\mathbf{B}$  values that give good fits to the observations at line center also reproduce the entire wavelength dependence of the observed  $Q/I$  and  $U/I$ .

The vector magnetic field constitutes 3 independent free parameters  $(B, \theta_B, \chi_B)$ . We have 3 constraints, namely the  $Q/I$ ,  $U/I$  profiles generated mainly by the Hanle effect, and the  $V/I$  profile generated by the longitudinal Zeeman effect. Through a combined modeling that uses the Zeeman effect (Step 1) and the Hanle effect (Steps 2, 3), we have been able to fit, with a single choice of  $\mathbf{B}$ , the three profiles ( $Q/I$ ,  $U/I$ ,  $V/I$ ) for the 8 observed locations that we have analyzed. In Table 10.2 we list these  $(B, \theta_B, \chi_B)$  values for the 8 observed profiles. The extracted field strengths are weak, namely  $B \in [10 \text{ G}, 50 \text{ G}]$ . The average  $\theta_B$  is  $136^\circ$ . The values of  $\chi_B$  are quite random. The Stokes  $I$  profile is not much affected by the range of field strengths that we are interested in (10–50 G).

In summary we have demonstrated that the forward scattering Hanle effect (for observations near disk center) combined with the longitudinal Zeeman effect can be used as a good diagnostic of weak vector magnetic fields in the solar chromosphere. Since the transverse Zeeman effect is too insensitive to such fields, they cannot be diagnosed by the Zeeman effect alone, only the Hanle-Zeeman combination can do the job.

## New Results

For the first time in the literature the forward scattering observations in a spectral line are analyzed and it is used as a diagnostic tool for estimating the chromospheric magnetic fields. The important results that are obtained in this chapter are as follows.

1. We present polarimetric  $(I, Q/I, U/I, V/I)$  observations of the Ca I 4227 Å line recorded around  $\mu = \cos \theta = 0.9$ . Here  $Q$  and  $U$  represent linear polarization and  $V$  the circular polarization. The high sensitivity of the polarimeter (ZIMPOL: Zurich IMaging POLarimeter) makes it possible to measure the weak polarimetric signals with great accuracy.

2. We model these high quality observations using the solution of polarized RT equation in the presence of a magnetic field. For this we use standard 1D model atmospheres.
3. We show that the linear polarization is mainly produced by the Hanle effect (rather than by the transverse Zeeman effect), while the circular polarization is due to the longitudinal Zeeman effect.
4. A unique determination of the full  $\mathbf{B}$  vector may be achieved when both effects are accounted for. The field strengths required for the simultaneous fitting of  $(Q/I, U/I, V/I)$  are in the range 10–50 G. The shapes and signs of the  $Q/I$  and  $U/I$  profiles are highly sensitive to the orientation of the magnetic field.

*Further studies related to the work presented in this chapter are published in:*

1. Bianda, M., Ramelli, R. Anusha, L. S., Stenflo, J. O., Nagendra, K. N., Holzreuter, R., Sampoorna, M., Frisch, H., & Smitha, H. N., 2011, **A&A**, 530, L13

## Chapter 11

# Conclusions and future outlook

The aim of this thesis is to explore the landscape of solar magnetic fields, through new formulations of theoretical methods and their applications to study the solar polarimetric observations. We are primarily interested in understanding scattering polarization in spectral lines that arises due to the geometry of the medium such as a multi-dimensional (multi-D) structure or sphericity of the medium. We consider scattering both in the absence and presence of weak magnetic fields. We also considered the effects of turbulent magnetic fields on the spectral line polarization. We have formulated several polarized radiative transfer (RT) problems and solved them using modern, efficient numerical methods that we have developed. In the following we give a brief summary of the work carried out in this thesis. Subsequently we give an outlook on the future plans to advance our knowledge in this field, based on the work already done in this thesis.

### 11.1 Summary of the thesis

In chapter 1 we have given a general introduction to the thesis. We have given basic definitions, concepts and illustrative examples which are necessary to understand the work presented in subsequent chapters. We have also discussed the motivation for taking up this research topic for the thesis. At the end of chapter 1 we also give an outline of the theoretical formulations, and new results presented in the thesis.

In chapter 2 we have studied the Hanle effect due to a random magnetic field with a finite correlation length, in order to assess limitations to the micro-turbulent approximation commonly used in the literature. The magnetic field is characterized by a correlation length and a magnetic field vector probability density function (PDF). We have constructed an RT equation for the mean radiation field, and show that a simple averaging of the solution

of this equation over the PDF yields the mean Stokes parameters. The transfer equation is solved numerically by a Polarized Approximate Lambda Iteration (PALI) method. We have found that micro-turbulent approximation is safe for optically thin lines and optically very thick lines formed in a scattering media. The lines with intermediate optical thicknesses show some sensitivity to the magnetic field correlation length (see Fig. 2.4). Studies carried out in the micro-turbulent limit with different types of magnetic field PDFs indicate that the polarization is quite sensitive to the shapes of the PDFs (Section 2.8).

In chapter 3 we propose a robust method called Stabilized Preconditioned Bi-Conjugate-Gradient (Pre-BiCG-STAB) to solve the classical problem of line transfer in spherical media. This method belongs to a class of iterative methods based on the projection techniques. We briefly present the method, and the computing algorithm. We have compared Pre-BiCG-STAB with another method (Pre-BiCG) which also belongs to the same class and is very efficient with respect to other contemporary methods. These two advanced methods are validated in terms of their efficiency and accuracy, by comparing with other iterative methods currently in use such as Jacobi, Gauss-Seidel and Successive Over Relaxation (see Figure 3.2). Although we have considered unpolarized RT and complete frequency redistribution (CRD) in line scattering in one-dimensional (1D) spherically symmetric media in this chapter, we find that the method developed is equally efficient when we extend it in later chapters to handle polarization and partial frequency redistribution (PRD) scattering in multi-D media.

In chapter 4 we have formulated the polarized transfer equation in three-dimensional (3D) media using the technique of irreducible spherical tensors  $\mathcal{T}_Q^K(i, \mathbf{\Omega})$ . The multipolar expansion for Stokes vectors and Stokes source vectors presented in this chapter allows us to write an RT equation in terms of  $I_Q^K$  and  $S_Q^K$ . We show that the advantage of formulating the RT equation in terms of  $\mathcal{T}_Q^K(i, \mathbf{\Omega})$  is that the irreducible source vector  $S_Q^K$  becomes completely independent of the angle variables, making it easier to extend the existing 1D PALI methods to the 3D case. However the irreducible components  $I_Q^K$  remain dependent on the inclination and also on the azimuthal angle of the ray. We present 3D solutions on some test cases, which may serve as benchmarks. The nature of line RT in 3D media, as compared to the 1D case is discussed in some detail. We show that the 3D PALI method gives correct results in the limit of a 1D medium (see Figure 4.3). The 3D anisotropy is characteristically different from the 1D anisotropy of the radiation field. The difference arises due to the finite optical depths in the horizontal directions ( $X, Y$ ). This causes large differences between the 3D and 1D values of the degree of linear polarization ( $Q/I, U/I$ ). In fact, in 3D media the radiation field is non-axisymmetric (even

in the absence of magnetic fields) because the finite optical depths in  $X, Y, Z$  directions break the azimuthal symmetry of the radiation field. In a 1D media, the radiation field is axisymmetric about the  $Z$ -axis. Due to these reasons, the shapes and magnitude of the  $(Q/I, U/I)$  spectra differ significantly from the corresponding 1D cases (see Figure 4.6).

In chapter 5 we develop an efficient method to solve polarized RT equation with PRD in a two-dimensional (2D) slab. We assume a two-level atom model with unpolarized lower level. We assume that the medium is finite in two directions ( $Y$  and  $Z$ ) and infinite in the third direction ( $X$ ). First we apply the Stokes vector decomposition technique developed in chapter 4 to the case of 2D media. We show that due to symmetry of the Stokes  $I$  parameter with respect to the  $\varphi = \pi/2$  axis, the Stokes  $Q$  becomes symmetric and the Stokes  $U$  becomes anti-symmetric about this axis ( $\varphi$  is measured from the infinite  $X$  direction anti-clockwise). Using this property we can represent the polarized radiation field by 4 irreducible components  $I_0^0, I_0^2, I_1^{2,y}$  and  $I_2^{2,x}$ . The Stokes source vectors are also decomposed into 4 irreducible components which are independent of the ray direction. Due to axi-symmetry  $I_1^{2,y}$  and  $I_2^{2,x}$  are zero in 1D media. This decomposition technique is interesting for the development of iterative methods. Here we describe the Pre-BiCG-STAB method developed earlier in chapter 3 and show that it is much faster and efficient than the Jacobi iteration method used in chapter 4. Further, in this chapter we generalize to PRD, the 2D short characteristics formal solver developed in Paletou et al. (1999) for CRD. This formal solver is much more efficient than the one used in chapter 4. With these two new features, it is possible to compute the solutions for a wide range of model parameters. With the method of chapter 4 only media with small optical depths can be considered. For example, in Figure 5.9 we consider the case of semi-infinite atmospheres with  $T_Z = T_Y = T = 2 \times 10^9$ . We compare the surface averaged emergent Stokes profiles in 2D media, and the corresponding 1D solutions for CRD and PRD. We show that the deviation of polarized radiation field in 2D media from the one in 1D media exists both for CRD and PRD, but is more stronger in the line wings of the PRD solutions.

Chapter 6 is dedicated to certain extensions of our previous works (chapters 4 and 5) on polarized RT in multi-D media with PRD. First, we present a generalization of the Stokes vector decomposition technique developed in chapter 4 to include the magnetic fields (Hanle effect). Secondly, we generalize to the magnetic 3D RT, the efficient Pre-BiCG-STAB method developed in chapter 5 for the non-magnetic 2D RT. Thirdly, we use the more efficient 2D and 3D short characteristics formal solvers, with appropriate generalizations to the present context. We give several benchmark solutions computed using the code, with all the above mentioned generalizations. The main results of these

solutions are the following (see Figure 6.13). In the non-magnetic case, at line center, the spatial distribution of  $Q/I$  and  $U/I$  is homogeneous in the interior of the top surface, but sharply raise near the edges. This is purely a multi-D geometric effect. The presence of a magnetic field modifies this spatial distribution by causing a depolarization (decrease in the magnitude), or re-polarization (increase in the magnitude) of  $Q/I$  and  $U/I$ . This is a natural consequence of the Hanle effect. In the line wing frequencies, magnetic and non-magnetic spatial distributions look the same, as Hanle effect is confined to the line core. However in the line wing frequency, the spatial distribution is more inhomogeneous, and the sharp raise of  $Q/I$  and  $U/I$  near the edges is more enhanced, as compared to those at the line center. This behavior at line wings is mainly due to the PRD effects. These characteristics are not noticeable if the CRD assumption is used in line formation studies.

In chapter 7 we formulate polarized RT equation in multi-D media that includes angle-dependent PRD and Hanle effect. We propose a method of decomposition of the Stokes source vector and Stokes vector in terms of irreducible Fourier components  $\tilde{\mathcal{S}}^{(k)}$  and  $\tilde{\mathcal{I}}^{(k)}$  using a combination of the decomposition of the scattering phase matrices in terms of irreducible spherical tensors  $\mathcal{T}_Q^K(i, \boldsymbol{\Omega})$  and the Fourier series expansions of angle-dependent PRD functions. We also establish that the irreducible Fourier components  $\tilde{\mathcal{S}}^{(k)}$  and  $\tilde{\mathcal{I}}^{(k)}$  satisfy a simple transfer equation, which can be solved by any iterative method such as a PALI or a Biconjugate-Gradient type projection method.

In chapter 8 we have further generalized (see Section 8.2.2) the Fourier decomposition technique developed in chapter 7. to handle AD PRD in multi-D polarized RT. We have applied this technique and developed the efficient Pre-BiCG-STAB method to solve this problem (see Section 8.3). We prove in this chapter that the symmetry of the polarized radiation field with respect to the infinite axis, which existed for a non-magnetic 2D medium in the case of AA PRD (as shown in chapter 5) breaks down in the case of AD PRD (see Appendix L). We present results of the very first investigations of the effects of angle-dependent PRD on the polarized line formation in multi-D media. We restrict our attention to freestanding 2D slabs with finite optical thicknesses on the two axes ( $Y$  and  $Z$ ). We consider effects of AD PRD on the scattering polarization in both non-magnetic and magnetic cases. We find that the relative AD PRD effects are prominent in the magnetic case (Hanle effect). They are also present in non-magnetic case for few choices of  $(\theta, \varphi)$ . We conclude that the AD PRD effects are important for interpreting the observations of scattering polarization in multi-D structures.

In chapter 9 we develop a mathematical framework for the last scattering approxima-



tion (LSA) approach, starting from the polarized RT equation. We derive simple formulae for  $Q/I$  by applying a few approximations to the governing equations of the RT approach. We have three levels of approximations named as LSA-1, LSA-2 and LSA-3. We validate the LSA approaches, by comparing with the exact RT approach (see Figure 9.5). However among the three LSA-3 is most useful as it is nearest to the exact RT solutions in reproducing the features of  $Q/I$  profiles in greater detail. LSA-3 is 8 times faster than the RT approach. To illustrate the usefulness of LSA-3 approach in modeling the second solar spectrum, we compare both the LSA-3 and the RT solutions with the recently observed  $Q/I$  spectra of Ca I 4227 Å line (see Figure 9.6). These recent observations are made in the quiet regions on the Sun. In this chapter we have shown that LSA-3 can provide a fit to the observed  $Q/I$  spectra, which is nearly as good as the exact RT approach itself. As mentioned above, LSA-3 solution can be obtained at a much less computational cost. Thus, LSA-3 may be applied

- (i) to interpret the second solar spectrum and the Hanle effect in lines with PRD,
- (ii) to test different theoretical formulations of the elastic collisions,
- (iii) to explore the formation of the second solar spectrum in media where 3D radiative transfer effects have to be taken into account,
- (iv) to estimate the strength of micro-turbulent magnetic fields in the solar chromosphere.

In chapter 10 we have analyzed spectropolarimetric observations of the Ca I 4227 Å line obtained near the center of the solar disk ( $\mu = 0.93$ ). The use of ZIMPOL allows us to reach the needed polarimetric precision. We analyze 8 positions along the slit, which represent different magnetic fields. These high quality observations are modeled using combinations of Hanle and Zeeman effect which act as complementary effects in the weak field regime. The vector magnetic field constitutes 3 independent free parameters ( $B, \theta_B, \chi_B$ ). We have 3 constraints, namely the  $Q/I, U/I$  profiles generated mainly by the Hanle effect, and the  $V/I$  profile generated by the longitudinal Zeeman effect. Through a combined modeling that uses the Zeeman effect and the Hanle effect we have been able to fit, with a single choice of  $\mathbf{B}$ , the three profiles ( $Q/I, U/I, V/I$ ) for the 8 observed locations that we have analyzed. In Table 10.2 we list these ( $B, \theta_B, \chi_B$ ) values for the 8 observed profiles. The extracted field strengths are weak, namely  $B \in [10 \text{ G}, 50 \text{ G}]$ . The average  $\theta_B$  is  $136^\circ$ . The values of  $\chi_B$  are quite random. The Stokes  $I$  profile is not much affected by the range of field strengths that we are interested in (10–50 G). In summary we have demonstrated that the forward scattering Hanle effect (for observations near disk center) combined with the longitudinal Zeeman effect can be used as a good diagnostic of weak vector magnetic fields in the solar chromosphere. Since the transverse Zeeman effect is too insensitive to

such fields, they cannot be diagnosed by the Zeeman effect alone, only the Hanle-Zeeman combination can do the job.

## 11.2 Future Outlook

As discussed in chapter 1 the current development in the field of realistic modeling of the second solar spectrum is restricted to the case of 1D RT and 1D solar model atmospheres using PRD in line scattering or to multi-D RT with 2D or 3D model atmospheres under the approximation of CRD in line scattering. With these two kinds of approaches, one has to restrict the attention to the observing regions which can well be represented by planar 1D media, or one has to restrict to the photospheric lines where PRD effects are negligible.

This situation in the field arose because, in the earlier decades (1) the resolution power of the telescopes and sensitivity of the polarimeters were insufficient to resolve the spatial structuring which manifest through the signals in the linear polarization profiles, (2) the complication of multi-D RT is such that the construction of realistic 3D atmospheric models and solution of polarized 3D RT equations were not computationally feasible.

The current studies of the linear polarization of the chromospheric lines suggest that, in many cases 1D model atmospheres fail to represent the solar atmosphere – which in reality is highly inhomogeneous and dynamic in nature. In the past three decades, there has been a revolution in technology which drastically improved the resolution power of the telescopes, precision and sensitivity of the spectro-polarimeters, and capability of the computers. Due to technological advancements it is now possible to record the faint linear polarization signals in the second solar spectrum in greater detail (both spectrally and spatially). Although it is impossible to perfectly simulate the solar atmospheric features in detail, using clever approximations it is still possible to have a 3D view of the solar atmosphere including the spatial inhomogeneities. To test these numerical simulations of the 3D solar model atmospheres, it is necessary to use them and solve the concerned polarized RT equation with PRD scattering, and then compare the results with the spatially resolved observations of the linear polarization in spectral lines. This major project is our next goal. We plan to take up such a project in three steps: (1) extend our numerical codes to handle realistic 3D model atmospheres; (2) perform polarimetric observations of the chromospheric line such as Ca II K which shows high degree of spatial variation, and construct a spatial map of the linear polarization; and (3) finally compute the linear polarization profiles using the numerical codes developed in step (1) and compare the results with the observations carried out in step (3). Such a study would answer to some

---

extent, whether these realistic 3D atmospheric models really realistic? How best we can mimic the solar atmospheric features and try to understand our nearest and dearest star, the Sun!!



## Appendix A

# Integral equations for the components of the source vector

In Equations (2.17) to (2.19) of chapter 2, we give the integral equation for the source vector  $\mathcal{S}(\tau|\mathbf{B})$ . The corresponding system of integral equations for its  $KQ$  components  $\mathcal{S}_Q^K(\tau|\mathbf{B})$  may be written as

$$\begin{aligned} \mathcal{S}_Q^K(\tau|\mathbf{B}) = & \mathcal{G}_Q^K(\tau) + \sum_{K'Q'} \mathcal{M}_{QQ'}^K(\mathbf{B}) \int_0^T \left\{ L_{Q'}^{KK'}(\tau - \tau'; \nu) \mathcal{S}_{Q'}^{K'}(\tau'|\mathbf{B}) \right. \\ & \left. + [L_{Q'}^{KK'}(\tau - \tau'; 0) - L_{Q'}^{KK'}(\tau - \tau'; \nu)] \int P(\mathbf{B}') \mathcal{S}_{Q'}^{K'}(\tau'|\mathbf{B}') d^3 \mathbf{B}' \right\} d\tau', \end{aligned} \quad (\text{A.1})$$

with

$$L_{Q'}^{KK'}(\tau; \nu) = \int_{-\infty}^{+\infty} \int_0^1 \frac{1}{2\mu} \Psi_{Q'}^{KK'}(\mu) e^{-\frac{|\tau|}{\mu}(\phi(x)+\nu)} \phi^2(x) d\mu dx. \quad (\text{A.2})$$

The  $\Psi_{Q'}^{KK'}(\mu)$  are real, even functions of  $\mu$  and satisfy  $\Psi_{Q'}^{KK'}(\mu) = \Psi_{-Q'}^{KK'}(\mu)$  (LL04, Appendix A20). For a non polarized primary source term,

$$\mathcal{G}_Q^K(\tau) = \delta_{K0} \delta_{Q0} G(\tau), \quad (\text{A.3})$$

with  $G(\tau)$  proportional to the Planck function. For a two-level atom with unpolarized ground level, the elements  $\mathcal{M}_{QQ'}^K(\mathbf{B})$  of the matrix  $\hat{M}(\mathbf{B})$  can be written as

$$\mathcal{M}_{QQ'}^K(B, \theta_B, \chi_B) = e^{i(Q'-Q)\chi_B} M_{QQ'}^K(B, \theta_B), \quad (\text{A.4})$$

with

$$M_{QQ'}^K(B, \theta_B) = \sum_{Q''} d_{QQ''}^K(\theta_B) d_{Q''Q'}^K(-\theta_B) X_{KQ''}(B). \quad (\text{A.5})$$

We recall that  $d_{QQ''}^K(\theta_B)$  are the reduced rotation matrices, with  $\theta_B$  and  $\chi_B$  the polar angles (inclination and azimuth) of the magnetic field direction in an atmospheric reference frame with the  $Z$ -axis along the normal to the surface (see Figure 2.1 in chapter 2). Explicit expressions for  $X_{KQ''}(B)$  can be found in LL04 (Chaps. 5, 10, 14; see also HF07). They can be written as

$$X_{KQ''}(B) = \frac{W_K(J_l, J_u)}{1 + \epsilon' + \delta_u^{(K)}} \left[ \frac{1}{1 + Q''\Gamma'_B} \right]. \quad (\text{A.6})$$

Here  $\Gamma'_B = \Gamma_B/(1 + \epsilon' + \delta_u^{(K)})$  with  $\epsilon' = C_{u,l}/A_{u,l}$  and  $\delta_u^{(K)} = D^{(K)}/A_{u,l}$  (Bommier 1997b; LL04 p. 520 and 532). We recall that  $C_{u,l}$  and  $A_{u,l}$  are the inelastic collisional and radiative de-excitation rates. The parameter  $D^{(K)}$ , with  $D^{(0)} = 0$ , is the effective number of depolarizing collisions, for the statistical tensor of rank  $K$ , taking place during the lifetime of the excited level. The magnetic field strength  $B$  enters through the efficiency factor  $\Gamma_B = 2\pi\nu_L g_u/A_{u,l} = (e_0/2mc)(g_u/A_{u,l})B$  where  $\nu_L$  is the Larmor frequency,  $e_0$  and  $m$  the charge and mass of the electron,  $c$  the speed of light and  $g_u$  the Landé factor of the upper level. Finally,  $W_K(J_l, J_u)$  are atomic depolarization parameters that can be found in LL04 (Table 10.1, p. 515). For a normal Zeeman triplet ( $J_l = 0, J_u = 1$ ),  $W_K = 1$  for all values of  $K$ . Explicit expressions of the  $\mathcal{M}_{QQ'}^K$  can be found in HF07 (see also Faurobert-Scholl 1991; Nagendra et al. 1998).

Equation (A.4) shows that the  $\chi_B$  dependence of the  $\mathcal{S}_Q^K$  appears as a phase factor. This suggests to introduce new functions  $S_Q^K(\tau|B, \theta_B)$  defined by the relation

$$\mathcal{S}_Q^K(\tau|B, \theta_B, \chi_B) = e^{-iQ\chi_B} S_Q^K(\tau|B, \theta_B). \quad (\text{A.7})$$

The integral equations for these new functions are

$$\begin{aligned} S_Q^K(\tau|B, \theta_B) &= \delta_{K0}\delta_{Q0} G(\tau) + \sum_{K'Q'} M_{QQ'}^K(B, \theta_B) \int_0^T \left\{ L_{Q'}^{KK'}(\tau - \tau'; \nu) S_{Q'}^{K'}(\tau'|B, \theta_B) \right. \\ &+ \left[ L_{Q'}^{KK'}(\tau - \tau'; 0) - L_{Q'}^{KK'}(\tau - \tau'; \nu) \right] \oint e^{-iQ'(\chi'_B - \chi_B)} P(B', \theta'_B, \varphi'_B) S_{Q'}^{K'}(\tau'|B', \theta'_B) \\ &\quad \left. \times B'^2 \sin \theta'_B d\theta'_B dB' \frac{d\chi'_B}{4\pi} \right\} d\tau'. \end{aligned} \quad (\text{A.8})$$

This equation becomes simpler if the magnetic field PDF is cylindrically symmetrical with respect to the  $Z$ -axis, i.e., of the form

$$P(\mathbf{B})d^3\mathbf{B} = h(B, \theta_B)B^2 \sin \theta_B d\theta_B dB \frac{d\chi_B}{4\pi}. \quad (\text{A.9})$$

We can integrate over  $\chi'_B$  the last term in Equation (A.8). It will be zero, unless  $Q' = 0$ . Equation (A.8) reduces thus to

$$\begin{aligned}
 S_Q^K(\tau|B, \theta_B) = & \delta_{K0}\delta_{Q0} G(\tau) + \sum_{K'Q'} M_{QQ'}^K(B, \theta_B) \int_0^T \left\{ L_{Q'}^{KK'}(\tau - \tau'; \nu) S_{Q'}^{K'}(\tau'|B, \theta_B) \right. \\
 & + \delta_{Q'0} \left[ [L_{Q'}^{KK'}(\tau - \tau'; 0) - L_{Q'}^{KK'}(\tau - \tau'; \nu)] \int_{B'} \frac{1}{2} \int_0^\pi h(B', \theta'_B) S_{Q'}^{K'}(\tau'|B', \theta'_B) \right. \\
 & \left. \left. \times B'^2 \sin \theta'_B d\theta'_B dB' \right] \right\} d\tau'. \tag{A.10}
 \end{aligned}$$

We remark here that the term involving the mean value of  $S_{Q'}^{K'}$  is zero when  $Q' \neq 0$ .

Once the  $S_Q^K(\tau|B, \theta_B)$  have been calculated, they have to be multiplied by  $e^{-iQ\chi_B}$  (see Equation (A.7)) and then averaged over the magnetic field PDF. Since  $P(\mathbf{B})$  has been assumed to have a cylindrical symmetry, the averaging process will give zero, except for the components with  $Q = 0$ . So the mean source vector  $\langle \mathcal{S} \rangle(\tau)$  and mean Stokes vector  $\langle \mathcal{I} \rangle(\tau, x, \mu)$  have only two non-zero components corresponding to  $K = 0, 2$  and  $Q = 0$ . The magnetic field PDF does not break the cylindrical symmetry of the atmosphere. We stress that there is no way to avoid the calculations of the  $S_Q^K(\tau|B, \theta_B)$  components with  $Q \neq 0$ . The reason is that the integral equation for the conditional mean source vector holds for both the micro and macro-turbulent limits.

## Appendix B

### Exact expressions of the mean coefficient $\langle \mathcal{M}_{00}^2 \rangle$

The coefficient  $\mathcal{M}_{00}^2$  is defined in the Appendix A. Exact expressions for the mean values  $\langle \mathcal{M}_{00}^2 \rangle$  can be obtained with the PDFs given in Table 2.1, when the magnetic field strength has a Dirac or Gaussian distribution. Because of the cylindrical symmetry of the PDFs,  $\langle \mathcal{M}_{00}^2 \rangle = \langle M_{00}^2 \rangle$ . The expressions given below correspond to  $W_K = 1$  and  $\delta_u^{(K)} = 0$ .

When the field strength has a Dirac distribution, the coefficients  $\langle \mathcal{M}_{00}^2 \rangle$  are of the form

$$\langle \mathcal{M}_{00}^2 \rangle_D = \frac{1}{1 + \epsilon'} \left[ 1 - C_1 \left( \frac{\Gamma_B'^2}{1 + \Gamma_B'^2} \right) - C_2 \left( \frac{4\Gamma_B'^2}{1 + 4\Gamma_B'^2} \right) \right]. \quad (\text{B.1})$$

The coefficients  $C_1$  and  $C_2$  depend only on the angular distribution. The coefficient  $\Gamma_B'$  is defined in the Appendix A. The index B stands for  $B_0$ .

When the field strength has a Gaussian distribution,

$$\langle \mathcal{M}_{00}^2 \rangle_G = \frac{1}{1 + \epsilon'} [1 - C_1 K_1 - C_2 K_2]. \quad (\text{B.2})$$

The coefficients  $K_m$ ,  $m = 1, 2$ , may be written as

$$K_m = 1 - \left[ \frac{\sqrt{\pi}}{m\gamma_\sigma} \exp\left(\frac{1}{(m\gamma_\sigma)^2}\right) \operatorname{erfc}\left(\frac{1}{m\gamma_\sigma}\right) \right], \quad (\text{B.3})$$

with

$$\gamma_\sigma = \sqrt{\pi} \Gamma_B'. \quad (\text{B.4})$$

One can check that the coefficients  $K_1$  and  $K_2$  go to zero when the magnetic field goes to zero.

We give in Table B.1 the coefficients  $C_1$  and  $C_2$  for the isotropic, cosine and sine power laws defined in Table 2.1, column 2, of chapter 2. Some of these results can be found in Stenflo (1982; 1994, Equation (10.54)).



**Table B.1:** Coefficients  $C_1$  and  $C_2$  for the calculation of  $\langle \mathcal{M}_{00}^2 \rangle$ 

	isotropic	cosine power law	sine power law
$C_1$	$\frac{2}{5}$	$\frac{6(p+1)}{(p+3)(p+5)}$	$\frac{3(p+2)}{(p+3)(p+5)}$
$C_2$	$\frac{2}{5}$	$\frac{6}{(p+3)(p+5)}$	$\frac{3(p+2)(p+4)}{4(p+3)(p+5)}$

For  $p = 0$ ,  $C_1$  and  $C_2$  go to  $2/5$  and we recover the isotropic angular distribution. For the cosine power law, when  $p$  goes to infinity,  $C_1$  and  $C_2$  go to zero and we recover the Rayleigh scattering. For the sine power law, when  $p$  goes to infinity,  $C_1$  goes to zero and  $C_2$  to 0.75.

## Appendix C

# Construction of $\hat{A}$ matrix and Preconditioner matrix $\hat{M}$

In Pre-BiCG method, it is essential to compute and store the  $\hat{A}^T$  matrix. A brute force - fully numerical way of doing this is as follows. Suppose that the dimension of  $\hat{A}$  matrix is  $n_d \times n_d$ , where  $n_d$  is the number of depth points. By sending a  $\delta$ -source function  $n_d$  times, to a formal solver subroutine,  $n_d$  columns of  $\hat{A}$  matrix can be calculated. But this takes a large amount of CPU time especially for large values of  $n_d$ .

Instead, there is a semi-analytic way of calculating the  $\hat{A}$  matrix. By substituting the  $\delta$ -source function in the expression for the intensity on a short characteristics stencil of 3-points (MOP in standard notation) we can obtain “recursive relations for intensity matrix elements  $\mathbf{I}_{ij}(i, j, = 1, 2, \dots n_d)$ , which can then be integrated over frequencies and angles to get the  $\Lambda$  matrix. Finally,  $\hat{A} = [\hat{I} - (1 - \epsilon)\Lambda]$ . The diagonal of  $\Lambda$  is  $\Lambda^*$  and the diagonal of  $\hat{A}$  is the preconditioner matrix  $\hat{M}$ .

For plane parallel full-slab problem, this is given in Kunasz & Auer (1988). In radiative transfer problems with spherical symmetry, it is sufficient to compute the solution on a quadrant. However this causes a tricky situation, in which we have to define a mid-line (see Figure 3.1) on which a non-zero boundary condition  $\mathbf{I}^+ = \mathbf{I}^-$  has to be specified. For the outgoing rays, the mid-vertical line is the starting grid point for a given ray. Since the intensity at the starting point is non-zero ( $\mathbf{I}^+ = \mathbf{I}^-$ ), intensity at any interior point depends on the intensity at all the previous points. Recall that

$$\mathbf{I}_k(\mu > 0) = \mathbf{I}_{k+1}(\mu > 0) \exp(-\Delta\tau_k(\mu > 0)) + \psi_{k-1}\mathbf{S}_{k-1} + \psi_k\mathbf{S}_k + \psi_{k+1}\mathbf{S}_{k+1} \quad (\text{C.1})$$

and

$$\mathbf{I}_{k+1}(\mu > 0) = \mathbf{I}_{k+2}(\mu > 0) \exp(-\Delta\tau_{k+1}(\mu > 0)) + \psi_k \mathbf{S}_k + \psi_{k+1} \mathbf{S}_{k+1} + \psi_{k+2} \mathbf{S}_{k+2} \quad (\text{C.2})$$

and so on until we reach the mid-line. It is easy to see from above equations that intensity calculation at a short characteristics stencil MOP is not confined only to the intensity on MOP, but also on all previous points, through spatial coupling. This is specific to performing radiative transfer on a spherical quadrant. Note that even for the construction of a diagonal  $\Lambda$ , all the elements  $\mathbf{I}_{ij}$  of the intensity matrix has to be computed. We present below the recursive relations to compute  $\mathbf{I}_{ij}(i, j = 1, 2, \dots, n_d)$ .

### For the incoming rays ( $\mu < 0$ ) - Reverse sweep

DO  $i = 1, 2, \dots, n_d$

Consider an arbitrary spatial point  $i$ . The delta-source vector is specified as

$$\mathbf{S}(\tau_i) = 1, \quad \mathbf{S}(\tau_j) = 0 \quad \text{for } i \neq j. \quad (\text{C.3})$$

DO  $ip = 1, 2, \dots, n_p$ , where  $n_p$  is the total number of impact parameters.

For the inner boundary points, define  $n_{vp} = n_d$  for the core rays and  $n_{vp} = n_d - (ip - n_c - 1)$  for lobe rays. The index  $n_{vp}$  represents the total number of points on a given ray of constant impact parameter  $p$ . The external boundary condition has to be taken as zero for constructing integral operators like  $\Lambda$ .

$$\mathbf{I}_{i1}(\tau_i, \tau_1, x, p) = 0. \quad (\text{C.4})$$

For those rays (with index  $ip$ ) for which  $p(ip) \leq r(i)$

DO  $j = 2, 3, \dots, n_{vp}$

IF

( $j = i + 1$ ) and ( $j = n_d$  or  $p(ip) = r(j)$ ), which are interior boundary points

$$\mathbf{I}_{i,j}(\tau_i, \tau_j, x, p) = \mathbf{I}_{i,j-1}(\tau_i, \tau_{j-1}, x, p) \exp(-\Delta\tau_j(\mu)) + \psi_u(j, x, p, \mu < 0) + \psi_d(j, x, p, \mu < 0) \quad (\text{C.5})$$

This is because at these interior boundary points we assume  $\mathbf{S}_d = \mathbf{S}_u$  and  $\mathbf{S}_d = \mathbf{S}_u = 1$  when  $j = i + 1$ .

ELSE

(Non interior boundary points)

If  $j = i + 1$

$$\mathbf{I}_{i,j}(\tau_i, \tau_j, x, p) = \mathbf{I}_{i,j-1}(\tau_i, \tau_{j-1}, x, p) \exp(-(\Delta\tau_j(\mu)) + \psi_d(j, x, p, \mu < 0)) \quad (\text{C.6})$$

Elseif  $j = i$

$$\mathbf{I}_{i,j}(\tau_i, \tau_j, x, p) = \mathbf{I}_{i,j-1}(\tau_i, \tau_{j-1}, x, p) \exp(-\Delta\tau_j(\mu)) + \psi_0(j, x, p, \mu < 0) \quad (\text{C.7})$$

Elseif  $j = i - 1$

$$\mathbf{I}_{i,j}(\tau_i, \tau_j, x, p) = \mathbf{I}_{i,j-1}(\tau_i, \tau_{j-1}, x, p) \exp(-\Delta\tau_j(\mu)) + \psi_u(j, x, p, \mu < 0) \quad (\text{C.8})$$

Else

if ( $j \leq i - 2$ )

$$\mathbf{I}_{i,j}(\tau_i, \tau_j, x, p) = 0 \quad (\text{C.9})$$

else

$$\mathbf{I}_{i,j}(\tau_i, \tau_j, x, p) = \mathbf{I}_{i,j-1}(\tau_i, \tau_{j-1}, x, p) \exp(-\Delta\tau_j(\mu)) \quad (\text{C.10})$$

end if

End if

END IF

END DO

For those rays for which  $p(ip) > r(i)$

DO  $j = 2, 3, \dots, n_{vp}$

$$\mathbf{I}_{i,j}(\tau_i, \tau_j, x, p) = 0 \quad (\text{C.11})$$

END DO

END DO

END DO

**For the outgoing rays ( $\mu > 0$ ) - Forward sweep**

Let  $i = n_d, n_d - 1, \dots, 1$

$$\mathbf{S}(\tau_i) = 1, \quad \mathbf{S}(\tau_j) = 0 \quad \text{for } i \neq j \quad (\text{C.12})$$

DO  $ip = 1, 2, \dots, n_p$

For  $j = n_{v_p}$  (Inner boundary point)

$$\mathbf{I}_{i,j}(\tau_i, \tau_j, x, p) \quad (\mu > 0) = \mathbf{I}_{i,j}(\tau_i, \tau_j, x, p) \quad (\mu < 0) \quad (\text{C.13})$$

For non boundary points

For those rays (with index  $ip$ ) for which  $p(ip) \leq r(i)$

DO  $j = n_{v_p} - 1, n_{v_p} - 2, \dots, 1$

If  $j = i + 1$

$$\mathbf{I}_{i,j}(\tau_i, \tau_j, x, p) = \mathbf{I}_{i,j+1}(\tau_i, \tau_{j+1}, x, p) \exp(-\Delta\tau_j(\mu)) + \psi_d(j, x, p, \mu > 0) \quad (\text{C.14})$$

Elseif  $j = i$

$$\mathbf{I}_{i,j}(\tau_i, \tau_j, x, p) = \mathbf{I}_{i,j+1}(\tau_i, \tau_{j+1}, x, p) \exp(-\Delta\tau_j(\mu)) + \psi_0(j, x, p, \mu > 0) \quad (\text{C.15})$$

Elseif  $j = i - 1$

$$\mathbf{I}_{i,j}(\tau_i, \tau_j, x, p) = \mathbf{I}_{i,j+1}(\tau_i, \tau_{j+1}, x, p) \exp(-\Delta\tau_j(\mu)) + \psi_u(j, x, p, \mu > 0) \quad (\text{C.16})$$

Else

$$\mathbf{I}_{i,j}(\tau_i, \tau_j, x, p) = \mathbf{I}_{i,j+1}(\tau_i, \tau_{j+1}, x, p) \exp(-\Delta\tau_j(\mu)) \quad (\text{C.17})$$

End if

END DO

For those rays for which  $p(ip) > r(i)$

DO  $j = n_{v_p}, n_{v_p} - 1, \dots, 1$

$$\mathbf{I}_{i,j}(\tau_i, \tau_j, x, p) = 0 \quad (\text{C.18})$$

END DO

END DO

END DO

The algorithm given above saves a great deal of computing time by cutting down the number of calls to the formal solver -2 instead of  $n_d$  -the first call to store the  $\psi$  and  $\Delta\tau$  at all depth points, and the second call to compute  $\mathbf{I}_{ij}$

## Appendix D

# A core-wing method for the 3D polarized line transfer

An unpolarized version of the core-wing method was originally developed by Paletou & Auer (1995). It was extended later to resonance polarization with PRD by Paletou & Faurobert-Scholl (1997) and to the Hanle effect by Nagendra et al. (1999). The above cited papers used simple forms of PRD functions (combination of  $r_{\text{II,III}}$  of Hummer 1962). Fluri et al. (2003) proposed a core-wing method for the Hanle scattering problem with the very general PRD matrices of Bommier (1997b).

The core-wing method assumes that CRD is a good description in the line core region ( $x \leq x_c$ ) and frequency coherent scattering (CS) is a good approximation in the line wings ( $x > x_c$ ). The choice of the separation frequency  $x_c$  is not critical. A practical choice is  $x_c = 3.5$ . In other words the  $r_{\text{II}}$  function of Hummer (1962) can be replaced by a weighted combination of CRD and CS.  $r_{\text{III}}$  function is set to CRD in the line core, and to zero in the line wings.

The application of the core-wing separation method to Equation (4.43) leads to

$$\int_{-\infty}^{+\infty} dx' \frac{\hat{R}(x, x')}{\phi(x)} \Lambda_{x'}^* p_{x'} \delta \mathcal{S}_l^{r,n}(\mathbf{r}, x') = (1 - g_x) \int_{\text{core}} dx' \hat{W} [\hat{\alpha} \phi(x') + (\hat{\beta} - \hat{\alpha}) \phi(x')] \Lambda_{x'}^* p_{x'} \delta \mathcal{S}_l^{r,n}(\mathbf{r}, x') + g_x \int_{\text{wing}} dx' \hat{W} \hat{\alpha} \frac{\delta(x - x') \phi(x')}{\phi(x)} \Lambda_{x'}^* p_{x'} \delta \mathcal{S}_l^{r,n}(\mathbf{r}, x'), \quad (\text{D.1})$$

where

$$g_x = \begin{cases} 0 & \text{for } x \leq x_c, \\ r_{\text{II}}(x, x) / \phi(x) & \text{for } x > x_c, \end{cases} \quad (\text{D.2})$$

is the separation coefficient. Simplifying the above integral we obtain

$$\delta \overline{\mathcal{J}}^{r,n}(\mathbf{r}, x) = \int_{\text{core}} dx' \hat{W} \hat{\beta} \phi(x') \Lambda_{x'}^* p_{x'} \delta \mathcal{S}_l^{r,n}(\mathbf{r}, x') \quad \text{for } x \leq x_c,$$

and

$$\delta \overline{\mathcal{J}}^{r,n}(\mathbf{r}, x) = (1 - g_x) \int_{\text{core}} dx' \hat{W} \hat{\beta} \phi(x') \Lambda_{x'}^* p_{x'} \delta \mathcal{S}_l^{r,n}(\mathbf{r}, x') + g_x \hat{W} \hat{\alpha} \Lambda_x^* p_x \delta \mathcal{S}_l^{r,n}(\mathbf{r}, x)$$

for  $x > x_c$ .

(D.3)

Substituting Equation (D.3) in Equation (4.43) we obtain separate equations for  $\overline{\mathcal{J}}^{r,n+1}(\mathbf{r}, x)$  in the core and the wing domains. After simple algebraic manipulations, Equation (4.44) can be re-written as

$$\delta \mathcal{S}_l^{r,n}(\mathbf{r}, x) = \delta \overline{\mathcal{J}}^{r,n}(\mathbf{r}, x) + \mathbf{r}_x^n, \quad (\text{D.4})$$

where  $\delta \overline{\mathcal{J}}^{r,n}$  is given by Equation (D.3). The residual vector  $\mathbf{r}_x^n$  is

$$\mathbf{r}_x^n = \overline{\mathcal{J}}^{r,n}(\mathbf{r}, x) + \epsilon \mathbf{B}(\mathbf{r}) - \mathcal{S}_l^{r,n}(\mathbf{r}, x). \quad (\text{D.5})$$

We now proceed to derive the line source vector corrections for the core domain. Defining a vector

$$\Delta \mathbf{T}^n = \int_{\text{core}} dx' \hat{W} \hat{\beta} \phi(x') \Lambda_{x'}^* p_{x'} \delta \mathcal{S}_l^{r,n}(\mathbf{r}, x'), \quad (\text{D.6})$$

the line source vector correction takes the form

$$\delta \mathcal{S}_l^{r,n}(\mathbf{r}, x) = \mathbf{r}_x^n + \Delta \mathbf{T}^n, \quad \text{for } x \leq x_c. \quad (\text{D.7})$$

Applying the integral operator  $\int_{\text{core}} dx' \hat{W} \hat{\beta} \phi(x') p_{x'} \Lambda_{x'}^*$  on both sides of the Equation (D.7), we finally obtain

$$\Delta \mathbf{T}^n = \frac{\overline{\mathbf{r}}^n}{1 - \int_{\text{core}} dx' \hat{W} \hat{\beta} \phi(x') p_{x'} \Lambda_{x'}^*}, \quad (\text{D.8})$$

where

$$\overline{\mathbf{r}}^n = \int_{\text{core}} dx' \hat{W} \hat{\beta} \phi(x') p_{x'} \Lambda_{x'}^* \mathbf{r}_{x'}^n. \quad (\text{D.9})$$

Notice that  $\overline{\mathbf{r}}^n$  and  $\Delta \mathbf{T}^n$  are independent of the frequency  $x$ . Using Equations (4.43), (D.3) and (D.7) we obtain

$$\delta \mathcal{S}_l^{r,n}(\mathbf{r}, x) = \frac{(1 - g_x) \Delta \mathbf{T}^n + \mathbf{r}_x^n}{[1 - g_x \hat{W} \alpha \Lambda_x^* p_x]}, \quad \text{for } x > x_c. \quad (\text{D.10})$$

The updated line source vector can be computed using

$$\mathcal{S}_l^{r,n+1}(\mathbf{r}, x) = \mathcal{S}_l^{r,n}(\mathbf{r}, x) + \delta\mathcal{S}_l^{r,n}(\mathbf{r}, x). \quad (\text{D.11})$$

The above core-wing equations are set up in the form of an iterative algorithm to compute the line source vector corrections. We define

$$c_1 = \max_{\tau_X, \tau_Y, \tau_Z, x} \left\{ \left| \frac{\delta\mathcal{S}_{0,l}^{0,r,n}(\mathbf{r}, x)}{\mathcal{S}_{0,l}^{0,r,n}(\mathbf{r}, x)} \right| \right\}, \quad \text{and} \quad p = \max_{\tau_X, \tau_Y} \left\{ \frac{1}{I} \sqrt{Q^2 + U^2} \right\}, \quad (\text{D.12})$$

where the  $I$ ,  $Q$  and  $U$  are computed at the top surface ( $\tau_Z = 0$ ). Further, we consider  $p$  only at the line center ( $x = 0$ ), and for  $\mu = 0.11$ , and  $\varphi = 7^\circ$ . Finally we define the maximum relative change (MRC) as

$$R_c^n = \max \{c_1, p\}. \quad (\text{D.13})$$

The iterative progress is followed through a convergence test on  $R_c^n$ . We have chosen a convergence criteria of  $10^{-4}$  on the  $R_c^n$ .



## Appendix E

# Expansion of Stokes parameters into irreducible components in non-magnetic 2D media

The Stokes parameters and the irreducible Stokes vector are related through the following expressions. They are already given in Frisch (2007). However we present these expressions here for an easy reference. The expressions given below are applicable for radiative transfer in 2D geometry (see Equation (5.14) and discussions that follows).

$$\begin{aligned} I(\mathbf{r}, \boldsymbol{\Omega}, x) &= I_0^0 + \frac{1}{2\sqrt{2}}(3 \cos^2 \theta - 1)I_0^2 \\ &+ \sqrt{3} \cos \theta \sin \theta \sin \varphi I_1^{2,y} + \frac{\sqrt{3}}{2}(1 - \cos^2 \theta) \cos 2\varphi I_2^{2,x}, \end{aligned} \quad (\text{E.1})$$

$$\begin{aligned} Q(\mathbf{r}, \boldsymbol{\Omega}, x) &= -\frac{3}{2\sqrt{2}}(1 - \cos^2 \theta)I_0^2 \\ &+ \sqrt{3} \cos \theta \sin \theta \sin \varphi I_1^{2,y} - \frac{\sqrt{3}}{2}(1 + \cos^2 \theta) \cos 2\varphi I_2^{2,x}, \end{aligned} \quad (\text{E.2})$$

$$U(\mathbf{r}, \boldsymbol{\Omega}, x) = \sqrt{3} \sin \theta \cos \varphi I_1^{2,y} + \sqrt{3} \cos \theta \sin 2\varphi I_2^{2,x}. \quad (\text{E.3})$$

The irreducible components in the above equations depend on  $\mathbf{r}$ ,  $\boldsymbol{\Omega}$  and  $x$ . The same transformation formulas can be used to construct the Stokes source vectors from the irreducible source vectors.

## Appendix F

# Symmetry of polarized radiation field in 2D geometries

Equation (5.14) concerns symmetry of polarized radiation field in 2D geometries. A proof of Equation (5.14) can be given as an algorithm.

Step (1): First we assume that the medium has only an unpolarized thermal source namely,  $\mathcal{S}(\mathbf{r}, x) = (\epsilon B(\mathbf{r}), 0, 0, 0, 0, 0)^T$ .

Step (2): Use of this source vector in the formal solution expression (Equation 5.23) yields  $\mathcal{I} = (I_0^0, 0, 0, 0, 0, 0)^T$ .

Step (3): Using this  $\mathcal{I}$ , we can write the expressions for the irreducible mean intensity components as

$$\begin{aligned} J_0^0(\mathbf{r}, x) &\simeq \int_{x', \Omega} \frac{\hat{R}(x, x')}{\phi(x)} I_0^0(\mathbf{r}, \theta, \varphi, x'), \\ J_0^2(\mathbf{r}, x) &\simeq c_2 \int_{x', \Omega} \frac{\hat{R}(x, x')}{\phi(x)} (3 \cos^2 \theta - 1) I_0^0(\mathbf{r}, \theta, \varphi, x'), \\ J_1^{2,x}(\mathbf{r}, x) &\simeq -c_3 \int_{x', \Omega} \frac{\hat{R}(x, x')}{\phi(x)} \sin 2\theta \cos \varphi I_0^0(\mathbf{r}, \theta, \varphi, x'), \\ J_1^{2,y}(\mathbf{r}, x) &\simeq c_4 \int_{x', \Omega} \frac{\hat{R}(x, x')}{\phi(x)} \sin 2\theta \sin \varphi I_0^0(\mathbf{r}, \theta, \varphi, x'), \end{aligned}$$

$$\begin{aligned}
J_2^{2,x}(\mathbf{r}, x) &\simeq c_5 \int_{x', \Omega} \frac{\hat{R}(x, x')}{\phi(x)} \sin^2 \theta \cos 2\varphi I_0^0(\mathbf{r}, \theta, \varphi, x'), \\
J_2^{2,y}(\mathbf{r}, x) &\simeq -c_6 \int_{x', \Omega} \frac{\hat{R}(x, x')}{\phi(x)} \sin^2 \theta \sin 2\varphi I_0^0(\mathbf{r}, \theta, \varphi, x'),
\end{aligned} \tag{F.1}$$

where

$$\int_{x', \Omega} = \int_{-\infty}^{+\infty} dx' \oint \frac{d\Omega}{4\pi}, \tag{F.2}$$

and  $c_i, i = 2, 3, 4, 5, 6$  are positive numbers (see Appendix J). We recall that  $d\Omega = \sin \theta d\theta d\varphi$ ,  $\theta \in [0, \pi]$  and  $\varphi \in [0, 2\pi]$ .

Step (4): Notice that  $\cos(\pi - \varphi) = -\cos \varphi$ ,  $\sin 2(\pi - \varphi) = -\sin 2\varphi$ .

Step (5): Using the formal solution computed with the thermal source vector  $(\epsilon B(\mathbf{r}), 0, 0, 0, 0, 0)^T$  and the fact that in a 2D geometry, the medium is homogeneous in the  $X$  direction, it follows that

$$\begin{aligned}
I_0^0(\mathbf{r}, \theta, \varphi, x') &= I_0^0(\mathbf{r}, \theta, \pi - \varphi, x'), \\
I_0^0(\mathbf{r}, \theta, \pi + \varphi, x') &= I_0^0(\mathbf{r}, \theta, 2\pi - \varphi, x'), \quad \varphi \in [0, \pi/2].
\end{aligned} \tag{F.3}$$

Step (6): Substituting Equation (F.3) in Equation (F.1), we can easily prove that

$$\begin{aligned}
(J_1^{2,x})^{(1)} &= 0, (J_2^{2,y})^{(1)} = 0, \\
\text{and hence} \\
(S_1^{2,x})^{(1)} &= 0, (S_2^{2,y})^{(1)} = 0,
\end{aligned} \tag{F.4}$$

where the superscript (1) means that it is a first order solution.

Step (7): Using Equation (F.4), along with Equations (E.1), (E.2) and (E.3) applied to

the source vectors we deduce

$$\begin{aligned}
S_I(\mathbf{r}, \theta, \varphi, x) &= S_I(\mathbf{r}, \theta, \pi - \varphi, x), \\
S_I(\mathbf{r}, \theta, \varphi + \pi, x) &= S_I(\mathbf{r}, \theta, 2\pi - \varphi, x), \\
S_Q(\mathbf{r}, \theta, \varphi, x) &= S_Q(\mathbf{r}, \theta, \pi - \varphi, x), \\
S_Q(\mathbf{r}, \theta, \varphi + \pi, x) &= S_Q(\mathbf{r}, \theta, 2\pi - \varphi, x), \\
S_U(\mathbf{r}, \theta, \varphi, x) &= -S_U(\mathbf{r}, \theta, \pi - \varphi, x), \\
S_U(\mathbf{r}, \theta, \varphi + \pi, x) &= -S_U(\mathbf{r}, \theta, 2\pi - \varphi, x).
\end{aligned}
\tag{F.5}$$

Step (8): Using formal solution for Stokes parameters  $I, Q, U$  and using the homogeneity of the 2D slab in the  $X$  direction, it follows that

$$\begin{aligned}
I(\mathbf{r}, \theta, \varphi, x) &= I(\mathbf{r}, \theta, \pi - \varphi, x), \\
I(\mathbf{r}, \theta, \varphi + \pi, x) &= I(\mathbf{r}, \theta, 2\pi - \varphi, x), \\
Q(\mathbf{r}, \theta, \varphi, x) &= Q(\mathbf{r}, \theta, \pi - \varphi, x), \\
Q(\mathbf{r}, \theta, \varphi + \pi, x) &= Q(\mathbf{r}, \theta, 2\pi - \varphi, x), \\
U(\mathbf{r}, \theta, \varphi, x) &= -U(\mathbf{r}, \theta, \pi - \varphi, x), \\
U(\mathbf{r}, \theta, \varphi + \pi, x) &= -U(\mathbf{r}, \theta, 2\pi - \varphi, x).
\end{aligned}
\tag{F.6}$$

Step (9): Now we recall the expression for the complex irreducible source vector components  $S_{Q,l}^K$  (see Equation (4.14) in chapter 4 and Equation (20) for zero magnetic field case in Frisch 2007) namely,

$$S_{Q,l}^K(\mathbf{r}, x) = G_Q^K(\mathbf{r}, x) + J_Q^K(\mathbf{r}, x), \tag{F.7}$$

where

$$\begin{aligned}
J_Q^K(\mathbf{r}, x) &= \frac{1}{\phi(x)} \int_{-\infty}^{+\infty} dx' \oint \frac{d\Omega}{4\pi} \\
&\times R^K(x, x') \sum_{j=0}^3 (-1)^Q \mathcal{T}_{-Q}^K(j, \Omega) I_j(\mathbf{r}, \Omega, x').
\end{aligned}
\tag{F.8}$$

Here  $I_0, I_1, I_2 = I, Q, U$ . The quantity  $R^{(0)}(x, x')$  is the first element of the matrix  $\hat{R}$ . All the other elements are given by  $R^{(2)}(x, x')$ .

Step (10): We consider the case  $K = 2, Q = 1$ . Substituting the expressions for  $\mathcal{T}_{-Q}^K(j, \boldsymbol{\Omega})$  from Landi Degl'Innocenti & Landolfi (2004) for the reference direction  $\gamma = 0$ , the integral over  $\varphi$  in Equation (F.8) can be written as

$$\int_0^{2\pi} d\varphi \sum_{j=0}^3 (\mathcal{T}_1^2)^*(j, \boldsymbol{\Omega}) I_j(\mathbf{r}, \boldsymbol{\Omega}, x') = \int_0^{2\pi} d\varphi \left[ (\mathcal{T}_1^2)^*(0, \theta, \varphi) I(\mathbf{r}, \theta, \varphi, x') \right. \\ \left. + (\mathcal{T}_1^2)^*(1, \theta, \varphi) Q(\mathbf{r}, \theta, \varphi, x') + (\mathcal{T}_1^2)^*(2, \theta, \varphi) U(\mathbf{r}, \theta, \varphi, x') \right]. \quad (\text{F.9})$$

Step (11): The  $\varphi$  integral in Equation (F.9) can be split into 2 parts, one from 0 to  $\pi$  and the other from  $\pi$  to  $2\pi$ . It can be shown that both these integrals yield purely imaginary functions. First we consider the integral from 0 to  $\pi$  and decompose into integrals over 0 to  $\pi/2$  and  $\pi/2$  to  $\pi$ . In the integral from  $\pi/2$  to  $\pi$  we perform a change of variable  $\varphi \rightarrow \pi - \varphi$ . We obtain

$$\int_0^{\pi} d\varphi \sum_{j=0}^3 (\mathcal{T}_1^2)^*(j, \boldsymbol{\Omega}) I_j(\mathbf{r}, \boldsymbol{\Omega}, x') \\ = \int_0^{\pi/2} d\varphi \left[ (\mathcal{T}_1^2)^*(0, \theta, \varphi) + (\mathcal{T}_1^2)^*(0, \theta, \pi - \varphi) \right] I(\mathbf{r}, \theta, \varphi, x') \\ + \left[ (\mathcal{T}_1^2)^*(1, \theta, \varphi) + (\mathcal{T}_1^2)^*(1, \theta, \pi - \varphi) \right] Q(\mathbf{r}, \theta, \varphi, x') \\ + \left[ (\mathcal{T}_2^2)^*(1, \theta, \varphi) - (\mathcal{T}_1^2)^*(2, \theta, \pi - \varphi) \right] U(\mathbf{r}, \theta, \varphi, x'), \\ = \int_0^{\pi/2} d\varphi \left[ \frac{\sqrt{3}}{2} \sin \theta \cos \theta (-e^{-i\varphi} - e^{-i(\pi-\varphi)}) \right] I(\mathbf{r}, \theta, \varphi, x') \\ + \left[ \frac{\sqrt{3}}{2} \sin \theta \cos \theta (-e^{-i\varphi} - e^{-i(\pi-\varphi)}) \right] Q(\mathbf{r}, \theta, \varphi, x') \\ + \left[ \frac{\sqrt{3}}{2} i \sin \theta (e^{-i\varphi} - e^{-i(\pi-\varphi)}) \right] U(\mathbf{r}, \theta, \varphi, x') \\ = \int_0^{\pi/2} d\varphi \left[ \frac{\sqrt{3}}{2} \sin \theta \cos \theta (2i \sin \varphi) \right] I(\mathbf{r}, \theta, \varphi, x') \\ + \left[ \frac{\sqrt{3}}{2} \sin \theta \cos \theta (2i \sin \varphi) \right] Q(\mathbf{r}, \theta, \varphi, x') \\ + \left[ \frac{\sqrt{3}}{2} i \sin \theta (2 \cos \varphi) \right] U(\mathbf{r}, \theta, \varphi, x'), \quad (\text{F.10})$$

which is purely an imaginary function. Similarly we can prove that the integral of  $\varphi$  from

$\pi$  to  $2\pi$  also yields a purely imaginary function. Thus  $J_1^2$  is purely imaginary. Since  $J_1^{2,x}$  is the real part of  $J_1^2$ , we have  $J_1^{2,x} = 0$ .

Following similar lines we can prove that  $J_2^2$  is purely real, which proves that  $J_2^{2,y} = 0$  where  $J_2^{2,y}$  is the imaginary part of  $J_2^2$ . Thus we get

$$(J_1^{2,x})^{(2)} = 0, (J_2^{2,y})^{(2)} = 0, \quad (\text{F.11})$$

and hence

$$(S_1^{2,x})^{(2)} = 0, (S_2^{2,y})^{(2)} = 0, \quad (\text{F.12})$$

where the subscript (2) means second order solution. Repeating the above steps (7)–(11), we can prove that Equations (F.11) and (F.12) are valid for any order  $n$ . Hence the proof.

## Appendix G

# Expansion of Stokes parameters into the irreducible components

The Stokes parameters and the irreducible Stokes vector are related through the following expressions. They are already given in Frisch (2007). However we present these expressions here for an easy reference.

$$\begin{aligned} I(\mathbf{r}, \boldsymbol{\Omega}, x) &= I_0^0 + \frac{1}{2\sqrt{2}}(3 \cos^2 \theta - 1)I_0^2 \\ &\quad - \sqrt{3} \cos \theta \sin \theta (I_1^{2,x} \cos \varphi - I_1^{2,y} \sin \varphi) \\ &\quad + \frac{\sqrt{3}}{2}(1 - \cos^2 \theta)(I_2^{2,x} \cos 2\varphi - I_2^{2,y} \sin 2\varphi), \end{aligned} \tag{G.1}$$

$$\begin{aligned} Q(\mathbf{r}, \boldsymbol{\Omega}, x) &= -\frac{3}{2\sqrt{2}}(1 - \cos^2 \theta)I_0^2 \\ &\quad - \sqrt{3} \cos \theta \sin \theta (I_1^{2,x} \cos \varphi - I_1^{2,y} \sin \varphi) \\ &\quad - \frac{\sqrt{3}}{2}(1 + \cos^2 \theta)(I_2^{2,x} \cos 2\varphi - I_2^{2,y} \sin 2\varphi), \end{aligned} \tag{G.2}$$

$$\begin{aligned} U(\mathbf{r}, \boldsymbol{\Omega}, x) &= \sqrt{3} \sin \theta (I_1^{2,x} \sin \varphi + I_1^{2,y} \cos \varphi) \\ &\quad + \sqrt{3} \cos \theta (I_2^{2,x} \sin 2\varphi + I_2^{2,y} \cos 2\varphi). \end{aligned} \tag{G.3}$$

The irreducible components in the above equations also depend on  $\mathbf{r}$ ,  $\boldsymbol{\Omega}$ ,  $x$  and  $\mathbf{B}$ .

## Appendix H

# The magnetic redistribution matrices in the irreducible tensorial form

Here we use the redistribution matrices defined under the approximation level III of Bommier (1997b). The expressions listed below are already given in Bommier (1997b). We give them here for the sake of completeness. The branching ratios (see Bommier 1997b) are given by

$$\alpha = \frac{\Gamma_R}{\Gamma_R + \Gamma_E + \Gamma_I}, \quad (\text{H.1})$$

$$\beta^{(K)} = \frac{\Gamma_R}{\Gamma_R + D^{(K)} + \Gamma_I}, \quad (\text{H.2})$$

with  $D^{(0)} = 0$  and  $D^{(2)} = c\Gamma_E$ , where  $c$  is a constant, taken to be 0.379 (see Faurobert-Scholl 1992).

The Hanle  $\Gamma_B$  coefficient (see Bommier 1997b) takes two different forms, namely

$$\Gamma_B = \Gamma'_K = \beta^{(K)}\Gamma, \quad \Gamma_B = \Gamma'' = \alpha\Gamma, \quad (\text{H.3})$$

with

$$\Gamma = g_J \frac{2\pi eB}{2m_e\Gamma_R} \quad (\text{H.4})$$

where  $eB/2m_e$  is the Larmor frequency of the electron in the magnetic field (with  $e$  and  $m_e$  being the charge and mass of the electron). Here  $B$  is the magnetic field strength. The expressions for the redistribution matrices given in Bommier (1997b) involve a cut-off frequency  $v_c(a)$ , which is given by the solution of the equation

$$\frac{1}{\sqrt{\pi}}e^{-v^2} = \frac{a}{\pi v^2 + a^2}, \quad (\text{H.5})$$



and a constant  $z = 2\sqrt{2} + 2$  coming from the angle-averaging process.

If

$$\begin{aligned} z v_c(a) |x'| - (x^2 + x'^2) &< (z - 1) v_c^2(a) \quad \text{and} \\ z v_c(a) |x| - (x^2 + x'^2) &< (z - 1) v_c^2(a) \quad \text{and} \\ |x'| < \sqrt{2} v_c(a) \quad \text{and} \quad |x| < \sqrt{2} v_c(a), \end{aligned} \quad (\text{H.6})$$

then domain 1 :

$$\begin{aligned} P_{Q,\text{III}}^K(j, \boldsymbol{\Omega}', \mathbf{B}) &= \sum_{Q'} \left\{ \beta^{(K)} \mathcal{M}_{QQ'}^K(\mathbf{B}; \Gamma'_K) - \alpha \mathcal{M}_{QQ'}^K(\mathbf{B}; \Gamma'') \right\} (-1)^{Q'} \mathcal{T}_{-Q'}^K(j, \boldsymbol{\Omega}'), \\ &= \sum_{Q'} \overline{\mathcal{M}}_{QQ',\text{III}}^{K(1)}(\mathbf{B}) (\mathcal{T}_{Q'}^K)^*(j, \boldsymbol{\Omega}'). \end{aligned} \quad (\text{H.7})$$

elseif

$$|x'| < v_c(a) \quad \text{or} \quad |x| < v_c(a), \quad (\text{H.8})$$

then domain 2 :

$$\begin{aligned} P_{Q,\text{III}}^K(j, \boldsymbol{\Omega}', \mathbf{B}) &= [\beta^{(K)} - \alpha] \sum_{Q'} \mathcal{M}_{QQ'}^K(\mathbf{B}; \Gamma'_K) (-1)^{Q'} \mathcal{T}_{-Q'}^K(j, \boldsymbol{\Omega}'), \\ &= \sum_{Q'} \overline{\mathcal{M}}_{QQ',\text{III}}^{K(2)}(\mathbf{B}) (\mathcal{T}_{Q'}^K)^*(j, \boldsymbol{\Omega}'). \end{aligned} \quad (\text{H.9})$$

else domain 3 :

$$\begin{aligned} P_{Q,\text{III}}^K(j, \boldsymbol{\Omega}', \mathbf{B}) &= [1 - \alpha/\beta^{(K)}] \\ &\times \left\{ [\beta^{(K)} - \alpha] \sum_{Q'} \mathcal{M}_{QQ'}^K(\mathbf{B}; \Gamma'_K) (-1)^{Q'} \mathcal{T}_{-Q'}^K(j, \boldsymbol{\Omega}') + \alpha \sum_{Q'} (-1)^{Q'} \mathcal{T}_{-Q'}^K(j, \boldsymbol{\Omega}') \right\}, \\ &= \sum_{Q'} \overline{\mathcal{M}}_{QQ',\text{III}}^{K(3)}(\mathbf{B}) (\mathcal{T}_{Q'}^K)^*(j, \boldsymbol{\Omega}'). \end{aligned} \quad (\text{H.10})$$

endif. If

$$x(x + x') < 2v_c^2(a) \quad \text{and} \quad x'(x + x') < 2v_c^2(a), \quad (\text{H.11})$$

then domain 4:

$$\begin{aligned}
 P_{Q,\text{II}}^K(j, \boldsymbol{\Omega}', \mathbf{B}) &= \alpha \sum_{Q'} \mathcal{M}_{QQ'}^K(\mathbf{B}; \Gamma'') (-1)^{Q'} \mathcal{T}_{-Q'}^K(j, \boldsymbol{\Omega}'). \\
 &= \sum_{Q'} \overline{\mathcal{M}}_{QQ',\text{II}}^{K(4)}(\mathbf{B}) (\mathcal{T}_{Q'}^K)^*(j, \boldsymbol{\Omega}'), \tag{H.12}
 \end{aligned}$$

else domain 5:

$$\begin{aligned}
 P_{Q,\text{II}}^K(j, \boldsymbol{\Omega}', \mathbf{B}) &= \alpha \sum_{Q'} (-1)^{Q'} \mathcal{T}_{-Q'}^K(j, \boldsymbol{\Omega}'), \\
 &= \sum_{Q'} \overline{\mathcal{M}}_{QQ',\text{II}}^{K(5)}(\mathbf{B}) (\mathcal{T}_{Q'}^K)^*(j, \boldsymbol{\Omega}'). \tag{H.13}
 \end{aligned}$$

endif.

The symbols  $\overline{\mathcal{M}}_{QQ',\text{II,III}}^{K(i)}$ ,  $i = 1, 2, 3, 4, 5$  have different expressions in different frequency domains. They implicitly contain the respective branching ratios and the Hanle  $\Gamma$  parameter depending upon the domain.

## Appendix I

# The magnetic redistribution matrices in the matrix form

We introduce the diagonal matrices

$$\hat{\alpha} = \alpha \hat{E}, \quad (\text{I.1})$$

with  $\hat{E}$  the identity matrix,

$$\hat{\beta} = \text{diag}\{\beta^{(0)}, \beta^{(2)}, \beta^{(2)}, \beta^{(2)}, \beta^{(2)}, \beta^{(2)}\}, \quad (\text{I.2})$$

$$\hat{\mathcal{F}} = \text{diag}\left\{1 - \frac{\alpha}{\beta^{(0)}}, 1 - \frac{\alpha}{\beta^{(2)}}, 1 - \frac{\alpha}{\beta^{(2)}}, 1 - \frac{\alpha}{\beta^{(2)}}, 1 - \frac{\alpha}{\beta^{(2)}}, 1 - \frac{\alpha}{\beta^{(2)}}\right\}. \quad (\text{I.3})$$

The real matrices  $\hat{M}_{\text{II}}^{(i)}(\mathbf{B})$  and  $\hat{M}_{\text{III}}^{(i)}(\mathbf{B})$  have following expressions in different domains.

In domain 1:

$$\hat{M}_{\text{III}}^{(1)}(\mathbf{B}) = \left\{ \hat{\beta} \hat{M}(\mathbf{B}, \Gamma'_2) - \hat{\alpha} \hat{M}(\mathbf{B}, \Gamma'') \right\}. \quad (\text{I.4})$$

In domain 2:

$$\hat{M}_{\text{III}}^{(2)}(\mathbf{B}) = \left\{ \left[ \hat{\beta} - \hat{\alpha} \right] \hat{M}(\mathbf{B}, \Gamma'_K) \right\}. \quad (\text{I.5})$$

In domain 3:

$$\hat{M}_{\text{III}}^{(3)}(\mathbf{B}) = \hat{\mathcal{F}} \left\{ \left[ \hat{\beta} - \hat{\alpha} \right] \hat{M}(\mathbf{B}, \Gamma'_2) + \hat{\alpha} \right\}. \quad (\text{I.6})$$

In domain 4:

$$\hat{M}_{\text{II}}^{(4)}(\mathbf{B}) = \hat{\alpha} \hat{M}(\mathbf{B}, \Gamma''). \quad (\text{I.7})$$

In domain 5:

$$\hat{M}_{\text{II}}^{(5)}(\mathbf{B}) = \hat{\alpha}. \quad (\text{I.8})$$

## Appendix J

# The reduced scattering phase matrix in real form

The elements of the matrix  $\hat{\Psi}$  in the real and reduced form are listed below.

$$\hat{\Psi} = \begin{pmatrix} \Psi_{11} & \Psi_{12} & \Psi_{13} & \Psi_{14} & \Psi_{15} & \Psi_{16} \\ \Psi_{12} & \Psi_{22} & \Psi_{23} & \Psi_{24} & \Psi_{25} & \Psi_{26} \\ \frac{1}{2}\Psi_{13} & \frac{1}{2}\Psi_{23} & \Psi_{33} & \Psi_{34} & \Psi_{35} & \Psi_{36} \\ \frac{1}{2}\Psi_{14} & \frac{1}{2}\Psi_{24} & \Psi_{34} & \Psi_{44} & \Psi_{45} & \Psi_{46} \\ \frac{1}{2}\Psi_{15} & \frac{1}{2}\Psi_{25} & \Psi_{35} & \Psi_{45} & \Psi_{55} & \Psi_{56} \\ \frac{1}{2}\Psi_{16} & \frac{1}{2}\Psi_{26} & \Psi_{36} & \Psi_{46} & \Psi_{56} & \Psi_{66} \end{pmatrix}, \quad (\text{J.1})$$

where the distinct matrix elements are:

$$\begin{aligned} \Psi_{11} &= 1; & \Psi_{12} &= \frac{1}{2\sqrt{2}}(3\cos^2\theta - 1); \\ \Psi_{13} &= -\frac{\sqrt{3}}{2}\sin 2\theta \cos \varphi; & \Psi_{14} &= \frac{\sqrt{3}}{2}\sin 2\theta \sin \varphi; & \Psi_{15} &= \frac{\sqrt{3}}{2}\sin^2\theta \cos 2\varphi; \\ \Psi_{16} &= -\frac{\sqrt{3}}{2}\sin^2\theta \sin 2\varphi; & \Psi_{22} &= \frac{1}{4}(9\cos^4\theta - 12\cos^2\theta + 5); \\ \Psi_{23} &= \frac{\sqrt{3}}{4\sqrt{2}}\sin 2\theta(1 - 3\cos 2\theta)\cos \varphi; & \Psi_{24} &= -\frac{\sqrt{3}}{4\sqrt{2}}\sin 2\theta(1 - 3\cos 2\theta)\sin \varphi; \\ \Psi_{25} &= \frac{\sqrt{3}}{2\sqrt{2}}\sin^2\theta(1 + 3\cos^2\theta)\cos 2\varphi; & \Psi_{26} &= -\frac{\sqrt{3}}{2\sqrt{2}}\sin^2\theta(1 + 3\cos^2\theta)\sin 2\varphi; \\ \Psi_{33} &= \frac{3}{4}\sin^2\theta[(1 + 2\cos^2\theta) - (1 - 2\cos^2\theta)\cos 2\varphi]; \end{aligned}$$

$$\begin{aligned}
\Psi_{34} &= \frac{3}{4} \sin^2 \theta (1 - 2 \cos^2 \theta) \sin 2\varphi; & \Psi_{35} &= \frac{3}{16} \sin 2\theta [(3 + \cos 2\theta) \cos \varphi - (1 - \cos 2\theta) \cos 3\varphi]; \\
\Psi_{36} &= -\frac{3}{16} \sin 2\theta [(3 + \cos 2\theta) \sin \varphi - (1 - \cos 2\theta) \sin 3\varphi]; \\
\Psi_{44} &= \frac{3}{4} \sin^2 \theta [(1 + 2 \cos^2 \theta) + (1 - 2 \cos^2 \theta) \cos 2\varphi]; \\
\Psi_{45} &= \frac{3}{16} \sin 2\theta [(3 + \cos 2\theta) \sin \varphi + (1 - \cos 2\theta) \sin 3\varphi]; \\
\Psi_{46} &= \frac{3}{16} \sin 2\theta [(3 + \cos 2\theta) \cos \varphi + (1 - \cos 2\theta) \cos 3\varphi]; \\
\Psi_{55} &= \frac{3}{16} [(1 + 6 \cos^2 \theta + \sin^4 \theta + \cos^4 \theta) + (1 - 2 \cos^2 \theta + \cos^4 \theta + \sin^4 \theta) \cos 4\varphi]; \\
\Psi_{56} &= -\frac{3}{16} [(1 - 2 \cos^2 \theta + \cos^4 \theta + \sin^4 \theta) \sin 4\varphi]; \\
\Psi_{66} &= \frac{3}{16} [(1 + 6 \cos^2 \theta + \sin^4 \theta + \cos^4 \theta) - (1 - 2 \cos^2 \theta + \cos^4 \theta + \sin^4 \theta) \cos 4\varphi]. \tag{J.2}
\end{aligned}$$

The elements of the matrix  $\hat{\Psi}$  satisfy certain symmetry properties with respect to the main diagonal. Hence the number of independent elements are only 21.

## Appendix K

# The magnetic redistribution matrices in the matrix form

The matrix forms of domain based angle-averaged PRD of Bommier (1997b) is already given in several references (see e.g., Anusha et al. 2011b). Here we present them in the case of angle-dependent PRD. We introduce the diagonal matrices

$$\hat{\alpha} = \alpha \hat{E}, \quad (\text{K.1})$$

with  $\hat{E}$  the identity matrix,

$$\hat{\beta} = \text{diag}\{\beta^{(0)}, \beta^{(2)}, \beta^{(2)}, \beta^{(2)}, \beta^{(2)}, \beta^{(2)}\}, \quad (\text{K.2})$$

$$\hat{\mathcal{F}} = \text{diag}\left\{1 - \frac{\alpha}{\beta^{(0)}}, 1 - \frac{\alpha}{\beta^{(2)}}, 1 - \frac{\alpha}{\beta^{(2)}}, 1 - \frac{\alpha}{\beta^{(2)}}, 1 - \frac{\alpha}{\beta^{(2)}}, 1 - \frac{\alpha}{\beta^{(2)}}\right\}. \quad (\text{K.3})$$

The expressions for the redistribution matrices given in Bommier (1997b) involve a cut-off frequency  $v_c(a)$ , which is given by the solution of the equation

$$\frac{1}{\sqrt{\pi}} e^{-v^2} = \frac{a}{\pi v^2 + a^2}. \quad (\text{K.4})$$

The real matrices  $\hat{M}_{\text{II}}(\mathbf{B}, x, x')$  and  $\hat{M}_{\text{III}}(\mathbf{B}, x, x')$  have following expressions in different domains.

If

$$\begin{aligned}
 |x' - x \cos \Theta| &< v_c \left( \frac{a}{\sin \Theta} \right) \sin \Theta \quad \text{and} \\
 |x| &< v_c(a) |\cos \Theta| + v_c \left( \frac{a}{\sin \Theta} \right) \sin \Theta \quad \text{and} \\
 |x - x' \cos \Theta| &< v_c \left( \frac{a}{\sin \Theta} \right) \sin \Theta \quad \text{and} \quad |x'| < v_c(a) |\cos \Theta| + v_c \left( \frac{a}{\sin \Theta} \right) \sin \Theta,
 \end{aligned} \tag{K.5}$$

then domain 1 :

$$\hat{M}_{\text{III}}(\mathbf{B}, x, x') = \left\{ \hat{\beta} \hat{M}(\mathbf{B}, \Gamma'_2) - \hat{\alpha} \hat{M}(\mathbf{B}, \Gamma'') \right\}. \tag{K.6}$$

elseif

$$|x'| < v_c(a) \quad \text{or} \quad |x| < v_c(a), \tag{K.7}$$

then domain 2 :

$$\hat{M}_{\text{III}}(\mathbf{B}, x, x') = \left\{ [\hat{\beta} - \hat{\alpha}] \hat{M}(\mathbf{B}, \Gamma'_K) \right\}. \tag{K.8}$$

else domain 3 :

$$\hat{M}_{\text{III}}(\mathbf{B}, x, x') = \hat{\mathcal{F}} \left\{ [\hat{\beta} - \hat{\alpha}] \hat{M}(\mathbf{B}, \Gamma'_2) + \hat{\alpha} \right\}. \tag{K.9}$$

If

$$|x + x'| < 2v_c \left( \frac{a}{\cos \frac{1}{2}\Theta} \right) \cos \frac{1}{2}\Theta, \tag{K.10}$$

then domain 4 :

$$\hat{M}_{\text{II}}(\mathbf{B}, x, x') = \hat{\alpha} \hat{M}(\mathbf{B}, \Gamma''). \tag{K.11}$$



---

else domain 5 :

$$\hat{M}_{\text{II}}(\mathbf{B}, x, x') = \hat{\alpha}. \quad (\text{K.12})$$

Here the matrix  $\hat{M}(\mathbf{B}, \Gamma)$  is the Hanle phase matrix whose elements can be found in several references (see e.g., Anusha et al. 2011b).

## Appendix L

# Symmetry breaking properties of the angle-dependent PRD

In this appendix we show that the symmetry properties that are valid in angle-averaged PRD case (proved in Appendix F) break down in the case of angle-dependent PRD. We present the proof in the form of an algorithm.

Step (1): First we assume that the medium contains only an unpolarized thermal source namely,  $\mathcal{S} = (\epsilon B(\mathbf{r}), 0, 0, 0, 0, 0)^T$ .

Step (2): Use of this source vector in the formal solution expression yields  $\mathcal{I} = (I_0^0, 0, 0, 0, 0, 0)^T$ .

Step (3): Using this  $\mathcal{I}$  we can write the expressions for the irreducible polarized mean intensity components as

$$\begin{aligned} J_0^0(\mathbf{r}, \boldsymbol{\Omega}, x) &\simeq \int_{x', \boldsymbol{\Omega}'} \frac{\hat{R}(x, x', \boldsymbol{\Omega}, \boldsymbol{\Omega}')}{\phi(x)} I_0^0(\mathbf{r}, \theta', \varphi', x'), \\ J_0^2(\mathbf{r}, \boldsymbol{\Omega}, x) &\simeq c_2 \int_{x', \boldsymbol{\Omega}'} \frac{\hat{R}(x, x', \boldsymbol{\Omega}, \boldsymbol{\Omega}')}{\phi(x)} (3 \cos^2 \theta' - 1) I_0^0(\mathbf{r}, \theta', \varphi', x'), \\ J_1^{2,x}(\mathbf{r}, \boldsymbol{\Omega}, x) &\simeq -c_3 \int_{x', \boldsymbol{\Omega}'} \frac{\hat{R}(x, x', \boldsymbol{\Omega}, \boldsymbol{\Omega}')}{\phi(x)} \sin 2\theta' \cos \varphi' I_0^0(\mathbf{r}, \theta', \varphi', x'), \\ J_1^{2,y}(\mathbf{r}, \boldsymbol{\Omega}, x) &\simeq c_4 \int_{x', \boldsymbol{\Omega}'} \frac{\hat{R}(x, x', \boldsymbol{\Omega}, \boldsymbol{\Omega}')}{\phi(x)} \sin 2\theta' \sin \varphi' I_0^0(\mathbf{r}, \theta', \varphi', x'), \end{aligned}$$

$$\begin{aligned}
J_2^{2,x}(\mathbf{r}, \boldsymbol{\Omega}, x) &\simeq c_5 \int_{x', \boldsymbol{\Omega}'} \frac{\hat{R}(x, x', \boldsymbol{\Omega}, \boldsymbol{\Omega}')}{\phi(x)} \sin^2 \theta' \cos 2\varphi' I_0^0(\mathbf{r}, \theta', \varphi', x'), \\
J_2^{2,y}(\mathbf{r}, \boldsymbol{\Omega}, x) &\simeq -c_6 \int_{x', \boldsymbol{\Omega}'} \frac{\hat{R}(x, x', \boldsymbol{\Omega}, \boldsymbol{\Omega}')}{\phi(x)} \sin^2 \theta' \sin 2\varphi' I_0^0(\mathbf{r}, \theta', \varphi', x'),
\end{aligned} \tag{L.1}$$

where

$$\int_{x', \boldsymbol{\Omega}'} = \int_{-\infty}^{+\infty} dx' \oint \frac{d\boldsymbol{\Omega}'}{4\pi}, \tag{L.2}$$

and  $c_i, i = 2, 3, 4, 5, 6$  are positive numbers (see Appendix J). We recall that  $d\boldsymbol{\Omega}' = \sin \theta' d\theta' d\varphi'$ ,  $\theta' \in [0, \pi]$  and  $\varphi' \in [0, 2\pi]$ . Here

$$\hat{R}(x, x', \boldsymbol{\Omega}, \boldsymbol{\Omega}') = \hat{W} \left[ \hat{\alpha} r_{\text{II}}(x, x', \boldsymbol{\Omega}, \boldsymbol{\Omega}') \left( \hat{\beta} - \hat{\alpha} \right) r_{\text{III}}(x, x', \boldsymbol{\Omega}, \boldsymbol{\Omega}') \right], \tag{L.3}$$

is the non-magnetic, polarized redistribution matrix.

Step (4): A Fourier expansion of the angle-dependent PRD functions with respect to  $\varphi'$  (instead of  $\varphi$ ) gives

$$r_{\text{II,III}}(x, x', \boldsymbol{\Omega}, \boldsymbol{\Omega}') = \sum_{k'=0}^{k'=\infty} (2 - \delta_{k'0}) \mathcal{R}e \{ e^{ik'\varphi'} \tilde{r}_{\text{II,III}}^{(k')}(x, x', \boldsymbol{\Omega}, \theta') \}, \tag{L.4}$$

with the Fourier coefficients

$$\tilde{r}^{(k)}(x, x', \boldsymbol{\Omega}, \theta') = \int_0^{2\pi} \frac{d\varphi'}{2\pi} e^{-ik'\varphi'} r_{\text{II,III}}(x, x', \boldsymbol{\Omega}, \boldsymbol{\Omega}'). \tag{L.5}$$

Substituting Equation (L.4) in Equation (L.1) we can show that the components  $J_1^{2,x}$  and  $J_2^{2,y}$  do not vanish irrespective of the symmetry of  $I_0^0$  with respect to the infinite spatial axis. In other words, to a first approximation, even if we assume that  $I_0^0$  is symmetric with respect to the infinite spatial axis as in angle-averaged PRD, the  $\varphi'$ -dependence of angle-dependent PRD functions  $r_{\text{II,III}}$  is such that the integral over  $\varphi'$  leads to non-zero  $J_1^{2,x}$  and  $J_2^{2,y}$ . This stems basically from the coefficients with  $k' \neq 0$  in the expansion of the angle-dependent PRD functions. Following an induction proof as in Appendix F, it follows that  $J_1^{2,x}$  and  $J_2^{2,y}$  are non-zero in general because the symmetry breaks down in the first step itself.

It follows from Equation (8.2), and from the above proof that the Stokes  $I$  parameter is not symmetric with respect to the infinite spatial axis in a non-magnetic 2D media,

## **322 Appendix L. Symmetry breaking properties of the angle-dependent PRD**

in the angle-dependent PRD case, unlike the angle-averaged PRD and CRD cases (see Appendix F for the proof in case of angle-averaged PRD).

## Appendix M

# The non-magnetic redistribution matrices

We are primarily interested in 1D polarized radiative transfer problem. In this Appendix we briefly discuss the polarized redistribution matrices in the Stokes  $(I, Q, U)$  basis. The use of  $(I, Q, U)$  becomes necessary whenever there is non-axisymmetry in the problem, the two well known examples of which are (i) the incidence of non-axisymmetric radiation at the boundary, and (ii) the presence of a oriented magnetic field. Both of these break the azimuthal (axi-) symmetry of the radiation field. In axi-symmetric problems, we can work with the  $(I, Q)$  basis, as  $U \equiv 0$ . Here  $Q$  positive is defined to be parallel to the limb. We begin by writing down the redistribution matrix for the non-magnetic scattering (see Domke & Hubeny 1988). We then describe the assumptions leading us from this general form, to simpler forms which are actually used in chapter 9. These details are scattered in several publications. Hence it is useful to list them here, for the sake of clarity. The angle-dependent Domke-Hubeny PRD matrix can be written (see Domke & Hubeny 1988) as

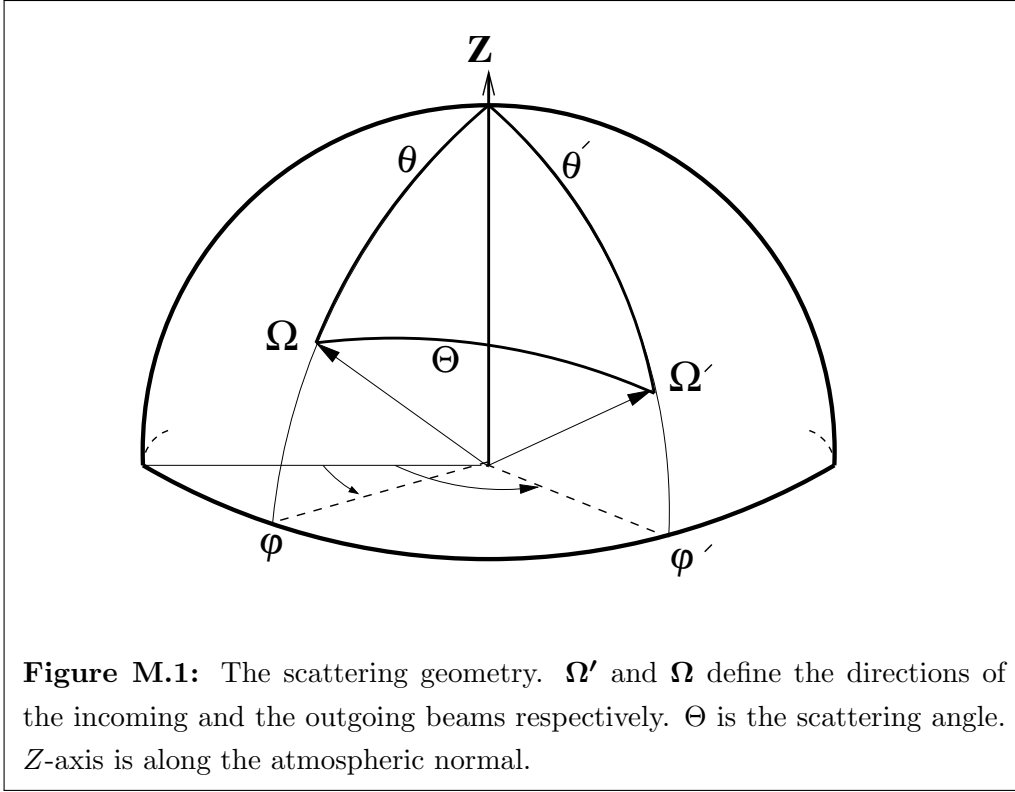
$$\begin{aligned} \hat{\mathbf{R}}(\lambda, \lambda', \Theta, z) = & \gamma_{\text{coh}} r_{\text{II}}(\lambda, \lambda', \Theta, z) \hat{\mathbf{P}}(\Theta; W_{\text{eff}} = W_2) \\ & + (1 - \gamma_{\text{coh}}) r_{\text{III}}(\lambda, \lambda', \Theta, z) \hat{\mathbf{P}}(\Theta; W_{\text{eff}} = k_c W_2). \end{aligned} \tag{M.1}$$

The depth dependent coherence fraction is defined as

$$\gamma_{\text{coh}} = \frac{\Gamma_R + \Gamma_I}{\Gamma_R + \Gamma_I + \Gamma_E}. \tag{M.2}$$

The collisional depolarization factor is defined as

$$k_c = \frac{\Gamma_R + \Gamma_I}{\Gamma_R + \Gamma_I + D^{(2)}} \frac{\Gamma_E - D^{(2)}}{\Gamma_E}, \tag{M.3}$$



where  $D^{(2)}$  is the rate of depolarizing elastic collisions. The factor  $W_2$  in Equation (M.1) depends on the angular momentum quantum numbers  $J_l$  and  $J_u$  of the lower and upper states. Note that  $W_2=1$  for Ca I 4227 Å line.  $r_{\text{II}}$  and  $r_{\text{III}}$  are the scalar redistribution functions of Hummer (1962).  $\hat{\mathbf{P}}(\Theta)$  is the scattering phase matrix (see Bommier 1997b). The scattering angle  $\Theta$  is given by

$$\cos \Theta = \mu\mu' + \sqrt{(1-\mu^2)(1-\mu'^2)} \cos(\varphi' - \varphi), \quad (\text{M.4})$$

where  $\mu = \cos \theta$ , and  $\mu' = \cos \theta'$  represent the inclinations of the outgoing and incoming rays;  $\varphi$  and  $\varphi'$  the respective azimuths in the atmospheric co-ordinate system fixed to the planar slab atmosphere, in which the scattering is described (see Figure M.1).

For the axi-symmetric (azimuthally independent) radiative transfer, the redistribution matrix can be written as

$$\hat{\mathbf{R}}(\lambda, \lambda', \mu, \mu', z) = \frac{1}{2\pi} \int_0^{2\pi} \hat{\mathbf{R}}(\lambda, \lambda', \Theta, z) d(\varphi' - \varphi). \quad (\text{M.5})$$

We make the approximation

$$\begin{aligned} \hat{\mathbf{R}}(\lambda, \lambda', \mu, \mu', z) &= \gamma_{\text{coh}} r_{\text{II}}(\lambda, \lambda', \mu, \mu', z) \hat{\mathbf{P}}(\mu, \mu'; W_{\text{eff}} = W_2) \\ &+ (1 - \gamma_{\text{coh}}) r_{\text{III}}(\lambda, \lambda', \mu, \mu', z) \hat{\mathbf{P}}(\mu, \mu'; W_{\text{eff}} = k_c W_2). \end{aligned} \quad (\text{M.6})$$

In writing this expression we assume that the azimuthal average of the redistribution matrix can be replaced by the product of the azimuthal averages of the redistribution functions and of the phase matrix. A similar factorization leads to the so called hybrid approximation for PRD suggested by Rees & Saliba (1982). Averaging the redistribution functions in Equation (M.6) over the scattering angle (defined by the angles  $\theta, \theta'$ ), one recovers the usual angle-averaged redistribution matrix

$$\begin{aligned} \hat{\mathbf{R}}(\lambda, \lambda', \mu, \mu', z) &= \gamma_{\text{coh}} r_{\text{II}}(\lambda, \lambda', z) \hat{\mathbf{P}}(\mu, \mu'; W_{\text{eff}} = W_2) \\ &+ (1 - \gamma_{\text{coh}}) r_{\text{III}}(\lambda, \lambda', z) \hat{\mathbf{P}}(\mu, \mu'; W_{\text{eff}} = k_c W_2), \end{aligned} \quad (\text{M.7})$$

where

$$r_{\text{II,III}}(\lambda, \lambda', z) = \frac{1}{2} \int_0^\pi r_{\text{II,III}}(\lambda, \lambda', \Theta, z) \sin \Theta d\Theta. \quad (\text{M.8})$$

(see Equation (103) in Bommier 1997b and the averaging method in Hummer 1962; Mihalas 1978). Equation (M.7), which is the hybrid approximation of Rees & Saliba (1982) is used in chapter 9 and in most of the work with PRD (see e.g., Faurobert-Scholl 1992; Nagendra 1994; Holzreuter et al. 2005; Sampoorna & Trujillo Bueno 2010). To recover the complete frequency redistribution limit, we set  $\gamma_{\text{coh}} = 0$ ; replace  $r_{\text{III}}(\lambda, \lambda', z) = \phi(\lambda, z)\phi(\lambda', z)$ , and also set  $(\Gamma_E - D^{(2)})/\Gamma_E = 1$  in the expression for  $k_c$ . The limit of frequency coherent scattering in the laboratory frame can be recovered by setting  $\gamma_{\text{coh}} = 1$  and through a replacement  $r_{\text{II}}(\lambda, \lambda', z) = \delta(\lambda - \lambda')\phi(\lambda', z)$ .

The scattering phase matrix is given by

$$\hat{\mathbf{P}}(\mu, \mu'; W_{\text{eff}}) = \hat{\mathbf{P}}^{(0)} + W_{\text{eff}} \hat{\mathbf{P}}^{(2)}(\mu, \mu'), \quad (\text{M.9})$$

which goes to the Rayleigh phase matrix  $\hat{\mathbf{P}}_R$  when  $W_{\text{eff}}$  is set equal to unity.  $\hat{\mathbf{P}}^{(0)}$  and  $\hat{\mathbf{P}}^{(2)}$  are the multipolar components of the scattering phase matrix. They are written as (Stenflo 1994)

$$\hat{\mathbf{P}}^{(0)} = \begin{pmatrix} 1 & 0 \\ 0 & 0 \end{pmatrix}; \quad \hat{\mathbf{P}}^{(2)}(\mu, \mu') = \frac{3}{8} \begin{pmatrix} \frac{1}{3}(1 - 3\mu^2)(1 - 3\mu'^2) & -(1 - 3\mu^2)(1 - \mu'^2) \\ -(1 - \mu^2)(1 - 3\mu'^2) & 3(1 - \mu^2)(1 - \mu'^2) \end{pmatrix}. \quad (\text{M.10})$$

### ***Redistribution matrix for the micro-turbulent magnetic fields :***

In chapter 9 we also use the micro-turbulent magnetic field averaged redistribution matrices. These matrices are found to be necessary in order to reproduce the core peak

amplitude in the  $Q/I$  spectra of the Ca I 4227 Å line. The relevant redistribution matrix can be obtained simply by replacing  $W_{\text{eff}}$  by  $W_{\text{eff}}f_B$  where

$$f_B = \begin{cases} 1 - \frac{2}{5} \left[ \frac{\gamma_h^2}{1+\gamma_h^2} + \frac{4\gamma_h^2}{1+4\gamma_h^2} \right] & \text{for } (\lambda, \lambda') \text{ in the line core,} \\ 1 & \text{elsewhere,} \end{cases} \quad (\text{M.11})$$

for the particular case of isotropic angular distribution of the micro-turbulent magnetic field (Stenflo 1982; Faurobert-Scholl 1993). The Hanle gamma parameter in the above equation is given by

$$\gamma_h = 0.88 g_J \frac{B_{\text{turb}}}{\Gamma_R + D^{(2)}}. \quad (\text{M.12})$$

Here,  $B_{\text{turb}}$  is the magnetic field strength in Gauss, and  $g_J$  is the Landé g factor of the upper level ( $g_J = 1$  for Ca I 4227 Å line).  $\Gamma_R$  and  $D^{(2)}$  are expressed here in units of  $10^7 \text{ s}^{-1}$ .



## Appendix N

### The magnetic redistribution matrices

In this Appendix we give the expression of the Hanle redistribution matrix used in Equation (10.8) of the text. We use the approximation III of the Hanle redistribution matrix defined in Bommier (1997b) for a two-level atom with unpolarized ground level. In matrix notation, this Hanle redistribution matrix may be written as

$$\hat{\mathcal{R}}(\lambda, \lambda', z, \mathbf{B}) = \hat{M}_{\text{II}}^{(i)}(\mathbf{B}, z)r_{\text{II}}(\lambda, \lambda', z) + \hat{M}_{\text{III}}^{(i)}(\mathbf{B}, z)r_{\text{III}}(\lambda, \lambda', z). \quad (\text{N.1})$$

$r_{\text{II,III}}(\lambda, \lambda', z)$  are the angle-averaged redistribution functions of Hummer (1962). Index  $i$  ( $= 1, 2, 3, 4, 5$ ) labels different  $(\lambda, \lambda')$  wavelength domains. We use the same domains as in Bommier (1997b). Indices 1 to 3 refer to the domains relevant to  $r_{\text{III}}$ , indices 4 and 5 to the domains relevant to  $r_{\text{II}}$  (see e.g., Fluri et al. 2003). In Bommier (1997b) the redistribution matrix elements are given in terms of the irreducible spherical tensors. Here we use a matrix notation and work in the irreducible Stokes vector  $\mathcal{I}$  basis. This implies that we deal with  $6 \times 6$  matrices. For clarity, the explicit expression of the  $\hat{M}_{\text{II,III}}^{(i)}(\mathbf{B}, z)$  matrices are given below.

We introduce the Hanle phase matrix  $\hat{M}(\mathbf{B}, \Gamma)$  (see e.g., Landi Degl’Innocenti & Landolfi 2004), where  $\Gamma$  is the Hanle parameter defined by

$$\Gamma = 0.88 g_J \frac{B}{\Gamma_R}. \quad (\text{N.2})$$

Here  $g_J$  is the Landé  $g$  factor of the upper level ( $g_J = 1$  for the Ca I 4227 Å line). The magnetic field strength  $B$  is expressed in Gauss and  $\Gamma_R$  in units of  $10^7 \text{ s}^{-1}$ . We also introduce the diagonal matrices

$$\hat{W} = \text{diag}\{W_0, W_2, W_2, W_2, W_2, W_2\}, \quad (\text{N.3})$$

$$\hat{\alpha} = \alpha \hat{E}, \quad (\text{N.4})$$

with  $\hat{E}$  being the identity matrix,

$$\hat{\beta} = \text{diag}\{\beta^{(0)}, \beta^{(2)}, \beta^{(2)}, \beta^{(2)}, \beta^{(2)}, \beta^{(2)}\}, \quad (\text{N.5})$$

$$\hat{\mathcal{F}} = \text{diag}\left\{1 - \frac{\alpha}{\beta^{(0)}}, 1 - \frac{\alpha}{\beta^{(2)}}, 1 - \frac{\alpha}{\beta^{(2)}}, 1 - \frac{\alpha}{\beta^{(2)}}, 1 - \frac{\alpha}{\beta^{(2)}}, 1 - \frac{\alpha}{\beta^{(2)}}\right\}, \quad (\text{N.6})$$

and the coefficients

$$\Gamma'_K = \beta^{(K)}\Gamma, \quad \Gamma'' = \alpha\Gamma. \quad (\text{N.7})$$

The coefficients  $\alpha$  and  $\beta^{(K)}$  are branching ratios introduced in Bommier (1997b, see her Equation (88)). They are given by

$$\alpha = \frac{\Gamma_R}{\Gamma_R + \Gamma_E + \Gamma_I}, \quad (\text{N.8})$$

$$\beta^{(K)} = \frac{\Gamma_R}{\Gamma_R + D^{(K)} + \Gamma_I}, \quad (\text{N.9})$$

with  $D^{(0)} = 0$  and  $D^{(2)} = c\Gamma_E$ , where  $c$  is a constant, taken to be 0.379 (see Faurobert-Scholl 1992).

The expressions given in Bommier (1997b) involve a cut-off frequency  $v_c(a)$ , which is given by the solution of the equation

$$\frac{1}{\sqrt{\pi}}e^{-v^2} = \frac{a}{\pi} \frac{1}{v^2 + a^2}, \quad (\text{N.10})$$

and a constant  $z = 2\sqrt{2} + 2$  coming from the angle-averaging process. The incident and scattered non-dimensional frequencies are denoted by  $x'$  and  $x$ . The matrices  $\hat{M}^{(i)}$ , together with the frequency domains, can be written in the following algorithmic form:

If

$$zv_c(a)|x'| - (x^2 + x'^2) < (z-1)v_c^2(a) \quad \text{and} \quad zv_c(a)|x| - (x^2 + x'^2) < (z-1)v_c^2(a) \quad \text{and} \\ |x'| < \sqrt{2}v_c(a) \quad \text{and} \quad |x| < \sqrt{2}v_c(a), \quad (\text{N.11})$$

then domain 1:

$$\hat{M}_{\text{III}}^{(1)}(\mathbf{B}, z) = \hat{W} \left\{ \hat{\beta} \hat{M}(\mathbf{B}, \Gamma'_2) - \hat{\alpha} \hat{M}(\mathbf{B}, \Gamma'') \right\}, \quad (\text{N.12})$$

elseif

$$|x'| < v_c(a) \quad \text{or} \quad |x| < v_c(a), \quad (\text{N.13})$$

then domain 2 :

$$\hat{M}_{\text{III}}^{(2)}(\mathbf{B}, z) = \hat{W} \left\{ \left[ \hat{\beta} - \hat{\alpha} \right] \hat{M}(\mathbf{B}, \Gamma'_2) \right\}, \quad (\text{N.14})$$

else domain 3 :

$$\hat{M}_{\text{III}}^{(3)}(\mathbf{B}, z) = \hat{W} \hat{\mathcal{F}} \left\{ \left[ \hat{\beta} - \hat{\alpha} \right] \hat{M}(\mathbf{B}, \Gamma'_2) + \hat{\alpha} \right\}, \quad (\text{N.15})$$

endif.

If

$$x(x + x') < 2v_c^2(a) \quad \text{and} \quad x'(x + x') < 2v_c^2(a), \quad (\text{N.16})$$

then domain 4 :

$$\hat{M}_{\text{II}}^{(4)}(\mathbf{B}, z) = \alpha \hat{W} \hat{M}(\mathbf{B}, \Gamma''), \quad (\text{N.17})$$

else domain 5 :

$$\hat{M}_{\text{II}}^{(5)}(\mathbf{B}, z) = \alpha \hat{W}, \quad (\text{N.18})$$

endif.

The Hanle phase matrix  $\hat{M}(\mathbf{B}, \Gamma)$  is given below :

$$\hat{M}(\mathbf{B}, \Gamma) = \hat{U}(\chi_B) \hat{m}(\theta_B, \Gamma) \hat{U}(-\chi_B), \quad (\text{N.19})$$

where

$$\hat{m} = \begin{pmatrix} 1 & 0 & 0 & 0 & 0 & 0 \\ 0 & m_{11} & m_{12} & m_{13} & m_{14} & m_{15} \\ 0 & \frac{1}{2}m_{12} & m_{22} & m_{23} & m_{24} & m_{25} \\ 0 & -\frac{1}{2}m_{13} & -m_{23} & m_{33} & m_{34} & m_{35} \\ 0 & \frac{1}{2}m_{14} & m_{24} & -m_{34} & m_{44} & m_{45} \\ 0 & -\frac{1}{2}m_{15} & -m_{25} & m_{35} & -m_{45} & m_{55} \end{pmatrix}, \quad (\text{N.20})$$

with

$$\begin{aligned}
m_{11} &= 1 - 3S_B^2\Gamma^2 \left[ \frac{C_B^2}{1+\Gamma^2} + \frac{S_B^2}{1+4\Gamma^2} \right]; & m_{12} &= -2\sqrt{\frac{3}{2}}C_B S_B \Gamma^2 \left[ \frac{2C_B^2 - 1}{1+\Gamma^2} + \frac{2S_B^2}{1+4\Gamma^2} \right], \\
m_{13} &= 2\sqrt{\frac{3}{2}}S_B \Gamma \left[ \frac{C_B^2}{1+\Gamma^2} + \frac{S_B^2}{1+4\Gamma^2} \right]; & m_{14} &= 2\sqrt{\frac{3}{2}}S_B^2 \Gamma^2 \left[ \frac{C_B^2}{1+\Gamma^2} - \frac{1+C_B^2}{1+4\Gamma^2} \right], \\
m_{15} &= -2\sqrt{\frac{3}{2}}S_B^2 C_B \Gamma \left[ \frac{1}{1+\Gamma^2} - \frac{1}{1+4\Gamma^2} \right]; & m_{22} &= 1 - \Gamma^2 \left[ \frac{(1-2C_B^2)^2}{1+\Gamma^2} + \frac{4S_B^2 C_B^2}{1+4\Gamma^2} \right], \\
m_{23} &= -C_B \Gamma \left[ \frac{1-2C_B^2}{1+\Gamma^2} - \frac{2S_B^2}{1+4\Gamma^2} \right]; & m_{24} &= -C_B S_B \Gamma^2 \left[ \frac{1-2C_B^2}{1+\Gamma^2} + \frac{2(1+C_B^2)}{1+4\Gamma^2} \right], \\
m_{25} &= S_B \Gamma \left[ \frac{1-2C_B^2}{1+\Gamma^2} + \frac{2C_B^2}{1+4\Gamma^2} \right]; & m_{33} &= 1 - \Gamma^2 \left[ \frac{C_B^2}{1+\Gamma^2} + \frac{4S_B^2}{1+4\Gamma^2} \right], \\
m_{34} &= S_B \Gamma \left[ \frac{C_B^2}{1+\Gamma^2} - \frac{1+C_B^2}{1+4\Gamma^2} \right]; & m_{35} &= C_B S_B \Gamma^2 \left[ \frac{1}{1+\Gamma^2} - \frac{4}{1+4\Gamma^2} \right], \\
m_{44} &= 1 - \Gamma^2 \left[ \frac{C_B^2 S_B^2}{1+\Gamma^2} + \frac{(1+C_B^2)^2}{1+4\Gamma^2} \right]; & m_{45} &= C_B \Gamma \left[ \frac{S_B^2}{1+\Gamma^2} + \frac{1+C_B^2}{1+4\Gamma^2} \right], \\
m_{55} &= 1 - \Gamma^2 \left[ \frac{S_B^2}{1+\Gamma^2} + \frac{4C_B^2}{1+4\Gamma^2} \right], & &
\end{aligned} \tag{N.21}$$

with  $C_B = \cos \theta_B$ ,  $S_B = \sin \theta_B$ . The matrix  $\hat{U}(\chi_B)$  is given by

$$\hat{U} = \begin{pmatrix} 1 & 0 & 0 & 0 & 0 & 0 \\ 0 & 1 & 0 & 0 & 0 & 0 \\ 0 & 0 & \cos \chi_B & \sin \chi_B & 0 & 0 \\ 0 & 0 & -\sin \chi_B & \cos \chi_B & 0 & 0 \\ 0 & 0 & 0 & 0 & \cos 2\chi_B & \sin 2\chi_B \\ 0 & 0 & 0 & 0 & -\sin 2\chi_B & \cos 2\chi_B \end{pmatrix}. \tag{N.22}$$

## Appendix O

# The Zeeman radiative transfer in the atmospheric reference frame

The definition of the Zeeman absorption matrix is usually given in an orthogonal reference frame with the  $z$ -axis along the line-of-sight (LOS). This reference frame is adequate for LTE transfer problems which can be solved ray by ray. Here we must solve the Zeeman transfer equation (Equation (10.12)) in the atmospheric reference frame (with the  $z$ -axis along the atmospheric normal). In the LOS reference frame the elements of the Zeeman absorption matrix depend on the angle  $\gamma$  between the LOS and the direction of the magnetic field vector  $\mathbf{B}$ , and on  $\chi$  that represents the azimuth of  $\mathbf{B}$  in the transversal plane. In practice the dependence is on  $\cos \gamma$  and on cosine and sine of  $\chi$  and  $2\chi$ . Here we show how to express the angular dependence of the Zeeman absorption matrix in terms of the polar angles  $(\theta, \varphi)$  of the ray direction  $\mathbf{\Omega}$  and  $(\theta_B, \chi_B)$  of the vector  $\mathbf{B}$  (see Figure O.1). We note in Figure O.1 that the values of  $\theta_B$ ,  $\theta$  and  $\gamma$  form a spherical triangle, if  $\theta$  and  $\gamma$  are non-zero. We use spherical trigonometry (see Smart 1960) to transform the terms depending on  $\gamma$  and  $\chi$ . The geometrical factors entering the Zeeman absorption matrix are  $\cos \gamma$ ,  $\cos^2 \gamma$ ,  $\sin^2 \gamma \cos 2\chi$ ,  $\sin^2 \gamma \sin 2\chi$ . The factor  $\cos \gamma$  is simply expressed by the cosine rule

$$\cos \gamma = \cos \theta_B \cos \theta + \sin \theta_B \sin \theta \cos(\varphi - \chi_B), \quad (\text{O.1})$$

from which we get the factor  $\cos^2 \gamma$

$$\cos^2 \gamma = [\cos \theta_B \cos \theta + \sin \theta_B \sin \theta \cos(\varphi - \chi_B)]^2. \quad (\text{O.2})$$

Using the sine rule and an analogue of the sine rule we get

$$\sin \gamma \sin \chi = \sin \theta_B \sin(\varphi - \chi_B), \quad (\text{O.3})$$

and

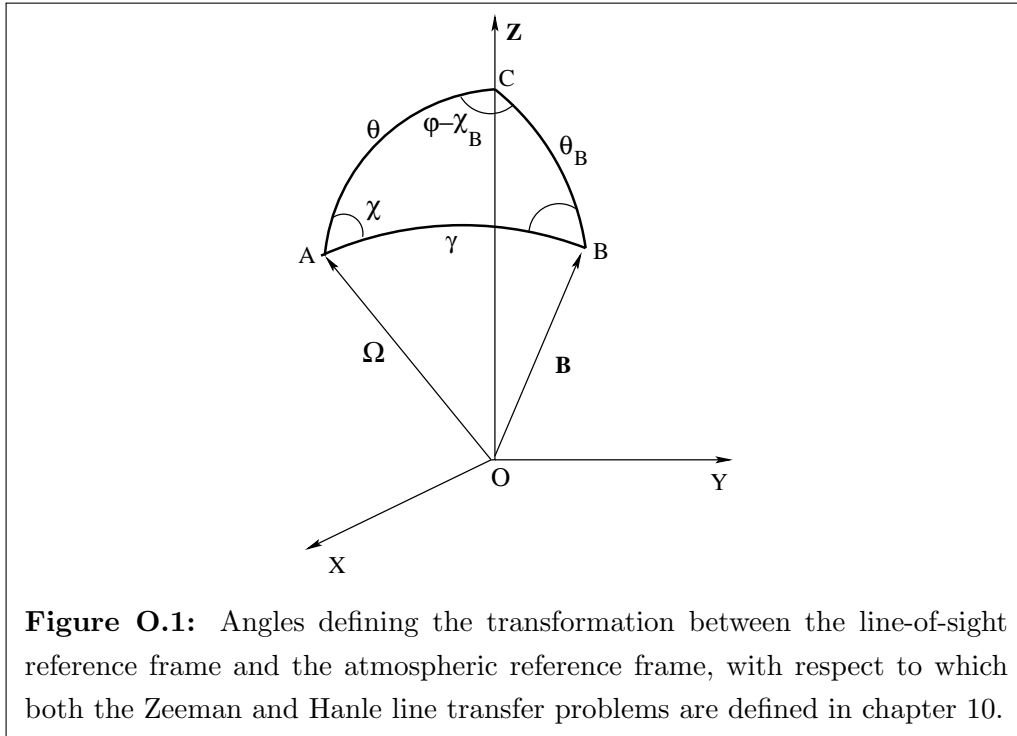
$$\sin \gamma \cos \chi = \sin \theta \cos \theta_B - \cos \theta \sin \theta_B \cos(\varphi - \chi_B). \quad (\text{O.4})$$

Subtracting the square of Equation (O.3) from the square of Equation (O.4) we get

$$\sin^2 \gamma \cos 2\chi = [\sin \theta \cos \theta_B - \cos \theta \sin \theta_B \cos(\varphi - \chi_B)]^2 - \sin^2 \theta_B \sin^2(\varphi - \chi_B). \quad (\text{O.5})$$

Multiplying Equation (O.3) by Equation (O.4) and multiplying by a factor of 2 on both sides of the resulting equation we get

$$\sin^2 \gamma \sin 2\chi = 2 \sin \theta_B \sin(\varphi - \chi_B) [\sin \theta \cos \theta_B - \cos \theta \sin \theta_B \cos(\varphi - \chi_B)]. \quad (\text{O.6})$$



# Bibliography

- Adam, J. 1990, “*Line formation in accretion disks*”, A&A, **240**, 541
- Anusha, L. S.**, & Nagendra, K. N., 2009, “*Projection methods for line radiative transfer in spherical media*”, Mem.S.A.It, **80**, 631
- Anusha, L. S.**, & Nagendra, K. N. 2011a, “*Polarized Line Formation in Multi-dimensional Media. I. Decomposition of Stokes Parameters in Arbitrary Geometries*”, ApJ, **726**, 6
- Anusha, L. S.**, & Nagendra, K. N. 2011b, “*Polarized line formation in Multi-dimensional media-III: Hanle effect with partial frequency redistribution*”, ApJ, **738**, 116
- Anusha, L. S.**, & Nagendra, K. N. 2011c, “*A Fourier decomposition technique to formulate the transfer equation with angle dependent partial frequency redistribution*”, ApJ, **739**, 40
- Anusha, L. S.**, & Nagendra, K. N., 2012, “*Polarized line formation in Multi-dimensional media-V: Effects of angle-dependent partial frequency redistribution*”, ApJ, **746**, 84
- Anusha, L. S.**, Nagendra, K. N., Bianda, M., Stenflo, J. O., Holzreuter, R., Sampurna, M., Frisch, H., Ramelli, R. & Smitha, H. N., 2011b, “*Analysis of the forward scattering Hanle effect in the Ca I 4227 Å line*”, ApJ, **737**, 95
- Anusha, L. S.**, Nagendra, K. N. & Paletou, F. 2011a, “*Polarized line formation in Multi-dimensional media-II: A high speed method to solve problems with partial frequency redistribution*”, ApJ, **726**, 96
- Anusha, L. S.**, Nagendra, K. N., Paletou, F., & Léger, L. 2009, “*Preconditioned Bi-conjugate Gradient Method for Radiative Transfer in Spherical Media*”, ApJ, **704**, 661

**Anusha, L. S.**, Nagendra, K. N., Stenflo, J. O., Bianda, M., Sampoorna, M., Frisch, H., Holzreuter, R., & Ramelli, R. 2010a, “*Generalization of the Last Scattering Approximation for the Second Solar Spectrum Modeling: The Ca I 4227 Å Line as a Case Study*”, ApJ, **718**, 988

**Anusha, L. S.**, Sampoorna, M., Frisch, H., & Nagendra, K. N., 2010b, “*The Hanle Effect as Diagnostic Tool for Turbulent Magnetic Fields*” in *Astrophysics and Space Science Proceedings: Magnetic Coupling between the Interior and the Atmosphere of the Sun*, eds. S. S. Hasan, & R. J. Rutten (Heidelberg, Berlin: Springer-Verlag), 390

**Anusha, L. S.**, Stenflo, J. O., Frisch, H., Bianda, M., Holzreuter, R., Nagendra, K. N., Sampoorna, M., & Ramelli, R., 2010c, “*Linear Polarization of the Solar Ca I 4227 Å line: Modeling based on radiative transfer and last scattering approximations*” in ASP Conf. Ser. **437**, “*Solar polarization 6*” (SPW6), ed. J. R. Kuhn, D. M. Harrington, H. Lin, S. V. Berdyugina, J. Trujillo-Bueno, S. L. Keil, and T. Rimmele (San Francisco: ASP), 57

Asensio Ramos, A., & Trujillo Bueno, J. 2005, “*Evidence for Collisional Depolarization in the MgH Lines of the Second Solar Spectrum*”, ApJ, **635**, 109

Asensio Ramos, A., & Trujillo Bueno, J. 2006, “*Very Efficient Methods for Multilevel Radiative Transfer in Atomic and Molecular Lines*” in EAS Pub. Ser. **18**, “*Radiative Transfer and Applications to Very Large Telescopes*”, ed. Ph. Stee (Les Ulis: EDP Sciences), 25

Asplund, M., Carlsson, M., & Botnen, A. V. 2003, “*Multi-level 3D non-LTE computations of lithium lines in the metal-poor halo stars HD 140283 and HD 84937*”, A&A, **399**, 31

Asplund, M., Grevesse, N., Sauval, A. J., Allende Prieto, C., & Kiselman, D. 2004, “*Line formation in solar granulation. IV. [O I], O I and OH lines and the photospheric O abundance*”, A&A, **417**, 751

Auer, L. H. 1984, “*Difference equations and linearization methods for radiative transfer*” in “*Methods in radiative transfer*”, ed. W. Kalkofen (Cambridge: Cambridge University Press), 237

Auer, L. H. 1991, “*Acceleration of Convergence*” in “*Stellar Atmospheres: Beyond classical models*”, ed. L. Crivellari, I. Hubeny, & D. G. Hummer (Dordrecht: Kluwer Academic Publishers), 9



- Auer, L. H., & Paletou, F. 1994, “*Two-dimensional radiative transfer with partial frequency redistribution I. General method*”, A&A, **285**, 675
- Auer, L. H., Fabiani Bendicho, P., & Trujillo Bueno, J. 1994, “*Multidimensional radiative transfer with multilevel atoms. 1: ALI method with preconditioning of the rate equations*”, A&A, **292**, 599
- Auvergne, M., Frisch, H., Frisch, U., Froeschlé, Ch., & Pouquet, A. 1973, “*Spectral line formation in a turbulent atmosphere*”, A&A, **29**, 93
- Avrett, E. H. 1995, “*Two-Component Modeling of the Solar IR CO Lines*” in “*Infrared tools for Solar Astrophysics: What’s Next?*”, ed. J. R. Kuhn, & M. J. Penn (Singapore: World Scientific), 303
- Barklem, P. S., & O’Mara, B. J. 1997, “*The broadening of p-d and d-p transitions by collisions with neutral hydrogen atoms*”, MNRAS, **290**, 102
- Belluzzi, L., Trujillo Bueno, J., Landi Degl’Innocenti, E. 2007, “*The Magnetic Sensitivity of the Ba II D1 and D2 Lines of the Fraunhofer Spectrum*”, ApJ, **666**, 588
- Ben-Jaffel, L., Harris, W., Bommier, V., Roesler, F., Ballester, G. E., & Jossang, J. 2005, “*Predictions on the application of the Hanle effect to map the surface magnetic field of Jupiter*”, Icarus, **178**, 297
- Bianda, M. 2003, “*Observations of scattering polarization and the Hanle effect in the Sun’s atmosphere*”, PhD Thesis, ETH Zürich (Cuvillier Verlag; Göttingen)
- Bianda, M., Solanki, S. K., & Stenflo, J. O. 1998a, “*Hanle depolarisation in the solar chromosphere*”, A&A, **331**, 760
- Bianda, M., Stenflo, J. O., & Solanki, S. K. 1998b, “*Hanle diagnostics of solar magnetic fields: the SR II 4078 Angstrom line*”, A&A, **337**, 565
- Bianda, M., Stenflo, J. O., Gandorfer, A., & Gisler, D. 2003, “*Enigmatic Magnetic Field Effects in the Scattering Polarization of the Ca I 4227 Å Line*”, in ASP Conf. Ser. **286**, “*Current Theoretical Models and Future High Resolution Solar Observations: Preparing for ATST*”, ed. A. A. Pevtsov & H. Uitenbroek (San Francisco: ASP), 61

- Bianda, M., Ramelli, R., Stenflo, J. O., **Anusha, L. S.**, Nagendra, K. N., Sampoorna, M., Holzreuter, R., & Frisch, H. 2010, “*Observations of the solar Ca I 4227 Å line*” in ASP Conf. Ser. **437**, “*Solar polarization 6*” (SPW6), ed. J. R. Kuhn, D. M. Harrington, H. Lin, S. V. Berdyugina, J. Trujillo-Bueno, S. L. Keil, and T. Rimmele (San Francisco: ASP), 67
- Bianda, M., Ramelli, R., **Anusha, L. S.**, Stenflo, J. O., Nagendra, K. N., Holzreuter, R., Sampoorna, M., Frisch, H., & Smitha, H. N., 2011, “*Observations of the forward scattering Hanle effect in the Ca I 4227 Å line*”, A&A, **530**, L13
- Bommier, V. 1977, “*Etude théorique de l’effet Hanle; traitement du cas de la raie  $D_3$  de l’Hélium en vue de la détermination du champ magnétique des protubérances solaires*”, Thèse de 3ème cycle, Université Pierre et Marie Curie Paris VI
- Bommier, V., Sahal-Bréchet, S. & Leroy, J. L. 1981, “*Determination of the complete vector magnetic field in solar prominences, using the Hanle effect*”, A&A, **100**, 231
- Bommier, V., Landi Degl’Innocenti, E., & Sahal-Bréchet, S. 1991, “*Resonance line polarization and the Hanle effect in optically thick media. II - Case of a plane-parallel atmosphere*”, A&A, **244**, 383
- Bommier, V. 1997a, “*Master equation theory applied to the redistribution of polarized radiation, in the weak radiation field limit I. Zero magnetic field case*”, A&A, **328**, 706
- Bommier, V. 1997b, “*Master equation theory applied to the redistribution of polarized radiation, in the weak radiation field limit II. Arbitrary magnetic field case*”, A&A, **328**, 726
- Bommier, V., Derouich, M., Landi Degl’Innocenti, E., Molodij, G., & Sahal-Bréchet, S. 2005, “*Interpretation of second solar spectrum observations of the Sr I 4607 Å line in a quiet region: Turbulent magnetic field strength determination*”, A&A, **432**, 295
- Botnen, A. 1997, “*Radiative Transfer in 3D*”, Masters Thesis, Institute of Theoretical Astrophysics, University of Oslo, Norway
- Brissaud, A., & Frisch, U. 1971, “*Theory of Stark broadening - II. Exact line profile with model microfield*”, J. Quant. Spec. Radiat. Transf., **11**, 1767
- Brissaud, A., & Frisch, U. 1974, “*Solving linear stochastic differential equations*”, J. Math. Phys., **15**, 524

- Cannon, C. J. 1970, “*Line Transfer in Two Dimensions*”, ApJ, **161**, 255
- Cannon, C. J. 1973, “*Angular quadrature perturbations in radiative transfer theory*”, J. Quant. Spec. Radiat. Transf., **13**, 627
- Cannon, C. J., & Rees, D. E. 1971, “*Line Transfer in the Presence of Two-Dimensional Velocity Gradients*”, ApJ, **169**, 157
- Carlsson, B. G. 1963, “*The numerical theory of neutron transport*” in Methods in Computational Physics, **1**, ed. B. Alder, S. Fernbach, & M. Rotenberg (New York: Academic), 1
- Carlsson, M. 1986, “*A computer program for solving multi-level non-LTE radiative transfer problems in moving or static atmospheres*”, Report No. 33, Uppsala Astronomical Observatory, Uppsala, Sweden
- Carlsson, M. 2009, “*Hydrodynamics and radiative transfer of 3D model atmospheres. Current status, limitations, and how to make headway*”, Mem.S.A.It, **80**, 606
- Chandrasekhar, S. 1934, “*On the hypothesis of the radial ejection of high-speed atoms for the Wolf-Rayet stars and the novæ*”, MNRAS, **94**, 522
- Chandrasekhar, S. 1946, “*On the Radiative Equilibrium of a Stellar Atmosphere. X.*”, ApJ, **103**, 351
- Chandrasekhar, S. 1950, “*Radiative transfer*” (Oxford: Clarendon Press)
- Chevallier, L., Paletou, F., & Rutily, B. 2003, “*On the accuracy of the ALI method for solving the radiative transfer equation*”, A&A, **411**, 221
- Collett, E. 1993, “*Polarized light: Fundamentals and applications*” (New York: Marcel Dekker, Inc.)
- Carroll, T. A., & Staude, J. 2005, “*Line formation in turbulent magnetic atmospheres*”, Astron. Nachr., **326**, 296
- Cayrel, R., Steffen, M., Chand, H., Bonifacio, P., Spite, M., Spite, F., Petitjean, P., Ludwig, H.-G., & Caffau, E. 2007, “*Line shift, line asymmetry, and the  $^6\text{Li}/^7\text{Li}$  isotopic ratio determination*”, **473**, 37
- Daniel, F., & Cernicharo, J. 2008, “*Solving radiative transfer with line overlaps using Gauss-Seidel algorithms*”, A&A, **488**, 1237

- Derouich, M., Sahal-Bréchet, S., Barklem, P. S., & O'Mara, B. J. 2003, “*Semi-classical theory of collisional depolarization of spectral lines by atomic hydrogen I. Application to p states of neutral atoms*”, A&A, **404**, 763
- Dittmann, O. J. 1997, “*The influence of cloud geometry on continuum polarization*”, JQSRT, **57**, 249
- Dittmann, O. J. 1999, “*3D polarised radiative transfer with weak magnetic fields*” in ASSL **243**, “*Solar polarization 2*” (SPW2), ed. K. N. Nagendra & J. O. Stenflo (Boston: Kluwer), 201
- Dominguez Cerdeña, I., Sánchez Almeida, J., & Kneer, F. 2006, “*Quiet Sun Magnetic Fields from Simultaneous Inversions of Visible and Infrared Spectropolarimetric Observations*”, ApJ, **646**, 1421
- Domke, H., & Hubeny, I. 1988, “*Scattering of polarized light in spectral lines with partial frequency redistribution - General redistribution matrix*”, ApJ, **334**, 527
- Dumont, S., Omont, A., Pecker, J. C., & Rees, D. E. 1977, “*Resonance line polarization: The line core*”, A&A, **54**, 675
- Fabiani Bendicho, P., Trujillo Bueno, J., & Auer, L. 1997, “*Multidimensional radiative transfer with multilevel atoms. II. The non-linear multigrid method*”, A&A, **324**, 161
- Fabiani Bendicho, P., & Trujillo Bueno, J. 1999, “*Three-dimensional radiative transfer with multilevel atoms*” in ASSL **243**, “*Solar polarization 2*” (SPW2), eds. K. N. Nagendra, & J. O. Stenflo (Boston: Kluwer), 219
- Faurobert, M. 1987, “*Linear polarization of resonance lines in the absence of magnetic fields. I - Slabs of finite optical thickness*”, A&A, **178**, 269
- Faurobert, M. 1988, “*Linear polarization of resonance lines in the absence of magnetic fields. II - Semi-infinite atmospheres*”, A&A, **194**, 268
- Faurobert-Scholl, M. 1991, “*Hanle effect with partial frequency redistribution. I - Numerical methods and first applications*”, A&A, **246**, 469
- Faurobert-Scholl, M. 1992, “*Hanle effect with partial frequency redistribution. II - Linear polarization of the solar Ca I 4227 Å line*”, A&A, **258**, 521

- Faurobert-Scholl, M. 1993, “*Investigation of micro-turbulent magnetic fields in the solar photosphere by their Hanle effect in the Sr I 4607 Å line*”, A&A, **268**, 765
- Faurobert-Scholl, M. 1994, “*Hanle effect of the magnetic canopies in the solar chromosphere*”, A&A, **285**, 665
- Faurobert-Scholl, M. 1996, “*Diagnostics with the Hanle effect*” in “*Solar polarization I*” (SPW1), eds. J. O. Stenflo, & K. N. Nagendra (Dordrecht: Kluwer), also Solar Physics, **164**, 79
- Faurobert, M., & Arnaud, J., 2002, “*Scattering polarization of molecular emission lines in the quiet solar chromosphere*”, A&A, **382**, 17
- Faurobert, M., Arnaud, J., Vigneau, J., & Frisch, H. 2001, “*Investigation of weak solar magnetic fields. New observational results for the Sr I 460.7 nm linear polarization and radiative transfer modeling*”, A&A, **378**, 627
- Faurobert, M., Derouich, M., Bommier, V., & Arnaud, J. 2009, “*Hanle effect in the solar Ba II D2 line: a diagnostic tool for chromospheric weak magnetic fields*”, A&A, **493**, 201
- Fluri, D. M., Holzreuter, R., Klement, J., & Stenflo, J. O. 2003a, “*Radiative transfer in Na I D<sub>2</sub> and D<sub>1</sub>*” in ASP Conf. Ser. **307**, “*Solar polarization 3*” (SPW3), eds. J. Trujillo Bueno, & J. Sánchez Almeida (San Francisco: ASP), 263
- Fluri, D. M., Nagendra, K. N., & Frisch, H. 2003b, “*An operator perturbation method for polarized line transfer VI. Generalized PALI method for Hanle effect with partial frequency redistribution and collisions*”, A&A, **400**, 303
- Folini, D. 1998, “*Computational approaches to multidimensional radiative transfer and the physics of radiative colliding flows*”, PhD Thesis, ETH No. 12606, ETH Zurich
- Fontenla, J. M., Avrett, E. H., & Loeser, R. 1993, “*Energy balance in the solar transition region. III - Helium emission in hydrostatic, constant-abundance models with diffusion*”, ApJ, **406**, 319
- Frisch, H. 2006, “*The Hanle effect in a random medium*”, A&A, **446**, 403 (HF06)
- Frisch, H. 2007, “*The Hanle effect. Decomposition of the Stokes parameters into irreducible components*”, A&A, **476**, 665 (HF07)

- Frisch, H. 2009, “*The Hanle effect. Angle-dependent frequency redistribution function. Decomposition of the Stokes parameters in irreducible components*” in ASP Conf. Ser. **405**, “*Solar Polarization 5*” (SPW5), ed. S. V. Berdyugina, K. N. Nagendra & R. Ramelli (San Francisco: ASP), 87 (HF09)
- Frisch, H. 2010, “*Spectral line polarization with angle-dependent partial frequency redistribution. I. A Stokes parameters decomposition for Rayleigh scattering*”, A&A, **522**, 41
- Frisch, H., & Frisch, U. 1975, “*LTE and non-LTE line formation with turbulent velocity fields*” in “*Physique des mouvements dans les atmosphères stellaires*”, eds. R. Cayrel, & M. Steinberg (Nice: Obs. Côte d’Azur)
- Frisch, H., & Frisch, U. 1976, “*Non-LTE transfer-II. Two-level atoms with stochastic velocity field*”, MNRAS, **175**, 157
- Frisch, H., **Anusha, L. S.**, Sampoorana, M., & Nagendra, K. N. 2009, “*The Hanle effect in a random magnetic field. Dependence of the polarization on statistical properties of the magnetic field*”, A&A, **501**, 335
- Gandorfer, A. 2000, “*The second solar spectrum*”, Vol I: 4625 Å to 6995 Å line (Zürich: vdf Hochschulverlag), ISBN No. 3 7281 2764 7
- Gandorfer, A. 2002, “*The second solar spectrum*”, Vol II: 3910 Å to 4630 Å line (Zürich: vdf Hochschulverlag), ISBN No. 3 7281 2844 4
- Gandorfer, A. 2005, “*The second solar spectrum*”, Vol III: 3160 Å to 3915 Å line (Zürich: vdf Hochschulverlag), ISBN No. 3 7281 3018 4
- Gandorfer, A. M., Povel H. P., Steiner, P., Aebersold, F., Egger, U., Feller, A., Gisler, D., Hagenbuch, S., & Stenflo, J. O. 2004, “*Solar polarimetry in the near UV with the Zurich Imaging Polarimeter ZIMPOL IP*”, A&A, **422**, 703
- Gros, M., Crivellari, L., & Simonneau, E. 1997, “*An Implicit Integral Method to Solve Selected Radiative Transfer Problems. IV. The Case of Spherical Geometry*”, ApJ, **489**, 331
- Gudiksen, B. V., Carlsson, M., Hansteen, V. H., Hayek, W., Leenaarts, J., & Martnez-Sykora, J. 2011, “*The stellar atmosphere simulation code Bifrost. Code description and validation*”, A&A, **531**, 154

- Hamann, W-R. 1985, “*Computed He II spectra for Wolf-Rayet stars*”, A&A, **145**, 443
- Hamann, W-R. 2003, “*Basic ALI in Moving Atmospheres*” in ASP Conf. Ser. **288**, “*Stellar Atmosphere Modeling*”, ed. I. Hubeny, D. Mihalas, & K. Werner (San Francisco: ASP), 171
- Hamilton, D. R. 1947, “*The resonance radiation induced by elliptically polarized light*”, ApJ, **106**, 457
- Hanle, W. 1923, “*Über den Zeemaneffekt bei der Resonanzfluoreszenz*”, Naturwissenschaften, **11**, 690
- Hanle, W. 1924, “*Über magnetische Beeinflussung der Polarisation der Resonanzfluoreszenz*”, Z. Phys., **30**, 93
- Hansteen, V. H., 2004, “*Initial simulations spanning the upper convection zone to the corona*” in IAU Symp. **223**, “*Multi-Wavelength Investigations of Solar Activity*”, ed. A. V. Stepanov, E. E. Benevolenskaya, & A. G. Kosovichev (Cambridge, UK: Cambridge University Press), 385
- Hansteen, V. H., Carlsson, M., & Gudiksen, B., 2007, “*3D Numerical Models of the Chromosphere, Transition Region, and Corona*” in ASP Conf. Ser. **368**, “*The Physics of Chromospheric Plasmas*”, ed. P. Heinzel, I. Dorotovic, & R. J. Rutten. (San Francisco: ASP), 107
- Hauschildt, P. H., & Baron, E. 2006, “*A 3D radiative transfer framework. I. Non-local operator splitting and continuum scattering problems*”, A&A, **451**, 273
- Hauschildt, P. H., & Baron, E. 2008, “*A 3D radiative transfer framework. III. Periodic boundary conditions*”, A&A, **490**, 873
- Hayek, W. 2008, “*First 3D radiative transfer with scattering for domain-decomposed MHD simulations*”, Physica Scripta, **133**, 4006
- Hestenes, M. R., & Stiefel, E. 1952, “*Methods of Conjugate Gradients for Solving Linear Systems*”, Journal of Research of the National Bureau of Standards, **49(6)**, 409
- Hillier, D. J. 1996, “*The calculation of line polarization due to scattering by electrons in multi-scattering axisymmetric envelopes*”, A&A, **308**, 521

Holzreuter, R., Fluri, D. M., & Stenflo, J. O. 2005, “*Scattering polarization in strong chromospheric lines. I. Explanation of the triplet peak structure*”, A&A, **434**, 713

Holzreuter, R., Fluri, D. M., & Stenflo, J. O. 2006, “*Ca II K polarization as a diagnostic of temperature bifurcation*”, A&A, **449**, L41

Holzreuter, R., & Stenflo, J. O. 2007a, “*Scattering polarization in strong chromospheric lines II. Influence of the temperature curve on the Ca II K line*”, A&A, **467**, 695

Holzreuter, R., & Stenflo, J. O. 2007b, “*Scattering polarization in strong chromospheric lines III. Spatial fluctuations of the polarized Ca II K line profiles*”, A&A, **472**, 919

Hubeny, I. 2003, “*Accelerated lambda iteration: An overview*” in ASP Conf. Ser. **288**, “*Stellar atmosphere modeling*”, eds. I. Hubeny, D. Mihalas & K. Werner (San Francisco: ASP), 17

Hubeny, I., & Burrows, A. 2007, “*A New Algorithm for Two-Dimensional Transport for Astrophysical Simulations. I. General Formulation and Tests for the One-Dimensional Spherical Case*”, ApJ, **659**, 1458

Hummer, D. G. 1962, “*Non-coherent scattering: I. The redistribution function with Doppler broadening*”, MNRAS, **125**, 21

Hummer, D. G., & Rybicki, G. B. 1971, “*Radiative transfer in spherically symmetric systems. The conservative grey case*”, MNRAS, **152**, 1

Ivanov, V. V. 1991, “*Analytical methods of line formation theory - Are they still alive*” in NATO ASI Ser. **C341**, “*Stellar atmospheres: Beyond classical models*”, eds. L. Crivellari, I. Hubeny, & D. G. Hummer (Dordrecht: Reidel), 81

Iyanaga, S., & Kawada, Y. 1970, “*Encyclopedic Dictionary of Mathematics*” (Cambridge, Massachusetts: The MIT Press)

Jackson, J. D. 1962, “*Classical Electrodynamics*” (New York: John Wiley & Sons)

Jeffrey, D. J. 1989, “*The Sobolev-P method - A generalization of the Sobolev method for the treatment of the polarization state of radiation and the polarizing effect of resonance line scattering*”, ApJ Suppl. Ser. **71**, 951



- Joos, F. 2002, “*Vector polarimetric observations of anomalous effects in the second solar spectrum*”, Master thesis, Institute of Astronomy, ETH Zürich
- Klein, R. I., Castor, J. I., Greenbaum, A., Taylor, D., & Dykema, P. G. 1989, “*A new scheme for multi-dimensional line transfer. I - Formulation and 1-D results*”, JQSRT, **41**, 199
- Kosirev, N. A. 1934, “*Radiative equilibrium of the extended photosphere*”, MNRAS, **94**, 430
- Kunasz, P., & Auer, L. H. 1988, “*Short characteristic integration of radiative transfer problems: Formal solution in two-dimensional slabs*”, J. Quant. Spec. Radiat. Transf., **39**, 67
- Kunasz, P. B., & Hummer, D. G. 1974a, “*Radiative transfer in spherically symmetric systems-III. Fundamentals of line formation*”, MNRAS, **166**, 19
- Kunasz, P. B., & Hummer, D. G. 1974b, “*Radiative transfer in spherically symmetric systems-IV. Solution of the line transfer problem with radial velocity fields*”, MNRAS, **166**, 57
- Kunasz, P. B., & Olson, G. L. 1988, “*Short characteristic solution of the non-LTE line transfer problem by operator perturbation. II - The two-dimensional planar slab*”, J. Quant. Spectrosc. Radiat. Transfer, **39**, 1
- Landi Degl’Innocenti, E. 1982, “*The determination of vector magnetic fields in prominences from the observations of the Stokes profiles in the D<sub>3</sub> line of helium*”, Solar Physics, **79**, 291
- Landi Degl’Innocenti, E. 1984, “*Polarization in spectral lines III. Resonance polarization in the non-magnetic, collisionless regime*”, Solar Physics, **91**, 1
- Landi Degl’Innocenti, E., & Bommier, V. 1994, “*Resonance line polarization for arbitrary magnetic fields in optically thick media. 3: A generalization of the square root of epsilon-law*”, A&A, **284**, 865
- Landi Degl’Innocenti, E., Bommier, V., & Sahal-Bréchet, S. 1990, “*Resonance line polarization and the Hanle effect in optically thick media. I - Formulation for the two-level atom*”, A&A, **235**, 459

- Landi Degl’Innocenti, E., Bommier, V., & Sahal-Br  chot, S. 1987, “*Linear polarization of hydrogen Balmer lines in optically thick quiescent prominences*”, A&A, **186**, 335
- Landi Degl’Innocenti, M., & Landi Degl’Innocenti, E. 1988, “*An analytical expression for the Hanle-effect scattering phase matrix*”, A&A, **192**, 374
- Landi Degl’Innocenti, E., & Landolfi, M. 2004, “*Polarization in spectral lines*” (Dordrecht: Kluwer) (LL04)
- Leenaarts, J., Carlsson, M., Hansteen, V., & Rutten, R. J. 2007, “*Non-equilibrium hydrogen ionization in 2D simulations of the solar atmosphere*”, A&A, **473**, 625L
- L  ger, L., Chevallier, L., & Paletou, F. 2007, “*Fast 2D non-LTE radiative modelling of prominences. Numerical methods and benchmark results*”, A&A, **470**, 1
- Lites, B. W., Kubo, M., Socas-Navarro, H., Berger, T., Frank, Z., Shine, R., Tarbell, T., Title, A., Ichimoto, K., Katsukawa, Y., Tsuneta, S., Suematsu, Y., Shimizu, T., & Nagata, S. 2008, “*The horizontal magnetic flux of the quiet-Sun internetwork as observed with the Hinode spectro-polarimeter*”, ApJ, **672**, 1237
- Manso Sainz, R., & Trujillo Bueno, J. 1999, “*The Hanle effect in 1D, 2D and 3D*” in ASSL **243**, “*Solar polarization 2*” (SPW2), ed. K. N. Nagendra & J. O. Stenflo (Boston: Kluwer), 143
- Manso Sainz, R., & Trujillo Bueno, J. 2003, “*A multilevel radiative transfer program for modeling scattering line polarization and the Hanle effect in stellar atmospheres*” in ASP Conf. Ser. **307**, “*Solar polarization*” (SPW3), eds. J. Trujillo Bueno, & J. S  nchez Almeida (San Francisco: ASP), 251
- Manso Sainz, R., & Trujillo Bueno, J. 2010, “*Scattering Polarization of the Ca II IR Triplet for Probing the Quiet Solar Chromosphere*”, ApJ, **722**, 1416
- McKenna, S. J. 1985, “*The transfer of polarized radiation in spectral lines: Formalism and solutions in simple cases*”, Ap&SS, **108**, 31
- Meinkohn, E. 2009, “*A General-Purpose Finite Element Method for 3D Radiative Transfer Problems*” in “*Numerical Methods in Multi-dimensional Radiative Transfer*”, ed. G. Kanschat, E. Meinkohn, R. Rannacher, & R. Wehrse (Berlin: Springer), 99

- Mihalas, D. 1978, “*Stellar atmosphere*” (2nd ed.; San Francisco: Freeman)
- Mihalas, D., Auer, L. H., & Mihalas, B. R. 1978, “*Two-dimensional radiative transfer. I - Planar geometry*”, ApJ, **220**, 1001
- Nagendra, K. N. 1986, “*Radiative transfer with Stokes vector*”, PhD Thesis (Bangalore: Bangalore University)
- Nagendra, K. N. 1988, “*Resonance line polarization in spherical atmospheres*”, ApJ, **335**, 269
- Nagendra, K. N. 1994, “*Resonance line polarization in spherical atmospheres: Partial redistribution effects studied with the Domke-Hubeny redistribution matrix*”, ApJ, **432**, 274
- Nagendra, K. N., Frisch, H., & Faurobert-Scholl, M. 1998, “*An operator perturbation method for polarized line transfer. III. Applications to the Hanle effect in 1D media*”, A&A, **332**, 610
- Nagendra, K. N., Paletou, F., Frisch, H., & Faurobert-Scholl, M. 1999, “*An operator perturbation method for polarized line transfer IV: Applications to the Hanle effect with partial frequency redistribution*” in ASSL **243**, “*Solar polarization 2*” (SPW2), eds. K. N. Nagendra, & J. O. Stenflo (Boston: Kluwer), 127
- Nagendra, K. N., Frisch, H., & Faurobert, M. 2002, “*Hanle effect with angle-dependent partial redistribution*”, A&A, **395**, 305
- Nagendra, K. N., Frisch, H., & Fluri, D. M. 2003, “*Numerical methods for solving the polarized line transfer equations with partial frequency redistribution*” in ASP Conf. Ser. **307**, “*Solar polarization 3*” (SPW3), eds. J. Trujillo Bueno, & J. Sánchez Almeida (San Francisco: ASP), 227
- Nagendra, K. N., & Sampoorna, M. 2009, “*Numerical Methods in Polarized Line Formation Theory*” in ASP Conf. Ser. **405**, “*Solar polarization 5*” (SPW5), eds. S. V. Berdyugina, K. N. Nagendra, & R. Ramelli, 261
- Nagendra, K. N., Bonifacio, P., & Ludwig, H.-G. eds. 2009, “*3D views on cool stellar atmospheres: theory meets observation*”, Mem.S.A.It., **80**

- Nagendra, K. N., **Anusha, L. S.**, & Sampoorna, M. 2009, “*Polarization : Proving ground for methods in radiative transfer*” in “*3D Views on Cool Stellar atmospheres: Theory meets Observation*”, ed. K. N. Nagendra, P. Bonifacio, & H.-G. Ludwig, Mem.S.A.It., **80**, 678
- Nagendra, K. N., Sampoorna, M., & **Anusha, L. S.**, 2010, “*Recent developments in polarized line formation in magnetic fields*” in *Recent advances in Spectroscopy; Astrophysical, Theoretical and Experimental Perspective*, eds. R. Chaudhary, M. V. Mekkaden, A. V. Raveendran, A. Satyanarayanan (Heidelberg, Berlin: Springer-Verlag), 139
- Nagendra, K. N., & Sampoorna, M. 2011, “*Spectral line polarization with angle-dependent partial frequency redistribution IV. Scattering Expansion Method for the Hanle effect*”, A&A, 535, 88
- Nordlund, Å. 1982, “*Numerical simulations of the solar granulation. I - Basic equations and methods*”, A&A, **107**, 1
- Nordlund, Å., & Stein, R. F. 1991, “*Dynamics of an Radiative Transfer in Inhomogeneous Media*” in “*Stellar Atmospheres: Beyond Classical Models*”, NATO ASI Series C, **341**, ed. L. Crivellari, I. Hubeny, & D. G. Hummer (Dordrecht: Kluwer), 263
- Olson, G. L., Auer, L. H., & Buchler, J. R. 1986, “*A rapidly convergent iterative solution of the non-LTE radiation transfer problem*”, J. Quant. Spec. Radiat. Transf., **35**, 431
- Omont, A., Smith, E. W., & Cooper, J. 1972, “*Redistribution of resonance radiation I. The effect of collisions*”, ApJ, **175**, 185
- Omont, A., Smith, E. W., & Cooper, J. 1973, “*Redistribution of resonance radiation II. The effect of magnetic fields*”, ApJ, **182**, 283
- Paletou, F., & Auer, L. H. 1995, “*A new approximate operator method for partial frequency redistribution problems*”, A&A, **297**, 771
- Paletou, F., Bommier, V., & Faurobert-Scholl, M. 1999, “*Polarized radiation transfer in 2D geometry*” in ASSL **243**, “*Solar polarization 2*” (SPW2), ed. K. N. Nagendra & J. O. Stenflo (Boston: Kluwer), 189

- Paletou, F., & Anterrieu, E. 2009, “A conjugate gradient method for solving the non-LTE line radiation transfer problem”, *A&A*, **507**, 1815
- Papkalla, R. 1995, “Line formation in accretion disks 3D comoving frame calculations”, *A&A*, **295**, 551
- Papoulis, A. 1968, “*Probability, Random Variables, and Stochastic Processes*” (Mac Graw Hill, New York)
- Peraiah, A. 2002, “*An Introduction to Radiative Transfer*” (Cambridge University Press)
- Peraiah, A., & Grant, I. P. 1973, “Numerical solution of the radiative transfer equation in spherical shells”, *JIMA*, **12**, 75
- Pereira, T. M. D., Kiselman, D., & Asplund, M. 2009a, “Oxygen lines in solar granulation. I. Testing 3D models against new observations with high spatial and spectral resolution”, *A&A*, **507**, 417
- Pereira, T. M. D., Asplund, M. & Kiselman, D. 2009b, “Oxygen lines in solar granulation. II. Centre-to-limb variation, NLTE line formation, blends, and the solar oxygen abundance”, *A&A*, **508**, 1403
- Pomraning, G. C. 1973, “*The equations of radiation hydrodynamics*” (Oxford: Pergamon Press)
- Povel, H. 1995, “Imaging Stokes polarimetry with piezoelastic modulators and charge-coupled-device image sensors”, *Opt. Eng.*, **34**, 1870
- Povel, H. 2001, “Ground-based Instrumentation for Solar Magnetic Field Studies, with Special Emphasis on the Zurich Imaging Polarimeters ZIMPOL-I and II” in ASP Conf. Ser. Vol. **248**, “Magnetic Fields Across the Hertzsprung-Russel Diagram”, ed. G. Mathys, S. K. Solanki & D. T. Wickramasinghe (San Francisco: ASP), 543
- Ramelli, R., Balemi, S., Bianda, M., Defilippis, I., Gamma, L., Hagenbuch, S., Rogantini, M., Steiner, P., & Stenflo, J. O. 2010, “ZIMPOL-3: a powerful solar polarimeter” in “*Proceedings of the SPIE*”, ed. I. S. McLean, S. K. Ramsay, & H. Takami, 7735, 77351Y-77351Y-12
- Rees, D. E. 1978, “Non-LTE resonance line polarization in the absence of magnetic fields”, *Publ. Astron. Soc. Japan*, **30**, 455

- Rees, D. E., & Saliba, G. J. 1982, “*Non-LTE resonance line polarization with partial redistribution effects*”, *A&A*, **115**, 1
- Rybicki, G. B., & Hummer, D. G. 1991, “*An accelerated lambda iteration method for multilevel radiative transfer. I - Non-overlapping lines with background continuum*”, *A&A*, **245**, 171
- Rybicki, G. B., & Hummer, D. G. 1992, “*An accelerated lambda iteration method for multilevel radiative transfer. II - Overlapping transitions with full continuum*”, *A&A*, **262**, 209
- Saad, Y. 2000, “*Iterative methods for Sparse Linear Systems*” (2nd ed.) (ebook:<http://www-users.cs.umn.edu/saad/books.html>)
- Sampoorna, M. 2011, “*Spectral line polarization with angle-dependent partial frequency redistribution. III. Single scattering approximation for the Hanle effect*”, *A&A*, **532**, 52
- Sampoorna, M., Nagendra, K. N., & Stenflo, J. O. 2007, “*Hanle-Zeeman Redistribution Matrix. II. Comparison of Classical and Quantum Electrodynamical Approaches*”, *ApJ*, **670**, 1485
- Sampoorna, M., Nagendra, K. N., & Frisch, H. 2008a, “*The Hanle effect with partial frequency redistribution: Construction of frequency dependent polarization matrix and numerical solution by a PALI method*”, *J. Quant. Spec. Radiat. Transf.*, **109**, 2349
- Sampoorna, M., Nagendra, K. N., Frisch, H., & Stenflo, J. O. 2008b, “*Zeeman line formation in solar magnetic fields: Studies with empirical probability distribution functions*”, *A&A*, **485**, 275
- Sampoorna, M., Nagendra, K. N., & Stenflo, J. O. 2008c, “*Hanle-Zeeman redistribution matrix III. Solution of the polarized line formation problem*”, *ApJ*, **679**, 889
- Sampoorna, M., Stenflo, J. O., Nagendra, K. N., Bianda, M., Ramelli, R., & **Anusha, L. S.** 2009, “*Origin of Spatial Variations of Scattering Polarization in the Wings of the Ca I 4227 Å Line*”, *ApJ*, **699**, 1650 (S09)
- Sampoorna, M., & Trujillo Bueno, J. 2010, “*Gauss-Seidel and Successive Overrelaxation Methods for Radiative Transfer with Partial Frequency Redistribution*”, *ApJ*, **712**, 1331

- Sampoorna, M., Nagendra, K. N., & Frisch, H. 2011, “*Spectral line polarization with angle-dependent partial frequency redistribution. II. Accelerated lambda iteration and scattering expansion methods for the Rayleigh scattering*”, A&A, **527**, 89
- Sánchez Almeida, J. 2007, “*A Simple Model for the Distribution of Quiet-Sun Magnetic Field Strengths*”, ApJ, **657**, 1150
- Schüssler, M., & Vögler, A. 2008, “*Strong horizontal photospheric magnetic field in a surface dynamo simulation*”, A&A, **481**, L5
- Scharmer, G. B. 1981, “*Solutions to radiative transfer problems using approximate lambda operators*”, ApJ, **249**, 720
- Schmid-Burgk, J. 1974, “*Line Formation in Turbulent Media: Mathematics of Profile Computation*”, A&A, **32**, 73
- Skartlien, R. 2000, “*A Multigroup Method for Radiation with Scattering in Three-Dimensional Hydrodynamic Simulations*”, ApJ, **536**, 465
- Smart, W. M. 1960, “*Text-Book on Spherical Astronomy, 6th ed.*” (Cambridge, England: Cambridge University Press)
- Stein, R. F., & Nordlund, Å. 1998, “*Simulations of Solar Granulation. I. General Properties*”, ApJ, **499**, 914
- Stein, R. F., & Nordlund, Å. 2000, “*Realistic Solar Convection Simulations*”, Sol. Phys., **192**, 91
- Stenflo, J. O. 1973, “*Magnetic-field structure of the photospheric network*”, Solar Physics, **32**, 41
- Stenflo, J. O. 1976, “*Resonance-line polarization I. A non-LTE theory for the transport of polarized radiation in spectral lines in the case of zero magnetic field*”, A&A, **46**, 61
- Stenflo, J. O. 1978, “*Resonance-line polarization III. The Hanle effect in a compact non-LTE radiative transfer formulation*”, A&A, **66**, 241
- Stenflo, J. O. 1982, “*The Hanle effect and the diagnostics of turbulent magnetic fields in the solar atmosphere*”, Solar Physics, **80**, 209

- Stenflo, J. O. 1987, “*Observational constraints on a ‘hidden’, turbulent magnetic field of the sun*”, *Solar Physics*, **114**, 1
- Stenflo, J. O. 1994, “*Solar magnetic fields - Polarized radiation diagnostics*” (Dordrecht: Kluwer)
- Stenflo, J. O. 2003a, “*Scattering polarization in magnetic fields : Anomalies, surprises and enigmas*” in ASP Conf. Ser. **307**, “*Solar polarization 3*” (SPW3), eds. J. Trujillo Bueno, & J. Sánchez Almeida (San Francisco: ASP), 385
- Stenflo, J. O. 2003b, “*Spectro-polarimetric Observations: What’s Next?*” in ASP Conf. Ser. **307**, “*Solar polarization 3*” (SPW3), ed. J. Trujillo Bueno & J. Sánchez Almeida (San Francisco: ASP), 583
- Stenflo, J. O. 2005, “*Polarization of the Sun’s continuous spectrum*”, *A&A*, **429**, 713
- Stenflo, J. O. 2006, “*Second solar spectrum: A brief overview*” in ASP Conf. Ser. **358**, “*Solar polarization 4*” (SPW4), eds. R. Casini, & B. W. Lites (San Francisco: ASP), 215
- Stenflo, J. O. 2010, “*Measuring the Hidden Aspects of Solar Magnetism*” in *Astrophys. Space Science Proceedings*, “*Magnetic coupling between the Interior and Atmospheres of the Sun*”, eds. S. S. Hasan & R. J. Rutten (Springer: Berlin Heidelberg), 101
- Stenflo, J. O. 2010, “*Distribution functions for magnetic fields on the quiet Sun*”, *A&A*, **517**, 37
- Stenflo, J. O., Twerenbold, D., & Harvey, J. W. 1983a, “*Coherent scattering in the solar spectrum : Survey of linear polarization in the range 3165-4230 Å*”, *A&AS*, **52**, 161
- Stenflo, J. O., Twerenbold, D., Harvey, J. W., & Brault, J. W. 1983b, “*Coherent scattering in the solar spectrum : Survey of linear polarization in the range 4200-9950 Å*”, *A&AS*, **54**, 505
- Stenflo, J. O., Harvey, J. W., Brault, J. W., & Solanki, S. 1984, “*Diagnostics of solar magnetic fluxtubes using a Fourier transform spectrometer*”, *A&A*, **131**, 333
- Stoer, J. & Bulirsch, R. 1983, “*Introduction to Numerical Analysis*” (Springer-Verlag)



- Trujillo Bueno, J. 2001, “*Atomic polarization and the Hanle effect*” in ASP Conf. Ser. **236**, “*Advanced solar polarimetry: Theory, Observations, and Instrumentation*”, ed. M. Sigwarth (San Francisco: ASP), 161
- Trujillo Bueno, J., Landi Degl’Innocenti, E., Collados, M., Merenda, L., & Manso Sainz, R. 2002, “*Selective absorption processes as the origin of puzzling spectral line polarization from the Sun*”, Nature, **415**, 403
- Trujillo Bueno, J. 2003, “*New diagnostic windows on the weak magnetism of the solar atmosphere*” in ASP Conf. Ser. **307**, “*Solar polarization 3*” (SPW3), eds. J. Trujillo Bueno, & J. Sánchez Almeida (San Francisco: ASP), 407
- Trujillo Bueno, J., & Fabiani Bendicho, P. 1995, “*A novel iterative scheme for the very fast and accurate solution of non-LTE radiative transfer problems*”, ApJ, **455**, 646
- Trujillo Bueno, J., Shchukina, N., & Asensio Ramos, A. 2004, “*A substantial amount of hidden magnetic energy in the quiet Sun*”, Nature, **430**, 326
- Trujillo Bueno, J., & Shchukina, N. 2007, “*The Scattering Polarization of the Sr I  $\lambda$  4607 Line at the Diffraction Limit Resolution of a 1 m Telescope*”, ApJ, **664**, 135
- Trujillo Bueno, J., & Shchukina, N. 2009, “*Three-dimensional Radiative Transfer Modeling of the Polarization of the Sun’s Continuous Spectrum*”, ApJ, **694**, 1364
- Uitenbroek, H. 2001, “*Multilevel Radiative Transfer with Partial Frequency Redistribution*”, ApJ, **557**, 389
- Uitenbroek, H., & Criscuoli, S. 2011, “*Why One-dimensional Models Fail in the Diagnosis of Average Spectra from Inhomogeneous Stellar Atmospheres*”, ApJ, **736**, 69
- van Noort, M., Hubeny, I., & Lanz, T. 2002, “*Multidimensional Non-LTE Radiative Transfer. I. A Universal Two-dimensional Short-Characteristics Scheme for Cartesian, Spherical, and Cylindrical Coordinate Systems*”, ApJ, **568**, 1066
- Vath, H. M. 1994, “*Three-dimensional radiative transfer on a massively parallel computer*”, A&A, **284**, 319

Vögler, A., Shelyag, S., Schüssler, M., Cattaneo, F., Emonet, T., & Linde, T. 2005, “*Simulations of magneto-convection in the solar photosphere: Equations, methods, and results of the MURaM code*”, A&A, **429**, 335

Wedemeyer, S., Freytag, B., Steffen, M., Ludwig, H.-G., & Holweger, H. 2004, “*Numerical simulation of the three-dimensional structure and dynamics of the non-magnetic solar chromosphere*”, A&A, **414**, 1121

Wedemeyer-Böhm, S., Rouppe van der Voort, L. 2009, “*On the continuum intensity distribution of the solar photosphere*”, A&A, **503**, 225

Werner, K., & Husfeld, D. 1985, “*Multi-level non-LTE line formation calculations using approximate Lambda-operators*”, A&A, **148**, 417

# Curriculum Vitae

## 1 Personal information

Name: Ms. L.S. Anusha  
Date of birth: 9th May 1983

## 2 Academic Record

Exam	Institute	Year	Percentage	Class
Grade X	Jawahar Navodaya Vidyalaya (CBSE)	1999	77	Distinction Distinction
Grade XII	Jawahar Navodaya Vidyalaya (CBSE)	2001	76	Distinction
BSc (CMS)	SDM College, Ujire	2004	85.4	Distinction
MSc in Mathematics	Mysore University	2006	89	Univ. 2nd Rank
National level PhD Entrance Exam in - Mathematics: GATE	New Delhi, India	2007	Qualified	
(PhD) Astrophysics	Indian Institute of Astrophysics	January 2007 - April 2012	Thesis submitted in April 2012	

## 3 Awards and Achievements

### 3.1 Post-graduate level :

Second rank in MSc (Mathematics) in the state level examination of the Mysore University.

### 3.2 Selection for PhD Programs :

Selected as Junior Research Fellow (JRF) by IIA, through a National level entrance test/interview, for conducting research leading to PhD degree. Also obtained JRF through the National level GATE exam in Mathematics.

### 3.3 PhD level :

Selected for the Indo-Swiss research scholarship in 2009 and 2010 to visit the research institute IRSOL, Switzerland for 2 months in 2009 and 50 days in 2010.

Selected for the Henri Poincaré Junior Fellowship 2010, to visit the Observatory of Nice for 40 days in 2010.

The research paper entitled “Polarized line formation in multi-dimensional media. I. Decomposition of Stokes parameters in arbitrary geometries ” published in the Astrophysical Journal, by Anusha L. S. & Nagendra, K. N. is selected for the “outstanding research paper award, 2010”.

## 4 Summer Project/Summer School

### 4.1 Project at IIA: :

Project entitled “ **Operator Perturbation Techniques for solving Radiative Transfer Equation** ” as a requirement for the Summer Project-2005 under the guidance of **Prof. K. N. Nagendra**, IIA, Bangalore.

### 4.2 Project at HRI: :

Participated in the **Visiting Summer Students Program (VSSP)-2006** in Mathemat-

ics, to work at the Harish Chandra Institute, Allahabad.

### 4.3 Special Projects::

Done several projects in theoretical astrophysics, and Observational Astronomy, as part of the one year long “Specialized Course work” in Astronomy and Astrophysics, organized at the Indian Institute of Astrophysics (IIA), and the Indian Institute of Science (IISc).

A project entitled ”Computerizing High-School for documentation and maintaining records” written in Visual Basic (VB), as a requirement for the BSc course work in 2004.

## 5 Visits to Institutions for Scientific Collaboration

### 5.1 Visits within India :

Visited Harishchandra Research Institutes (HRI), for advanced level training in problem solving techniques, as part of the Visiting Summer Students Program-2006 of HRI.

### 5.2 Visits Abroad :

- (1) Visited the Observatory of Nice, France, for 2 months to work with Prof. H. Frisch during October - November 2008. During this period also visited Observatory of Paris, Meudon.
- (2) Visited (a) Instituto Ricerche Solari Locarno (IRSOL) at Locarno, Switzerland for two months to work with Dr. M. Bianda during August - September 2009; in this period also visited La Specola Solare Ticinese, and MET-SVIZERA, the Meteorological Observatory at Locarno, Switzerland. (b) the Observatoire de la Côte d’Azur (OCA) at Nice, France for one month to work with Prof. H. Frisch during November 2009.
- (3) Visited (a) the Observatoire de la Côte d’Azur (OCA) at Nice, France for 40 days to work with Prof. H. Frisch during August - September 2010; (b) Instituto Ricerche Solari Locarno (IRSOL) at Locarno, Switzerland for 50 days to work with Dr. M. Bianda during October - November 2010.
- (4) Visited Hawaii, USA for participating in the international conference on ”Solar Polarization Workshop 6”, held at Maui, Hawaii, USA, during May 30 - June 4, 2010.

- (5) Visited Bamboo Sea, China for participating in the “International Summer School on Solar and Stellar polarization”, held at Bamboo Sea and Yibin University, Southern Sichuen Province China, during 8–18 July 2011.
- (6) Visited the Max Planck Institute for Solar System Research, Germany, for two months to work with Prof. Sami Solanki, Dr. Alex Feller and their group during January - March 2012.

## 6 Talks Presented in Conferences and Symposia

- (1) Presented a talk on “Preconditioned Bi-Conjugate Gradient method for Radiative Transfer in Spherical media”, on 29.05.2009 as a part of ‘student talk’ at the Indian Institute of Astrophysics, Bangalore, India.
- (2) Presented a talk on “Modeling the Second Solar Spectrum: Last Scattering Approximation and its validation”, on 23.03.2010 as a part of ‘student talk’ at the Indian Institute of Astrophysics, Bangalore, India.
- (3) Presented a talk on “Modeling linear polarization of the Solar Ca I 4227 Å line”, on 09.04.2010 as a part of ‘In-House meeting’ at the Indian Institute of Astrophysics, Bangalore, India.
- (4) Participated and presented a contributed talk entitled “Linear Polarization of the Solar Ca I 4227 Å line: Modeling based on radiative transfer and last scattering approximations”, at the international conference on “Solar Polarization Workshop 6”, held in Maui, Hawaii, USA, during May 30 - June 4, 2010.
- (5) Presented a talk on “Polarized line formation in multi-dimensional media”, on 23.06.2011 based on the paper Anusha & Nagendra 2011a, which was awarded the ‘outstanding research paper’ for the year 2010, at the Indian Institute of Astrophysics, Bangalore, India.
- (6) Presented a talk on “Polarized line formation in multi-dimensional media”, on 16.07.2011 at the “International Summer School on Solar and Stellar Polarization”, held at Bamboo Sea and Yibin University, Southern Sichuen Province China, during 8–18 July 2011.

## 7 Meetings/Workshops Attended

- (1) Participated in the international conference on “Magnetic Coupling between the Interior and the Atmosphere of the Sun”, held at the Indian Institute of Astrophysics, Bangalore, India, during December 2 – 5 , 2008.
- (2) Participated and presented talk at the international conference on ”Solar Polarization Workshop 6”, held in Maui, Hawaii, USA, during May 30 – June 4, 2010.
- (3) Participated in the international conference on “Chandrasekhar centenary conference” held at the Indian Institute of Astrophysics, Bangalore, India, during December 7 – 11 , 2010.
- (4) Participated in the “International Summer School on Solar and Stellar Polarization”, held at Bamboo Sea and Yibin University, Southern Sichuen Province China, during 8–18 July 2011.

## 8 Refereeing experience

1. Refereed a paper in the international journal **ApJ** in 2011
2. Refereed two papers in the international journal **Mem.S.A.It** in September 2009